Author:
Sheikh, Sadiyah

Title:
Novel Multivalent Glyco-Nanomaterials as Potential Theranostics

University of BRISTOL

Novel Multivalent Glyco-Nanomaterials as Potential Theranostics

Sadiyah Sheikh
Supervisors: Professor M. Carmen Galan and Dr. Henkjan Gersen

A dissertation submitted to the University of Bristol in accordance with the requirements for award of the degree of PhD in the Faculty of Science.

School of Chemistry, 2020

Word count: 74,371

Abstract

Cell surface carbohydrates play a key role in cell-cell recognition, this occurs via lectin proteins from one cell interacting with terminal sugar molecules on another. These interactions are ubiquitous throughout life with roles ranging from fertilisation to bacterial invasion. However, the downstream effects of carbohydrate interactions are not fully understood, partly due to the difficulty in isolating interactions for study. Using well characterised non-toxic carbon dots (CDs) we developed probes towards the identification of cell surface carbohydrate profiles and to assess the multivalent lectin binding strength via Förster resonance energy transfer (FRET) between two non-toxic, fluorescent probes in solution. We developed an assay and probed the specific interaction of Concanavalin A (ConA) lectin in this system.

Secondly, we explored the anti-cancer therapeutic potential of these glyco-carbon dots for improved chemotherapy drug – doxorubicin, delivery. Exploiting the enhanced permeability and retention (ERP) effect exhibited with nanoparticles for enhanced delivery as well as carbohydrate functionalisation for targeted delivery. We observe anti-cancer potential in this work and uncover a slow release mechanism for the delivery of doxorubicin to the site of action.

Finally, we assessed the photothermal therapy (PTT) potential of a novel carbon dot for anti-cancer treatment observing both cancer cell targeting and cytotoxicity. This work contributes to the development of non-invasive localised cancer treatments which involve a nanoparticle and external trigger component. This is important for the development of improved cancer therapies.

Acknowledgements

Thank you to the University of Bristol and the BCFN for facilitating my PhD and allowing me to live in Bristol for another 4 years. Special thanks to Annela Seddon and Duncan Casey. The support and opportunity I have been afforded through the BCFN has been invaluable and something I will never forget. The BCFN social network has made the last 4 years thoroughly enjoyable and facilitated some great memories.

Thank you to Carmen for allowing me to complete my PhD in her group, I always leave her office feeling inspired.

Thank you to all I have worked with, without whom this thesis would not have come together. Thank you to Carmen, Robin^[REF] and Tom Swift for proof-reading my thesis, your feedback was invaluable.

Thanks to Henkjan for support and great advice and discussion around the FRET portion of my work.

Thank you to the Galan group past and present. The culture in the group is very supportive which has facilitated great discussion and allowed me to learn a lot. Thank you to Stephen Andrew Hill and Tom Swift, the carbon dot "elders" before me for their guidance. Thank you to everyone in the Galan group for their friendship, many of which I hope to maintain for life. I cannot imagine coming into work each morning could get much better.

Special thanks to Noha Abu El Magd, Maristela Braga Matins Teixeira, Michael O'Hagan, Robin Jeanneret, Jennifer Samphire, Eliza Hunt and Teodoro Garcia Millan with whom I have spent many enjoyable hours of work and chat. You have all shaped me and for that I am thankful.

Thank you to all the Chemistry staff for their help.

Thank you to Georgia Hardstark and Karen Killgariff for keeping me entertained working late in the library.

Thank you to Chilli Daddy for their tofu hotpot number 4 which I have enjoyed both in celebration and commiseration countless times over the last 4 years.

For my mum, thank you for your support, encouragement and belief throughout my life.
For Reanna.

Author's declaration

I declare that the work in this dissertation was carried out in accordance with the requirements of the University's *Regulations and Code of Practice for Research Degree Programmes* and that it has not been submitted for any other academic award. Except where indicated by specific reference in the text, the work is the candidate's own work. Work done in collaboration with, or with the assistance of, others, is indicated as such. Any views expressed in the dissertation are those of the author.

SIGNED: ..... DATE:.....

CONTENTS PAGE

Abbreviations

ACC-2 – Cellosaurus cell line
AcCDala- Acid terminated carbon dots made through synthetic scheme 2
AcFCD – Acid terminated fluorescent carbon dots made through synthesis in scheme 1
AFM- Atomic force microscopy
ALL – Acute Lymphoblastic Leukaemia
AMF – alternating magnetic field
AmFCD- Amine terminated fluorescent carbon dots made through synthesis in scheme 1
ATP – Adenosine triphosphate
BBB – Blood brain barrier
BDA – 1,4-butanediamine
BRET – Bioluminescence resonance energy transfer
CA – citric acid
CAR - Chimeric antigen receptor
CAR-T – Chimeric antigen receptor T cells
p-CBA- 4-Carboxybenzaladehyde
CD- Carbon dot
CDala – Carbon dots made through synthetic scheme 2
CDI- 1,1'-Carbonyldiimidazole
CGE – Cluster glycoside effect
CLEM – Correlative electron microscopy
COVID-19 – Coronavirus disease 2019
DCC - dicarboxy aminocarbodiimide
DCM – Dichloromethane
DEA - Diethylamine
DHLA- Dihydrolipoic acid
DHE - Dihydroethidium
DLS - Dynamic light scattering
DNA - Deoxyribonucleic acid
DOSY – Diffusion ordered spectroscopy
EA - ethanolamine
EBOV-GP - Ebola virus glycoprotein
ECM – Extra cellular matrix
EDA - Ethylenediamine
EDC – 1-Ethyl-3-(3-dimethylaminopropyl)carbodiimide)
EDX – Energy dispersive x-rays
EG – Ethylene glycol
EM – Electron microscopy
EM – electron microscopy
EPR – Enhanced permeability and retention
ER – Endoplasmic reticulum
FAC – Frontal affinity chromatography
FCD – Blue-fluorescent carbon dots made through synthesis in scheme 1
FDA – Federal drug association
FRET – Förster resonance energy transfer
FTIR – Fourier transformed infra-red
GBP – Glycan binding protein
GC – Guanine-cytosine DNA base pair
GlcNAc – β-N-acetyl glucosamine
GPRC – G protein coupled receptor

HA – Haemagglutinin
HeLa cells – Henrietta Lacks cells
HSQC – Heteronuclear single quantum coherence
IL6 – Interleukin 6
ITC- Isothermal calorimetry
L929 cells – Mouse fibroblast cell line
LM – Light microscopy
MAA- Mercaptoacetic acid
MDR – multi drug resistance
MRI – Magnetic resonance imaging
MW – Microwave
MWCO – Molecular weight cut-off
N - number
NA – Neuraminidase
NHS – N-hydroxysuccinimide
NIR – Near infra-red
NLP - nuclear localised signal peptide
NMR – Nuclear magnetic resonance
OD – Optical density
PDA – polydopamine
PDI – perylenediimides
PDT – Photo dynamic therapy
PEG- Polyethylene glycol
PFH – perfluorohexane
PTT - Photo thermal therapy
QCE- Quantum confinement effect
QY – Quantum yield or (Φ)
RNA - Ribonucleic acid
ROS – Reactive oxygen species
SARS-CoV-2 - Severe acute respiratory syndrome coronavirus 2
SAXS – Small-angle x-ray scattering
SD – Standard deviation
SEM – Standard error mean
Sia – Sialic acid
SM – Starting material
SNA – Sambucus Nigra Lectin
STEM – Scanning transmission electron microscope
SUPR - Superenhanced permeability and retention
TEA - Triethylamine
TEM – Transmission electron microscope
TFA – Trifluoro acetic anhydride
TFE – Trifluoroethanol
TGA – Thermogravimetric analysis
TOPO- Trioctylphosphine oxide
TTDDA – 4,7,10-Trioxa-1,13-tridecanediamine
UCNPs – Upconverting nanoparticles
WGA- Wheat germ agglutanin
XPS – X-ray photoelectron spectroscopy
ZP – Zona pellucida

Molecules and glycan functionalised carbon dots synthesised

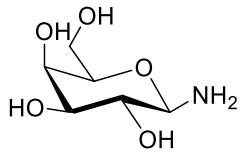

1

1-Amino-1-deoxy-ß-D-galactopyranoside

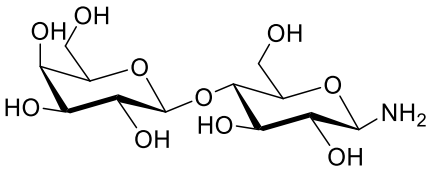

2

1-Amino-1-deoxy-ß-D-lactopyranoside

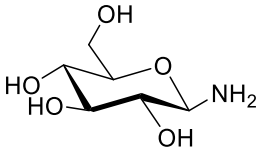

3

1-Amino-1-deoxy-ß-D-glucopyranoside

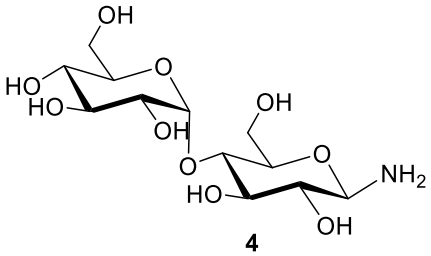

4

1-Amino-1-deoxy-ß-D-maltopyranoside

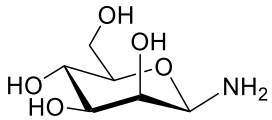

5

1-Amino-1-deoxy-ß-D-mannopyranose

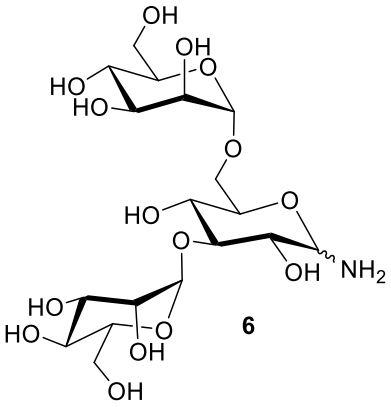

6

3,6-Di-O-(α-D-mannopyranosyl)-1-amino-1-deoxy-D-mannopyranose

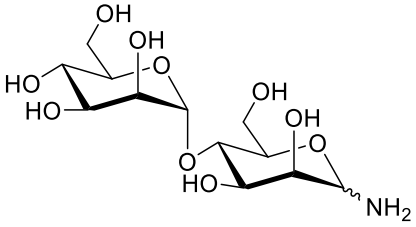

7

4-O-(α-D-Mannopyranosyl)-1-amino-1-deoxy-D-mannopyranose

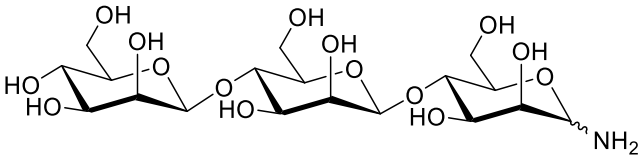

8

ß-D-Mannopyranose-(1-4)-ß-D-mannopyranose-(1-4)-1-amino-1-deoxy-ß-D-mannopyranose

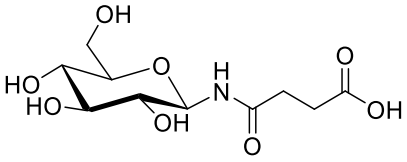

9

1-amino-(4-oxobutanoic acid)-ß-D-glucopyranose

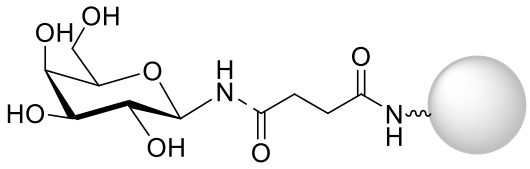

CDala -galactose **14**

CD-glactose **21**

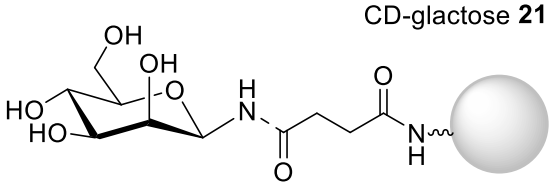

CDala-mannose **15**

CD-mannose **22**

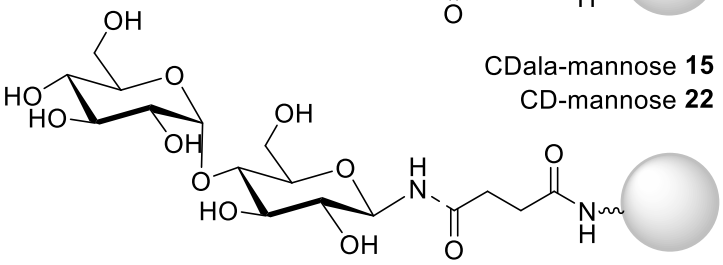

CD-maltose **23**

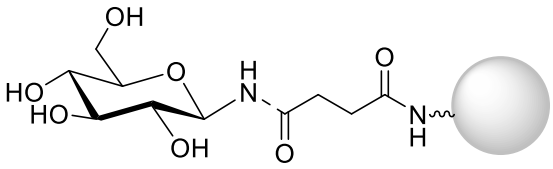

CD-glucose **24**

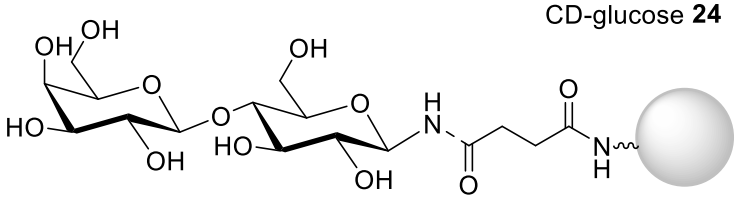

CD-lactose **25**

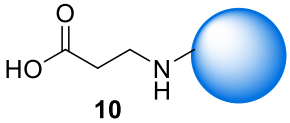

10

AcCDala

"short linker"

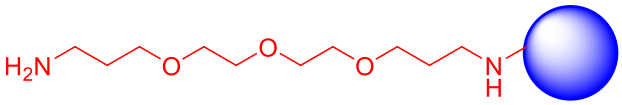

16

AmCD

"long linker"

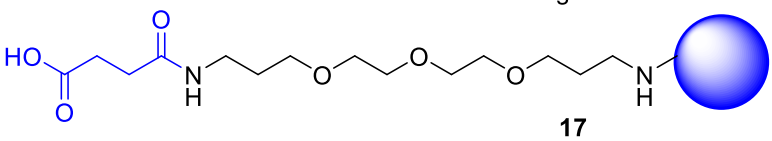

17

AcCD

"long linker"

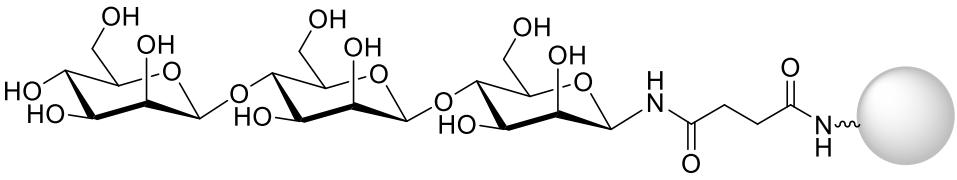

CDala-1,4-mannotriose **11**

CD-1,4-mannotriose **18**

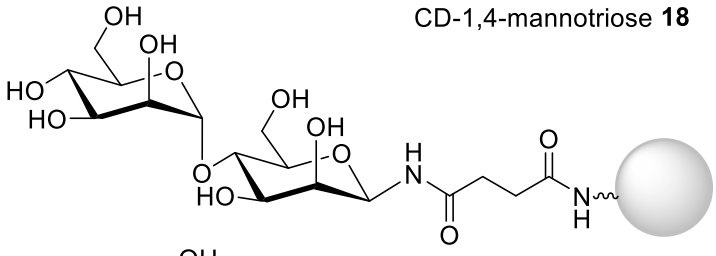

CDala-4-*O*-mannobiose **12**

CD-4-*O*-mannobiose **19**

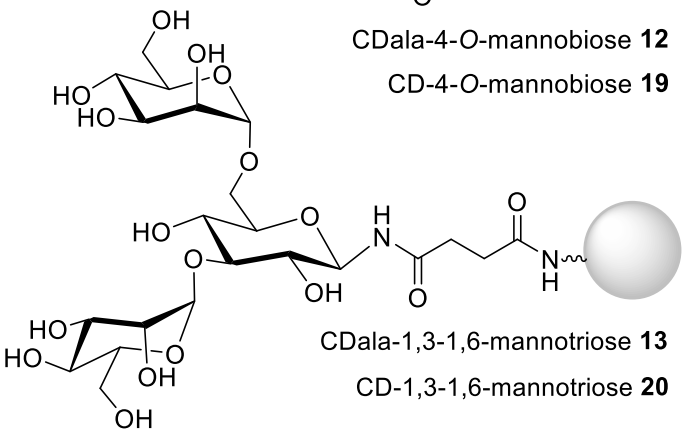

CDala-1,3-1,6-mannotriose **13**

CD-1,3-1,6-mannotriose **20**

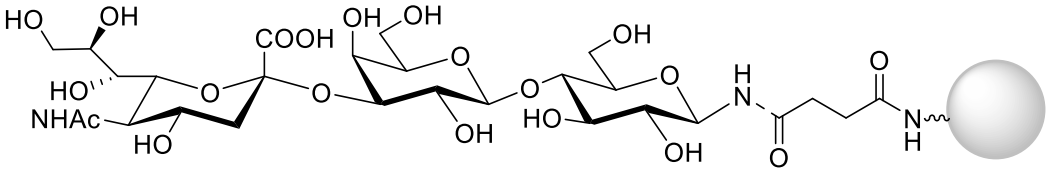

26

CD-3'-sialyl-D-lactose

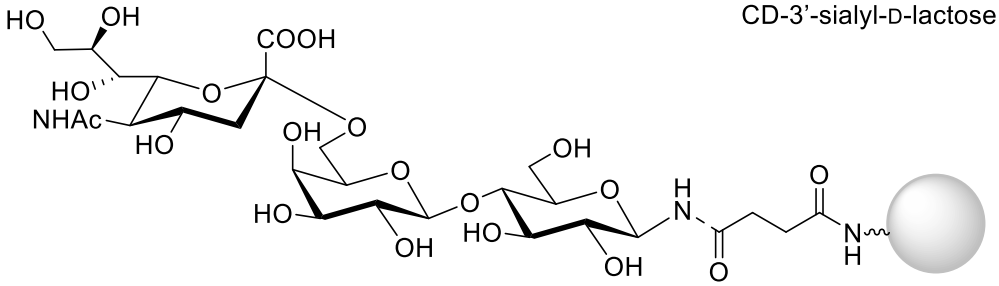

27

CD-6'-sialyl-D-lactose

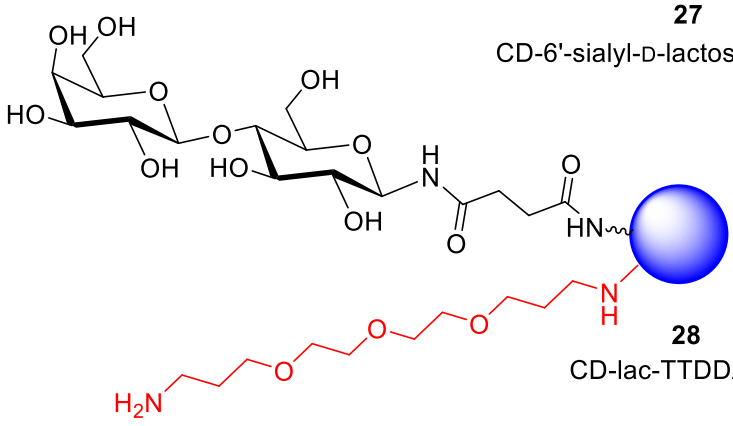

28

CD-lac-TTDDA

1. Introduction

1.1 Carbohydrates

Carbohydrates are molecules defined as containing carbon, oxygen and nitrogen atoms in the formula $C_m(H_2O)_n$ but often contain groups at different positions such as N-acetyl, carboxylic acid or sulfate in nature. They usually consist of a 5 or 6 carbon membered ring but can consist of only 3 carbons. The specific definition relates to the field and context but biochemically they are small molecule aldose or ketoses. They are referred to as saccharides and hence monosaccharides which form di-, oligo- and poly- saccharide. They are also referred to collectively as glycans and end in the suffix -ose. They exist as two enantiomers D- and L- which must be denoted to describe the molecule referred to[1,2].

1.2 Biological importance of carbohydrates

1.2.1 Carbohydrates in nature

Carbohydrates are a key component in cellular communication and act as the first interaction a cell has with its external environment. Their role is less well understood compared to proteins as the field of glycobiology is much newer and our understanding of their functionality is still developing[3]. Their complexity is not encoded directly in the genome, but occurs predominantly in the golgi body via numerous controlled steps to build complex macromolecules which play a role in protein folding, structure and function. Understanding glycosylation patterns and sequence to function relationship is much more complicated than seen in proteins[4]. They play a key role in immune response, disease pathways and pathogen mediation hence understanding the pathways they are involved in is crucial frontier to tackle to pave the way for new medicines[5].

Monosaccharides are the simplest component constituting polysaccharides. Glucose is a common monosaccharide which is broken down in the Krebs cycle to generate ATP. Monosaccharides have a complex signalling role when they are linked to form polysaccharides. A range of biologically common hexose monosaccharides including D-glucose, D-mannose, D-galactose, N-acetyl-D-glucosamine, N-acetyl-D-galactosamine, L-fucose and D-glucuronic acid. Biologically important nine-carbon monosaccharides such as sialic acids also exist. Monosaccharides can be linked via biologically distinct alpha and beta linkages to produce branched or linear oligosaccharides which can have various covalent modifications at any of its carbon positions[1]. Appreciation of the potential diversity in

polysaccharide structure is apparent from the fact a hexasaccharide made from six distinct monosaccharides, linked by either an alpha or beta linage has 1 trillion possible combinations[1].

Carbohydrates are most commonly found as part of the extra cellular matrix (ECM) forming a glycocalyx which is integral to cellular health. In this structure carbohydrates are involved in a number of roles including acting as a protective barrier, modulating inter cellular interaction, maintaining cell matrix integrity and modulating cell-microbe interactions. Carbohydrates can be attached to soluble cytosolic proteins, commonly o-linked which is carried out in the cytosol[6].

Extracellular facing membrane bound polypeptides are glycosylated, and these form the basis for cell signalling. These glycoproteins are for the most part synthesised in the endoplasmic reticulum (ER) - golgi pathways in Eukaryotes. These can be N- (asparagine) or O- (e.g. serine and threonine) linked. Before attachment to a peptide, a monosaccharide is linked to a nucleotide or lipid in an activation step to allow their crossing the endoplasmic reticulum (ER) or golgi membrane. Nascent polypeptide is synthesised directly into the ER lumen where folding is facilitated by carbohydrate attachment by glycosyltransferases. Once the glycopeptide is fully formed it is transported to the cis-golgi for carbohydrate remodelling and elaboration. It then exits the trans-golgi and is transported to and presented on the cell surface membrane[7,8].

1.2.2 Carbohydrate mediated communication in pathogens

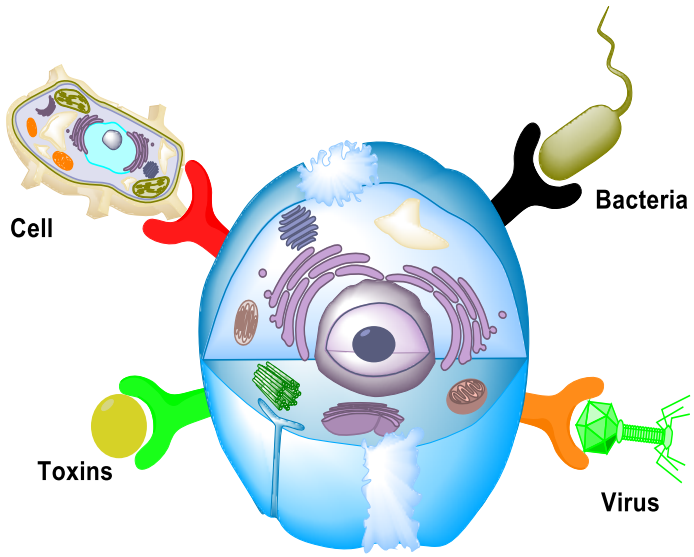

Figure 1.1 Cell interactions are mediated by lectin-carbohydrate binding include inter-cellular, pathogenic, and toxin mediation interactions. In this figure the lectin receptor is attached to and presented on the cell membrane and binding as stated partners. On the cell, virus, bacteria and toxin carbohydrates (which are not presented in this figure) are attached and bound by the lectin.

Glycans are the first line of communication between neighbouring cells, or toxins (Figure 1.1). Most commonly glycan binding proteins (GBPs) recognise carbohydrates and modulate cell to cell communication. Glycan binding proteins can be classed as lectins or glycosamineglycan-binding proteins.

One example of carbohydrate function can be seen through their promoting the recirculation of lymphocytes through the bloodstream and lymphatic system. This is important for immune system function facilitated by L-fucose, D-mannose and fucoidan (fucose polysaccharide) carbohydrates. These line the post capillary venule and inhibit lymphocyte binding hence promoting circulation and improved chance of pathogenic encounter eliciting greater immune response. Another commonly referenced example is the carbohydrate mediated sperm and egg binding event[9]. The egg is heavily glycosylated existing as the zona pellucida (ZP) comprised of mainly glycosaminoglycan hyaluronan. The sperm surface contains O-linked hyaluronan binding proteins and cleavage proteins to navigate the ZP and fuse with the egg plasma membrane. Post fertilisation, the O-linked sugars are deglycosylated to prevent further sperm adhesion therefore conferring fertilisation by a single sperm. Carbohydrate recognition has been observed in certain diseases as the basis of pathogenic invasion of healthy cells and hence also immune response offering a good target for disease treatment. Examples of well-studied multivalent carbohydrate mediated pathogen invasion include Shiga toxin and cholera toxin diseases, FimH lectin mannose binding by *E.Coli*, HIV and Ebola can be bound by DCSIGN and DCSIGNR lectins with respective specificity, owing to their high mannose coating.[10]

One example of viral glycan mediated infection is seen with *Influenza A*. The virus contains sialic binding haemagglutinin (HA) and sialic acid cleaving neuraminidase (NA) which work in tandem to mediate host cell invasion where replication can be hijacked. New viruses which have a mixture of the HA and NA antigenic receptors on the surface can then propagate further. Sialic acids (Sia's) bound by HA include sialic acid 2,3- linked galactose (Siaα-2,3Gal) and sialic acid 2,6 linked galactose (Siaα-2,6Gal) conformers. Siaα-2,6Gal is the main carbohydrate of the two presented in human airways, hence, viruses with HA and NA which can bind terminal 2,6- linked SAs are able to infect humans. Avian cells present 2,3- linked sialic acid hence corresponding HA and NA can bind. Swine trachea presents both Siaα-2,3Gal and Siaα-2,6Gal hence, both influenza A strains are supported[11]. This allowed for new stains to develop which present both HA and NA types hence, avian flu became an epidemic in 2003, 2004 and swine flu a pandemic in 2009-2010 which had human to human pathogenicity. The most recent coronavirus disease 2019 (COVID-19) caused by the virus Severe acute respiratory syndrome coronavirus 2 (SARS-CoV-2), immediate animal host is currently not known,

finding the animal responsible could help develop a vaccine and minimise the spread of future outbreaks[12].

1.2.3 Multivalent carbohydrate binding & the cluster glycoside effect

Often carbohydrate recognition occurs via the multivalent interaction between glycans and a given receptor as a means to enhance binding. Each individual binding events are too weak to confer association between carbohydrate and protein, however, when multiple binding event occur strong association is conferred (Figure 1.2). This is termed the cluster glycoside effect (CGE) as in nature carbohydrates are clustered together at the cell surface to promote multivalent binding[13]. Multivalent binding also confers selectivity. If multiple carbohydrates recognised by a particular protein are clustered together, they communicate a strong signal which cannot be accidental. Paradoxically, binding has also been observed to be diverse where one protein can bind more than one type of carbohydrate. For example, with the lectin Concanavalin A, binding of mannose is preferential, however, glucose binding also occurs. Binding affinity is based on subtle structural differences between carbohydrates such as the secondary carbon -OH position in this case and its implications in the binding pocket. Hierarchical binding confers selectivity, but also allows for binding affinity to be modulated.

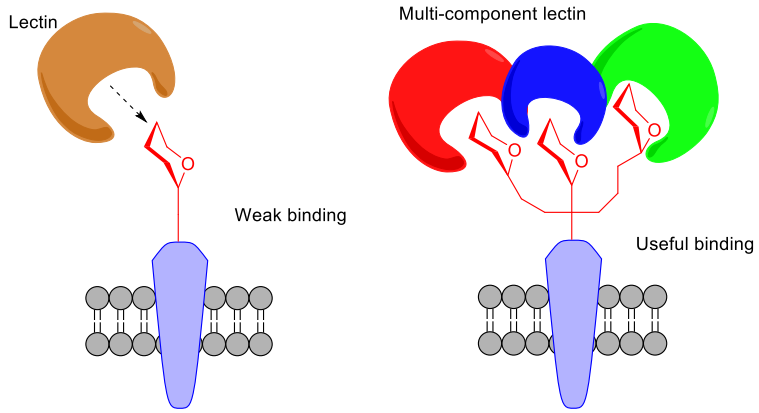

Figure 1.2 Multivalency is key to mediating lectin-carbohydrate interactions at the cell surface. Multivalent binding as seen on the right confers tighter binding between lectin and carbohydrate than the sum of the same number of individual interactions. Multivalent binding is defined as when both ligand and receptor exhibit multiple binding interactions. [14]

Binding affinity is often quantified in terms of a binding constant which is a measure of the strength of interaction. The binding constant can either be presented as the binding affinity (k_a), meaning how tightly a protein and carbohydrate are bound, or the dissociation constant (k_d), describing how likely the two components are to separate. They are both the reciprocal of each other and lectin affinity is most commonly described in terms of dissociation constant for comparison. The k_{off} and k_{on} are the dissociation rate and association rate respectively.

$$k_d\ (M) = \frac{[L][P]}{[LP]} = \frac{k_{off}}{k_{on}}$$

Equation 1.1 Dissociation constant k_d equation. L is ligand P is protein. The k_{off} and k_{on} are dissociation and association constants. Unit of k_d is measured in molarity (M).

In one study by Mori *et al.*[15] the binding of Concanavalin A (ConA) to a mannotriose (3,6-Di-*O*-(α-D-mannopyranosyl)-D-mannopyranose) via quartz crystal microbalance (QCM) the 2:1 and 1:1 (carbohydrate:Con A) binding stoichiometry was investigated (Figure 1.3). Carbohydrates were bound to the quartz microbalance and Concanavalin A was added in 10 mM HEPES buffer and allowed to bind. In the 1:1 ratio Concanavalin A was able to bind one terminal mannose of the mannotriose. In the 2:1 interaction, two terminal mannoses were bound by the same ConA protein at two different binding sites. The interaction was controlled by adding a galactose spacer to create the 1:1 interaction and no spacer in the 2:1 interaction. The k_a of 2:1 stoichiometry was 10 times higher compared to the 1:1 ratio evidencing the cluster glycoside effect.[15]

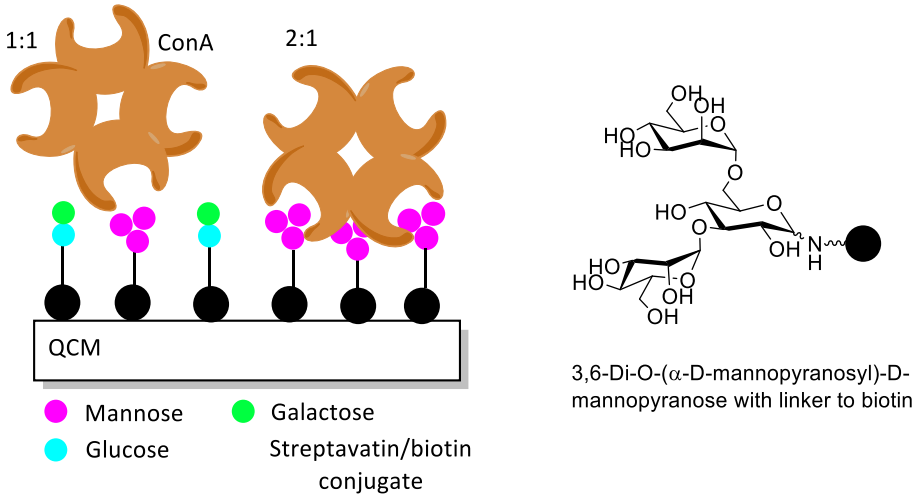

Figure 1.3 Carbohydrate cluster glycoside effect was measured through affinity contsants by Mori et al.[15]. Concanavalin A binding of terminal mannose of mannotriose in a 1:1 or 2:1 (carbohydrate:lectin) bound to a quartz crystal microbalance (QCM) via streptavidin:biotin functionalisation. The galactose terminated disaccharides act as spacers as Concanavalin A does not bind galactose.[15]

Studies into the FimH lectin seen on the pili of *E. coli* is an interesting case where increased multivalency is not the basis for increased binding affinity. FimH has two domains, one which is for carbohydrate binding ($FimH_L$) and the other for association with pili FimG protein ($FimH_P$). It is known to bind high mannose type glycans mono- and divalently, which have a divalent (C3 and C6 linked) trimannoside domain. These glycans are presented on the urinary tract cell surfaces and one *E. coli* is able to exhibit up to 200 interactions to this surface. However, these individual binding interactions means that the *E. coli* is still relatively weakly bound to the urinary tract lining. The k_d for divalent

binding to α-6Man$_2$, α-2Man$_2$ and α-3Man$_2$ is 2.7 x 10^{-4}, 7.0 x 10^{-5} and 2.8 x 10^{-5} M respectively owing to the fast off rate of the lectin. This allows for the *E. coli* to traverse the lining and imposes good invasiveness. Strong binding termed "catch-bonding" is induced through shear stress acting on the interaction. When urine is excreted the force pulls the *E. coli* and the FimH$_P$ domain dissociates from FimG, but it remains tethered. This improves the binding affinity 2000-fold and allows *E. coli* to evade removal from the urinary tract. Treatments for urinary tract infection is therefore desirable and targets to the FimH lectin must have better affinity than this trimannoside but importantly a slower off rate.[16]

1.2.4 Concanavalin A lectin carbohydrate interactions

Concanavalin A is a lectin of molecular weight 104-122 kDa isolated from Jack beans (*Canaualia ensiformis*) known to bind mannose and glucose seen to generate an immune response, agglutinating mannose presenting erythrocytes involved in conferring blood group types[17], insulin receptor-mediation[18] and in mediating *Escherichia coli* pathogenesis[19].

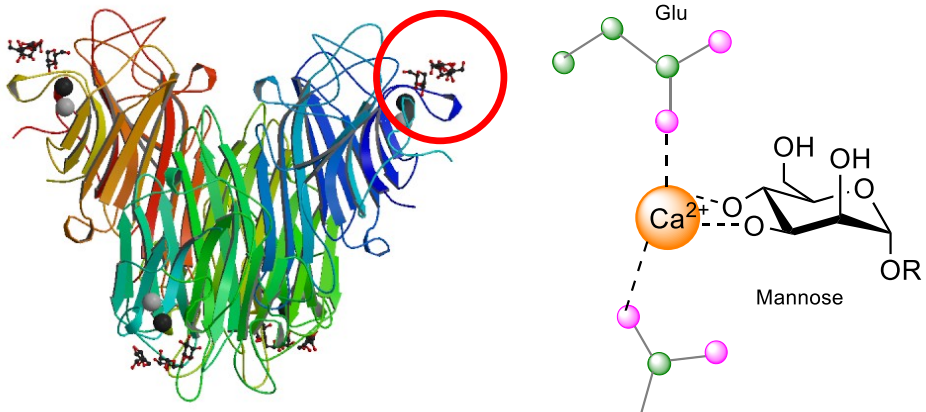

Concanavalin A
structure PDB n°: 1CVN

Figure 1.4 Concanavalin A structure with four homotetrimers which each have a binding site, circled in red. The binding of a terminal mannose residue is mediated by a Ca^{2+} ion and two glutamic acid residues.[20]

ConA preferentially binds terminal α-D-mannose over α-D-glucose whilst α-D-galactose is used as a negative control experimentally as the axial 4-position hydroxyl means that it does not fit in the binding site.[21] Concanavalin A has 4 binding sites one from each of its subunits which make up a homotetramer at pH 7.4, with a crystal structure determined size of 7x7x6 nm (Figure 1.4). At pH < 4.5 below its isoelectric point it dissociates into a dimer.[15,22]

ConA is known to favour polysaccharides over monosaccharides as it forms hydrogen bonds with carbohydrates which precede the terminal mannose both on the surface of the protein and within the binding site. Both branched and linear oligomannosides are preferred over monomannoside and evidence suggests increasingly branched oligomannosides confers tighter binding. For example, in a study by Munoz *et al*.[23] dendrimeric presented mannose showed a non-linear binding affinity to ConA. As the generations of mannose increased so did the multivalent binding effect. Generation 1 (G1) – 3 mannoses, G2 – 9-mannoses and G3, 27 mannoses were used in an SPR experiment and K_d was measured. G3 had a of 372-fold binding enhancement compared to methyl-mannose, whereas G2 has a 112-fold and G1 a 13.8-fold improvement This fits with the notion of greater clustering conferring tighter binding (Figure 1.5).

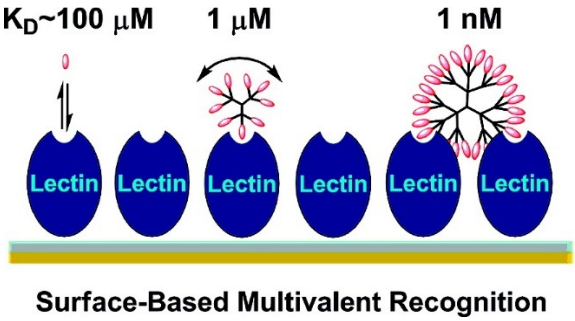

Figure 1.5 Lectin glycodendrimer shows improved binding conferring the cluster glycoside effect, Munoz et al.[23]

A multivalent effect is seen for ConA when the C-3-position hydroxyl is free to hydrogen bond with the protein, which is linked by a C-6-linkage to the preceding mannose which also has another mannose at the C-3-position creating a mannotriose (3,6-Di-*O*-(α-D-mannopyranosyl)-D-mannopyranose) as shown in figure 1.6. This was shown through a study with variable branched glycoproteins isolated from hen egg ovalbumin in a frontal affinity chromatography (FAC) experiment. K_d for this trimannoside was 0.24 μM, when a mannose was linked at the C-3-position of the terminal C-6-linked mannose the K_d increased to 35 μM. Also, in this study it was seen that introducing a C-2-linked mannose on the C-3-position hydroxyl of the C-6-linked mannose promotes tighter binding likely by having additional hydrogen bonding with the protein. K_d decreased from 0.2 μM to 0.029 μM.[21] Hence, branching such as at the C-2-position of the terminal mannose induces tighter binding over linear mannosides. One final observation saw that modification of the C4 position of the C-3-linker mannose removed binding.

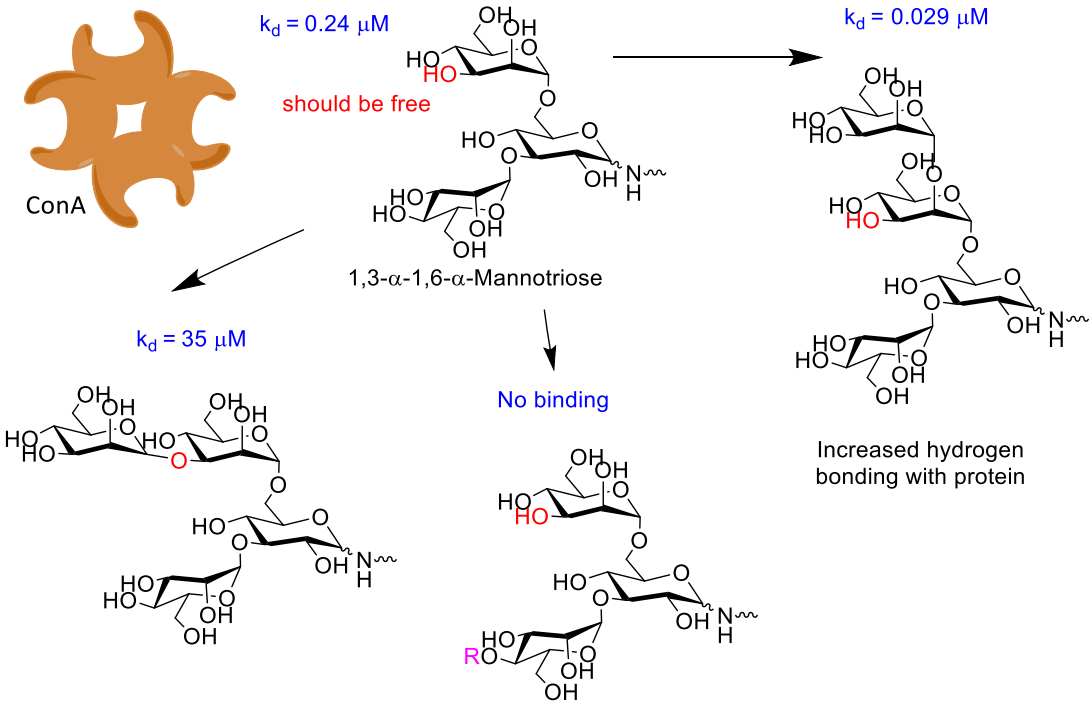

Figure 1.6 Concanavalin A binding of trimannose (3,6-Di-O-(α-D-mannopyranosyl)-D-mannopyranose). Red indicates the -OH which should be accessible for ConA binding. Certain other changes either improve, reduce or remove binding. Changes may be far away from the binding site and still impact binding dramatically due to hydrogen bonding effects with Concanavalin.[21]

Concanavalin A is known to exhibit weak hydrophobic affinity seem through binding of lipid vesicles. This fits with the role of Con A, a cell surface glycan bind protein, closely proximate to the lipid plasma membrane. These lipid interactions are weak, for example 7 x 10^2 M^{-1} between ConA and B-indoleacetic acid a lipid analogous to tryptophan which is found in plants[24].

3,6-Di-*O*-(α-D-mannopyranosyl)-D-mannopyranose is common to all glycopeptides and composes the first branching step after two sequential N-acetylglucosamines which are asparagine linked. This motif is known to be bound tightly by Concanavalin A and hence a good experimental control. From nature, structures with this trisaccharide have been observed to bind tightly with Concanavalin A including the branched mannose 9-mer called “high mannose” found in the endoplasmic reticulum, and other hybrid N-glycans composed of differing monosaccharides[25]. This 9-mer is important for protecting proteins from degradation and signalling a protein is ready for the next step in the glycosylation pathway[26]. If not added to a protein post translation, then the protein will not fold correctly[27]. Elevated levels of high-mannose have also been observed in breast cancer[28]. Therefore, investigating high-mannose during disease with ConA offers a target for disease treatment.

1.2.5 Carbohydrates in Cancer

During the progression of cancer, certain pathways are up and down regulated to allow the cancerous cell to grow, reproduce, form a tumour and become malignant and metastasise. This involves a lot of protein synthesis and elevated metabolic turnover which in turn impacts the glycosylation pathways. These glycosylation changes are reflected on the cell surface through the overall carbohydrate profile depending on the cell type and stage of tumour progression.

Understanding the differences between cancer cells and healthy cells as well as how the glycocalyx profile changes with each stage of cancer progression is important for cancer diagnosis and treatment. Glycosylation changes in cancer can take the form of structure truncation, elongation and also structure modification. Also, certain epitopes may be over presented on the cell surface which for example may play a role in tumour endothelial escape and metastasis. A well-known example is that of the overexpression of terminal sialic acid on tumour cells in a number of cancers which was first observed through wheat germ agglutinin (WGA) agglutinating on the tumour. Sialic acids monitoring (down to picogram amounts) is carried out clinically during cancer treatments. Tumours benefit from having a high density of negatively charged sialic acids on their surface as this causes inter-cellular repulsion and promotes metastasis. Sialic acids are bound by siglecs and selectins which normally mediate immune response hence, hyper sialylation helps evade immune recognition.[28]

Another example In this context can be found with mucin glycoproteins. These are heavily glycosylated glycoproteins which are found on mucosal surfaces and modified in cancer. The oligosaccharides are decorated with sialic acid and are able to traverse the epithelial cell layer and enter the blood vessel below. These changes can be detected using monoclonal antibodies and used as a diagnosis. Overexpression of Lewis^{x} and Lewis^{a} and sialyl Lewis^{x} and sialyl Lewis^{a} have also been observed on cancerous cells and have been linked to metastasis, which is mediated through binding endogenous selectins.[29] In the case of N-acetyllactosamine the increase in sialic acid is α-2,6-linked rather than α-2,3-linked which experimentally can be distinguished by the Sambucus Nigra Lectin (SNA) which preferentially binds the 2,6-linked variant. [30]

1.3 Synthetic platforms to mimic glycan presentation

1.3.1 Glycoarrays

Glycoarrays consist of a support to which carbohydrates can be covalently or electrostatically bound for subsequent investigation. Using arrays to immobilise either the lectin or carbohydrate offers certain advantages for measuring binding affinity such as high throughput, low material requirements, streamlining, repeatability and potential for commercialisation. They allow for a number of analysis techniques to be conducted to measure lectin-glycan interactions. Methods for conjugation are varied depending on the carbohydrate and linker involved, but most examples reported include click chemistry (e.g. Cu(I)-catalysed cycloaddition between an azido and alkyne), amide coupling, ionic interaction(with poly-L-lysine), fluorous based coupling and DNA-DNA based immobilisation[30] (Figure 1.7).

Considering the multivalent nature of lectin-carbohydrate binding, the spatial organisation is an important consideration when developing carbohydrate arrays. Designing arrays with defined organisation allows for the investigation of multivalency as seen in the work by Mori et al.[15] where they controlled the density of 3,6-Di-*O*-(α-D-mannopyranosyl)-1-amino-1-deoxy-D-mannopyranose with spacers to achieve either 1:1 or 2:1 protein-carbohydrate valency as seen in 2.3.1.

By confining carbohydrates to a surface, a number of techniques can be used to probe them such as mass spectrometry, surface plasmon resonance, or quartz crystal microbalance (QCM). Furthermore, binding experiments can be conducted with a range of complimentary partners such as lectins, antibodies or pathogens. This is useful for the discovery of novel physical information and interactions which are not isolatable in solution.

However, one major drawback of plate assays results from the fact they are 2 dimensional, whereas in nature lectin-carbohydrate interactions often occur in 3 dimensions. Concanavalin A for example has 4 binding sites which are arranged tetragonally to each other, hence, to utilise all binding sites it would need to encounter carbohydrates in 3 dimensions. The development of nanoparticles as glyco platforms overcomes this issue and provides glycan presentation that is more similar to that seen in nature. This is achieved through the fact nanoparticles provide a multivalent nanoscale 3D arrangement. The nanoprobes potentially mimic pathogens in terms of curvature and size providing a good model for multivalent pathogenic invasion mechanisms. Being on the sub-cellular size regime, nanoparticles are able to assimilate well offering potential as a drug delivery or diagnostic tool. They

also offer programmable nanoscale functionality, presenting multiple types of carbohydrate multivalently in a spatially controlled way.

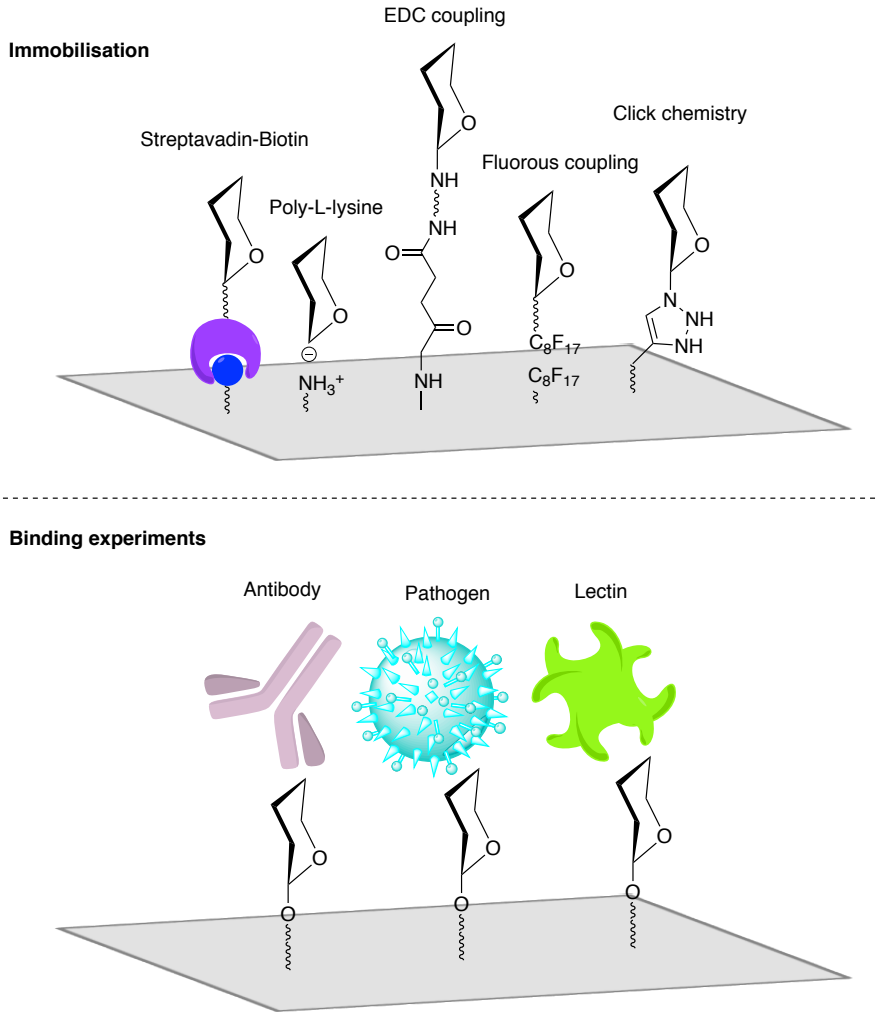

Figure 1.7 Glycoarrays involve the immobilisation of the carbohydrate of interest and then the probing by either an antibody e.g. in an enzyme linked lectin assay (ELLA), a pathogen such as HIV or with a lectin to investigate binding.

1.3.2 Nanoparticle glycan presentation

Nanoscale multivalent glyconanoparticles have been synthesised to mimic carbohydrate clustered presentation in 3D with the aim to develop synthetic platforms that enable the study of multivalent carbohydrate/protein interactions. A range of materials and methods have been explored as multivalent platforms that mimic glycan presentation in nature and that are generally non-toxic. In some instances, the platforms introduce novel properties such magnetism or incorporate a conjugated drug for therapeutic effects. In general, designing these particles from the bottom up allows for tighter control of the glycan presentation which allows for study of the principles underpinning multivalent glycan binding.

Nanoparticles used for glycan presentation include metallic and polymeric particles, as well as carbon-based dots and dendrimers. In addition, synthetic glycopolymers can be synthesised through block copolymer methods where self-assembly is controlled by the starting material properties to produce vesicles, micelles and rod-like shapes. Starting components can include glycan-functionalised monomers which following self-assembly present the sugar moiety on the surface in a highly ordered way[31,32]. Changing the starting copolymer structure can influence the glycan density, the nanoparticle shape and introduce multiple glycan moieties to create a synthetic glycocalyx.

Metallic glyconanoparticles can be made from iron oxide, gold, or semi-conductor material to form quantum dots and quantum rods. In these cases the nanoparticle is synthesised before glycan functionalisation commonly through thiol group interaction or with quantum dots via metallic coordination. Gold coated iron oxide nanoparticles offer the potential for magnetic control and also surface plasmon resonance measurements. Gold nanoparticles also exhibit colour change properties as a result of clustering which can be used as a measure of interparticle interaction[33]. One example uses the photoluminescence (PL) properties of gold nanoparticles functionalised with mannose to probe binding with *E.Coli.*[34]

Dendrimeric glyconanoparticles are often designed to have symmetry in their structure owing to their highly ordered arrangement which can be useful when studying the cluster glycoside effect. For instance, this is evident on probes based on a C60 fullerene scaffold, where highly branched structures could be prepared. In one example by Sánchez-Navarro *et al.*[35] 360 mannobioses were displayed on one particle. Therapeutically this system has potential to block the binding of pathogenic Dengue and Zika virus which share this carbohydrate in common and is known to bind to the dendritic cell-specific intercellular adhesion molecule-3-grabbing nonintegrin (DC SIGN) receptor in a multivalent manner on human dendrimeric cells[36]. Another glycodendrimer using a C60 fullerene scaffold, presented 12 or 24 α-mannoses as well as α-galactose as a negative control was used to assess the multivalent binding of Concanavalin A. Cu-assisted click chemistry synthesis methodology was employed and isothermal calorimetry (ITC) was used to measure the binding parameters. The K_a of the 12-mer was 421.6±21.2 $M^{-1}\times10^{-4}$, the 24-mer was 137.5±25.4 $M^{-1}\times10^{-4}$ and the galactose was reported as showing no binding. These values along with ΔG values and showed that the lower valency 12-mer has better binding to Con A likely due to high entropic value for the 24-mer meaning less binding occurred. This effect is interesting despite relatively high (and therefore poor binding) K_a values. The authors suggest

that high entropy originates with the 24-mer binding as it has greater flexibility and 15 Con A proteins clustering compared to 6.5 for the 12-mer[35].

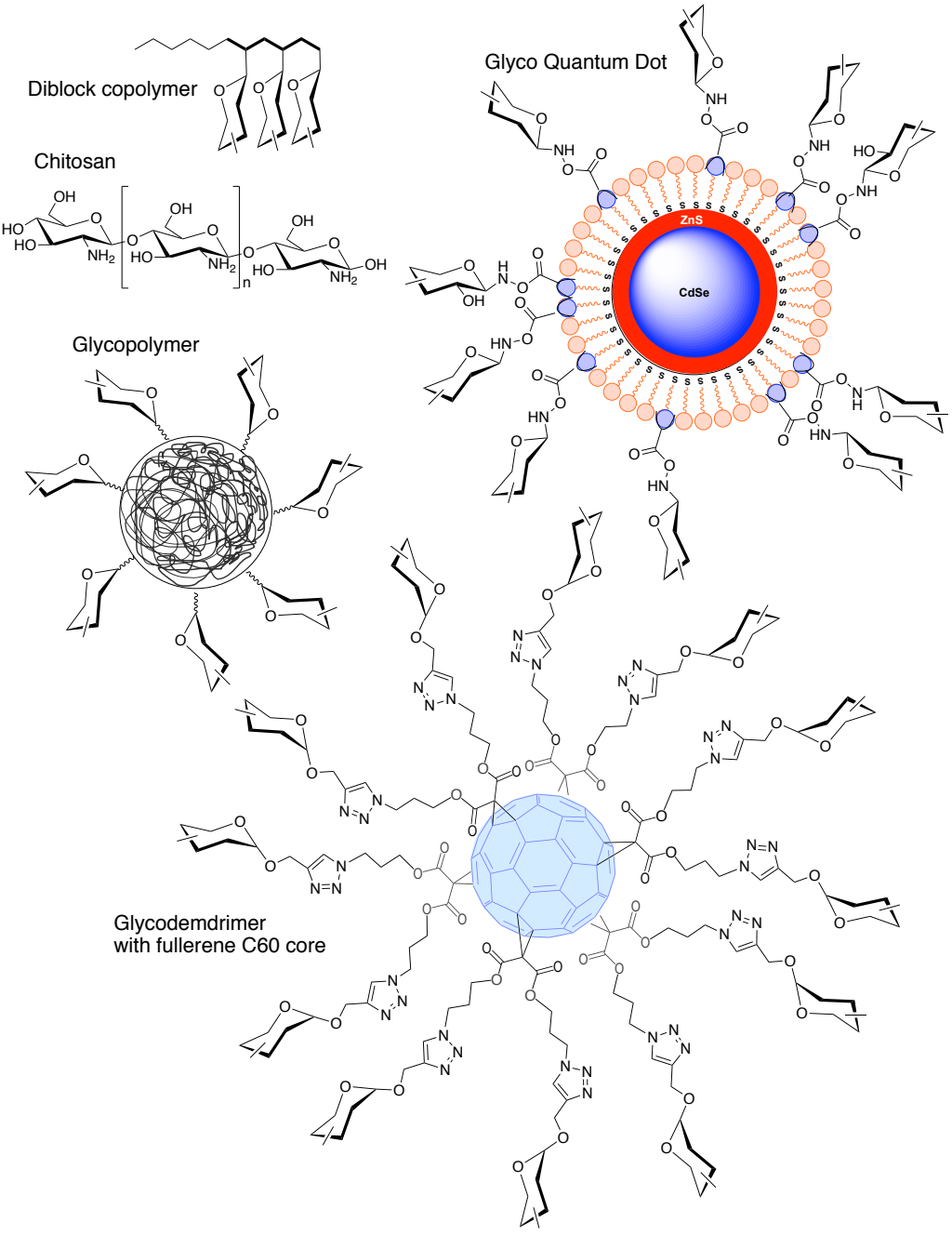

Figure 1.8 Common glyconanoparticles; polymeric glyconanoparticles, example starting material polymers such as chitosan and diblock copolymers. Quantum dot based glyconanoparticle and dendrimeric glyconanoparticles which in this example has a fullerene core.[35]

1.3.3 Quantum Dot glycan presentation

Quantum dots are semi-conductor crystalline nanoparticles which offer unique properties in that they exhibit the quantum confinement effect (QCE) and have size dependent fluorescence properties. Sizes are commonly between 2-10 nm but they can be larger at 200 nm when synthesised via electronic lithography routes[37]. CdSe quantum dots sized 2.1, 2.5, 2.9, 4.7 and 7.5 nm have blue, green, yellow, orange and red photoluminescence respectively[38]. In a semi-conducting material, an electron-hole pair (also known as an exciton) can be generated upon irradiation. When the exciton is confined to a particle smaller than its Bohr radius the energies become quantized into discrete energy levels. The energy levels are then related to the particle size. A photon is emitted when the electron-hole pair recombines[39]. QDs consist of a core and shell structure such as CdSe/CdS or CdSe/ZnS, where the shell material has a band gap that straddles the core band gap hence acting as a passivating layer (Figure 1.9). QDs are used as they commonly are photostable and have a high quantum yield comparable with fluorescent proteins and some commercial dyes used in bioimaging[40].

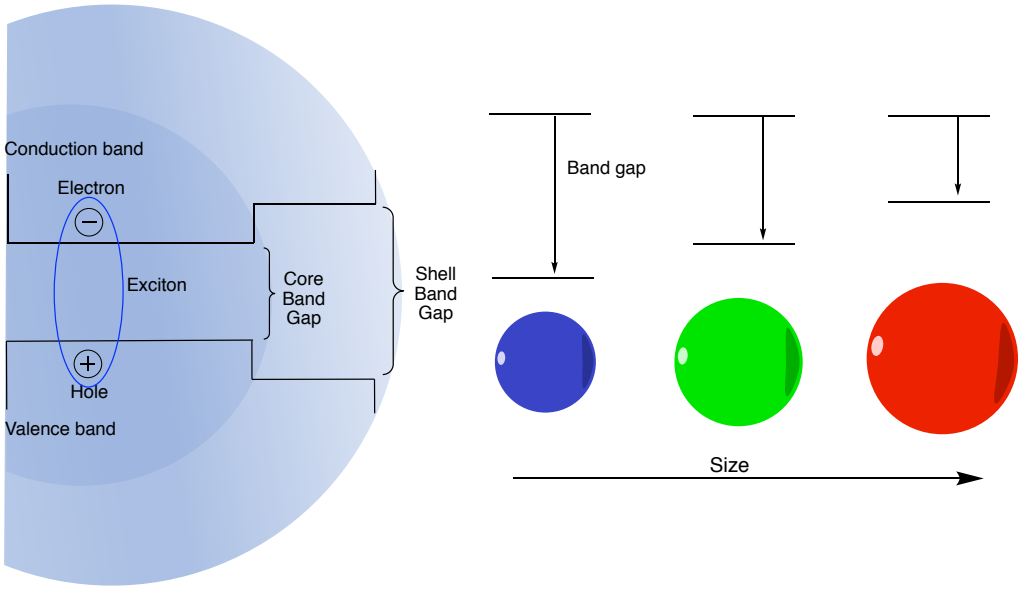

Figure 1.9 The quantum confinement effect seen in semi conducting Quantum Dots (QDs).

The glycan density on the QD surface can be controlled in a number of ways, for example by changing the conjugation method (CDI or EDC/NHS amide coupling agents)[41], using spacers, or varying the length of linker between carbohydrate and nanoparticle surface[42]. Previous work in the Galan group investigated control over carbohydrate presentation by introducing molecules as spacers and also achieving bi-functionalisation with 2 different carbohydrates through ratio control during conjugation. Using these glyconanoparticles they were able to investigate the role of individual carbohydrates on the nanoparticle interaction with cancerous and non-cancerous mammalian cells.

In their work, cadmium selenide (CdSe) QDs with a Zinc Sulfide (ZnS) shell were made and coated with a trioctylphosphine oxide (TOPO) corona which provides colloidal stability through Zn-O interaction. This was then exchanged with ligand of interest which contained a thiol which is able to coordinate with the ZnS. In this work the thiols used were either Mercaptoacetic acid (MAA) or dihydrolipoic acid (DHLA). MAA was used as a linker for the conjugation of dextran as a positive control, whilst DHLA had 2 versions, a PEG linker terminated in either a carboxylic acid or a hydroxyl. The carboxylic acid was used as a handle to react with 1-aminoglycosides of interest in an EDC coupling reaction, and the unreactive hydroxyl acts as a spacer. By controlling the molar ratio of these 2 types of DHLA linkers the overall density of glycosylation could be controlled. Ratios of 100:0, 60:40, 40:60 and 0:100 spacer:linker were used to generate 4 QDs with varying linker density. Furthermore, these carboxylic acids sites could either be reacted with 1 or 2 different aminoglycosides. Carbohydrates investigated in this system include, glucose, mannose, maltose, maltotriose galactose and lactose and dextran as a positive control (Fig.1.9).

Initial cytotoxicity studies with HeLa and AS cell lines showed that there was no toxic effect with QDs coated in 60% lactose after a 24 hours incubation period compared to control without QDs. At the same concentration, capped QDs without glycan functionalisation were toxic under the same conditions. Hence, in subsequent cell studies the QD density was fixed at 60% carboxylic acid terminated DHLA linker and 40% hydroxyl terminated DHLA linker. In the case of hydroxyl, glucose, mannose, maltose and maltotriose functionalised QDs, no uptake was observed. In the case of dextran and galactose functionalised QDs, uptake was observed and early and late endosomal and some Golgi retention was observed, with slight variation between cell lines. After 24 hours the number of QDs had reduced, suggesting exocytosis of the QDs. Lactose functionalised QDs were taken up and retained in the endosomes, Golgi and endoplasmic reticulum (ER) in both cell lines evading exocytosis beyond 24 hrs.

Bi-functionalised QDs with lactose and a carbohydrate which when mono-functionalised previous did not allow QDs entry into the cells, allowed QD uptake. In this way lactose was used as a “Trojan horse” to facilitate the uptake of bi-functionalised QDs seen with 1:1 functionalised lactose:mannose and lactose:maltotriose. Notably, these QDs had a different intracellular localisation to lactose-conjugated QDs, suggesting an intracellular targeting role of the mannose and maltotriose post internalisation. Furthermore, the lactose/maltotriose showed vesicular retention proximal to the nucleus in some cell lines.

1.4 Synthesis of Carbon dots

Carbon dots (CDs) were discovered in 2004 by Sun *et al.*[43] during the preparation of single walled carbon nano tubes (SWCNT). In the last 15 years research developing syntheses and exploring the applications of CDs has become a huge field in its own right. Carbon dots syntheses are categorised into two main approaches: top down where carbon-based materials with defined structure are broken down into nanoparticles retaining structure from the original material or bottom up where small

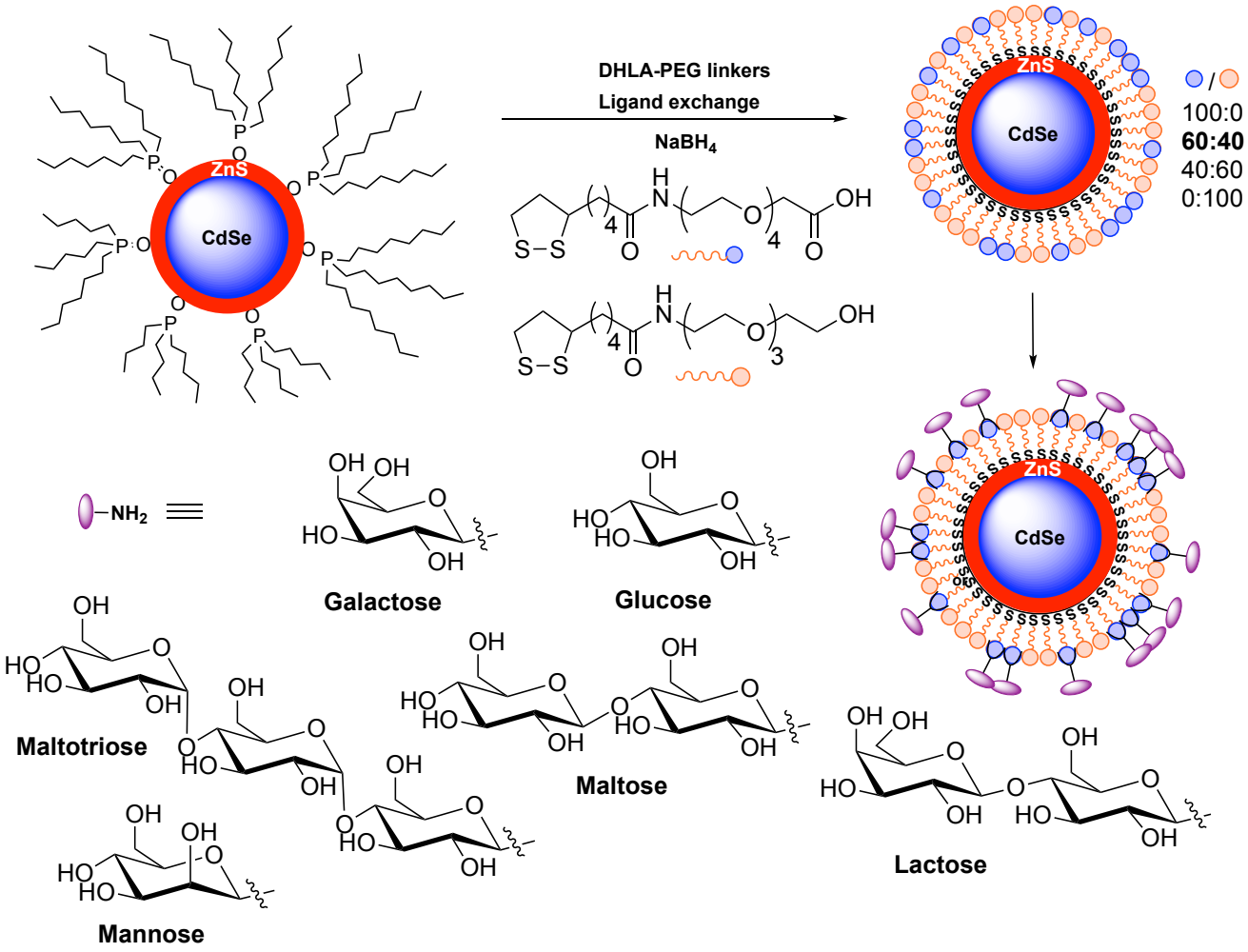

Figure 1.10 Synthesis and glycan functionalisation of quantum dots as carried out by Benito-Alifonso et al.[44] These materials were used in cancer cells and uptake depending on the glycan present was investigated.

molecules are carbonised and dehydrated to form carbon-based particles. The Sun *et al.*[45] synthesis can be classed as a top down approach. Bottom up methods are more accessible and allow for easier CD core manipulation through established doping effects although these are intrinsically less well defined and often less structured than those synthesised by top down methods. Top down methods include, electrolysis with graphitic electrodes, ultrasonication where soundwaves facilitate carbonisation, laser ablation of a carbon source into particulate form, and acid treatment involving

oxidising a carbon source into particulate form. Common precursors include, graphene and graphene oxide (GO), soot, carbon nanotubes, fullerenes and activated charcoal (Figure 1.11). The structures drawn in figure 1.11 are not a hard and fast rule, for example sp^3 core can result from bottom up synthesis.[46]

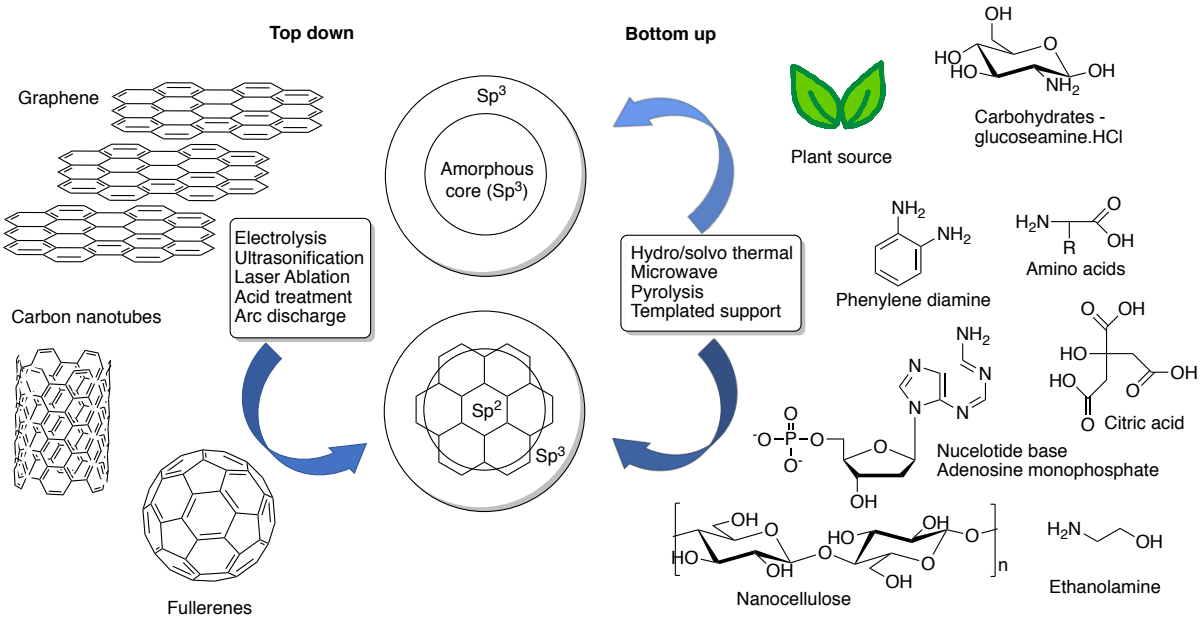

Figure 1.11 Carbon dot synthesis route, top down from structured bulk precursor materials, or bottom up from small molecules without inherent structure. Commonly used methods are included, and the general resulting structure is drawn which results from these methods[46].

A wide range of techniques are available to probe the structure of carbon dots (Figure 1.11). Certain techniques are able to probe the core or shell i.e. surface independently, whilst the majority provide information on the whole structure. AFM, FTIR NMR and XPS probe the surface structure and provide useful information on the surface which is important when considering environmental interactions. TEM and Raman spectroscopy probe the core structure such as crystallinity. Overall properties such as size, elemental content, structural information and photoluminescence can be measured through fluorescence and UV-Vis spectroscopy, DLS, DOSY, TGA, Zeta potential, EDX and small angle x-ray scattering (SAXS). Refer to appendix for a brief explanation of the techniques used in this work.

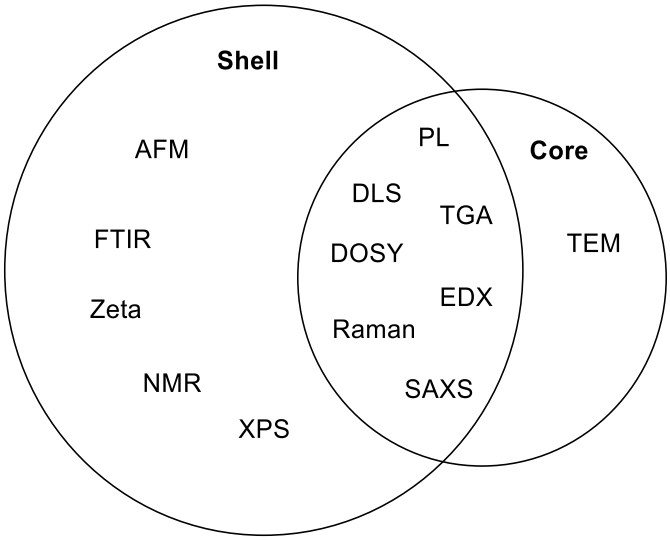

Figure 1.12 Venn diagram of the techniques available to characterise carbon dots. Relevant techniques are categorised as able to probe the core or shell independently or both.

1.4.1 Top Down carbon dot synthesis

1.4.1.1 Graphene containing carbon dots

Carbon dots made via top down methods retain some graphene structure in their core which is hypothesised to be the basis for quantum confinement in material termed either carbon quantum dots (CQDs) or graphene quantum dots (GCDs)[47]. Bulk graphene itself has a band gap of 0 eV owing to its linear energy dispersion of the charge carriers. However, fragments of nanoscale graphene are known to exhibit quantum confinement in a size dependent manner due to π conjugation electron delocalisation (and $\pi - \pi^*$ transitions in the sp^2 domain). Time dependent density function theory (TDDFT) can be used to determine the band gap and therefore emission wavelength of a graphene sp^2 domain of certain diameter (Figure 1.13). However, factors such as edge functional groups, hybridisation and graphene shape will also affect the PL[47].

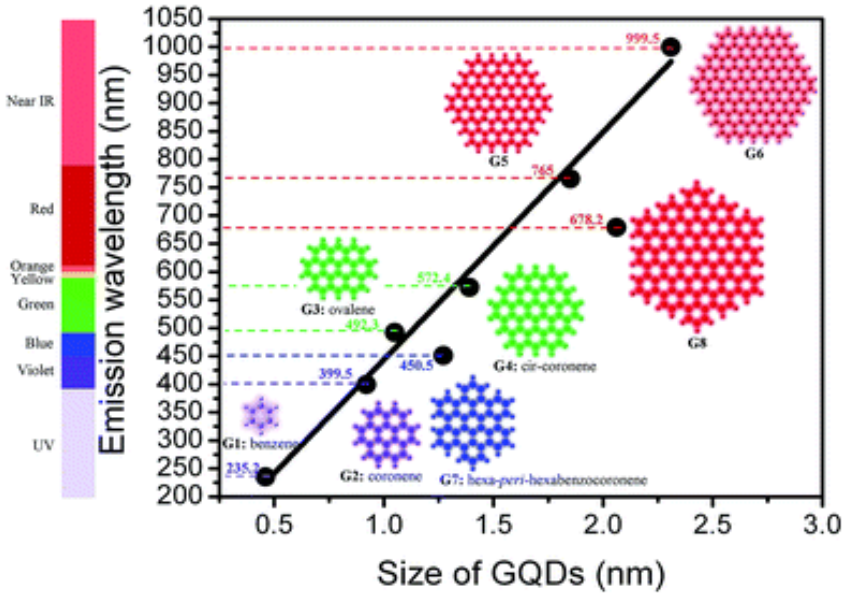

Figure 1.13 Graphene sp^2 domain size to fluorescence emission wavelength positive relationship Reproduced with permission from Sk et al.[47]

The mechanism involves the carbon dot being similar in size to QDs where the Bohr radius of an exciton in the material is larger than the particle therefore exhibiting size dependent photoluminescence (PL). The size of the carbon dot correlates with the size of the sp^2 domains within the core, and evidence suggests that the larger the sp^2 domain, the smaller the energy gap, hence, lower energy (red-shift). Li *et al.* observed for 1.2 nm CQDs a 350 nm fluorescence peak, 1.5-3 nm 400-700 nm peak, and for 3.8 nm core 800 nm. GCDs were synthesised via electrochemical means involving graphitic rods and separated on the basis of size post synthesis using silica-gel chromatography with petroleum ether/diethyl ether. Evidence for this effect was determined through predicting the highest occupied molecular orbital-lowest unoccupied molecular orbital (HOMO-LUMO) band gap for isolated graphene sp^2 domains between 1.4-2.2 nm and observing that they match up with the PL energies observed in a size dependent manner.[48]

Furthermore, another study observed the same size-PL dependence analogous to QDs. GCDs were synthesised from 3 coal based starting materials; anthracite, bituminous coal and coke, each of which has a different structure. Under top down synthesis conditions involving sonication in acid followed by heating to 100 – 120 °C before neutralisation with NaOH and filtration, a-GCD, b-GCD and c-GCD were afforded of diameters 29 ± 11 nm, 2.30 ± 0.78 nm, 5.8 ± 1.7 nm respectively. Each fit a size dependent PL profile where a-GCD fluoresced yellow, b-GCD blue and c-GCD green (λ_{ex} 345 nm). Interestingly, individual b-GCD particles of 2.96 nm, 2.30 nm had different fluorescence emission peaks of 500 nm and 460 nm, further conferring quantum confinement effect. However, the evidence

does not exclude oxidative groups at the graphene edge as the mechanism for the photoluminescence observed[49].

Peng *et al.*[50] developed CQDs synthesised from carbon fibres in acid before heating for 24 hours, with size dependent fluorescence profiles (Fig 1.14). 1.4 nm had blue fluorescence 405 nm (λ_{ex} 318 nm), 4-8 nm had green 500nm (λ_{ex} 331 nm) and 7-11 nm had yellow 575 nm emission (λ_{ex} 429 nm). These CQDs of different sizes were synthesised at three temperatures 80 ^{O}C, 100 ^{O}C and 120 ^{O}C respectively. The authors hypothesis that the temperature controls the size and the nature of the sp^2 domains in the particle and hence synthesis temperature could be a way to tune the spectral properties of CQDs.[50]

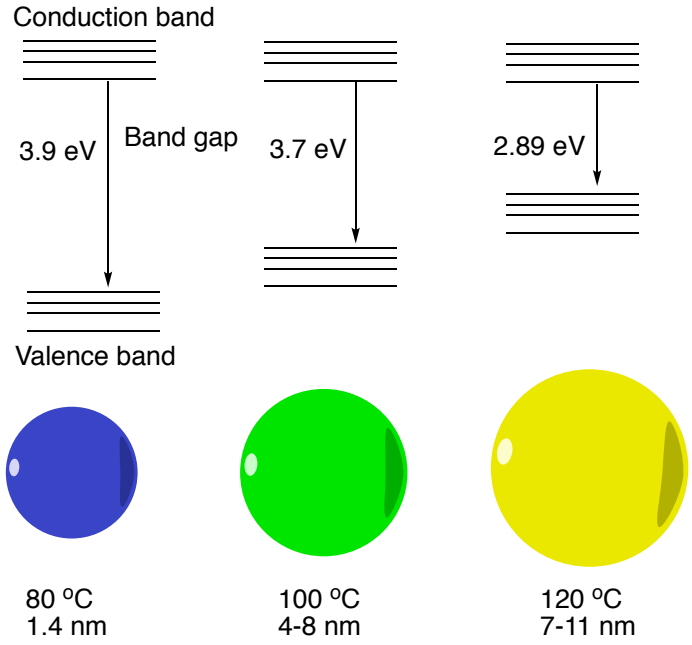

Figure 1.14 Carbon Quantum Dots (CQDs) synthesised by Peng et al.[50] at 80 ^{O}C, 100 ^{O}C and 120 ^{O}C via top down methods exhibit size dependent fluorescence and band gap energies. [50]

1.4.1.2 Graphene oxide containing carbon dots

Graphene oxide derived CQDs exhibit similar size-dependent emission as graphene derived ones. The structure of graphene oxide contains some sp^3 domains as epoxy and hydroxyl groups and also oxidated sites in the form of carboxyl and carbonyl groups commonly found at the particle edges. Sp^2 domains exist within the graphene layer as smaller domains separated by sp^3 regions (Figure 1.15). Larger graphene quantum dots (GCDs) contain larger and more sp^2 domains which are responsible for their PL. Edge functional groups are good handles for manipulating the PL spectra and GCDs can also be doped in a similar way to non-sp^2 containing carbon dots. Depending on whether electron enriching (nitrogen) or lacking (boron) atoms are incorporated, the PL can be blue or red-shifted.[51]

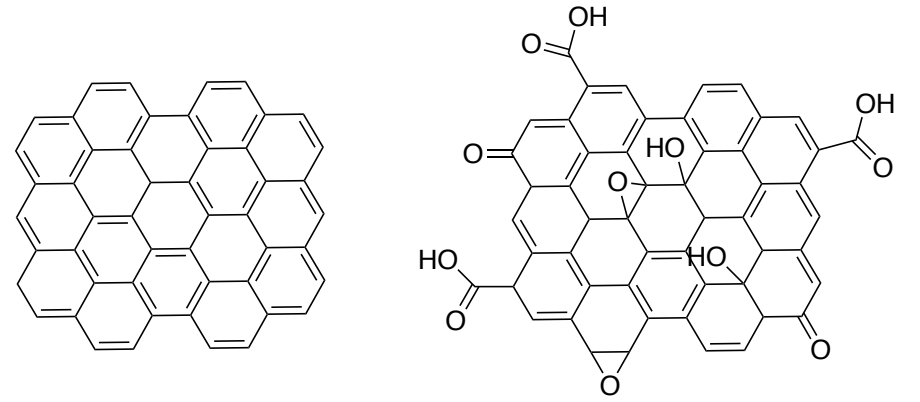

Figure 1.15 The sp^2 domains in graphene and graphene oxide (GO) act as chromophores/centres at which electron-hole pairs can recombine radiatively. The PL energy can therefore be tuned by controlling the amount of sp^2 present in the graphene carbon dot (GCD).[47]

Literature sometimes refers to the sp^2 domain within GCDs as the conjugated domain and references the size dependent quantum confinement PL effect which is seen in GCDs. The larger the conjugated system, the more red-shifted the PL reported. For example, graphite was used to prepare CDs by Zhou *et al.*[52] CDs were separated using filters of molecular weight cut-off (MWCO) <5 kDa and 5-10 kDa which yielded blue (1.9 ± 0.3 nm) and yellow (3.2 ± 0.5 nm) fluorescent particles. Filter sizes larger than this yielded particles which did not exhibit fluorescence. They proposed sp^2 conjugate domain size as the basis for this effect FTIR peak at 1630 cm^{-1} shifted to 1620 cm^{-1} (C=C stretch) which is indicative of a larger conjugation system in the yellow CDs.[52]

1.4.2 Bottom up synthesis of carbon dots

A wide range of materials have been used to synthesis carbon dots as the single prerequisite is that it contains carbon. As previously mentioned, top down methods confer structural properties to the CD which are intrinsic to the starting material such as graphene producing CDs with sp^2 conjugate core. For bottom up methods, the precursors can be small organic molecules including amino acids, sugars and DNA as well as polymers and waste biomass (termed green methods). With biomass-based syntheses, the starting material is often a mixture of precursors. Natural materials used include pomelo peel,[53] watermelon peel,[54] coffee grounds,[55] egg,[56] milk,[57] seafood waste[58] and urine.[59] These are commonly conducted using hydrothermal or microwave methods and generate heterogenous materials which do not confer any PL, size or structural consensus with each other as the small molecules are polymerised and carbonised at different rates and to different extents depending on the particular synthesis (e.g. reaction time, concentration of reagents, temperature, etc).[60]

Amino acids contain acid and amine groups. The acid group facilitates polymerisation, conjugation and aromatic formation and the amine group also facilitates polymerisation as well as N-doping and passivation potential. All-natural amino acids were compared as starting material for hydrothermally synthesised carbon dots at 180 ^{O}C for 12 hrs. The variable R-group of amino acids was found to be crucial, by stabilising surface defects and achieve N-doping and to differing extents which was seen through the QY and PL intensity. For example, serine and threonine have terminal hydroxyl groups which were thought to promote dehydration and carbonisation hence good photostability and QY of 30 % and 22 % respectively.[61]

DNA macromolecules or nucleotides have been used for CD synthesis which have in some cases been shown to retain the heterocyclic features of the starting material and retain phosphate groups. One study observed that purine bases induced better N-doping that pyrimidine in a synthesis involving nucleotide bases. Furthermore, the sugar component confers greater QY compared to synthesis involving the equivalent nitrogenous base.[60]

1.4.2.1 Carbohydrate based bottom up carbon dot synthesis

A number of small carbohydrate molecules including glucose, mannose, fructose and glucosamine have been used for carbon dot synthesis due to their wide availability and low cost as well as their ability to ring-open in water forming an aldehyde which is important in condensation reactions involved in carbon dot syntheses. Resulting from these reactions are polymers and small molecules which can have a number of fates. Commonly glucose has been used and has a relatively low carbonisation temperature, lending its use for greener synthesis methods[62]. A CD synthesis involving H_2SO_4 refluxing from glucose only yielded carbon dots with low QY (0.01) which could be improved with a second TTDDA passivation step (0.13). This supports literature examples where having a simple carbonaceous material such as soot, citrate or carbohydrate alone, yields a material with poor PL properties[63].

A secondary passivating agent is usually included in carbohydrate-based syntheses and a wide range of bottom up synthesis methods have been employed in the literature. This secondary molecule in combination with glucose will dictate the CD structure and PL properties. One study by Klinger *et al.*[64] showed that glucose reaction with ammonia (ammoxidation reaction) produced a huge number of pyrazines such as 2-pyrazinol, 2,5- and 2,6-fructosazine and 2,5- and 2,6-deoxyfructosazine. When a polysaccharide was used in its stead, lower yield was obtained showing that monosaccharide is preferred for carbon dot synthesis[64]. Other carbohydrates such as glucosamine have been used to

produce pyrazines as they contain an amine group. Glucosamine has also been observed to have a doping effect and red-shift CD fluorescence due to the N containing amine group. The formation of pyrazine containing molecules is also possible in a self-condensation reaction which is a common group in molecular fluorophores[65].

A fructose and maltose-based synthesis produce graphite-like sp^2 core carbon dots. Using either NaOH or $NaHCO_3$ base and both carbohydrates at 500 mM concentration (whilst under room temperature and pressure) synthesised a green fluorescent CD. However, this synthesis had a relatively low QY of 2.2 %[66].

1.4.2.2 Photoluminescence and carbon dot structure relationship

The structure to PL relationship of carbon dots is one of their most intriguing properties. The photoluminescence makes carbon dots useful for biological context and understanding the basis of this property and improving it is a main focus in the field. Synthesis and application should be considered in tandem when developing carbon dots. CD PL properties are influenced by starting materials and synthetic conditions through passivation, doping, molecular fluorophore generation and crosslink enhanced emission. Figure 1.16 summarises the structural basis for carbon dot PL.

As previously mentioned, precursor molecules are very wide ranging and each influence the PL profile of the resulting CD. More than one PL centre can exist within a carbon dot owing to the multiple distinct structures that can exist in a single carbon dot. Commonly but not as a rule, top down synthesis methods confer conjugated sp^2 structure in the core. These domains commonly absorb at lower wavelengths between 200-250 nm and exhibit blue-fluorescence as seen with graphene (Figure 1.16 blue shaded area highlights core region). Bottom up methods confer more variability in the structure often with a mixture of sp^3 and sp^2 regions. Sp^2 core domains generated from bottom up methods will show similar PL profiles to top down synthesised CDs. Sp^2 hybridised O and N at the edge of crystalline domains are known as the “edge domain” and absorb between 250 – 350 nm with a correspondingly red-shifted fluorescence (Figure 1.16 green shaded area). Oxidised “surface domain” (Figure 1.16 orange shaded area) groups such as pyrrolic, amine and carboxylic groups confer even more red-shifted absorption and fluorescence, in the region above 350 nm into the visible region. Furthermore, surface groups can result in surface emissive traps which require passivation for good QY. Self-absorption can occur when the PL profiles of different surface domains overlap so that the emission of one is the excitation energy of another causing a cascade excitation, this can be seen in both the absorption and fluorescence profiles in as a tail towards 800 nm.

Molecular fluorophores can be generated during synthesis and presented at the CD surface which may have their own PL profile independent from the main carbon dot. Polymeric content can confer improved PL if crosslinked polymer is present in the CD structure through the crosslink enhanced emission effect. Finally, the PL profile can be blue or red-shifted through heteroatom doping which has been demonstrated through a number of syntheses (see section 1.4.2.5 on doping).

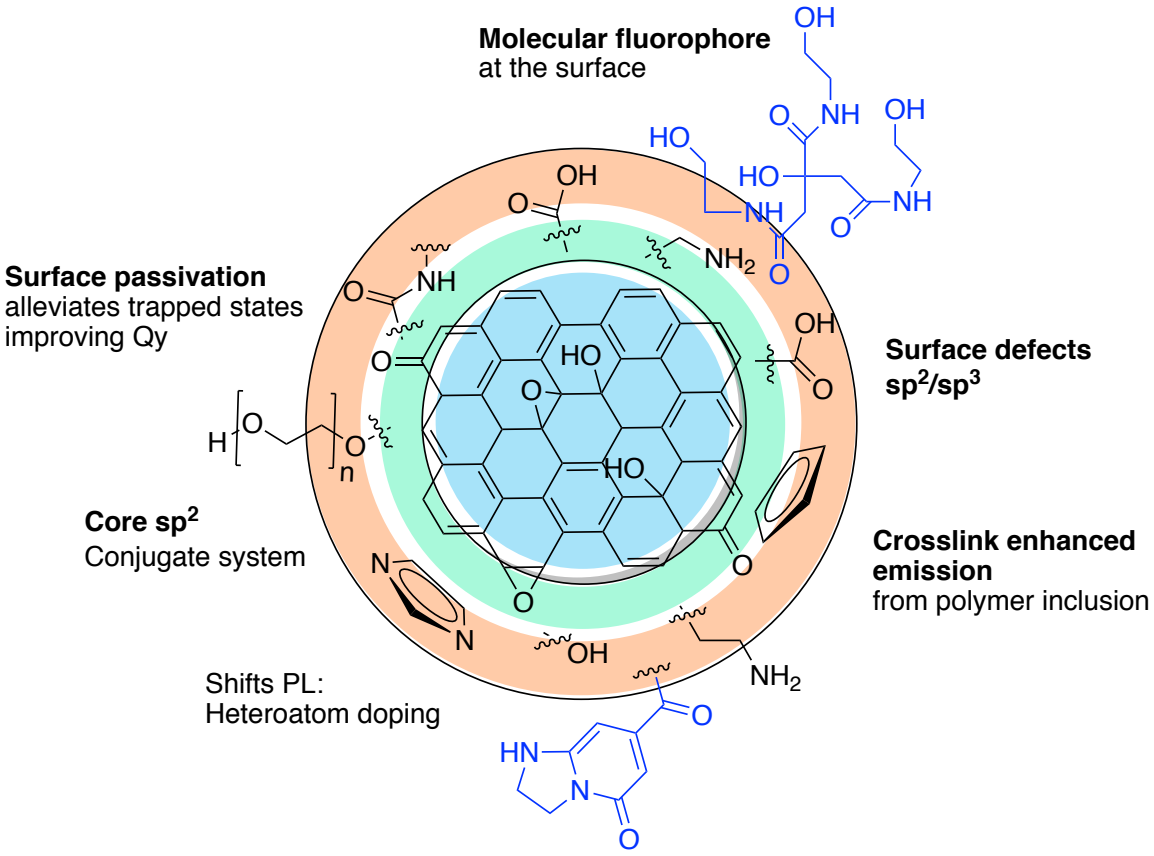

Figure 1.16 Carbon dot structure to photoluminescence relationship. Multiple contributing factors influence a carbon dots PL profile which are determined in synthesis and can be modified post synthesis. Three shaded areas indicate three areas fluorescence can originate from. Blue = core, green = edge domain, orange = surface domain. Blue molecules illustrate surface molecules on the CD surface with their own PL profile.

1.4.2.3 Passivation for improved carbon dot quantum yield

Passivation is well known as a mechanism to make emissive and improve the QY in CDs with highly oxidised surfaces. The oxygen containing surface groups are known as surface defects and capture excitons and have associated red-shifted PL. Exciton trapping means that the QY of the CD is low and must be improved to make CDs biologically useful. Passivation can be achieved using organic and

inorganic materials which can be added in synthesis or conjugated to existing functional groups post synthesis. This feature gives carbon dots tunability and has facilitated improved QY from < 1% to over 90 % in the best cases. Polyethylene glycol$_{1500}$ (PEG_{1500}) was one of the first passivating molecules, conjugated to CDs synthesised using laser ablation from graphite powder and cement in the presence of water. The initial material generated in this manner was not fluorescent however, after heating nitric acid (up to 2.6 M) treated CDs with PEG_{1500}, the material exhibited excitation dependent emission between 400-694 nm (Figure 1.17). Interestingly, better QY was induced by subjecting this material to repeated PEG_{1500N} functionalisation.[43]

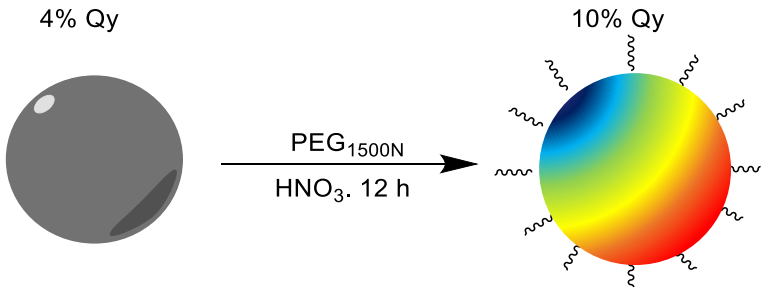

Figure 1.17 Passivation with PEG_{1500} of carbon dots synthesised from graphite powder and cement to reveal fluorescence upon λ_{ex} 400 nm shown by Sun et al.[43]

Passivating molecules work by facilitating electron-hole recombination located at the surface of CDs. Carboxyl surface groups non-radiatively allow electron-hole recombination by acting as electron acceptors. Hydroxyl functionalisation facilitates radiative recombination due to its electron donating property conferring improved QY. Evidence for this was shown by Fe^{3+} detection through coordinating with hydroxyl terminated CDs which quenches fluorescence. Hydroxylation had been shown to induce CD fluorescence in the first instance.[67] Similarly, amine and amide groups have been shown to induce improved CD QY due to electron donating properties. CD passivating molecules with terminal amine groups include polyethyleneimine (PEI), poly(2-ethyl-2-oxazoline (PPEI-EI, average MW ~ 5000) initially explored by Sun *et al.*[43] A plethora of amine containing molecules have since been conjugated via simple N-(3-dimethylaminopropyl)-N'-ethylcarbodiimide hydrochloride (EDC) coupling to carboxylic acid groups on CDs to improve QY.

Passivation through incorporating small molecules into the synthesis has been shown with numerous amine containing molecules such as 4,7,10-trioxa-1,13-tridecanediamine (TTDDA), 1,2-ethylenediamine (EDA), diethylamine (DEA), 1,4-butanediamine (BDA), and triethylamine (TEA).[68] Through NMR and FTIR (C-N peak at 1580 cm^{-1} stretch) these functional groups have been seen to be conjugated onto the CD surface. Interestingly, primary amines were seen to improve QY more than secondary or tertiary amines in a comparative study. In a microwave synthesis amine containing

molecule was added to citric acid before 2-4 minute microwave pyrolysis. QY values obtained for primary amine EDA was 30.2% whilst secondary amine DEA was 4.2% and tertiary amine TEA was 3.2% all compared to unpassivated CDs of 2.2%.[69]

One other key property which can be affected by passivation is PL, which can change from excitation dependent to excitation independent. This is the case if the PL originated from the surface group induced trapped states of differing energy levels which can be removed through passivation. In this case any excitation independent PL observed originates from the core, either from sp^2 domains, or in the case of amorphous CDs the sp^3 enriched domains.[70]

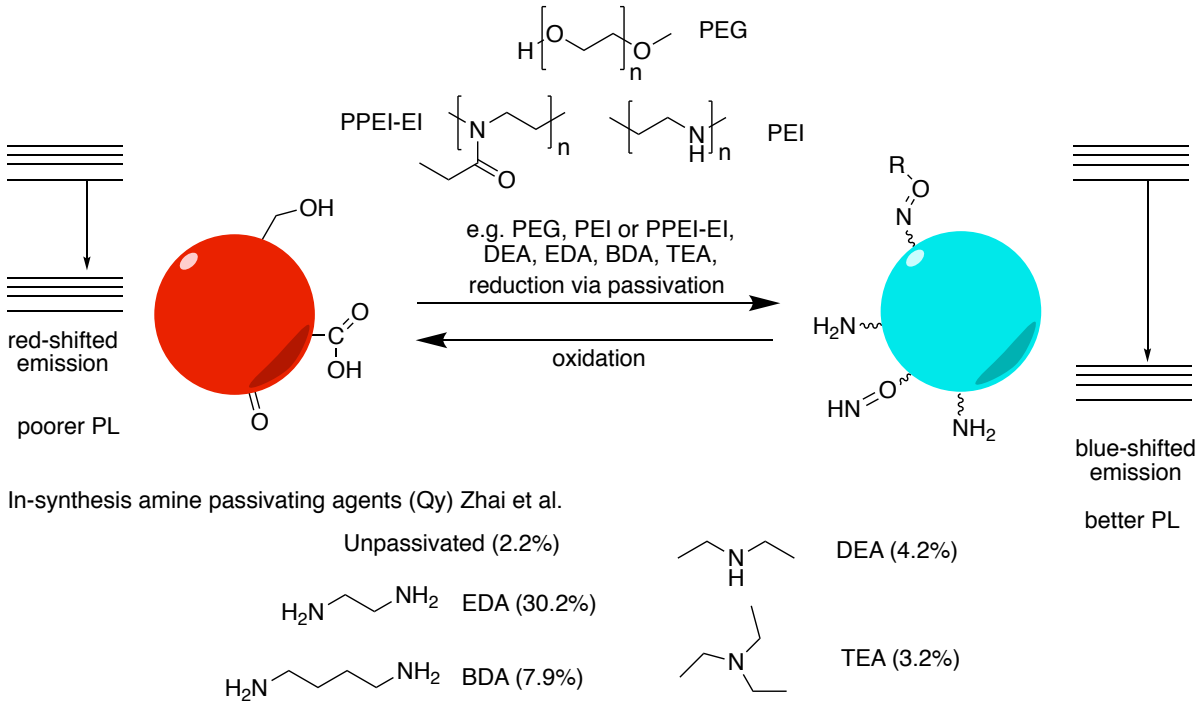

Figure 1.2 Effect of passivating on the photoluminescence (PL) profile of carbon dots. Passivating agents include PEG, PEI and PPEI-EI as well as other small amine containing molecules. Zhai et al.[71] show that primary amine EDA improved the QY of unpassivated CDs from 2.2 % to 30.2 % whilst secondary amine DEA and tertiary amine TEA only improve the QY to 4.2 % and 3.2 % respectively.[71]

1.4.2.5 Doping carbon dots changes the photoluminescence properties

Doping is another one step way to modify CD properties. Doping allows for PL tuning based on the electronegativity of the atom incorporated and the introduction of new bands in the energy gap. Electron withdrawing elements (high electronegativity) such as S, N, Cl and F blue-shift the PL profile as they introduce lower energy bands, n-type doping. Whilst electron donating elements (low electronegativity) such as Se, B, Cu and Co confer more red-shifted emission introducing higher energy bands, p-type doping. This doping effect can influence the surface electronics of surface groups or the sp^2 or sp^3 hybridised core therefore affecting the PL irrespective of its origin.

It has been reported that N and B (heteroatom) doping of GCDs show a blue and red PL shift respectively compared to undoped GCDs.[72] Core sp^2 regions confer a $\pi - \pi^*$ transition in an excitation independent manner, however, N or B doping introduce n $- \pi^*$ transitions which introduce a lower energy levels and therefore an excitation dependent PL peak. Generally speaking, electron rich nitrogen typically induces a blue-shift on the CD, while electron poor boron tends to cause a red-shift. However, this is not always the case. Another example describing the synthesis of yellow fluorescent carbon dots employs F, S (electron withdrawing) and Se (electron donating) as doping agents.[73] In the synthesis of these CDs, Poly(o-phenylenediamine) was combined with either potassium hydrogen difluoride (KHF_2), sodium hydrosulfide or sodium hydroselenide in a hydrothermal synthesis at 180 ^{O}C for 12 hrs. Resulting CDs had fluorescence peak maxima at 411 nm (λ_{ex} 362 nm), 530 nm (λ_{ex} 483 nm) and 594 nm (λ_{ex} 541 nm) respectively whilst undoped was at 570 nm (λ_{ex} 521 nm). Selenium red-shifted the undoped fluorescence peak whilst fluorine blue-shifted to a greater degree than sulfur showing that doping can be tuned to a certain degree based on the known electron properties of the dopant properties[73].

Nitrogen is one of the most commonly used doping agents for carbon dot as it can be easily incorporated from a range of starting materials found in nature such as carbohydrates and amino acids and thought to be inherently non-toxic. It is also of a similar atomic size to and has good valency with carbon meaning for a good doping agent. Trialling a number of amino acids Yang *et al.*[74] observed that temperature during synthesis played a role in incorporation of nitrogen into the CD. A single starting material, the amino acid of choice was used in a hydrothermal synthesis at 180 ^{O}C before dialysis purification. At longer times, up to 6 hrs, more nitrogen was incorporated seen through FTIR amide peaks and I (1700 cm^{-1}) and II (1580 cm^{-1}) forming as a result of carbonisation and polymerisation. XPS also showed the nitrogen percentage content increased to 13.67% with temperature and time. After 18 h complete carbonisation was observed. Interestingly, varying the reaction time allowed for the degree of passivation to be tuned also. They propose that the amino acids polymerise in the reaction and these longer molecules can act as the passivating coating as seen in other syntheses with TTDDA and PEG. The degree of passivation is seen to be greater for a shorter reaction time of 3 hrs, and decreases up to 6 hr reaction time when the peptide carbonises. Passivation is attributed to the amine and oxygen containing groups in protein[74].

Simultaneous co-doping with groups of varying electron withdrawing ability such as N and S respectively, can be achieved. Qu *et al.*[75] carried out a solvothermal synthesis from citric acid and N

and S containing thiourea. They achieved CDs with 3 PL peaks at 340 nm, 440 nm and 540 nm which can be attributed to the N-doped and S-doped verses undoped influence on the PL profile. Furthermore, they observed an increased QY effect suggesting a passivation role of the dopants due to the introduction of new energy bands.[75]

Red-shifting the PL profile of CDs has been shown to be, paradoxically, possible through fluorine doping. The electron-withdrawing property of fluorine is known to induce fluorescence red-shift in polyconjugate sp^2 systems. Work by Yang *et al.*[76] achieved this with CDs synthesised through microwave synthesis from citric acid, urea and sodium fluoride. They suggest the basis for this effect is that fluorine doping is extended to expand the conjugate system and also to include the surface electronic states. This larger sp^2 conjugate system has lower energy levels explaining the red-shifted fluorescence. This is evidenced by an increase in the $\pi - \pi^*$ transition peak in the absorbance spectra at ~220 nm and XPS confirming fluorine incorporation in the CD. Hence, the doping effect must be considered in the context of the CD structure i.e. sp^2 core, alongside the intrinsic dopant properties.[76]

Mondal *et al.*[77] studied the effect of Boron B and Phosphorus P doping in relation to already nitrogen doped carbon dots. These carbon dots were synthesised from a 1:1:1 of citric acid and EDA at 1:4. A bathochromic shift is seen in the emission spectra of both B and P doped nitrogen containing carbon dots at 340 nm and 420 nm which corresponds to possibly two fluorescence centres causing dual fluorescence. This provides more evidence that both fluorescence centre resulting from sp^2 core and surface states are affected simultaneously by the same dopant. Interestingly the quantum yield is reduced upon B and P doping from 95% and 11% for nitrogen only carbon dots, to 63% and 9% for B and 63% and 6% P doped versions at 340 nm and 420 nm emission respectively. The reduced QY they attribute to increased trapped states from the dopants rather than more emissive levels relieving trapped states. Hence, the relationship between dopant and passivation is not always clear cut. Worth noting from this work is the high QY possible in carbon dots within the blue region of the visible spectrum.[77]

1.4.2.4 Molecular fluorophores on carbon dots

During bottom up CD syntheses, small fluorescent molecules can be generated which are then incorporated into the CD structure through carbonisation. If the molecule is not broken down or covalently attached to the surface, as in passivation as described earlier, they may associate onto the CD as well as be free within the product mixture (which persist despite certain purification techniques such as dialysis and centrifuge filtration). These molecules usually form in the initial reaction step at lower temperatures (~180 ^{O}C), before the carbonisation at higher temperatures (300-400 ^{O}C) where the carbon dot core forms. As a result, the CD PL profile can result from the combined contribution of the small fluorescent molecule and the CD itself[78].

This effect was first observed by Krysmann *et al.*[79] where they found that at lower reaction temperatures only a small molecule was made and upon temperature increase CD was formed and became the main reaction component. Citric acid (CA) and ethanolamine (EA) were combined in a pyrolysis reaction for 30 minutes. At the lowest temperature of 180 ^{O}C, the excitation independent PL profile emission peak of 455 nm was attributed to a fluorophore termed PL-CNP180, this was generated during synthesis whilst no nanoparticle (by DLS and TEM) was generated. When the reaction temperature was increased to 230 ^{O}C, a CD was generated named CNP230, which showed a new excitation dependent PL feature red-shifted (ex > 400 nm) in relation to the PL-CNP180 peak. This new PL peak was found to be from the core of the new CD. Hence, this system was seen to exhibit dual fluorescence. At the highest temperature of 300 ^{O}C, the CD was the main component seen through XPS (carbon content increase), TEM, FTIR and the second luminescence peak when excitation > 400 nm (excitation dependent) is the main feature. At 400 ^{O}C full carbonisation predominated hence no fluorophore was observed[79].

These results were confirmed by direct heating of CNP180 at 300 ^{O}C which under the same conditions afforded the same material as the original synthesis. They also conducted the reaction between CA and EA under hydrothermal conditions at 140 ^{O}C which yielded the same products (Figure 1.12). Hence, different from doping, the dual fluorescence is a result of two PL centres which are independent of each other.

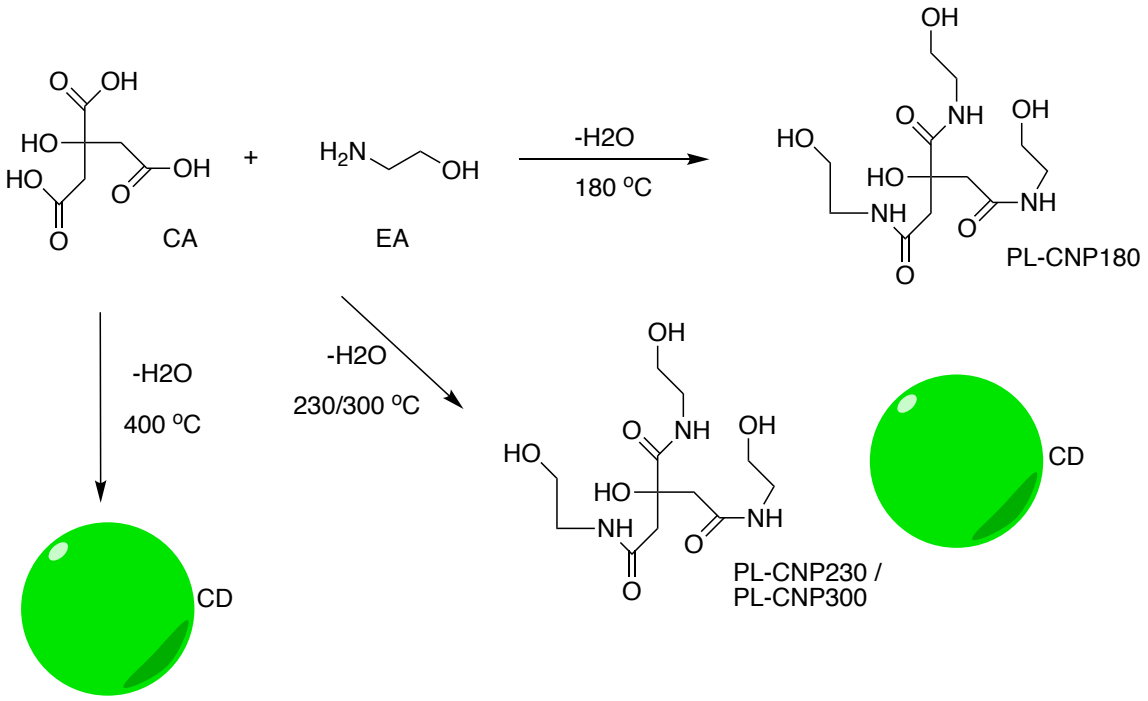

Figure 1.12 Molecular fluorophore generation during a pyrolysis carbon dot synthesis by Krysmann et al.[79] was temperature dependent from the starting materials citric acid (CA) and ethanolamine (EA). At 180 °C only fluorophore was generated (PL-CNP180). At 230 °C and 300 °C fluorophore and carbon dot were generated. At 400 °C only carbon dot was generated.[79]

Similarly, Song *et al.*[80] observed very similar temperature effects when using citric acid (CA) and ethylenediamine (EDA) in a 4:1 mmol ratio employing a hydrothermal process. In their report, small aromatic fluorophores were produced at lower temperatures 100-200 °C. Separation of the major component, imidazo[1,2-*a*]pyridine-7-carboxylic acid, 1,2,3,5-tetrahydro-5-oxo- (IPCA) from the CD using silica gel column chromatography allowed for the PL profiles of IPCA and CD core to be investigated in isolation. IPCA had excitation independent emission and a high QY of 36%. They appreciate that complete purification of IPCA from the CD core is not possible hence the core was synthesised from heating CA at 200 °C. The obtained CD showed excitation dependent PL and was weakly blue-fluorescent with lower than 1% QY. Comparing CD cores synthesised both ways showed the same characteristics hence it was suggested that CA forms the CD core. It is well known that CA forms large conjugate systems through dehydration upon heating which is the basis for CD structure and sp^2 conjugate fluorescence. Et-EDA and Ac-EDA are two variants on EDA which contain an ethyl group and an acetyl group respectively which when substituted for EDA in the synthesis, derive molecules which are variants of IPCA with the respective functional group attached. This confirms that EDA and CA are the precursor for IPCA and tuning of the small molecule generated is possible[80].

Interestingly, oligomers of IPCA were fractionated during separation suggesting polymerisation occurs from IPCA (in this context considered a dimer) which can then either carbonise or they propose become crosslinked at the surface of the CD core. Crosslinking of polymers is referenced in other CD

syntheses containing polymers as the starting material, and if retained post synthesis to infer crosslink enhanced emission (CEE) on CDs. Crosslinked polymer CD cores are different from conjugated centres as they are aggregated structures. The amine-based PL centres of the polymer when restricted in vibration and rotation due to crosslinking, promote radiative exciton recombination and hence, improved PL is a known effect.[81]

The difference between molecular state fluorescence or CEE and passivation or doping, is that the PL centre originates from the fluorophore in isolation to the CD which can have its own PL centre. Hence, doping and passivation are not features seen in any of the materials described in this section. This is supported by the fact red-shifting of fluorescence is not seen as would be for doping and QY does not improve with a greater degree of polymeric content which would be the case in passivation.

Furthermore, fluorescence lifetimes were determined for the fractions post separation. Each fraction contained two decay lifetimes which were identified as from the IPCA molecule and the CD core. Having determined that later factions contained more CD core and earlier fractions contained more IPCA, they correlated the average lifetime of the mixture increasing with each sequential fraction as a result of the increased CD core content. Similar lifetime experiments were conducted by Schneider *et al.*[82] who used the known molecular lifetimes to distinguish between cursory fluorophores made during CD syntheses hydrothermally from different starting material mixtures all with citric acid (5.5 mmol) in common. Either ethylenediamine, hexamethylenetetramine or triethanolamine were added (5 mmol) which afforded e-CDs, h-CDs and tCDs respectively. E-, and h-CDs syntheses generated surface fluorophores IPCA as with Song *et al.*[80] and citrazinic acid respectively whilst tCDs only generated the CD core. They were able to observe lifetimes from the CD surface states were influenced by the fluorophore generated in the synthesis by comparing with CD when no surface fluorophore is present.[82]

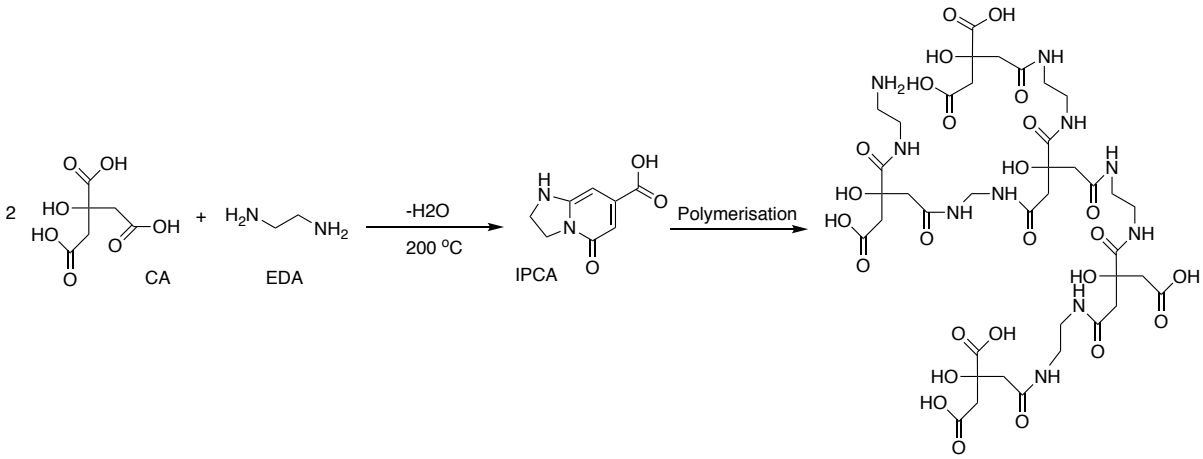

Figure 1.3 Polymerisation of IPCA generated from citric acid (CA) and ethylenediamine (EDA) generated during carbon dot synthesis, seen by Song et al. Subsequent crosslinking of these polymers on the surface of carbon dots have been shown to exhibit a crosslink enhanced emission (CEE) effect. [80]

1.5 Thesis aims

The aim of this work is to develop a novel carbohydrate-based cancer cell targeting nanoplatform which can be used for diagnosis and for drug delivery. Well studied changes associated with cancer commonly target protein transcription up or down regulation, caused by increased cellular growth and division and cell membrane remodelling. One other facet of the cell membrane is the glycocalyx. This highly dense multifunctional carbohydrate layer adopts changes which promote cancer cell invasion and metastasis. Hence, identifying and targeting these glycan interactions is one route to achieving successful tumour targeting. Targeted treatment leads to improved drug efficacy and selectivity which should lead to fewer associated treatment side-effects.

Understanding carbohydrate multivalent binding by their protein receptors called lectins, is important for developing specific targeting technology. Studying these interactions using synthetic probes and in isolation from the complete cell allows these interactions to be measured independently and should provide a fundamental understanding. Towards this goal, we proposed to use nanoscale particles for glycan presentation. We aim to develop and evaluate carbon dots, a fluorescent and non-toxic nanoscale particle, to probe carbohydrate lectin interactions. Utilising their photoluminescence properties, we aim to develop a FRET assay to investigate lectin binding interactions.

Full characterisation of glyconanoparticles must be conducted when developing a novel carbon dot-based FRET assay to measure the binding affinity of carbohydrate lectin interactions. Structural and spectral information on the glyconanoparticles inform the parameters of the FRET assay and must also be considered when interpreting the data. First developing the assay using lectins with known binding specificity with the aim to apply this to less well studied lectins and novel carbohydrates. Through using a nanoparticle, the multivalency exhibited in nature will be mimicked and provide a reasonable approximation of binding information Glycan-coated quantum dot nanoparticles have been shown in previous work within the Galan group by Benito-Alifonso *et al.*[44] to act as a targeting moiety specifically for cancer cells. Hence, we aim to work towards a non-toxic version for drug delivery. The non-toxic nature of the carbon dots thus offers the possibility of future *in vivo* application, which we aim to explore for drug delivery purposes and for photothermal therapy applications for anti-cancer treatments.

2. Carbon dot synthesis for glycan presentation

2.1 Aims

The work described in this chapter is aimed at developing novel carbon-based glyconanoparticles for biological applications. Functionalisation with several carbohydrates of interest was carried out, and full characterisation of the novel materials conducted. Little is known of the carbohydrate presentation on these nanoparticles, to that end novel structural information was obtained to inform an updated model of our glyconanoparticles. Specifically, carbohydrate valency, conjugation and organisation on the carbon dot surface were investigated. This work was conducted with consideration of how these carbohydrates are presented for multivalent binding with lectin proteins, specifically the lectin Concanavalin A which binds terminal mannose.

The carbon dots synthesised and functionalised were characterised using common nanoparticle analytical techniques including dynamic light scattering (DLS), zeta potential, several spectroscopic techniques (such as fluorescence and UV-Visible spectroscopy), transmission electron microscopy (TEM), atomic force microscopy (AFM). The materials were also characterised by techniques commonly used for carbohydrate analysis including nuclear magnetic resonance (NMR) and the Molisch's test. This information was used to infer novel structural information on the glycan carbon dots synthesised and was also used to inform binding studies with Concanavalin A and Sambucus nigra Lectin in chapter 4.

2.2 Results

2.2.1 Synthesis

Carbon dots were synthesised according to a protocol developed in the Galan group using carbohydrate based starting material glucosamine.HCl with a passivating agent, in a carbonisation reaction.[46,83] It has been shown that carbohydrate density on the carbon dot surface can be controlled by the length and functionality of linker used.[44] Hence, two variants of this carbon dot were synthesised using two different types of linkers, an amino acid based-one and a PEG-containing chain. The two CD syntheses were conducted according to a protocol developed by Hill *et al.*[46] in the group. "Short linker" CD synthesis involved the microwave-assisted thermolysis of β-alanine and glucosamine.HCl which afforded acid terminated CDs termed "AcCDala" **10** and could be directly functionalised by 1-aminoglycans **1-8** in an EDC coupling reaction[84]. The "Long linker" CD synthesis employed 4,7,10-Trioxa-1,13-tridecanediamine (TTDDA) in the microwave reaction with

glucoseamine.HCl to afford CDs termed "AmCD" **16** with a long TTDDA, amine terminated group on the surface. **16** could then be further functionalised with succinic acid to introduce acid groups and undergo the same EDC coupling with 1-aminoglycans **1-8** [85]. In each case NMR allowed for the confirmation of conjugation. These two materials were characterised at each step using a number of techniques and the glycan presentation investigated.

2.2.1.1 Long linker Carbon Dot synthesis - AcCDs **17**

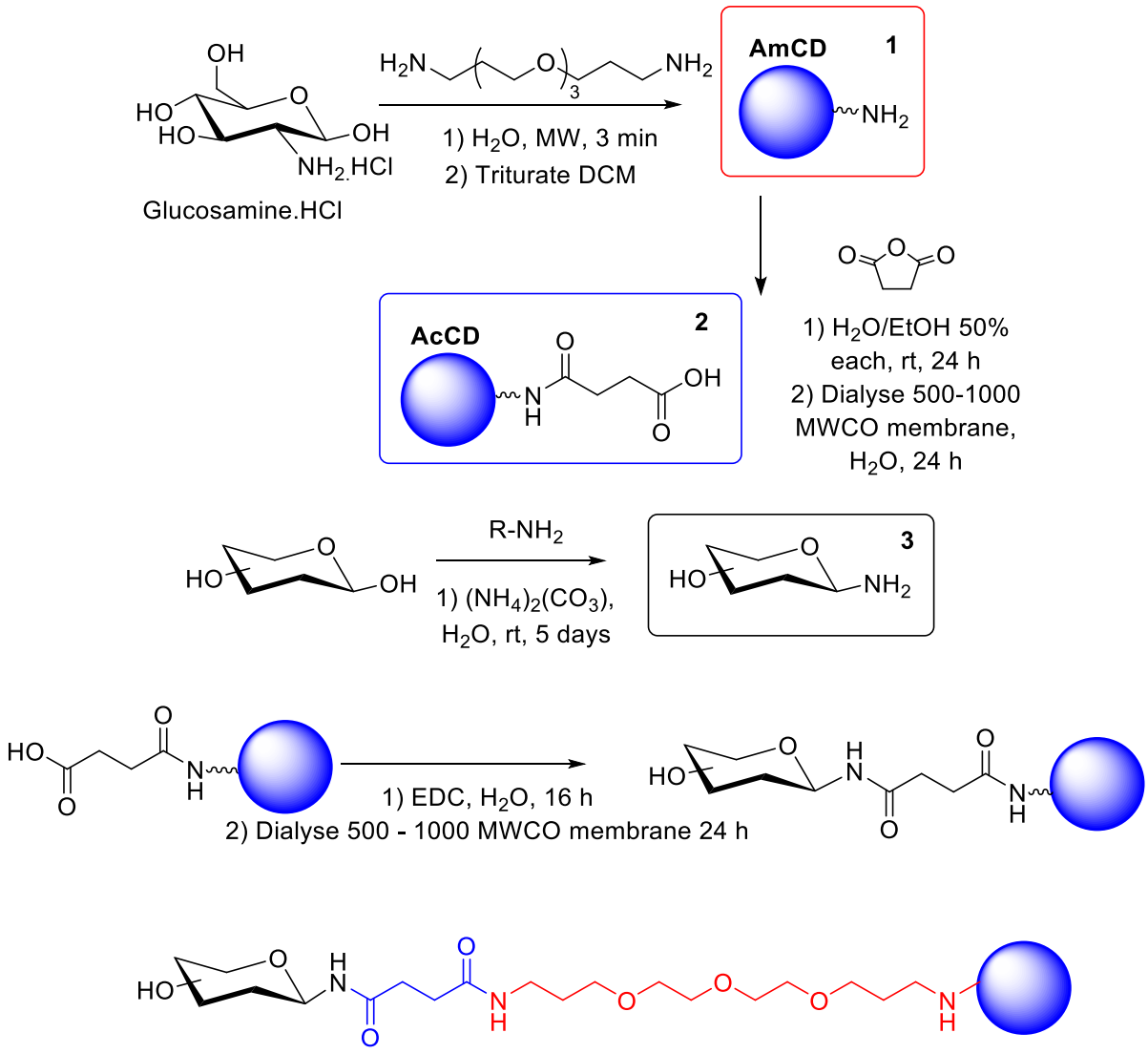

Figure 2.1 Synthesis scheme of AmCD to AcCD "long linker" carbon dots and glycan functionalisation.

Blue-fluorescent carbon dots were synthesised from glucosamine.HCl and TTDDA starting materials in a 3-minute domestic microwave synthesis on a gram scale following a modified reported procedure.[46] Carbohydrates was chosen as a precursor molecule for carbon dot synthesis due to their availability and low cost combined with their inherent biocompatibility making them non-toxic materials. Glucosamine.HCl ($GluNH_2$.HCl) contains an amine group which has the potential to act as a doping

agent in addition to the two primary amine groups in TTDDA included here. Literature evidence for the passivating ability of TTDDA supports the inclusion of TTDDA for achieving a material with good QY as well as providing a linker for subsequent biomolecule conjugation.

Starting from $GluNH_2.HCl$ (0.24 M) and TTDDA (1.1 equiv.) in 20 ml H_2O, microwave-thermolysis (800W, 80% power) was conducted. The microwave time had been optimised to 3 minutes where an oil like dark brown fluorescent (under UV light) material was afforded which was soluble in water.[46] The material was purified using spin centrifugation through a cellulose membrane (10,000 MWCO was initially used), before dialysis on a cellulose membrane 1,000 MWCO in H_2O was conducted over 16 hrs. Extraction of the CDs with DCM and H_2O was conducted to separate material generated which was not water soluble from the water soluble CDs. The final material termed AmCD **16** was freeze dried before further use.

AmCD **16** was functionalised with succinic anhydride 1:1 mass equivalents in a ring opening reaction to convert these amine terminated CDs to acid terminated CDs to form AcCD **17.**

2.2.1.2 Short linker carbon dot synthesis – AcCDala **10**

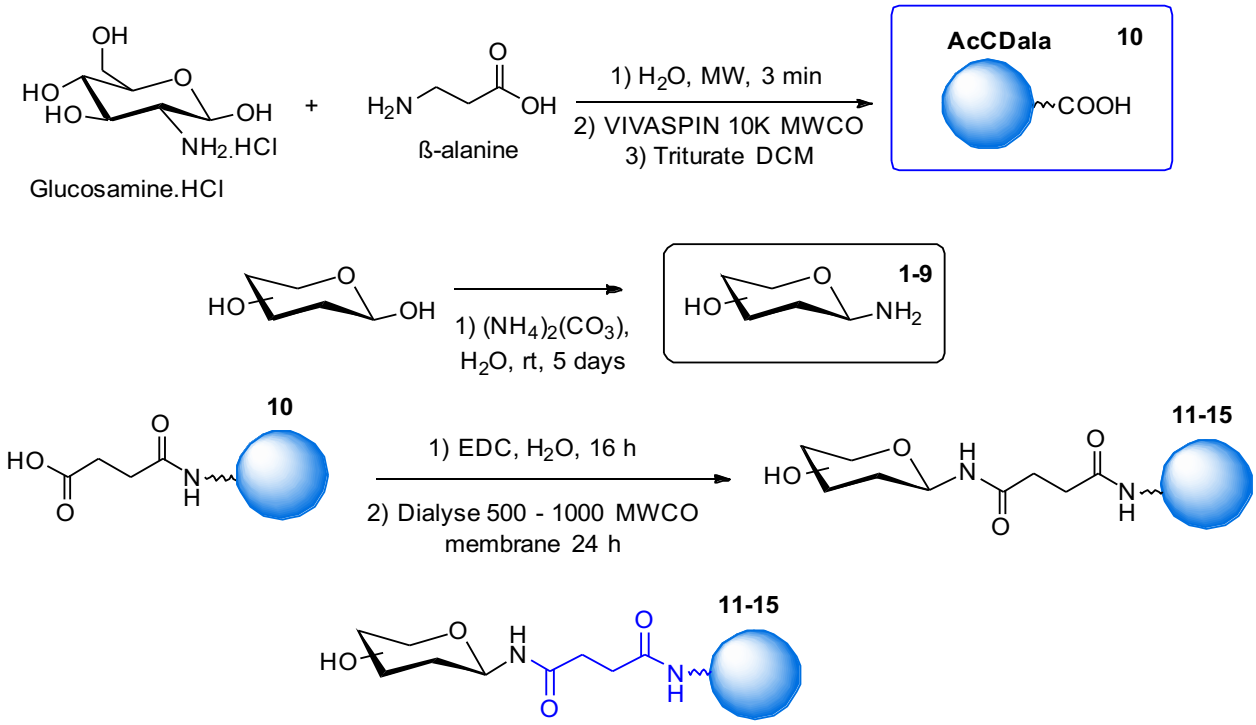

Figure 2.2 Synthesis and glycan functionalisation scheme of AcCDala "short linker" carbon dots.

A second blue-fluorescent carbon dot was synthesised from glucosamine.HCl and amino acid β-alanine in a 3-minute domestic microwave synthesis on a gram scale following reported procedures.[83] The β-alanine was included in the synthesis as a means to directly introduce an acid functional group at the surface of the CDs. It was also reported that following this method higher biomolecule functionalization could be achieved as the CD appears to bear more acid groups on the surface when compared to acid-coated AmCD **16**. In brief, sugar and amino acid reagents were microwaved at 800W in a domestic microwave at 80% power for 3 minutes. Purification involved H_2O/DCM extraction as with the previous CDs followed by further purification using a 10,000 Da MWCO Vivaspin20 for 10 minutes at 8,000 rpm to yield **10**.

2.2.1.3 Kochetkov amination

Both AcCDala **10** and AcCD **17** were functionalised with 1-aminoglycans **1-8** which had been synthesised from starting carbohydrates: β-D-galactose, β-D-lactose, β-D-glucose, β-D-maltose, β-D-mannose, 3,6-Di-*O*-(α-D-mannopyranosyl)-D-mannopyranose, 4-*O*-(α-D-Mannopyranosyl)-D-mannopyranose and β-D-Mannopyranose-(1—4)-β-D-mannopyranose-(1—4)-β-D-mannopyranose in a Kochetkov amination reaction. This was carried out on a 10 g scale (5g scale for disaccharides) over 5 days at room temperature in a saturated ammonium carbonate solution in H_2O (1% w/v) to afford 70-84 % yields, as shown in table 2.1. Data for **1-5** are shown in table 2.1. For mannose disaccharide and trisaccharides **6,7 & 8** calculating the yield was not appropriate as a number of side products which were not distinguishable from starting material or product were generated. It was hypothesized that only 1-aminoglycosides would react with the acid functionality on the CDs and thus we decide to look at the carbohydrate remaining post conjugation and purification to carbon dot. Aminated saccharides were lyophilised before storage at -4°C until use.

1-aminoglycan starting carbohydrate	% Yield
Galactose	70
Glucose	76
Lactose	74
Maltose	75
Mannose	84

Table 2.1 Kochetkov amination reaction percentage yield as determined through NMR.

Literature showed that a number of aminated products could result in this reaction alongside the desired glycosylamine. These include the glycosyl ammonium carbonate salt, the dimer di-glycosylamine or the glycosyl carbamate which can exist as either the α or β conformations[86]. Coupling

with the carboxylic acid handle on the carbon dot can occur with any of the glycosyl amine, the glycosyl ammonium carbonate salt or the dimer di-glycosylamine. The % yield in table 2.1 is the calculated % glycosylamine calculated from the total starting carbohydrate anomeric and the glycosylamine anomeric integration in NMR. According to these % yields, the amount of **1-5** used in the conjugation was modulated.

2.2.1.4 Carbohydrate conjugation

In the Kochetkov amination, in all di and tri- mannose cases **6,7 & 8** there was an amide peak in the anomeric region for the conjugated carbohydrate which matched literature for general glycosylamide formation. Hence, modulation of these before conjugation was not possible. This was seen in the ^{13}C NMR as a peak between 70-82 ppm smaller than that observed from unconjugated carbohydrate anomeric peaks which came between 105-82 ppm.

In order to glycan functionalise CDs, AcCD **17** was reacted with 1-aminoglycans **1-8,** 200 mg aminated monosaccharide (400 mg disaccharide, 600 mg disaccharide) in an EDC coupling reaction in 3 ml H_2O having calculated the moles of acid handles available to react. In this reaction steric effects are most likely to be the limiting factor in conjugation. Unconjugated saccharide was removed through dialysis 500-1000 MWCO membrane and NMR was used to confirm conjugation.

For sialyllactose carbohydrates which contain a carboxylic acid, reductive amination with sodium cyanoborohydride was used to functionalise AmCDs **16** on a 10 mg scale for 3 hours to afford **26** & **27**. Purification was carried out by the same dialysis method but using a 5000 Da MWCO membrane.

2.2.2 Characterisation

2.2.2.1 NMR carbon dot characterisation

NMR spectroscopy was used to characterise the synthesised carbon dots at each stage of synthesis and conjugation. NMR provides information on the surface chemistry of the carbon dot, which is useful for observing subsequent conjugation steps. It can be used to quantify the presence of different chemical moieties. D_2O was used as the solvent owing to the good water solubility of carbon dots. Proton (^1H), carbon (^{13}C) and Heteronuclear single quantum coherence (HSQC) NMR was conducted as detailed to characterise carbon dots. Glycan carbon dots synthesised within this work (Figure 2.1 and 2.2) were characterised by NMR and are presented in Figures A.11-A.15 of the appendix, for AcCDala **10** and A.18-A.27 for AcCD **17** in the experimental section.

Figure 2.3 shows the ^{1}H spectra of AmCD **16** post purification. The characteristic peaks of the TTDDA linker are observed in the region between 1.83 – 3.60 ppm. Aromatic features at 8.50 ppm are observed reflecting the presence of aromatic groups at the surface which were generated during the synthesis carbonisation process. Upon acid functionalisation with succinic anhydride two notable things occur in the ^{1}H NMR spectra (Figure 2.4). Triplets corresponding to the methylene groups of succinic anhydride are seen at 2.38 ppm and 2.53 ppm and also the desymmetrisation of TTDDA occurs confirming conjugation of both TTDDA and succinic acid. This is seen through new peaks distinguishing the peaks labelled i, b, a & j in figures 2.4 and 2.5. From figure 2.3, b & i are at 1.83 ppm and a & j are at 2.97 ppm. In figure 2.4, upon succinic anhydride conjugation, these split into four peaks: i, 1.62 ppm b, 1.82 ppm, a, 2.89 ppm and j, 3.13 ppm. Peaks associated with carbohydrate ring structure usually seen between 3-4 ppm are not distinguishable, suggesting carbonisation of this structure. However, the disordered region between 3.5-3.6 ppm is a useful region to use as a carbon dot identifier in ^{1}H NMR.

^{1}H NMR of AcCDala **10** is presented in figure 2.5. Identifiable key signals assigned to the methylene triplets from β-alanine were observed at 2.65 ppm and 3.15 ppm. These being distinguishable from each other suggests different environments and hence presentation on the carbon dot surface. Signals between 3.45-3.80 ppm were assigned to the carbon dot and used as an identifier for the presence of AcCDala **10**.

Glycan functionalisation of carbon dots was also supported by ^{1}H NMR. Distinct peaks corresponding to the carbohydrate ring structure between 3.2-4.1 ppm as well as anomeric peaks between 4.0-5.3 ppm specific to each carbohydrate allowed for the identification and in some cases quantification of carbohydrate present (see section 2.4.1.5). HSQC was used to correlate proton and carbons to identify anomeric peaks according to literature where possible. This was dependent on the anomeric peaks not being overlaid with other peaks such as the H_2O peak and the signal being strong enough to be detected.

In many cases despite repeated dialysis, unconjugated carbohydrate and in some cases EDC was observed which appears to be non-covalently attached to the CD surface. Free carbohydrate observed, results from the Kochetkov amination of the 1-aminoglycan being incomplete as well as being hydrolysed in water. According to literature glycosylamide anomeric carbon peaks come between 70-80 ppm[87,88]. For instance, the case for AcCDala **10** and AcCD **17** conjugated with 3,6-di-O-

(α-D-mannopyranosyl)-D-mannopyranose, β- D-mannopyranose-(1—4)-β-D-mannopyranose-(1—4)-β-D-mannopyranose and 4-*O*-(α-D-mannopyranosyl)-D-mannopyranose **11-13** and **18-20**. However, other signals associated to unbound sugars were also observed and unfortunately, for all other CD-carbohydrates no peak corresponding to an amide linked anomeric peak can be seen, which suggests no successful covalent conjugation is likely to have taken place.

For example, figure 2.6 shows the ^{1}H NMR spectra of CDala-1,4-mannotriose **12**. This trisaccharide has six anomeric peaks (one under the H_2O peak) in the anomeric region which correspond to two molecules, one of which is conjugated to the CD and the other free carbohydrate. Using an HSQC (Figure 2.7) to correlate these peaks with their carbons its apparent that the peak at 5.02 ppm correlates to a carbon signal at 71.32 ppm much smaller than usual for unconjugated anomeric peaks which usually come between 105-80 ppm. The other trisaccharide present in this NMR shows no evidence of being conjugated and peaks match those of the carbohydrate starting material identified in Figure A.8 at 5.04 ppm, 4.76 ppm and 4.59 ppm.

The CD-glycans which have non-covalently associated carbohydrate only were investigated further to see if the amide linked carbohydrate has shifted upfield in the ^{1}H NMR to come within the carbohydrate ring peaks between 3.2-4.1 ppm. Glucosyl amide **9** was synthesised and purified by another member of the Galan group. The ^{1}H NMR of this molecule showed an anomeric peak shift to 4.94 ppm from 4.57 ppm for β-D-glucose. Using HSQC NMR the correlated carbon shifted to 79.94 ppm from 83.04 ppm for β-D-glucose. This suggests the signal of the amide should be observed within the anomeric region 4.0-5.3 ppm. However, when comparing the amide coupled glucose anomeric position to when it is carbon dot conjugated this anomeric peak is not visible. This suggests that in the case of glucose, mannose, galactose, maltose and lactose there is no covalent conjugation to the carbon dot **14-15** and **22-25**. We therefore propose that the carbohydrate observed through NMR is electrostatically associated with the carbon dot surface. Figure 2.9 shows the conjugated (solid line) and non-covalently associated (dashed line) structure of CD-carbohydrates which were synthesised using both AcCD **17** and AcCDala **10.**

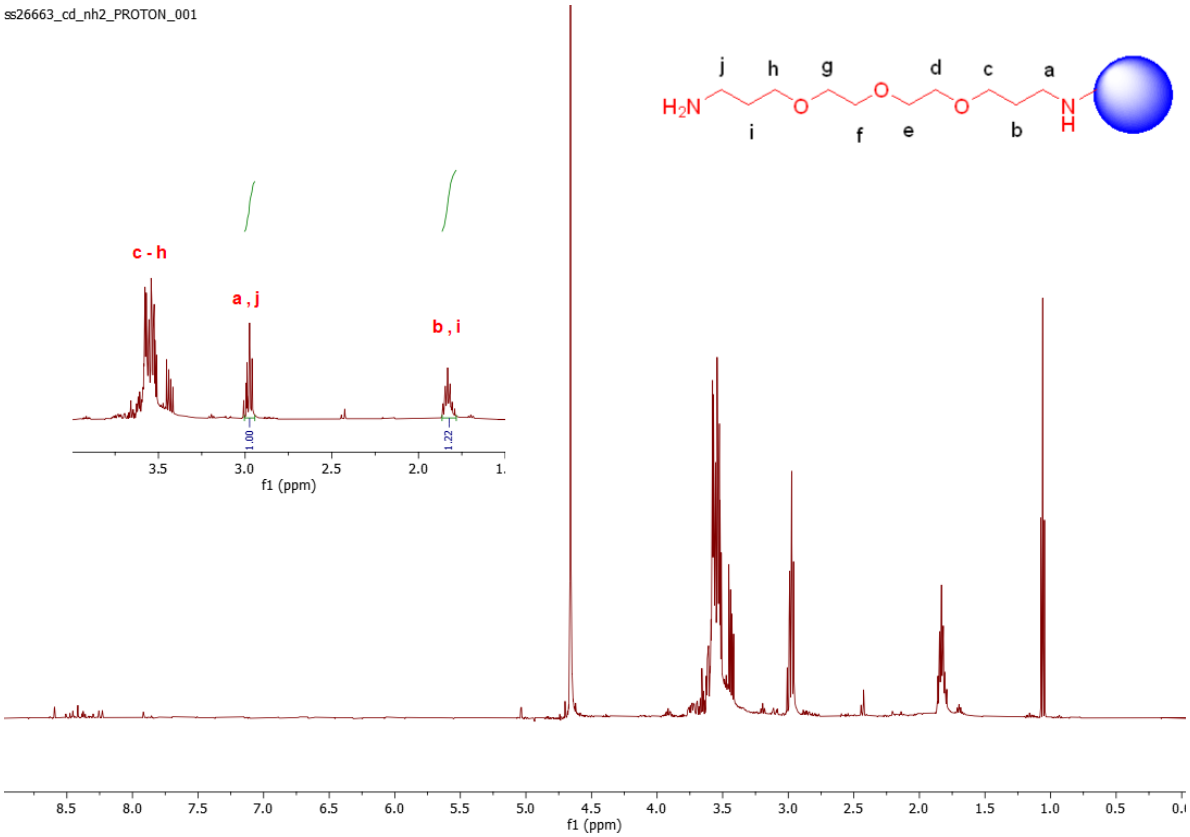

*Figure 2.3 [1]H NMR of **AmCD 16** (500 MHz, D2O): δ = 3.50-3.60 (m, c-h), 2.97 (t, J = 7.2 Hz a,j), 1.83 (q, J = 6.0 Hz, b,i).*

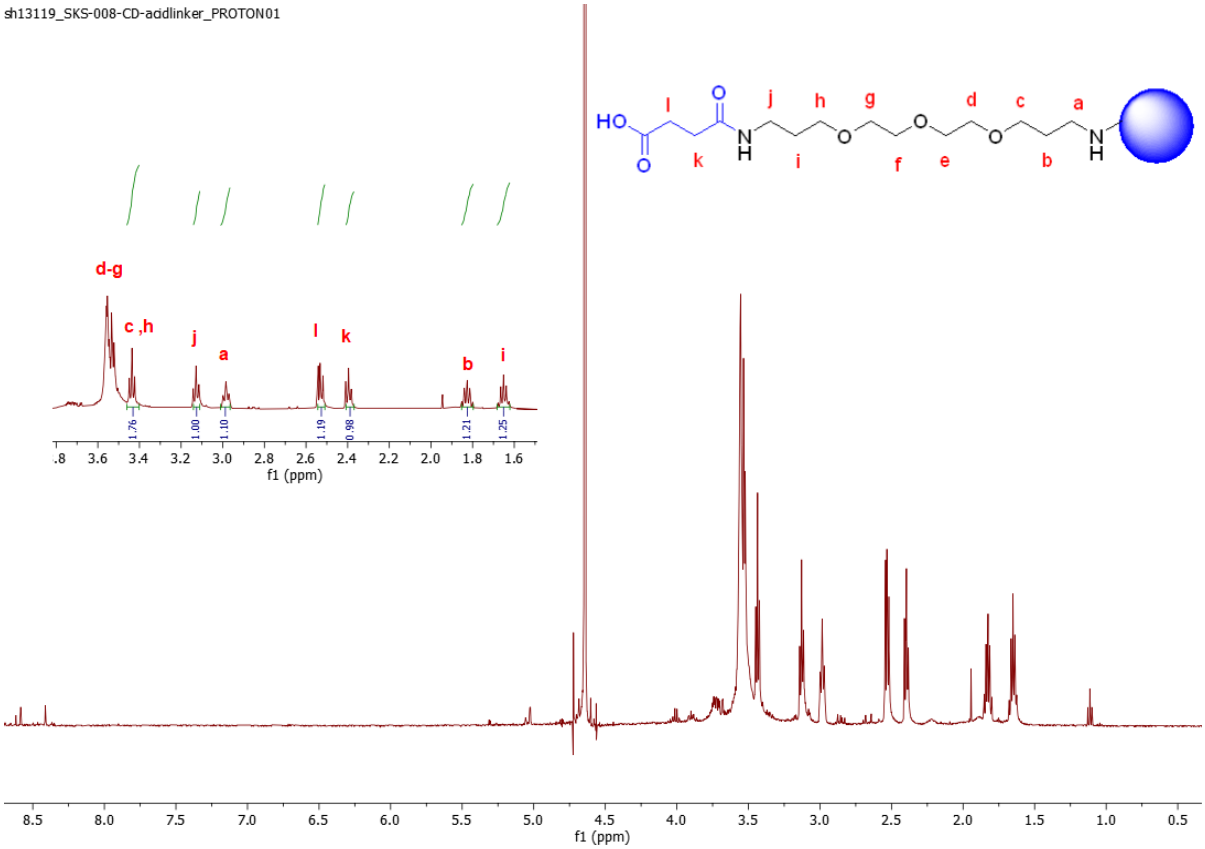

*Figure 2.4 [1]H NMR of **AcCD 17** (500 MHz, D2O): δ = 3.60-3.50 (d-g), 3.45 (t, J =8 Hz, c,h), 3.13 (t, J =8 Hz, j), 2.89 (t, J =8 Hz, a), 2.53 (t, J =8 Hz, l), 2.38 (t, J =8 Hz, k), 1.82 (p, J =8 Hz,b), 1.65 (p, J =8 Hz, i).*

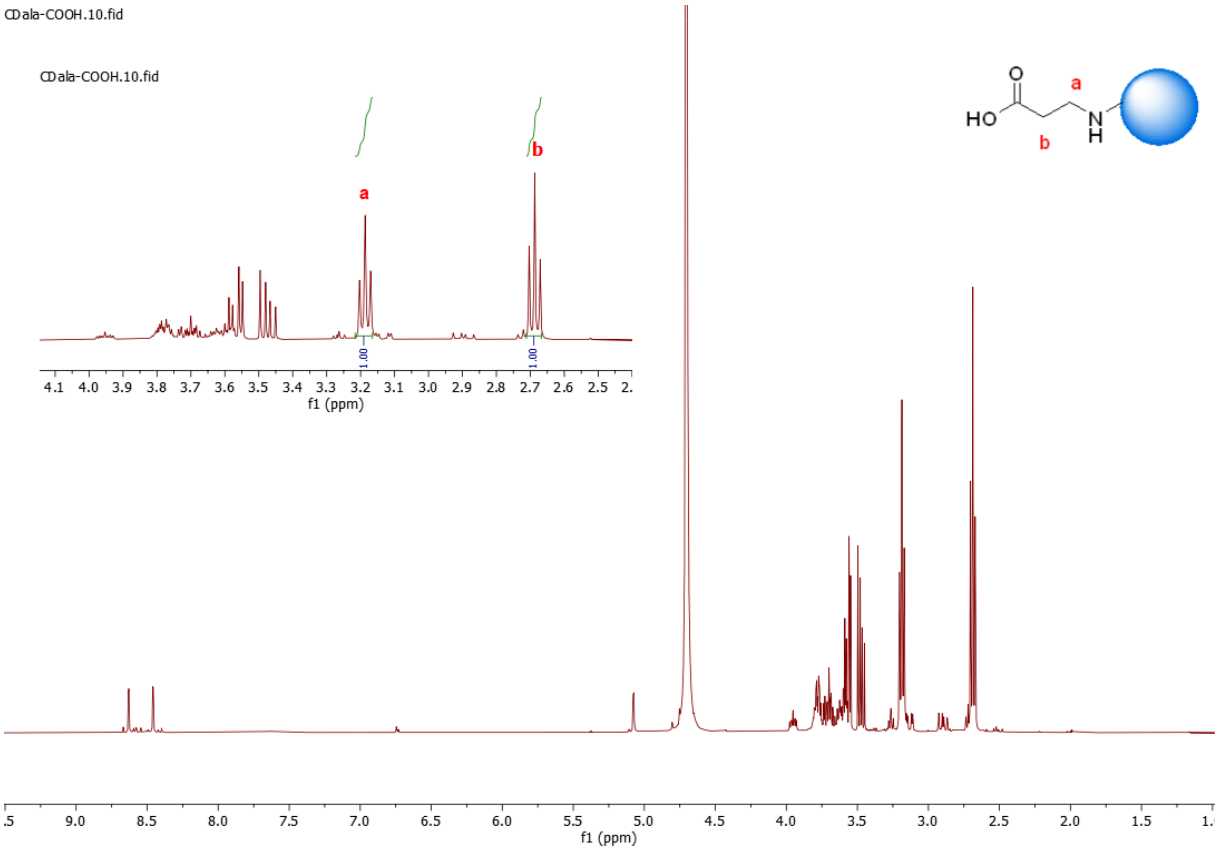

*Figure 2.5 ^{1}H NMR of **AcCDala 10** (400 MHz, D2O): δ = 2.65 (t, 2H, J= 6.5, b) δ = 3.15 (t, 2H, J= 6.5, a)*

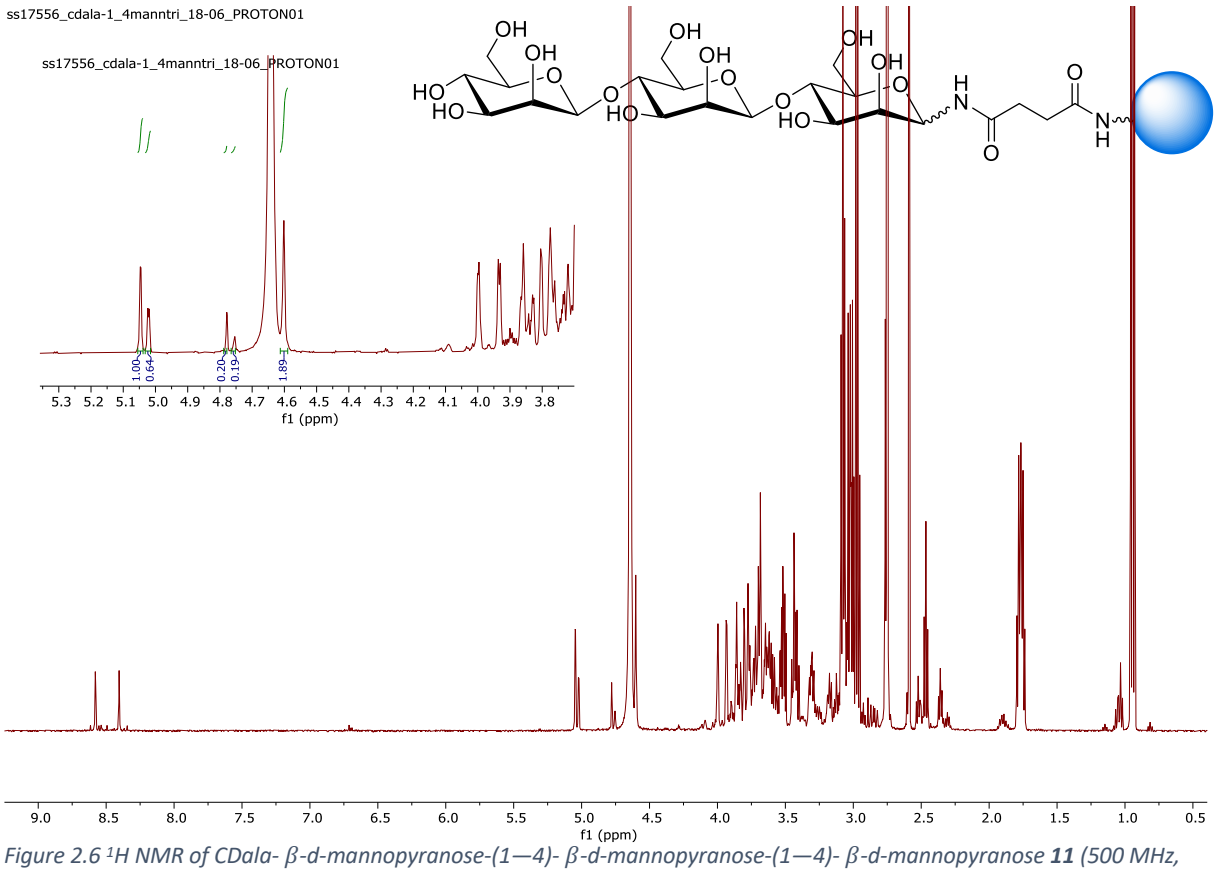

*Figure 2.6 ^{1}H NMR of CDala- β-d-mannopyranose-(1—4)- β-d-mannopyranose-(1—4)- β-d-mannopyranose **11** (500 MHz, D2O): δ = 4.60 (s, 1H), 4.63 (1H, H1), 4.75 (s, 1H), 4.78 (d, J = 0.9 Hz, 1H), 5.02 (d, J = 2.3 Hz, 1H), 5.05 (d, J = 1.5 Hz, 1H)*

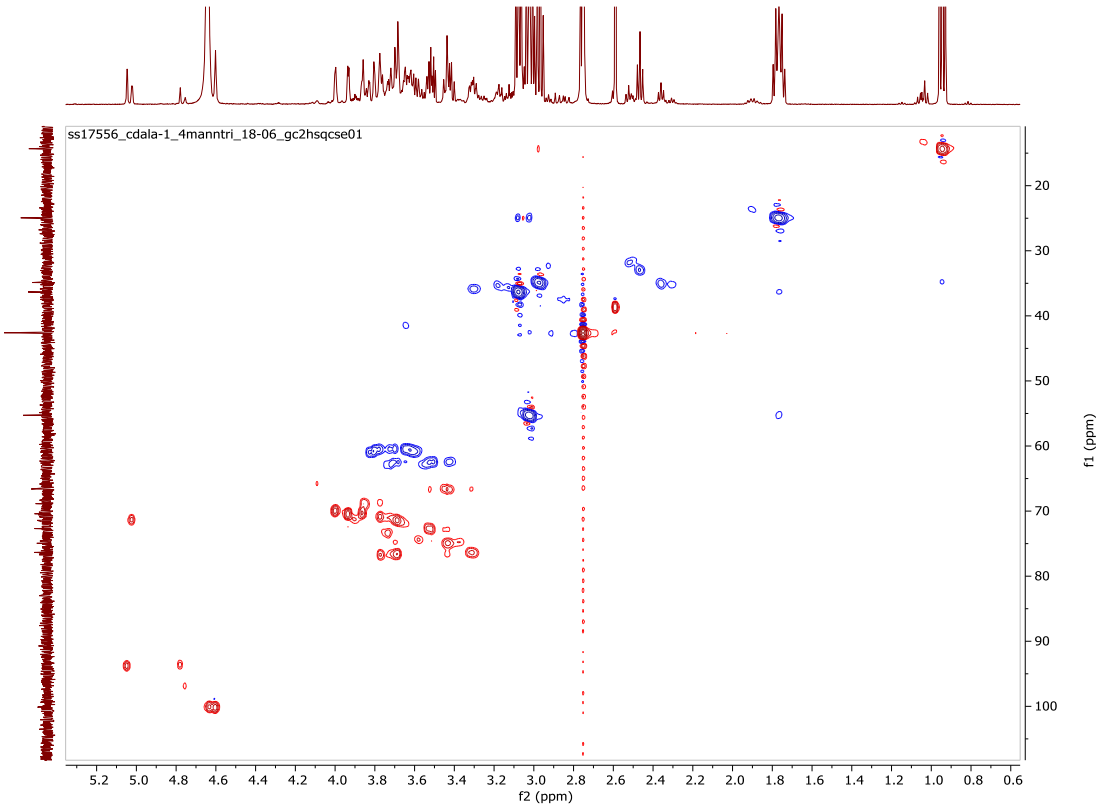

*Figure 2.7 HSQC NMR of CDala-β-d-mannopyranose-(1—4)- β-d-mannopyranose-(1—4)- β-d-mannopyranose **11** (126 MHz, D20): δ = 93.77, 71.32, 93.68, 96.88, 100.06, 100.12 ppm*

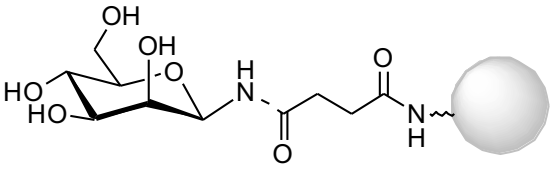

15 & 22
CD-mannose

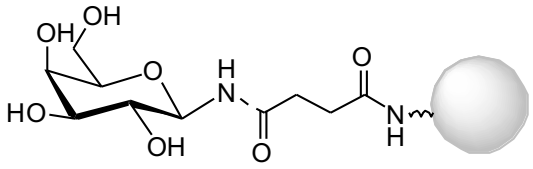

14 & 21
CD-galactose

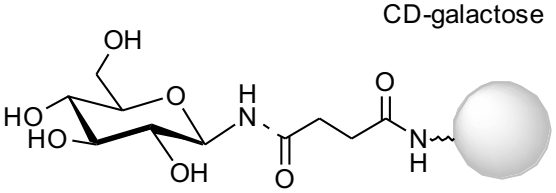

24
CD-glucose

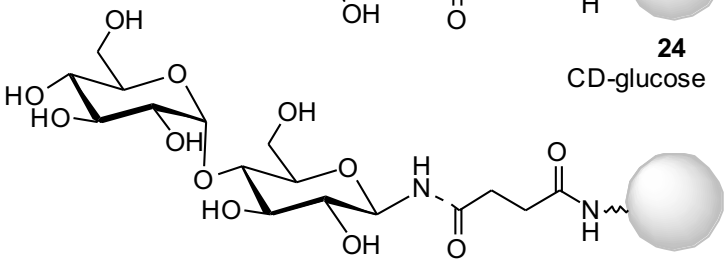

23
CD-maltose

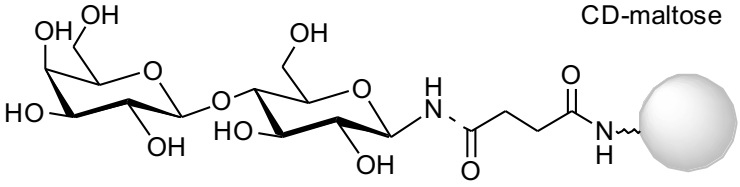

25
CD-lactose

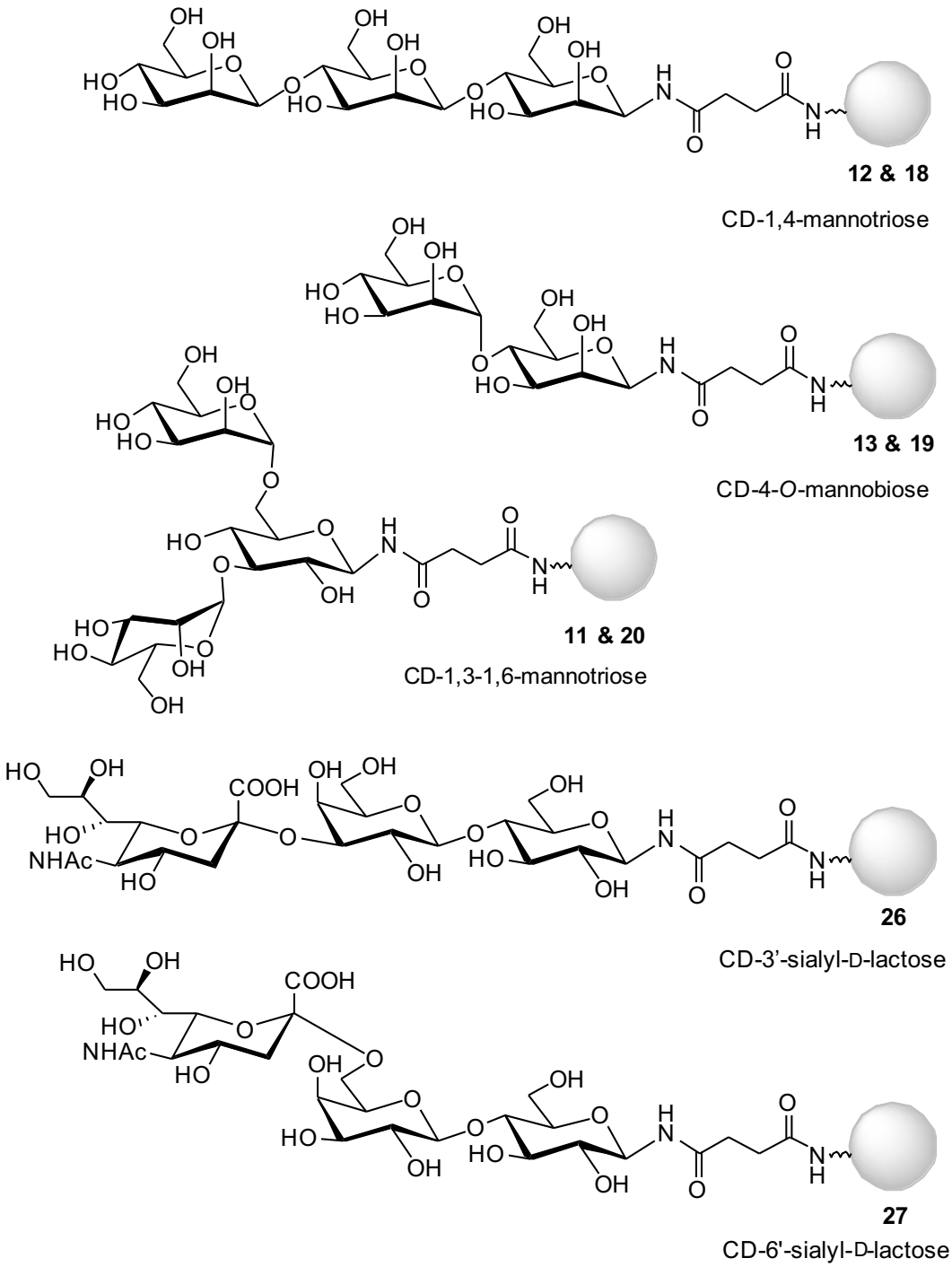

*Figure 2.9 Scheme of synthesised glycan functionalised carbon dots. Both CD-carbohydrate number and shortened name are included and used henceforth. Grey colour references that glyco carbon dots can be synthesised with both short and long linker CDs. Where two numbers are written the smaller number refers to AcCDala **10** syntheses and the larger refers to the AcCD synthesis. Dotted line refers to lack of amide linkage seen in NMR; hence covalent linkage cannot be confirmed.*

2.2.2.2 Glycan quantification -Molisch's test

The Molisch's test allows for the quantification of any carbohydrate present on the carbon dot. It is a colorimetric test which uses sulfuric acid and phenol. The sulfuric acid dehydrates the carbohydrates which then condenses with two molecules of phenol to produce a yellow coloured product which absorbs at 490 nm. Using this test with our amide coupled carbohydrate-CD system it is necessary to appreciate the amide bond on the conjugated glycoside needs to be broken before the reaction can proceed. Hence, this method could underestimate the carbohydrate present on the CD. It also won't differentiate between covalent and non-covalent bound carbohydrates. Indeed, comparing CD-glycans which bear sugars non-covalently associated may report a more accurate signal of the carbohydrate present and correspondingly a higher amount compared to covalently linked CDs. Furthermore, comparing our system with other glycan functionalised nanoparticles in the literature which are commonly O-linked[89,90], our N-linked glycans which are conjugated via a stronger amide bond could comparatively underestimate the carbohydrate present on our CDs. Therefore, producing a calibration curve from carbohydrates which contain an acetyl group at the anomeric position would perhaps be more accurate for our system.

Figures S2.2 and S2.3 shows carbohydrate calibration data for all sugars used as well as absorption data for functionalised carbon dots, both long and short linked. Furthermore, background absorption was measured for unfunctionalised AmCD **16**, AcCD **17** and AcCDala **10**. Signal from which could originate from CD absorption at 490 nm or cleavable glucosamine on the CD surface originating from the synthesis.

CD-sugar	Carbohydrate µmol/g	R^2	Carbohydrate per CD-sugar µg/g	CD per CD-sugar µg/g	Percentage mass sugar on CD
24	**2**	**0.988**	**373± 88**	**999.7**	**0.037%**
22	**1**	**0.965**	**193 ± 43**	**999.8**	**0.019%**
23	**1**	**0.926**	**421 ± 79**	**999.6**	**0.042%**
25	**2**	**0.910**	**822 ± 229**	**999.2**	**0.082%**
21	**5**	**0.997**	**890 ± 247**	**999.1**	**0.089%**
19	**2**	**0.953**	**644 ± 207**	**999.4**	**0.064%**
18	**3**	**0.970**	**1360 ± 486**	**998.6**	**0.136%**
20	**2**	**0.840**	**1120 ± 485**	**998.9**	**0.112%**
26	**2**	**0.910**	**1212 ± 229**	**998.8**	**0.121%**
27	**5**	**0.961**	**3335 ± 1252**	**996.7**	**0.334%**

Table 2.2 Molisch test data for CD-carbohydrate synthesied from longer linker synthesis. The carbohydrate measured is presented in terms of micromole (column 1) and micrograms (column 3). R^2 represents the data goodness of fit, 1 being optimum fit (column 3). The amount of corresponding carbon dot is presented in terms of micrograms (column 4). The percentage mass of carbohydrate is calculated (column 5).

CDala-sugar	Carbohydrate µmol/g	R^2	Carbohydrate per CD-sugar µg/g	CDala per CD-sugar µg/g	Percentage mass sugar on CD
15	**2**	**0.969**	**303 ± 60**	**999.7**	**0.030%**
14	**4**	**0.896**	**744 ± 201**	**999.3**	**0.074%**
12	**14**	**0.966**	**4994 ± 1592**	**995.0**	**0.499%**
11	**2**	**0.970**	**1118 ± 257**	**999.0**	**0.112%**
13	**6**	**0.980**	**3461 ± 895**	**997.0**	**0.346%**

Table 2.3 Molisch test data for CD-carbohydrate synthesied from shorter linker synthesis. The carbohydrate measured is presented in terms of micromole (column 1) and micrograms (column 3). R^2 represents the data goodness of fit, 1 being optimum fit (column 3). The amount of corresponding carbon dot is presented in terms of micrograms (column 4). The percentage mass of carbohydrate is calculated (column 5).

The carbohydrate present (μmol/g) the first column in tables 2.2 and 2.3 shows how many moles of carbohydrate are available for binding comparatively. Values range from 1 – 14 μmol/g and do not show a trend based on either the carbohydrate present, whether covalent conjugation to the CD was seen, nor the type of CD (AcCD **17** or AcCDala **10**) present. Carbohydrate functionalisation was also calculated in terms of mass (μg/g) and in terms of percentage mass which composes CD-carbohydrate. Based on the above, this test cannot be used to elucidate the covalent or non-covalently attached carbohydrate nor can it reveal the specific sugar present as the test does not discriminate between carbohydrates. Tables 2.2 and 2.3 are therefore a measurement of the total amount of non-covalent bound carbohydrate and conjugated carbohydrate present in each sample.

The carbohydrate mass percentage and the differences between them have been studied in AFM by Swift *et al*.[91] Through AFM of CD-glucose **24**, CD-mannose **22**, CD-galactose **21**, CD-maltose **23** and CD-lactose **25**, differences in adhesion between the tip and the glycan corona were observed[92]. These differences are supported by the Molisch's test. When greater adhesion is observed more

carbohydrate mass μg/g is measured (Figure 2.10). Note that the same CD-carbohydrate batches were used to allow comparison between AFM and the Molisch's test.

As a mass percentage of CD-carbohydrate, carbohydrate values vary between 0.019 – 0.499 %. This range is much wider than that seen for the samples studied through AFM, 0.019 – 0.089 %. Hence, we would anticipate that the larger percentage carbohydrate masses of di- and tri- saccharides as well as sialyllactose cleavable conjugated onto the carbon dot we observe in the Molisch's test would also be observed in AFM.

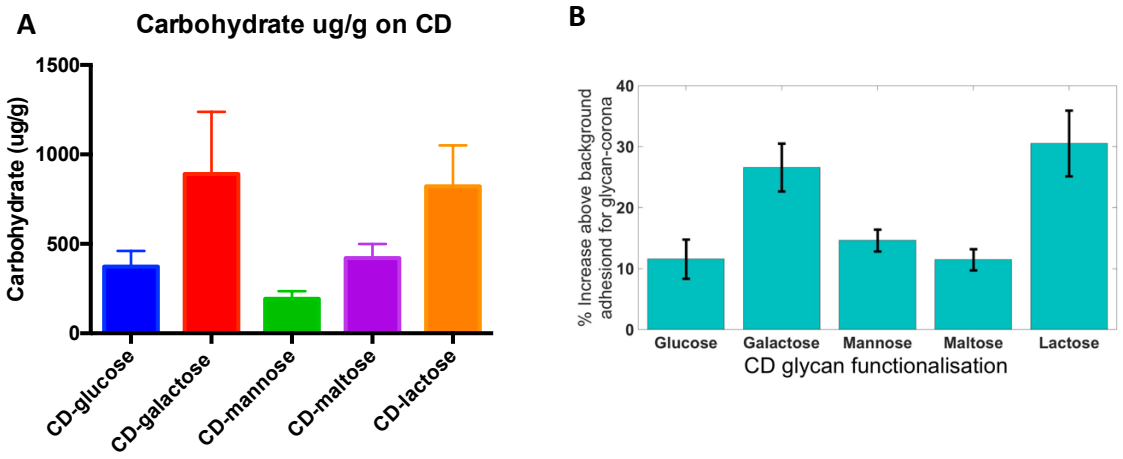

Figure 2.10 a) Carbohydrate per CD (µg/g) determined from the Molisch's test. B) AFM adhesion studies[92] of CD-carbohydrate from Swift et al[92].

CDs AmCD **16**, AcCD **17** and AcCDala **10** have a carbohydrate signal which linearly increases with concentration (Fig S2.2). Negative control experiments with just water revealed a background level of absorption which is similar in absorption. Hence these measurements could be in error of the background. However, AcCD **17** and AcCDala **10** have a linear absorption greater than the background which is likely due to the glucosamine.HCl starting material used in the microwave synthesis of the CDs but also could reflect difference in their QY. This carbohydrate by inference must be present on the surface of the carbon dot and accessible for cleavage.

Assuming the carbohydrate present is glucosamine we can calculate the amount of carbohydrate present on the surface of each of these materials per gram. Using literature values for the signal of glucosamine in the Molisch's test[93], we estimate the amount of sugar present on unfunctionalised CDs, see table 2.4. CDs (Figure S2.2) compared to CD-carbohydrate and CDala-carbohydrate the carbohydrate (Figure S2.3) absorption signal in the Molisch's test is low as might be expected. However, it is important to note that glucosamine has a 30 times lower signal compared to mannose for the same concentration of carbohydrate in the Molisch's test[93]. As both the short and long linker CD syntheses contain glucosamine.HCl this may be the result of this carbohydrate in the CD samples.

Hence, the absorption could represent a significant carbohydrate amount when compared to that observed for carbohydrate functionalised carbon dots.

CD-sugar	Carbohydrate µmol/g	R^2	Carbohydrate per CD-sugar µg/g	CD per CD-sugar µg/g	Percentage mass sugar on CD
16	**6**	**0.475**	**2279**	**998**	**0.228%**
17	**86**	**0.837**	**30848**	**969**	**3.085%**
10	**19**	**0.905**	**6791**	**993**	**0.679%**

*Table 2.4 Molisch test data for AmCD, AcCD and AcCDala **10**. The carbohydrate measured is presented in terms of micromole (column 1) and micrograms (column 3). R^2 represents the data goodness of fit, 1 being optimum fit (column 3). The amount of corresponding carbon dot is presented in terms of micrograms (column 4). The percentage mass of carbohydrate is calculated (column 5).*

When comparing the lower signal seen for glycan functionalised CDs and free CDs and taking into account that the Molisch's test represents the cleavable and free carbohydrate present, it follows that the glucosamine on functionalised CD is mostly shielded sterically offering explanation for the reduced carbohydrate signal in functionalised CDs.

2.2.2.3 Glycan quantification – using NMR

In order to get a more accurate quantification of conjugated glycan functionalization. ^{1}H and HSQC NMR measurements using imidazole as an internal standard were carried out. The same sample of CD-4-*O*-mannobiose which was used to assess carbohydrate conjugation in the Molisch's test was used here (Figure A.19). 4-*O*-mannobiose anomeric peak at 5.04 ppm (^{1}H) and 71.23 ppm (^{13}C) and imidazole peak at 7.77 ppm (^{1}H) were integrated and the moles of carbohydrate determined. In terms of mass, the carbohydrate mass was 51 mg per gram of CD-4-*O*-mannobiose **19** or 5.1 % content. Comparing this to the 0.064 % carbohydrate content determined through the Molisch's test, NMR suggests a greater carbohydrate content than the Molisch's test can measure. The carbohydrate quantified in NMR refers to only the conjugated carbohydrate, however, looking at the spectra Figure A.19 there is more unconjugated carbohydrate present than conjugated. Hence, the measure of carbohydrate content is suggested to be a gross underestimation in the Molisch's test. Quantifying the total amount of carbohydrate using ^{1}H NMR was not possible for CD-4-*O*-mannbiose **19** with imidazole as the anomeric peaks were not identifiable due to poor signal to noise resolution, resulting from low sample concentration and water peak at 4.79 ppm.

2.2.2.4 FTIR

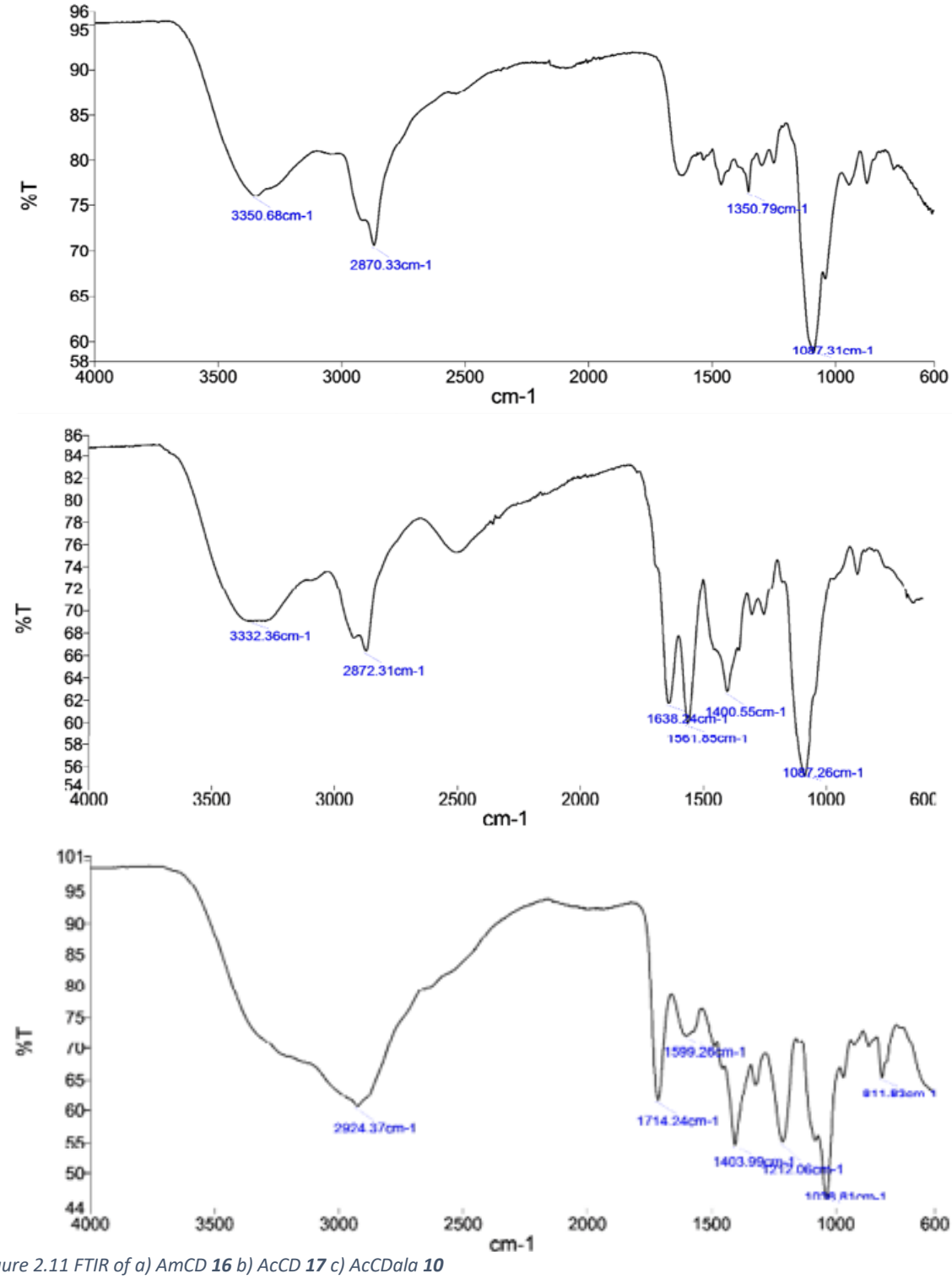

*Figure 2.11 FTIR of a) AmCD **16** b) AcCD **17** c) AcCDala **10***

FTIR was carried out on AmCD **16**, AcCD **17** and AcCDala **10** in order to investigate the surface groups present on each carbon dot (Figure 2.11). All CDs had peaks at 3350 cm^{-1} (O-H stretch), 3332 cm^{-1} (N-H stretch) and 2924 cm^{-1} (N-H stretch) which corresponds to the presence of amine and or alcohol. For AcCDala **10** this peak has combined with the peak at 2870 cm^{-1} (C-H stretch) which is seen

separately for AmCD **16** and AcCD **17**. The other peak that all spectra share is the one at 1087 cm^{-1} (C-O). Upon succinic acid ring opening reaction to convert AmCD **16** to AcCD **17** new peaks appear in the FTIR spectrum. 1638 cm^{-1} (HNCO stretch) amide, 1561 cm^{-1} (N-H stretch) amine, and 1400 cm^{-1} (O-H bend) carboxylic acid. The formation of an amide bond confirms conjugation of succinic acid which is also seen through the new carboxylic acid peak. For AcCDala **10**, a carboxylic acid peak is also seen at 1403 cm^{-1} (O-H), suggesting β-alanine is presented on the surface. Three additional peaks are also seen compared to AcCD **17** due to the different synthesis reflected on the carbon dot surface. These are 1714 cm^{-1} (C=O stretch), 1212 cm^{-1} (C-O stretch) and 611 cm^{-1} (C-Cl stretch). These results match expected surface functionality.

2.2.2.5 UV-Vis spectroscopy

UV-Vis data of AmCD **16**, AcCD **17**, AcCDala **10** and example CD-carbohydrate, CD-, CDala-, 4-*O*-mannobiose in H_2O are presented in Figure 2.12. Common features include an absorption peak at 280 nm corresponding to carbonyl and carbohydrate n $\rightarrow \pi^*$ transition and also a large peak at < 200 nm corresponding to $\pi \rightarrow \pi^*$ transitions. The absorption tail seen towards longer wavelengths up to 600 nm belong to the numerous optical sites which exist at the surface of CDs. Swift *et al.*[91] investigated the absorption of CD-, glucose, mannose, maltose, galactose and lactose and through 2D fluorescence plots observed that at wavelengths greater than 300 nm the absorption varied between carbohydrate present. This suggests that the surface electronics are influenced by the carbohydrate present independent of the core,[94] hence carbohydrates are not just passivating agents.

The absorption peak at 280 nm varies in shape dependent on carbohydrate conjugated (independent of concentration intensity). For example, both CD-lactose and CD-maltotriose have smaller broader peaks compare to CD-4-*O*-mannobiose. The differences here may reflect the carbohydrate concentration on the CD. Interestingly, the AcCDala **10** spectra all have a more pronounced peak at 280 nm in common, seen through comparing CD-mannose and CDala-mannose. Perhaps reflecting the different CD cores and the electronic characteristics they impose on the edge band emission. Furthermore, no difference can be concluded in the UV-Vis spectra between covalent and adsorbed carbohydrate onto CDs.

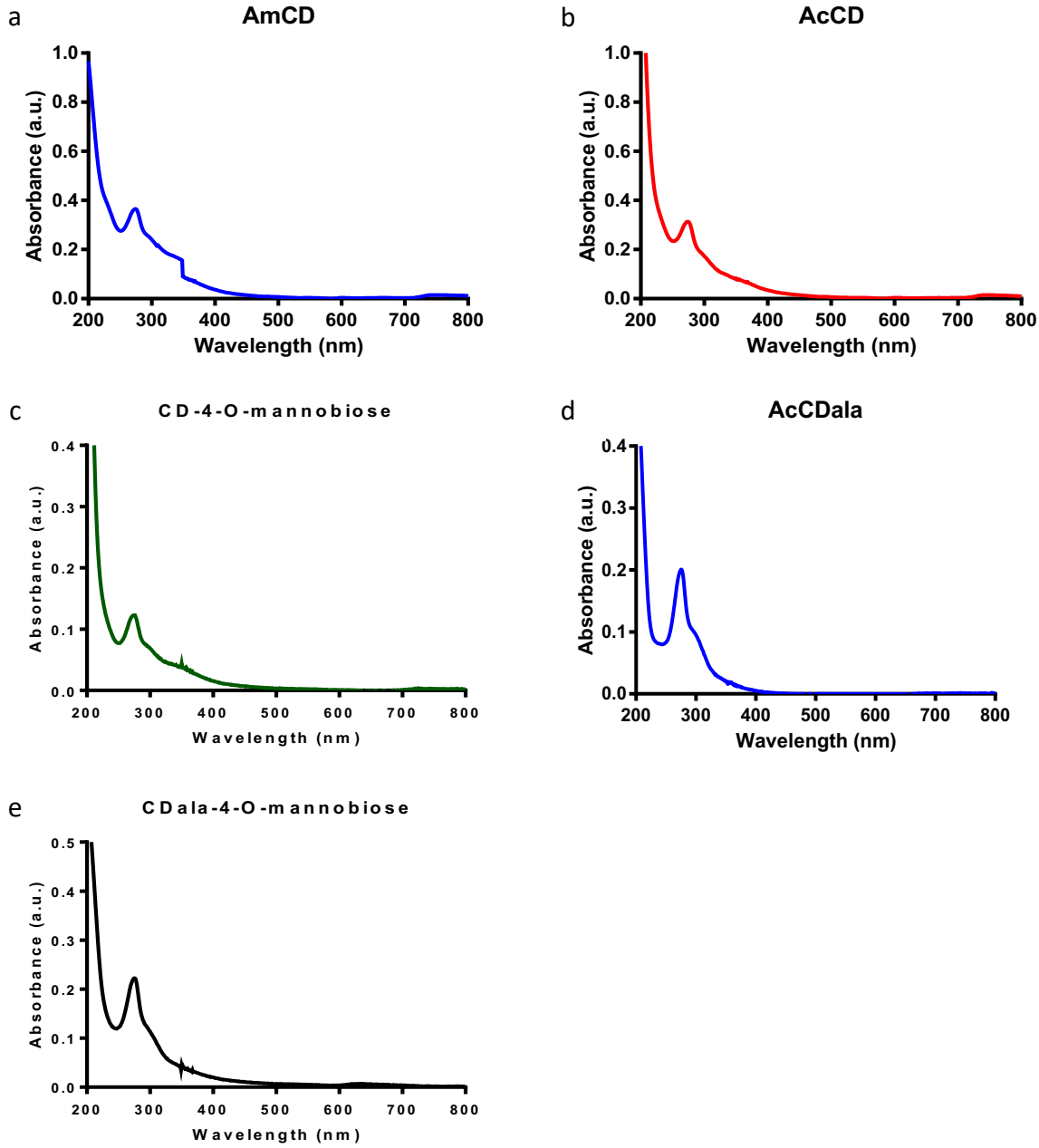

*Figure 2.12UV-vis absorption spectra for a) AmCD **16**, b) AcCD **17**, c) AcCDala **10**, d) CD-4-O-mannobiose **19** and e) CDala-4-O-mannobiose **14**.*

2.2.2.6 Fluorescence spectroscopy

The excitation and emission of AmCD **16**, AcCD **17**, AcCDala **10** and example CD-carbohydrate CD and CDala-, 4-*O*-mannobiose in water are presented in Figure 2.12. The excitation spectra has a peak at 340 nm which is seen for all CDs synthesised. Swift *et al.*[94] propose that the carbohydrate conjugation affects this region specifically which corresponds to the absorption peak seen at 340 nm. From our data it looks as though a substantially greater glycan dependent excitation change is seen for the peak at 290 nm. AcCDala **10** shows this starkly, where glycan presence has a much greater peak at 290 nm

in CD-4-*O*-mannobiose **19**. Interestingly, for CD-4-*O*-mannobiose **19**, the same peak at 290 nm is reduced compared to the starting AmCD **16** or AcCD **17**. Hence, both the surface domain and edge band are influenced by the carbohydrate at the surface.

These carbon dots have excitation-dependent emission similar to other carbon dots synthesised via bottom up methods, reflecting the variety of molecular states present in carbon dots. The peak emission upon excitation at 340 nm is 450 nm with a slight shoulder at ~ 525 nm. If carbohydrate is present this shoulder is more pronounced owing to the dual fluorescence of these carbon dots resulting from the surface state variability induced by the carbohydrate present.

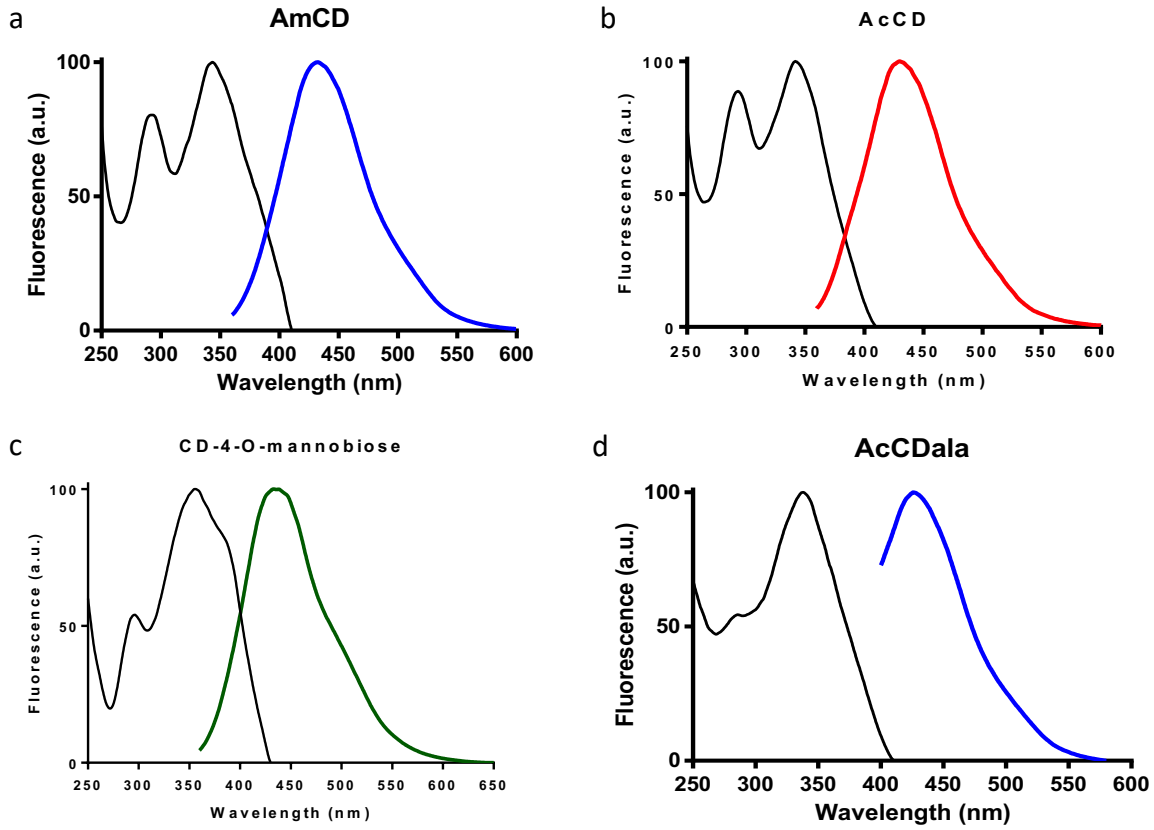

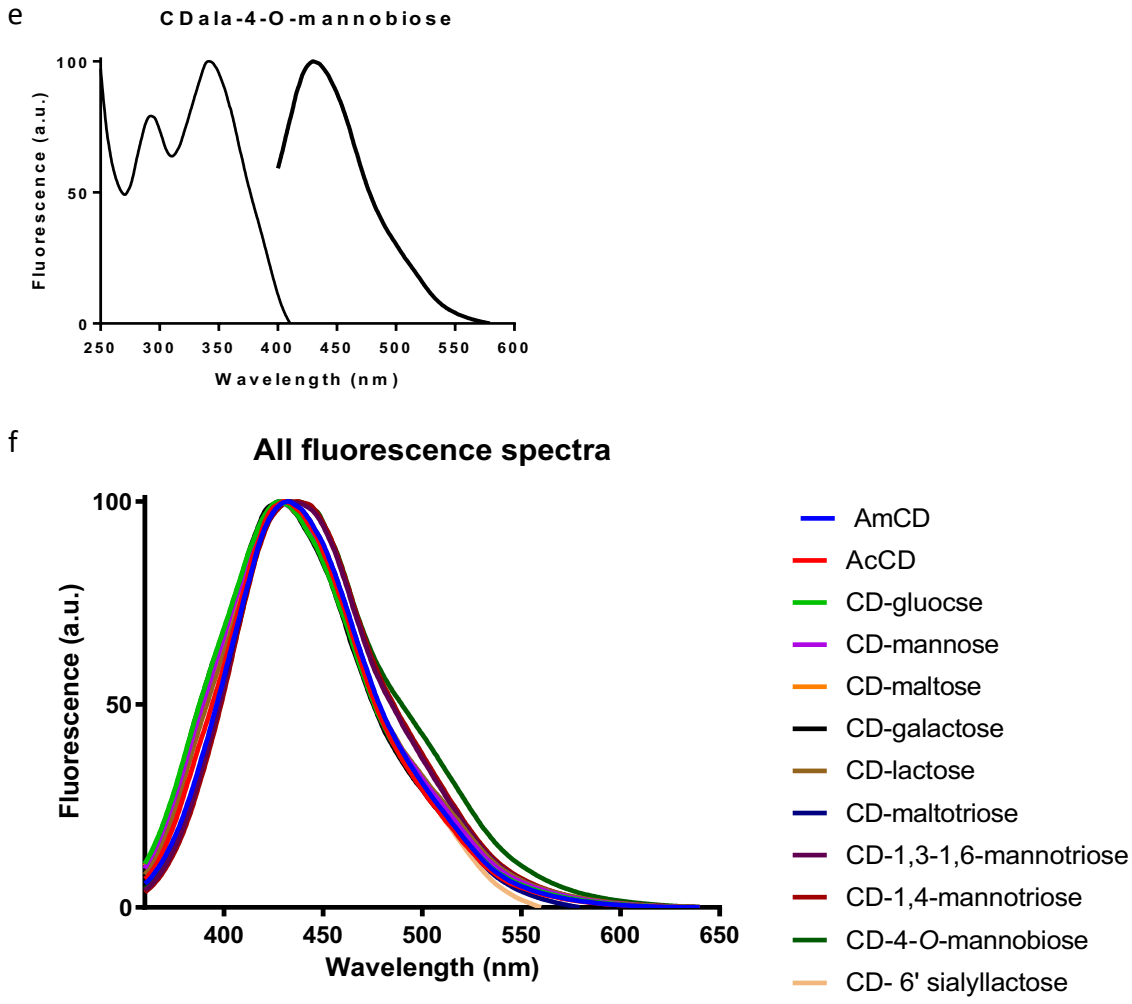

*Figure 2.13 Fluorescence spectra of a) AmCD **16** b) AcCD **17** c) CD-4-O-mannobiose **19** d) AcCDala **10** e) CDala-4-O-mannobiose **12** f) and all CD-carbohydrate emission spectra overlapped.*

2.2.2.7 Quantum yield

Quantum yield (QY or **Φ**) of a nanomaterial is an independent ratiometric assessment of its ability to emit photons of light based on the number of photons absorbed. This characteristic is important when considering bioimaging applications. Some of the brightest commercially available fluorophores have QYs up to 0.92 and QDs have good QY, greater than 0.5 in some cases which has been matched by recent carbon dot syntheses across the fluorescence spectrum based on improved passivation. Depending on the application QY may be considered sufficient. Using spectrophotometer instrumentation available to us, we are able to analyse materials of low QY down to 0.01.

When calculating the QY, the excitation and emission wavelengths of a material must be considered, different dyes with known QY are used as a standard against which the material of interest is

compared. Two common dyes are Rhodamine B λ_{ex} 514 nm and Quinine sulfate (QS) λ_{ex} 350 nm. In this work quinine sulfate was used as its photoluminescence is similar to short and long linker carbon dots synthesised in this work, see section 2.4.9. Experimentally the standard must be run in 0.1 M H_2SO_4 at 22 °C. Experimentally, a calibration curve of fluorescence versus absorbance is made when the absorbance is less than 0.1 (see Figure S2.9, where there is a linear relationship can be observed bwhen abs <0.1). The gradient of the line is then used to calculate the QY. The QY was determined to be between 0.66-8.79 for all material to be used in further experiments. The QY was dependent on the carbohydrate present but showed no correlation between carbohydrate size or structure and QY value.

$$\Phi_{CD} = \Phi_{QS} \cdot \frac{(m_{CD})}{(m_{QS})} \cdot \frac{(\eta_{CD})^2}{(\eta_{QS})^2}$$

Equation 2.1 Quantum yield (QY or Φ) equation. Using quinine sulfate (QS) as a standard (QY = 0.54), the refractive index (η) of H_2O being 1.33 and using the gradient (m) from the data generated measuring fluorescence against absorbance.

Sample	QY%	R^2
Quinine Sulfate	54.60	0.99
AmCD	3.87 ± 0.44	0.85
AcCD	8.79 ± 0.16	0.74
CD-glucose	3.92 ± 0.47	0.84
CD-mannose	6.36 ± 0.19	0.99
CD-galactose	7.05 ± 0.31	0.97
CD-maltose	5.75 ± 0.69	0.84
CD-lactose	6.26 ± 0.29	0.97
CD-maltotriose	7.05 ± 0.31	0.97
CD-1,3-1,6-manntriose	4.04 ± 0.79	0.99
CD-1,4-manntriose	3.88 ± 0.07	0.99
CD-4-O-mannobiose	2.39 ± 0.44	0.99
AcCDala	6.29 ± 0.42	0.94
CDala-mannose	0.66 ± 0.04	0.96
CD-ala-galactose	3.50 ± 0.04	0.98
CDala-1,3-1,6-mannotriose	4.50 ± 0.79	0.76
CDala-1,4-manntriose	2.26 ± 0.19	0.91
CDala-4-O-mannbiose	3.06 ± 0.44	0.74
CD-3'sialyllactose	2.30 ± 0.19	0.87
CD-6'sialyllactose	5.24 ± 0.34	0.94

Table 2.5 Quantum yield (QY or Φ) data measured for the carbon dot materials synthesised. R^2 is the goodness of fit with 1 being the best fit.

2.2.2.8 DLS and zeta potential

Dynamic light scattering (DLS) and zeta potential (ζ) were used to try and observe monodispersed carbon dots and determine their hydrodynamic size in HEPES buffer 0.1M concentration with 5 mM $CaCl_2$ and 5mM $MnCl_2$. This buffer is used in all later binding studies (see Chapter 3). TEM and AFM

reported size distribution of carbon dots between 1.54 – 3.69 ± 2.8 and 2.27 ± 0.89 (for AmCD **16**) respectively. Hence, from DLS we expected a hydrated diameter larger than this, but of the same order of magnitude. Furthermore, previous work in the group measured monodispersed CDs using DLS in distilled H_2O: 3.85 ± 0.89[85] and MeOH: 3-4 nm[92].

Factors affecting carbon dot dispersion include the dispersant interaction, pH and particle concentration. In this work we were interested in the distribution of CDs in HEPES buffer, hence we did not change this parameter. 0.1 M HEPES buffer has a pKa of 7.48 at 25 ^oC, buffering over the pH range 6.8- 8.2. Amines on the surface of AmCD **16** at this pH are neutral and acids on the surface of AcCDs **16** are charged. However, for both types of acid functionalised CDs (AcCD **16** and AcCDala **10**), electrostatic repulsion did not induce a monodispersed sample.

Literature evidence shows that a size distribution trend exists for nanoparticles as a function of concentration. At high concentration the size distribution is distorted and at low concentration the data is too noisy. Where the size distribution is independent of the concentration, particle diameter can be measured. Optimisation with CD-galactose in 0.1M HEPES and comparing with H_2O, MeOH and 0.01M HEPES between 0.3 – 5 $mgml^{-1}$, the particle size in each diluent was measured. Peak 1 data for both intensity and number measurements are shown in figure 2.14. Peak 1 refers to the first peak measuring the smallest size but greater than 1 nm, allowing for solvent peaks which fall below 1 nm to be omitted.

In MeOH and H_2O, the peak 1 diameter was measured between 100 – 500 nm and between 400 – 1000 nm respectively, suggesting aggregation is the presiding form in both solutions, and data aggregation occurs in a concentration dependent manner. Number data did not reveal any particle size smaller than that observed from intensity data at these concentrations and conferred the same size distribution. In HEPES buffer at 0.1 M and 0.01 M smaller sizes were measured at the same order of magnitude as seen with other techniques, suggesting greater monodispersed sample. In the two buffers, diameters of 0.7 nm ± 0.2 and 1.2 nm ± 0.2 respectively for number data and 4.3 nm ± 0.6 and 2.7 nm ± 0.6 respectively for intensity data are averages from data collected between 0.3 – 2.5 $mgml^{-1}$ where sizes are in the same regime.

Looking at size distribution for CD-galactose **21** in 0.1 M HEPES only, peak 1 number data at concentrations 0.3 – 2.5 $mgml^{-1}$ (Figure 2.14d) shows only one peak. This peak corresponds to solvent, shown by the green data points all below 1 nm. This is likely due to the proportion of particles in the

monodispersed form being very low. Looking at the intensity data of the same sample, larger particles 4.278 nm ± 0.555 nm are measurable.

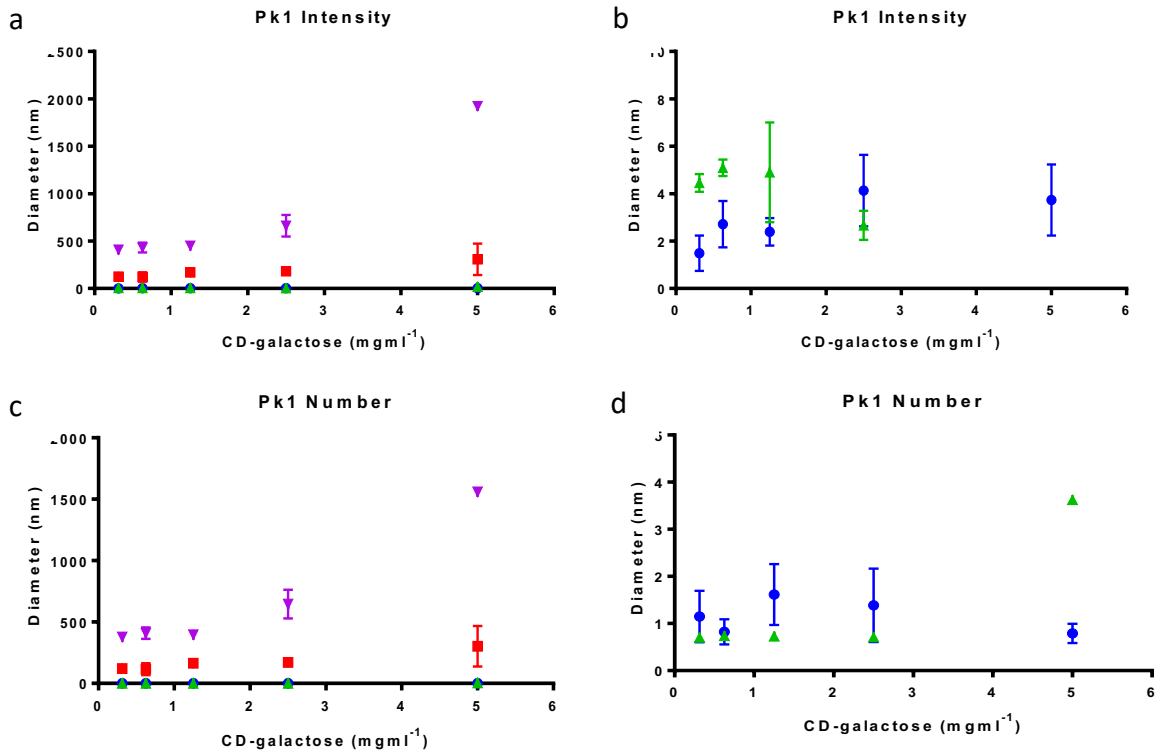

*Figure 2.14 DLS of CD-galactose **21** at concentrations 0.3125 – 5 mgml^{-1}. Peak 1 % intensity (a&b) and % number (c&d) data are presented for CD-galactose in 0.1 M HEPES (green), 0.01 M HEPES (blue), MeOH (red) and H_2O (purple).*

For each CD-carbohydrate the concentration in 0.1 M HEPES to measure particle hydrodynamic diameter, must be determined through the same optimisation process. However, to allow comparison of the degree of aggregation between CD-carbohydrates, DLS (% intensity data) and zeta potential were carried out, with sample concentration 0.4 mgml^{-1} in 0.1 M HEPES for all CD-carbohydrates (Figure 2.15). For these samples the reported sizes all report hydrodynamic diameters between 500-1000 nm suggesting aggregation. This is likely due to electrostatic and hydrophobic inter carbohydrate and carbon dot surface group interactions.

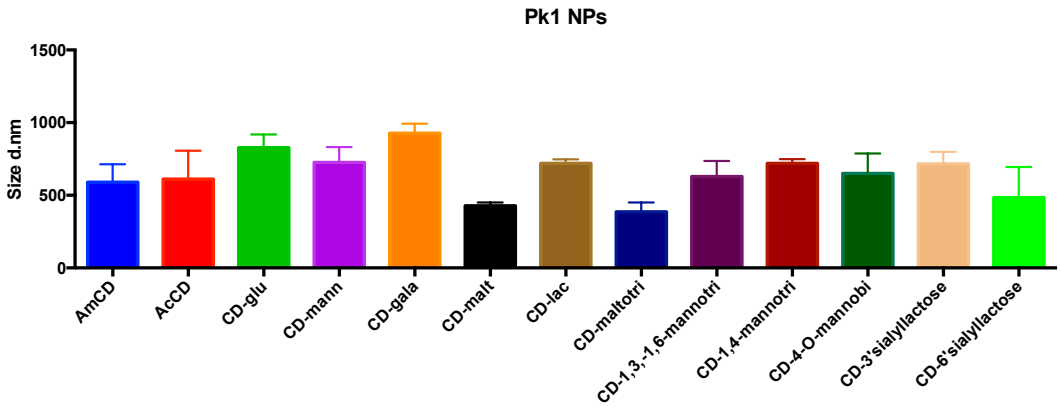

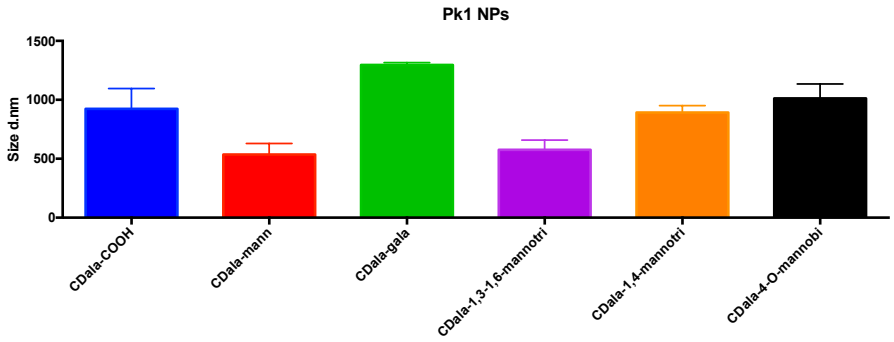

Figure 2.15 DLS (% intensity) peak 1 data of CD-carbohydrate in 0.1M HEPES at 0.4 mgml^{-1}

Observing intensity data of CD-galactose **21** in 0.1 M HEPES best elucidates the CD hydrodynamic size is supported by zeta potential results. Generally speaking, more positive zeta potential is indicative of more monodispersed particles in a sample, hence by varying concentration of CD-galactose **21**, it is possible to infer at which concentration the size should be measured using DLS. Within the concentration range measured, 0.4 mgml^{-1} in 0.1 M HEPES, was the highest zeta potential measurement of 7.0 ± 0.6 mV. Correspondingly in DLS, this concentration falls in the range where the particle size measured doesn't vary with concentration. Hence, supporting the diameter for CD-galactose **21** as 4.3 nm ± 0.6 nm.

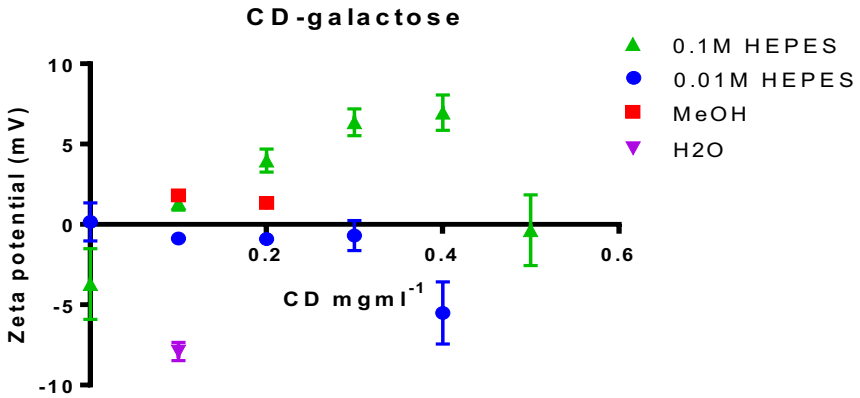

Figure 2.16 Zeta potential (ζ) data for CD-galactose over a range of concentrations 0.1 – 0.5 mgml^{-1}. Data for CD-galactose in buffer 0.1 M HEPES (green), 0.01 M HEPES (blue), MeOH (red), and H_2O (purple) are shown.

At the same concentration of 0.4 mgml^{-1} in 0.1 M HEPES, the zeta potential was measured for all CD-carbohydrates (2.17). For CD-carbohydrates with a AmCD **16** core the ζ was between 5-15 mV. Apart from the CD-sialyllactose sample which is slightly negative reflecting the carboxylic acid group on the terminal sugar and hence presented on the CD surface. As zeta potential is a measure of difference in charge between particle surface and the diluent, this negative charge suggests that the carbohydrate is presented on the surface of the particle and is a distinct environment to the diluent.

AcCDala **10** data zeta potential values all suggest a slightly negative surface charge (but close to 0 mV) hence are likely aggregating. This reflects that these particles are made through a different synthesis and have a different structure and surface properties such as carboxylic groups seen from FTIR peak at 1403 cm $^{-1}$. Comparing CD-carbohydrate and CDala-carbohydrate which have been functionalised with the same carbohydrate either having a positive or negative zeta potential depending on the CD, suggests that the carbon dot surface is highly exposed to the diluent.

In summary, table 2.6 shows the hydrodynamic diameter and corresponding zeta potential for each sample at 0.4 mgml^{-1} in 0.1 M HEPES. This concentration of HEPES buffer is used in later experiments where binding is assessed through DLS hydrodynamic aggregate size measurements. Compared to previous size distributions for CD-carbohydrate materials[46,92] measured in H_2O and MeOH these sizes are much larger in 0.1 M HEPES.

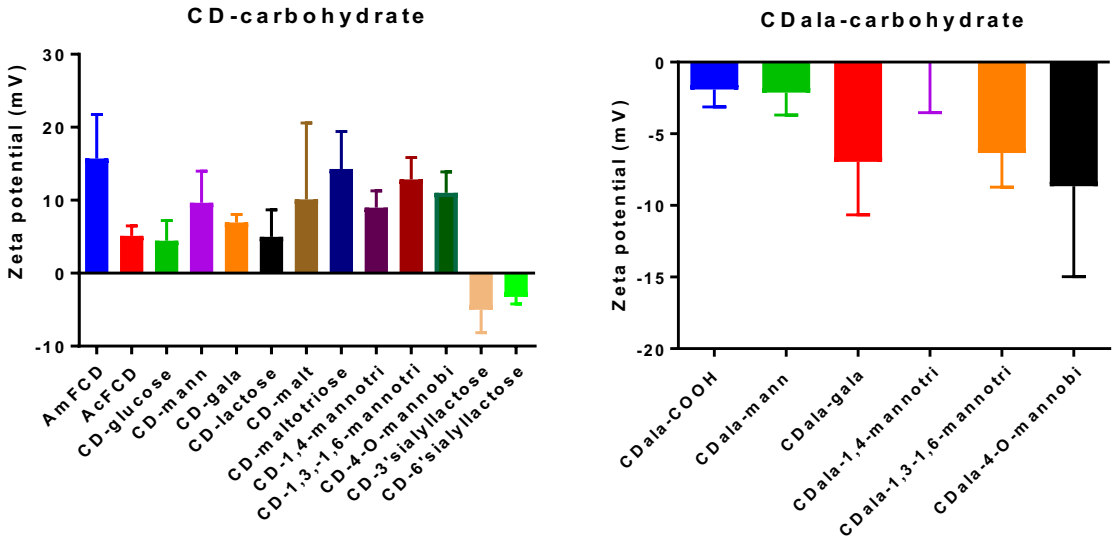

Figure 2.17 Zeta potential (ζ) data for a) CD-carbohydrate and b) CDala-carbohydrate with SEM error bars.

CD-sugar	Intensity pk1 (d.nm)	Zeta potential (mV)
AmCD	590 ± 71	15.7 ± 3.5
AcCD	611 ± 113	5.1 ± 0.8
CD-glucose	827 ± 53	4.4 ± 1.6
CD-mannose	726 ± 61	9.6 ± 2.5
CD-galactose	927 ± 38	7.0 ± 0.6
CD-maltose	428 ± 13	10.1 ± 6.0
CD-lactose	719 ± 16	5.0 ± 2.2
CD-maltotriose	385 ± 37	14.3 ± 3.0
CD-1,4-mannotriose	717 ± 17	9.0 ± 1.3
CD-1,3-1,6-mannotriose	628 ± 61	12.8 ± 1.7
CD-4-O-mannobiose	650 ±79	11.0 ± 1.7
AcCDala	923 ± 100	-1.9 ± 0.7
CDala-mannose	536 ± 54	-2.1 ± 0.9
CD-ala-galactose	1296 ± 11	-7.0 ± 2.1
CDala-1,3-1,6-mannotriose	576 ± 47	-6.3 ± 1.4
CD-1,4-mannotriose	893 ± 34	-0.1 ± 2.0
CD-4-O-mannobiose	1012 ± 71	-8.7 ± 3.7
CD-3'sialyllactose	716 ± 48	-5.0 ± 1.8
CD-6'sialyllactose	484 ± 121	-3.3 ± 0.6

Table 2.6 Summary table of carbon dot DLS Intensity peak 1 and zeta potential data.

2.2.2.10 TEM

Previous high-resolution transmission electron microscopy (TEM) work in the group with these CD-carbohydrates show these have an sp^3 crystalline diamond-like core evidenced by lattice spacing of 0.21 nm and 0.25 nm for the (111) and (110) planes respectively. The diameter of AmCD **16** core was previously reported as 2.45 ± 0.54 nm[83], agreeing with diameter range measured from samples in this work which are reported as between 1.54-3.69 $\pm$ 2.87 as seen in Figures 2.19, 2.20 and 2.21 (histograms) and presented in table 2.7.

TEM provides a diameter based on the contrast against a carbon background which is relatively difficult to achieve. Best contrast is achieved when using homemade carbon coated (4 nm coating) copper grids. Considering that the edge domain surrounding the core and the glycan coating may give poor contrast TEM usually reports a smaller diameter than DLS. High resolution images taken by Hill et al. show that AmCD **16** observed by TEM are wholly made up of sp^3 region. Hence, the particle diameter seen through TEM is that of the sp^3 core.

Data presented in figure 2.19 are TEM images of AmCD **16**, AcCD **17** and CD-carbohydrates; CD-lactose, CD-glucose, CD-mannose, CD-galactose and CD-maltose **21-25** all made from long linker CDs.

Selected samples were chosen for TEM to allow for complete processing. Samples were prepared in MeOH at 5 $mgml^{-1}$ before drop casting onto carbon coated copper grids and left to dry overnight before imaging. In each case the left-hand image shows the lowest magnification of each sample and magnification increases as you move right. From these images the carbon dots can be confirmed as quasi-spherical nanoparticles. Upon glycan functionalisation the high contrast cores observed for AmCD **16** and AcCD **17** are less well resolved owing to the glycan coating present. This coating is seen as a cloudy corona around the particles but also present separate from CD cores. This is most clearly seen in CD-galactose where a shadowy film covers the grid and is not correlated to the location of the CD cores. As TEM reveals the core sp^3 domain, the diameter reported for each of AmCD **16**, AcCD **17** and CD-carbohydrate are all within error of each other. The large error is likely due to the highly heterogeneously sized population of particles known to result from bottom up syntheses.

Scanning transmission electron microscopy (STEM) a form of dark-field microscopy was trialled for imaging AcCDs **17**. This technique is good for imaging samples with low contrast as it collects scattered electrons from the sample and the background remains dark. The AcCDs **17** here are bright and more easily distinguishable from the background then in standard TEM. The diameters measured using this technique was 3.47 ± 2.79, within error compared to 2.84 ± 2.0 for standard TEM.

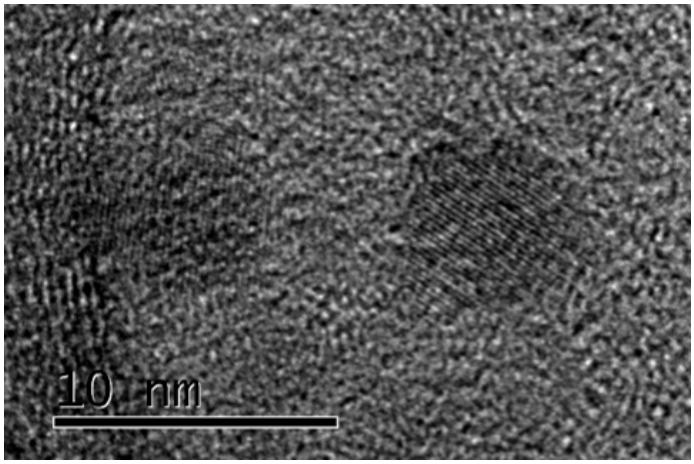

*Figure 2.18 High resolution TEM image of AmCD **16** reproduced with permission from Hill et al.*[85]

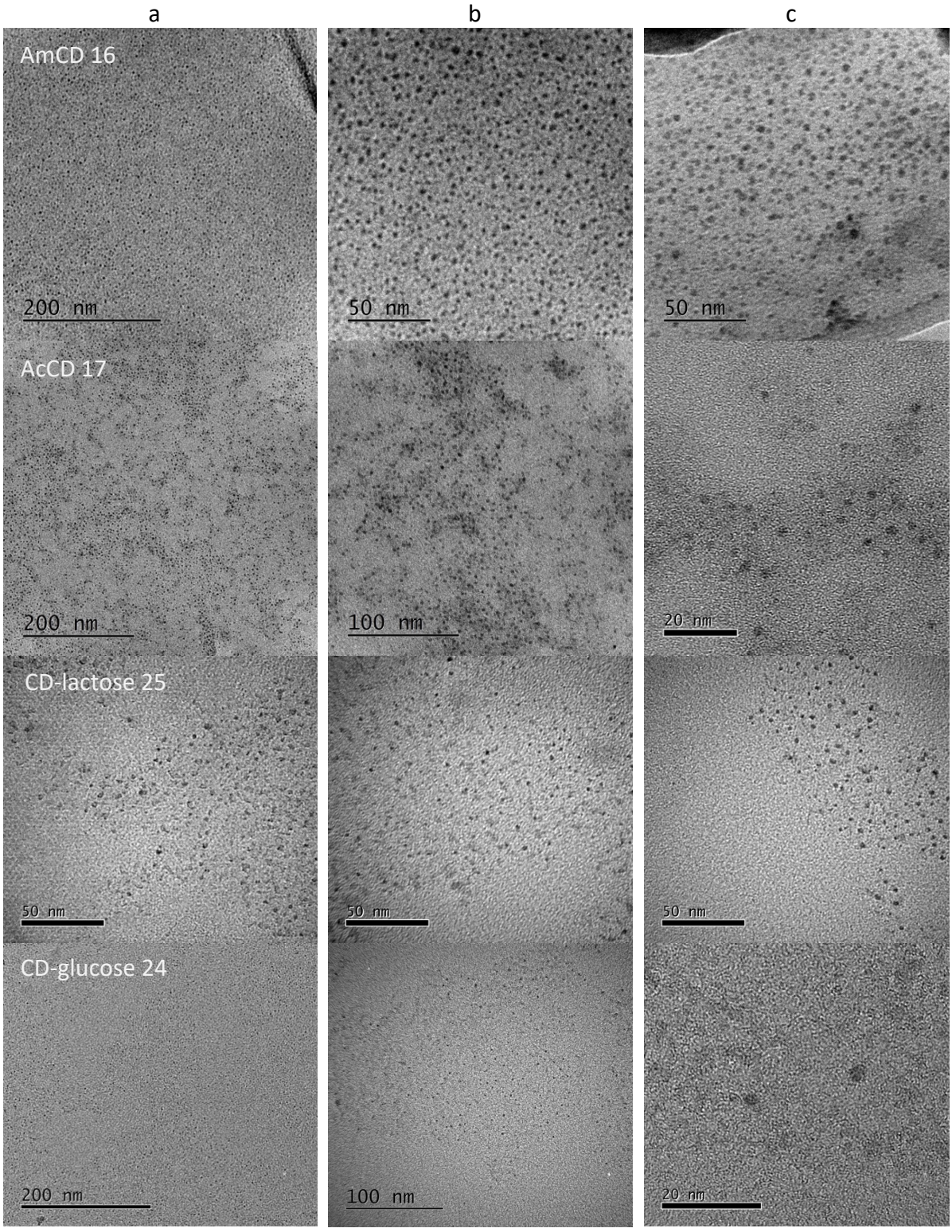
a
b
c
AmCD 16
200 nm
50 nm
50 nm
AcCD 17
200 nm
100 nm
20 nm
CD-lactose 25
50 nm
50 nm
50 nm
CD-glucose 24
200 nm
100 nm
20 nm

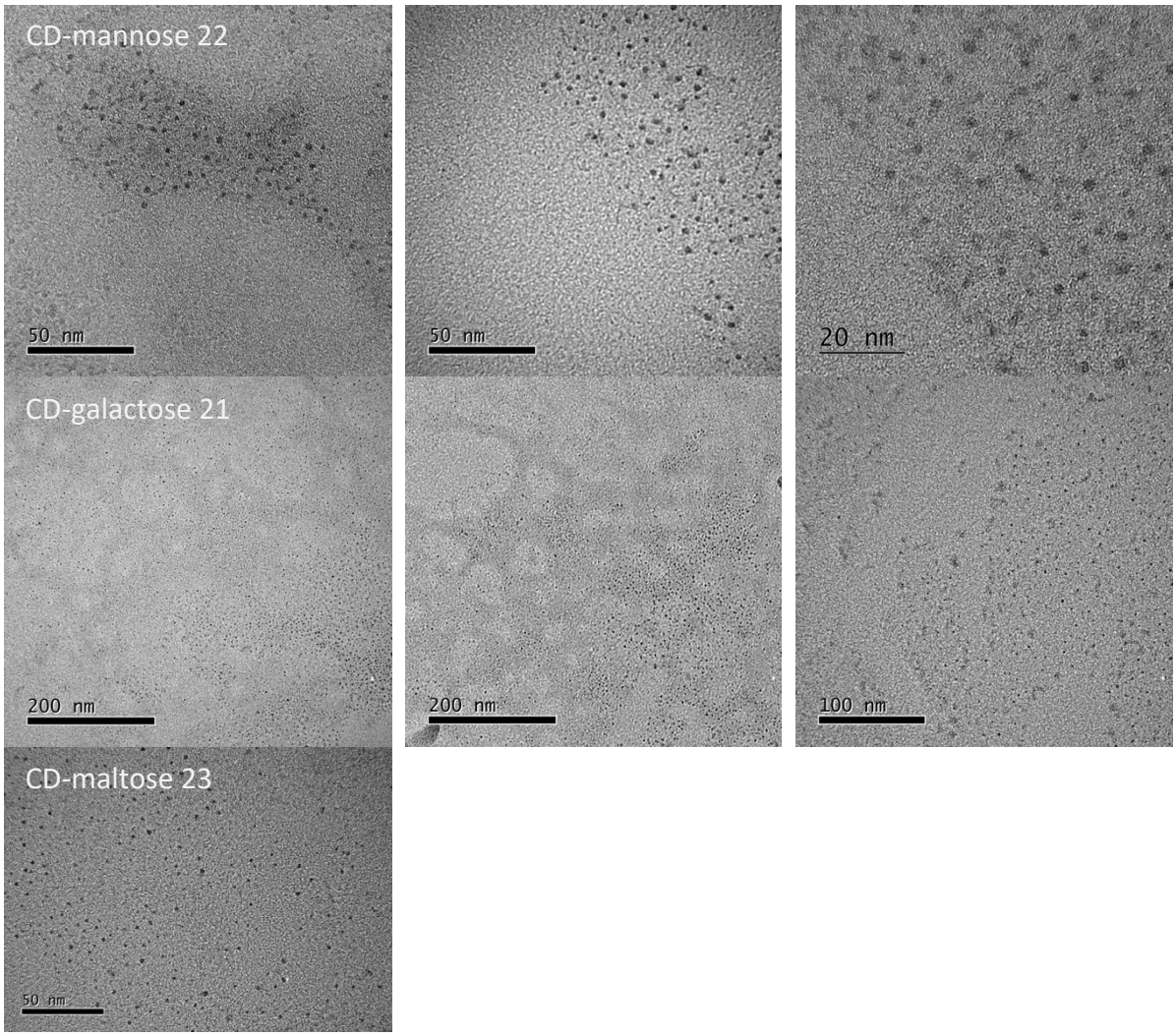

*Figure 2.19 TEM images of long linker carbon dots; AmCDs **16**; AcCDs **17**; CD-lactose **25**; CD-glucose **24**; CD-mannose **22**; CD-galactose **21** and CD-maltose **23**. Increasing magnification from a to c.*

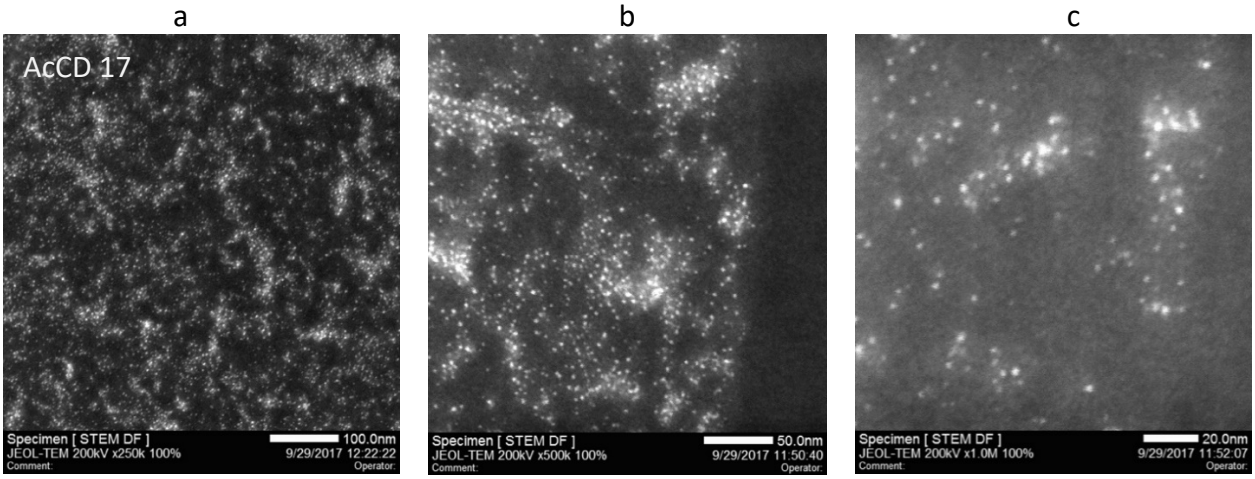

*Figure 2.20 STEM images of AcCD **17**. increasing magnification from a to c.*

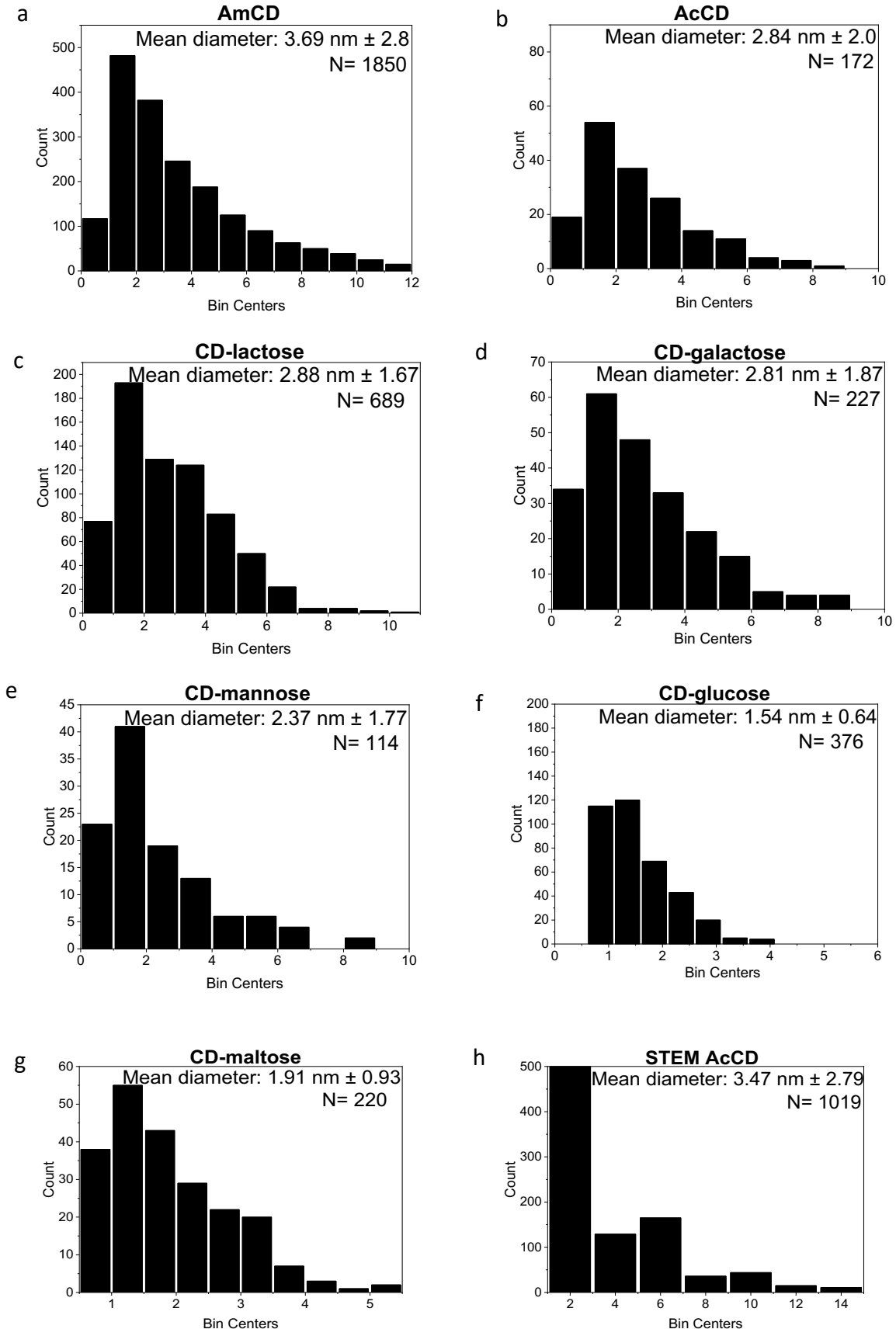

*Figure 2.21 Histograms of diameter from images in figure 2.19 for a) AmCD **16**, b) AcCD **17**, c) CD-lactose **25**, d) CD-galactose **21**, e) CD-mannose **22**, f) CD-glucose **24**, g) CD-maltose **23** h) AcCD **17** (from STEM figure 2.20) Image J software was used to measure particle diameter using thresholding*

CD-sugar	Diameter from TEM (nm)
AmCD **16**	3.69 ± 2.8
AcCD **17**	2.84 ± 2.0
CD-glucose **24**	1.54 ± 0.64
CD-mannose **22**	2.37 ± 0.77
CD-galactose **21**	2.81 ± 1.87
CD-maltose **23**	1.91 ± 0.93
CD-lactose **25**	2.88 ± 1.67

*Table 2.7 Summary table of carbon dot and CD-carbohydrate **21-25** diameters from TEM. Error represents SEM.*

2.2.2.11 AFM

Tapping mode atomic force microscopy (AFM) provides the most accurate size information with the possibility of atomic resolution in the height dimension. There are some caveats when considering CD AFM data; the sample is dry during imaging hence the height does not represent the hydrated diameter of the particle. As the AFM tip has a radius of 0.35 μm (in these experiments) there is an overestimation of the size of the CD using this technique. AFM of AmCD **16** revealed a diameter of 2.27 ± 0.89 nm which is similar to previous work in the group of 3.0 ± 1 nm. Comparing this to TEM data 3.69 ± 2.8 nm, 1.57 nm height of AmCD **16** is considerably smaller. This may reflect either an overestimate of size from the TEM data or an underestimation of the size from AFM. Considering that TEM data shows a smaller average size post carbohydrate functionalisation, suggests that the TEM data for AmCD **16** is an overestimation.

AFM can also be used to probe the composition and heterogeneity of the CD-carbohydrates through adhesion studies as carried out by Swift *et al.*[91] Through adhesion mapping the areas of high adhesion which can be thought of as "sticky" are carbohydrate and areas of low adhesion are the CD surface. This was determined from probing the surface of CD-carbohydrates and observing areas of high and low adhesion on one particle. Some particles had more sticky areas than others which showed variability and inhomogeneity between carbohydrates and between individual particles also. One consideration of this conclusion must be that the CD-carbohydrate linker is relatively long. When dried the TTDDA linker and carbohydrate may not represent the hydrated organisation of these molecules, hence the particle surface composition inhomogeneity maybe in part due to sample preparation.

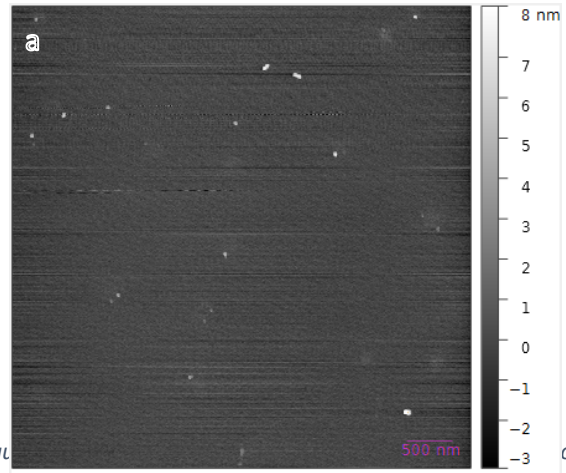

*Figu opography b) 3D height profile of AmCDs **16** c) histogram of particle height (error is SEM).*

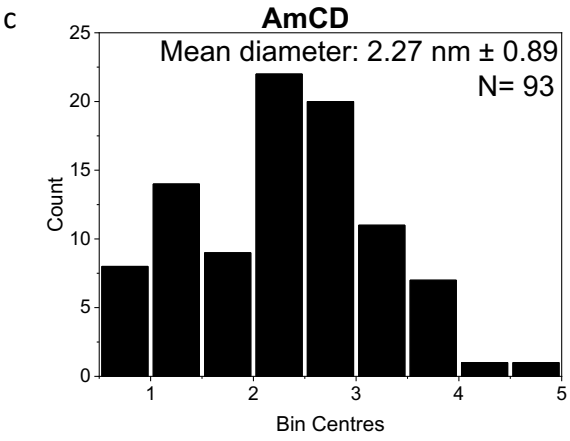

2.2.2.12 Carbon dot structure and spectroscopic properties

Publication by Swift *et al.*[94] uses a number of techniques to conclude information about the CD electronics and structure relationship. Specifically, the influence of the presence of carbohydrate on the electronic and spectroscopic properties on the long linker carbon dots. Glucose, mannose, galactose, maltose and lactose were tested in this work. TEM images presented in this publication were carried out by myself. The main work in this paper involved the use of ultra-fast spectroscopy to elucidate the lifetimes of the long linker CDs.

Transient absorption (TA) of carbon dots involves a pump and probe laser which are sent to the sample in femto or nanosecond succession to sequentially excite the sample from the ground state to the excited state and then the probe laser is sent to collect a snapshot of the exited energy profile at the set delay time point between pump and probe. This snapshot is based on how much the sample absorbs the probe laser energy. The delay is varied to build up an image of the sample excited states over time. Shorter delay times between pump and probe imposes greater resolution. The time taken

for non-radiative decay between energy levels within the molecule is called the excited state lifetime and a single molecule has as many lifetimes as it has energy levels in the conduction band. Apart from the fluorescence mechanism, the intrinsic lifetimes along with QY of a CD will determine the appropriateness of the material for bioimaging[68].

Bioimaging application of CD is advantageous if the intrinsic lifetime is greater than commercial fluorophores such as fluorescein 4.1 ±0.1 ns, Rhodamine B 17.4 ±0.02 ns, Alexafluro 488 4.1 ns and Alexafluor 647 1 ns. Commonly for CDs with dual fluorescence the core PL will have a relatively longer decay lifetime such as 14 ns compared to the lifetime of 1.3 ns originating from shell and surface PL centre. The lifetime of interest can be selected through either relatively blue or red shifting the excitation wavelength as the core has a fluorescence maxima blue shifted relative to the surface PL centre[68].

The excitation wavelength used is close to the excitation maxima of the sample in our case 340 nm pump wavelength and white light (CW) probe. This wavelength is known to excite both fluorescence mechanisms present in our material, hence, multiple lifetimes were observed. T_1 lifetimes on the picosecond order between 4.2 - 15 ps (for both AmCD **16** and CD-carbohydrates) were attributed to core relaxation, dependent on solvent access to the CD surface groups below the inhomogeneous glycan corona. T_2 had ps lifetimes which scaled with T_1 hence, were also attributed to the core. Longer ns lifetimes T_3 was thought to be from the surface groups. Exciton trapping here confers a longer lifetime and we propose the majority of the fluorescence[91].

2.3 Conclusions and future work

In this chapter the CD structure and glycan functionalisation were investigated and characterised further when compared to previous work in the Galan group and the literature. Key findings include the need for better methods that can provide direct evidence of covalent functionalisation of carbon dots. Evidence of covalent linkage through an amide linked anomeric carbon was identified for mannose oligosaccharides on both short and long linker CDs, however it was also observed that non-covalently attached sugar might also be present on the CD surface. This information must be used to inform any experiments involving these materials. The glycan presentation is known to impact lectin binding through the cluster glycoside effect. Hence, interpreting binding studies with these glyconanoparticles must be correlated to nanoparticle-based glycan conjugation and thus presentation on the CD surface.

Furthermore, physical characterisation of long linker carbon dots was carried out to build up a full picture of the glyconanoparticle structure. Electronic properties of the carbon dot depend on the carbohydrate, changing the photoluminescence excitation in some cases, the fluorescence peak at 500 nm (dual fluorescence) and the quantum yield. These spectroscopic properties were determined for the specific batch of carbon dots which are used in the following chapter. Having developed and characterised these materials in the same way from the same synthesis batch of carbon dots allows for relative comparison between these material.

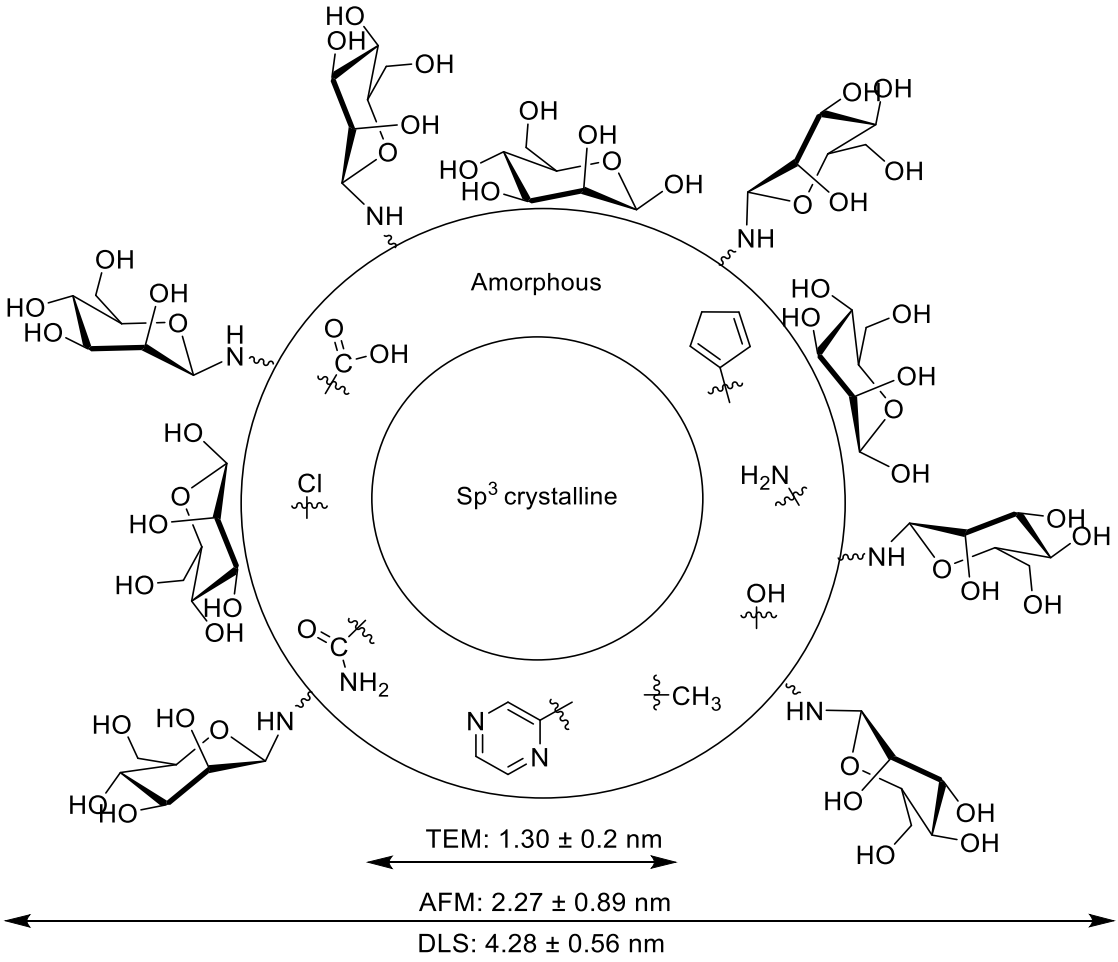

Figure 2.23 Summary figure of longer linker carbon dot functionalised with a generic carbohydrate (mannose in this case). Data from DLS and AFM from this chapter are used in combination with high-resolution TEM data from the thesis of S.Hill[83]. Surface functional group information informed through FTIR, the Molisch test and NMR.

The conclusive structure of long linker CD-carbohydrate is summarised in Figure 2.23. Previous high resolution TEM work by Stephen Andrew Hill[83] shows a core sp^3 crystalline structure, with an average size of 1.3 $\pm$ 0.2 nm and an sp^2 amorphous layer around that. AFM and DLS data show height and hydrated diameters of 2.27 $\pm$ 0.89 nm and 4.28 $\pm$ 0.56 nm respectively. These data can vary based on carbohydrate as shown by Swift *et al.*[94] and also between batches. NMR data showed that the carbohydrate present can be quantified relative to the carbon dot in the sample hence allowing

comparison between CD-carbohydrates. This method allows for the quantification of all carbohydrate present on the carbon dot surface both covalently bound and non-covalently associated. The Molisch test quantification method is appropriate for O-linked carbohydrates as this is more readily cleavable than our N-linked carbohydrates. TEM and zeta potential data shows that carbohydrate exists associated to the surface of the carbon dot. TEM also shows that material of low density exists in the CD-carbohydrate samples but not AmCD **16** or AcCD **17** samples suggesting the presence of glycans. Work by Swift *et al.*[94] shows that the glycan coating of the CD-carbohydrate is likely inhomogeneous as the surface of carbon dot is exposed post carbohydrate functionalisation. This makes sense as the structure of carbons dots is known to be quasi-spherical and the functional amine and acid handles are also likely inhomogeneously distributed on the CD surface.

Caveats include that it can be difficult to determine the ratio of covalently bound and non-covalently bound carbohydrate in each CD-carbohydrate sample. Also, the presentation of these glycans cannot directly be inferred. The ratio of linked and associated carbohydrate will differ between CD-carbohydrate samples; hence, binding studies would be specific to that sample. The long linker carbon dots would extend the carbohydrate away from the carbon dot surface if unfolded. However, with free carbohydrate associated through hydrogen, hydrophobic interaction this may not be the case. Indirect methods have been used to determine the lectin binding to these glyconanoparticles through a FRET assay in the next section.

2.4 Chapter 2 Experimental

2.4.1 Synthesis

1) Amine terminated CD core synthesis (AmCD 16)

Amine terminated carbon dots (AmCDs) numbered **16** were synthesised in a microwave assisted reaction from Glucosamine.HCl (1 g) and TTDDA (1.35 ml) dissolved in 20 ml deionised H_2O. Reaction was carried out in a 250 ml conical flask at the centre of an 800 W Wilkinson domestic microwave at 80% power for 3 minutes. CDs were extracted using H_2O/DCM and purified further using a Vivaspin 20 ml column 10,000 Da MWCO filter (GE Healthcare Life Sciences) centrifuged for 10 mins at 8,000 rpm. CD were lyophilised before further use. AmCD **16** synthesis was also scaled up using a hydrothermal method. Glucosamine.HCl (6 g) was heated in H_2O (8 ml) to 100 ^oC before TTDDA (8 ml) was added for 30 minutes. After synthesis, the same extraction and purification was carried out.

2) Acid terminated FCD functionalisation (AcCD 17)

AmCDs **16** (200 mg) were functionalised with a terminal acid group - AcCDs numbered **17** using succinic anhydride (200 mg) in 1:1 EtOH:H_2O overnight. CDs were purified using dialysis in a 500-1000 MWCO membrane (Biotech Spectra/Por dialysis membrane) overnight.

3) Kochetkov sugar amination

β-D-glycosylamines **1-8** were synthesised using the Kochetkov amination method to allow for conjugation onto the AcCD **17**. Reaction mix consisted of 15 g trisaccharide **6** & **8**, 10 g disaccharide **2,4** & **7** or 5 g for monosaccharides **1,3 & 5** (1% w/v) in saturated $(NH_4)_2CO_3$ stirred for 5 days at RT, over which solid $(NH_4)_2CO_3$ was added at 40 mg per mg of saccharide to ensure the reaction remains in excess. After the reaction the solution was lyophilised to remove excess $(NH_4)_2CO_3$ encouraged by re-dissolving in warm aq. MeOH as required. β-D-glycosylamines **1-8** were stored at -4 °C.

4) AcCD-saccharide functionalisation – EDC coupling

AcCD **17** (60 mg) was reacted with aminated saccharide (250 mg for monosaccharides) accounting for the Kochetkov amination yield in each case (Table 1) in 3ml H_2O with a 2-fold amount of EDC overnight. Unreacted material was removed through dialysis against deionised H_20 using a 500-1000 MWCO membrane (Biotech Spectra/Por dialysis membrane) overnight.

4b) AcCD-sialyl-D-lactose functionalisation – Reductive amination

AcCD **17** (10 mg) was dissolved in 1 ml deionised H_2O before either 3'-sialyllactose or 6'-sialyllactose (100 mg) was added to the solution and finally sodium cyanoborohydride (13 mg). The reaction was stirred for 3 hours. Unreacted material was removed through dialysing against deionised H_2O using a 5000 MWCO membrane overnight.

5) AcCDala synthesis[84]

"Short linker" acid terminated CDs – AcCDala numbered **10,** were synthesised from glucosamine.HCl and β-alanine in a 3 minute domestic microwave synthesis. Glucosamine.HCl (1.00 g, 4.63 mmol) was dissolved in 20 ml deionised H_2O before the addition and dissolving of β-alanine (0.45 g, 5.09 mmol). The reaction was carried out in a 250 ml conical flask at the centre of an 800 W Wilkinson domestic microwave at 80% power for 3 minutes. CDs were extracted using H_2O/DCM and purified further using a Vivaspin 20 ml column 10,000 Da MWCO filter centrifuged for 10 mins at 8,000 rpm. CD were lyophilised before further use.

6) AcCDala-saccharide functionalisation

AcCDala (30 mg) was dissolved in 3 ml deionised H_2O before the addition of coupling agent EDC (60 mg) and finally the aminated saccharide of interest (125 mg for monosaccharides). The reaction was left stirring for 16 h. Unreacted material was removed through dialysing against deionised H_2O using a 500-1000 MWCO membrane overnight.

2.4.2 Post Kochetkov amination characterisation of glycosylamines 1-8.

NMR was used to determine reaction yield for glycosylamines **1-5** using diagnostic β-anomeric peak shift as seen in table 1. The product and starting material anomeric peaks and α and β anomer signals are clearly distinguishable according to literature seen in ^{1}H NMR between 4.0-5.3 ppm and in ^{13}C between 82-105 ppm hence these are assigned. Where signals can be identified they are denoted as either starting material **†** and aminated product of interest *****. Where possible, using literature references other proton and carbon signals have been assigned. For novel glycosylamines **6-8** the anomeric proton and carbon signals have been assigned. Remaining starting material anomeric peaks are also identified **†**. Molecule **9** is also fully assigned in this section.

Notes on NMR assignments - ***** notates anomeric aminated product. **†** notates anomeric starting material. C1 and H1 refers to the 1st carbon position on the carbohydrate ring, moving around the ring clockwise to position 6. C1' refers to the second and C'' the third monosaccharide in an oligosaccharide beginning at the reducing end of the molecule. See Appendix for NMR spectra.

1 1-Amino-1-deoxy-β-D-galactopyranoside[95]

^{1}H NMR (400 MHz, D_2O): α-D-Galactopyranose δ = 5.25† (d, H1, 1H, J = 3.6) ppm**.** β-D-Galactopyranose δ = 4.61† (d, H1, 1H, J = 9.1) ppm**.** 1-Amino-1-deoxy-α-D-galactopyranose δ = 3.47 (dd, 2H, J = 9.6, 8.3)**.** 1-Amino-1-deoxy-β-D-galactopyranose δ = 4.25* (d, H1, 1H, J = 8.7), 3.38 (dd, 2H, J = 9.8, 8.7) ppm.

^{13}C NMR (126 MHz, D_2O): 1-Amino-1-deoxy-β-D-galactopyranose δ = 87.55* (C1), 75.85 (C5), 73.53 (C3), 71.90 (C2), 70.45 (C4), 61.15 (C6) ppm. 1-Amino-1-deoxy-α-D-galactopyranose δ = 68.96 (C4), 68.78 (C2) ppm. α-D-Galactopyranose δ = 92.41† (C1) ppm. Mass ES^+ prediction: 179.156 MW Measured mass ES^+: 202 and 364.1 MW.

2 1-Amino-1-deoxy-β-D-lactopyranoside[96]

^{1}H NMR (400 MHz, D_2O): α-D-Lactose δ = 5.22* (d,H1, 1H, J = 3.8) ppm. β-D-Lactose δ = 4.45 (d, 1H, J = 7.8), δ = 4.66 (d, 1H, J = 8.0) δ = 5.2 (d, 1H, J = 3.8) ppm. 1-amino-1-deoxy-β-D-lactose δ = 4.44* (d, 1H, J = 7.8), 4.11 (d, 1H, J = 8.8), 3.92 (d, 1H, J = 3.4), 3.96 (d, 1H, J = 2.4), 3.85-3.55 (m, 9H), 3.22 (m, 1H) ppm.

^{13}C NMR (126 MHz, D_2O): β-D-Lactose δ = 102.47 (C1) ppm. 1-amino-1-deoxy-β-D-lactose δ = 102.47, 84.42, 68.41, 68.62, 73.57 ppm. Mass ES^+ prediction: 341.3 MW Measured mass ES^+: 364.1 MW.

3 1-Amino-1-deoxy-β-D-glucopyranoside[97]

^{1}H NMR (400 MHz, D_2O): α-D-Glucopyranose δ = 5.18† (d, 1H, H1 J = 3.8) ppm. β-D-Glucopyranose δ = 4.59† (d, 1H, H1 J = 7.9), 3.85 (s, 1H), 3.73 (s, 1H), 3.56 (d, 1H, J = 3.7), 3.49 (s, 1H), 3.43 (s, 1H), 3.27 (t, 1H J = 8.6) ppm. 1-Amino-1-deoxy-β-D-glucopyranose δ = 4.24* (d, 1H, H1 J = 8.9), 3.60 (d, H6a, 1H, J = 6.0), 3.78 (d, H6b, 1H, J =), 3.14 (t, H2, 1H, J = 9.0) ppm.*^{13}C NMR (126 MHz, D_2O):* α-D-Glucopyranose δ = 91.84 (C1) ppm. β-D-Glucopyranose δ = 95.66 (C1), 75.67, 74.06, 72.60, 71.32, 71.32 69.54 ppm. 1-Amino-1-deoxy-β-D-glucopyranose δ = 84.85* (C1), 72.41 (C2) 60.49 (C6) ppm. Mass spectroscopy ES^+ prediction: 179.156 MW Measured mass: 202, 364, 381 MW.

4 1-Amino-1-deoxy-β-D-maltopyranoside[96]

^{1}H NMR (400 MHz, D_2O): β-D-maltopyranose δ = 4.59 (d, 1H, H1 J=8.0) ppm. α-D-maltopyranose δ = 5.16† (d, 1H, H1 J=3.8), 5.34† (d, 1H, H1' J=3.8) ppm. 1-amino-1-deoxy-α-D-maltose δ = 5.28† (d, 1H, H1', J = 5.5) ppm. 1-amino-1-deoxy-β-D-maltose δ = 4.64* (d, 1H, H1 J = 9.1), 4.23* (d, 1H, H1', J= 8.9), 4.04* (d, 1H', J =8.8) ppm.*^{13}C NMR (126 MHz, D_2O):* β-D-maltopyranose δ = 95.47 (C1) ppm. α-D-maltopyranose δ = 78.94 (C1), 99.69 (C1') ppm. 1-amino-1-deoxy-α-D-maltose δ = 71.52 (C1) ppm. 1-amino-1-deoxy-β-D-maltose δ = 82.75 (C1), 84.00 (C1'), 86.61 (C1') ppm. Mass spectroscopy ES^+ prediction: 341.3 MW Measured mass: 364 MW.

5 1-Amino-1-deoxy β-D-mannopyranose[98]

^{1}H NMR (400 MHz, D_2O): β-D-mannose δ = 4.88† (d, 1H, H1 J= 1.1 ppm. α-D-mannose δ = 5.16 (d, 1H, H1 J=1.9) ppm. 1-amino-1-deoxy-β-D-mannose δ = 4.32* (d, 1H, H1 J=1.1) 3.93 (dd, 1H, J = 1.1), 3.40 (d, 1H, J = 2.2) ppm.*^{13}C NMR (126 MHz, D_2O):* β-D-mannose δ = 82.01† (C1) ppm. α-D-mannose δ = 80.30† (C1) ppm. 1-amino-1-deoxy-β-D-mannose δ = 82.36* (C1) ppm.

6 3,6-Di-*O*-(α-D-mannopyranosyl)-1-amino-1-deoxy-D-mannopyranose

^{1}H NMR (500 MHz, D2O): δ = 4.38 (d, 1H, H1 J = 1.1) ppm δ = 4.90 (d, 1H, H1 J= 1.7) ppm δ = 5.14 (d, 2H, H1 J= 1.7) ppm. All product, no sm.*^{13}C NMR (126 MHz, D_2O):* δ = 85.75 (C1), 102.50 (C1'), 105.30 (C1'') ppm. MS ES+ found *m/z*: 504.1916 527.1586, 528.1605.

7 4-*O*-(α-D-Mannopyranosyl)-1-amino-1-deoxy-D-mannopyranose

^{1}H NMR (500 MHz, D_2O): 4-*O*-(α-D-Mannopyranosyl)-1-amino-1-deoxy-D-mannopyranose δ = 4.20 (d, 1H, H1 J = 1.1), 4.22 (d, 1H, H1 J = 1.1), 4.39 (d, 0.25H, H1), 4.42 (s, 0.39H), 4.62 – 4.59 (m, 2H), 5.04 (dd, J = 6.2, 2.0 Hz, 1H), 5.12 (dd, J = 4.4, 1.8 Hz, 2H) ppm.*^{13}C NMR (126 MHz, D_2O):* 4-*O*-(α-D-Mannopyranosyl)-D-mannopyranose δ = 101.43, 93.97 ppm**.** 4-*O*-(α-D-Mannopyranosyl)-1-amino-1-deoxy-D-mannopyranose δ = 100.11, 85.24, 82.48 ppm. MS ES+ found *m/z*: 365.1099

8 β-D-Mannopyranose-(1—4)-β-D-mannopyranose-(1—4)-1-amino-1-deoxy-β-D-mannopyranose

^{1}H NMR (500 MHz, D_2O): Product: δ = 4.36 (d, 1H, H1 J = 1.1, C1), δ = 4.56 (s, 0.39H), δ = 4.92 (d, 1H, H1 J= 1.1) δ = 4.73 (d, 1H, H1) ppm**.** *SM:* δ = 4.62 – 4.59 (m, 2H) δ = 5.04 (dd, J = 6.2, 2.0 Hz, 1H) δ = 5.19 (dd, J = 4.4, 1.8 Hz, 2H) ppm. *^{13}C NMR (126 MHz, D_2O): Product* δ = 82.46 (C1), 84.98, 100.16 ppm. *SM:* δ = 93.72, 93.88 ppm. MS ES+ found *m/z*: 504.1916, 505.1911

9 1-amino-(4-oxobutanoic acid)-*β*-D-glucopyranose (synthesised by another member of the Galan group) *^{1}H NMR (500 MHz, D_2O):* δ = 4.94 (1H, d, H1, J = 9.1 Hz), 3.85 (1H, dd, H6a, J = 2.2 Hz), 3.6 (1H, dd, J = 12.4 Hz, H6b, 5.3 Hz), 3.56-3.46 (2h, m, H3, H5) 3.43-3.34 (2H, m, H2, H5) 2.70 – 2.58 (4H, m, CH_2) ppm. **^{13}C NMR (126 MHz, D_2O):** δ = 30.89, 61.13, 61.16, 69.92, 72.43,77.20, 78.22 and 79.94 ppm.

2.4.3 Post synthesis and purification characterisation of carbon dots 10, 16 & 17

10 AcCDala

^{1}H NMR (400 MHz, D_2O): δ = 2.65 (t, 2H, J= 6.5, b) *δ* = 3.15 (t, 2H, J= 6.5, a) ppm. *^{13}C NMR (126 MHz, D_2O): δ* = 35.24 (a), 31.37 (b) ppm.

16 AmCD

^{1}H NMR (500 MHz, D_2O): δ = 5.09 (s, 1H) 3.50-3.60 (m, c-h), 2.97 (t, J = 7.2 Hz a,j), 1.83 (q, J = 6.0 Hz, b,i) ppm. *^{13}C NMR (126 MHz, D_2O): δ* = 27.82, 37.50, 68.31, 69.27 71.37 ppm.

17 AcCD

^{1}H NMR (500 MHz, D_2O): δ = 5.10 (d, 1H, J = 2.3 Hz), 3.60-3.50 (d-g), 3.45 (t, J = 8 Hz, c,h), 3.13 (t, J = 8 Hz, j), 2.89 (t, J = 8 Hz, a), 2.53 (t, J = 8 Hz, l), 2.38 (t, J = 8 Hz, k), 1.82 (p, J = 8 Hz, b), 1.65 (p, J = 8 Hz, i) ppm. *^{13}C NMR (126 MHz, D_2O):* δ = 26.53, 28.29, 29.46, 30.24, 36.29, 37.66, 68.32, 69.49, 71.45 ppm.

2.4.4 Post purification characterisation of CD-carbohydrates 11-15 and 18-27.

Presented is the NMR characterisation of all CD-carbohydrates **11-15** and **18-27** synthesised in this work. For **11-13** (short linker) and **18-20** (long linker) where an amide linkage can be indirectly inferred through ^{13}C NMR between 70-82 ppm this is identified with a *. For glycan functionalised carbon dots where the conjugated anomeric cannot be seen, where possible the starting material and aminoglycosyl anomeric peaks are identified. For sialyllactose conjugated carbon dots **26** and **27** the anomeric peaks are identified. No sialyllactose conjugation is observed through NMR as the anomeric proton next to the amide bond is not seen in the ^{13}C in the region 82-105 ppm.

11 CDala-1,4-mannotriose

^{1}H NMR (500 MHz, D_2O): δ = 4.60 (s, 1H), 4.63 (1H, H1), 4.75 (s, 1H), 4.78 (d, J = 0.9 Hz, 1H), 5.02* (d, J = 2.3 Hz, 1H), 5.05 (d, J = 1.5 Hz, 1H) ppm**.** *^{13}C NMR (126 MHz, D_2O): δ* = 93.77, 71.32*, 93.68, 96.88, 100.06, 100.12 ppm.

12 CDala-4-O-mannobiose

^{1}H NMR (500 MHz, D_2O): δ = 4.61 (s, 1H), 4.73 (s, 1H), 4.75 (d, 1H, J = 1.1 Hz), 4.78 (d, 1H, J = 1.1 Hz), 5.06 – 5.01* (m, 3H), 5.12 (t, 1H, J = 2.5 Hz) ppm. *^{13}C NMR (126 MHz, D_2O): δ* = 71.25*, 93.71, 93.51, 100.16, 101.33 ppm.

13 CDala-1,3-1,6-manntriose

^{1}H NMR (500 MHz, D_2O):δ = 4.60 (s, 1H, H1), 4.63 (1H, H1), 4.75 (s, 1H, H1), 4.78 (d, 1H, H1 J= 0.9), 5.03* (d, 1H, H1 J= 2.3), 5.05 (d, 1H, H1 J= 1.5) ppm. *^{13}C NMR (126 MHz, D_2O): δ* = 93.79, 71.34* (C1), 93.64, 96.90, 100.07, 100.15 ppm.

14 CDala-galactose

^{1}H NMR (400 MHz, D_2O): δ = 4.25 (d, 1H, J = 8.8), 4.60 (d, 1H), 4.89 (s, 1H), 5.28 (d, 1H, J = 3.7) ppm. *^{13}C NMR (126 MHz, D_2O): δ* = 70.39 (C1), 94.90, 91.51 ppm.

15 CDala-mannose

^{1}H NMR (500 MHz, D_2O): δ = 5.04 (s, 1H), 4.76 (s, 1H), 4.41 (s, 1H) ppm. *^{13}C NMR (126 MHz, D_2O): δ* = 85.02, 93.81, 93.42 ppm.

18 CD-1,4-mannotriose

^{1}H NMR (500 MHz, D_2O): δ = 5.05 (d, 1H, J= 1.5 Hz), 5.02* (d, 1H, J = 2.3 Hz), 4.78 (s, 1H), 4.76 (s, 1H) ppm. *^{13}C NMR (126 MHz, D_2O): δ* = 71.45* (C1), 93.71, 93.71, 96.84, 100.16, 100.16 ppm.

19 CD-4-*O*-mannobiose

^{1}H NMR (500 MHz, D_2O): δ = 5.12 (d, J = 2.5 Hz, 1H), 5.05 (d, J = 2.0 Hz, 1H), 5.02* (d, J = 2.0 Hz, 1H), 4.78 (s, 1H), 4.75 (s, 1H), 4.61 (s, 1H) ppm. *^{13}C NMR (126 MHz, D_2O): δ* = 71.23*, 93.71, 93.71, 93.71, 100.16, 101.33 ppm.

20 CD-1,3-1,6-mannotriose

^{1}H NMR (500 MHz, D_2O): δ = 5.05 (d, J = 1.,6 Hz, 1H), 5.02* (s, 1H), 4.78 (s, 1H), 4.76 (s, 1H) 4.60 (s, 2H) ppm. *^{13}C NMR (126 MHz, D_2O): δ* = 71.35*, 93.81, 93.61, 96.84, 100.06, 100.16 ppm.

21 CD-galactose

^{1}H NMR (400 MHz, D_2O): δ = 5.12 (d, J = 3.8 Hz, 1H), 4.44 (d, J = 7.9 Hz, 1H) ppm. *^{13}C NMR (126 MHz, D_2O): δ* = 92.20, 96.35 ppm.

22 CD-mannose

^{1}H NMR (400 MHz, D_2O): δ = 5.10 (d, J = 1.6 Hz, 1H), 4.82 (d, J = 1.2 Hz, 1H) ppm. *^{13}C NMR (126 MHz, D_2O): δ* = 82.57, 85.15, 93.69, 94.02 ppm.

23 CD-maltose

^{1}H (Presat) NMR (500 MHz, D_2O): β-D-maltose *δ* = 3.24 (m, 1H), 3.38 (t, 1H, J = 9.4), 4.68 (d, 1H, J = 7.9) ppm. α- D-maltose *δ* = 5.21 (d, 1H, J = 3.7), 5.36 (d, 1H, J = 3.8) ppm. Amino-1-deoxy-β-D-maltose *δ* = 4.11 (d, 1H, J = 8.9), 4.17 (d, 1H, J = 8.8) ppm. *Other new significant peaks δ* = 4.26 (d, 1H, J = 8.9), 4.87 (d, 1H, J = 5.4) ppm. *^{13}C NMR (126 MHz, D_2O):* β-D-maltose *δ* = 69.22, 72.39, 95.60 ppm. α- D-maltose *δ* = 91.56, 99.30 ppm. Amino-1-deoxy-β-D-maltose *δ* = 86.73, 86.73 ppm. *Other new significant peaks δ* = 85.41, 86.34 ppm.

24 CD-glucose

^{1}H (Presat) NMR (500 MHz, D_2O): β-D-glucose *δ* = 3.25 (t,1H, J = 8.9), 4.62 (dd, 1H, J = 8.0) ppm. Amino-1-deoxy-β-D-glucose *δ* = 3.14 (t, 1H, J = 9.0) ppm. Other new significant peaks *δ* = 4.30 (d, 1H, J = 8.9) ppm. *^{13}C NMR (126 MHz, D_2O):* β-D-glucose *δ* = 73.27 ppm. Amino-1-deoxy-β-D-glucose *δ* = 95.79 ppm. Other new significant peaks *δ* = 86.82 ppm.

25 CD-lactose

^{1}H (Presat) NMR (500 MHz, D_2O): β-D-Lactose *δ* = 4.68**†** (d, 1H, J = 7.8), *δ* = 4.46**†** (d, 1H, J = 7.9). α-D-Lactose *δ* = 5.23 (d, 1H, J = 3.8). amino-1-deoxy-β-D-lactose *δ* = 4.45* (d, 1H, J = 7.9) 4.16* (d, 1H, J = 9.0) 3.98 (d, 1H, J = 2.8) 3.94 (d, 1H, J = 3.4) ppm**.** *^{13}C NMR (126 MHz, D_2O):* β-D-Lactose *δ* = 102.80**†**, 95.57**†** ppm. α-D-Lactose *δ* = 91.66 ppm**.** amino-1-deoxy-β-D-lactose *δ* =102.98*, 86.8*, 68.61, 59.99 ppm.

26 CD-3'-sialyllactose

^{1}H (Presat) NMR (500 MHz, D_2O): δ = 5.09 (d, J = 3.8 Hz, 1H), 4.53 (d, J = 7.9 Hz, 1H), 4.40 (d, J = 7.8 Hz, 1H) ppm.*^{13}C NMR (126 MHz, D_2O): δ* = 102.61, 95.77, 91.86 ppm.

27 CD-6'-sialyllactose

^{1}H (Presat) NMR (500 MHz, D_2O): δ = 5.10 (d, 1H, J = 3.8 Hz) 4.54 (d, 1H, J = 8.0 Hz), 4.30 (d, 1H, J = 7.9 Hz) ppm. *^{13}C NMR (126 MHz, D_2O): δ* = 102.96, 95.74, 91.83 ppm

2.4.5 Molisch's Test

In a proposed mechanism of the Molisch's test[99,100] the mono-, di- or tri- saccharide is first dehydrated using H_2SO_4 to the hydroxymethylfurfuryl via intermediates of type X and Y. Subsequently the hydroxymethylfurfuryl reacts with 2 equivalents of phenol in a condensation reaction to form a product which is oxidised to chromophore Z which absorbs at 490 nm. In this method irrespective of sugar structure or functional groups around the ring the same enol form intermediate X is formed and subsequently chromophore Z. However, this reaction efficiency is known to depend on the initial carbohydrate hence a calibration curve must be produced in each case (Figure S.2a). In this way the carbohydrate conjugated onto a nanoparticle can be quantified in terms of μmol or ug per gram of CD-carbohydrate. Other methods involve using anthrone, ornicol, resorcinol for the condensation step. However, these methods are reported to be less sensitive as well as less convenient in that the molar absorptivity varies greatly between carbohydrates in these methods[93,101].

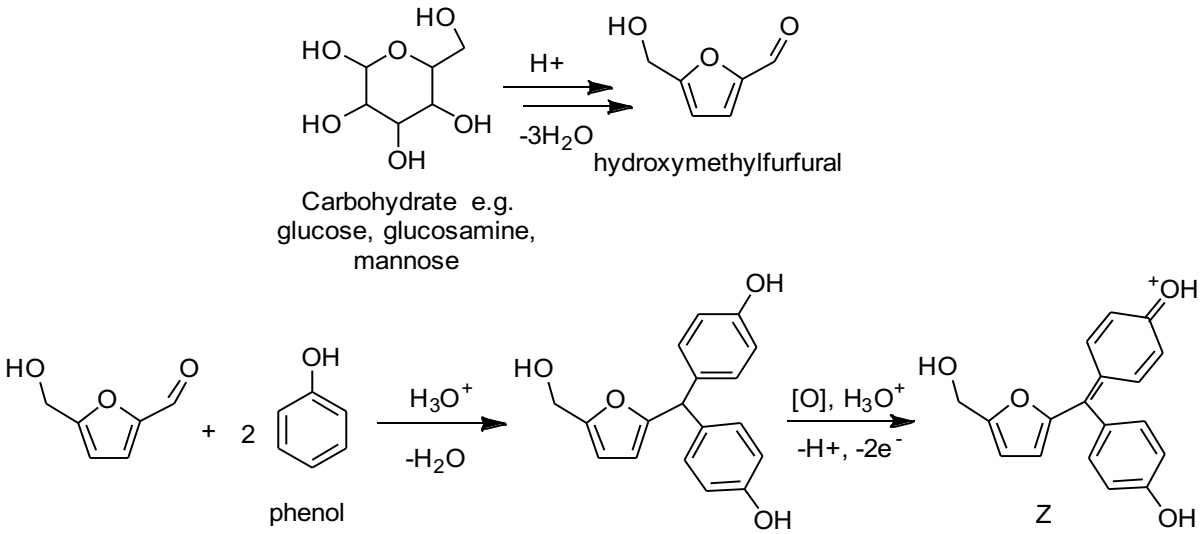

Supplementary Figure 2.1 Molisch's Test Mechanism. Carbohydrate is dehydrated with H_2SO_4 and then chromophore Z is made by reacting with two molecules of phenol with the hydroxymethylfurfural.[99,100]

Method according to Masuko *et al.*[93] CD-carbohydrate at stock concentration 600 μgml^{-1} in H_2O (50 μL) was placed in a 96-well plate well and 5 subsequent 2-fold serial dilutions were made. 150 μL of concentrated H_2SO_4 was added to each well and plate was shaken for 30 min. Then 30 μL of phenol solution 5% w/v in water was added to each well and plate was heated to 90 °C in a static water bath for 5 min, before cooling to RT in another water bath for 5 min. Absorption at 490 nm was measured using a plate reader.

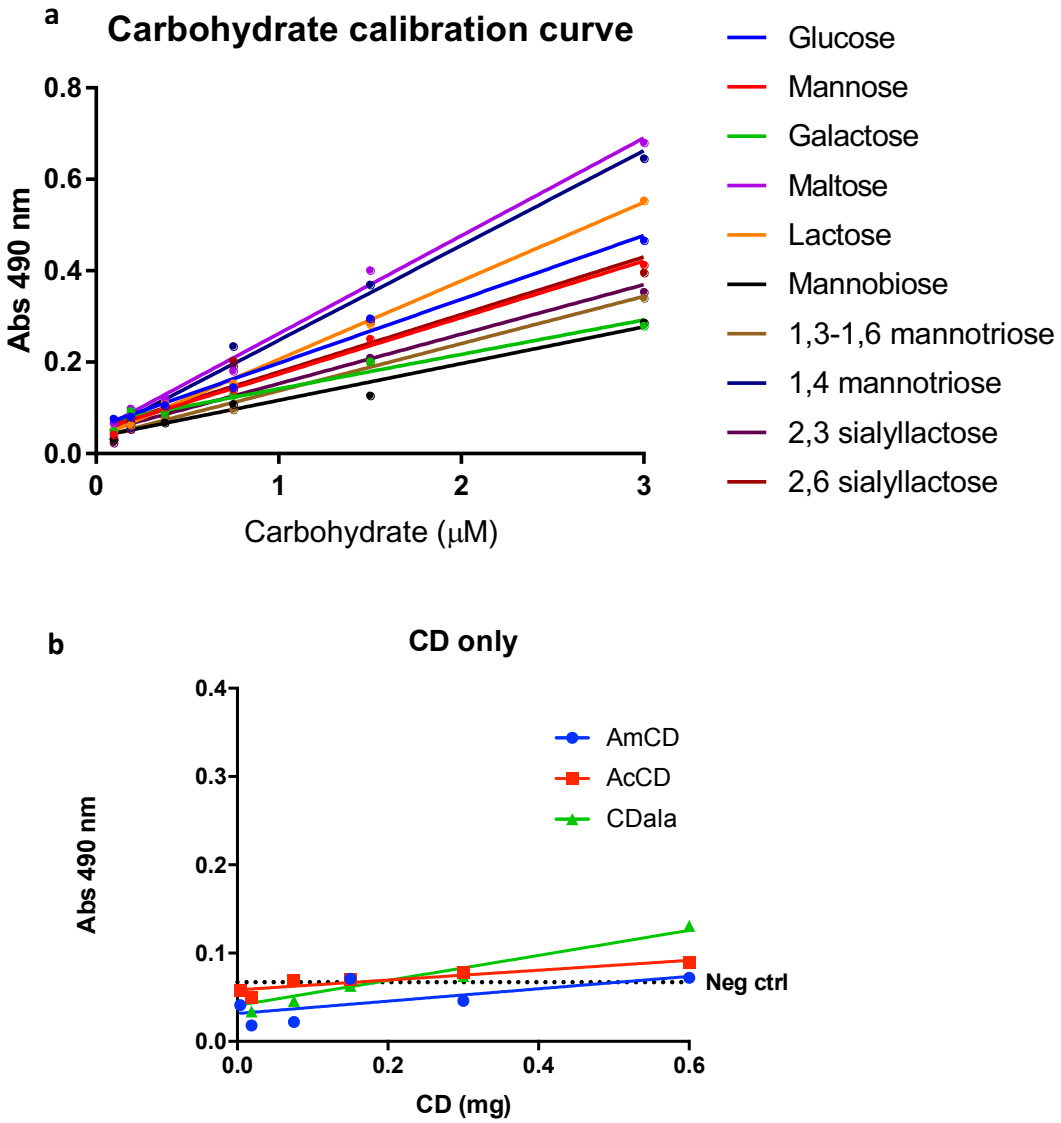

Supplementary Figure 2.2 Molisch's test graphs. a) calibration curve for carbohydrate absorption at increasing concentration. b) Unfunctionalised carbon dot, AmCD (blue line), AcCD (red line) and AcCDala (green line) was measured as a function of concentration. Negative control of H_2O was measured and shown as a black dotted line on the graph.

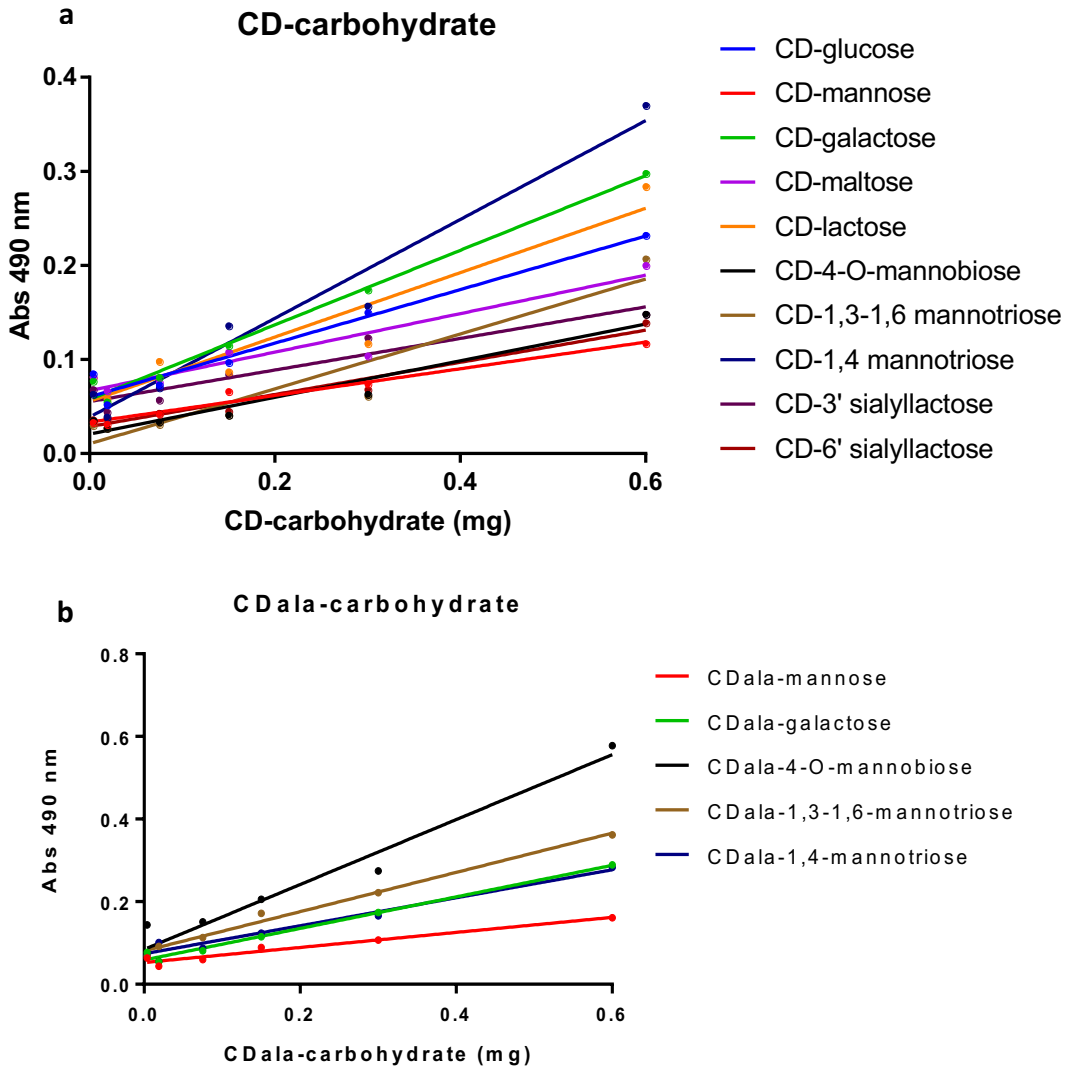

Supplementary Figure 2.3 Molisch's test graphs. a) CD-carbohydrate (long linker CD) results. b) CDala-carbohydrate (short linker CD) results. Using the calibration curve (Figure S2.2a) the absorption measured experimentally was used to determine the carbohydrate present.

2.4.6 NMR experimental

50 μg of Imidazole was dissolved in D_2O along with 0.5 mg CD-4-*O*-mannobiose before ^1H NMR was carried out to quantify the moles of carbohydrate conjugated to the carbon dot through having identified the anomeric carbon close to the amide linkage to the carbon dot. The imidazole singlet at 7.18 ppm and the anomeric peak at 5.04 ppm (identified using HSQC Figure A.19) from the CD-4-*O*-mannobiose were integrated, (assuming that the conjugated sugar was 4-*O*-mannobiose), the moles of sugar was determined to be 7.47 $x10^{-8}$ moles in 0.5 mg or 51 mg/g CD-4-*O*-mannobiose. This is 5.1 % by mass sugar which is 80 times more than 0.064% determined using the Molisch's test.

2.4.7 UV-Vis spectra

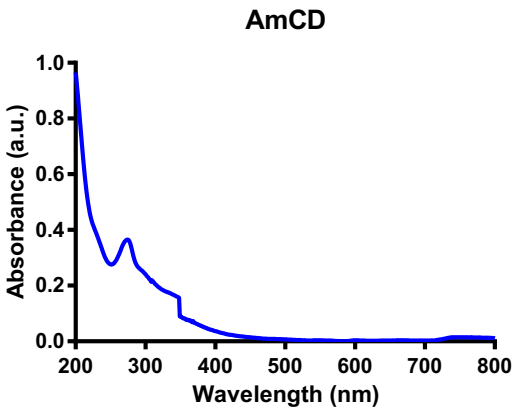

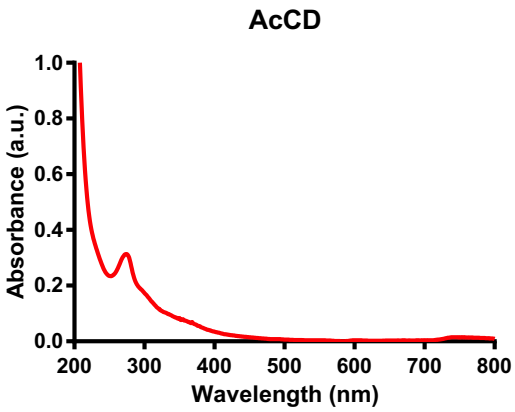

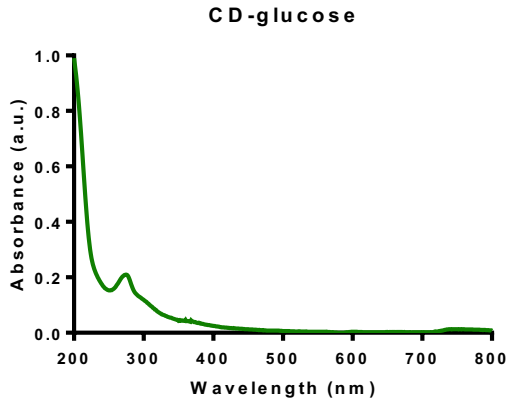

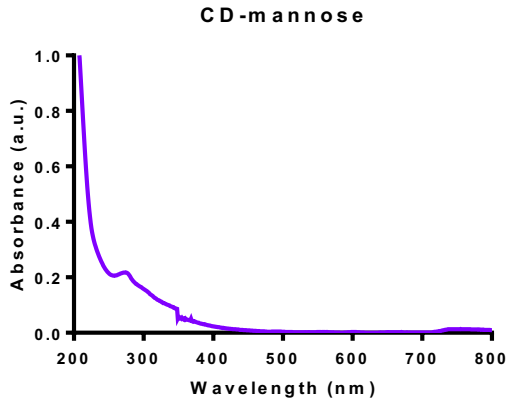

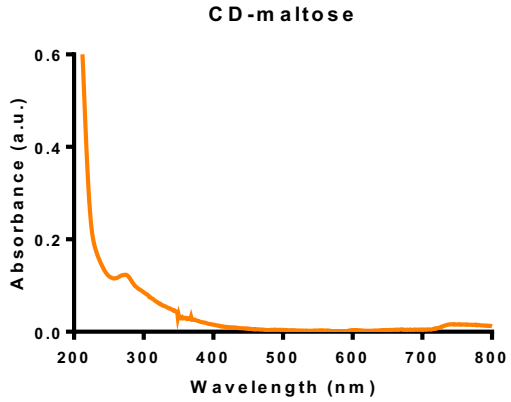

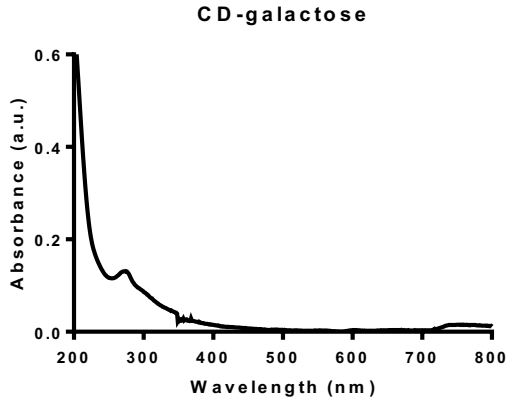

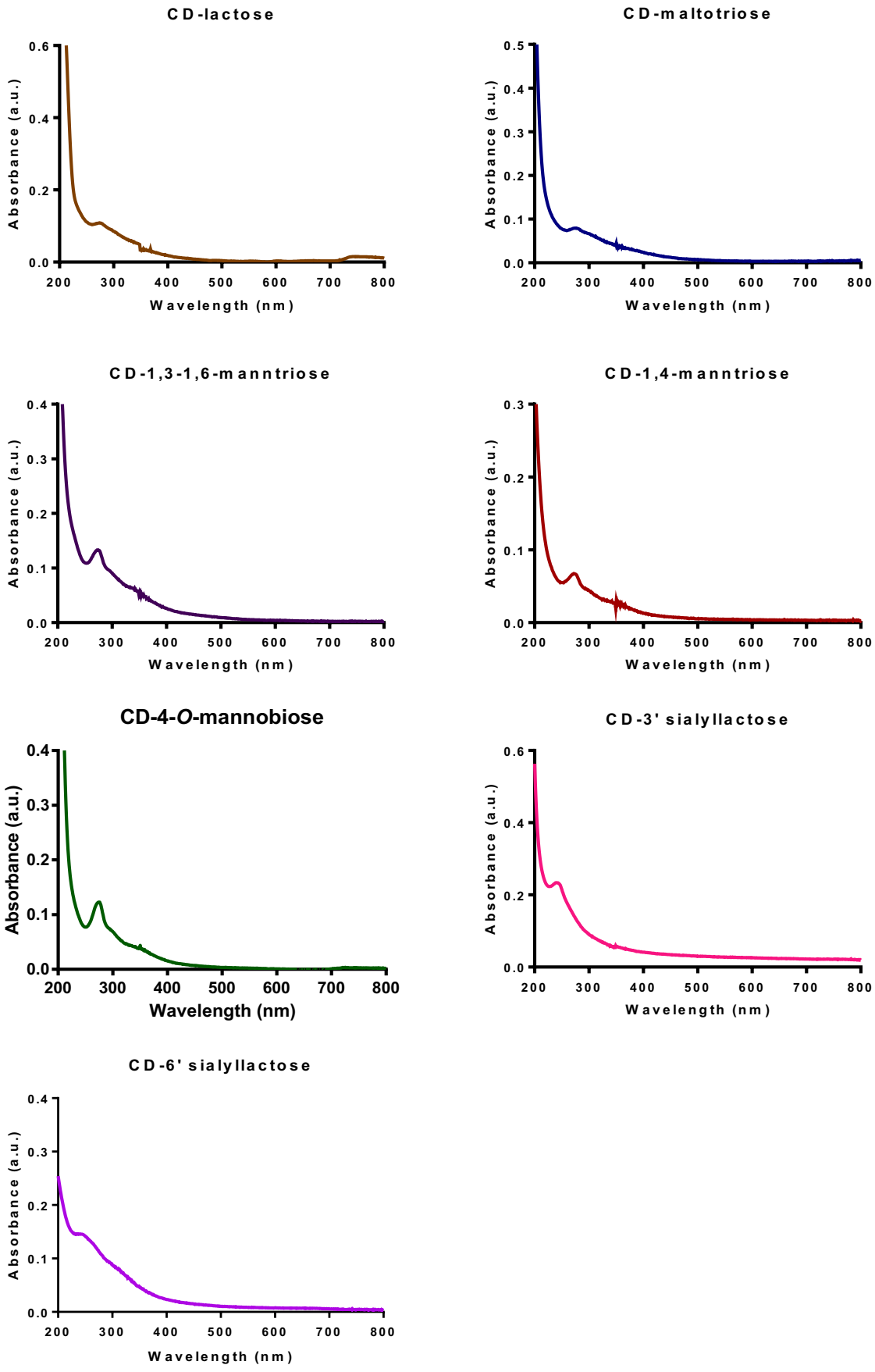

Supplementary Figure 2.4 UV-Vis data for all longer linker carbon dots and CD-carbohydrates synthesised.

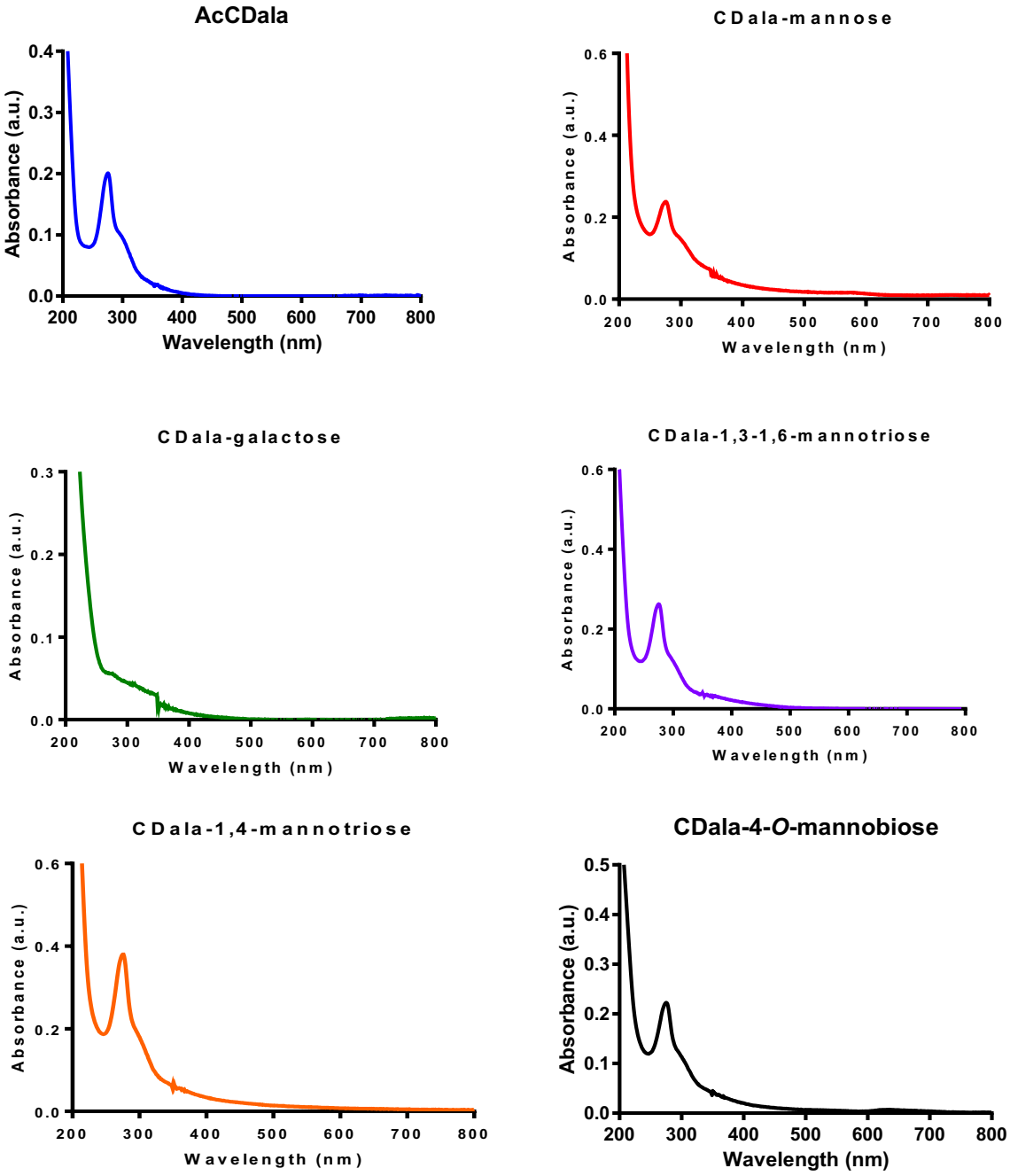

Supplementary Figure 2.5 UV-Vis data for all shorter linker carbon dots and CDala-carbohydrates synthesised.

2.4.8 Fluorescence spectra

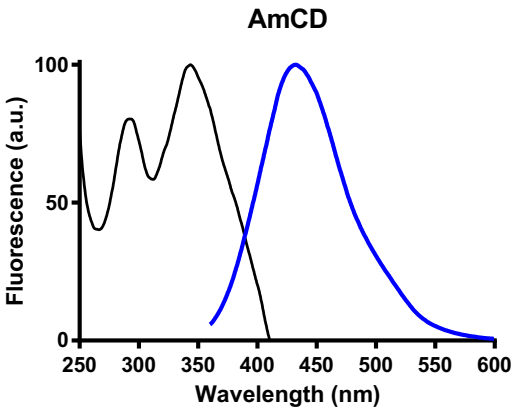

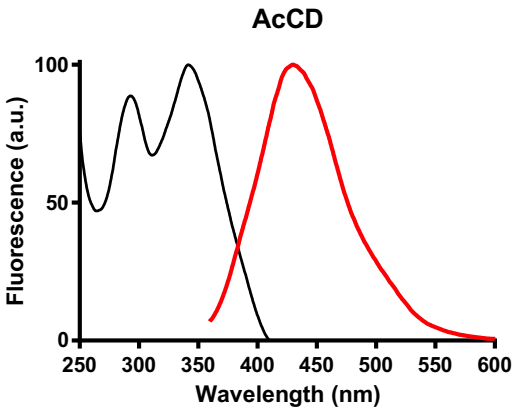

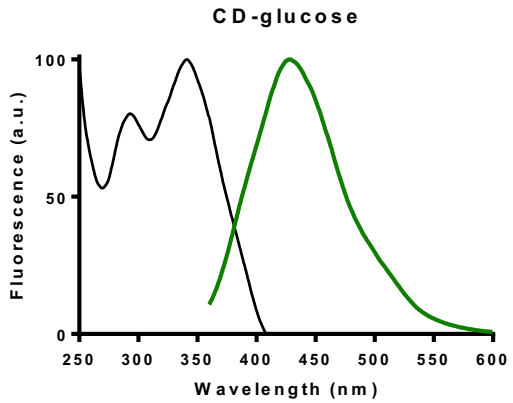

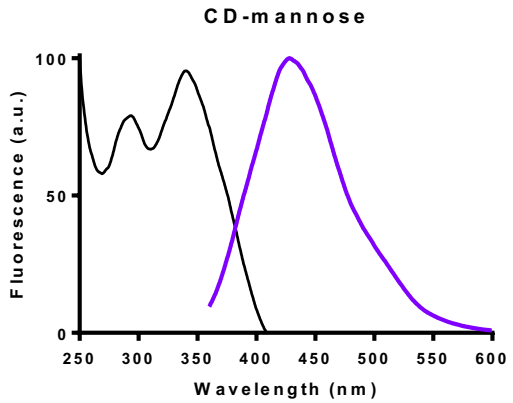

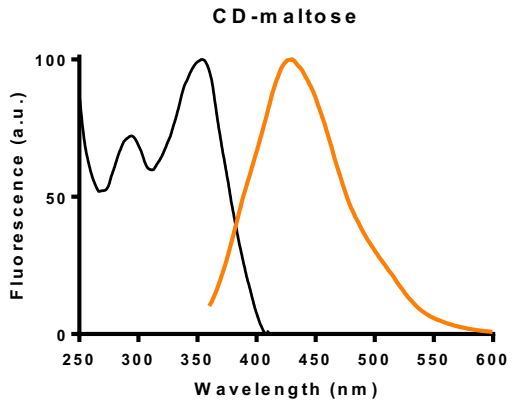

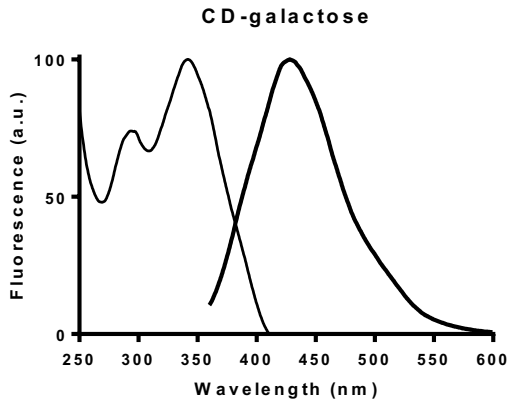

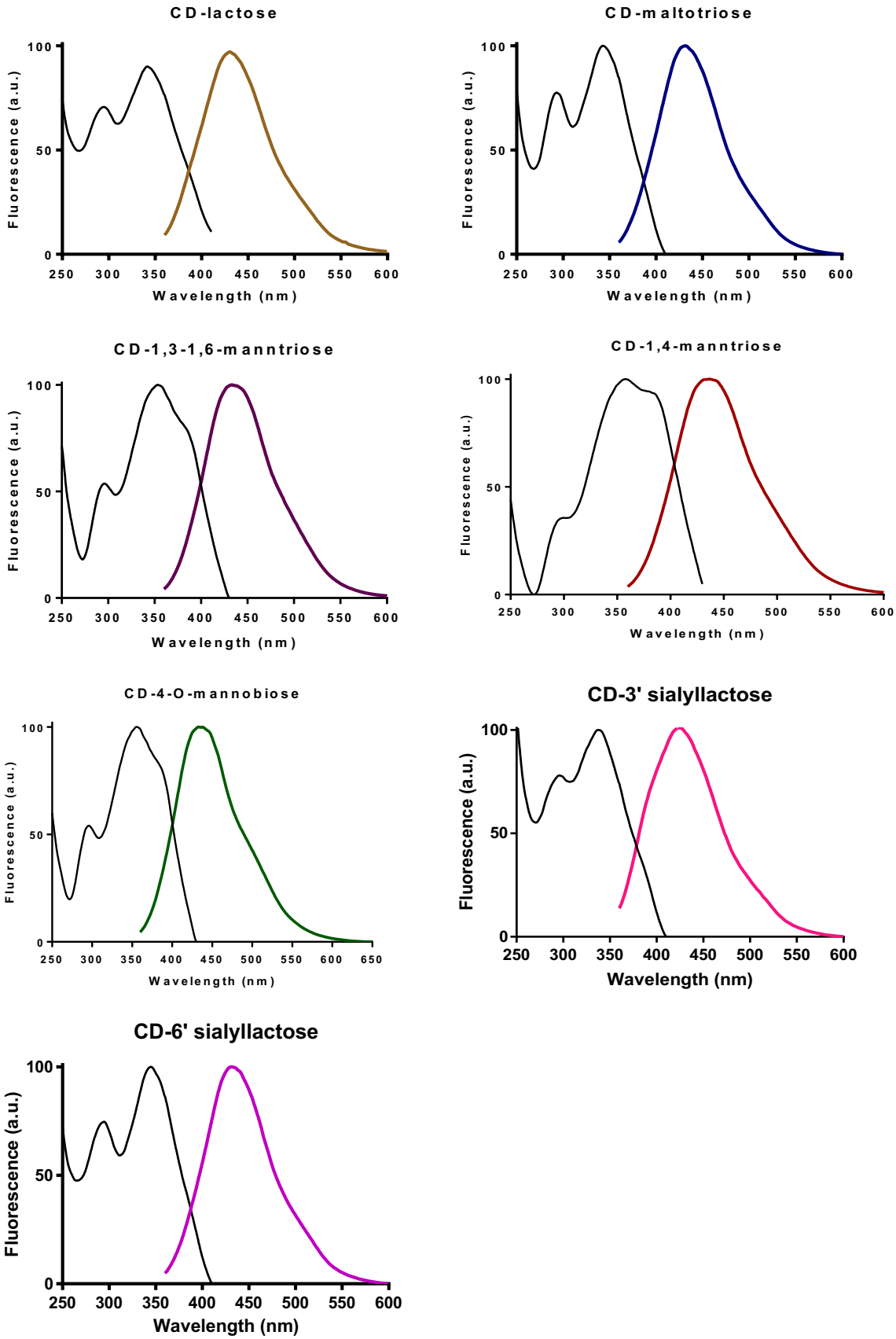

Supplementary Figure 2.6 Fluorescence spectra for all longer linker carbon dots and CD-carbohydrate synthesised.

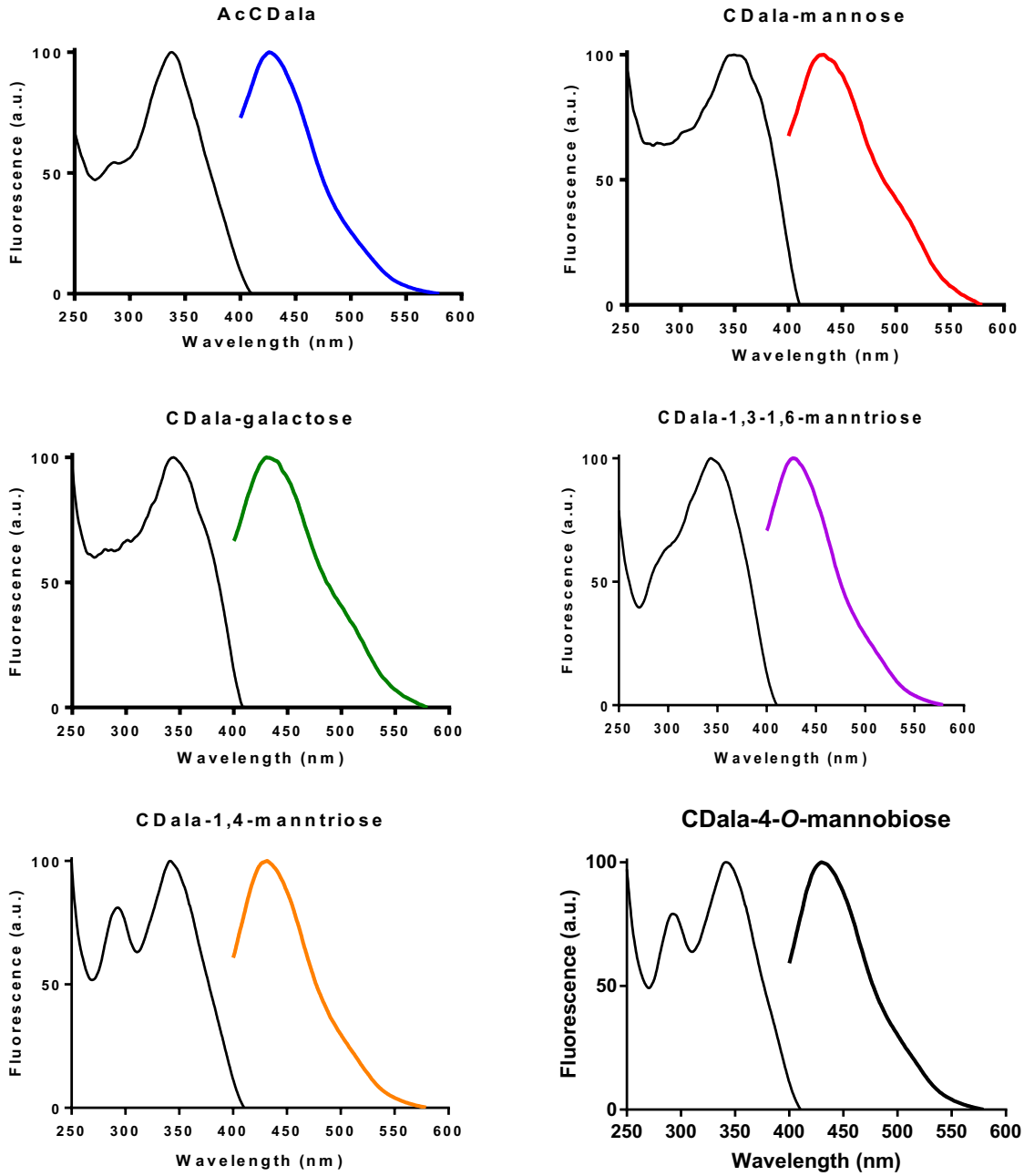

Supplementary Figure 2.7 Fluorescence spectra for all shorter linker carbon dots and all CDala-carbohydrates synthesised.

2.4.9 Quantum yield raw data

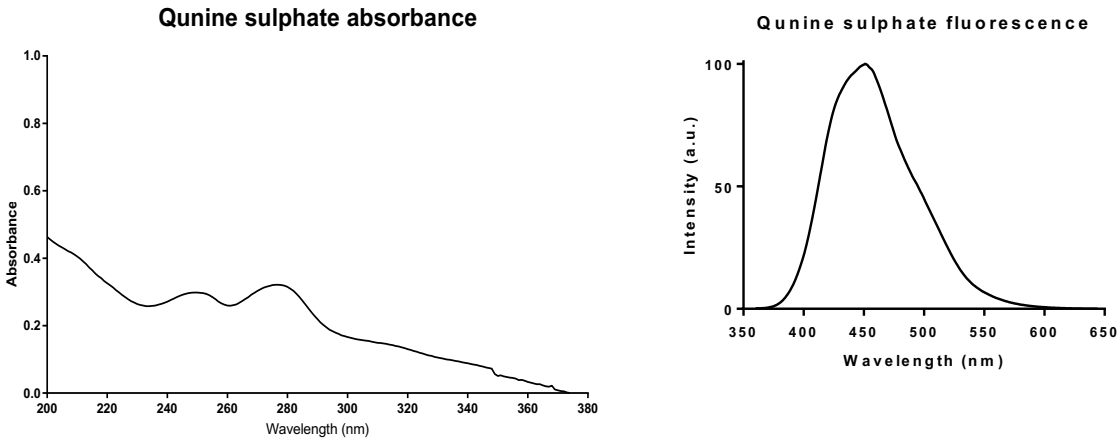

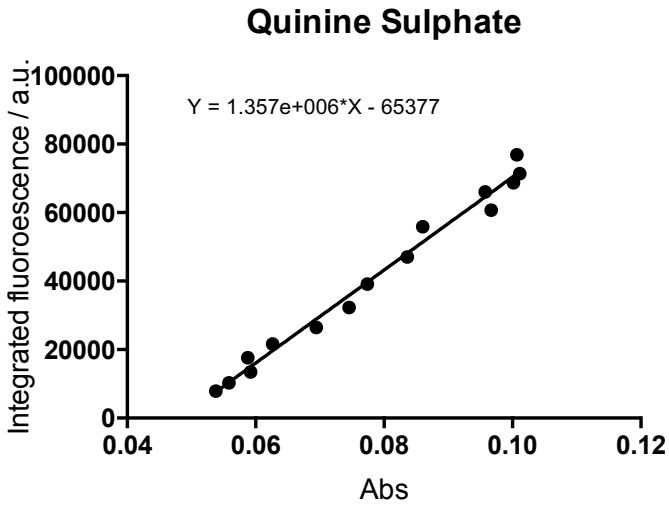

Supplementary Figure 2.8 Quantum yield standard quinine sulfate (QS) absorbance and fluorescence profile. Calibration curve generated from experimental data, plotting fluorescence v. absorbance when absorbance was > 0.1. The gradient of this line was used to determine the QY of carbon dot samples using the QY equation.

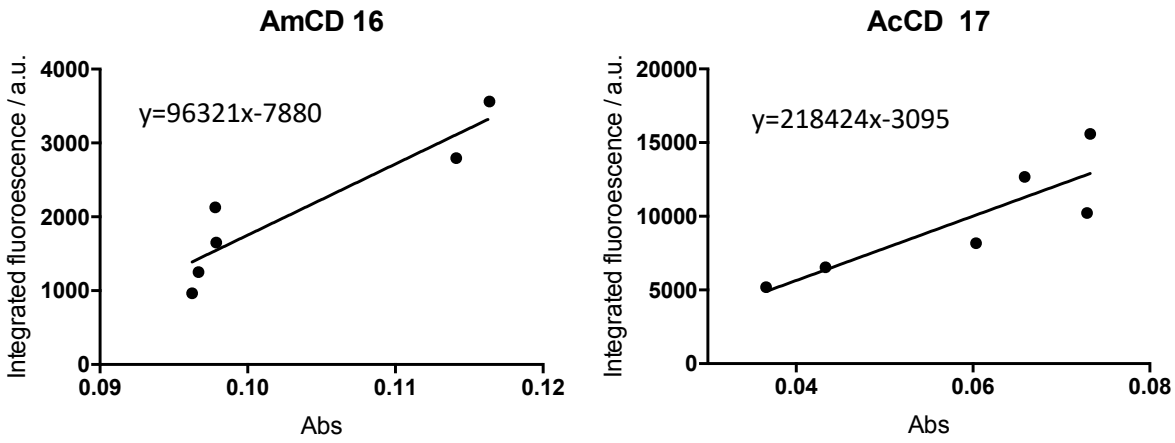

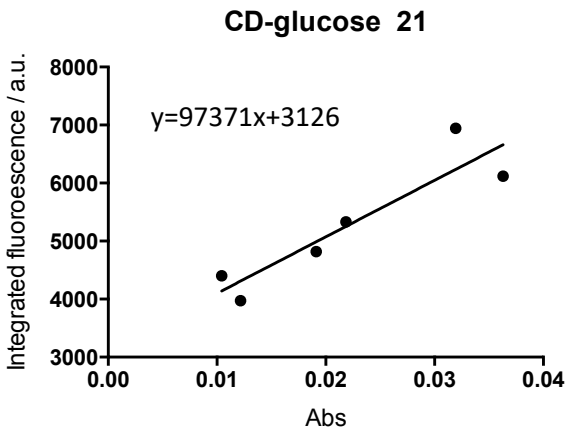
CD-glucose 21
y=97371x+3126
Integrated fluoroescence / a.u.
Abs

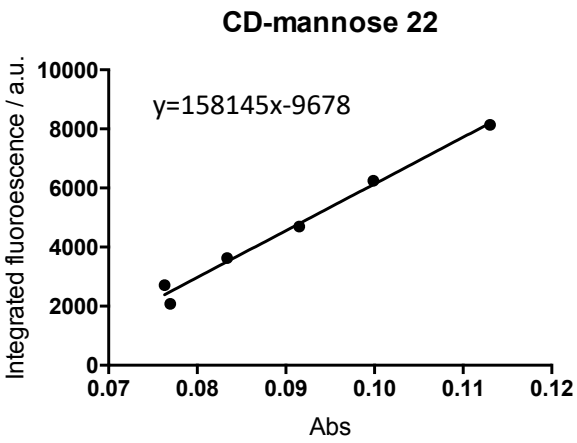
CD-mannose 22
y=158145x-9678
Integrated fluoroescence / a.u.
Abs

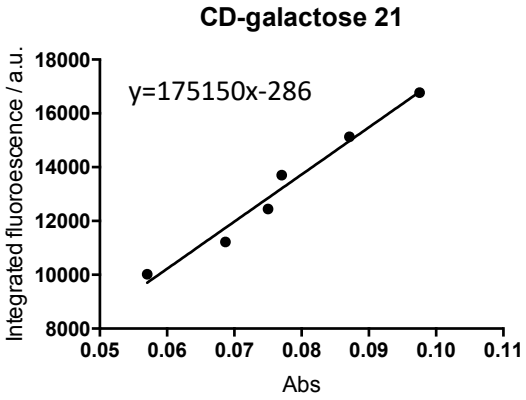
CD-galactose 21
y=175150x-286
Integrated fluoroescence / a.u.
Abs

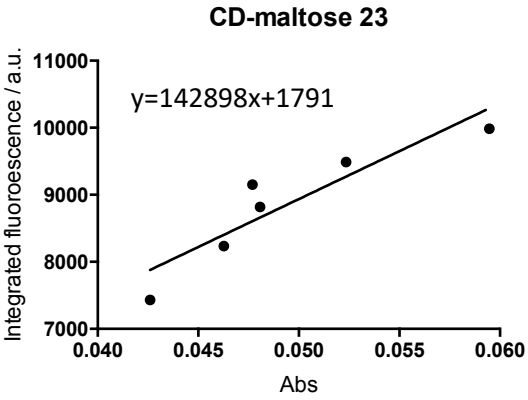
CD-maltose 23
y=142898x+1791
Integrated fluoroescence / a.u.
Abs

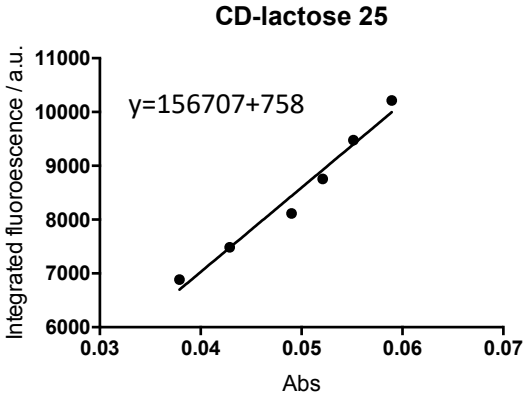
CD-lactose 25
y=156707+758
Integrated fluoroescence / a.u.
Abs

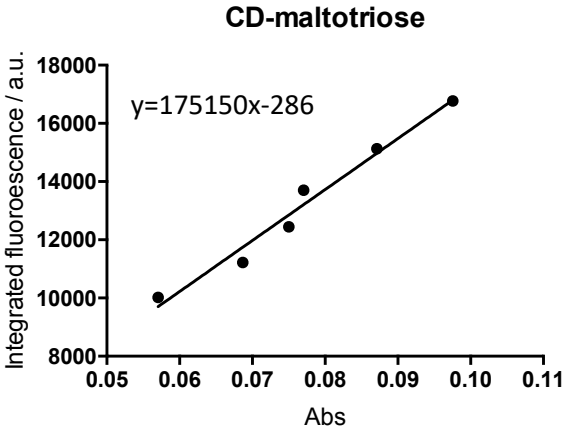
CD-maltotriose
y=175150x-286
Integrated fluoroescence / a.u.
Abs

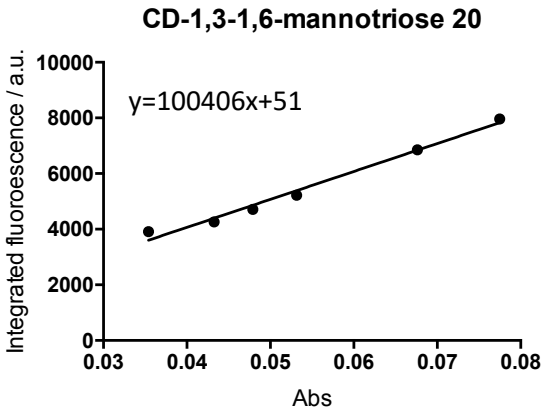
CD-1,3-1,6-mannotriose 20
y=100406x+51
Integrated fluoroescence / a.u.
Abs

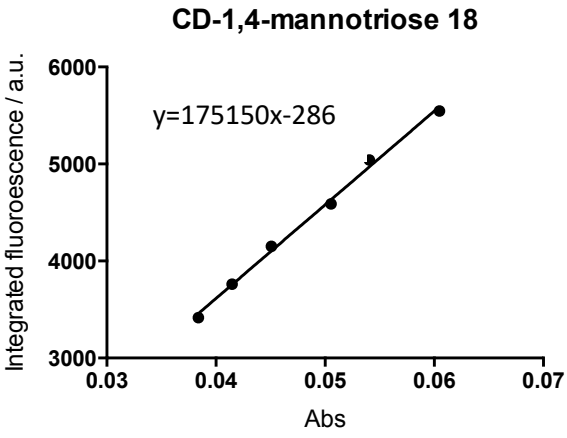
CD-1,4-mannotriose 18
y=175150x-286
Integrated fluoroescence / a.u.
Abs

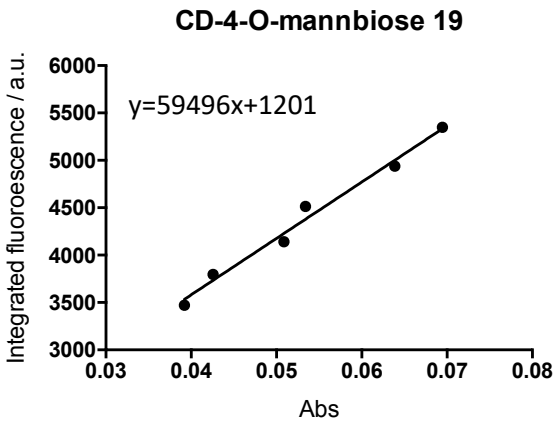
CD-4-O-mannbiose 19
y=59496x+1201
Integrated fluoroescence / a.u.
Abs

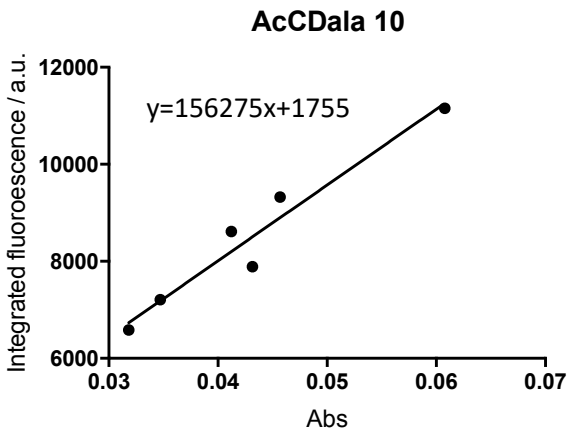
AcCDala 10
y=156275x+1755
Integrated fluoroescence / a.u.
Abs

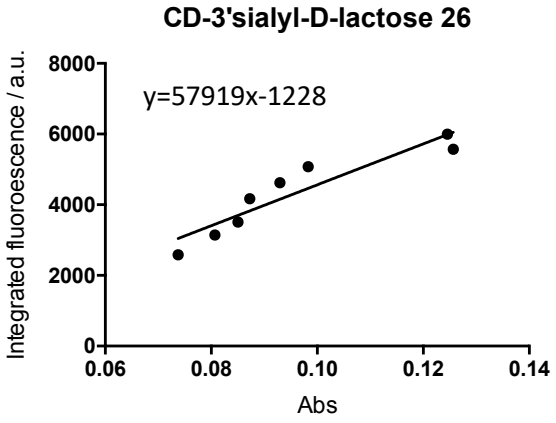
CD-3'sialyl-D-lactose 26
y=57919x-1228
Integrated fluoroescence / a.u.
Abs

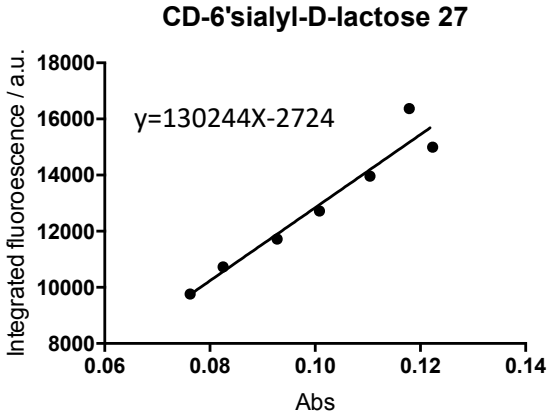
CD-6'sialyl-D-lactose 27
y=130244X-2724
Integrated fluoroescence / a.u.
Abs

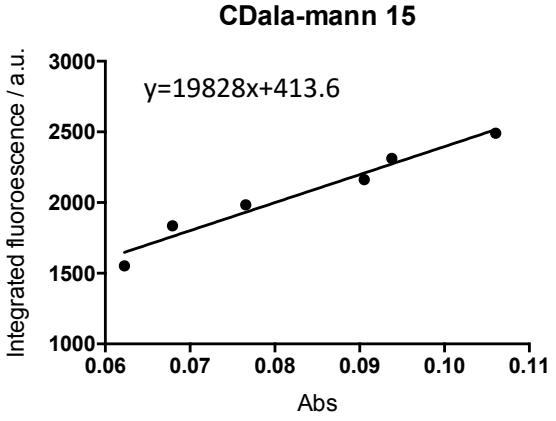
CDala-mann 15
y=19828x+413.6
Integrated fluoroescence / a.u.
Abs

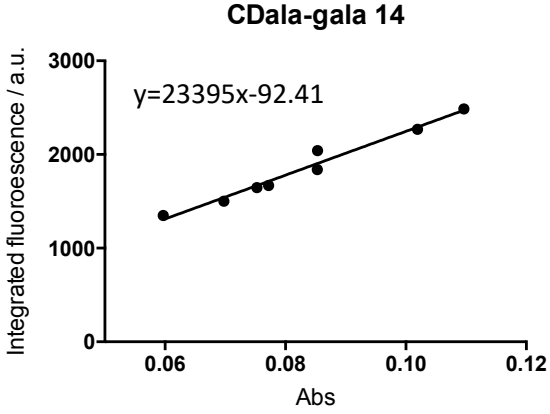
CDala-gala 14
y=23395x-92.41
Integrated fluoroescence / a.u.
Abs

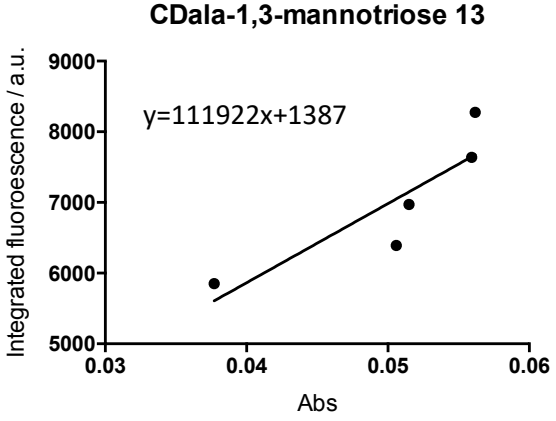
CDala-1,3-mannotriose 13
y=111922x+1387
Integrated fluoroescence / a.u.
Abs

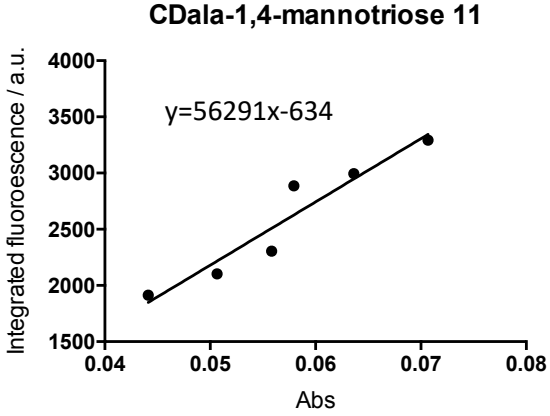
CDala-1,4-mannotriose 11
y=56291x-634
Integrated fluoroescence / a.u.
Abs

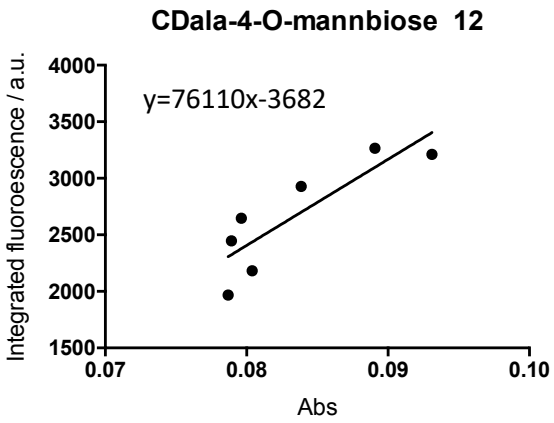

Supplementary Figure 2.9 Quantum yield curves for both shorter and longer linker carbon dot samples. Curve generated from experimental data, plotting fluorescence v. absorbance when absorbance was > 0.1 a.u. Gradient from each curve was used in the QY equation to determine the quantum yield.

CD-carbohydrate	Line gradient	Y-intercept	QY error
Quinine sulfate	$1.357 \times 10^6 \pm 45776$	-65377 ± 3673	
AmCD 16	96321 ± 20223	-7880 ± 2094	0.44
AcCD 17	218424 ± 64168	-3095 ± 3875	0.16
CD-galactose 21	175150 ± 14230	-286 ± 1112	0.31
CD-glucose 21	97371 ± 21590	3126 ± 517	0.47
CD-mannose 22	158145 ± 8825	-9678 ± 804	0.19
CD-maltotriose	175150 ± 14230	-286 ± 1112	0.31
CD-maltose	142898 ± 31803	1791 ± 1581	0.69
CD-lactose	156707 ± 13377	758.3 ± 666.8	0.29
CD-4-O-mannobiose 19	59496 ± 3695	1201 ± 201	0.08
CD-1,4-mannotriose 18	96555 ± 3073	-249 ± 150	0.07
CD-1,3-1,6-mannotriose 20	100406 ± 6027	51 ± 338	0.13
AcCDala 10	156275 ± 19133	1755 ± 840	0.42
CDala-galactose 14	23395 ± 1627	-92 ± 137	0.04
CDala-mannose 15	19828 ± 1979	414 ± 167	0.04
CDala-4-O-mannobiose 12	76110 ± 20031	-3682 ± 1674	0.44
CDala-1,4-mannotriose 11	56291 ± 8633	-635 ± 499	0.19
CDala-1,3-1,6-mannotriose 13	111922 ± 36175	1387 ± 1839	0.79
CD-3'-sialyl-D-lactose	57919 ± 8997	-1228 ± 879.3	0.19
CD-6'-sialyl-D-lactose	130244 ± 15328	-185.8 ± 1559	0.34

Supplementary Figure 2.10 Quantum yield curve data and QY error summary table.

2.4.10 DLS experimental

DLS experimental: Malvern Zetasizer Nano-S Dynamic Light scattering instrument was used to record the hydrodynamic diameter of CDs. Samples were diluted to concentrations between 0.3125 – 5 mg ml^{-1} in (0.2 µm Minisart filter) filtered H_2O, MeOH, 0.1 M or 0.01 M HEPES buffer (supplemented with 5 mM $CaCl_2$ and 5 mM $MnCl_2$ ions) and measured in a 70 μL volume Malvern disposable plastic cuvette at 25 °C. Minimum ten repeats were conducted in triplicate and averaged.

2.4.11 Zeta potential experimental

Zeta potential experimental: Malvern Zetasizer Nano-S Dynamic Light scattering instrument, was used to record the seta potential of CDs. Samples were diluted to concentrations between 0.1 – 5 mg ml^{-1} in the same diluents as in DLS. 750 μL of sample was placed in a DTS1060 Malvern folded capillary cell. Minimum 100 repeats were conducted in triplicate and averaged.

2.4.12 TEM experimental

TEM was performed on either the Jeol 2100 (200 kV) for AmCD and AcCD or Jeol 1400 TEM Voltage (120 kV) for all other carbohydrate functionalised CD samples. In all cases, samples were prepared at 5 mg ml^{-1} in MeOH before drop casting (20 μL) onto 4 nm carbon-coated copper grids (non-glow discharged) and left to dry for 24 hr before imaging.

2.4.13 AFM experimental

On a clean surface 100 μL of sample was drop cast onto freshly cleaved mica (1.5 cm^2) and left for 2 minutes. Angling the mica at 45° N_2 was used to remove excess solution from the mica. Samples were left to dry overnight. Samples were imaged using a Bruker Multimode with Quadrexed Nanoscope 3D controller in tapping mode using NuNano AC mode silicon scout 350 probes, spring constant 42 N/m Resonant frequency: 350 kHz.

3. Glyco-carbon dot lectin interactions

This chapter explores work with the aim of developing a FRET based assay *in vivo* where the delivery of a drug can be measured via a FRET signal output. FRET has been used as a molecular ruler in cell-based experiments involving the cell membrane and protein binding. This is owing to its sensitive distance dependence under 10 nm. The glycan functionalised CDs from chapter 2 are used with a commercial fluorophore to explore the capacity of this nanomaterial towards a FRET assay. Physical characterisation including DLS, AFM and TEM is carried on the same system to probe the structure and size of these aggregates formed as a result of binding between the CD-carbohydrate-lectin pair.

3.1 FRET

Förster resonance energy transfer (FRET) occurs when there is emission and excitation overlap between two fluorophores (Figure 3.1).

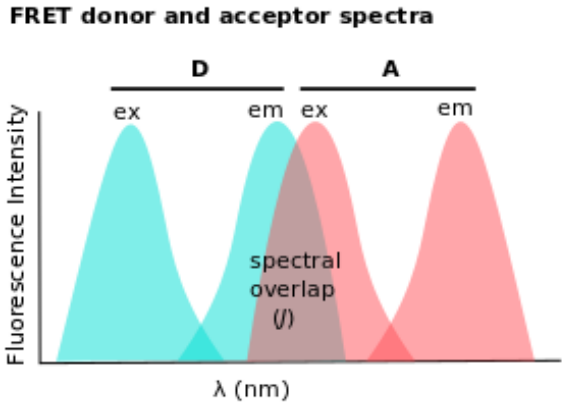

Figure 3.1 FRET donor and acceptor photoluminescence example spectra with overlap between donor emission and acceptor excitation allowing for non-radiative energy transfer.

This process involves non-radiative energy transfer from one molecule to another with reduced fluorescence from the donor (S_1 to S_0) which can be reabsorbed by the acceptor (Figure 3.2). Instead, the donor molecule donates energy to the acceptor molecule through a dipole-dipole coupling interaction.[102] The energy transfer between the molecules is distance (r) dependent, with an inverse r^6 distance relationship. Typically distances up to 10 nm can be measured through changes in FRET.[103]

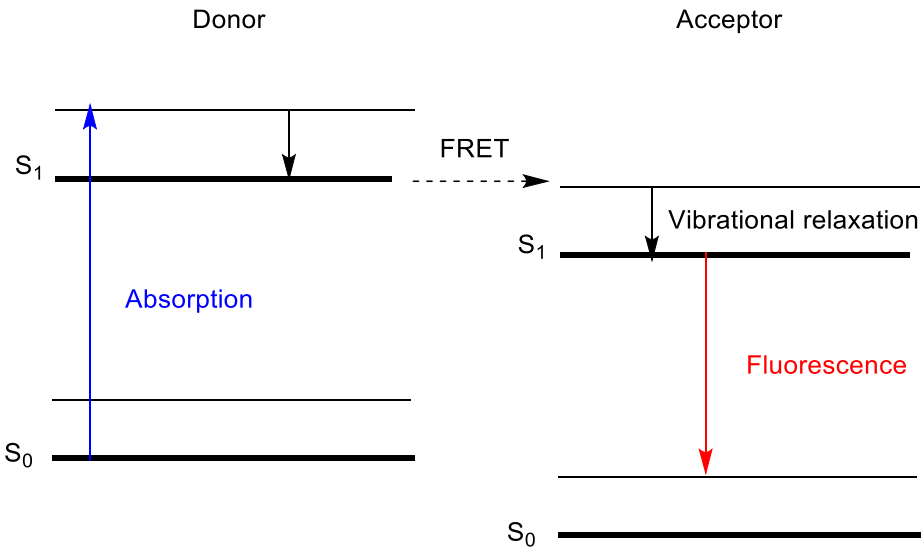

Figure 3.2 Jablonski diagram of FRET from donor molecule to acceptor molecule. FRET involves non-radiation energy transfer between molecular excited states and results in red-shifted fluorescence energy to that of the absorbed energy.

Overlaying a donor and acceptor fluorescence emission excitation profile of two given molecules can reveal if there is potential for FRET to occur when the molecules are in close proximity. FRET is used in biology as a molecular ruler first shown by Stryer[104] and Clegg[105], and has since been used as a tool to probe many types of biomolecule-biomolecule interactions[106]. The acceptor excitation and emission spectra should be Stokes shifted compared to the donor. This can be determined through the emission of the donor overlapping with the excitation of the acceptor (*J*). Optimal conditions would also have a peak within the donor spectra at a wavelength which the acceptor is not excited, as well as a peak in the acceptor fluorescence which the donor does not fluoresce. This does not exclude certain FRET pairs being used together, however, deconvoluting these spectra must be carried out in order for FRET quantification. Other conditions of FRET include good donor QY, donor and acceptor within 10 nm of each other (Figure 3.3) characterised through R_0 and good dipole-dipole alignment which is inherent and characterised in k^2.[107]

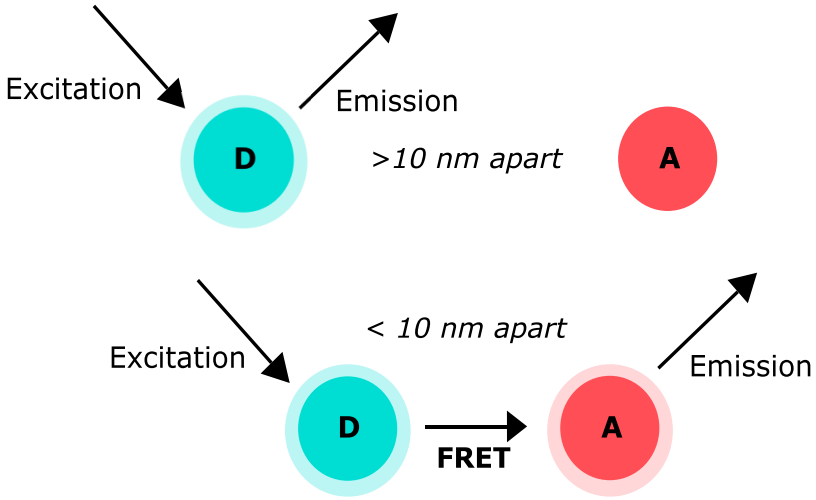

Figure 3.3 Distance dependence of FRET interaction between a donor with excited energy and acceptor with accepts this energy non-radiatively when < 10 nm away and emits red-shifted energy radiatively.

3.1.1 FRET efficiency

The FRET efficiency is defined as the QY of the FRET interaction and can be defined using the theoretical FRET equation below (Equation 3.1), where k_{ET} is the rate of FRET, k_f is the radiative decay of the donor and k_i are any other rates of donor decay or transfer.[107]

$$E = \frac{k_{ET}}{k_f + k_{ET} + \sum k_i}$$

Equation 3.1 The FRET efficiency (E) as shown in terms of rates.

It is possible to calculate the average distance (r) of a FRET interaction. However, this requires knowledge of the FRET efficiency (E). Using the FRET efficiency obtained, the distance (r) can be calculated.[102]

$$E = \frac{1}{[1 + (\frac{r}{R_0})^6]}$$

Equation 3.2 FRET efficiency (E) relationship to the average distance between the donor and acceptor (r) with an inverse r ^{6} power law as shown where R_0 is the Förster radius.

The FRET efficiency can be measured experimentally. There are several ways this can be carried out, including ratiometrically, fluorescence lifetimes or through measuring the change in fluorescence intensity of one species as a function of the starting signal. Depending on the fluorophores being used either the donor or acceptor can be measured. Below the most commonly used methods are described.

Ratiometric FRET provides a relative FRET efficiency ($E_{rel.}$). However, this means that using the $E_{rel.}$ value to determine r is not feasible. I_A is the fluorescence from the acceptor at the acceptor fluorescence wavelength and I_D is the donor fluorescence at the donor florescence when both have been excited at the donor excitation wavelength (in our case) 430 nm. This readout would require linear unmixing of the signal at (in our case) 525 nm to obtain I_A from I_{DA} and of the signal at 430 nm to obtain I_D from I_{DA}. This is unless the emission at 525 nm contains no directly excited donor emission i.e. $I_A = I_{DA}$ and the emission at 430 nm contains no directly excited acceptor signal $I_D = I_{DA}$. Using fluorophores with a discrete single emission and excitation peaks makes this possible such as with QDs.[90]

$$E_{rel.} = \frac{I_A}{I_D + I_A}$$

Equation 3.3 Ratiometric FRET efficiency ($E_{rel.}$) equation.

Guo *et al.*[90] developed a novel ratiometric FRET readout method which reduces the impact of certain problems such as low signal readout, instrument laser variability and signal fluctuation (termed self-calibration). This was used to extract an apparent k_d binding values which are comparable to each other. The acceptor fluorescence at 626 nm and donor fluorescence at 554 nm as $I_{626}/\ I_{554}$ were calculated having subtracted the direct acceptor excited background signal. The data was fitted using Hill's equation as follows where n is the Hill's coefficient, K_d is the apparent binding dissociation constant, R_{max} is the saturated FRET ratio and $[C]$ is the acceptor concentration.[90]

$$\frac{I_{626}}{I_{554}} = (R_{max}\ [C]^n)/({K_d}^n + \ [C]^n\ )$$

Equation 3.4 Hill's equation used by Guo et al.[90] to plot novel ratiometric FRET and extract an apparent k_d.

Excited state lifetime of the donor by itself (τ_D), and when the acceptor is present (τ_{DA}), can be used to probe the energy transfer to acceptor. As more energy transfer occurs to the acceptor the donor lifetime will decrease. This method is devoid of crosstalk from the acceptor as the lifetime can be donor independently measured. However, if multiple lifetimes exist for the donor then adaptations of equation 3.6 are required. Lifetimes are independent of donor concentration hence are less sensitive to experimental error. They can also be used as FRET readout to compare different environments which is useful for *in vivo* study.[108–110]

$$E = 1 - \frac{\tau_{DA}}{\tau_D}$$

Equation 3.5 Donor lifetime FRET efficiency equation.

FRET efficiency (E) can be measured at one wavelength corresponding to the donor i.e. 430 nm in the presence ($I_{DA} = I_{430}$) and absence ($I_D = I_{430_0}$) of acceptor, to find the proportion of excited state energy transferred from the donor to an acceptor molecule. This is used when the acceptor molecule is non-fluorescent or not fluorescent at the donor emission wavelength. For more accurate measurements avoiding signal fluctuation the integral over a range of donor emission wavelengths better quantifies I_D and I_{DA}. Caveats of this method include that the emission peak wavelength must remain consistent upon acceptor addition.[109]

$$E = 1 - \frac{I_{DA}}{I_D} = 1 - \frac{I_{430}}{I_{430_0}}$$

Equation 3.6 Donor Fluorescence to measure FRET efficiency (E) equation. I_{430} refers to the donor emission intensity upon ConA-F addition (λ_{em} 430 nm) and I_{430_0} refers to the donor emission with no ConA-F addition.

Measuring the acceptor emission is possible for measuring FRET efficiency (E) and requires the absorption of the acceptor to be included in the equation. Either absorption of the acceptor when there is no donor (at both donor and acceptor excitation wavelength) is included or the absorption of acceptor at a wavelength where the donor does not absorb.

The three-cube FRET method is commonly used in live cell imaging where bleed-through and crosstalk are harder to correct for. It involves collecting fluorescence at three filter sets or cubes; the donor filter set (I_{DD}) which measures at the donor excitation and emission, the acceptor filter set (I_{AA}) which measures at the acceptor excitation and emission and the FRET filter set (I_{DA}) which measures at the donor excitation and acceptor emission[111]. Obviously within these measurements lies crosstalk and bleed-through, with the aim of isolating the donor fluorescence, direct acceptor excitation and the sensitised (FRET) acceptor intensity there are many methods as outlined by Gordon *et al.*[112] and Zeug *et al.*[113] which use correction factors to obtain a FRET efficiency value. These correction factors can include fluorophore coefficients, QY or filter set percentage transmission. Often this is referred to as FRETN which demotes it is normalised but is not comparable to FRET efficiencies determined through other means.[112]

3.1.2 Experimental ways to measure FRET

Experimentally there are a number of types of experiments which can be used to put information into the equations in section 3.1.1 to obtain (E). These include sensitised emission, photobleaching, lifetime imaging which are applicable in biology and chemistry. Furthermore, bioluminescence resonance energy transfer (BRET), fluorescence polarisation and homo-FRET can be used if these other techniques are not appropriate[114].

Sensitised emission refers to an experimental method where the donor and acceptor molecule fluorescence is measured as the variable is changed. From this the donor fluorescence, acceptor fluorescence or a ratiometric fluorescence change can be used to calculate (E). Associated crosstalk is a major drawback of this method, however it is efficient for looking at systems where (E) changes rapidly such as protein conformation studies.[115]

Photobleaching is useful to measure FRET *in vivo* as it is relatively non-invasive although it can only be used once per cell. This involves having a FRET pair where the donor is transferring energy to the acceptor. Then the acceptor is permanently photobleached whilst the donor is unaffected. This causes the donor fluorescence to increase in relation to the amount of FRET that was occurring before photobleaching.[115,116]

Fluorescence lifetime imaging looks at the inherent nanoscale lifetime or decay pattern of the donor species only. When the donor's environment changes such as when it is transferring energy to an acceptor, its lifetime decreases. This method is commonly used in live cell imaging in a process called fluorescence-lifetime imaging microscopy (FLIM). This technique is vulnerable to artefacts from other cellular environmental impacts on the donor.[115]

Single-molecule FRET is a growing area of research aiming to look at a single FRET interaction in order to measure specific interactions of interest in a complex environment and observe transient states. Commonly this is desired for *in vivo* application where interactions can involve sub-nanometer distinct states. Methods commonly used are similar to bulk population in that fluorescence intensity or lifetime are used.[117]

Bioluminescence resonance energy transfer (BRET) involves most commonly luciferase being the source of light and also the donor partner in a FRET pair and can be used with other commercial FRET acceptor molecules. The luciferase protein being the sole acceptor excitor and not requiring an

external illumination source means that no direct excitation of the acceptor molecule occurs. This means one direction of crosstalk is eliminated from the experiment and quantification become easier. Other benefits of the source of light not being from an external source include removal of non-specific *in vivo* background autofluorescence and photobleaching of the donor molecule, however, one drawback is the low fluorescence of luciferase compared to some commercial fluorophores.[118]

Homo-FRET makes use of a molecule's self-absorption properties as it is seen in carbon dots as well. When two identical molecules are within 10 nm of each other, they have the capacity to transfer energy from excited donor to acceptor molecule. This occurs on a nanosecond timescale whereas rotation of the molecule is much slower. Hence, using a detector which only observes light polarised parallel to the linearly polarised excitation light, the signal of the originally excited molecules can be measured as a function of time. If a donor is transferring energy via homo-FRET, then its signal will decrease over time.[115]

Fluorescence polarisation involves the excitation of a fluorophore in solution at one linear polarisation. After a certain amount of time the excited fluorophores are detected at two perpendicular linear polarisations. Based on the diffusion coefficient of the molecule and hence their size, polarisation will either remain the same if large, or depolarise if they are small and fast diffusing. Using fluorescence polarisation, binding can be quantified as a fluorophore will diffuse slower if bound and depolarise less quickly than if free in solution.[119]

Any of these methods can be used to measure biological and chemical distance dependent phenomena. Commercial fluorophores are often used in this work as they have narrow and sharp fluorescence peaks and a narrow absorption band. In biology fluorescent proteins such as green fluorescent protein, yellow fluorescent protein and mCherry can be used for the precise sequence specific tagging of proteins[120], an important advantage considering the distance dependence in FRET. This has allowed for protein conformational change to be monitored as well as binding interactions with a target protein[121] or DNA[122] or carbohydrate.[90,123–125]

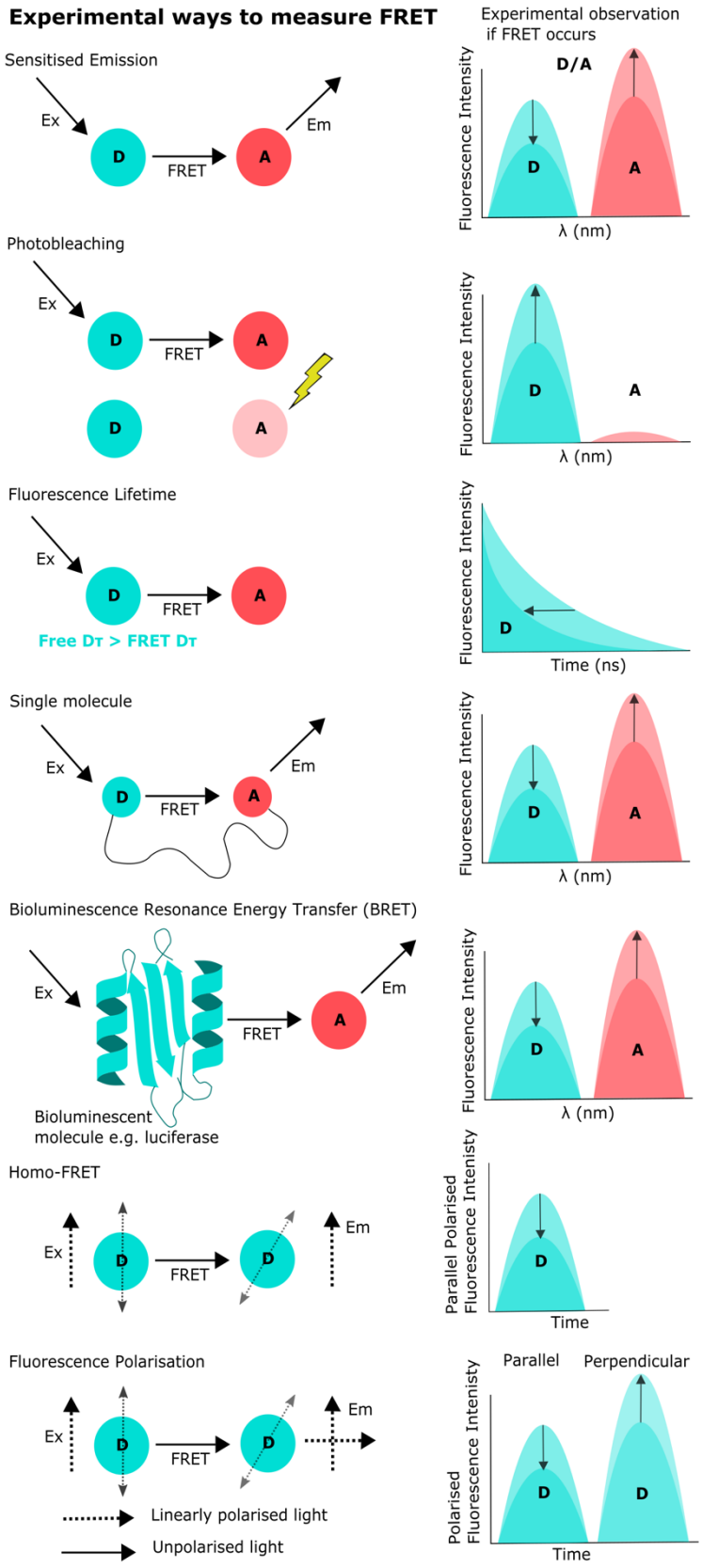

Figure 3.4 Experimental ways to measure FRET summary. Donor (and) acceptor are shown if present in the experiment. Graph shows the measured effect when FRET occurs.

3.1.3 Caveats of FRET measurements

By choosing a suitable nanoparticle it is possible to minimise problems associated with FRET experiments as outlined in section 3.1.2. However, it is important to be mindful of certain issues and recognise them in data e.g. artefacts can result from ions in a titration experiment which may be overlooked.[126] Outlined are the most common problems of experimental FRET measurements.

3.1.3.1 Crosstalk

Crosstalk refers to the acceptor being directly excited by the donor excitation wavelength. This is a result of the fact that the absorbance and excitation of a fluorophore will be likely be non-zero. Also, even though the acceptor will be Stokes shifted, the width of its spectral peaks will be wide in comparison to the shift. The crosstalk can be estimated for a FRET pair by finding the intensity ratio between the emission upon donor and acceptor excitation when a sample of acceptor only is present. To remove crosstalk, linear unmixing and Spectra FRET can be carried out on the data obtained.[127]

3.1.3.2 Bleed-through

Another effect of spectral overlap is bleed-through, which refers to the donor signal which is seen at the wavelength measured as acceptor fluorescence i.e. acceptor channel. The severity of bleed-through is judged in comparison to the intensity of acceptor in the acceptor channel. If significant it should be subtracted from the total intensity in the acceptor channel. However, this is difficult because isolating the donor bleed-through from the acceptor fluorescence in the overall acceptor channel during FRET cannot be done.[127]

3.1.3.3 Non-specific FRET

Non-specific FRET can result if the concentration of acceptor is very high or non-specific aggregation occurs between the donor and acceptor fluorophores inducing false positive FRET signal. This can be observed as the case if the FRET readout is linearly dependent on the concentration of acceptor fluorophore measured through its intensity. Furthermore, at high donor and or acceptor concentrations or large sample volume, the donor molecule can emit a photon which is absorbed by the acceptor in a non-FRET process.[127]

3.1.3.4 Mixture of fluorophore populations

In some cases, a single donor and acceptor do not interact in isolation, a donor can be bound by multiple acceptors or vice versa. In this it is assumed that there is a distinct donor to acceptor FRET interaction which occur independently, and the overall average FRET interaction is observed from each of these individual interactions. Generally speaking, FRET models follow kinetic assumptions as such. It is proposed that additional energy transfer pathway can exist but are not well understood.[127]

With multivalent binding mixtures of fluorophore populations must be considered. A multivalent interaction can mean multiple binding events between two molecules which in turn have a single donor and acceptor molecule associated. Or if the multivalent binding occurs across multiple molecules then more than a 1:1 donor:acceptor interaction occurs. In this situation we assume that FRET transfer occurs as discrete events between the donor and multiple acceptors or vice versa.[127]

3.1.3.5 Change in fluorescent properties upon binding

Upon binding of the donor and acceptor structural changes, or environmental changes such as temperature and ionic strength can impact the donor or acceptor fluorescence, potentially having a quenching effect or shifting the fluorescence peak.[127]

3.1.4 Nanoparticle FRET systems

Nanoparticles have certain spectroscopic and physical properties which mean they could potentially become more popular for research than commercial molecular fluorophores and fluorescent proteins and hence be used in FRET experiments. Associated problems with dyes include in some cases weak signal, photobleaching, too short lifetimes for FRET, poor stability and huge toxicity issues. Issues associated with fluorescent proteins include that they are very labour intensive to produce, suffer from spectral crosstalk, and are very large in some cases for the length scale of FRET.

QDs[128–130], gold nanoparticles (AuNPs)[131], graphene oxide nanoparticles[132], upconverting nanoparticles[133] have all been used in the context of FRET. The functional handles for modification on their surface means that any toxicity issues associated can be avoided by conjugation of biocompatible material. They are known to have comparatively good photostability which can be extended through passivation. Their photoluminescent properties can be tuned in some cases with high precision during synthesis such as size with QDs offering greater flexibility and tunability for bespoke FRET needs. QDs

also have narrow and symmetric emission peaks of many colours which allow for multiplexing[134]. AuNPs and graphene oxide nanoparticles have been used as efficient FRET quenchers also. Their small size allows for FRET scale (<10 nm) interaction as well as tightly controlled conjugation of molecules of interest for highly controlled FRET experiments.[135,136]

3.1.5 Nanoparticle FRET for measuring lectin binding

Not many nanoparticle FRET assays to measure lectin carbohydrate binding have been developed as of yet. The work by Guo *et al.*[90] have shown QDs as an effective platform upon which to test multivalent lectin interactions involved in disease pathways. This could be extended to investigate binding in rare or unusual carbohydrates but also base novel nanoparticle FRET systems for lectin binding. Other work combining nanoparticles and lectin binding studies include using QDs to investigate maltose binding protein (MBP) affinity for maltose.[137] MBP was bound covalently to QDs and through a fluorophore attached to maltose the binding was measured through FRET. In a similar system QDs were again used to measure MBP affinity for maltose, but through a competition assay. MBP was conjugated onto the QD and a maltose analogue, β-cyclodextrin which was quencher conjugated was added hence FRET-based quenching QD fluorescence. Once free maltose was introduced this analogue was displaced and a QD fluorescence signal was observed which was used to quantify binding.[138]

Subsequently, work by Guo *et al.*[90] developed a QD based ratiometric FRET assay to investigate the carbohydrate lectin interactions which mediate the pathogenic invasion seen in HIV and Ebola viruses. The binding affinity of lectins DC-SIGN and DC-SIGNR which mediate virulence were investigated in relation to multivalency. Results showed DC-SIGN binds > 100-fold tighter than DC-SIGNR to glyconanoparticles, which supported observed pathogen transfection in nature. Using QD glyconanoparticles they were able to elucidate novel structural binding information and assess the synthetic platforms suitability to intervene in pathogen lectin binding.

In order to investigate the effect of multivalency both the lectin and carbohydrate valency was varied. Two lectins DC-SIGN and DC-SIGNR which have similar structure with 4 carbohydrate recognition domains (CRDs) but different special presentation were used. The carbohydrate density on the QD was controlled so that the inter glycan distance was either 0.98 ± 0.11 or 1.29 ± 0.36 nm and the number of glycans per QD was 330 ± 70 and 222 ± 62. Two types of QDs were made using ethylene glycol (EG) linker lengths with 3 or 11 carbons (C_3 & C_{11}) whilst using an inert DHLA linked zwitterionic

spacer to modulate glycan density further. Finally, either a monosaccharide or disaccharide was presented on the QD. Glycan density was calculated theoretically from the QD hydrodynamic radius and the number of carbohydrate molecules per QD. This was determined using the Molisch's Test, a colorimetric assay. The unbound carbohydrate detected was used to infer the conjugated carbohydrate.

A ratiometric FRET assay was used to measure the strength of binding between the lectins DC-SIGN, DC-SIGNR and an isolated CRD to specific carbohydrates mannose and dimannose. The dye Atto-594 was attached to the lectin which is a spectrally suitable FRET acceptor for the QD and the λ_{em} ratio I_{626}/I_{554} was used to monitor acceptor fluorescence/donor quenching. Experimentally an interaction was inferred if titration of acceptor into donor solution induced a stepwise increase in I_{626}/I_{554}. This signal then plateaus once all the donor sites have been saturated.

Interaction between QD-dimannose and DC-SIGNR produced the largest FRET signal whilst QD-mannose and DC-SIGNR produced poor signal similar to that with CRD only. CRD experiments show that monovalent interactions are not measurable in this assay and any interactions with mono mannose were also too weak to be measured. This suggests multivalent interaction between DC-SIGNR and QD-dimannose. Secondly, DC-SIGN and QD-dimannose had an even greater FRET ratio suggesting DC-SIGN binds dimannose via more interactions that DC-SIGNR. The binding fit between DC-SIGNR and QD-mannose and QD-dimannose is positively cooperative which was not the case for DC-SIGN which showed no cooperativity. From this work DCSIGN was suggested to have all 4 CRDs facing upwards which allowed it to bind multivalently whilst DC-SIGNR CRDs face sideways and binds cooperatively and multivalently.

Observations show that crowding, seen by dye saturation, induces a FRET signal decrease for DC-SIGN only with QD-dimannose for both C_3 and C_{11} EG linker. This is removed when spacer is introduced to reduce to 25% glycan coating suggesting that the dimannose binding above saturation level causes CRD rearrangement.

By keeping the ratio of QD-carbohydrate and lectin constant but varying the concentration in solution they were able to see when the fluorescence ratio I_{626}/I_{554} saturated and hence, when the QD-carbohydrate were fully bound by lectin. From this data they were able to extract the apparent dissociation constant (k_d) for each lectin.

From the apparent K_d values they were able to compare lectins, linker length, carbohydrate mono- and di- saccharides and therefore investigate multivalency. The best binding they saw was with DCSIGN and the QD-dimannose with the shortest linker C_3 where a low k_d of 610 pM was observed. This fit with the binding mode seen from previous data and observations in nature where DCSIGN is able to exhibit secondary interactions with the dimannose to promote enhanced multivalent binding. They then tested QD-dimannose, when EG_n = 3 and 11, as an inhibitory vector to prevent pathogenicity.

A model system was set up with a murine leukaemia virus (MLV) virus which had the luciferase gene inside and an Ebola virus glycoprotein (EBOV-GP) presented on the surface which is bound by DCSIGN/R. A human embryonic kidney cell line (293T) was transfected so that they presented the DCSIGN/R lectin. The MLV was taken up and the luciferase gene expressed to confirm uptake. To test the QD-dimannose for inhibitory effect, the 293T cells were first predisposed to the QD-dimannose before the MLV virus was introduced. Through the removal of luciferase detection, it was observed that the inhibition in DCSIGN 293T cells by CD-dimannose with ethylene glycol linker (EG linker C_3) had an IC_{50} (inhibitory concentration) of 0.7 $\pm$ 0.2 nM. This is comparable with the best synthetic glyconanoparticles available[36,139,140].

3.2 Physical characterisation for lectin binding

3.2.1 DLS, zeta potential and TEM

DLS is a relatively easy experiment to run to assess the size distribution of particles in solution. In a binding interaction, size distribution can be assessed to show new aggregates including the proportion of aggregation occurring. In one study liposomes were used where ConA and a mannosylated glycodendrimer linked porphyrin were embedded in the surface of two populations of liposome 148 nm and 146 nm respectively.[141] This was investigated to model the mannose receptor on retinal cell membranes as a drug target in retinoblastoma. Upon mixing they observed a new aggregate size as a function of ConA-mannose binding. The first was similar in size to the original liposomes 157 nm (representing the unbound liposomes) and a large aggregate 5180 nm was observed where ConA had specifically bound the terminal mannose causing aggregation. They anticipate that ConA can bind multiple terminal mannoses as seen in figure 3.5 caused such large aggregates to form.

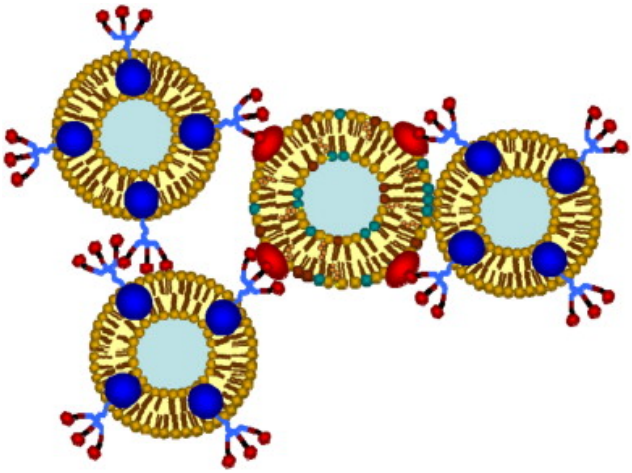

Figure 3.5 Liposome aggregation bridged by ConA- terminal α-D-mannose binding. Copied with permission from Makky et al.[141]

Zeta potential was also used in this work to observe ConA functionalisation onto the liposome surface. Liposome by itself had a zeta potential of − 66.8 ± 2.9 mV, free ConA was − 14.2 ± 0.3 mV and conjugated − 79.4 ± 2.5 mV. Mixing alone did not show this same additive decrease in zeta potential − 62.2 ± 2.5 mV. Hence conjugation was inferred from zeta potential measurements.[141]

DLS was used to observe aggregation induced between QDs functionalised with β-N-acetylglucosamine (GlcNAc) and Wheat germ agglutinin (WGA) lectin. Hydrodynamic diameter increased from 14-16 nm to 240-260 nm. QDs have very high contrast owing to the metallic content, hence these 240-260 nm aggregates were imaged in TEM and confirmed to consist of GlcNAc conjugated QDs with WGA tightly aggregated compared to free GlcNAc conjugated QDs, indicating GlcNAc-WGA interaction.[142]

Guo *et al.*[90] use physical evidence for the interaction between their QD-carbohydrate and DCSIGN-R lectin, whilst DCSIGN had a smaller aggregate size. This provided supporting data for the FRET result they observed. They were able to isolate distinct size distributions from the raw data to infer multimodal distribution with aggregate diameters of 124 and 205 nm. Showing two distinctly different aggregate sizes existed in one sample. Guo *et al.*[90] also observe aggregates for DCSIGNR with QD-dimannose in TEM and STEM, whilst DCSIGN showed QDs were isolated suggesting a lack of aggregation. This result was quantified using nearest neighbour particle distance and matched data observed in DLS.

3.2.1 AFM

AFM can be used not just as an imaging tool, but also as a means to probe force measurements. Single binding events can be measured using AFM down to pN forces. These experiments are usually labour intensive and require specialist AFM knowledge. They have been used to probe lectin interaction with carbohydrate. The AFM tip is functionalised with either the lectin or carbohydrate of interest and the binding partner is functionalised onto a mica, silicon or gold surface. The tip is brought within nm distance from the surface (depending on the linker length) and binding can occur in solution between the AFM tip and the substrate. Via feedback loops the force required is measured and a force-distance curve is generated. In one study the tip was functionalised with hexasaccharide and ConA was functionalised on a gold substrate. Hexasaccharide was used so that the terminal mannose was more accessible than in the monosaccharide form. Unbinding force was determined to be 96 $\pm$ 55 pN. This technique can also be used to probe whole cells. In one study AFM force interactions were used to map the glycocalyx on a whole bacterium (*Bacillus cereus*). A force map was built up across the whole cell using known force interactions characteristic of a lectin with various terminal N-acetylglucosamine, mannose and glucose molecules.[143]

AFM has been used to characterise AmCD **16**, CD-glucose **24**, CD-mannose **22**, CD-galactose **21**, CD-maltose **23** and CD-lactose **25** is work carried out by Tom Swift *et al*.[92] From 6 images of each CD-carbohydrate the radius was calculated as seen in figure 3.6 Table 3.1 summarises the radii of the particles and the number in brackets shows the maximum radius from the core of the glycan functionalised CDs. Topography images show that the glycan corona is inhomogeneously distributed around the core. Figure 3.7 shows phase contrast images of AmCD **16** CD-glucose **24**. The dark area corresponds to an individual CD whilst the lighter corona (in contrast to the background) in CD-glucose **24** indicates carbohydrate.

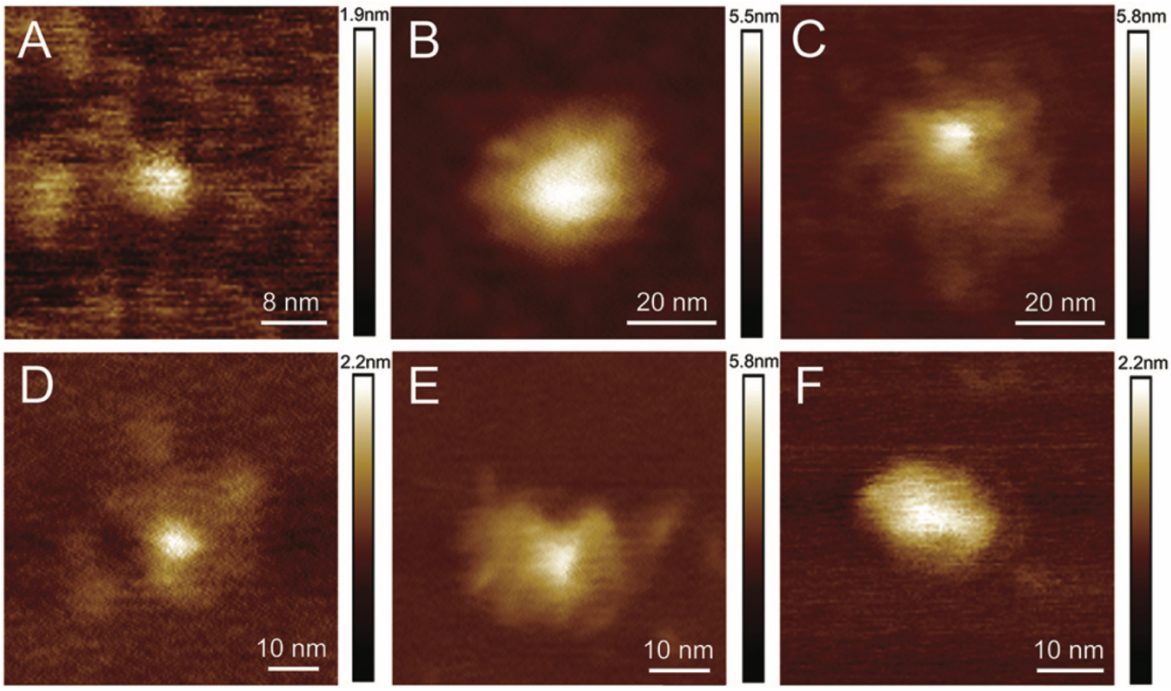

Figure 3.6 AFM topography image reproduced from Tom Swift's thesis,[92] images produced by Rob Harniman. A) AmCD, B) CD-glucose, C) CD-mannose, D) CD-galactose E) CD-maltose E) CD-lactose. Images reproduced from Tom Swift's thesis.[92]

CD sample	*Radius (nm)*
AmCD	3.03±0.05
CD-glucose	5.69
CD-mannose	3.38
CD-galactose	2.94
CD-maltose	2.7
CD-lactose	2.94

Table 3.1 AFM reported CD-carbohydrate radius for glycan functionalised CDs, from AFM as measured by Swift et al.[94] Table reproduced from Thomas Swift thesis.[92]

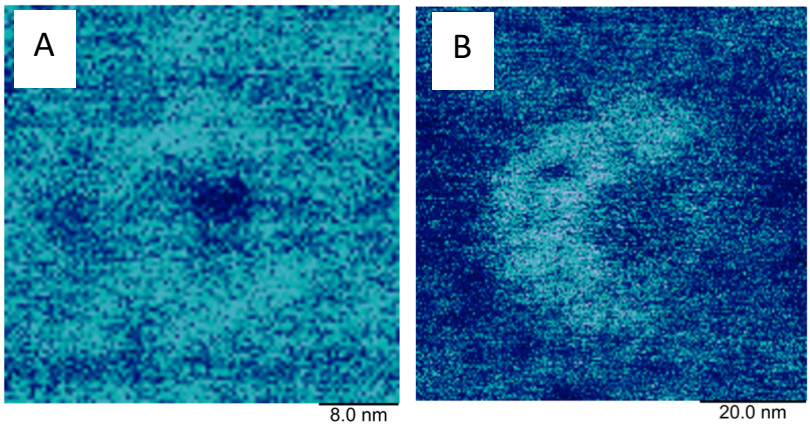

*Figure 3.7 Phase contrast image of the same carbon dot as shown in figure 3.5 A) AmCD **16** and B) CD-glucose **24** Reproduced from Thomas Swift thesis[92]*

3.3 Aims

In this chapter we aimed to investigate carbohydrate lectin binding using a FRET readout mechanism. The work presented are experiments towards developing a carbon dot FRET assay which can be applied to investigate more complex lectin binding. The results in this work we aim to correlate with those seen in other systems in the literature, hence we use ConA, a well-studied lectin. The materials synthesised and characterised in chapter 2 were used as the donor partner in this work owing to the blue fluorescent properties of the carbon dots AcCD **17** and AcCDala **10**. For ease we use commercial fluorescein bound ConA as the acceptor partner in this work. Binding interaction was also investigated through physical aggregation probing via DLS, TEM and AFM. We aimed to develop a ratiometric assay as seen in a number of literature examples. Specifically, we look to Guo *et al.*[42] who develop a ratiometric FRET assay using QDs to probe DCSIGN and DCSIGNR lectin binding.

3.4 Results and discussion

Work in this chapter was conducted by myself and is unpublished.

3.4.1 CD-carbohydrate Concanavalin A binding – physical characterisation

In vitro physical characterisation of multivalent lectin binding interactions is made possible using a glyconanoparticle. Observing the aggregation of a glyco-nanoparticle as a function of binding protein allows for the interaction to be imaged and quantified. ConA which is tetravalent and can bind four terminal mannose residues in a tetrahedral organisation was used as the model system. We proposed this would induce 3-dimensional quasi-spherical aggregation which would increase in diameter as a function of lectin concentration. In figure 3.8, a 2D illustration of the proposed structure is presented to aide in visualisation of the CD-mannose **22** and the ConA seen in green. By using DLS the hydrodynamic size of these aggregates can be measured, whilst TEM can reveal the structure of the aggregates, distinguishing carbon dots from the background through their crystalline core. AFM provides accurate height information of the aggregates which can be correlated to the known size of carbon dots to determine the composition versus size of these aggregates. Each technique has associated caveats such as TEM and AFM being conducted on dried samples. However, combining the information from these three techniques confers aggregate structural information which can be correlated to FRET assay results.

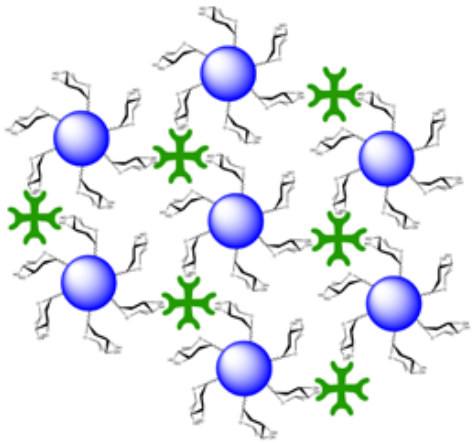

Figure 3.8 2D illustration of how the ConA (green) and CD-mannose may interact to form an aggregate. The ConA and CD-mannose are shown as ordered as a result of the ConA specificity for mannose rather than forming a CD-mannose aggregate with a corona of protein.

3.4.2 Concentration range measured

CD-glycans used in this work were CD-mannose **22** and CD-galactose **21**. The CD contain the longer TTDDA-type linker and their synthesis and characterization have been described in detail using a variety of techniques such as DLS and TEM (chapter 2) and by Swift *et al.*[91] α-D-mannose is the specific terminal glycan that ConA binds in its binding site. The equivalent α-D-galactose is not bound by ConA at its binding site due to unfavourable interactions from the C-4 position hydroxyl of galactose preventing hydrogen bonding.[21] ConA was allowed to bind to CD-mannose and CD-galactose in 0.1 M HEPES buffer pH 7.4, which contained 5 mM $CaCl_2$ and 5 mM $MnCl_2$ which dissociate into Mn^{2+} and Ca^{2+} ions in solution which play a role in ConA binding. All references of 0.1 M HEPES refer to this buffer with ions. The concentration of CD-mannose **22** and CD-galactose **21** were kept the same at 1 mg ml^{-1}, and the mass of ConA varied from an equivalent mass down to 0.00625 mg ml^{-1}. The equivalent molarity is presented alongside ConA in table 3.2.

Mass ratio CD:ConA	*ConA (mg ml^{-1})*	*ConA(μM)*
1:1	1	9.62
1:0.2	0.2	1.92
1:0.1	0.1	0.962
1:0.05	0.05	0.480
1:0.025	0.025	0.240
1:0.0125	0.0125	0.120
1:0.00625	0.00625	0.060

Table 3.2 Table of the mass ratios used of CD: ConA and the equivalent ConA mass and molar concentration this represents.

A range of CD:ConA ratios were chosen as the moles of carbohydrate per CD could not be determined. Hence, to observe an interaction a wide range of mass ratios was used. Using DLS and zeta potential, these samples were all investigated. For TEM and AFM the ratio 1:0.025 was used having determined from DLS and zeta potential that an interaction was induced by ConA addition.

3.4.3 CD-carbohydrate ConA interactions monitored using DLS

CD-mannose **22** and CD-galactose **21** were investigated as multivalent glycan platforms for ConA binding. Considering the α-D-mannose specificity of ConA, CD-mannose was anticipated to have greater binding that CD-galactose **21**. Through DLS the binding was investigated in terms of aggregation, hence CD-mannose **22** was expected to show greater aggregate sizes than CD-galactose. All DLS experiments were carried out in 0.1 M HEPES buffer. ConA was added to CD-carbohydrate in an Eppendorf tube and vortexed to promote disaggregation of any self-assembly and allow for lectin-carbohydrate binding.

Previous data in chapter 2 (section 2.2.2.8) the hydrodynamic diameter (peak 1 % intensity data) for CD-mannose **22** was 725.90 ± 60.85 nm and CD-galactose **21** was 926.50 ±38.05 nm. This size was larger than TEM and AFM, and therefore proposed to be the result of self-aggregation. These samples are the same material as suggested in the aggregation DLS studies. Hence the disassembly of CD-carbohydrate is a prerequisite for specific ConA binding.

We also carried out DLS on ConA by itself at concentrations 0.00625-1 mg ml^{-1}, the same concentration as used with CD-carbohydrate. This showed that the lectin also self-aggregates with diameters between 200-325 nm between 9.62-0.060 μM. This is shown by the fact than the literature reported size of ConA 7x7x6 nm[15] which is 2 orders of magnitude smaller than the aggregates. ConA aggregates in a slight concentration dependent manner, where greater concentration reports smaller sizes down to ~ 200 nm and lower concentrations report larger sizes up to ~ 300 nm (figure 3.8). However, the sizes seen are much smaller than that observed when ConA is combined with CD-glycans.

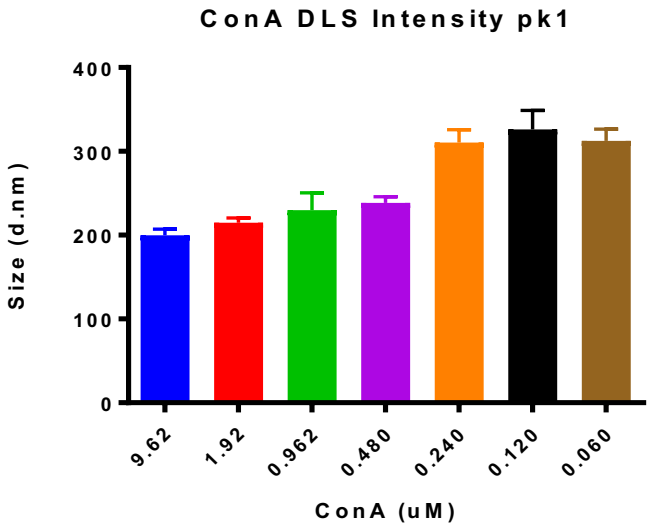

Figure 3.9 DLS data (peak 1) intensity of ConA at concentrations between 9.62-0.060 μM. The same concentrations used in binding experiments with CD-carbohydrate

Interaction between the CD-glycan and ConA in solution reported different size aggregates than either the CD-carbohydrate by itself or the ConA by itself (0.060-9.62 μM). This was seen for all CD-carbohydrate samples as a function of increasing ConA concentration (figure 3.9). At the highest ConA concentration of 9.62 μM aggregate size reaches 2248 nm for CD-galactose **21** and 3308 nm for CD-mannose **22** (peak 1 size). For comparison, this is much larger than ConA by itself at 9.62 μM of 200 nm. However, the inverse result is seen between 0-1.92 μM ConA concentration where CD-galactose **21** has the greatest aggregate size. Hence, from this data it is difficult to conclude whether there is a specific or non-specific basis for aggregation.

Raw data seen in supplementary figures S.3.1 & S.3.2 of the CD-glycan and ConA samples show that there are sometimes multiple peaks in the data showing multiple aggregate sizes exist in solution. The size of these peaks does not correspond to the size of either the CD-glycan or ConA (at the same concentration as the sample) in any case as far as we can see. Hence, the new aggregates must be composed of both CD-glycan and ConA.

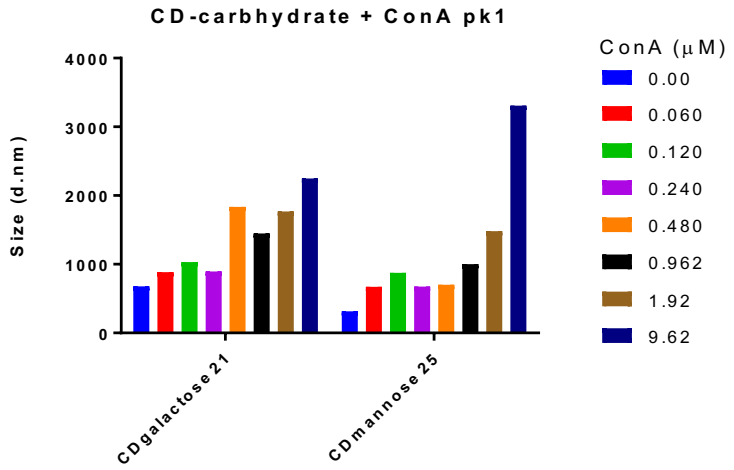

*Figure 3.10 DLS data (peak 1) intensity of ConA at concentrations between 9.62-0.060 μM with 1 mg ml^{-1} CD-mannose **22** and CD-galactose **21** in the sample.*

To analyse our data, we applied the analysis methods reported by Guo *et al.*[42] In their work, functionalised QDs are employed in binding studies, which are more easily monodispersed for DLS characterisation hence, the percentage size increase reflects the percentage size increase as a function of the diameter of one particle. We use this method in a similar manner, however as our glycan-CDs are aggregated to start with, our results show a disassembly of aggregates to form a new aggregate of distinctly larger size in a concentration dependent manner.

The increase in diameter of the aggregate upon the addition of ConA as a function of CD-carbohydrate starting diameter is plotted in Figure 3.11. This data shows that as a function of CD-mannose 725.90 ± 60.85 nm (self-aggregated) which was smaller than CD-galactose **21** 926.50 ±38.05 nm, the aggregate size upon ConA addition has increased more. CD-galactose **21** reaches 232 % increase and CD-mannose **22** reaches 946 % aggregate diameter increase. The initial size difference between CD-galactose and CD-mannose **22** (CD-galactose **21** is 200.6 nm larger) could explain why there is a large % increase for CD-mannose **22**. If ConA is non-specifically interacting with the CD-carbohydrate surfaces, then ConA addition will cause a greater % increase for a smaller aggregate. However, if CD-carbohydrates do disaggregate, then the greater aggregate diameter reported for 9.62 μM ConA concentration could mean that the larger aggregate size is a result of specific binding.

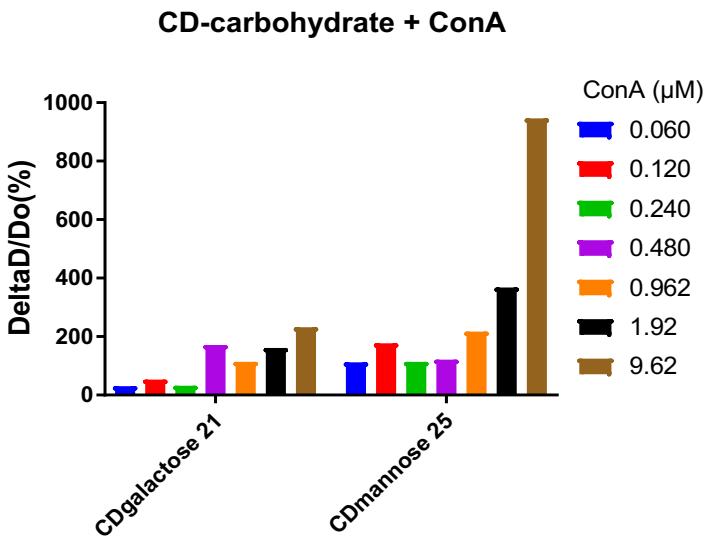

*Figure 3.11 The $\Delta D/D_0$ (percentage increase) DLS data from figure 3.9 of aggregate size for CD-mannose **22** and CD-galactose **21**.*

3.4.4 Zeta potential of CD-carbohydrate concanavalin A binding

Zeta potential was used as a measure of CD-galactose **21** and CD-mannose **22** binding with ConA between 0.00625 – 9.62 μM i.e. the same samples used in DLS. Zeta potential is a good measure of nanoparticle surface charge and can be used as a means for measuring surface functional change in CDs.[144] Hence in this context an overall change is CD surface charge would indicate ConA interaction.

Firstly, ConA between the concentration range 0.06 – 9.62 μM was measured by itself in zeta potential measurements. The values did not vary with concentration, mean value of 9.99 ± 0.36 (SEM) mV observed (Figure 3.12). ConA is fairly consistent in surface charge over the concentration range used in these binding experiments, meaning any changes in surface charge originate from the CD-carbohydrate influence.

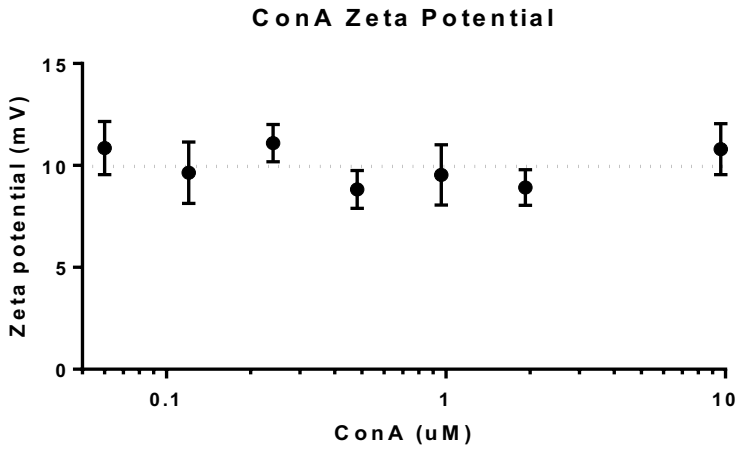

Figure 3.12 Zeta potential of ConA as a function of concentration between 0.06 – 9.62 μM in 0.1 M HEPES buffer.

Starting with 1 mg ml^{-1} CD-mannose **22** and CD-galactose **21** in 0.1 M HEPES the zeta potential are -6.28 mV and -4.40 mV respectively. For CD-carbohydrate + ConA 9.62-0.060 μM, the zeta potential increases as a function of ConA looking as though it is reaching a plateau at higher concentration in both cases (Figure 3.13). This plateau occurs before 10 mV even though the concentration of ConA reaches 9.62 μM, a relatively high concentration. 10 mV being the charge of a ConA only aggregate would be expected if the CD-carbohydrate was fully coated by ConA.

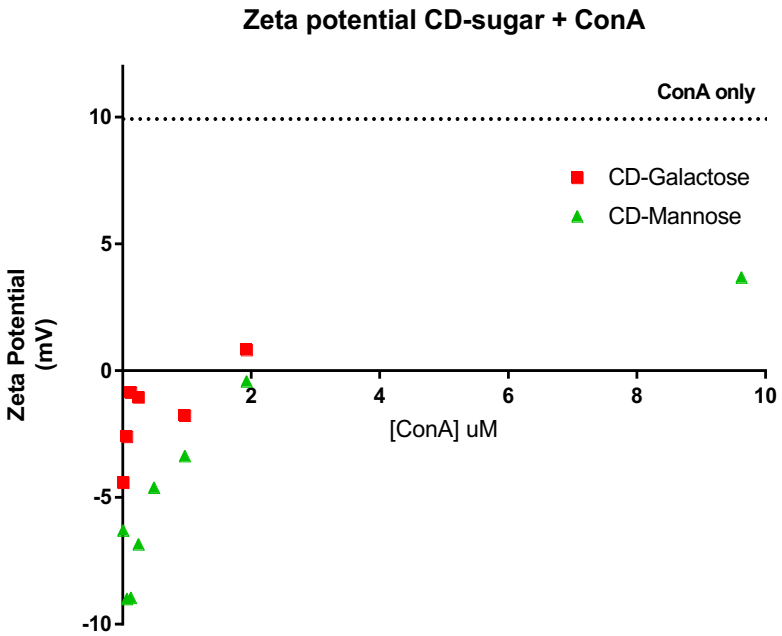

*Figure 3.13 Zeta potential of CD-mannose **22** and CD-galactose **21** upon the addition of ConA over the range 0.06 – 9.62 μM in 0.1 M HEPES buffer.*

This suggests that the aggregates are not fully coated in ConA and the negative influence of both CD-carbohydrates is present on the surface. DLS data suggests that a distinct aggregate diameter was observed for CD-carbohydrate + ConA. Zeta potential data of the aggregates further supports the presence of CD/lectin aggregates showing that the complex has both protein and CD-carbohydrate. This suggests that the two components are distributed through the aggregate rather than a "core" CD-carbohydrate with a corona of lectin. This fits with the idea that the lectin carbohydrate interaction mediates the aggregate formation. However, it is not clear still whether this is a specific interaction or not. Non-specific hydrogen bonding between the carbohydrate and protein could be the reason for aggregation. However these results, do not rule out specific binding occurring within the CD-mannose **22** + ConA aggregate either.

3.4.5 AFM

AFM was used to further investigate ConA binding of CD-carbohydrate in an effort to observe the aggregates and structural features which would reveal differences in binding mode between CD-mannose and CD-galactose. DLS and zeta potential data show that both these carbohydrates induce an interaction between the carbon dot and ConA hence no specific binding can be concluded between CD-mannose and ConA. Based on the fact a strong ConA dependent interaction was observed in zeta potential over the mass ratio range (CD:ConA) 1:0.00625 - 1:0.1 the ratio 1:0.025 was chosen for further AFM studies. AcCD **17** was used as a control in these experiments, at the same mass ratio ConA was added to AcCD **17** and all 3 samples were prepared for AFM in the same manner. AFM involved the drying of aggregates onto mica with the aim to probe their surface and obtain information on how the aggregate is organised when in solution. Accurate (dried) height and adhesion information can be obtained through AFM which provided structural aggregate information.

Sample preparation is highly important for obtaining reliable AFM images. Cleanliness was optimised to produce artefact free samples which involved preparing the samples in a clean room. The sample preparation procedure was optimised iteratively, variables explored were deposition method, sample concentration, buffer concentration and drying rate. Successful imaging was possible through the following method. The samples of AcCD **17** and CD-carbohydrate + ConA with ratio 1:0.025 was diluted 1000-fold in 0.1 M HEPES buffer. Mica was cleaved using Scotch tape and the sample was drop deposited on the freshly cleaved surface and left for two minutes. Then the solution was wicked away from the corner of the mica using white roll with minimal interference to the mica surface. The samples were left overnight to dry before AFM imaging was carried out. All AFM imaging presented in the results chapter 3.5.4 was carried out by AFM technician Dr. Rob Harniman using a Bruker Multimode AFM.

Topography and adhesion AFM images are shown for each of 0.1 M HEPES only, AcCD **17** + ConA in 0.1 M HEPES (Figure 3.14), CD-mannose **22** + ConA in 0.1 M HEPES (Figures 3.15 and 3.16) and CD-galactose **21** + ConA in 0.1 M HEPES (Figure 3.17). Topography reveals sub nm resolution in the Z-domain (height). Adhesion measures the AFM tip's interaction with the sample surface in mV, the lighter the shade of colour on the image the greater the interaction and vice versa.

AcCD **17** AFM images are shown in figure 3.13. Key features include large structures up to 10.8 nm in height which were seen throughout the sample. These structures were attributed to HEPES buffer aggregating, possibly containing AcCD **17** and ConA material. The concentration of 0.1 M HEPES is much greater than the AcCD **17** or ConA which has been diluted 1000-fold, hence it is not surprising that HEPES buffer makes up a large proportion of deposited material.

In AcCD **17** + ConA between these large structures, small particles of mean height 5 nm were observed which are within the same radius size range of 2.7 – 5.69 nm as measured of CDs by Swift *et al*.[94] Phase contrast image 3.14b maps the adhesion of the AFM tip with the sample. These smaller particles are dark which indicates that the AFM tip has lower adhesion to these than to the mica background. This low adhesion for "bare" carbon dots was described again by Swift *et al.*[91] The HEPES buffer structure is lighter in this image indicating higher adhesion. This image also shows that the AcCD **17** do not have light corona around the particle which is seen for CD-carbohydrates and was determined to be the carbohydrate corona as shown by Swift *et al.*[91] and presented in figure 3.7. Hence, it can be concluded that AcCD **17** do not have a glycan or a protein corona.

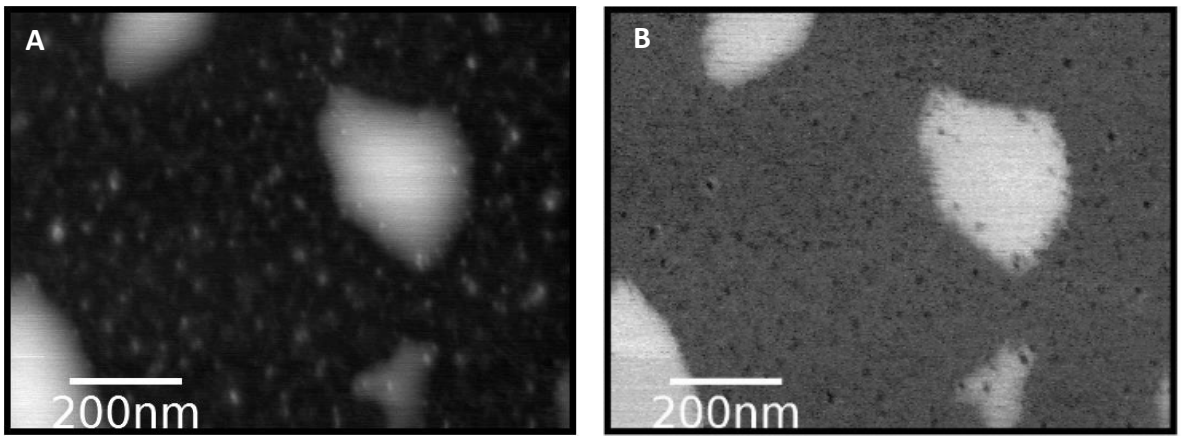

*Figure 3.14 AcCD **17** and ConA 1:0.025 mass ratio AFM images. A) Topography image B) Phase contrast image*

Next CD-mannose **25** + ConA and CD-galactose **21** + ConA samples were imaged. In both samples, at the micron scale, large structures which we can attribute to HEPES buffer were observed. These can be seen in figure 3.15a. Magnification of the space around these structures revealed features of a different structure on the nm scale (Figure 3.15b). Between 50-200 nm, these structures had a height

of ~ 10 nm and were not seen in any images of AcCD **17** + ConA. These were magnified further, and high-resolution images were taken for both CD-mannose **25** + ConA and CD-galactose **21** + ConA samples.

Figure 3.15c,d show these 50-200 nm structures for CD-mannose **22**. Structurally they have a denser core which has a greater height compared to the surrounding material. These CD-mannose + ConA aggregates vary in size and have an irregular edge shape. Following discussion with Dr. Rob Harniman (AFM specialist), we concluded that the CD-mannose **22** + ConA aggregates resulted from a drying effect. During the sample preparation, the aggregates dry onto the mica surface from the outside in towards the centre. As the water dries, material including CD-mannose **22** and ConA are dragged to the middle hence when the water finally evaporates, a "core" structure results in the middle of a flatter structure, with a similar structure to a fried egg. Figures 3.15b c & d show these structures.

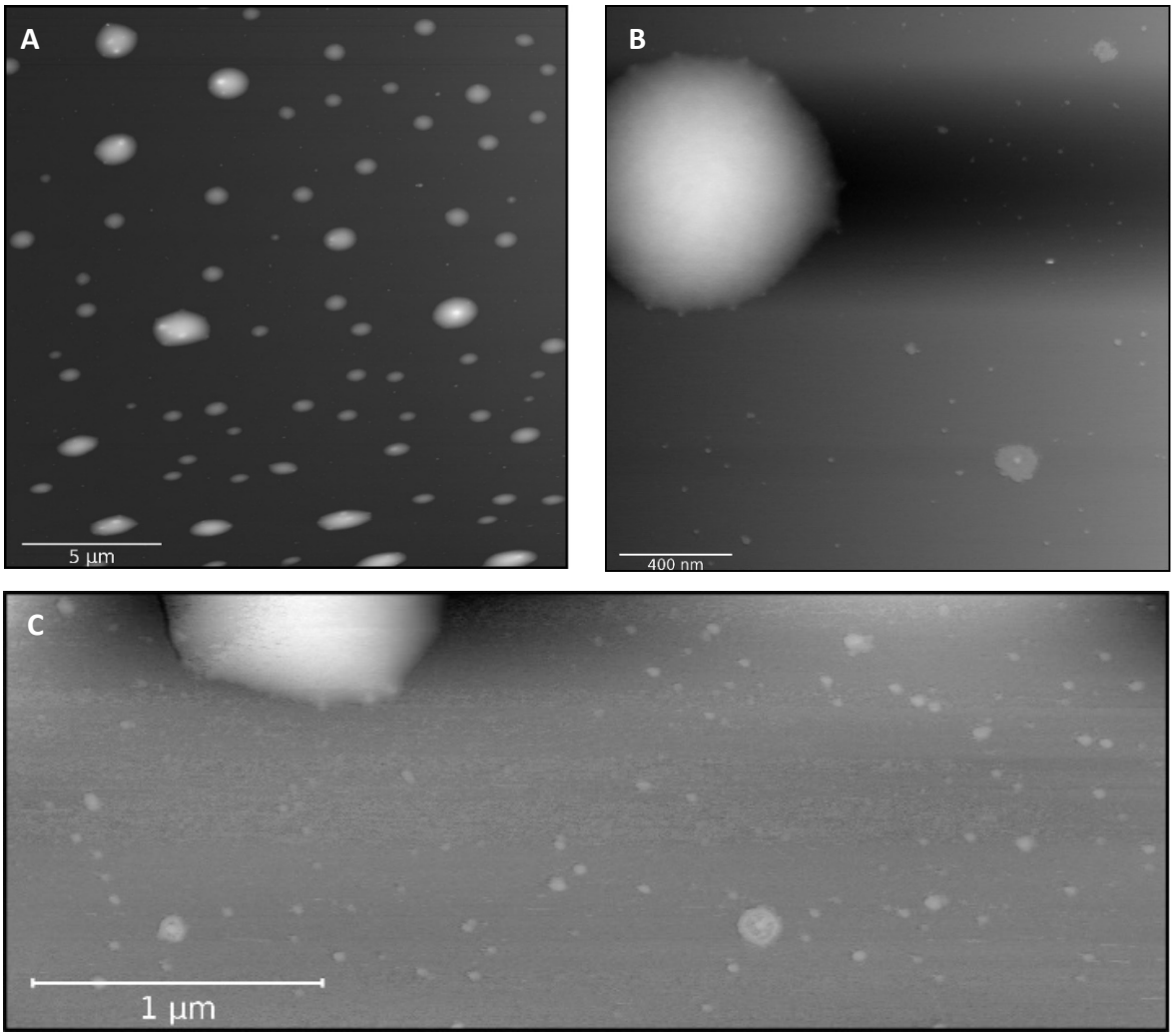

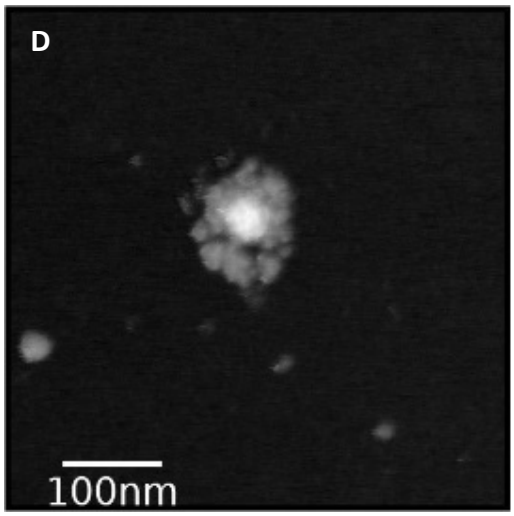

Figure 3.15 CD-mannose and ConA 1:0.025 mass ratio. A-D) Topography images.

Looking at figure 3.16 in more detail and rendered in 3D (figure 3.16b) shows more information on the aggregate structure. Height and phase information of CD-carbohydrates reported before was used to identify substructure of the aggregate. The aggregate is 120 nm in diameter in the AFM image from figure 3.16. Topographical image shows quasi-spherical particles within the aggregate which can be better distinguished in the 3D image. Within the "core" of the aggregate there seem to be CD sized particles which fits with our drying effect suggestion. Hence, we propose that the aggregate in figure 3.16 contains CD-mannose **22**. Furthermore, we can observe from phase contrast images (Figure 3.16c) in blue, that the CD-mannose particles are dark blue, having low adhesion to the AFM tip, characteristic of CD[91]. There is a lighter area around each of these particles which is again more apparent in the 3D map corresponding to areas of higher adhesion as would be the case for carbohydrate, protein or as we have seen with HEPES buffer. Hence, we propose there is order within these aggregates were the CD-mannose **22** and ConA are distributed within the aggregate in a manner indicative of CD-mannose **22** to ConA interaction. This is not indicative of specific binding of ConA in itself.

For CD-galactose **21** + ConA these "fried egg-type" structures were also observed. However, these were not the only nm scale structures observed. Figure 3.17 shows an image where both structures were seen. CD-galactose **21** + ConA also had aggregates of the same size but without this dense "core" structure. This suggests a smaller aggregate in solution hence a faster drying time, meaning that the dense core effect does not occur. One of these structures is magnified in Figure 3.17b,c. In this aggregate carbon dot sized particles can be observed. In the blue phase contrast image (Figure 3.17c) a lighter blue corona is observed which could be carbohydrate and/or ConA and HEPES buffer. However, interestingly this looks to be more loosely associated and less densely packed. This indicates that in solution the aggregate is less tightly bound which could be the result of non-specific adhesion.

This difference in structure occurrence between CD-carbohydrates + ConA could be a manifestation of ConA specificity for α-D-mannose and is non-specific for β-D-galactose. In order to determine this, quantification of these two discrete structures should be performed over a greater number of images to allow statistical significance testing.

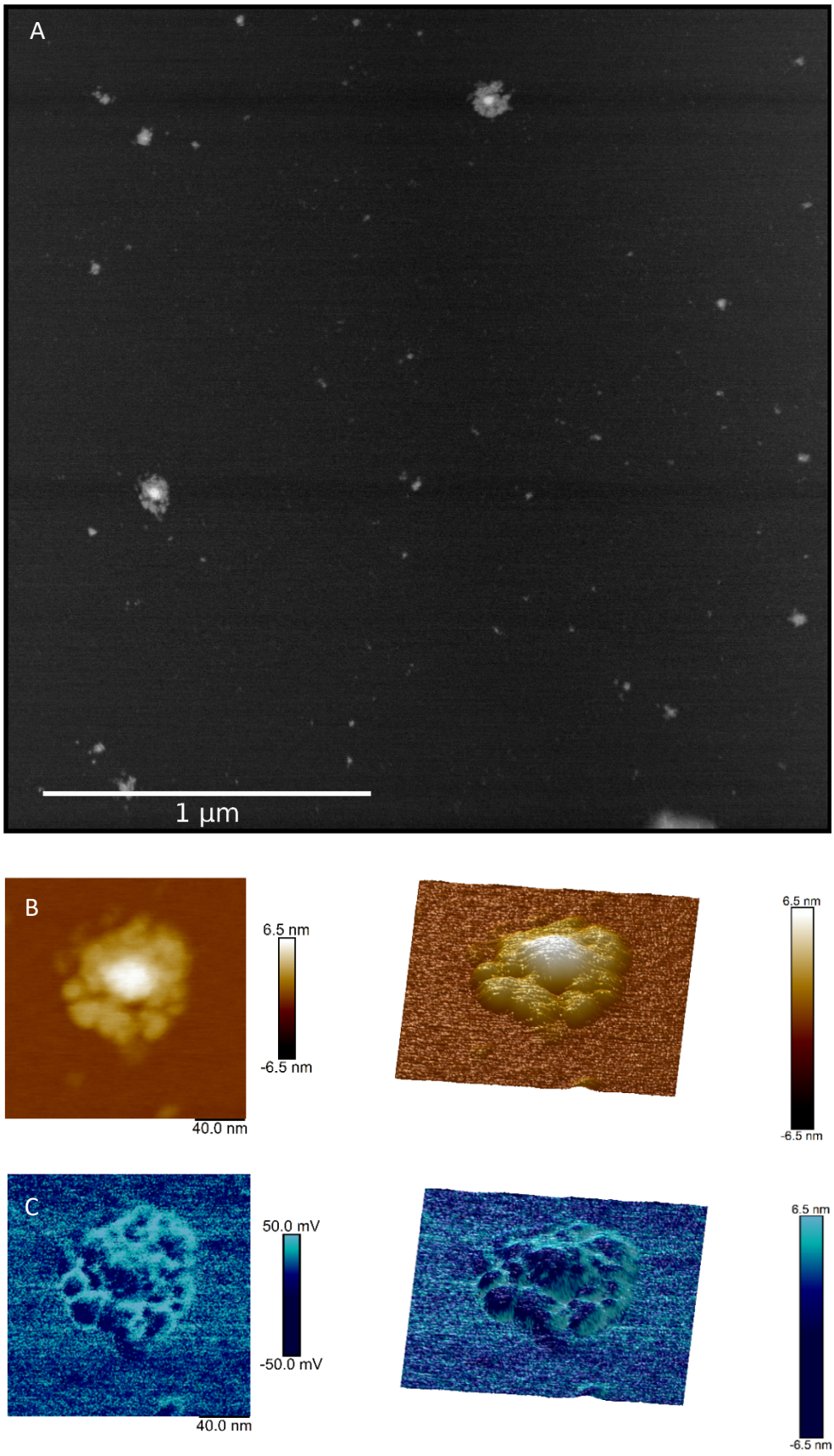

*Figure 3.16 AFM images of CD-mannose **22** + ConA. A) shows a wide field of view. White structures are aggregates of CD-mannose **22** and ConA. B) Topography of an aggregate 2D and 3D. C) Phase contrast 2D and 3D images of aggregate.*

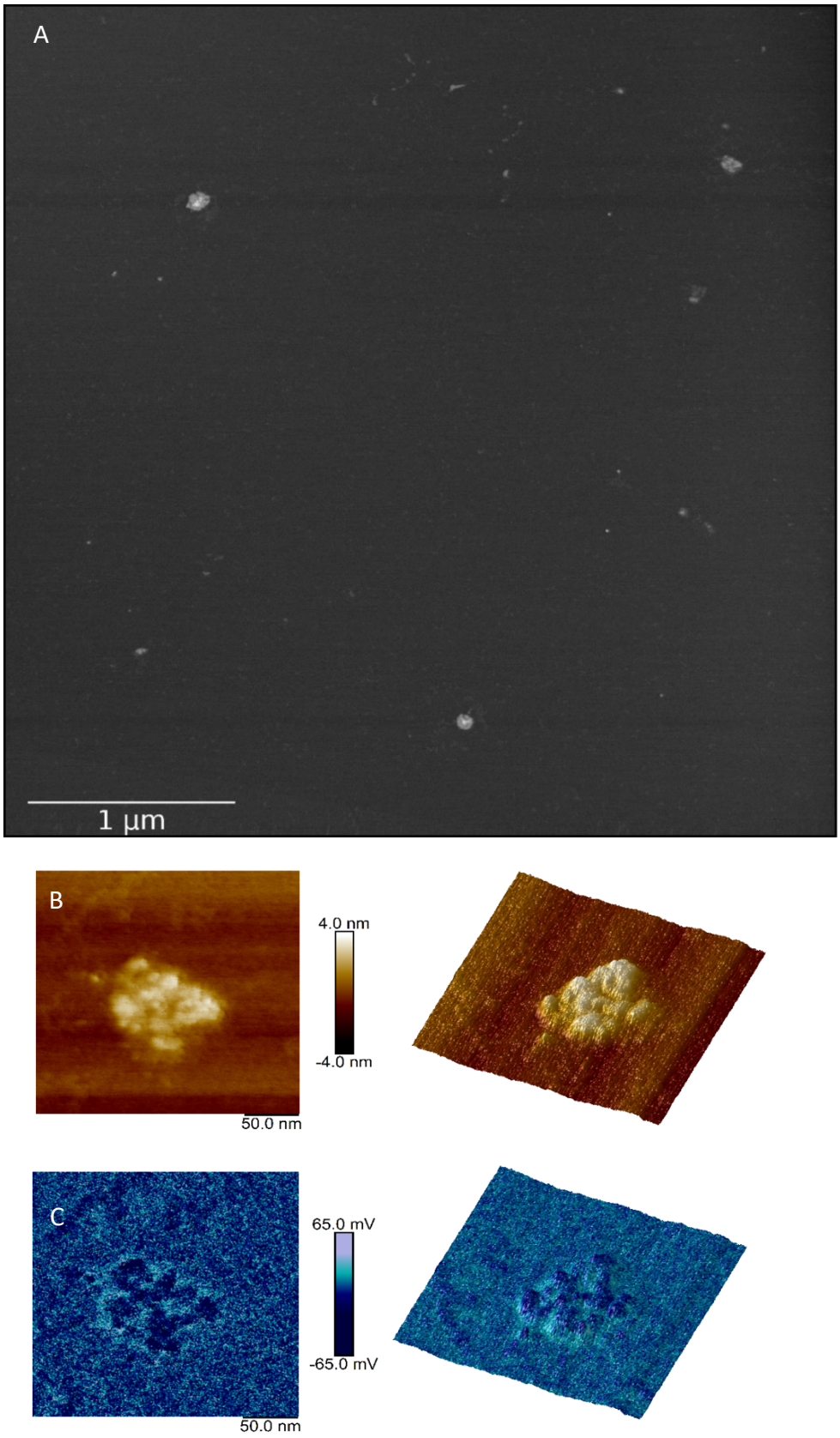

*Figure 3.17 AFM images of CD-galactose **21** + ConA. A) shows a wide field of view. White structures are aggregates of CD-galactose **21** and ConA. B) Topography of an aggregate 2D and 3D. C) Phase contrast 2D and 3D images of aggregate.*

A 0.1 M HEPES control sample was prepared and imaging revealed large aggregates with height 40 nm (figure 3.18). These having the same height and adhesion properties as the large structures in other samples showed that 0.1 HEPES was the material composing these aggregates. In this sample no smaller nanometer structures were seen on the mica suggesting them to be the CD-carbohydrate and ConA material.

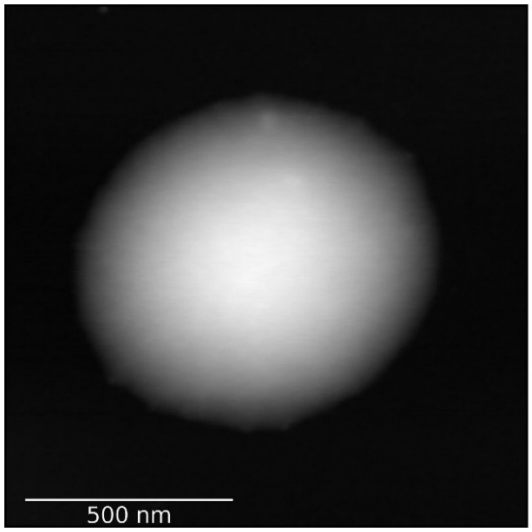

Figure 3.18 AFM topography image of 0.1 M HEPES only on mica. Large micron structures observed.

Efforts to remove some 0.1 M HEPES buffer for better visualisation of 50-200 nm structures were carried out. The sample CD-mannose **22** + ConA sample (as used for figure 3.15) was dialysed with H_2O before deposition. The assumption was that the aggregates in solution would not disassemble at lower HEPES concentration and through this the large aggregates could be removed before imaging. However, a complete disaggregation of HEPES and nanoscale structures was induced. Figure 3.19 shows the images of CD-mannose post dialysis with H_2O. Individual carbon dots can be clearly observed in both topography and phase contrast images and no agregation at the micro or nanoscale was observed. Phase contrast images show that the CDs lie in an area of high adhesion which could be carbohydrate, protein or HEPES buffer. Hence, this was not a viable means for improving sample aggregate distribution.

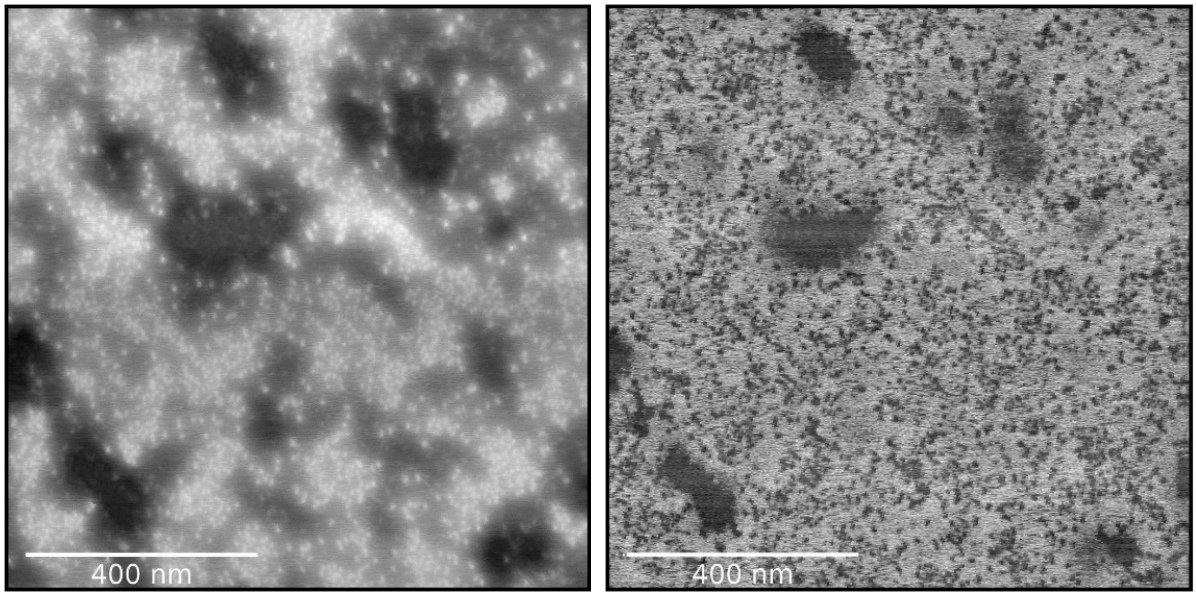

*Figure 3.19 AFM image of CD-mannose **22** + ConA post 16 hr dialysis and remade sample. A) Topography B) Phase contrast image.*

3.4.6 TEM

TEM was carried out on both CD-mannose **22** and CD-galactose **21** + ConA with the aim of observing aggregates. The carbon dots are known to be between 1.54 – 3.69 nm in diameter in TEM and this was used as a means for identifying CDs in these images. Aggregates were not observed in CD-galactose **21** + ConA as was the case in AFM. CDs were identified and were monodispersed suggesting no ConA induced aggregation was seen (Figure 3.20). During sample preparation the aggregates which exist in solution must disassemble. Sample preparation involves drop depositing 20 μL of sample undiluted onto a 4 nm carbon coated copper grid and drying overnight before imaging. The same is not seen in CD-mannose **22** + ConA. Here no monodispersed CD-mannose was observed and there were aggregates between 30-50 nm, hence, smaller than the aggregates seen in AFM. From these images there were not enough aggregates to conduct statistical significance calculation. These were imaged via TEM and STEM as shown in figure 3.21. High-resolution TEM was conducted on one of these aggregates and within the aggregate CDs can be seen through their density and crystalline core. The areas around the CDs do not have crystallinity implying that this is material associate with the carbon dots which have no crystallinity, potentially ConA or carbohydrate. This result suggests that something in the TEM preparation process causes differential effect on the aggregates. This could be a result of tighter binding of ConA to CD-mannose **22** which is the result of specific binding.

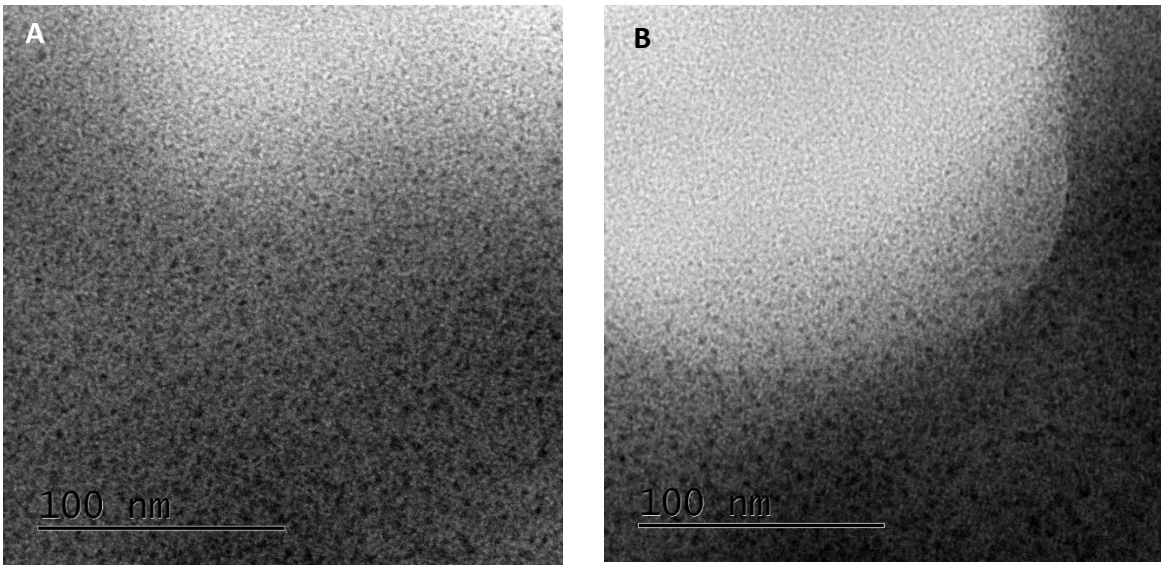

Figure 3.20 TEM of CD-galactose + ConA low

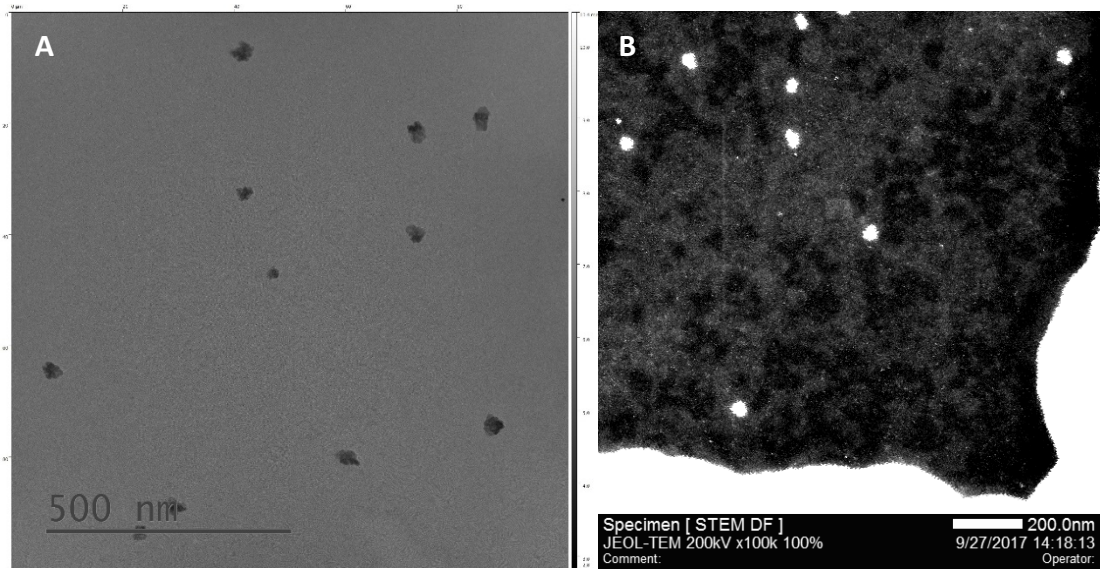

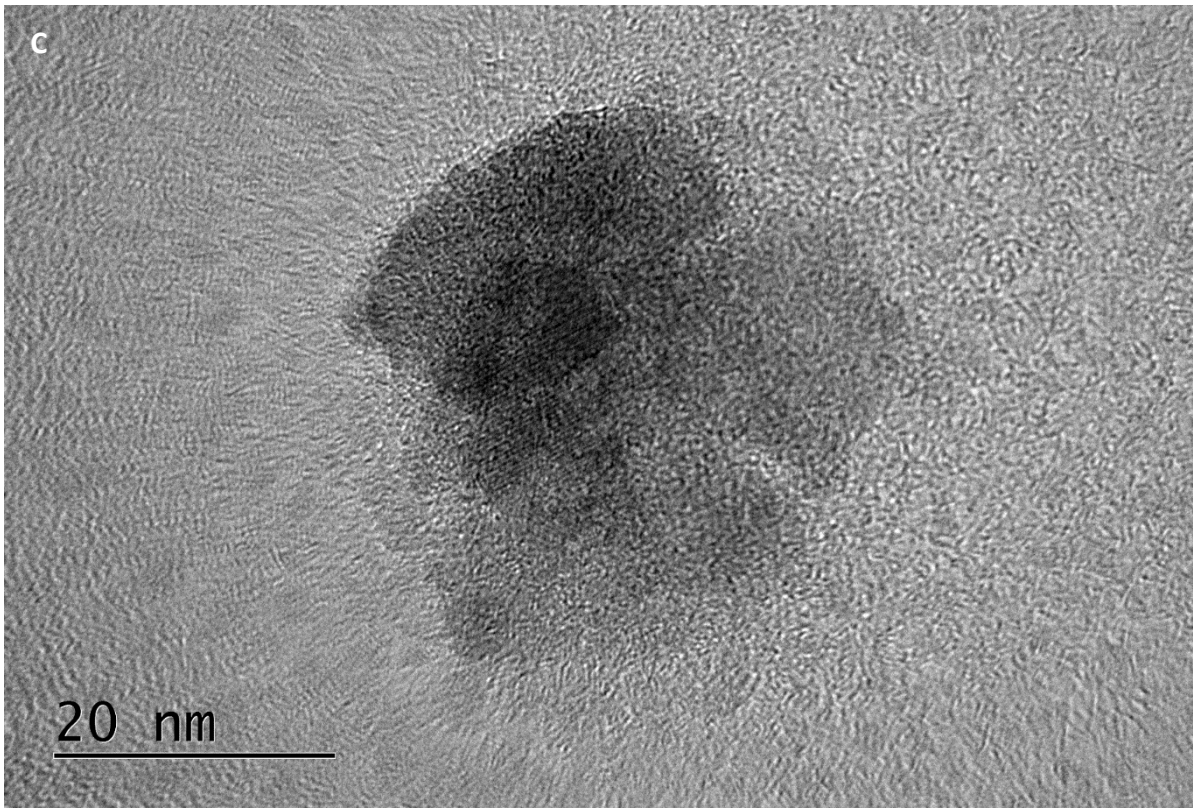

Figure 3.21 A) TEM and B) STEM image of CD-mannose + ConA low. C) High resolution TEM showing CD particle crystal lattice core.

3.5 FRET Results

In developing a novel carbon dot FRET assay for measuring lectin carbohydrate binding, nanomaterials synthesised and characterised in chapter 2 were used. The photoluminescence properties and full structural characterisation of these materials means that interpreting the meaning behind the results seen in this chapter can be discussed. As is the case with other nanomaterial-based FRET assays the material properties should be included as part of a correction factor which allow the variants in the assay to be comparable. These include QY and spectral overlap between donor and acceptor. The means for assessing the FRET efficiency can be conducted in a number of ways such as ratiometrically, by measuring the fluorescence increase or decrease in one fluorophore, through a 3-cube method – which measures in three channels with the aim of removing crosstalk signals. Often this means that the result of the assay is apparent to that assay only and an apparent k_d is extracted. This means raw results from this assay cannot be compared with others, but rather trends can be compared. In this work we explore the two carbon dots synthesised, CDala-carbohydrate and CD-carbohydrate from chapter 2 as well as using **FCD-3** from chapter 5 as a FRET acceptor. The effect of having a longer or shorter linker is explored. Some literature evidence shows that having a longer linker allows the carbohydrate to be more easily bound as it is further from the carbon dot surface and sterically

favourable. However, in the context of a distance dependent FRET readout, a small increase in distance could result in a removal of FRET altogether. Figure 3.22 shows the relationship between distance and propensity for FRET to occur with our system. Theoretical R_0 was calculated for the CD with fluorescein to determine the maximum distance at which FRET would be possible. Vice versa, the measured FRET signal indicates that the donor and acceptor must be within measurable distance hence can inform on the binding distance and conformation[102].

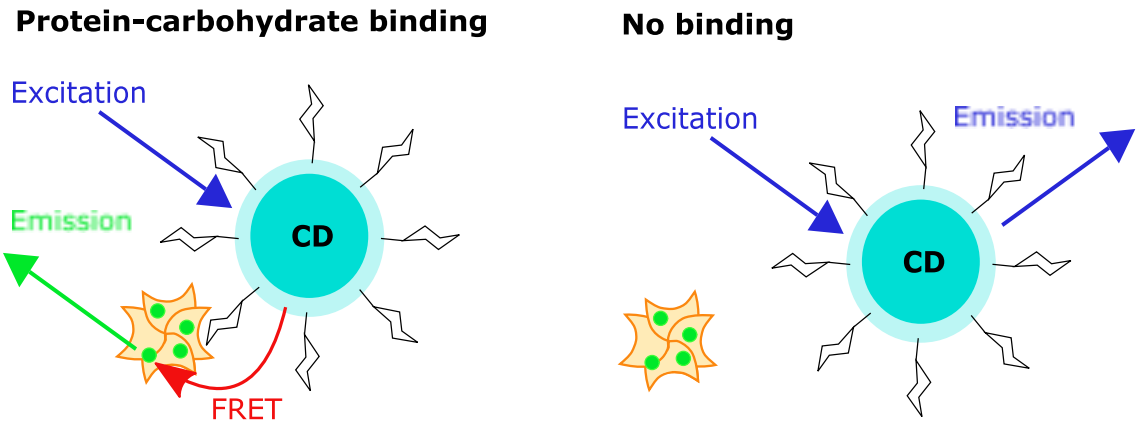

Figure 3.22 CD-carbohydrate binding by specific lectin in this case ConA attached with fluorescein allows distance dependent FRET interaction to occur.

3.5.1 FCD-3 and AcCD 17 FRET experiment

Initial efforts were made using long linker AmCD **16** synthesis carbon dots as the donor and using green fluorescent carbon dots **FCD-3** as the acceptor partner. This would allow for two functionalisable platforms for multivalent presentation. By having the lectin presented on a carbon dot this would be more closely sterically similar to how the interaction occurs in nature. The spectral excitation and emission profiles are shown in figure 3.23a. The excitation spectra of AcCD **17** and **FCD-3** are shown on the same graph. Using these spectra optimal excitation of the AcCD would occur at 320-340 nm where **FCD-3** has low excitation. This is important to ensure minimal direct acceptor excitation. The fluorescence of **FCD-3** peaks at 525 nm, at which AcCD **17** has minimal emission. This indicates good potential for FRET.

A preliminary experiment was conducted to observe whether any FRET occurred between the two nanoparticles without the carbohydrate or lectin conjugated to either substituent. **FCD-3** was titrated into a stock solution of AcCD **17** and the λ_{em} 525 nm measured as a function of λ_{ex} 340 nm. The raw fluorescence data is shown in figure 3.23. The blue line shows the emission of AcCD **17** (1 mg ml^{-1}) in 0.1 M HEPES buffer. Upon each addition of **FCD-3** (each aliquot was 8 μL of 5 mg ml^{-1}) the emission at

430 nm corresponding to AcCD **17** decreased but the fluorescence at 525 nm did not increase. This indicates no FRET occurred from blue CD to green. The decrease at 430 nm indicates energy transfer or quenching of AcCD **17** as a result of the addition of **FCD-3**, and any type of non-FRET energy transfer cannot be inferred. This decrease could be used as a measure of nanoparticle interaction, however, as it is not FRET it is not r^6 distance dependent and will not be able to sensitively measure lectin-carbohydrate interaction. Evidence from chapter 5 on the characterisation of **FCD-3** shows that this material is composed of a small molecule coating a nanoparticle. Hence, this small molecule could be dissociating from the nanoparticle surface during the assay and inducing quenching. This was determined as not a good assay system as FRET could not be concluded.

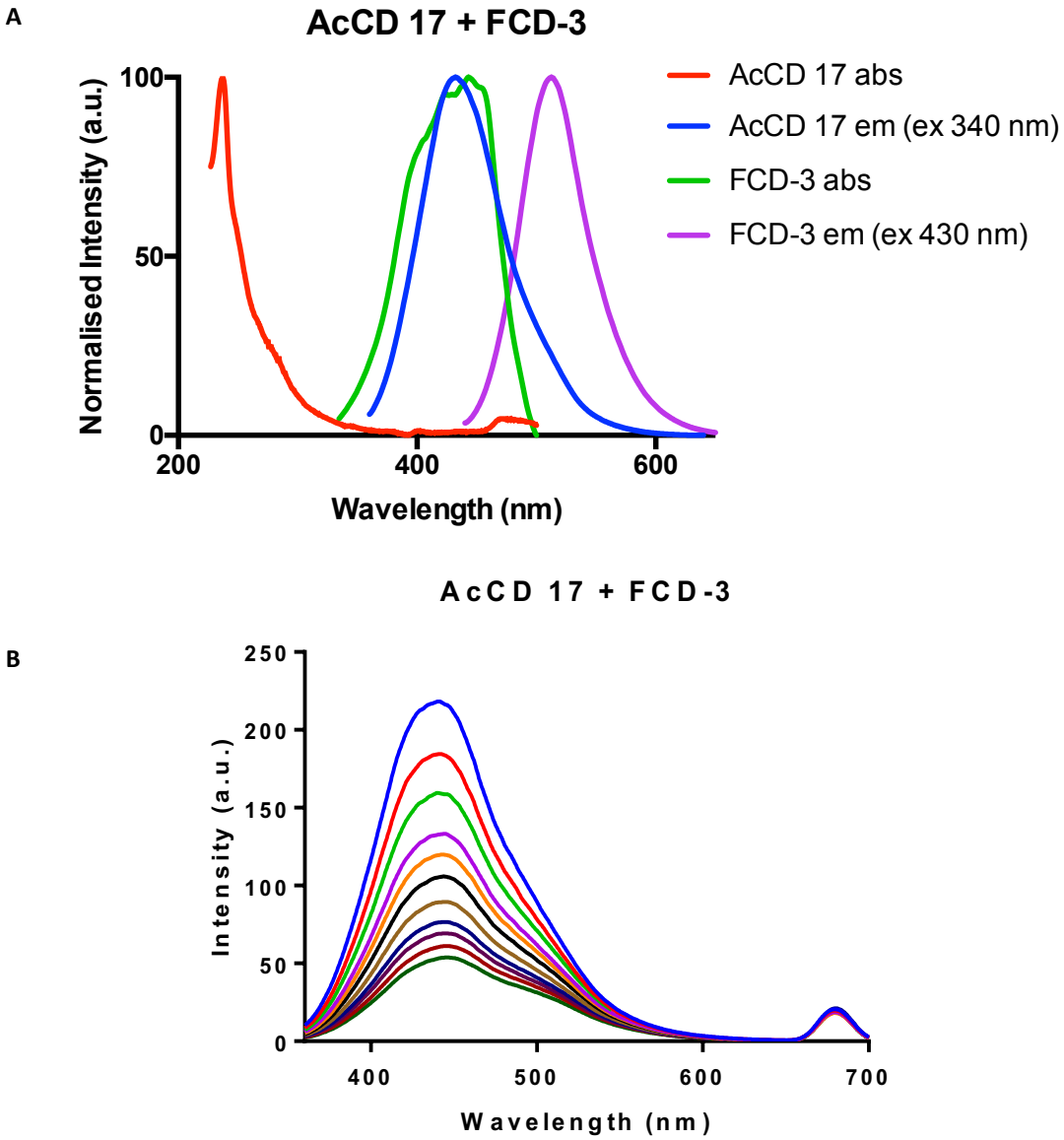

*Figure 3.23 Graphs relating to AcCD **17** and FCD-3. A) Absorptionand emission spectra for AcCD **17** and **FCD-3** overlaid. AcCD **17** λ_{ex} 340 nm and λ_{em} 430 nm. **FCD-3** λ_{ex} 430 nm and λ_{em} 525 nm. Overlap between AcCD **17** emission and **FCD-3** absorption profiles is indicative of potential energy transfer via FRET. B) Shows the FRET assay raw data of 10 aliquots of **FCD-3** titrated into AcCD **17** where λ_{ex} is 340 nm. Starting spectra blue, last titration dark green.*

3.5.2 FRET pair Förster radius (R_0)

A consideration of FRET is the spectral overlap between the donor emission and acceptor excitation. This is usually shown through overlaid spectra as seen in figure 3.23. With CD-carbohydrate it has been shown that the conjugated carbohydrate can affect the electronic properties of the CD so that the emission shoulder ~ 520 nm differs between CD-carbohydrates synthesised from the same AcCD **17**. We have seen differences between carbohydrate functionalised AcCDala **10** too. Hence, we calculated the difference in integral of each of CD-carbohydrates and CDala-carbohydrates with the acceptor fluorescein. Fluorescein conjugated ConA can be commercially purchased and was used in subsequent FRET assays. The spectral overlap (*J*) nm^4 cm^{-1} M^{-1} is shown in table 3.3. The integrated area was calculated according to equation 3.7 in the program $a|e$, where $PL_{D(\lambda)}$ is the donor emission integral when the area is normalised to 1 and ϵ_A is ConA's extinction coefficient.

$$J(\lambda) = \int_0^\infty PL_{D(\lambda)}\, \epsilon_A\, \lambda^4\, d\lambda$$

Equation 3.7 Equation used by software $a|e$ to generate integrated area overlap between emission of CD-carbohydrate and CDala-carbohydrate and fluorescein (J) nm^4 cm^{-1} M^{-1}. Data obtained is summarised in table 3.3.

The spectral overlap data were similar ranging between 1.476 - 1.787 x 10^{12} nm^4 cm^{-1} M^{-1}. This small range suggests that this would not have a large effect on the FRET potential. However, some methods for analysing FRET include this as part of a correction factor[113] when calculating apparent FRET values.

In order to determine the R_0 of the CD-carbohydrate and CDala-carbohydrate with ConA-F equation 3.8 found in Guo *et al*.[90] was used. The equation provides the R_0 in Angstrom (Å) however, this is often reported in nanometers for relevance. Where n_r= 1.33 the refractive index, K^2 = 2/3 and is the random dipole moment orientation of free fluorophore, Q_{QY} is the QY of the donor and I is the integral of the spectral overlap (*J*) nm^4 cm^{-1} M^{-1}.

$$R_0\,(\text{Å}) = \left(8.79 \times 10^{-5}\, {n_r}^{-4} \times Q_{QY} \times K^2 \times I\right)^{\frac{1}{6}}$$

Equation 3.8 Förster radius (R_0) equation. Data obtained is summarised in table 3.3.

The R_0 values are presented in table 3.3 and show a range of values from 1.995-2.925 nm. This is relatively short compared to the 10 nm distance that FRET can potentially occur over. However, this means that up to 3.99-5.85 nm FRET can be measured using these materials as synthesised all be it with 1.54 % efficiency.[102]

Sample	*Spectral overlap (J) $x10^{12}$ / nm^4 cm^{-1} M^{-1}*	*R_0 with Fluorescein (nm)*
AmFCD	1.623	2.55
AcFCD	1.593	2.93
CD-glucose	1.559	2.55
CD-mannose	1.597	2.77
CD-galactose	1.546	2.81
CD-maltose	1.587	2.72
CD-lactose	1.610	2.77
CD-maltotriose	1.608	2.82
CD-1,3-1,6-manntriose	1.719	2.60
CD-1,4-manntriose	1.740	2.59
CD-4-O-mannobiose	1.787	2.40
AcCDala	1.491	2.74
CDala-mannose	1.763	2.00
CDala-galactose	1.748	2.03
CDala-1,3-1,6-mannotriose	1.543	1.93
CDala-1,4-manntriose	1.604	2.55
CDala-4-O-mannbiose	1.614	2.60
CD-3'sialyllactose	1.476	2.34
CD-6'sialyllactose	1.634	2.46

Table 3.3 Spectral overlap of CD-carbohydrate and ConA and calculated R_0 values using equation 3.8. Errors could not be calculated in from this data as repeats were not conducted.

3.5.3 Theoretical FRET distance using physical information

Using the R_0, and structural information we have for CD-carbohydrate and CDala-carbohydrate donor and ConA-fluorescein acceptor whether there is a physical barrier to FRET can be thought about. We observe aggregation when donor and acceptor are in buffered solution together and DLS reports aggregate sizes between 200-1000 nm. However, thinking about a donor and acceptor pair in isolation, FRET distance (r) can be thought about.

Generic CD structure proposed in the conclusion of chapter 2 (section 2.3) shows the overall hydrodynamic size to be 4.28 $\pm$ 0.56 nm. If the CD fluorescence were to originate from the centre of the CD, the distance to the CD surface (i.e. the radius) is 2.14 nm. This calculated hydrodynamic radius includes the TTDDA linker which is ~ 2.13 nm long when extended (based on theoretical calculations where one C-C bond is 0.14 nm). Hence this likely means that the linker is not fully elongated at the surface. It is not known whether the carbohydrate on the CD surface is covalently or non-covalently bound. Assuming that both the TTDDA linker has a carbohydrate molecule covalently bonded and becomes fully extended in solution then this adds ~2.13 nm for the linker ~0.42 nm for succinic anhydride and ~0.42 nm for the carbohydrate onto the theoretical distance between donor and acceptor.

Furthermore, the short linker synthesis does not have the TTDDA linker or succinic anhydride on the surface hence this means a greater theoretical likelihood of FRET. Assuming specific binding occurs, the carbohydrate will be bound within the binding site on the ~7x7x6 nm ConA which is at the surface of the protein. Finally, the fluorescein acceptor is conjugated onto the protein in a 4.5:1 fluorophore:protein ratio. This means it is likely that there is a fluorophore less than 7 nm from the carbohydrate.

The minimum distance between the CD fluorescence centre (donor) and fluorescein molecule (acceptor) is therefore 0.84 nm. This is based on the fluorescence of the CD originating at the surface, a succinic acid linker (~0.42 nm) and carbohydrate molecule (~0.42 nm) and the fluorophore being next the carbohydrate in certain orientations, total 0.84 nm. This is nearer than the R_0 for all CD-carbohydrates reported hence, FRET is possible with these materials. However, the further possible distance between donor and acceptor is 12.11 nm. This is greater than the FRET distance possible as well as much greater than the R_0 value seen for our donors in table 3.3. Hence it is feasible FRET could occur with these values.

3.5.4 FRET between ConA and CDala-carbohydrate (Shorter linker)

The shorter linker spectral profile was overlaid with that of ConA conjugated fluorescein (ConA-F) to assess the FRET potential, data is presented in figure 3.22. The excitation and emission spectra for AcCDala **10** are shown in blue and red respectively. CDala-carbohydrate spectra are similar enough that AcCDala **10** is a good indication of the FRET potential for these also. ConA-F direct excitation below 400 nm has a low chance of occurring allowing for optimal excitation of the donor to be achieved with the peak at 340 nm. However, the AcCDala **10** emission spectra shoulder above 500 nm (as is also the case with CDala-carbohydrate) means there will be some bleed-through into the signal at 525 nm.

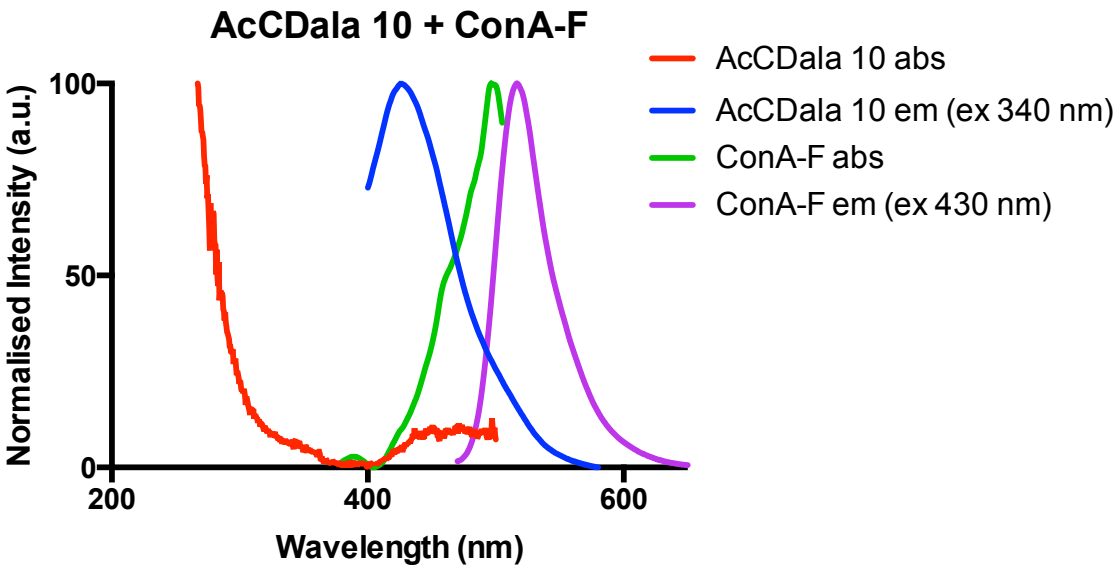

*Figure 3.24 Absorption and emission spectra for AcCDala **10** and ConA-F overlaid. AcCDala **10** λ_{ex} 340 nm and λ_{em} 430 nm. ConA-F λ_{ex} 430 nm and λ_{em} 525 nm. Overlap between AcCDala **10** emission and ConA-F absorption profiles is indicative of potential energy transfer via FRET.*

Example FRET titration data is shown in figure 3.23 for AcCDala **10**, CDala-mannose **15** and CDala-galactose **14** with ConA-F. Starting spectra with donor only is shown in blue in each titration. Upon ConA-F additions the donor fluorescence at 430 nm decreases for CDala-mannose **15** and CDala-galactose **14** and the acceptor signal at 525 nm increases with an isosbestic point clearly seen at 495 nm. This is not the case for AcCDala **10** where the donor signal decreases to a lesser extent and the signal at 525 nm does not increase. This suggests that the CDala-carbohydrate donors are able to transfer energy to the acceptor fluorophore under the terms of distance dependent FRET meaning that ConA-F is closer to the CD than in the case of unfunctionalised CD. This indicates that the carbohydrate functionalisation does not impede FRET by increasing the distance between the CD and the acceptor. This also indicates no non-specific FRET with AcCDala **10**. CDala-mannose **15** also shows an initial fast rate of FRET, seen through the red spectra being considerably lower compared to CDala-galactose **14**.

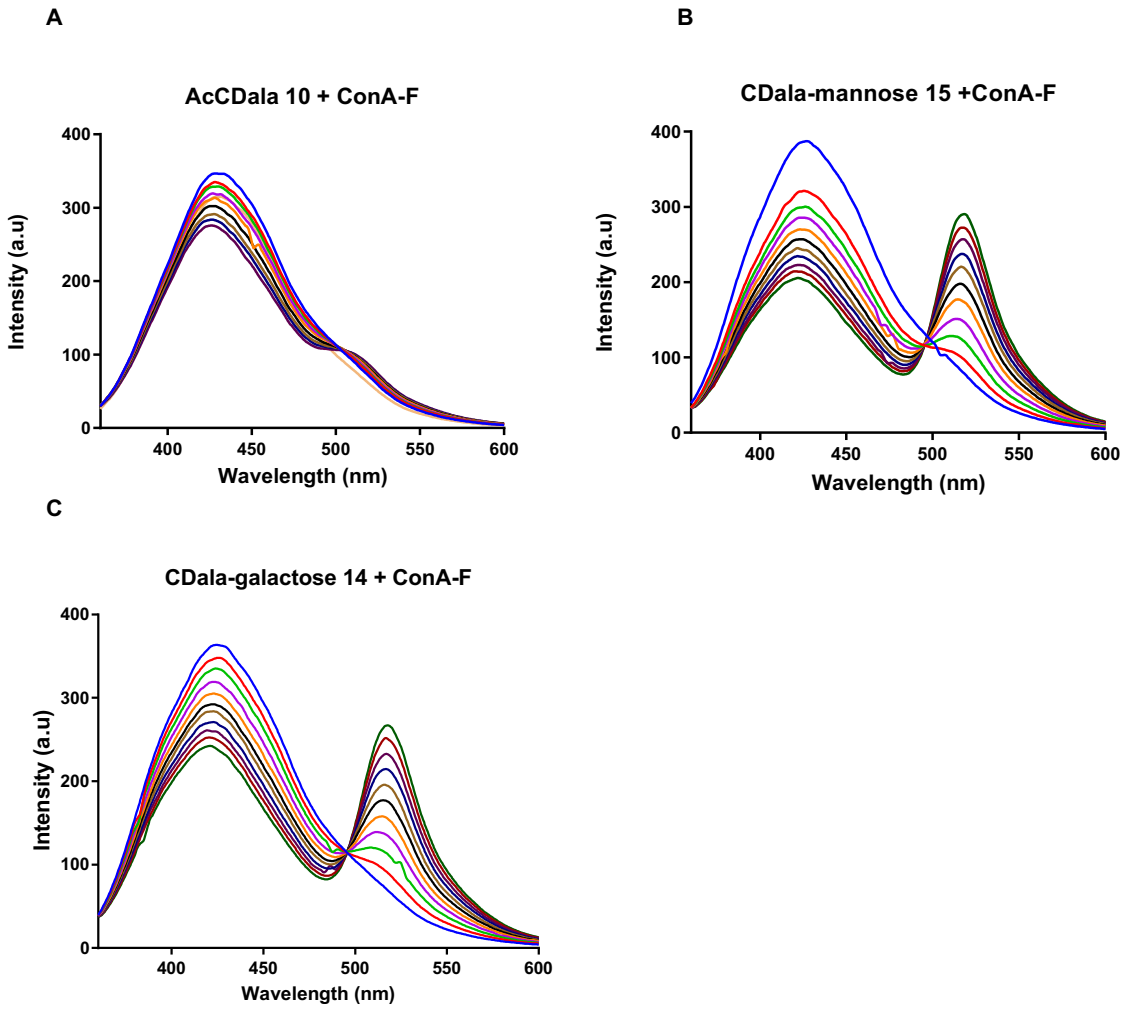

*Figure 3.25 Raw FRET assay raw data of 10 aliquots of ConA-F titrated into AcCDala **10** (A), CDala-mannose **15** (B) and CDala-galactose **14** (C). Starting spectra blue, last titration dark green in all cases.*

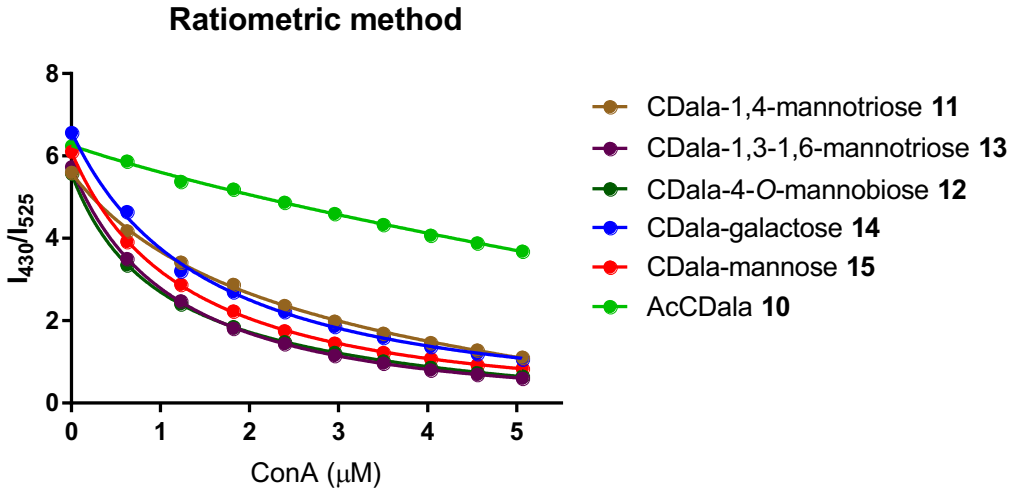

Figure 3.26 CD-carbohydrate + ConA-F FRET assay plotted using one site total binding – variable slope Hill plots of direct dye excited corrected ratiometric FRET I_{430} / I_{525}

The data was processed according to ratiometric method outlined in section 3.1.1 and developed by Guo *et al.*[42] Presented in figure 3.24 is I_{430} / I_{525} having subtracted the direct dye excitation background. Upon additional aliquots of acceptor (40 μg) the ratio decreases, initially faster and begins to plateau. The AcCDala **10** control (light green line) has a more linear curve suggesting that the acceptor has a signal independent of binding. The gradient of each slope is used by GraphPad Prism software to determine the apparent dissociation constant k_d which are shown in table 3.4.

It is worth noting that whilst carrying out the experiment, upon the addition of ConA-F aliquots, a precipitate formed and dropped out of solution. This could be the result of the donor and acceptor interacting and forming aggregates this means that not all the binding can be observed on a time scale which is measurable by the instrument setup.

	I_{430} / I_{525}			
CD-carbohydrate	Apparent k_d (μM)	B_{max}	NS	R^2
AcCDala 10	4.36 $\pm$ 7.22	-1.7 $\pm$ 3.3	-0.3 $\pm$ 0.2	1.00
CDala-galactose 14	1.63 $\pm$ 0.36	-7.6 $\pm$ 1.2	0.04 $\pm$ 0.14	1.00
CDala-mannose 15	1.36 $\pm$ 0.07	-6.9 $\pm$ 0.2	0.04 $\pm$ 0.03	1.00
CDala-4-O-mannobiose 12	0.97 $\pm$ 0.03	-5.6 $\pm$ 0.06	-0.05 $\pm$ 0.01	1.00
CDala-1,4-mannotriose 11	1.99 $\pm$ 0.37	-5.3 $\pm$ 0.8	-0.14 $\pm$ 0.08	1.00
CDala-1,3-1,6-mannotriose 13	1.23$\pm$ 0.04	-6.7 $\pm$ 0.1	0.05 $\pm$ 0.02	1.00

Table 3.4 Apparent dissociation constants k_d (with SEM) for CDala-carbohydrate from FRET assay with ConA-F determined from graph in figure 3.24. Where B_{max} is the maximum specific binding in terms of I_{430}/I_{525} and NS is the slope of the non-specific binding in terms of I_{430}/I_{525} per μM ConA. $\pm$ SE

The apparent k_d values for short linker CDs are within the low μM range, which confers binding you may expect for ConA where multivalent interaction may be responsible.[21] Nanomolar values are the golden standard for this work and are achieved by using glycodendrimers with 12, 24 or more molecules per molecule.[35] However, these results are apparent k_d values and can be compared using this assay only. And the AcCDala **10** control has a comparatively strong interaction with a k_d of 4.363 μM – on the same order of magnitude as all CDala-mannosides tested. The apparent k_d for the CDala-mannosides although similar between the range 0.97-1.99 μM. However, CDala-galactose **14** also falls within this range meaning this result indicates a non-specific interaction mediated by the presence of carbohydrate.

3.5.5 FRET between ConA and CD-carbohydrate (Longer linker)

The long linker spectral profile was overlaid with that of ConA-F to assess the FRET potential, data is presented in figure 3.25. The excitation and emission spectra for AcCD **17** are shown in blue and red respectively. CD-carbohydrate spectra are similar enough that AcCD **16** is a good indication of the FRET potential for these also. Long linker CDs have similar photoluminescence profiles to short linker CDs hence the same excitation 340 nm can be used. Similar to the short linker CD, spectral bleed-through at 525 nm will occur.

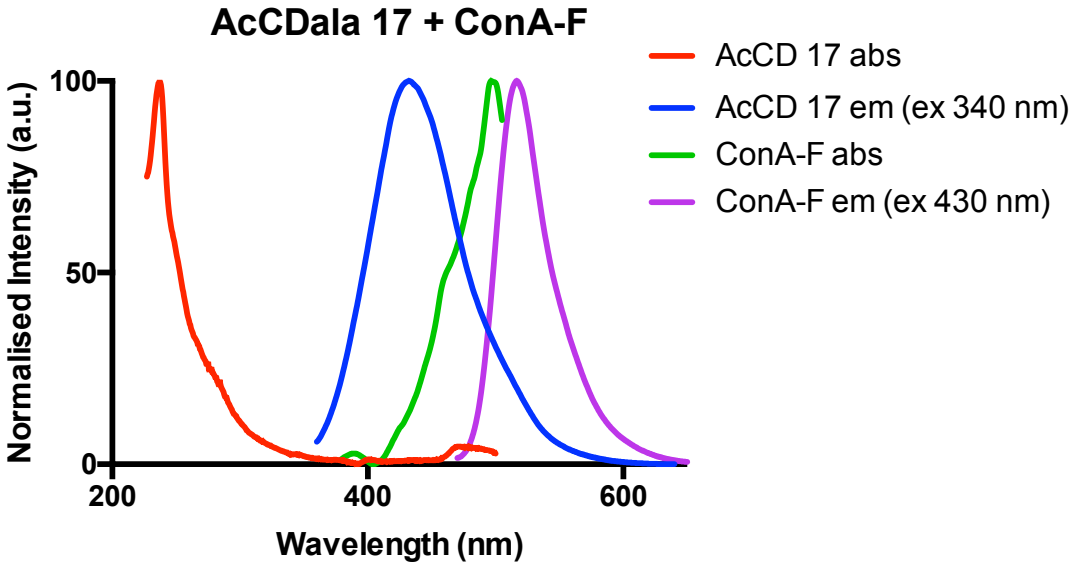

*Figure 3.27 Absorption and emission spectra for AcCD **17** and ConA-F overlaid. AcCD **17** λ_{ex} 340 nm and λ_{em} 430 nm. ConA-F λ_{ex} 430 nm and λ_{em} 525 nm. Overlap between AcCD **17** emission and ConA-F absorption profiles is indicative of potential energy transfer via FRET.*

Considering the longer linker on these CDs compared to the short linker CDs, the distance between the donor and acceptor will be further away hence a reduced FRET signal would be expected. This is assuming that the carbohydrate is covalently conjugated to the linker, interacting with the ConA-F and fully extended from the CD surface. The FRET titration data however, indicates FRET has occurred due to a decrease in donor signal and increase in acceptor signal with isosbestic point at 515 nm (Figure 3.26).

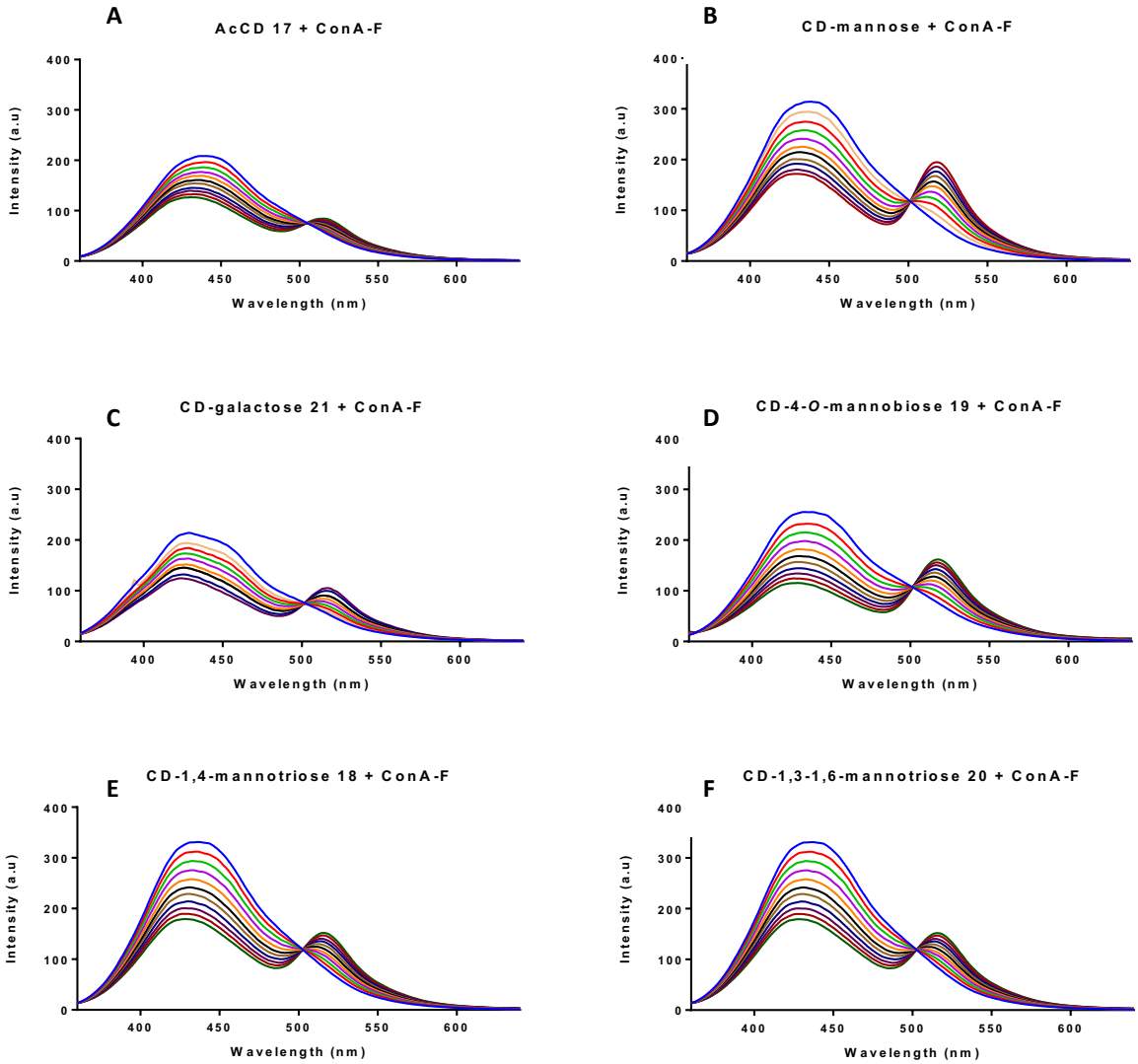

*Figure 3.28 Raw FRET assay raw data of 10 aliquots of ConA-F titrated into AcCD **17** (A), CD-mannose **22** (B), CD-galactose **21** (C), CD-4-O-mannobiose **19** (D), CD-1,4-mannotriose **18** (E) and CD-1,3-1,6-mannotriose **20** (F). Starting spectra blue, last titration dark green in all cases.*

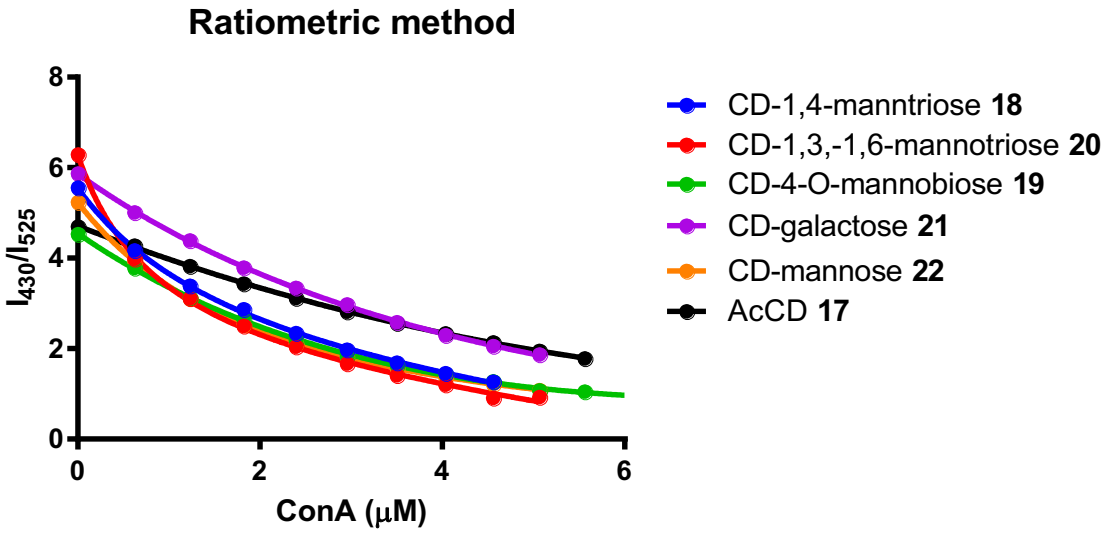

Figure 3.29 CDala-carbohydrate + ConA-F FRET assay plotted using one site total binding – variable slope Hill plots of direct dye excited corrected ratiometric FRET I_{430} / I_{525}

As before, the same ratiometric method I_{430} / I_{525} and was plotted as a function of acceptor concentration as shown in figure 3.27. The slope of the control, AcCD **17** (black line) looks more linear than the carbohydrate containing samples indicating a lack of FRET similar to the data seen with short linker data. The k_d was extracted from the slope of the curve in GraphPad Prism and collated into table 3. Interestingly, there are greater differences between CD-carbohydrate samples with a long linker than with the short linker. From table 3.5 the AcCD **17** shows a 10-fold higher k_d of 36.67 μM than observed in short linker results. This suggests a weaker interaction between the AcCD **17** surface and ConA-F than with AcCDala **10**. CD-galactose **21** k_d of 7.84 μM can be compared with the CD-mannoside samples. CD-4-O-mannobiose **19** had a k_d of 9.29 μM which is greater than the CD-galactose **21** control. Assuming α-mannose binding occurs, this result indicates a lack of specific binding by ConA to this disaccharide. The other CD-mannosides have comparable values as seen with short linker CDala-mannosides which indicates that the FRET distance is not much different between CD linker length. This suggests that the linker does not play a role in mediating a distant dependent result. Otherwise a large difference would be seen for a small change due to the nature of FRET.

I_{430} / I_{525}

CD-carbohydrate	Apparent k_d (μM)	B_{max}	NS	R^2
AcCD 17	36.67 ± 46.44	-73.2 ± 167	1.2 ± 167	0.9998
CD-galactose 21	7.84 ± 2.78	-13.0 ± 6.4	0.2 ± 6.4	0.9997
CD-mannose 22	2.44 ± 0.04	-6.6 ± 0.1	0.06 ± 0.1	1
CD-4-O-mannobiose 19	9.29 ± 2.78	-18.8 ± 7.7	0.6 ± 7.7	0.9993
CD-1,4-mannotriose 18	1.85 ± 0.39	-4.9 ± 0.8	-0.2 ± 0.8	0.9994
CD-1,3-1,6-mannotriose 20	0.89 ± 0.16	-5.1 ± 0.5	-0.2 ± 0.5	9.9987

Table 3.5 Apparent dissociation constants k_d (with SEM) for CD-carbohydrate from FRET assay with ConA-F determined from graph in figure 3.27. Where B_{max} is the maximum specific binding in terms of I_{430}/I_{525} and NS is the slope of the non-specific binding in terms of I_{430}/I_{525} per μM ConA. ± SE

Considering FRET data for both the short and long linker CDs in combination with structural information gleaned from chapter 1 which showed that carbohydrate exists in the sample which is not covalently bound to the CD. ConA may have greater affinity for this free carbohydrate and if it is in greater concentration than the ConA binding sites available, a lack of FRET may result. If ConA-F binds unconjugated but CD associated carbohydrate, this could bring fluorescein in closer proximity to the CD donor, hence, FRET does not infer conjugated carbohydrate binding. Furthermore, CDala-galactose **14** and CD-galactose **21** both have a better FRET signal compared to unfunctionalised CDs. This suggests that non-specific carbohydrate interaction is involved in FRET observed independent of linker length.

3.5.6 Caveats of our system

We use glycan functionalised carbon dots as our donor system and the fluorophore fluorescein conjugated to the lectin Concanavalin A (ConA-F) as our acceptor. In our system we do observe crosstalk as shown by control data with ConA-F only. This is relatively high considering the minimal excitation seen for Con-F in its spectra. However, this is subtracted from the raw data before FRET efficiency equations are applied.

There is a baseline level of bleed-through of CD donor fluorescence at 525 nm in the acceptor channel which is difficult to remove. Although the donor concentration does not change over the course of the experiment (the acceptor aliquot added contains donor so that the overall donor concentration remains consistent), the CD fluorescence reduces as FRET occurs to the acceptor. Hence, three-cube methods could overcome this. In our system we observe non-specific aggregation in DLS with CD-galactose **21** + ConA. Hence, a lack of distinguishable FRET efficiency observed with CD-mannose **22** could be a result of non-specific FRET occurring.

In our case we have a multivalent donor which presents binding sites in 3-dimensions. The acceptor fluorescein is conjugated to ConA to make ConA-F which can bind in 3-dimensions also, having four identical independent binding sites. This means that there is potential for an aggregate to form as a result of these specific interactions which means multiple donor to acceptor potential FRET opportunities and a mixed fluorophore population. Furthermore, commercially acquired acceptor ConA-F has on average 4.5 fluorophores conjugated per ConA tetramer. Which means FRET interactions from one donor to one acceptor binding event will still have multiple fluorophore populations.

With our carbon dots the surface functionalisation is known to impact the fluorescence peak shoulder ~ 520 nm hence binding with an acceptor fluorophore such as fluorescein (λ_{ex} 530 nm) could impact this. This would affect the acceptor channel potentially to a greater extent than the donor channel as a result. Control experiments with a non-fluorescent ConA or further investigations with methyl α-D-mannose could investigate the effect of protein binding in this case. Furthermore, raw FRET titration data shows a donor peak blue-shift upon each addition of ConA-F. This could be a property on the aggregate which could cause detection in the donor channel to be misleading.

2.5.7 Methyl-α-D-mannose competitive studies

Post FRET titration methyl-α-D-mannose was added to the sample in a competition assay. Methyl-α-D-mannose is bound irreversibly by ConA.[145] When added into solution with CD-mannose **22**, and AcCD **17** it competes with specific mannose binding in CD-mannose **22** or can simply remove non-specific interactions between AcCD **17** and ConA-F. Figure 3.28 shows that for AcCD **17**, addition of methyl-α-D-mannose, up to 1000 ug, causes a removal of FRET signal upon 340 nm irradiation. The donor fluorescence peak at 430 nm increases, meaning the CD can undergo radiative emission and the isosbestic point at 515 nm is no longer observed. However, the peak at 525 nm corresponding to the acceptor peak fluorescence increases with each addition of methyl-α-D-mannose too. This suggests that as the donor becomes unbound, ConA-F becomes more fluorescent. This seems counter intuitive as the donor is further away hence cannot FRET, meaning lower fluorescence signal at 525 nm would be expected. However, direct dye excitation of fluorescein could be occurring. Figure S.3.3 shows that ConA-F fluorescence at 525 nm reaches 200 a.u. upon the highest ConA-F concentration. This is much greater than the fluorescence seen in in figure 3.28 of AcCD **17** + ConA-F at the final titration (>100 a.u.). Hence, restoration of this direct dye excitation may be occurring when ConA-F binds methyl-α-D-mannose. Furthermore, this could indicate ConA-F fluorescence is quenched when it is bound to

the CD, perhaps by the CD or self-quenching due to a high level of fluorescein aggreged at the CD surface.

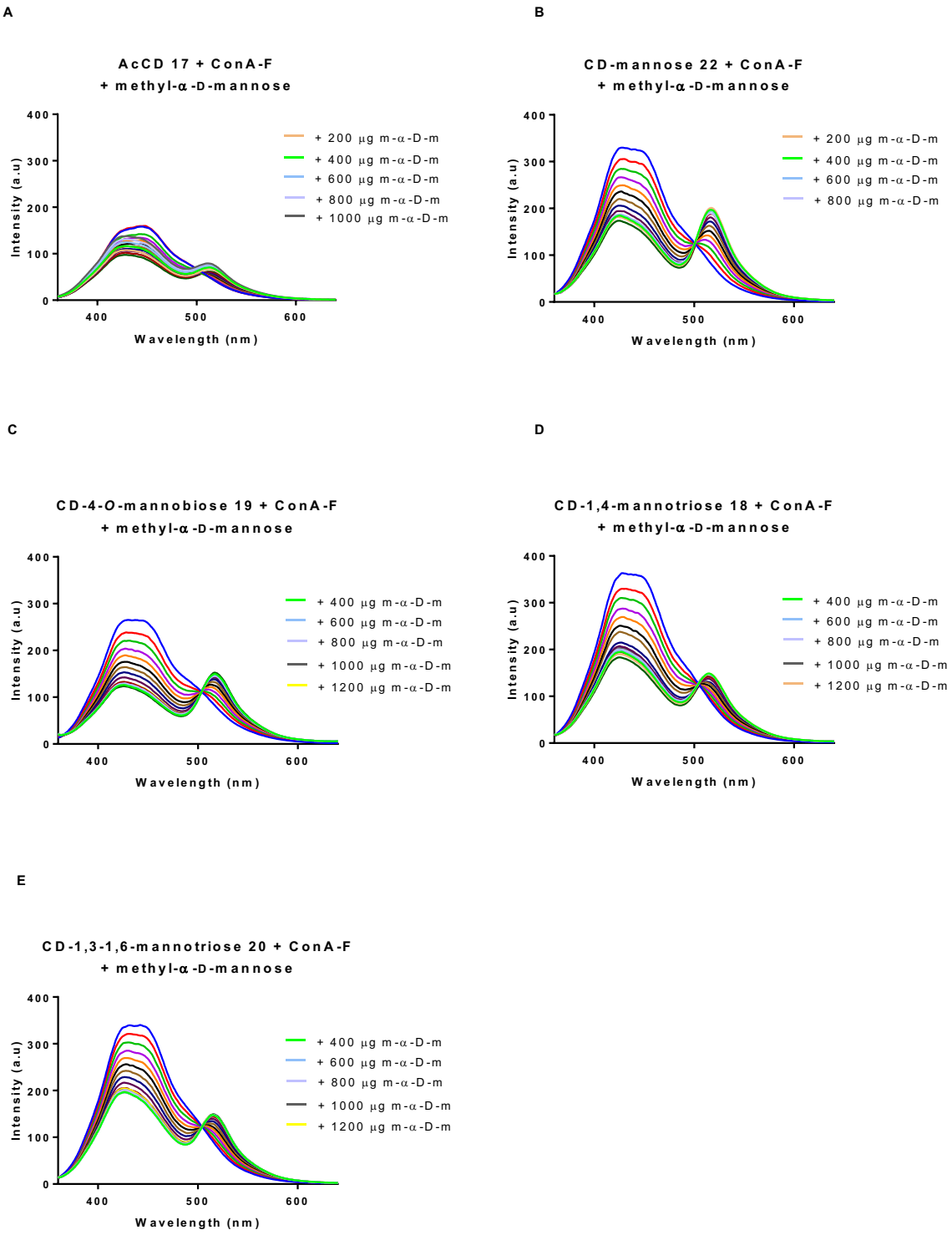

Figure 3.30 Addition of methyl-α-D-mannose which irreversibly binds ConA was added to FRET titrations post ConA FRET experiments.

3.5.8 CD-sialyl-D-lactose FRET

CD-3'-sialyl-D-lactose **26** and CD-6'-sialyl-D-lactose **27** were tested in the same ratiometric FRET assay with the Elderberry Bark lectin - Sambucus Nigra lectin (SNA) conjugated with fluorescein (SNA-F). SNA is a tetrameric lectin of size 140 kDa which is known to specifically bind α-2,6-sialyllactose over α-2,3-sialyllactose.[146] This is due to interaction between the terminal sialic acid in 2,6-sialyl-D-lactose which is bound with greater affinity by SNA based on binding site interaction with the carboxylic acid and glyceryl (C7-C9) side chain.[147] Sialic acid is one biomarker of cancer cell progression and metabolism in some breast cancer cases.[148] Furthermore, sialic acid linkage is important in cancer. For example, non-small cell lung cancer tumours it was observed that α-2,6- galactose linked sialic acid was overexpressed in well differentiated cells and not in poorly differentiated cells within the same tumour.[149] Hence this has the potential to be exploited for targeted cancer treatment.

The FRET assay raw data can be seen in figure 3.31. The same FRET donor and acceptor are used in this assay as previous work. The donor peak has a double humped fluorescence peak which means that measuring the signal by integrating over a range would be more accurate than at one wavelength. However, the intensity at 430 nm and 525 nm were plotted using non-linear fitting according to Hill's equation as seen in figure 3.32. The apparent k_d from SNA with CD-3'-sialyl-D-lactose **26** was 1.185 $\pm$ 0.008 μM (R^2 = 0.9999) B_{max} is -5.0 $\pm$ 0.1 and NS is -0.03 $\pm$ 0.01 and with CD-6'-sialyl-D-lactose **27** was 0.6044 $\pm$ 0.007 μM (R^2 = 0.9996) B_{max} is -5.2 $\pm$ 0.1 and NS is -0.03 $\pm$ 0.02. This result fits with the knowledge that SNA has greater specificity for the α-2,6- version of sialyllactose having almost half the affinity in this assay. This indicates differential binding information can be observed and could be assessed using data from this assay.

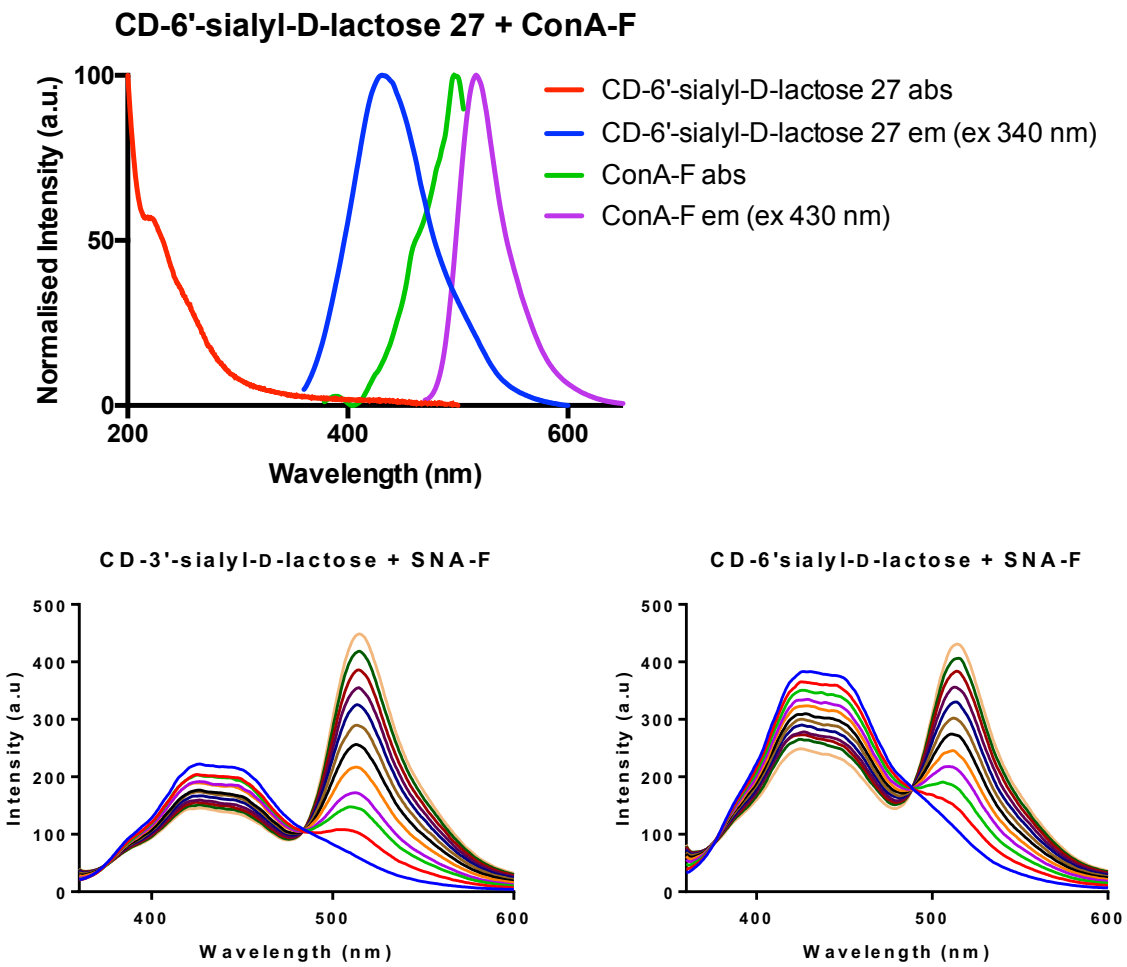

*Figure 3.31 FRET Raw FRET assay raw data of 10 aliquots of SNA-F titrated into CD-3'-sialyl-D-lactose **26** and CD-6'-sialyl-D-lactose **27**. Starting spectra blue, last titration dark green in all cases. Molar concentrations of SNA-F were the same as those used for ConA-F and the CD-carbohydrate concentration was also the same 1 mg ml^{-1}.*

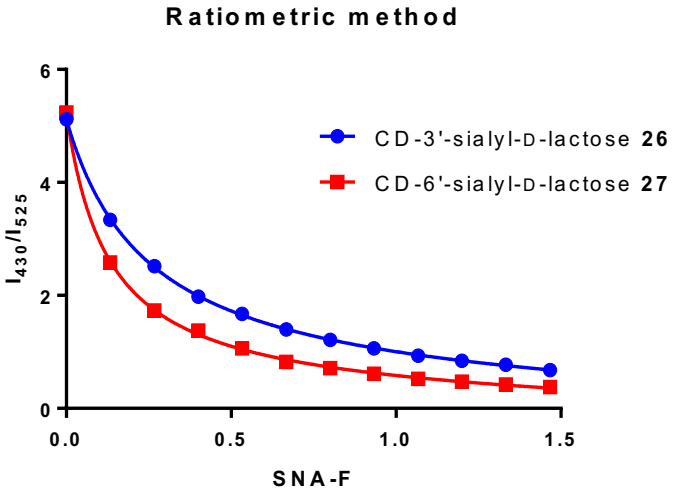

*Figure 3.32 CD-3'-sialyl-D-lactose **26** + ConA-F and 4 CD-6'-sialyl-D-lactose **27** + ConA FRET assay plotted using one site total binding – variable slope Hill plots of direct dye excited corrected ratiometric FRET $\frac{I_{430}}{I_{525}}$*

3.6 Conclusions and Future Work

Physical DLS, TEM and AFM characterisation revealed carbohydrate-based aggregation between CD-mannose and CD-galactose with ConA. Although this has not been carried out for shorter linker CD's we anticipate similar aggregation induced by ConA-F, based on known surface functionality. AFM studies revealed CD-carbohydrate-based aggregation between 200-500nm which was not seen in AcCD **17**. These structures were also seen in TEM and DLS. This data alluded to different modes of binding between CD-mannose **22** and CD-galactose **21** reflecting ConA specificity for α-D-mannose, seen through two distinct types of aggregates. These were thought to reflect tight and loose aggregates in solution. The prevalence of these aggregate types differed between CD-mannose **22** and CD-galactose **21** needs further investigation.

FRET results indicate differences between short and long linker CD-carbohydrate binding by ConA. The comparison between control AcCDala **10** and AcCD **17** in FRET assay with ConA-F with apparent dissociation constants of k_d of 4.36 μM and k_d of 36.67 μM reveals a 10-fold difference in affinity. Considering they have the same terminal carboxylic acid group the basis for this difference is unclear. The TTDDA and succinic anhydride linker on AcCD **17** may add increased distance between the CD fluorescence centre and fluorescein.

For the shorter linker FRET result, AcCDala **10** and CDala-galactose **14** having comparable affinity to the CD-carbohydrates indicates a non-specific interaction. Longer linker CDs seem to not impose an improved affinity compared to CDala-carbohydrates, rather better controls where AcCD **17** has a 10-fold greater dissociation constant (36.67 μM) and CD-galactose **21** (7.84 μM) is also larger than CD-mannosides. This suggests CD-mannoside results result from specific binding of ConA. In order to investigate these results further, reliability should be improved by repeating these assays so that significant differences can be concluded. Whether these results can be reproduced using a different synthesis is also an important point. Carbohydrate functionalisation is an unknown variable with this material. Between syntheses this could vary and assessing this would be difficult. Chapter 2 outlined how the Molisch's test can be used to determine the carbohydrate present on the surface of the CD. However, this does not differentiate if and how much is covalently or associated with the CD. Furthermore, a second interaction was assessed in this assay using the same FRET donor and acceptor. Results of this fit with known binding affinity of SNA for α-2,6-sialyl-D-lactose over α-2,3-sialyl-D-lactose suggesting this result may be able to probe novel lectin carbohydrate interactions.

R_0 range between 2-2.9 nm and spectral overlap indicate that FRET could occur with the materials used, the minimum distance possible being 0.84 nm calculated from known physical characteristics of our system. Hence, it is feasible that FRET could be the basis for the results we observe. So far ratiometric FRET seems to provide apparent FRET binding constants which show similarity between two types of CD, which suggests reliability.

Interestingly, competition studies with the long linker CD show a distinct removal of FRET interaction with AcCD **17**. This suggests a different binding mechanism between ConA-F to carboxylic acid functionalised CDs and a carbohydrate. However, differences in this study could not be distinguished at the concentration range of competitive inhibitor used.

In order to investigate this further CD-galactose **21** should be tested in a competition assay with methyl-α-D-mannose to observe whether an effect similar to AcCD **17** in which case the result with CD-mannose **22** would be specific to the ConA specificity for mannose. If CD-galactose **21** has a result similar to CD-mannose **22** then this suggests this effect is an indication of non-specific binding and suggest CD-mannose **22** is non-specifically bound by ConA-F.

Furthermore, if these results can differentiate between lectin-carbohydrate binding and non-specific binding then inhibition experiments could be used to measure the binding affinity, where the donor fluorescence recovery could be the parameter indicative of binding. This could also be used to quantify the CD-carbohydrate interaction with ConA. The amount of methyl-α-D-mannose required to restore donor fluorescence, through an inhibitory binding study, could reveal how much carbohydrate was bound on the CD surface by ConA.

To overcome the α-D-galactose non-specific interaction and confirm that the FRET signal is specific between ConA and our CD-mannose it would make sense to instead carry out Ca^{2+} omitted experiments between ConA and CD-mannosides. This should show a removal of FRET. Also, ConA-succinyl could be used as a means for assessing multivalent binding of CD-carbohydrates. Succinylating the lectin causes a dimer to exist in solution instead of a tetramer at pH 7.4. The lectin binding will be much lower if reflecting the reduced multivalency. This could also be assessed in terms of aggregate size formed. ConA-succinyl would cause a reduction in aggregate size if the aggregation is the basis of specific α-D-mannose binding or would not if it simply aggregates to any carbohydrate non-specifically.

3.7 Experimental

Lectins Concanavalin A fluorescein conjugated (ConA-F) and Sambucus Nigra Lectin fluorescein conjugated (SNA-F) were purchased from Vector Labs.

3.7.1 DLS and zeta potential sample preparation

CD-carbohydrate was diluted to 1 $mgml^{-1}$ in 0.1 M HEPES buffer with 5 mM $MnCl_2$ and 5 mM $CaCl_2$ and ConA was diluted in the same buffer and added in mass ratios 1:1 to 1:0.00625 to the CD-carbohydrate sample.

1 ml of sample was made total. A plastic 70 μL cuvette was used to measure hydrodynamic size in DLS and a plastic zeta potential cell was used to measure the zeta potential, 700 μL required. Before DLS and zeta potential measurements samples were vortexed for 10 seconds in a 1.5 mL Eppendorf tube.

3.7.2 AFM sample preparation

AFM sample preparation was carefully and iteratively optimised to the following. Fresh buffer (0.1 M HEPES buffer with 5 mM $MnCl_2$ and 5 mM $CaCl_2$) was prepared from 0.2 μm cellulose membrane filtered ultrapure water and samples with CD-mannose **22**, CD-galactose **21** and AcCD **17** were prepared with ConA at the ratio 1:0.025 (0.24 μM). Samples were vortexed for 10 seconds in 1.5 mL Eppendorf tubes for before deposition. Fresh mica surface was prepared by cutting up 1 cm^2 squares and cleaved with Scotch tape to reveal a fresh atomically flat surface. Samples were diluted 1000-fold. 20 μL of sample was drop deposited on the surface and left for 2 minutes. White roll was used to carefully remove excess sample from the side of the mica. N_2 was gently blown on the surface for drying. Samples were left overnight before imaging to dry completely. Variables optimised in AFM sample preparation include drying time, concentration of sample, buffer cleanliness and drying method i.e. spin drying.

3.7.3 TEM and STEM sample preparation

CD-mannose **22**, CD-galactose **21** and AcCD **17** were prepared in the same way in 0.1 M HEPES buffer with 5 mM $MnCl_2$ and 5 mM $CaCl_2$ and ConA added at the ratio 0.25 (0.24 μM). Sample was vortexed before deposition. 20 μL of sample was drop deposited onto a 4 nm carbon coated copper grid and the whole droplet was left on the grid and allowed to dry down overnight.

3.7.4 FRET assay experimental conditions

CD-carbohydrate of interest was diluted to 5 mg ml^{-1} in 0.1 M HEPES buffer with 5 mM $MnCl_2$ and 5 mM $CaCl_2$. Molar concentration was calculated using a ConA mass of 104 kDa and SNA mass of 140 kDa into a quartz cuvette was added 120 μL of sample and 480 μL of buffer only (1 mg ml^{-1}). Fluorescence was measured using a fluorometer set to 700 V laser power, slit width 10 nm. ConA-F was dissolved to 5 mg ml^{-1} in 0.1 M HEPES buffer with 5 mM $MnCl_2$ and 5 mM $CaCl_2$ which also contained CD-carbohydrate of interest at 1 mg ml^{-1}. i.e. preparing the guest solution in the host solution as seen in supramolecular titrations.[150] 8 μL of ConA-F solution was titrated into the CD-carbohydrate solution and mixed by pipette mixing 3 times. Fluorescence was measured upon each titration up to 10 additions.

Fluorescence at 430 nm and 525 nm were taken as the donor and acceptor signal respectively. These were plotted ratiometrically I_{430}/I_{525} having subtracted the direct dye excitation background. This data was plotted in GraphPad Prism software using non-linear fitting, one-site total binding fitting (Model: $Y = Bmax\ X/(k_d + X)\ + NS\ X + Background$) and the k_d values reported were those reported by the software.

3.7.5 Supplementary graphs

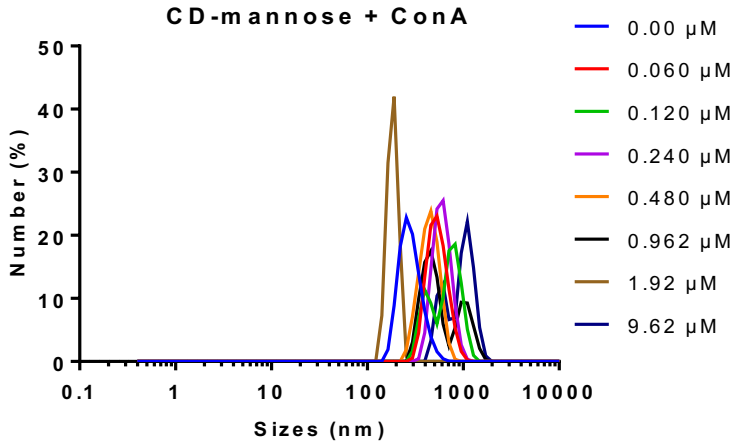

*Supplementary Figure 3.1 DLS raw data of % intensity data for CD-mannose **22** + ConAat a range of concentrations in a binding study.*

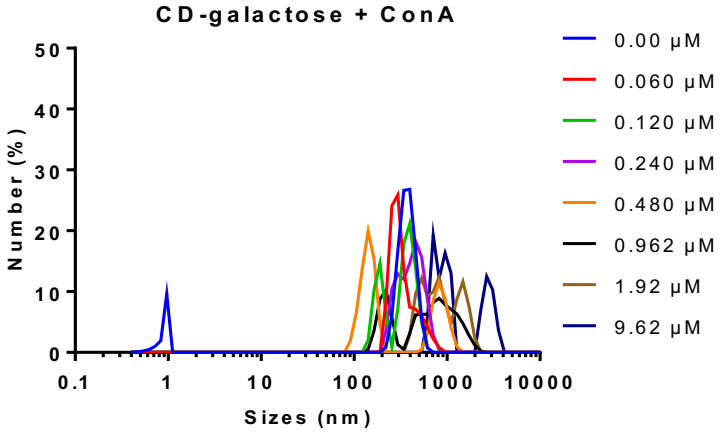

*Supplementary Figure 3.2 DLS raw data of % intensity data for CD-glactose **21** + ConA at a range of concentrations in a binding study.*

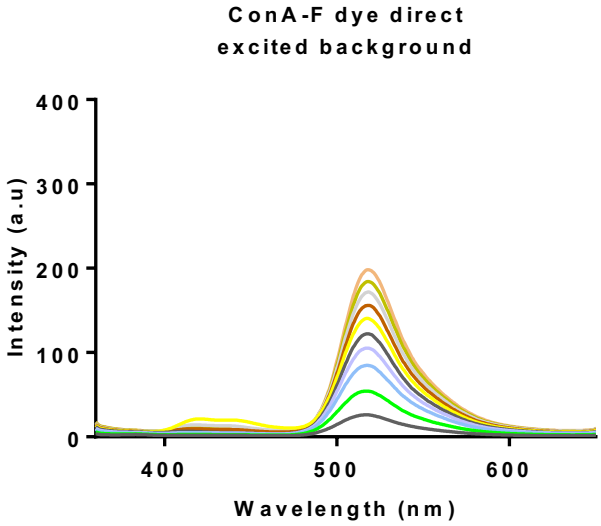

Supplementary Figure 3.3 Direct dye excitation (λ_{ex} 340 nm) of ConA-F acceptor.

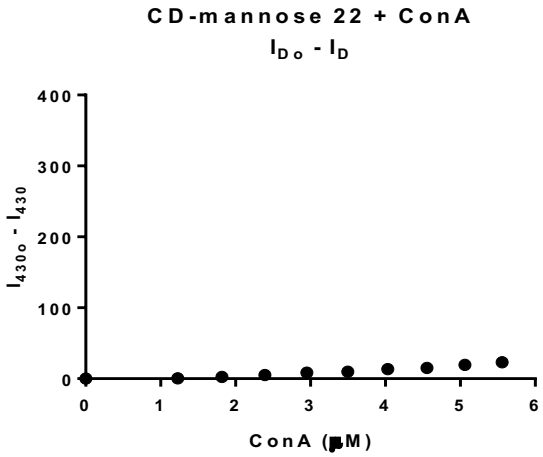

Supplementary Figure 3.4 Control experiment. Additions of ConA without fluorescein to CD-mannose 22 to observe if CD-mannose quenching occurs without an acceptor fluorophore.

4. Carbon Dots for Anti-Cancer Drug delivery

4.1 Introduction

4.1.1 Cancer

Cancer is one of the most prevalent and deadly diseases in the world, with 1 in 2 people developing the disease over the course of their lifetime and is still one of the leading global cause of death. Therefore, research into treatments for cancer represents a big proportion of efforts in medical research[151,152]. The variety of cancers are vast, commonly of the liver, prostate, colorectal, stomach are believed to be caused by intricate multifactorial biological pathways[151]. Hence, cancer treatments are often not universal, and research is devoted to develop novel therapies that can intervene at different stages of cancer progression. In addition to existing treatments such as radiotherapy and chemotherapy clinically used, personalised medicines e.g. immunotherapy and targeted therapy are technologies at the forefront of clinical research[153]. They both offer tailored treatments which can be used more sensitively in terms of earlier treatment, reduced side effects and have high efficacy. However, the expense of developing these treatments in a highly tailored way may not be sustainable in a medical climate where resources are increasingly restricted, and cases are increasing (due to aging and growing population and unhealthy lifestyle)[154]. Furthermore, a good understanding of the underlying mechanisms of action of the cancer pathway is required for the development of suitable treatments, however this is not always be possible. In this context, patients with novel or complex cancer origins often have to rely on traditional therapies which effect have high levels of non-specific cellular damage and hence side effects associated.

In the first instance novel treatments need not focus on exploiting an underlying mechanism, rather the novelty can come from exploiting known cancer associated biological markers in a new way. These can include increased vasculature around the tumour, faster cell growth and division and invasiveness and metastatic cellular behaviour[155]. Hence, novel treatments which are more broadly applicable are a good alternative to tailored treatments but also have improved treatment over traditional clinical methods. These novel treatments could also reduce the cost of current treatments such as radiotherapy and chemotherapy. This is not to say novel technologies cannot be used in combination with targeting treatments in a combined treatment which may then lead to very highly targeted therapies with minimal side effects[156].

4.1.2 Current treatments

4.1.2.1 Radiotherapy

Radiotherapy was first used as a therapeutic agent against stomach cancer in 1896 and the reduction of the associated tumour was noted[157]. Since then radiotherapy has been widely used as a means to kill target cancer cells within a tumour through damaging their DNA with radiation. The radiation source can be X-ray or gamma radiation. The electromagnetic waves cannot penetrate deep into the body hence the tumour site can be spatially targeted via external source manipulation. Downsides to radiotherapy include fatigue, skin blistering, hair loss and sickness[158] as irradiation of DNA can cause DNA damage but not cell death. This can lead to the development of a secondary tumour so must be carefully considered before treatment[159].

4.1.2.2 Immunotherapy

Immunotherapies are a more targeted type of cancer treatments which prompt the patient's immune system to recognise and destroy cancer cells.[153] It is a relatively non-invasive technique and evades resistance issues as with drug treatments. The main types of immunotherapy that are available include monoclonal antibodies for which a Nobel prize was won in 1984[160], cancer vaccines[161] and (chimeric antigen receptor t-cell) Car-T cell therapy.[162] Monoclonal antibodies are proteins which bind cancer cells and elicit a natural immune response.[163] They are generated in response to a specific cancer cell antigen within a patient in a mouse host. The cancer cells are injected into the mouse and an antibody response is generated. The mouse spleen cell is then fused with blood cells of the host which can then generate an endless supply of antibodies. These are then injected back into the human host periodically and cause cancer cell detection and destruction.[164] However, fusion of mouse and host cells is difficult to achieve, and contamination can occur.

Newer CAR-T cell therapy works differently to also induce an immune response. This can be more specific to the cancer markers of interest as it uses gene editing. T-cells (part of the immune response) are removed from the patient and engineered with the chimeric antigen receptor or receptors of interest. These are then grown *in vitro* before reintroduction into the patient where they can bind cancer cells and kill them.[162,165]

4.1.2.3 Chemotherapy

Chemotherapy refers to the use of drugs killing cancer cells as treatment. The treatment targets fast growing cells and is often specific to certain cancers. Chemotherapy drugs can be used in combination and usually elicit the greatest treatment response of therapies available. They work on the basis of interfering with DNA transcription and translation or arresting the cellular growth cycle which is more frequent in cancer cells compared with healthy cells. With chemotherapy, the therapeutic window must be considered, this refers to the concentration range where the drug is toxic enough to induce enough damage to cancer cells but preserve healthy cell modes of action. Damage includes covalently bonding with DNA or RNA and proteins by alkylating agents or alkaloids,[166] cross-linking DNA strands with each other by platinum agents,[166] antimetabolites competing with DNA or RNA nucleotides to disrupt synthesis or antibiotics which form free radicals and damage DNA.[166] For example, the drug doxorubicin (dox), which is part of the anthracycline antibiotic class, intercalates within the minor DNA grooves preventing transcription machinery association.

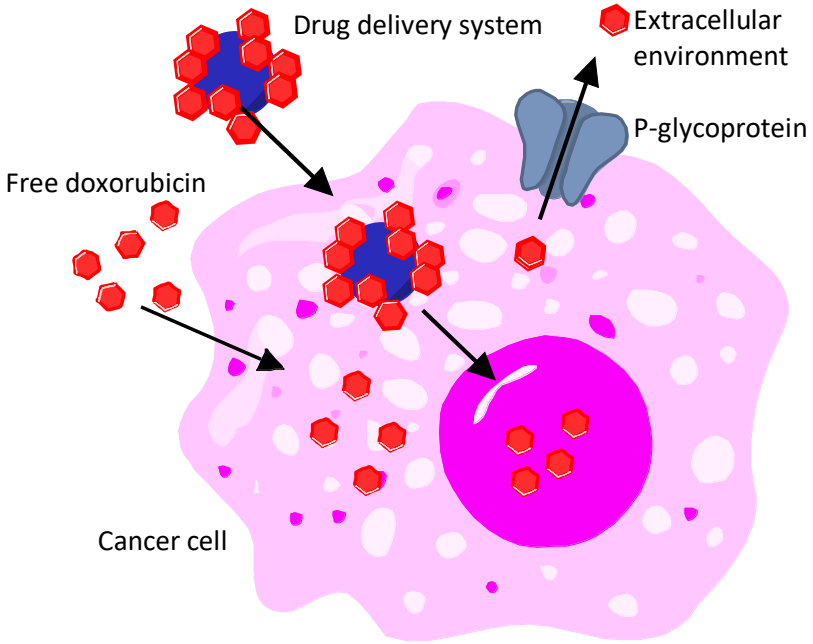

Figure 4.1 Multidrug resistance (MDR) refers to the upregulation of the p-glycoprotein in cancer cells. Doxorubicin is readily removed from the cytosol. When a drug is nanoparticle bound it is able to evade removal.

However, resistance to small molecule drugs can build-up over time and this will lead to reduced treatment options. This is commonly referred to as multidrug resistance (MDR) and is often due to the upregulation of the MDR-1 gene encoding the membrane p-glycoprotein which is presented at the surface of cancer cells[166] (Figure 4.1). This effectively pumps out the small drug indiscriminately and often drugs of the same class cannot then be subsequently used. If the drug molecule can however

not be recognised by this protein due to NP carrier methods, then evasion of removal can be achieved. This is something we address through our work to achieve improved drug delivery.

4.1.2.4 Doxorubicin

Doxorubicin is a chemotherapy drug used since the 1970's which was isolated originally from bacterium *Streptomyces peucetius*[167] and is part of the anthracycline family (Figure 4.2). Doxorubicin.HCl is a commercial hydrophilic drug molecule which contains a carbohydrate moiety with an amine group and tetracyclic aglycon component. Its mode of action involves binding to the minor groove of Deoxyribonucleic acid (DNA) and preventing topoisomerase II association and therefore arresting DNA transcription[168]. Doxorubicin is a planar molecule that intercalates between two pairs of GC (guanine-cytosine) bases forming hydrogen bond interactions with guanine and can form covalent linkage through its amino sugar to a guanine base. Doxorubicins protonated amine has a pKa at 9.93 and a pKa at 8 (hydroquinone -OH), meaning at physiological pH 7.4 the molecule becomes protonated at the amine, making it positively charged[169].

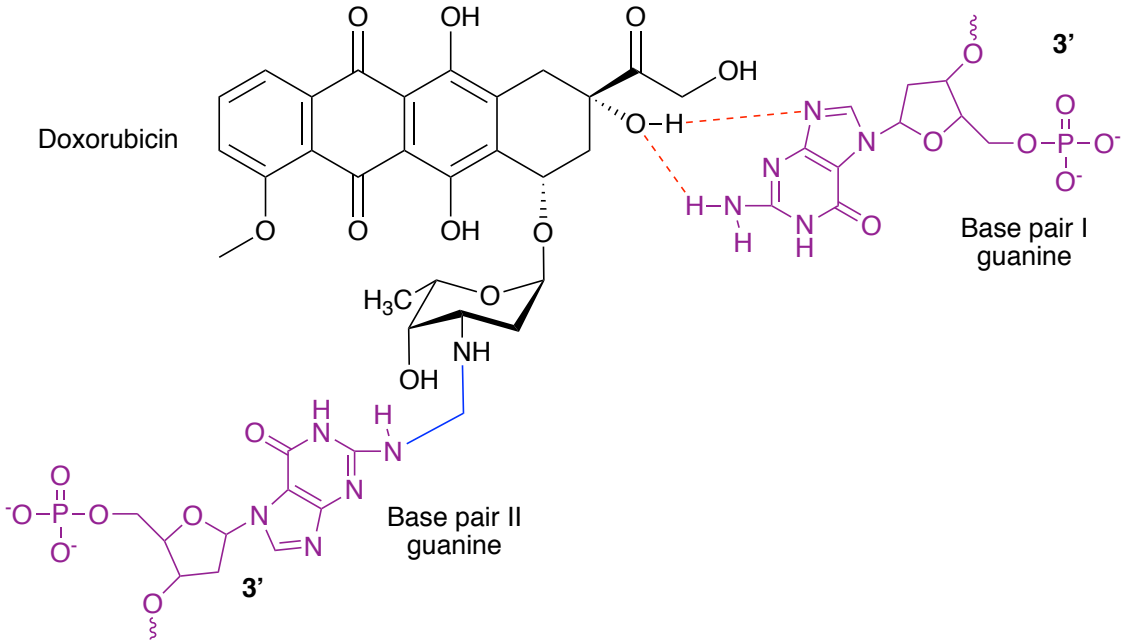

Figure 4.2 Doxorubicin binds dsDNA by intercalating between 2 pairs of guanine and cytosine DNA base pairs. Red dotted lines indicate hydrogens bonding between doxorubicin and guanine base I. Blue covalent line indicates bond between doxorubicin amino sugar and guanine base II via a formaldehyde[170] on the opposite DNA strand.

Doxorubicin is widely used commonly to treat breast, bladder, lymphoma, Kaposi's sarcoma and acute lymphoblastic leukaemia cancers. The drug has certain side effects associated with its use including hair loss, weakened immune system, darkened skin, diarrhoea and loss of appetite as well as the potentially fatal cardiomyopathy. Cardiomyopathy occurs on average in 11 % of cases (depending on

the dosage) and can occur long after remission 17 years post treatment in one study.[171] Once cardiomyopathy develops prognosis is 50 % survival.[172]

The cause of cardiotoxicity from doxorubicin is believed to be oxidative stress in the cardiomyocytic cells which particularly harms mitochondrial enzymes such as NADPH oxidase.[173] It also induces apoptosis via p53 (a cancer upregulated protein) activation once superoxides have been generated meaning poorer heart function[174]. This is dose dependent so if doxorubicin's therapeutic index can be improved and hence less drug needs to be administered, then the risk of cardiomyopathy will be reduced. Because doxorubicin is used so widely research into reducing the known associated side effects of doxorubicin is a large field. Some other areas of research include developing analogues of doxorubicin hence improving the therapeutic index, combining doxorubicin with cardio-protectant and also targeting circular cardiomyocyte Ribonucleic acid (RNA) associated with doxorubicin toxicity[173].

Doxorubicin effectiveness has been assessed *in vitro* extensively in two breast cell lines; MDA-MB-231 and MCF-7.[175] These cancer cell lines involve different pathways which make them cancerous and as a result differ in metastatic severity. MDA-MB-231 is more aggressive and metastatic, whilst MCF-7 is less so, growing slower and providing better prognosis on average. Doxorubicin is known to work more successfully on MCF-7, whilst MDA-MB-231 has a developed resistance at clinically relevant concentrations.[175] Hence developing treatments which are able to improve the efficacy of doxorubicin in MDA-MB-231 are sought after whilst MCF-7 is used often as a comparative cell line.

Anti-cancer treatments include looking for unique biomarkers associated with these cell types. Growth signals such as G protein coupled receptor (GPCR) and interleukin 6 (IL6) are examples of markers which can be targeted. However, these pathways can be circumvented by cancer cells and therefore targeting these pathways for downregulation do not necessarily offer long-term targets. Cancer cell drug resistance methods include DNA damage repair upregulation, histone reorganisation, epithelial-mesenchymal transition and drug efflux -also known as multi drug resistance as seen for doxorubicin removal.[176]

Furthermore, when considering the structure of a tumour is important when approaching treatment design. Being able to understand the 3D arrangement of these cells shows that the most resistant cells are the outermost cells of the tumour where the extracellular doxorubicin concentration is highest.[176] One study used 3D cell cultures in an effort to identify markers responsible for the resistance of MDA-MB-231 to doxorubicin. Key observations included that resistance in both MCF-7 AND MDA in the 3D

culture compared to 2D culture. They determined that underlying causes for poor doxorubicin efficacy were due to pathways for decreased cellular proliferation of cells at the core of the tumour and poor ECM adhesion. Hence treatments could include molecules which would intercept these pathways and make the tumour cells more amenable to doxorubicin treatment[175].

4.1.2.5 Methods for improving efficacy

Improving the efficacy of a clinically used drug is one way to improve chemotherapy treatments. Addressing either the problems associated with a particular drug involved such as multi drug resistance in tumours, or by looking at the pathways involved exclusively in cancer progression can offer potential for improving efficacy. Furthermore, the drug efficacy must be considered in combination with the toxicity to healthy cells, which is known as the therapeutic window. In the case of doxorubicin, the dosage is directly linked to the rate of a cardiomyopathy side-effect. In one study the rate of heart failure was 26 % for a cumulative dose of 500 mg/m^2, 48 % for 600 mg/m^2 and 100 % when 800 mg/m^2 was administered in a study of 530 patients. Clinically, the cumulative dose does not usually exceed 300 mg/m^2 keeping the risk of cardiotoxicity low.[177]

Assessing the toxicity of a drug *in vitro* can be conducted through calculating the IC_{50} values which is the half maximal inhibitory concentration of a drug of interest compared to control. The IC_{50} value obtained depends on the cell line and experimental conditions used, but through controlled repeats values become comparable. Doxorubicin is a well-studied drug *in vitro* and the IC_{50} values for a number of cell lines has been conducted. These control values can be used to measure the efficacy of a new drug or modified version of a drug to see how it would compare to the clinical version. The IC_{50} value is the concentration of drug required to cause 50% cell death. For doxorubicin, the IC_{50} values in HeLa, MDA and MCF-7 are 0.14 μM, 1.26 μM, and 0.01 μM[178] respectively according to the Genomics of Drug Sensitivity in Cancer Project database. The IC_{50} value does not tell much about the therapeutic window. The steepness of the dose-response curve measured through the Hill slope or slope factor (m) does however. The larger this value the more steep the curve is and the greater the effect of a drug at concentrations either side of the IC_{50}. For example, to maintain the drug activity between $\pm$ 10 % of the IC_{50} when m = 3 requires the drug concentration to not vary more than 15 % , however, if m = 1, then the drug concentration can vary up to 40 % for the same activity[179]. Hence, when m = 1 i.e. is smaller (and less steep), there is a greater therapeutic window. Clinically speaking this means there is a greater difference between the concentration required to elicit a therapeutic response and the concentration which would be overly toxic. Hence, the greater the therapeutic window, the safer the drug.

Since 1995 two FDA-approved liposome-based products have been marketed, which deliver doxorubicin with a wider and therefore improved therapeutic window, these are called Doxil® and Myocet®. The drug formulations work on two factors; doxorubicin is sequestered from multi drug resistance pathways and the nanoparticle facilitates improved drug uptake. Hence, less doxorubicin is required to elicit the same toxic response. These were the first generation of nanoparticle-based drug delivery vehicles used and since the liposome and micellar drug delivery is commercially common. These two examples are described in more detail in sections 4.1.3.

Having a nanoparticle can improve efficacy via passive and active targeting methods. Passive methods involve using known different biological differences between cancerous and healthy cells such as pH, ionic strength and temperature as a mechanism for drug release. Active methods involve adding, usually covalently, a specific molecule to the nanoparticle surface which has a known targeting effect such as promoting uptake or evading removal. Targeting agents include folic acid (FA), transferrin and hyaluronan have been used as targeting agents, conjugated to carbon dots by simple a EDC/NHS coupling mechanism[180] (see section 4.3.1.3).

4.1.3 Nanoparticles for drug delivery

4.1.3.1 The ERP effect for nanoparticles

The enhanced retention and permeability (ERP) effect is widely known to be the basis for favourable nanoparticle uptake in cancer cells (Figure 4.3). It was first observed by Matsumara and Maeda in 1986 when a chemotherapy protein conjugated to a polymer was observed to accumulate mainly at the tumour site in mice.[181] The team proposed that the macromolecule they generated worked better based on a size selecting basis within which nanoparticle delivery systems reside and allows non-specific uptake of the nanoparticle and also associated cargo. Firstly, the nanoparticle, > 5 nm, is too large to undergo renal excretion. Secondly, tumours have increased vasculature as they require increased nutrition and oxygenation as the cells grow and divide faster than healthy cells. Associated with the additional blood vessels is abnormal transport pathways favouring larger particles being transported to the tumour. Once there, the nanoparticles are easily able to escape the blood vessels and cross into the cancer cells due to abnormal, leaky vessels. This results from incomplete epithelial lining with pores 0.1 – 3 μm wide. In healthy cells the epithelial layer is not compromised so larger nanoparticles less easily enter healthy cells. Overall delivery of nanoparticles to cancer cells is twice as efficient to healthy cells due to the ERP effect.[182,183]

ERP effect – Enhanced Permeability and Retention Effect

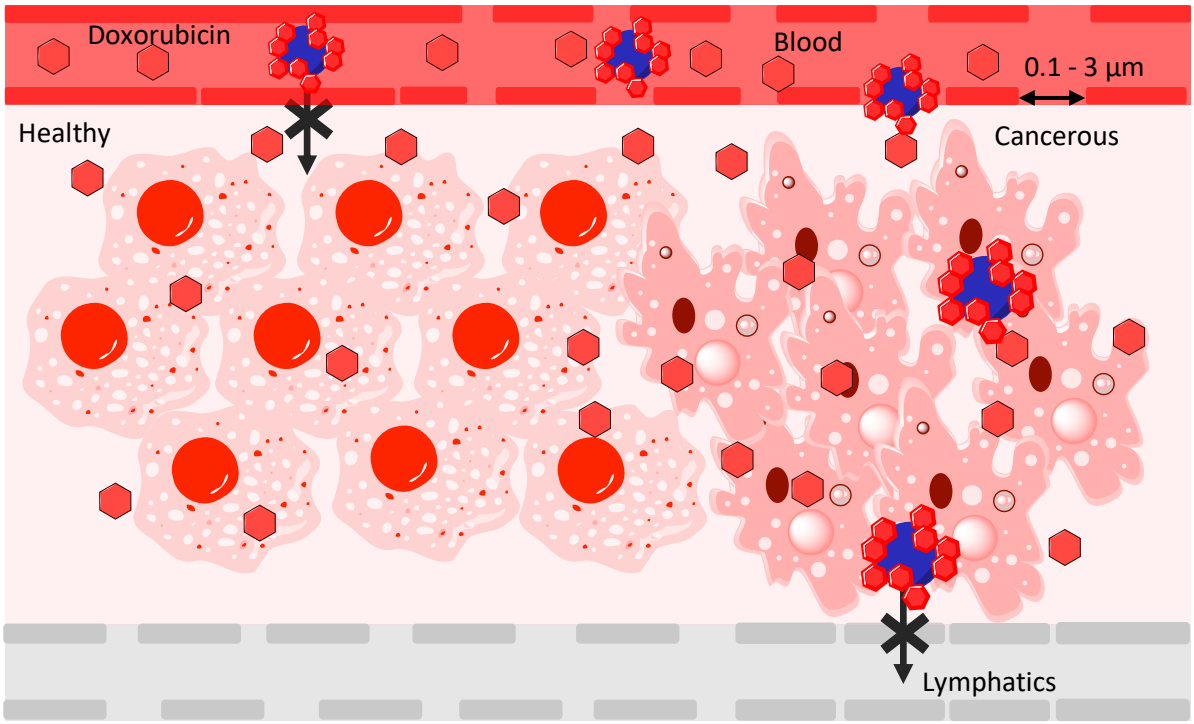

Figure 4.3 Enhanced permeability and retention effect (ERP) illustration. Free doxorubicin can traverse the blood vessel endothelial cells due to "leaky" vessels and increased vasculature seen at the tumour site. Once there, doxorubicin accumulates as it cannot leave via the lymphatic capillaries causing a high local concentration. This is the basis for passive nanoparticle drug delivery to cancer cells.

Within the tumour, ECM larger particles are retained for longer than smaller particles as their usual removal through the lymphatic drainage system is not possible as it is not developed in tumours. This retention of larger sized particles means that their residence time in the tumour extracellular environment is extended and their effective uptake and toxicity is enhanced.[183] Many drug delivery systems rely on this as no targeting moiety is required. Liposomal delivery systems work through this method and have been used to deliver doxorubicin to tumour sites more effectively than to healthy cells.[184]

The ERP effect means that nanoparticle uptake can be promoted by upregulating the pathways underlying it. Nanoparticles already accumulate within tumours, molecules and proteins which promote certain features of the ERP can be delivered.[183] This includes attaching vasodilators such as nitric acid or botulinum neurotoxin which increase blood flow through the tumour.[182] By delivering growth factors, tumour necrosis factors or inducing hyperthermia, blood vessel walls can be made more permeable for nanoparticle uptake. These agents can be co-delivered to improve the uptake of a nanoparticle in a drug delivery capacity. Interestingly vasculature can be damaged with external thermal prompting termed superenhanced permeability and retention (SUPR). Photo dynamic, photo thermal and near infra-red (NIR) heating anti-cancer technologies have been applied to tumours to

promote up to three times as much nanoparticle delivery. One example used NIR and an immunotherapeutic agent to achieve SUPR. The agent is a monoclonal antibody which has a NIR absorbing molecule attached which binds perinuclear cells. Upon NIR irradiation the cells die and cause the vessels to become more permeable. A nanoparticle can then be administered and have greater invasion. This SUPR technology is FDA approved[182].

4.1.3.2 Drug loading on Nanoparticles

Generally speaking, the greater the drug loading capacity of a nanoparticle the more efficient its capacity for drug delivery and the overall toxicity due to the higher local drug concentration. Furthermore, in the case of doxorubicin, if the tumour is treated with high local dosage then resistance is less likely to develop before the tumour is destroyed.

Drug loading is usually measured through equation 4.1a to obtain the % weight of the drug on the nanoparticle carrier.[185] Experimentally, the loading capacity of a drug can be inferred through how much drug is left after loading has occurred. However, this value is dependent on the amount of drug used in the conjugation and is not therefore comparable between studies. There are a number of ways drugs can be loaded either onto or into a nanoparticle, or in fact if the drug is crystallised then there is no physical carrier at all so that the drug composes the nanoparticle. Types of nanoparticle scaffolds include metal organic frameworks (MOFs), porous particles made from a variety of materials such as silica or protein, liposome and micelles, polymer meshes and or block co-polymer type self-assembling nanoparticles, drug crystals or metal-bio frameworks or ionically associated nanoparticles[186]. Once the drug is delivered, the removal of the nanoparticle must be considered to avoid toxicity.

$$A\ )Drug\ loading\ DL\ (weight\ \%\ ) = \frac{Mass\ of\ drug}{Mass\ of\ nanoparticle}\ x\ 100\ \%$$

$$\text{B) D}rug\ loading\ efficiency\ DLE\ (weight\ \%\ ) = \frac{Mass\ of\ drug\ loaded}{Initial\ mass\ of\ drug}\ x\ 100\ \%$$

Equation 4.1 Two methods used for measuring the loading of drug onto a nanoparticle drug delivery system. A) Drug loading weight % of drug onto a nanoparticle equation. B) Drug loading efficiency DLE, the loading of a drug can be inferred by how the percentage of drug left after loading.

The different methods of drug loading dictates the off-loading properties of the drug from the nanoparticle. Hence, the drug delivery system must be designed with the cargo and the target site in mind. In non-covalently loaded systems such as encapsulation, electrostatic, hydrogen bonding, hydrophobic interactions and metal coordination, natural changes in the environment can be utilised for specific drug release at the tumour site through pH, temperature or ionic induction.[187] Covalently

loaded drugs can also use biological environmental changes to achieve off-loading at the target site. With the strength of the covalent bond sequestering the drug when the nanoparticle is not at the target site, this is an efficient means for achieving low non-specific delivery. Release has been shown to be achievable via nanoparticle degradation and the use of cleavable linkers such as low pH cleavable amide bonds, imines, hydrazones, and others[187].

External sources are another method to achieve triggered release and can be a good way of administering a drug as it can give both spatial and temporal control. There are a number of light, magnetic, electric field and ultrasound responsive nanoparticles which have shown potential for this type of treatment.[188] Usually this involves a complete disassembly of the nanoparticle to induce drug release[188] hence is good for covalently linked drug release.

Other methods have been developed that are based on pH-dependent release mechanisms have been well studied for tumour site release as cancer cells induce low pH in their extracellular environment with respect to healthy cells. Hence, the drug can be delivered to the cancer cell and normal uptake proceeds. This pH-controlled release mechanism is relatively sensitive to the local pH, and hence a relative drug concentration can be delivered with high precision.[168,189]

pH release can easily be achieved by using an acidic group on the nanoparticle, which becomes protonated in acidic conditions so that an electrostatic interaction is removed which releases a drug molecule. In the gastrointestinal tract the pH varies considerably with the stomach being acidic and the small intestine slightly basic. This can be used as the basis for delivery. In one study, pH was used to trigger the disassembly of a polymer-based polyelectrolyte nanoparticle complex for insulin delivery to the extracellular environment of epithelial cells at pH 7.4. The polymers γ-polyglutamic acid (PGA) which contains carboxylic acids and the polymer chitosan which contains amines made up the nanoparticle complex. At pH 7.4, the amine groups become neutral upon reaching the target area and the polyelectrolyte complex disassembles as the inter polymer chain electrostatic interactions are removed, releasing the insulin.[190] Similarly causing disassembly, at low pH (< 2) the carboxylate anions form carboxylic acid groups on γ-PGA as they become protonated. Peptides are often used in a similar pH responsive capacity as they possess pKas within a biologically relevant range allowing for pH based nanoparticle drug release to be tuned.[189]

Alternatively, the carboxyl group can be used as a means to swell or shrink polymersomes, micelles and hydrogel nanoparticles in response to pH to cause drug release. In one system, a polymersome[191]

was made from a polymer containing carboxylic acids. At biologically high pH (>7), the carboxylic acid is deprotonated and this causes the hydrogel to swell. This increases the intraporosity and the drug sequestered is able to diffuse out. The remaining hydrophobic interactions prevented complete disassembly of the polymers[192]. Ionic strength is another cellular environmental change which can induce nanoparticle swelling. In cancer cell membrane depolarisation can occur which, depending on the type of cancer, can cause various ion (K^+, Cl^-, Ca^{2+} and Na^+) efflux and influx changes. A nanoparticle was made from L-glutamic acid (COO^-) and L -lysine (NH_3^+). Release in one system was investigated as a function of NaCl concentration, which was varied between 0.1 and 1 M whilst pH was maintained at 7.4. A positive swelling effect was observed with ionic strength. When the ionic strength was low, the NH_3^+ and COO^- groups were able to interact more without interference from Na^+ and Cl^- ions from the solution.[193]

A common doxorubicin loading strategy used to investigate novel nanoplatforms and novel theranostic platforms is the formation of a Schiff base imine between the doxorubicin amine and an aldehyde or ketone of a polymer which can self-assemble into a micelle or polymersome nanoparticle[180,194]. Aromatic imines have been shown to have good stability in water at neutral pH, due to extended $\pi - \pi$.[195]

Loading of doxorubicin can be achieved through hydrophobic interactions and $\pi - \pi$ stacking between the drug and mesoporous polydopamine[196] or graphene oxide nanoparticles[197]. The underlying release of doxorubicin in these systems also relies on low pH. Under acidic conditions the doxorubicin amine is protonated and doxorubicin dissociates from the nanoparticle. In one study Xing *et al.* were also able to attach a p-glycoprotein inhibitory molecule D-α-tocopheryl polyethylene glycol 1000 succinate (TPGS) for improved *in vitro* doxorubicin delivery to the nucleus and then induce doxorubicin unloading via two techniques. Near-infra red irradiation (808 nm laser at 2 W cm^{-2}) induced localised heating and the addition of glutathione disrupted stacking interactions promoting dissociation. Endosomal escape of the nanoparticle was inferred through visualisation of doxorubicin in the cytosol.[196]

Iron oxide nanoparticles have superparamagnetic properties allowing an external magnet to be used to induce drug release. Superparamagnetism also facilitates specific and controlled delivery of the NP-drug system and is also a contrast agent for magnetic resonance imaging (MRI). More recently it has been used as a means for localised heating induced apoptosis and tumour treatment. Using an external alternating magnetic field (AMF), the nanoparticle magnetic moment can be made to flip fast

enough to generate significant Brownian motion of the particle which causes local temperature increase.[198] This system can be used in combination with covalently linked drugs as the nanoparticle heating can lead to covalent bonds breaking.

Schiff base bond between doxorubicin-like molecule and fluorescein amine or carbonyl on a diblock copolymer was used as a pH sensitive drug delivery mechanism. The nanoparticle combined diblock copolymer and iron oxide and was used to achieve tumour targeted release where the pH reached 5.5. The imine between the amine of the dye and the carbonyl of the polymer was seen not to hydrolyse at pH 7.4. Upon AMF treatment at pH 5.5 the release was described as having a burst effect greater than pH 5.5 alone, induced by the heat generated from the nanoparticle.[199]

Click chemistry has been used as a facile way to attach drugs or dyes to nanoparticles as a means for covalent conjugation free from complex reaction conditions such as heat, organic solvent and or catalysts.[200] This makes click chemistry more amenable for reactions involving biologically relevant materials such as proteins. The main copper-free click reaction is based on the strain-promoted alkyne cycloaddition with a given azide. Commonly, commercial biological molecules can be purchased with azide groups installed for easy conjugation. *In vitro* click chemistry can also be used as an investigative tool using bioengineering of molecules of interest to have an alkyne group.[201] Nanoparticles containing an azide can be clicked and used for covalent labelling[200].

Gold nanoparticles lend themselves to thiol based covalent binding as AuNPs become stabilised upon thiol coating as the sulphur-gold bond is stronger than gold-gold. The thiol group becomes a good functional handle making AuNPs easy to work with. The thiol handle offers the potential for exchange with thiol containing molecules so that the molecule is presented on the surface of the AuNP. Interestingly, there is precedent showing that rare earth elemental ions are able to break the gold-sulphur bond and displace it, hence leading to drug release application and possible dual therapy applications with their photon up-converting properties.[202]

Ultrasound can be used as a means for theranostic nanoparticle drug delivery and imaging method. In one study doxorubicin was loaded onto the surface of an alginate nanodroplet containing non-polar perfluorohexane (PFH). Upon ultrasound irradiation which are high-frequency sound waves, the droplet vaporises *in vivo* to a gas forming microbubbles and facilitating doxorubicin release. This vaporisation degree was linearly proportional to the doxorubicin release thereby allowing controlled release.[203]

Light can be used as an external trigger for nanoparticle drug release. Depending on the wavelength used different penetration depths are possible with the best being near-infra red penetration centimetres deep (Chapter 5). The nanoparticle itself can be photo responsive, for example gold and rare earth metal containing nanoparticles produce heat which can induce release of their cargo, or a photosensitiser molecule or linker such as 2-nitrobenzyl ester[195] can be incorporated on the nanoparticle to initiate nanoparticle instability and drug release.[204]

The toxicity of the nanoparticle post-delivery must be considered for the system to be feasible. Often the drug is occluding the nanoparticle from the biological environment and from inducing toxic effects. If the particle is highly toxic such as with quantum dots, then its toxicity must be evaluated against the treatment payoff. The half-life is one measure of the circulation time of a nanoparticle in the body to assess the toxicity of a nanoparticle[187].

Overall, drug loading can be achieved through a number of non-covalent and covalent means. Non-covalent methods allow for easy synthesis, commonly passive delivery and drug release via pH, ionic or redox features of cancer cells. Covalent methods can confer greater targeting, evade multi drug resistance and less non-specific delivery induced by light, ultrasound, magnetic fields, electrical fields, but require an external source to induce drug off-loading. Having a covalent targeting molecule and electrostatically bound drug is one way to achieve a high level of targeting and high off-loading.

4.1.3.3 Liposomal NPs for Doxorubicin delivery

Doxil® (1995) and Myocet® (2000) are the two main FDA approved doxorubicin drug delivery treatments used clinically today. They have better cardiotoxic outcomes due to their improved therapeutic index and have an improved or the same efficacy as doxorubicin alone. Doxil is a PEGylated liposome which delivers doxorubicin to the tumour site based on the ERP effect. The PEG coating contributes improved circulation time, prevents aggregation and reduced immune response.[205] Doxil has a high residency time in the body, still observed up to 3 days post treatment.[206] The liposome component can biologically assimilate and offers a simple and adaptable scaffold upon which desired properties can be added. Liposomes are also able to carry a large drug payload as they can simply sequester the same volume of drug that they have volume inside them.

One drawback of this system is that the PEG coating causes the nanoparticle to accumulate in the skin, mainly the hands and feet and hand-foot syndrome can result. This results in release of high concentrations of doxorubicin at these sites causing sore skin and breakage.[207] Furthermore, the long

residency time in the body means that doxorubicin is being continuously released from the nanoparticle for longer times than when doxorubicin is used alone, thus killing healthy cells dramatically as a result. Hence, combining slow release with improved targeting would avoid the side effects.

Myocet® is a liposomal doxorubicin delivery nanoparticle which does not have PEGylation hence hand and foot syndrome is not seen in this treatment. This system has a residency time of around 1 hr, a lot less than with Doxil®.[206] This however also means that this treatment needs to be administered more often than Doxil® in order for the same cytotoxic levels to be reached.[208] The liposomal seclusion of doxorubicin in the blood system again means that multidrug resistance is not seen as much over the course of doxorubicin delivery and improved efficacy is observed compared to doxorubicin alone.

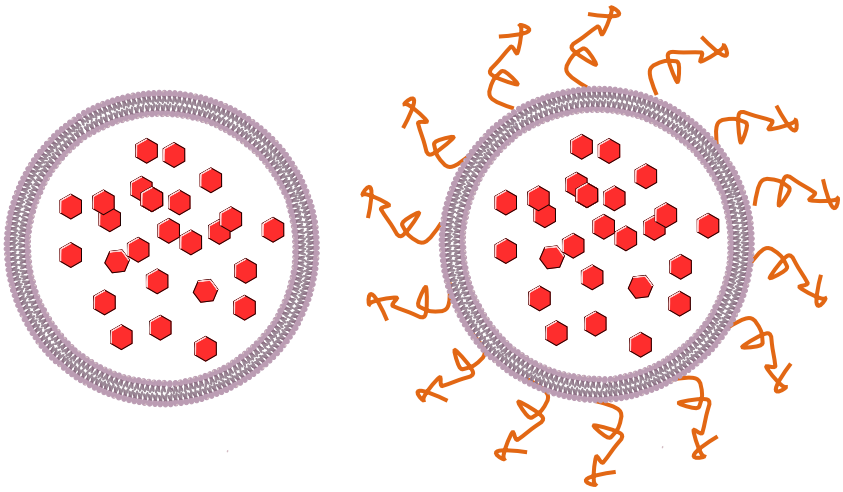

Myocet (Teva, UK) 2000 Doxil (Janssen) 1995

Figure 4.4 Two commercially available nanoparticle liposome doxorubicin delivery systems. Orange chains are PEG linkers which imposes improved circulation time. [205]

4.1.3.4 Carbon dots for doxorubicin delivery

Carbon dots have been trialled in a number of studies for doxorubicin delivery[168,180,185,209,210]. Both covalently linked and electrostatically adsorbed doxorubicin have been shown to have improved bioavailability and toxicity over doxorubicin alone owing to improved cancer cell uptake and good off-loading once at the tumour. Doxorubicin being red fluorescent (λ_{ex} 480, λ_{em} 590 nm)[211] offers a good model drug to observe *in vitro* cellular uptake allowing for ease of identification and quantification through flow cytometry.

Electrostatic adsorption of doxorubicin onto carbon dots is an efficient means for delivery *in vitro,*[185,212,213] owing to the easy of loading doxorubicin simply by mixing with CDs at the desired

concentration. Direct characterisation of electrostatic loading is not observed; however, zeta potential and *in vitro* effects can be used to infer information.

Carbon dots synthesised by Kong *et al*.[185] via hydrothermal methods from citric acid and ethylene diamine were shown to have good electrostatic doxorubicin loading and improved toxicity in MCF-7 cancer cell line than free drug. DL was 2.88 % and DLE was 57.7 %. Zeta potential data showed the CD was -5.12 mV, doxorubicin alone was 5 mV and the CD-dox was 1.07 mV. This suggests loading onto the carbon dot occluding the negative surface charge of the particle from the solvent. They demonstrated their lowest tested pH 5.0 achieved the best unloading of doxorubicin of 82.0 % after 72 hrs. Confocal microscopy showed colocalization between the carbon dots (λ_{ex}360 nm, λ_{em} 450 nm) and doxorubicin in MCF-7 cells, providing evidence for carbon dot mediated intracellular delivery. This was carried out after 4 hrs supporting the theory that doxorubicin is sequestered on the carbon dot surface post internalisation and can evade MDR removal.

Another study using electrostatically loaded doxorubicin on carbon dots was carried out by Yuan *et al*.[213] Carbon dots were synthesised from supermarket bought milk in a hydrothermal synthesis to generate 450 nm (λ_{ex} 360 nm) fluorescent carbon dots which were determined through FTIR to have carboxyl groups (1100 cm^{-1}) on the surface. The carboxyl groups were thought to be the basis of electrostatic interactions with doxorubicin for loading achieving DL of 4.35 % and DLE of 87 %. They also propose the hydrophilicity of their carbon dots allows for additional hydrogen bonding with doxorubicin. Similarly to Kong *et al*.[185], they observed pH dependent release of doxorubicin from the CD at pH 5.0 in a dialysis experiment. Cytotoxicity experiments in ACC-2 (cancerous) at 24, 48 and 72 h, all showed greater toxicity with the CD-dox system than free dox. In L929 (healthy) cell line lower toxicity was seen with the CD-dox than free doxorubicin at the same concentration (1.5 μM). Interestingly, at 72 h in L929, free dox had significantly greater toxicity compared to CD-dox than at either 48 or 24 h. This suggests that the sequestering of doxorubicin on the CD persists up to 72 h.

The ketone appended onto the tetracyclic aglycone component of doxorubicin has the potential to be involved in imine bond formation with an amine on the surface of carbon dots.[214] Zhang *et al*. synthesised hollow carbon dots from L-ascorbic acid and urea (1:7 molar ratio) in a hydrothermal synthesis and were able to load doxorubicin through imine formation and observed pH sensitive intracellular release[168]. They show evidence of this covalent linkage via FTIR peak presence at ~ 1651 cm^{-1} characteristic of imine bond presence. They also suggest that covalent bonding could also occur between the doxorubicin amine and carboxylic acid groups on the CD surface, coupling agents

potentially used include EDC and CDI among others. Furthermore, electrostatic interaction between the amine and carboxylic acid at physiological pH 7.4 could in part be responsible for doxorubicin loading. In addition to these interactions on the CD surface, they propose doxorubicin encapsulation by the hollow CDs. Overall the DL achieved was 42.9 %. They observed improved drug delivery potential compared to free doxorubicin through pH dependent drug off-loading in dialysis with best dox release 74.7 % achieved at pH 5.0. Reduced cytotoxicity at 48 h was seen at concentrations of 5, 10, 20 and 40 μgml^{-1}, where CD-dox had ~ $\frac{2}{3}$ toxicity as that of free dox. CD-dox having lower toxicity then free dox and vice versa have both been used as an indication of efficient drug delivery. They suggest the cause of a reduction in toxicity is greater sustained release properties of CD-dox making it less toxic initially.

Hydrophobic interactions including $\pi - \pi$ stacking between doxorubicin and carbon dots was attributed as the main adsorption method in a study by Sun *et al*.[212] They highlight evidence of doxorubicin $\pi - \pi$ stacking was shown with carbon nanotubes[215] early as 2009 which was evidenced by *in vitro* improved efficacy. They also reference Strauss *et al*[216]. who show favourable $\pi - \pi$ stacking and also ionic interaction between carbon dots and perylenediimides (PDI) through computational modelling. Carbon dots were synthesised hydrothermally from D-glucose and L-glutamic acid in a 1:1 molar ratio and DLE was determined to be 260 %. Prolonged dox release was observed compared to free dox through dialysis which they attribute to a low pH of 5.0, protonating the doxorubicin amine and improving drug hydrophilicity and release. Interestingly, similar to Zhang *et al*.[168] cytotoxicity data shows a reduced toxicity effect compared to free dox at 48 h between 0.005 - 0.5 μgml^{-1}. At greater concentration of 5 μgml^{-1} they then observe that CD-dox and free dox have similar cytotoxicity, which suggests that at a high enough dose there is enough free dox released from CD-dox to make the delivery system non-effective. Furthermore, they then showed they were able to further modulate and reduce dox release and cytotoxicity from CD-dox by adding a polydopamine (PDA) coating simply by mixing CD-dox with PDA for 3 h in TRIS buffer (10 mM pH 8.5).

Covalently conjugated doxorubicin to carbon dots is seen in the study by Li *et al*.[217] EDC/NHS conjugation between the doxorubicin amine and the carboxylic acid on the carbon dot surface or the already conjugated transferrin protein carboxylic acid groups. The toxic effect of this system was assessed in paediatric brain tumour cells. After conjugation size exclusion was used to purify the conjugate so that no free doxorubicin or transferrin was present. They observed a 14-45 % reduced cell viability compared to doxorubicin alone at a concentration of 10 nM. Interestingly, they have no

evidence for the doxorubicin dissociation from the nanoparticle and therefore the effect observed is that of the CD-doxorubicin and transferrin conjugate as a whole.

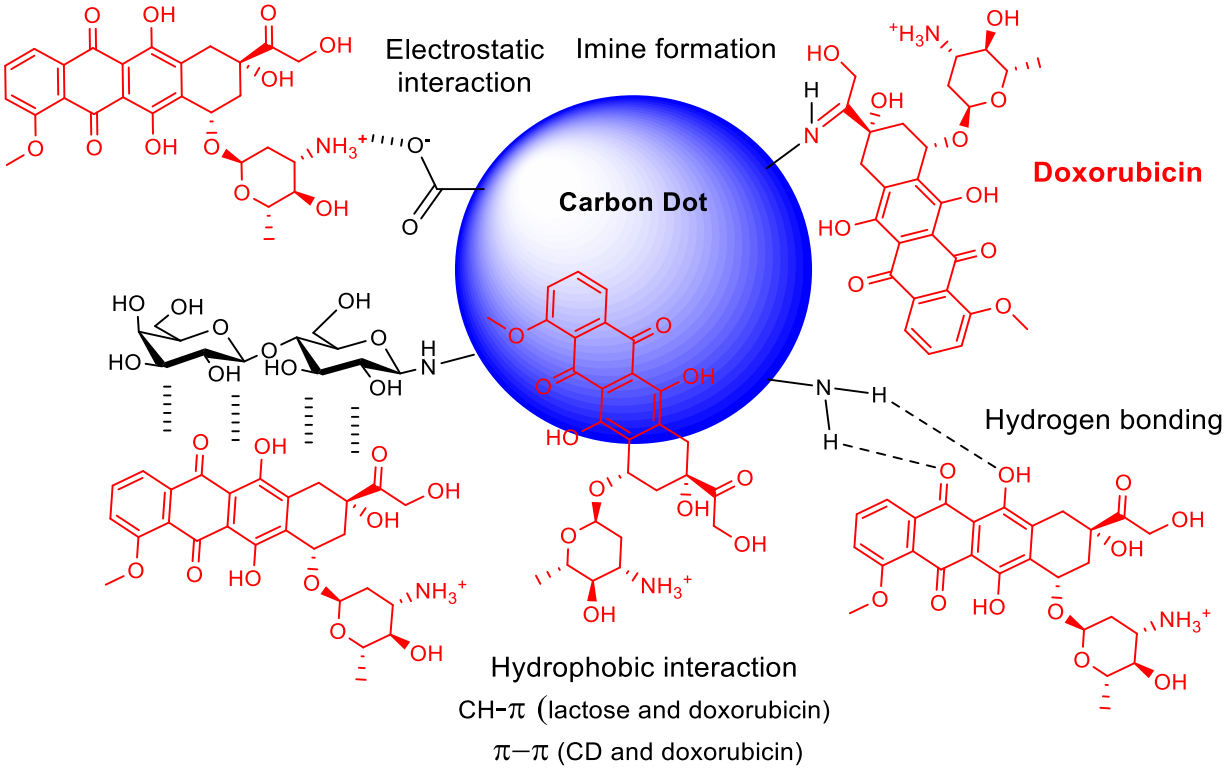

Figure 4.5 Possible doxorubicin - carbon dot interactions. Carbon dot shown is a general structure with functional groups for illustration purpose. Electrostatic interaction between doxorubicin amine and carboxylic acid at physiological pH. Imine formation between an amine and a ketone of the doxorubicin. Hydrogen bonding between hydrogens and oxygens from either of the doxorubicin or the CD surface. CH-π bonding between cyclic carbohydrate and doxorubicin. And π − π between aromatic groups on the CD and doxorubicin.

When looking to improve targeting of CD-doxorubicin delivery systems, biofunctionalisation is a good starting point[218]. In each example outlined below, folic acid (FA), transferrin or hyaluronan (HA) has been conjugated alongside doxorubicin onto carbon dots as a means for improved doxorubicin delivery *in vitro*.[180] FA targets FA receptors which are over expressed in some cancers namely; colorectal, breast, cervical, ovarian, epithelial, lung, kidney and brain. FA is a heme containing protein hence can bind iron and oxygen which is required in cancer cells for oxygenation where metabolism is high. Furthermore, due to its iron binding properties FA has MRI agent applications.[180,219] Iron shows good contrast in MRI due to its ferromagnetic property. In one literature procedure, green fluorescent carbon dots were synthesised from sorbitol and sodium hydroxide in a microwave reaction. Bovine serum albumin (BSA) was coated onto the surface of the carbon dot before folic acid was conjugated using DCC/NHS to BSA and the doxorubicin to BSA also using TEA. 85.6 % dox loading was achieved and improved toxicity in HeLa cells and reduced non-specific toxicity were observed. Hence this system appears to have an improved efficacy and therapeutic window compared to free dox.[194]

Transferrin is able to cross the blood brain barrier (BBB) and be bound by transferrin receptors which are overexpressed on brain tumour cells, hence is useful to promote nanoparticle crossing and treating hard to reach brain cancers and is known to have MDR evasion properties[217]. Carbon dots were synthesised from carbon powder with nitric acid and sulfuric acid (top-down method) to afford green fluorescent particles (λ_{ex} 540 nm, λ_{em} 580 nm). Transferrin and then doxorubicin were covalently conjugated onto carboxylic acid coated carbon dots using EDC/NHS. Uptake and cytotoxicity of a paediatric brain tumour cell line was greater for CD-transferrin conjugated dox than free dox. After 18 hrs, the uptake was 5-fold greater for the delivery system and the cytotoxicity 14-45 % at 10 nM. Interestingly, they considered an increase in cytotoxicity as evidence for improved delivery, likely owing to the greater doxorubicin uptake.

HA is a glycosaminoglycan present in the ECM which binds CD44 protein presented on cancer cell membrane, hence can actively targeting carbon dots or graphene carbon dots to lung carcinoma A549 cells[220,221]. *In vitro* studies of cancer cells with CD44 overexpressed on their surface have been used to test the applicability of CD bifunctionalised with doxorubicin and HA for targeted delivery. The HA was covalently conjugated onto the CD before doxorubicin was linked via the pH cleavable linker 4-carboxybenzaladehyde (p-CBA). It was observed *in vitro* in 4T1 cells that free dox uptake peaks at 1 h and the CD-HA-dox uptake increased over 4 hr which was mainly localised in the lysosome. This suggests that the HA-CD44 mediated uptake caused lysosomal accumulation. Here the low pH induced dox release via the pH cleavable linker and accumulation in the nucleus occurred. The slow uptake and slow release from the lysosome to the nucleus correlated with a reduced cytotoxicity for CD-HA-dox then free dox at 24 h. Furthermore, *in vivo* studies supported *in vitro* results described and also showed that for CD-HA-dox, strong accumulation was seen in the tumour site and liver (where there are HA receptors on endothelial cells) compared to non-specific targets e.g. lung and kidney. This supports HA based uptake and tumour specific delivery[221].

Nuclear targeting can be achieved with nuclear localised signal peptide (NLP) which was applied to a carbon dot-based doxorubicin delivery by Yang *et al*.[210] Similarly to hyaluronan conjugated CDs the doxorubicin was attached via a pH hydrolysable bond. *In vitro* and *in vivo* studies observed improved targeting and efficacy for the CD drug delivery system over free dox. Interestingly they saw that the NLP facilitated the whole CD-NLP-dox system was taken up by the nucleus which is not seen with other delivery systems which target the cell membrane. Hence, the NLP is able to facilitate direct delivery of dox to the nucleus. This improves the efficacy and therapeutic window as the p-glycoprotein is less able to remove free doxorubicin.

Overall, a number of carbon dot-based doxorubicin delivery systems have emerged in the last five years offering improved doxorubicin delivery, measured through good loading efficiency, better *in vitro* uptake than free doxorubicin and pH dependent release all on non-toxic platforms. Interestingly, cytotoxicity is not a conclusive measure of delivery by itself. Studies conclude both an increase and decrease in cytotoxicity compare to free dox as an improvement in drug delivery. Hence, cytotoxicity must be considered in the context of uptake and the time point after doping. Areas which need more definition include understanding of the basis of CD-doxorubicin binding, doxorubicin release mechanism *in vitro* and measuring this over time. Furthermore, comparing cancer cell lines could allow specific targeting and hard to treat cancers to be investigated.

4.2 Aims

In this work we aim to develop a non-toxic platform for the selective delivery of anti-cancer drugs to cancerous cells. Doxorubicin is a well-known anti-cancer drug used in a myriad of cancer treatments; hence we use this model drug as part of an initial foray into testing our carbon dots for drug delivery. We aim to develop a platform which can be bi-functionalised, combining glycan functionalisation and drug loading for the aim of targeted drug delivery to avoid non-specific drug delivery to healthy cells and minimise side-effects. The glycan and drug bi-functionalisation would represent a proof of concept and hope to showcase that a carbohydrate with known targeting ability could be used for targeted anti-cancer delivery. We focus on using lactose to target our system to HeLa, MCF-7 and MDA cancer cells. Lactose has been shown in previous work in the Galan group to allow for selective cell uptake of QD.[44] Cytotoxicity assays and confocal microscopy will be used as a means to measure the delivery system efficacy compared to control.

4.3 Results and discussion

This chapter outlines the development of an anti-cancer drug delivery system using carbon dots as the nanoparticle carrier and doxorubicin as the drug. Carbon dots used are the particles described in chapter 1 as the long linker blue fluorescent carbon dots (**AmCD 16**). The work in this chapter was conducted in collaboration with another Galan group member, Sylvain Penasse. Data for sections 4.3.2.5 – dialysis to determine release rate and 4.3.2.6 – FTIR to show imine formation, was generated by Sylvain Penasse. This is indicated again at the beginning of both sections.

Four carbon dots with the surface functionality of amine (AmCD **16**), carboxylic acid (AcCD **17**), lactose (CD-lactose **25**) and a fourth CD with both lactose and TTDDA (defined as CD-lac-TTDDA **28**) were

tested for their dox loading capacity. Nuclear delivery potential of these systems can be assessed through confocal microscopy since doxorubicin is red fluorescent. The drug nanoparticle complexes were characterised via NMR, DOSY, DLS and zeta. Three cancerous cell lines MDA-MB-231, MCF-7 and HeLa are used in this work to assess the efficacy of our drug delivery system compared to free dox.

4.3.1 Synthesis

Four differently functionalised nanoparticles were loaded with doxorubicin; AmCD **16** (Chapter 2.2.1.1), AcCD **17,** CD-Lactose (**25**) and CD-lac-TTDDA **28**, first introduced in this chapter, termed **28**. CD-lactose was synthesised via EDC coupling of AcCD **17** and 1-amino lactose **2.** The aim of this was to achieve a carbon dot with both carbohydrate targeting moiety and amine group presented on the surface. Similarly, CD-lac-TTDDA **28** was synthesised from CD-lactose **25** via EDC coupling with TTDDA (equimolar ratio to the lactose used in the previous step).

Doxorubicin loaded nanoparticles AmCD-dox (**N1-8**), AcCD-dox (**C1-8**), CD-lactose-dox (**L1-8**) and CD-lac-TTDDA-dox (**LT1-8**) were prepared by combining the carbon dot and a 0.1 mg ml^{-1} solution of doxorubicin in H_2O and freeze drying overnight (hence consistent dox amount was achieved). The ratio of CD:Dox and the nomenclature used are summarised in Table 4.1. Loading of doxorubicin was carried out on a 1 mg scale. Post lyophilisation the material afforded was a red powder which was stored at 4 ^oC and redissolved in H_2O to 0.1 mg ml^{-1} immediately before use.

Mass ratio of CD/Dox	***Amine CD*** *AmCD*	***Acid CD*** *AcCD*	***CD-β-D-lactose*** *CD-lactose*	***CD-lactose-TTDDA*** *CD-lac-TTDDA*
0	16	17	25	28
1:1	N1	C1	L1	LT1
1.25:1	N2	C2	L2	LT2
2:1	N3	C3	L3	LT3
3.33:1	N4	C4	L4	LT4
10:1	N5	C5	L5	LT5
20:1	N6	C6	L6	LT6
100:1	N7	C7	L7	LT7
1000:1	N8	C8	L8	LT8

*Table 4.1 Nomenclature used when describing the ratio of AmCD (**N**), AcCD (**C**), CD-lactose (**L**) and CD-lac-TTDDA (**LT**) to doxorubicin used in drug loading step. Ratios from 1:1 to 1000:1 CD/dox were made.*

4.3.1.1 DOSY to assess doxorubicin loading

Sample	Corrected diffusion coefficient / $x10^{-6}$ cm^2 s^{-1}	
Doxorubicin	1.66	
AmCD	3.83	
AcCD	2.86	
N5	Dox: 0.94	CD: 1.88
C5	Dox: 2.49	CD: 4.18

Table 4.2 Diffusion coefficients of doxorubicin, carbon dot, N5 and C5 determined through DOSY which have been corrected to allow comparison against the water diffusion coefficient. Repeat measurements were not conducted hence error was not calculated for this data.

N5 and **C5** CDs were assessed for doxorubicin loading using diffusion ordered spectroscopy (DOSY) (Table 4.2). Using this technique, the diffusion coefficient of a molecule or particle can be measured in solution. If a sample contains two non-interacting particles or molecules, then their diffusion coefficient will be at least an order of magnitude different. Water can be used as a reference by which diffusion coefficients can be adjusted in order to make two spectra comparable (if the water diffusion coefficients are different between spectra). In this work the doxorubicin diffusion coefficient was measured to be 1.66 $x10^{-6}$ cm^2 s^{-1}. The diffusion coefficient of doxorubicin in the form **N5** and **C5** was determined as 0.94 $x10^{-6}$ cm^2 s^{-1} and 2.49 $x10^{-6}$ cm^2 s^{-1}. These are both not an order of magnitude slower as you may expect if associated with a larger particle such as a carbon dot. However, the diffusion coefficient of AmCD **16** and AcCD **17** are 3.83 $x10^{-6}$ cm^2 s^{-1} and 2.86 $x10^{-6}$ cm^2 s^{-1} respectively. These are within the same order of magnitude as free doxorubicin hence, results cannot be conclusive. However, for both the doxorubicin and carbon dots the diffusion coefficient changes when combined therefore some interaction is suggested.

4.3.2 Drug loading studies

Using UV-Vis or fluorescence to determine doxorubicin loading was not possible with our system as the spectral overlap between the carbon dots and doxorubicin was too great. Although the peak absorption and fluorescence for each are separated by 160 nm, the baseline absorption and fluorescence of carbon dots is relatively high due to self-absorption properties. Increasing the CD-dox concentration does not improve this due to self-quenching effects causing absorption and fluorescence values which are non-linear as a function of concentration. As a result, other techniques were used to assess the loading of doxorubicin onto the carbon dot.

FTIR provided definitive evidence of interaction between doxorubicin and AmCD **16** in the form of imine formation, suggesting that a covalent imine conjugation underlies doxorubicin loading.

Doxorubicin ketone signal at 1717 cm^{-1} disappearance and imine peak formation at 1690-1640 cm^{-1} (which are not seen in free dox or the CD spectra) provides evidence for this. This is not to say other hydrophobic; electrostatic and hydrogen bonding does not take place between these two substituents. It has been shown previously that doxorubicin can interact in these ways with carboxylic acids[185] (hydrogen and electrostatic) and cyclic[212] CH-π groups and sp^2 conjugated systems (hydrophobic) which we have shown in chapter 2 are present on the AmCD **16** and AcCD **17** surface. Confocal results showed a positive concentration cytosol localisation for carbon dots AmCD **16**, AcCD **17** and CD-lac-TTDDA **28** without dox, implying an interaction between the CD and doxorubicin. DOSY was used to determine the diffusion coefficient of doxorubicin when carbon dots were similar, hence suggesting interaction. Dialysis studies were carried out to observe the diffusion of doxorubicin over time from the surface of carbon dots which was slower than that seen for doxorubicin alone at physiological pH (7.4) and at low pH (5.0). All of this data was used to infer interaction between the doxorubicin and the CD. The release was investigated through dialysis and confocal microscopy and cytosolic versus nuclear doxorubicin localisation was observed over 2 hrs.

4.3.2.1 Confocal to determine optimal loading

Initial confocal microscopy experiments were trialled to evaluate if the combination of carbon dots with doxorubicin had an effect on the intracellular uptake. **N1-8**, **C1-8**, **L1-8** and **LT1-8** (10 μg ml^{-1}) were incubated with $1x10^5$ HeLa cells (100 μL) for 1 h to allow for uptake. Live confocal images were taken after 1 h to observe whether uptake of doxorubicin had been achieved. In all cases, negative control images with no dox or CD present, saw no red fluorescence (emission window measured 570 – 600 nm) upon excitation at 450-480 nm. Positive control with doxorubicin showed red fluorescence localised in the nucleus only. This agrees with literature evidence that doxorubicin readily internalises HeLa cells and localises at the nucleus.[222] Bright field images where the nucleus and cell membrane can be seen were used to confirm nuclear localisation by overlaying with fluorescence images (Figure 4.6).

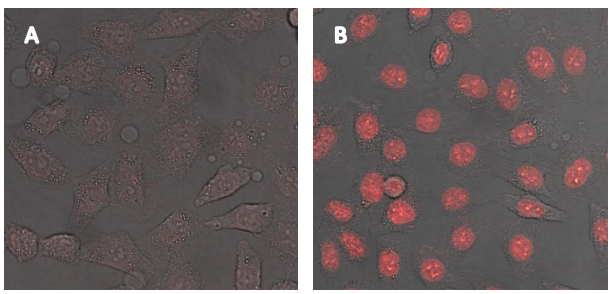

Figure 4.6 Confocal image and brightfield images of HeLa cells overlaid. Fluorescence measured between 570-600 nm A) Negative control, HeLa cells with no dox or CD present B) Doxorubicin incubated HeLa cells (1 hr) at working concentration 10 $\mu g\ ml^{-1}$

With CD-dox systems not only was uptake of doxorubicin facilitated by the CD seen, but also doxorubicin localisation in the cytosol (figure 4.7). This cytosol localisation is not seen for free doxorubicin. This is important for slow release of doxorubicin to the nucleus allowing for evasion removal by the p-glycoprotein. When cytosolic fluorescence is seen, it was thus established that an interaction between the CD and doxorubicin can be inferred, i.e. if the drug were free then nuclear delivery would be seen. Furthermore, this shows that the carbon dots are unable to cross the nuclear membrane. Doxorubicin loading onto the CDs at ratios between 1:1 and 1000:1 showed different localisations at 1 h upon incubation with HeLa cells (figure 4.7). This was used to infer the concentration for optimal drug loading on the carbon dots, but with no excess free drug. This is important for optimising the drug delivery system for good efficacy. Section 4.3.2.1.1. explains these experiments further.

4.3.2.1.1 Acid & Amine CD-Dox

The CD-dox materials **N1-8** and **C1-8** were tested in HeLa cells for uptake and their intracellular localisation observed. In figure 4.7, the intracellular localisation of doxorubicin can be observed as the red fluorescent areas in the images. Nuclear fluorescence shows free doxorubicin whilst cytosol fluorescence shows carbon dot bound doxorubicin. For both **N1-8** and **C1-8**, there is a gradual shift in florescence from nuclear to cytosol localisation (from 1 to 8) correlating with the amount of carbon dot present. When there is more carbon dot present more doxorubicin is sequestered on the carbon dot surface. At **N5** and **C5** doxorubicin is seen predominantly in the cytosol. At **N6-8** and **C6-8**, there is excess carbon dot and hence loading is less efficient. From this experiment it was determined that for both AmCD **16** and AcCD **17**, the optimal loading of dox was seen in **N5** and **C5** respectively which have a 10:1 (CD:dox) ratio. Interestingly, the same loading was seen for both AmCD **16** and AcCD **17** despite differences in surface functional groups. The loading could involve electrostatic and hydrogen bonding as both carboxylic acid and amine functional groups have the potential to be charged and electrostatically interact[168] with doxorubicin and also hydrogen bond[213] via oxygen and hydrogen atoms present as seen in literature.

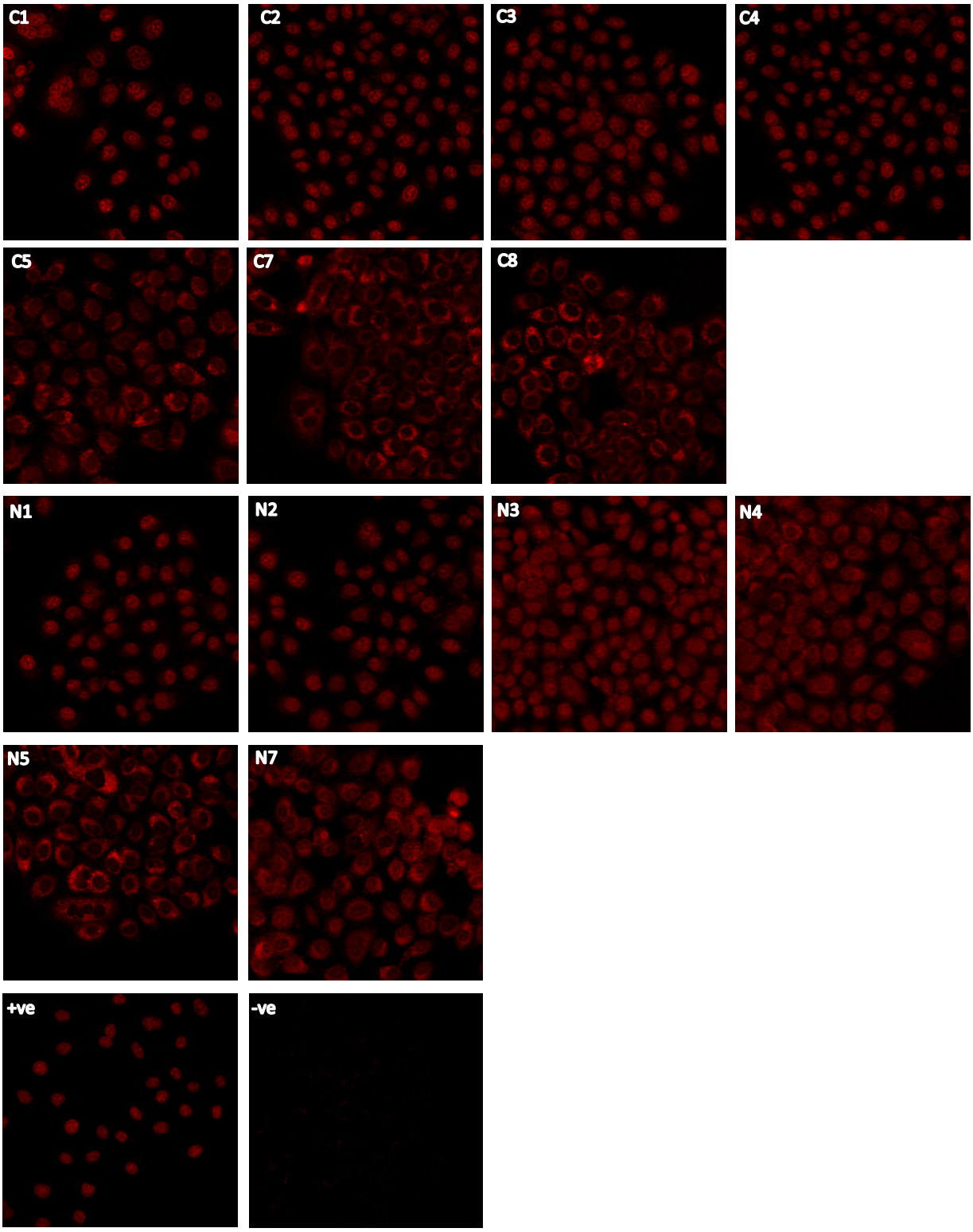

Figure 4.7 Confocal images of live HeLa cells incubated with N1-8 and C1-8 (10 µgml^{-1}) for 1 hr before imaging. Red florescence is doxorubicin. From 1 to 8, a gradual shift in fluorescence localisation from nucleus to cytosol can be seen. This correlates to the increase in carbon dot present from 1 to 8. Positive control shows free doxorubicin and negative control shows HeLa cells with no CD-dox. C6, N6 and N8 are not presented in this figure as the images for these were not acquired.

Quantification of the shift of localisation from the cytosol to the nucleus was quantified over time from a second experiment where the fluorescence per cell was measured at 15 minutes, 30 minutes, 1 h and 2 h. The doxorubicin fluorescence seen in the confocal images (Figure 4.7) is a good reporter of the *in vitro* off loading and delivery of doxorubicin. The ratio of nuclear:cytosolic (N/C) fluorescence was calculated in Fiji software. The cytosol and nuclear regions were identified through bright field images and the fluorescence intensity per area quantified in terms of grey values. When the fluorescence intensity in the nucleus per area is equal to that in the cytosol the ratio is 1. This is denoted as the dotted line in figure 4.8. Free doxorubicin has a Nuc/Cyt value greater than 1 owing to the fact that it can freely localise in the nucleus even at 15 minutes. **C5** (red bars) show that over time, doxorubicin moves from the cytosol to the nucleus. At 15 minutes there is equal distribution of doxorubicin through the cell. Over time, up to 2 hr this continues to increase up to Nuc/Cyt value of 3. This same trend is seen for **N5** (green bars); however, the initial starting point is a ratio of 0.2 showing clear cytosolic localisation. The translocation to the nucleus is also much slower suggesting slower release from the carbon dot surface. This is a much greater difference between **N5** and **C5** than the confocal images in figure 4.7 would suggest. Hence, quantification and observation over time is a good way to understand intracellular delivery.

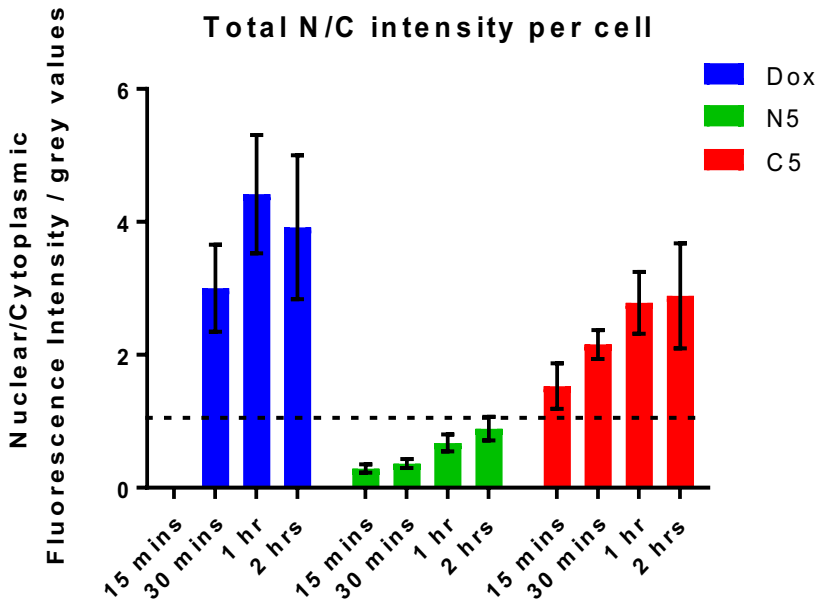

Figure 4.8 Quantification of doxorubicin intracellular localisation. Cytosolic and nuclear fluorescence per unit area was quantified in each cell incubated with either free dox (blue bars) C5 (red bars) or N5 (green bars).The nuclear: cytosolic ratio (N/C) was calculated for N=50 cells at time points 15 minutes, 30 minutes, 1 hr and 2 hr. Dotted line indicates where ratio N/C = 1.

4.3.2.1.2 Doxorubicin loading on lactose-coated CDs

Looking to exploit the role of sugars as targeting moieties, we loaded doxorubicin onto carbon dot CD-lactose **25** using the same freeze-drying method as for **N1-8** and **C1-8 (**section 4.3.10). Lactose functionalisation has been shown to induce cell selective uptake and intracellular localisation of quantum dots and facilitate uptake of bifunctionalised QDs which were not taken up without the lactose.[44] Therefore, **L1-8** were incubated with HeLa cells under the same conditions as with **N1-8** and **C1-8** for 1 hr. Live confocal microscopy imaging showed that doxorubicin was localised to the nucleus in all cases of **L1-8** (Figure 4.9). This result shows a lack of interaction between the CD-lactose **25** and doxorubicin, hence the drug was free and able to enter the nucleus. This also suggests that hydrophobic CH-π interactions and hydrogen bonding between the doxorubicin and the lactose on the CD-lactose **25** surface does not allow for doxorubicin loading. This suggests that the doxorubicin loading observed in both AmCD **16** and AcCD **17** is electrostatic and any hydrophobic interaction between doxorubicin and the carbon dot surface is likely not the underlying basis for loading.

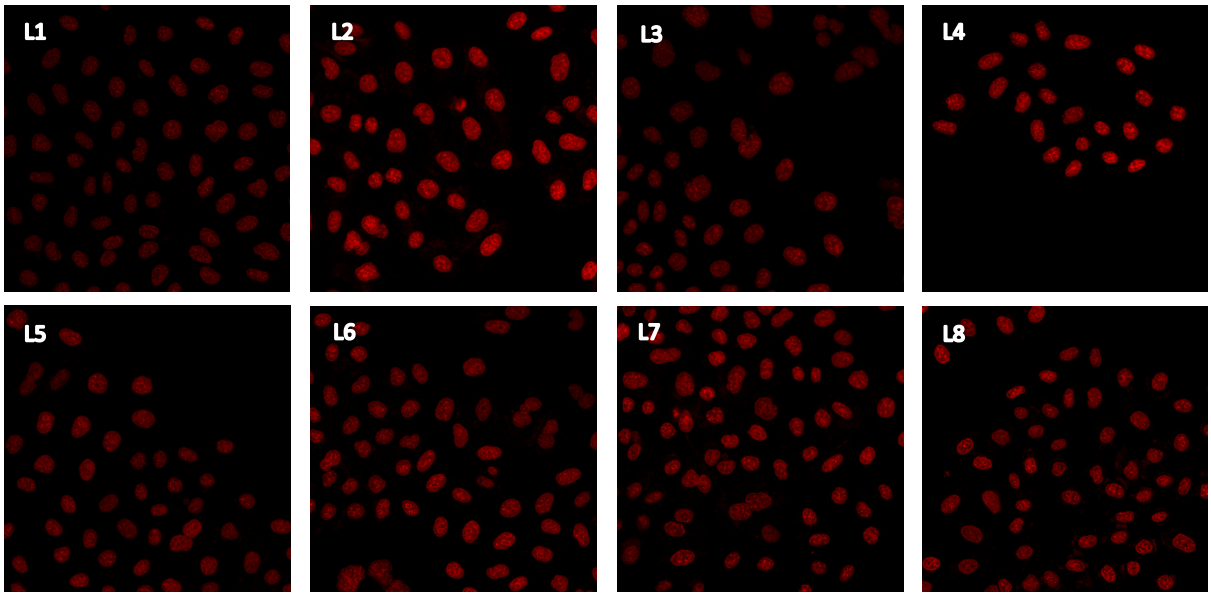

Figure 4.9 Confocal images of HeLa cells incubated with L1-8 (10 μgml^{-1}) for 1 hr before imaging. Red florescence is doxorubicin. In all experiments in this figure, doxorubicin fluorescence is localised in the nucleus. This was confirmed through bright field images (not presented here).

4.2.2.1.3 Doxorubicin loading on CD-lac-TTDDA

Conjugating TTDDA onto the surface of CD-lactose **25** should allow for doxorubicin loading yet have lactose present as a targeting moiety. **LT1-8** were incubated with HeLa cells under the same conditions at **N1-8**, **C1-8** and **L1-8** for 1 hr. For all of **LT1-8** cytosolic doxorubicin localisation was observed as seen in figure 4.10. **LT1-4** were not able to load doxorubicin as well as in **N1-4**, **C1-4** and **L1-4**. This suggests that doxorubicin loading onto CD-lactose is less efficient than with AmCD **16** and AcCD **17**. We propose

that the conjugation of TTDDA provides a higher density of free amines on the surface than is seen in AmCD **16**, hence this is the basis for introducing doxorubicin loading to CD-lactose **25**. NMR provides evidence of the presence of TTDDA on the surface of CD-lac-TTDDA **28** (Figure A.28). Furthermore, figure 4.10 shows that at **LT7** and **LT8**, there is no doxorubicin fluorescence. This implies that uptake is not possible when carbon dots are in a high excess and doxorubicin is not highly concentrated on the nanoparticle surface. To allow for comparison between the CD-doxorubicin drug delivery systems, **LT5** was used henceforth in dialysis and cytotoxicity experiments.

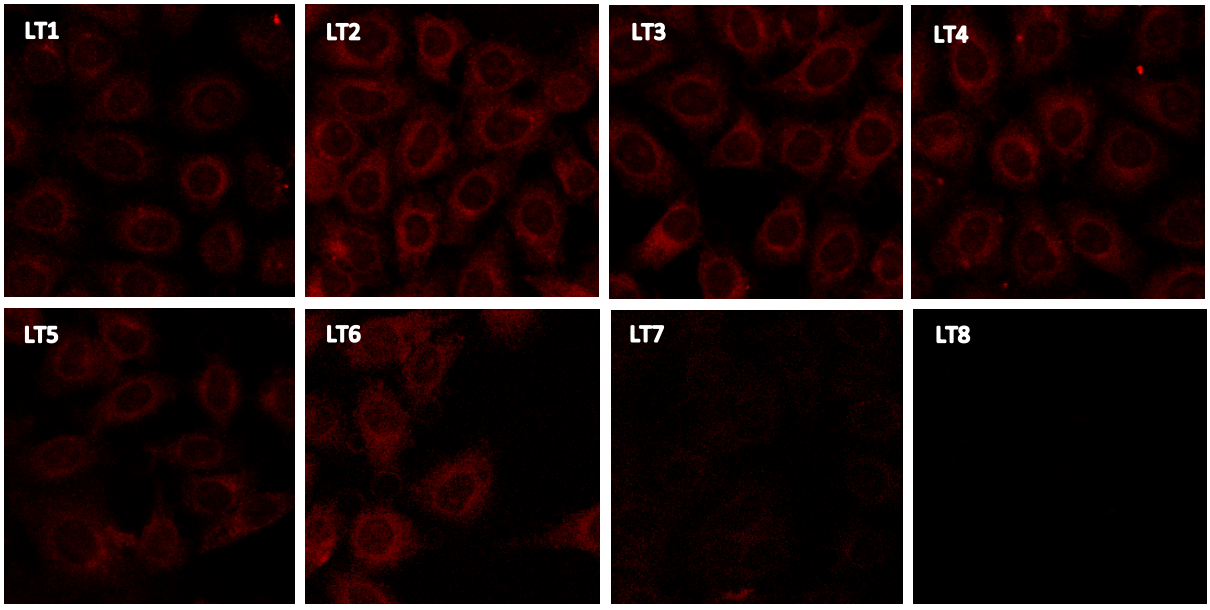

Figure 4.10 Confocal images of live HeLa cells incubated with LT1-8 (10 μgml^{-1}) for 1 hr before imaging. Red fluorescence is doxorubicin. In all these experiments doxorubicin is localised to the cytosol and in LT7 and LT8 no fluorescence con be seen indicating poor or no uptake. Note, these images were taken with a higher gain than images in figure 4 and 5, hence are not comparable in that respect.

4.3.2.2 Dialysis to determine release rate

The data in figure 4.11 was collected and collated by Sylvain Penasse. Dialysis (3,500 MWCO cellulose membrane) in PBS at pH 5.0, 6.8 and 7.4 was carried out to investigate the pH dependence of the doxorubicin release from **N5** up to 157.5 hrs. Release was measured from doxorubicin concentration in dialysis solution outside the membrane, i.e. free doxorubicin, via doxorubicin fluorescence. Greatest doxorubicin release was observed at pH 5.0 from time point 47.7 h; 20 % to 45 %; 157.7 h. This fits with the formation of an imine bond between the carbon dot and doxorubicin. Between pH 6.8 and 7.4 there is not much difference in release, never reaching 20 %. The imine bond is acid-labile and should be stable at physiological pH[195], hence low pH induced doxorubicin release. Dialysis to probe the release of free doxorubicin and **C5** at pH 5.0, 6.8 and 7.4 has yet to be carried out.

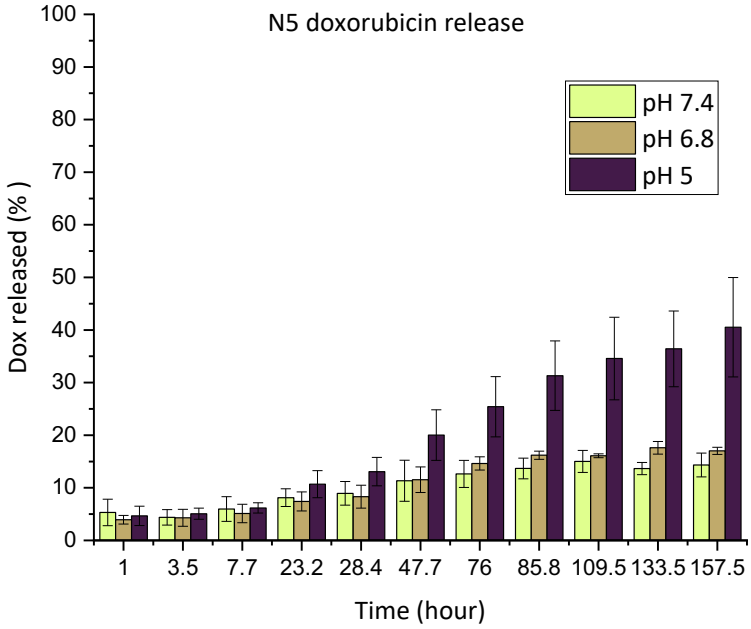

*Figure 4.11 Dialysis based doxorubicin release data at pH 5.0, 6.8 and 7.4 for **N5** in PBS. Graph and data shown generated by Sylvain Penasse.*

4.3.2.3 FTIR to show imine formation

The data for this section was generated by Sylvain Penasse. FTIR was used to probe the disappearance of the doxorubicin ketone peak at 1717 cm^{-1} (Figure 4.12) upon the addition of AmCD **16** at ratios 1:1 (**N1**) and 5:1 (**N5**). In figure 4.13, the ketone peak of doxorubicin decreases as shown by the arrow towards the baseline. Upon addition of AmCD **16**, reduction of ketone peak was observed correlating to the amount of AmCD **16** in **N1** (green line) and **N5** (purple line) this was taken to indicate imine formation with the doxorubicin. Furthermore, a peak at 1690-1640 cm^{-17} corresponding to imine[3] bond appears in **N1** (green line) and **N5** (purple line) when comparing to AmCD **16** (blue) or free dox (red) spectra. This is difficult to conclude as there is an overlapping peak at 1620 cm^{-1} from the free dox. AmCD **16** (blue line) does not have a peak at 1717 cm^{-1} so does not contribute to this signal. The concentration of doxorubicin was kept constant 0.1 mg ml^{-1}. Overall, this supports imine linkage as being responsible for doxorubicin loading onto the AmCD **16**. In the case of AcCD **17**, the peaks at 1638 cm^{-1} (HNCO) amide and at 1561 cm^{-1} (N-H) as seen in FTIR spectra of AcCD **17** in section 2.2.2.4 meant that the ketone peak at 1717 cm^{-1} could not be monitored accurately in the same way as they come at the same position as an imine 1690-1640 cm^{-1}.[223] Hence, imine formation could not be probed. FTIR to probe CD-lac-TTDAA to dox interaction has yet to be carried out, we anticipate a similar result to AmCD **16** as there both have a free amine on their surface, and we can infer interaction between CD-lac-TTDDA **28** and dox through confocal similarly to AmCD **16**.

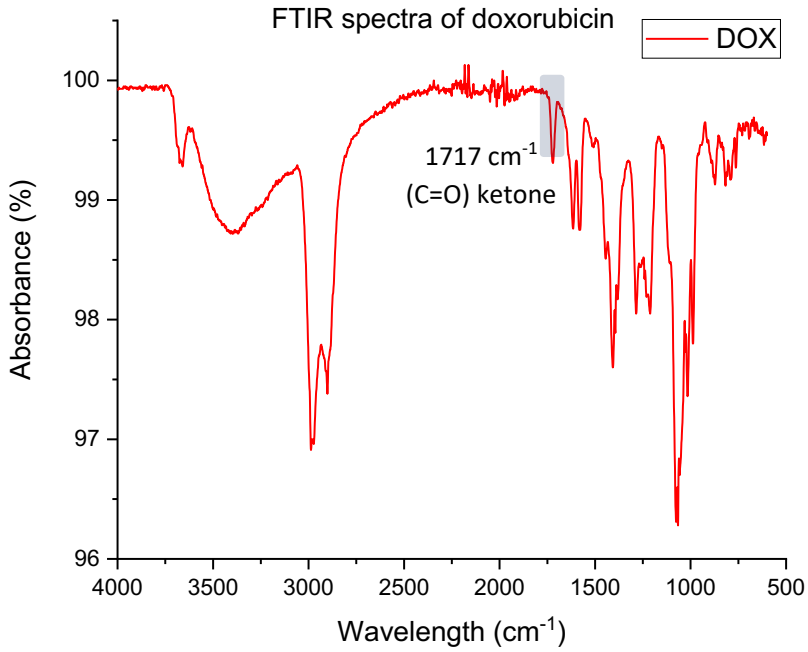

Figure 4.12 FITR spectra of free doxorubicin. Peak at 1717 cm^{-1} (C=O) ketone is identified here and can be used to probe the formation of an imine via this ketone. Data for this graph generated by Sylvain Penasse.

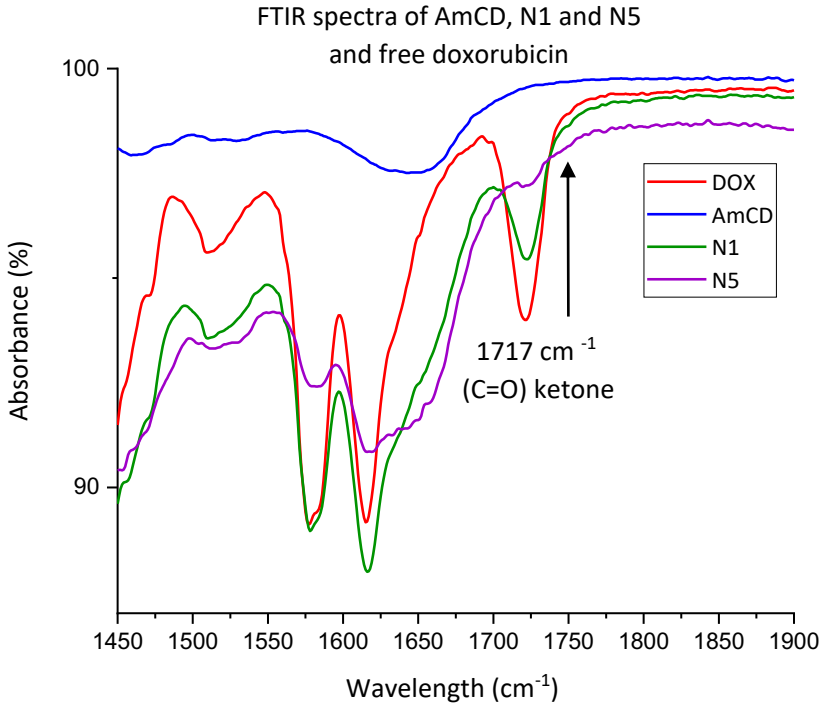

*Figure 4.13 FTIR spectra of free doxorubicin (red), AmCD **16** (blue), **N1** (green) and **N5** (purple). The ketone signal from doxorubicin, as shown in figure 10, decreases stepwise upon the addition of AmCD **16** as shown by the black arrow first in **N1** then **N5**. Imine formation is supported by this data. Data for this graph generated by Sylvain Penasse.*

4.3.3 Cellular studies

4.3.3.1 Cytotoxicity of AmCD **16**, AcCD **17** and CD-lac-TTDDA **28**

Cytotoxicity of carbon dots without doxorubicin loaded was conducted to observe if there was any toxic effect on HeLa cells which may interfere with measuring the toxicity of **N5**, **C5** and **LT5**. Relative to control (untreated cells) there was no significant toxic effect observed in either the AB or Calcein assay for AmCD **16**, AcCD **17** and CD-lac-TTDDA **28** (Figure 4.14).

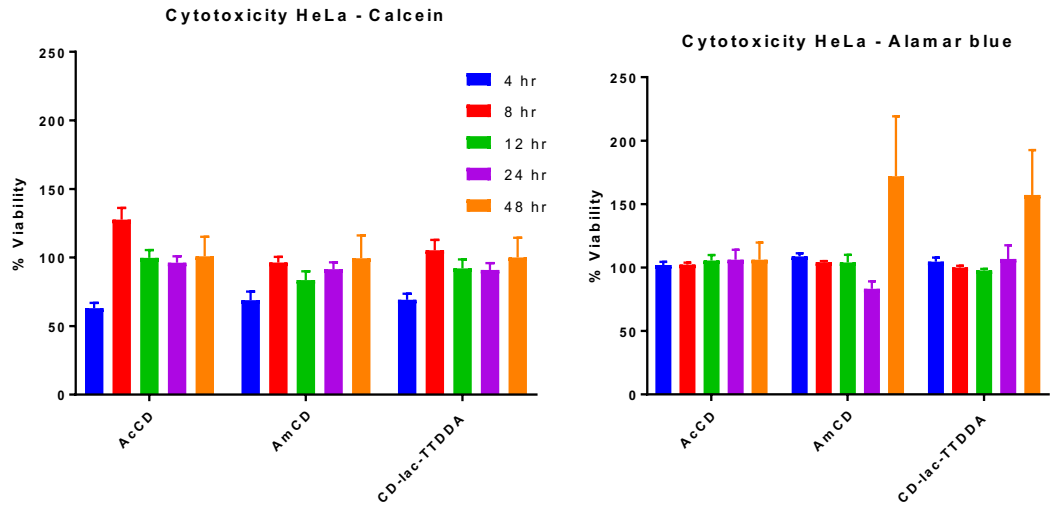

*Figure 4.14 Cytotoxicity of AmCD **16**, AcCD **17** and CD-lac-TTDDA **28** as measured via Calcein AM and Alamar blue tests at time points: 4hr (blue), 8 h (red), 12 h (green), 24 h (purple) and 48 h (orange). Experiments were conducted in triplicate.*

4.3.3.2 Cytotoxicity of N5, C5, LT5

Cytotoxicity studies were conducted in three cell lines MDA-MB-231, MCF-7 and HeLa, at four time points 24 h, 48 h, 4 days and 7 days, for samples **N5**, **C5** and **LT5** which had suggested promise for slowed drug delivery (Section 4.3.2.1.1). Two cytotoxicity tests were conducted in parallel; Alamar blue (AB) and Calcein AM (Calcein) and a dose-response curve generated in each case (figures S4.1, 4.2 & 4.3). Data was conducted in triplicate and averaged. From the dose-response curve inhibitory concentration (IC_{50}) values were extracted.

The data in this section offers information on the efficacy of **N5**, **C5** and **LT5** as a means for improved doxorubicin delivery. Firstly, in all cases as time increases, toxicity increases. This is observed in both AB and Calcein AM assays. Doxorubicin by itself is highly toxic and IC_{50} values are within the same order of magnitude at 24 h as those reported in the Genomics of Drug Sensitivity in Cancer Project database.[178]

LT5 compared to all other delivery systems has the least toxic effect at all time points in some cases never reaching the same toxicity as free doxorubicin at the first time point of 24 hrs. Hence, the delivery is on a slower time scale than 7 days, potentially never fully releasing all the bound doxorubicin. This also agrees with confocal images which show that cytosolic retention of doxorubicin is greater than that seen for **N1-8** or **C1-8**.

As expected, free doxorubicin had a greater toxicity than all of **N5**, **C5** and **L5** at time points 24 h and 48 hr. This suggests that the carbon dots sequester doxorubicin on their surface fitting with the proposed slowed release theory. However, and most interestingly, **N5** has a greater toxic effect at day 4 (AB only) seen in table 4.9 and in both cytotoxicity tests at day 7 in MDA – AB 0.00109 μM and Calcein 0.00298 μM compared to free doxorubicin with 0.00561 μM and 0.0132 μM respectively (Table 4.9).

MDA	*IC_{50} (AB assay)*	*IC_{50} (Calcein)*
N5	0.00109	0.00298
Dox	0.00561	0.0132

Table 4.3 IC_{50} values (μM) at day 7 for N5 and free doxorubicin in MDA-MB-231 cells.

This "swap" in toxicity shows that **N5** reaches greater toxicity at longer time points than free doxorubicin. In HeLa this effect is also seen with **N5** at day 4 as well as day 7 (AB and Calcein). Furthermore, in MCF-7 at day 4 **N5** has greater toxicity, however, at day 7 free doxorubicin is once again more toxic. **C5** does not show increased toxicity to the same extent as compared to doxorubicin. In some cases, the toxicity is comparable, but not an order of magnitude greater as seen with **N5** (table 4.3).

Free doxorubicin is known to be effluxed from the cancer cell via the p-glycoprotein. However, if doxorubicin is sequestered on AmCD, then this is reduced and as the drug is slowly released there is a greater likelihood that it can enter the nucleus where it is effective. Literature evidence has shown both a decrease or an increase in toxicity with a drug delivery nanoparticle as evidence for improved efficacy as discussed earlier in this chapter 4.1.3.4. Up to 72 hr a reduction in toxicity is used as evidence of sequestering of the drug[168]. But also, greater toxicity is seen by Li *et al.*[217] who attribute this to greater uptake of the nanoparticle form.

In vitro, the context is not similar to nature in that the extracellular environment is fairly consistent compared to *in vivo*. Hence, *in vitro* any free doxorubicin exocytosed by the p-glycoprotein could re-enter the cell. This means that the benefits of our system could be underestimated in this experiment. Overall, by running our experiments at 4 day and 7 days our work is able to offer an explanation and

evidence for the seemingly conflicting increased and decreased cytotoxicity seen for doxorubicin-carbon dot delivery systems in the literature. Finally, MDA-MB-231 is known to be resistant to doxorubicin through MDR yet **N5** worked best on this cell line, showing that the CD sequesters irrespective of the level of p-glycoprotein present. This suggests that **N5** CD conjugate offers potential to treat this type of breast cancer.

AB IC_{50} MCF7 (μgml^{-1})	24 hr	48 hr	4 day	7 day
N5	0.236	0.141	0.00309	0.00176
C5	0.0692	0.0118	0.00924	0.00437
LT5	> 10	> 10	> 10	0.125
Dox	0.0470	0.0123	0.0136	0.000558

Calcein IC_{50} MCF-7 (μgml^{-1})	24 hr	48 hr	4 day	7 day
N5	> 10	1.653	0.001365	0.00830
C5	> 10	0.0490	0.00662	0.0129
LT5	> 10	> 10	0.4080	14.80
Dox	6.48	0.0130	0.00749	0.00472

AB IC_{50} MDA (μgml^{-1})	24 hr	48 hr	4 day	7 day
N5	> 10	0.0244	0.00255	0.00109
C5	0.0887	0.0133	0.00278	0.00230
LT5	> 10	4.980	0.212	0.0710
Dox	> 10*	0.00441	0.00427	0.00561

Calcein IC_{50} MDA (μgml^{-1})	24 hr	48 hr	4 day	7 day
N5	> 10	> 10	0.0205	0.00298
C5	16.8	> 10	0.00534	0.00365
LT5	> 10	> 10	> 10	0.1780
Dox	0.0251	> 10*	0.00124	0.0132

AB IC_{50} HeLa (μgml^{-1})	24 hr	48 hr	4 day	7 day
N5	0.124	0.0284	0.00268	0.000231
C5	0.186	0.0211	0.00410	0.00114
LT5	> 10	1.27	0.239	0.0216
Dox	0.0450	0.0177	0.00486	0.000695

Calcein IC_{50} HeLa (μgml^{-1})	24 hr	48 hr	4 day	7 day
N5	0.136	0.0543	0.00146	0.000386
C5	0.121	0.0543	0.00535	0.00136
LT5	> 10	6.42	0.517	0.0244
Dox	0.0430	0.0376	0.00381	0.000482

Table 4.4 Cytotoxicity data for N5, C5 L5 and free doxorubicin in HeLa, MDA and MCF-7 cancerous cell lines. Values stated are Inhibitory concentrations - IC_{50} (µM). Two cytotoxicity assays were conducted in tandem Alamar blue (AB) and Calcein AM (Calcein) as seen in each tables title.

4.4 Conclusions and future work

In this work, four different carbon dot delivery-based doxorubicin delivery systems have been synthesised and tested with cancer cells with different doxorubicin loading. The structure and mechanism of loading was explored by varying the surface functionality of the carbon dot to match common trends in the literature. Our group expertise in carbohydrate functionalising carbon dots was used in this context to develop a lactose-based target system. Lactose functionalisation improved the specificity of delivery in previous work[44] and has the potential for developing multivalent carbohydrate-based delivery systems.

CD-lactose **25** was shown not to bind doxorubicin well i.e. hydrophobic (CH-π) interactions are not sufficient for loading. In other words, removing the electrostatic interactions that occur between dox and **N5** and **C5** removes the loading potential. The fact **N5** has slower drug release (dialysis and confocal N/C) and greater cytotoxicity at 7 days than **C5** shows that additional interactions than just electrostatic must occur between the CD amines and Dox. We propose this is due to the imine formation between the doxorubicin ketone and the surface amines of **N5**. We suggest that this interaction is more favourable than forming corresponding carboximidate which would form between the doxorubicin amine and the carboxylic acid of **C5**. The carbonyl of carboxylic acids is much less electrophilic towards nucleophilic attack by an amine than the carbonyl of ketones, therefore forming a covalent linkage between dox and **C5** in this manner is less favourable. Another factor could be the sterics of doxorubicin loading onto a nanoparticle in that AmCD **16** may offer more electrostatic interactions with doxorubicin than the AcCD **17** can provide.

By synthesising CD-lac-TTDDA **28** by conjugating TTDDA onto CD-lactose **25**, dox loading was restored to the carbon dot as seen in confocal microscopy. Cytotoxicity revealed that this system had the lowest toxicity for the same concentration of doxorubicin at 24 h, 48 h 4 day and 7 day time points. This indicates strong interaction, greater than amines only in the form of **N5**.

N5 showed interesting cytotoxicity results compared to free doxorubicin explaining seemingly contradictory literature results. Both greater and lower cytotoxicity has been shown as evidence of improved efficacy for carbon dot doxorubicin delivery systems as discussed in section 4.1.3.4. However, this is because carbon dots improve doxorubicin uptake and also sequester it from p-glycoprotein removal. Hence depending on the time point and concentrations the dominant effect changes. Initially **N5** shows reduced toxicity compared to free doxorubicin which we suggest is due to sequestering effects. By carrying out these assays up to 7 days we observe that at longer time points

the toxicity of **N5** becomes greater than free doxorubicin owing to the slow by continued release of doxorubicin to the nucleus. This is supported by confocal evidence where over 4 hrs doxorubicin translocated into the nucleus at different rates depending on the CD surface functionality.

FTIR was shown for the first time to the best of our knowledge as indicating imine formation between doxorubicin and a carbon dot. This was inferred from disappearance of the signal resulting from the doxorubicin ketone removal upon sequential carbon dot addition. Previous studies comment that covalent bonding could occur between the Dox ketone and the CD amine, or the carboxylic acid on the CD and the Doxorubicin amine.[168] Dialysis studies *in vitro* of **N5** also showed low pH release which agrees with imines being acid-labile and is a good cancer targeting property to have as cancer cells are more acidic than healthy cells. Understanding the basis of doxorubicin loading is important for developing a system which has both specific and passive uptake properties.
Zeta potential may be an interesting experiment to run. Literature evidence[185] shows that doxorubicin increases the zeta potential upon conjugation to carbon dots which have a zeta potential close to 0 eV. One experiment could be carried out to compare the zeta potential (at pH 7.4) of **N5** with **N5**-dox and **C5** with **C5**-dox. This would reveal the surface charge when doxorubicin has been loaded. The AmCD **16** surface would be occluded from the solvent upon loading and the doxorubicin amine would be bound to the carbon dot surface as an imine. In this case, a more negative zeta potential for **N5** would be expected compared to AmCD **16**. For AcCD **17** upon loading, the doxorubicin amine would be solvent exposed and the carboxylic acid surface groups occluded from the surface. In this experiment the zeta potential of **C5** would be expected to increase with respect to the AcCD **17**. It is worth bearing in mind that the implications of cell media would need to be considered for these experiments and further along, the *in vivo* context.

A further zeta potential experiment could be conducted at high pH (> 9.93) with **C5** and **N5**. At pH above the Doxorubicin amine pKa of 9.93, the amine deprotonates. This negative change in charge would be expected to be greater for **C5** then **N5** reflected in zeta potential compared to when at pH 7.4.

Future work would include further quantification of nuclear/cytosol doxorubicin localisation *in vitro* over time of **N5**, **C5** and **LT5**. Also, flowcytometry would allow high throughout data to be collected of uptake rates of CD-dox systems and hence delivery potential over time. Investigating lysosomal escape of CD-dox could be explored for improving delivery as it is a means by which delivery systems are

exocytosed as seem for many literature examples. Carbohydrate based targeting of cancer cells affects uptake method, hence endosome-lysosome pathway evasion could be achieved this way.

4.5 Chapter 4 Experimental

Doxorubicin.HCl was purchased from Sigma Aldrich.

4.5.1 Synthesis

4.5.1.1 Doxorubicin loading onto AmCD **16**, AcCD **17**, CD-lactose **25** & CD-lac-TTDDA **28**

A mixture of carbon dot (AmCD **16** or AmCD **17**, CD-lactose **25** & CD-lac-TTDDA **28**) and doxorubicin.HCl (0.1 $mgml^{-1}$) were dissolved in H_2O and then freeze dried overnight to afford a red powder **N1-8** (from AmCD **16**) or **C1-8** (from AcCD **17**) or **L1-8** (from CD-lactose **25**) or **LT1-8** (CD-lac-TTDDA **28**). The material was redissolved to 0.1 $mgml^{-1}$ doxorubicin concentration directly before use.

4.5.1.1.1 NMR characterisation of doxorubicin, N5, C5 and L5.

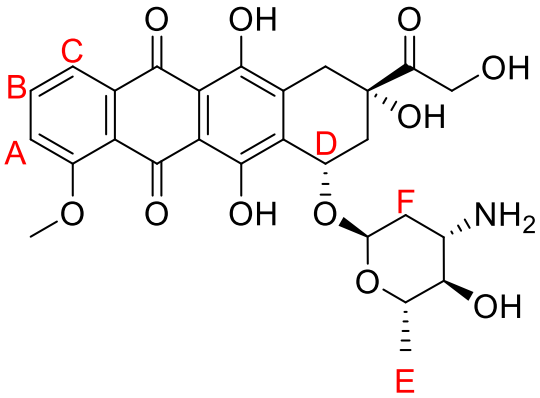

NMR of commercial Doxorubicin.HCl: ^1H NMR (500 MHz): δ = 7.67 (d, 1H, J = 6.3 Hz, **B**), 7.45 (s, 1H, **C**), 7.41 (d, 1H, J = 8.7 Hz, **A**), 4.27 (d, 1H, J = 7.0 Hz, **D**), 3.73 (s, 2H, **F**), 1.33 (d, 2H, J = 6.3 Hz, **E**) ppm. NMR matches previously reported data in the literature see ref .[224] For DOSY the peak used to determine the diffusion coefficient of doxorubicin was at 7.67 ppm in ^1H NMR. Appendix shows ^1H NMR and DOSY spectra of Doxorubicin.HCl.

NMR of N5, C5 and L5 show the same assignments as seen for doxorubicin.HCl and AmCD 16, AcCD 17 and CD-lactose 25 respectively (see section 2.4.3 for assignments and appendix for spectra).
For **N5** DOSY the peak used to determine the diffusion coefficient of carbon dot was 3.5-3.6 ppm.
For **C5** DOSY the peak used to determine the diffusion coefficient of carbon dot was 3.5-3.6 ppm.

4.5.1.2 CD-lac-TTDDA **28** synthesis and doxorubicin loading – **LT1-8**

To CD-lactose 25, TTDDA (1:1 molar equivalent to lactose used in glycan functionalisation) was conjugated onto the surface to any remaining carboxylic acids via EDC coupling (4 equivalents) for 2 hr in H_2O (10 ml) on a 60 mg CD-lactose scale. CD-lac-TTDDA **28** was purified using dialysis using 500-1000 MWCO cellulose membrane overnight**.** A mixture of CD-lactose **25** and doxorubicin.HCl (0.1 $mgml^{-1}$) were dissolved in H_2O and then freeze dried overnight to afford a red powder **N1-8** (from AmCD **16**) or **C1-8** (from AcCD **17**) or **L1-8** (from CD-lactose **25**) or **LT1-8** (CD-lac-TTDDA **28**). The material was redissolved to 0.1 $mgml^{-1}$ doxorubicin concentration directly before use.

NMR of CD-lac-TTDDA **28**: *^{1}H NMR* (*500 MHz*): δ = 5.24 (d, 1H, J = 3.8 Hz) 4.68 (d, 1H, J = 7.9 Hz), 4.57 (d, 1H, J = 7.8 Hz), δ = 4.46 (d, 1H, J = 7.8 Hz) 3.50-3.70 (m), 3.00 (t, J = 7.2 Hz), 2.40 (s, 1H, Hz), 1.96 (q, 1H, J = 6.7 Hz) ppm. Spectra

4.5.2 DOSY

Sample	*Diffusion coefficients / x 10^{-6} cm^2 s^{-1}*		*Water diffusion coefficient/ x $10^{-6}$$cm^2$ s^{-1}*
Doxorubicin	1.86		16.5
AmCD	3.83		16.3
AcCD	2.86		16.3
N5	Dox: 2.14	CD: 3.08	17.5
C5	Dox: 1.39	CD: 1.11-3.08	15.3

Supplementary table 4.1 DOSY derived diffusion coefficients – raw values. These are corrected against the water peak and presented in the main text table 3. Data measurements were not conducted in triplicate hence errors were not calculated.

4.5.3 Cell studies

CD loaded doxorubicin toxicity in HeLa, MDA and MCF7 cancer cells was determined by way of IC_{50} measurement using a Calcein assay and an Alamar Blue assay which were performed in tandem. HeLa cells were plated at $1x10^5$ cells per well in a 96-well plate and incubated overnight. The next day cells were incubated with nanomaterial in dilution to produce inhibition curves. Samples used for these experiments were those named **C5**, **N5** and **LT5** (see table 4.1 for reference), which were at 10:1 Dox:CD mass ratio. Concentrations used in these experiments were between 100-0.1 μgml^{-1} with respect to doxorubicin. After incubation with nanomaterial for either 24 hr, 4 day or 7 day cells were washed thrice with PBS and then Calcein and Alamar blue assays were carried out as described previously.

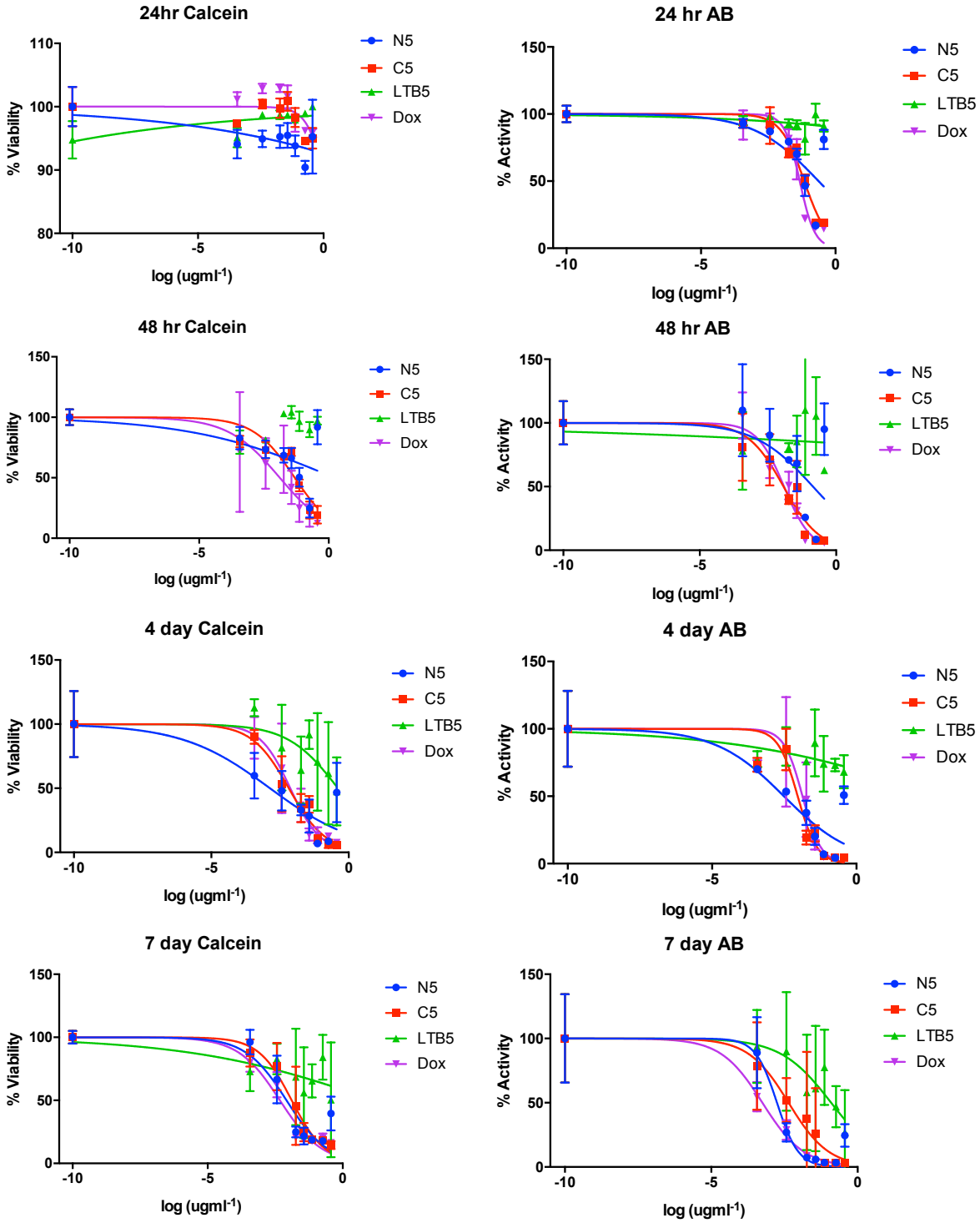

Supplementary Figure 4.1 MCF-7 Toxicity dose-response (inhibition) curves plotted in GraphPad Prism using Non-linear regression. Experiments were carried out in triplicate and normalised before IC_{50} values were determined.

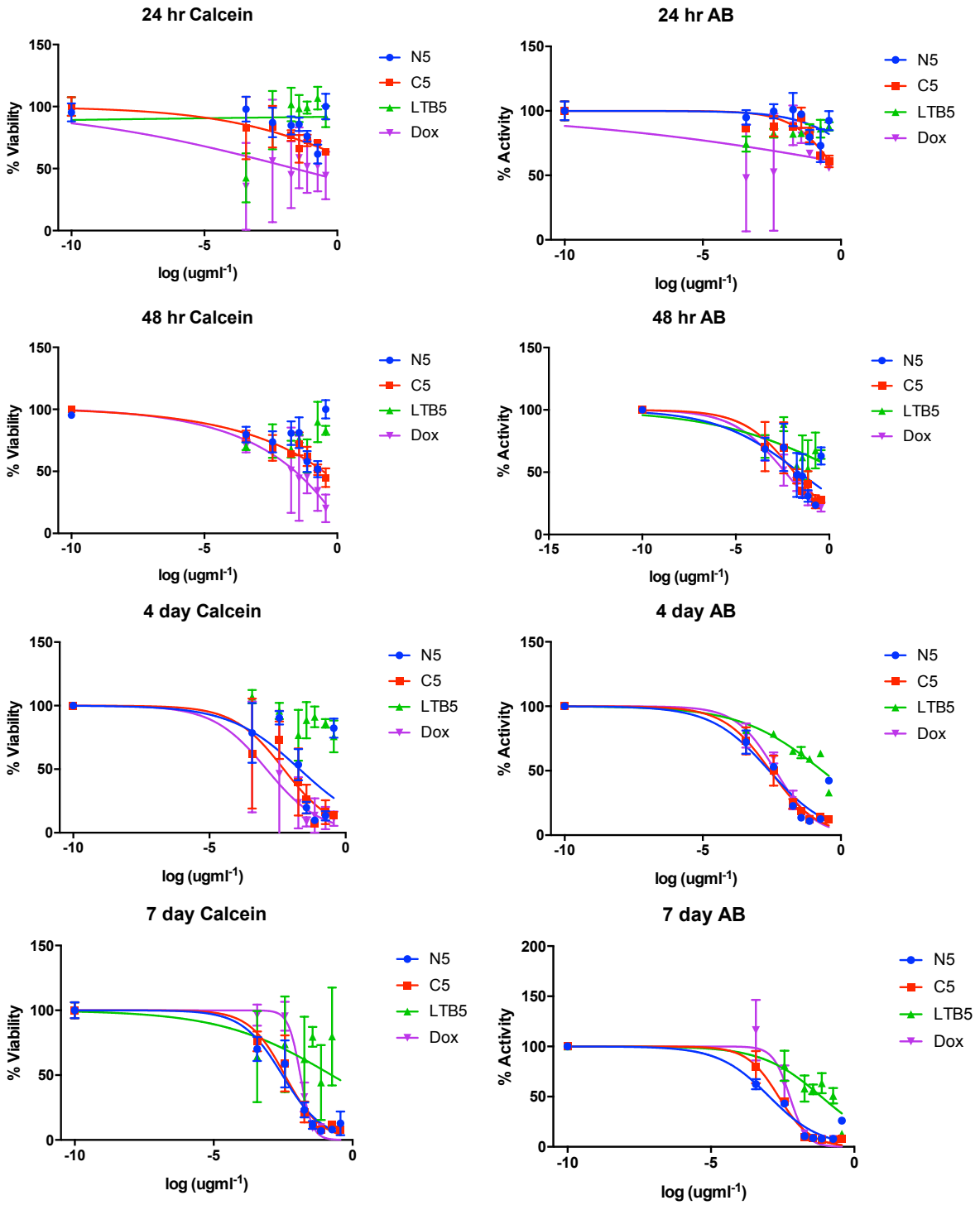

Supplementary Figure 4.2 MDA Toxicity dose-response (inhibition) curves plotted in GraphPad Prism using Non-linear regression. Experiments were carried out in triplicate and normalised before IC_{50} values were determined.

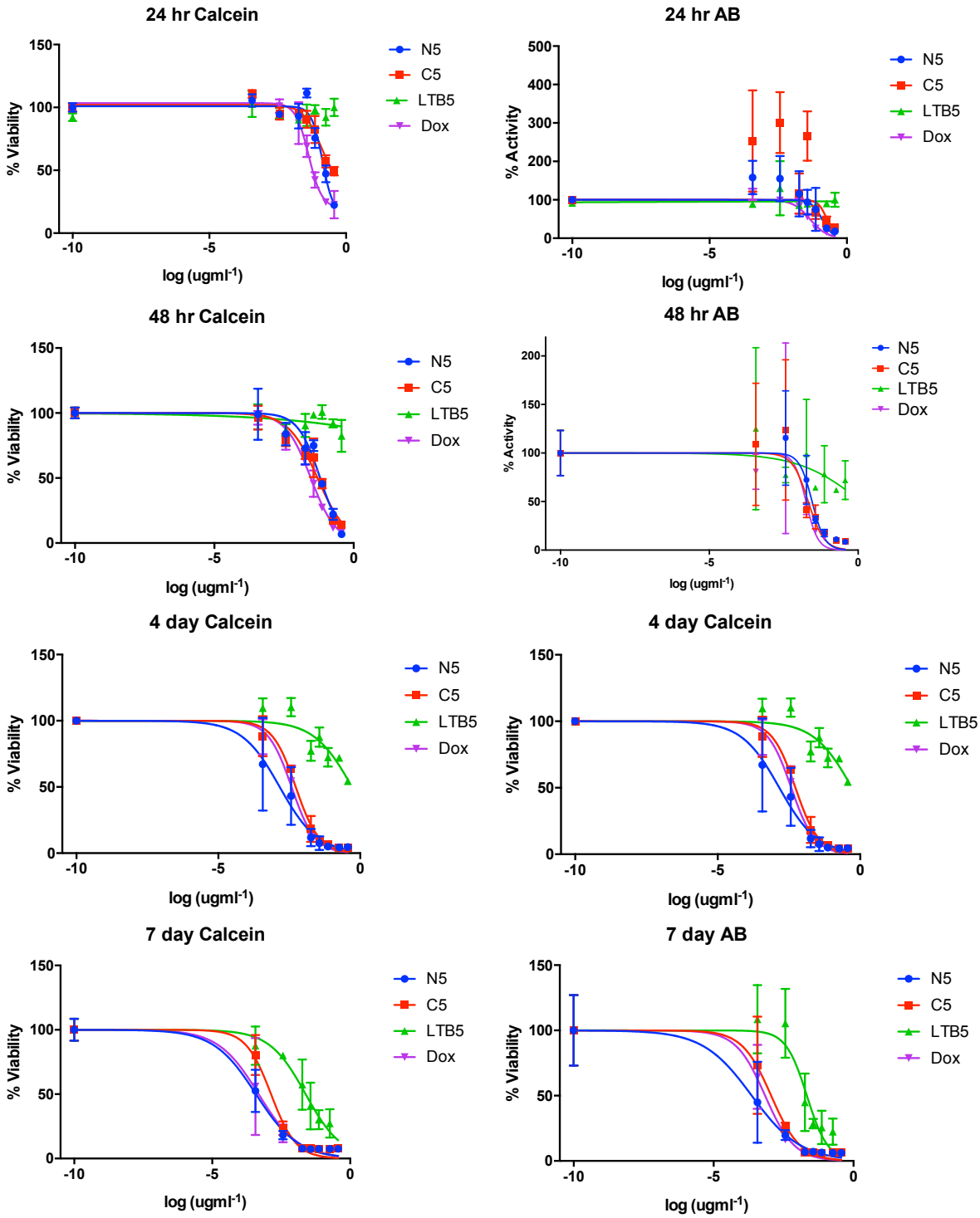

Supplementary Figure 4.3 HeLa Toxicity dose-response (inhibition) curves plotted in GraphPad Prism using Non-linear regression. Experiments were carried out in triplicate and normalised before IC_{50} values were determined.

Errors AB logIC_{50} MCF7 ($\mu g\ ml^{-1}$)	24 hr	48 hr	4 day	7 day
N5	8.80	1.65	0.45	0.16
C5	-	0.05	0.12	0.12
LT5	5.30	-	0.44	2.45
Dox	0.77	0.013	0.13	0.09

Errors Calcein logIC_{50} MCF-7 ($\mu g\ ml^{-1}$)	24 hr	48 hr	4 day	7 day
N5	0.33	0.41	0.29	0.15
C5	0.05	0.14	0.10	0.26
LT5	10	-	3.19	0.33
Dox	0.04	0.09	0.12	0.16

Errors AB logIC_{50} MDA ($\mu g\ ml^{-1}$)	24 hr	48 hr	4 day	7 day
N5	1.32	0.33	0.20	0.14
C5	0.20	0.15	0.07	0.07
LT5	-	1.1	0.14	0.14
Dox	4.0	0.1	0.07	0.08

Errors Calcein logIC_{50} MDA ($\mu g\ ml^{-1}$)	24 hr	48 hr	4 day	7 day
N5	-	-	0.37	0.11
C5	1.0	-	0.24	0.10
LT5	-	-	-	0.74
Dox	1.1	-	0.35	0.04

Errors AB logIC_{50} HeLa ($\mu g\ ml^{-1}$)	24 hr	48 hr	4 day	7 day
N5	0.18	0.24	0.06	0.28
C5	0.40	0.16	0.08	0.15
LT5	-	1.16	0.14	0.11
Dox	0.05	0.15	0.06	0.12

Errors Calcein logIC_{50} HeLa ($\mu g\ ml^{-1}$)	24 hr	48 hr	4 day	7 day
N5	0.09	1.3	3.1	3.6
C5	0.21	1.4	2.4	3.0
LT5	-	7.8	0.6	1.8
Dox	0.06	1.6	2.5	3.7

Supplementary Figure 4.4 Standard errors of cytotoxicity data presented in table 4.4 (of main chapter text). Log IC_{50} values shown as this is most appropriate for this data set.

5. Green fluorescent Carbon Dots for PTT

5.1 Photothermal therapy

Photothermal therapy (PTT) treatments have been explored over the last 10 years (Figure 5.1). These types of therapy are based on using the lower energies (biologically compatible) of the electromagnetic spectrum (400-1350 nm) for biomedical applications.[225] The technology often works in combination with nanoparticle agents or small molecules which due to their size and physiochemical properties are able to target or accumulate in a particular tissue or cell (e.g. cancer) and upon activation elicit local heating, which can lead to a therapeutic response.[225,226]

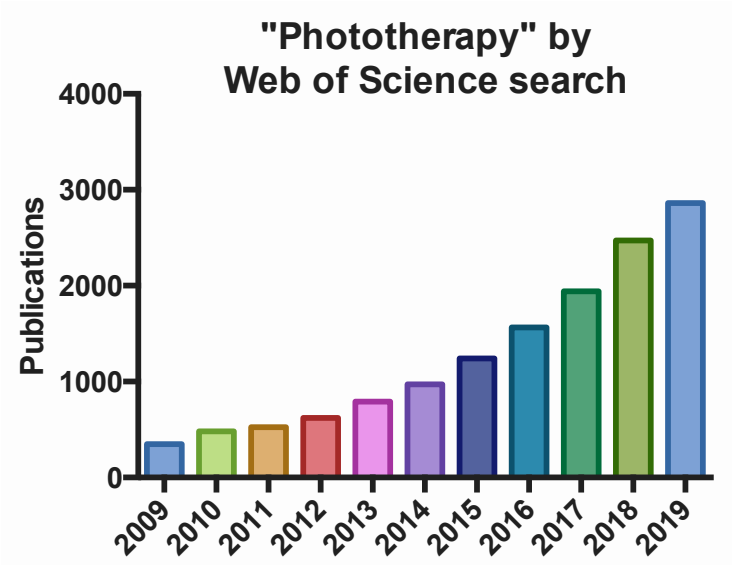

Figure 5.1 Publications with the word "phototherapy" included between 2009-2019

The application of PTT has been exemplified both *in vitro* / *in vivo.*[226] Commonly the energy used for these type of applications is in the UV-visible-near infrared (NIR) range (700-1100 nm), with a variety of nanoparticle types being used, metallic nanoparticles including gold, silver, palladium, copper, iron oxide, and molybdenum oxide[227], as well as carbon nanotubes (CNTs) and single layer graphene nanotubes (GNTs) and polymer nanoparticles[226]. These nanomaterials can also act in a multimodal way including drug or DNA delivery, imaging agent or MRI contrast agent. The energy applied in the form of a photon of light is absorbed and can then be emitted spectroscopically in a number of ways, however, a high conversion to heat is required for inducing hyperthermia and delivering photothermal therapy (Figure 5.2).

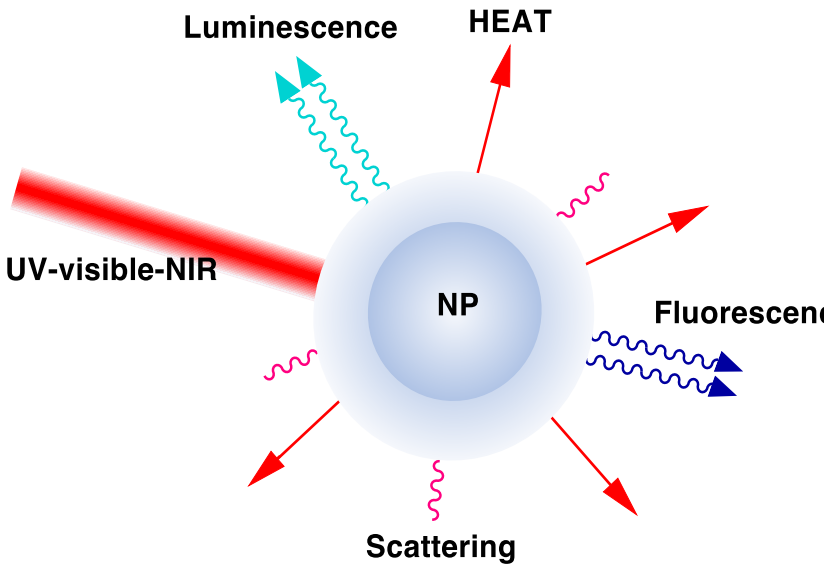

Figure 5.2 UV-visible-NIR irradiation of a nanoparticle energy conversion.[227]

PPTs can induce local hyperthermia with detrimental effect on the target cell. Hyperthermia is categorised into primary and a secondary effects. Primary effects refer to the local effects seen in the immediate context of a nanoparticle i.e. causing intracellular protein denaturation (between 48-60 ^{o}C) also known as thermal ablation. While secondary effects elicit the general biological homeostatic responses observed in surrounding tissue which occur at temperatures around 41-48 ^{o}C [226] and require longer treatment times of 15-60 minutes for cytotoxicity compared to 4-6 minutes for primary.[228] Primary effects induce more severe toxicity; hence, nanoparticles have been widely studied for PTT as they are able to induce higher local temperature increase.

PPTs can be induced by a wide range of wavelengths, however, one important consideration is the effect of each therapy on a biological sample. In the context of cancer, tumours can be up to centimetres below the skin surface and therefore wavelength penetration depth must be considered(Figure 5.3). Furthermore, the healthy tissue must not absorb too much energy such that necrosis of cells is induced. Hence, through NIR irradiation in combination with a nanoparticle conferring efficient NIR to heat conversion, targeted PTT becomes viable. However, as these wavelengths are lower energy than UV and visible wavelength, longer treatment times are required for the same therapeutic effect. NIR-I and NIR-II refer to the 2 biological windows which PTTs are generally targeted towards, with the NIR-II providing greater therapeutic potential in terms of depth of treatment and lower non-specific biological interaction.

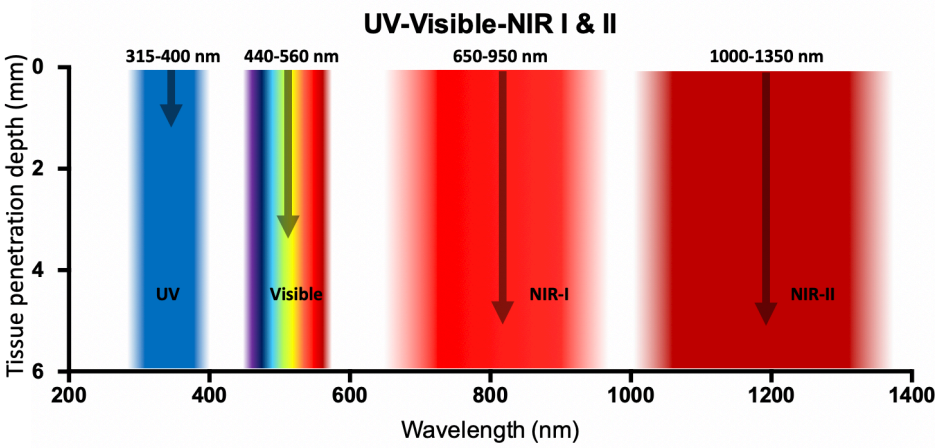

Figure 5.3 UV-Visible-NIR wavelengths and tissue penetration depth. [226,228]

Achieving nanoparticle based targeted anti-cancer treatments has been of particular interest. New technologies are moving away from magnetic field induced metallic nanoparticle-based treatments developed in the 1950's, which are limited to superparamagnetic ferromagnetic nanoparticles such as iron oxide nanoparticles. These offer useful properties in that they have good light to heat conversion, magnetism and NIR absorption. However, this PTT is only able to raise intracellular temperature to 42-45 ^{o}C, and often have toxicity issues associated[229].

Other nanomaterials have also been used for photothermal therapy, common to all is a good photoluminescence and biocompatibility. Nanogold is a popular option due to its surface plasmon resonance (SPR) properties, which confers excellent light to heat conversion. This is due to efficient absorption, good photostability, low luminescence yield and rapid relaxation of surface plasmon resonance[230]. For nanogold-based applications, visible or IR wavelengths are readily absorbed and the emitted light profile changes depending on the size, shape and local environment of the nanoparticle which allows for sensing applications.[231]

Graphene also has good photothermal properties and has been used in conjunction with IR irradiation to induce hyperthermia in cancer cells. Graphene's aromatic lattice is a good scaffold for drug loading through hydrophobic and pi-pi interactions offering potential for dual treatment[232]. Single-walled carbon nanotubes (CNTs) are able to absorb in the NIR and emit between 1100-1400 nm in the NIR region also due to strong absorption, allowing for PTT and deep tissue imaging. Their PTT potential was first compared to gold nanorods where a 10 times lower dose was observed to elicit the same tumour elimination through local heating[233]. In addition being able to drug load via $\pi - \pi$ stacking,[234] CNTs also have a hollow cavity which is suitable for drug sequestering and through PEG coating their

associated toxicity can be addressed[235]. Associated toxicity is known to come from their high aspect ratio, meaning they can pierce cells[236].

Upconverting nanoparticles (UCNPs)[237] provide a novel way to deliver high energy UV and visible wavelength energy in a targeted way using relatively benign NIR irradiation. As NIR has good penetration of biological material they are able to interact with UCNPs deep within tissue. These nanoparticles act as optical centres and often contain an absorbing metal antenna such as Erbium (Er^{3+}) and photon upconverting ion such as Ytterbium (Yb^{3+}). The upconverting lanthanide metal ion has the ability to absorb two photons sequentially with an intermediate electronic state which in an anti-stoke shift, produces a photon in an energy conserving manner. Up conversion is 5 orders of magnitude more efficient compared to multiphoton (two photon) irradiation which requires coincident photon irradiation for high energy emission[238].

Another material that has found applications in PTT are carbon dots due to their photostability, facile synthesis and low toxicity properties as well as non-bleaching properties allowing for their use in bioimaging, drug delivery and other therapeutic purpose. Achieving NIR wavelength absorbing CDs within the biological transparency window between 650 – 1350 nm where tissue is most penetrable by light, is particularly difficult. Hence, deep tissue penetration limitations exist currently for CD photothermal therapy. Furthermore, due to poor IR absorption, CD irradiation requires high power densities which are energy intensive to produce. However, efforts to red-shift the carbon dot spectroscopic profile have been explored through p-type doping or with small organic molecules containing a variety of heteroatoms[72].

5.1.1 Carbon dots for PTT

Recent efforts have been directed to modifying the synthesis of CDs to yield nanomaterials that are amenable to IR absorption. This has been achieved via the addition of known IR absorbing small molecules such as ureas within the synthesis and optimising the number of nitrogen containing pyrrole groups on the CD surface which are generated by careful control of the reaction conditions such as starting material ratios, reaction time and temperature.[239]

For instance, Permatasari *et al.*[239] synthesised carbon dots through a 30 minute microwave assisted methodology at 140 ^{o}C using a range of ratios of citric acid:urea (between 1:1 and 1:10). A ratio of 1:5 w/w citric acid:urea was found to be optimal in order to achieve the most red-shifted and most pronounced absorbance peak at 650 nm. Secondly, the temperature during formation was optimised

to 140 °C. Initial efforts to reduce the temperature to 130 °C changed the absorbance shape to broaden across the visible and NIR range (400-700 nm). This suggests sufficient energy is provided above 140 °C to form these pyrrolic structures. Increasing the temperature above 140 °C marginally improved the absorbance at 650 nm but the material was less stable after 5 days. Finally, the reaction time was optimised to 240 minutes based on the intensity of the absorbance peak at 650 nm. Physical characterisation including FTIR and XPS was carried out on three of the CD materials produced from these experiments which had varying degrees of NIR absorption to determine that pyrrolic structures were the basis of the NIR absorbance observed. Evidence included FTIR stretching vibrations at 1350 cm^{-1} and 1630 cm^{-1} corresponding to nitrogen containing functional groups C-N and C=N/C=O respectively. XPS is able to measure nitrogen content and can be deconvoluted to show the proportion of nitrogen in the pyrrolic-N form which was highest at 70.9 % for the best NIR emitter. Overall optimisation produced carbon dots with high 54.3 % photothermal conversion.

Bao *et al.*[240] conducted *in vivo* (mice) experiments with a 655 nm laser with NIR-absorbing CDs with excellent photothermal conversion of 59.2 %. After 3 hr incubation the CD accumulation was assessed in the tumour and the subject's organs. Accumulation was greatest in the tumour compared to any of the excised organs. Furthermore, thermographic measurements observed temperatures of 59-71 °C at the tumour site with CD present after 5 min irradiation (655 nm laser, 1 W cm^{-2}) compared to control where no CDs were present.[240] Hence, this material offers great potential for NIR induced cellular ablation and targeted tumour treatment. Interestingly, the starting materials used by Bao *et al*. were the same as those conducted by Permatasari *et al.*[239] consisting of only citric acid and urea at a 1:3 ratio w/w, but conducted under different solvothermal method, at 160 °C for 240 minutes. Fluorescence and absorption profiles were almost identical in shape to Permatasari *et al.* with a peak absorption between 600-700 nm and fluorescence peak at 720 nm. They claim that the dimethyl sulfoxide (DMSO) sulfur containing solvent is a doping agent in their synthesis and they report an improved photothermal conversion of 59%. XPS data revealed pyrrolic-N as expected but also 1.2% sulfur composition. Both nitrogen and sulphur are known carbon dot doping agents which red-shift spectral properties by passivating the trapped states so that lower energies can escape[75]. Furthermore, the lower band gap energy associated with these surface states means that the photoluminescence profile is more red-shifted than non-pyrrolic-N containing carbon dots.

Alternatively, passivation with highly branched bis-MPA polyester hydroxyl polymer was shown to improve carbon dot QY within the NIR region compared to equivalent oxygen content seen with linear PEGylation. Oxygen content was improved through increased hydroxyl content in this new started

material which was added into the commercial grade honey carbon dot synthesis. Honey:polymer was microwaved for 10 minutes at a 1:8 w/w ratio. Post synthesis hydroxyl groups were more highly presented on the CD surface. NIR emission at 820 nm (λ_{ex} 745 nm) was considerably enhanced dependent on increasing hydroxyl terminated hyperbranching[241]. These materials showed excitation dependent emission between the ranges λ_{ex} 350-700 and λ_{em} 521 -751 nm, but passivation with sequential generations of hyperbranching did not red-shift these profiles, rather improved quantum yield at the NIR of the emission spectra. This indicated better surface passivation of trapped surface states with greater levels of branching but no new associated surface states introduced by these hydroxyl groups.

Doping carbon dots with metals has been explored as a means for improving quantum yield whilst avoiding the inherent toxicity effects of the metal. After doping with Ga, Sn, Ag, Zn, and Au through a sonochemical synthetic method, CD toxicity was determined to be low in all materials[242]. Furthermore, evidence has been shown that metallic nanoparticles have good optical properties and photothermal conversion and hence promise as PTT agents. Rare earth metals have poor quantum yield but good photothermal conversion upon NIR irradiation[243]. They have many energy levels which when used as a doping agent, can exist within the band gap of the bulk material. Nd^{3+} doped LaF_3 nanocrystals show excellent photothermal properties, allowing for sensitive thermal detection applications[226]. Hence, using lanthanides as a means to introduce energy levels within the carbon dot band gap could improve their photothermal properties. However, research into PTT applications of metal doped carbon dots is fairly new and literature has scope to develop in this area.

The majority of carbon dots are within a UV-light spectral window which is less amenable to more biologically penetrating treatments. However, within the visible absorption region between 440 – 560 nm up to 2.5 mm depth penetration through the dermis can be still achieved, which is suited to treating surface and sub-cutaneous tumours[244]. These wavelengths are usually associated with ROS production from either direct radical formation or through triplet to singlet O_2 conversion. This process is termed photo dynamic therapy (PDT) and is distinctly different from the thermal method seen in PTT. Carbon dots which are able to achieve PTT are highly sought after.

Furthering the efficacy of PTTs against tumours can be achieved through combining it with a secondary treatment in a two-pronged attack. For example, sequestering a secondary treatment on the surface of a nanoparticle means drug delivery is achieved. If the nanoparticle is delivered to the tumour through the ERP effect or targeted through a targeting molecule, then targeted drug delivery can be

combined with PTT. Many groups have looked to combine photothermal treatment with a secondary mechanism such as drug release[225] or immunoadjuvant activation[245] through local acidic pH at the target site[246]. Often times the irradiation forms an in-situ activation step. Work by Hu *at el*. shows that using a graphene-PEG-doxorubicin proteinosome, doxorubicin release can be induced intracellularly by NIR irradiation in doxorubicin resistant MCF-7 cell line. Zhou *et al.* used Copper sulfide (CuS) nanoparticles containing radioactive copper salts which upon irradiation emitted radiation which caused secondary tissue damage in conjunction with hyperthermia[225]. Other examples include having small molecule dyes such as indocyanine green, associated with a nanoparticle which enhances the photothermal effect[225]. One important prerequisite for all of these therapies is that the nanomaterial is non-toxic to healthy cells. Carbon dots are reported as low in toxicity and biocompatible[248], lending their use for PTT. Their facile synthesis also means they are an easily accessible material to work with.

5.1.2 Doping carbon dots with small molecules for PTT

5.1.2.1 Phenylenediamine carbon dot doping for PTT

Literature precedent shows phenylene diamine can be used in carbon dot syntheses to produce materials fluorescent between the green-red visible range depending on the synthesis (Figure 5.4). A number of studies explore phenylene diamine isomers as starting materials in carbon dot syntheses. Jiang *et al*. carried out CD synthesis with o-, m- and p- of phenylene diamine in ethanol in a 12 hr thermal reaction at 180 °C to afford green/yellow (λ_{em} 535 nm), blue (λ_{em} 435 nm) and red (λ_{em} 604 nm) fluorescent CDs (under λ_{ex} 365 nm) respectively[249]. FTIR data revealed that these particles shared common chemical functional groups on the surface, however the nitrogen content measured by XPS was 7.32 %, 3.69 % and 15.57 % for o-, m- and p- phenylene diamine starting material CDs respectively. Furthermore, the average carbon dot size were 8.2 nm 6.0 nm and 10 nm for o-, m-, p- phenylene diamine derived CDs. These results support that nitrogen doping red-shifts fluorescence and is likely due to a greater amount of pyrrolic-N groups on the surface of p-phenylene diamine containing CDs allowing for improved trapped state emission and also direct excitation of these groups.

Furthermore, Jiang *et al.* then took CD synthesis using o- and m- phenylene diamine and added tartaric acid under the same conditions of 12 hr solvothermal reaction at 180 °C in ethanol which allowed them to red-shift the CD fluorescence profile. Spectra shift for m-phenylenediamine (under λ_{ex} 365 nm) went from blue (λ_{em} 435 nm) to (λ_{em} 510 nm) green and for o-phenylenediamine from green/yellow (λ_{em} 535 nm) to a multipeaked red-NIR shape. They suggest that the surface groups increased oxidation and carboxylation as the basis for this effect[250].

Interestingly, yellow fluorescent ($\lambda_{ex.}$ 400 nm, λ_{em} 573 nm) CDs were also synthesised from o-phenylenediamine in a twenty-minute microwave assisted reaction by Song *et al.*[251] This reaction was in water rather than ethanol, and FTIR data indicates surface groups are composed of unsaturated C=O, C=C, C-N= and C-O/C-O-C groups and XPS indicates 14.93 % nitrogen content. They hypothesise that o-phenylene forms a polymer in the carbonisation process which incorporates oxygen and explains the poly unsaturated bond peaks in FTIR[251].

Ding *et al.*[252] took p-phenylenediamine and added urea into the synthesis with the aim of improving the QY of the red fluorescent carbon dots produced by Jiang *et al.*[249] through increased nitrogen doping. Optimal conditions were selected as 1:1 w/w ratio at 160 ^{o}C for 10 hr in a hydrothermal synthesis. Upon purification using silica gel chromatography they separated 8 fractions of CDs which had distinct fluorescence peaks from 440 – 625 nm. Interestingly, the size distribution of these nanoparticles was similar but they differed in the degree of surface oxidation which conferred a greater red shift in fluorescence peak.

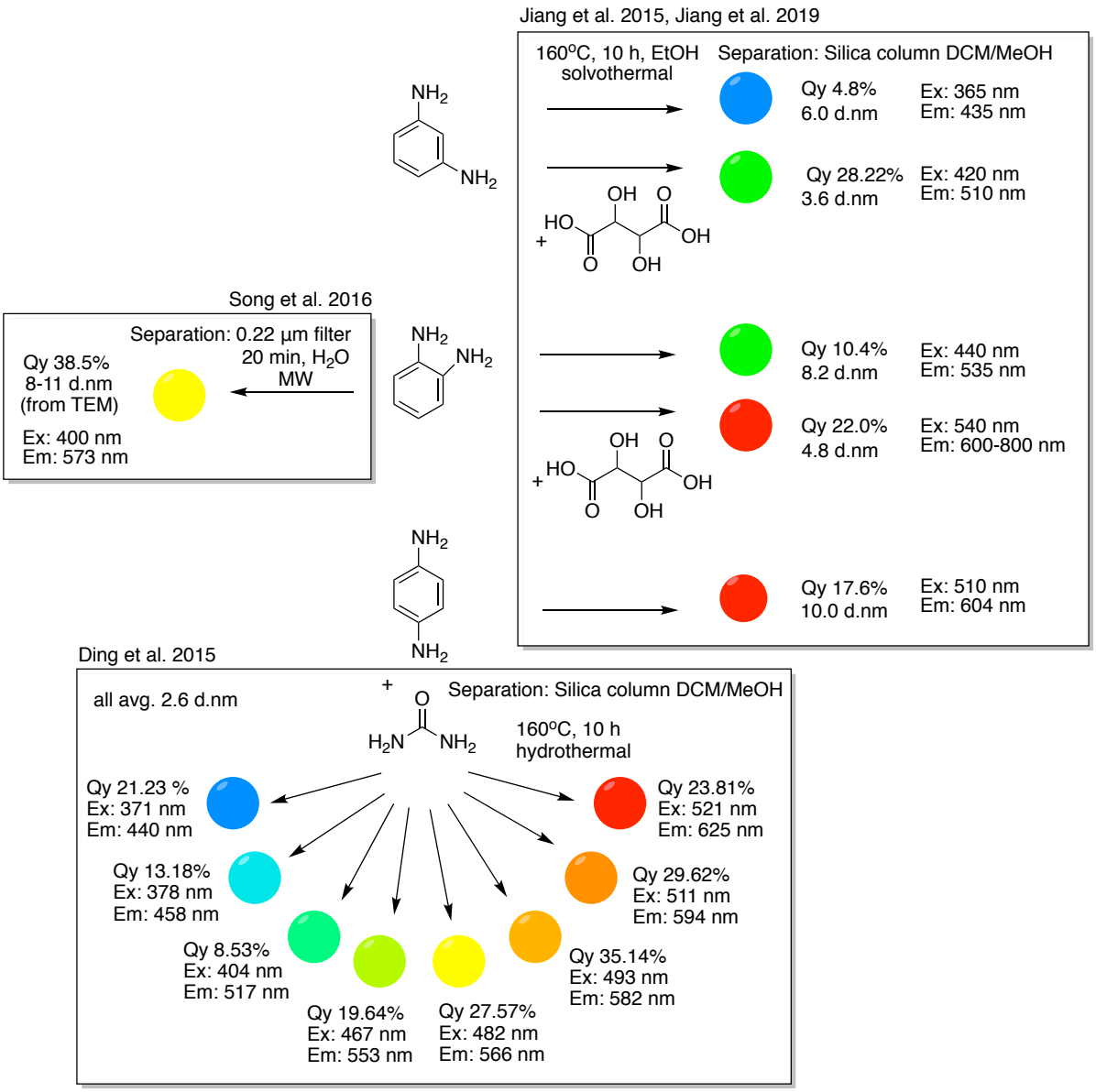

Figure 5.4 Phenylenediamine carbon dot syntheses summary including diameter by DLS (unless indicated), Quantum yield (QY), photoluminescence excitation and emission peak (excitation independent emission). Jiang et al. 2015[249], Jiang et al. 2019[250], Song et al. 2016[251].

The results presented in this chapter are published[253]. The work presented in this chapter was carried out by myself, Stephen Andrew Hill and David Benito-Alifonso (indicated in the text of the results chapter). Stephen Andrew Hill and I share joint first authorship of this publication. Section 5.2 previous work, covers work carried out by Stephen Andrew Hill and are presented in his thesis[83]. All the work in results section 5.4 was carried out by myself.

5.2 Previous work

Previous work carried out by Stephen Andrew Hill[83] in the Galan group looked to modify the blue carbon dot synthesis from section 2.2.1.1 to achieve carbon dots with a more red-shifted spectral profile. This should allow bioimaging to be conducted and intracellular targeting to be observed. Beginning with the material in hand synthesised from glucosamine hydrochloride and TTDDA in a facile domestic microwave synthesis, the protocol was adapted. Following literature president showing phenylenediamine as a good nitrogen doping source, its three isomers were incorporated into the established glucosamine hydrochloride 3-minute microwave assisted carbon dot synthesis (as outlined in chapter 2) instead of TTDDA. The same protocol was followed with a 1:1 w/w glucosamine to phenylenediamine ratio in 20 ml H_2O in a 3-minute microwave assisted reaction. For o- and p-phenylenediamine a blue fluorescent material was afforded which had excitation dependent properties. This suggested poor incorporation of these materials into the nanoparticle as the spectral profile had not been red shifted compared to the original material. The m-phenylenediamine and glucosamine synthesis produced a fluorescence peak at 525 nm with excitation independent properties. A green fluorescent carbon dot was afforded (**FCD-3**) from this synthesis. Stephen Andrew Hill carried out initial characterisation of **FCD-3** as described in section 4.2.1. However, further characterisation revealed that **FCD-3** was made up of mostly two distinct materials termed **4** and **FCD-5**. These materials were characterised separately by myself in the results section 4.4.

5.2.1 Characterisation

Characterising this new CD termed **FCD-3**, dynamic light scattering (DLS) showed a hydrodynamic diameter of 6-9 nm Fig.S5.2 and a zeta potential (ζ) of 12.05 mV Fig.S5.3. High resolution TEM shows that these carbon dots have an amorphous internal structure, as no lattice patterns can be seen at high-magnification. TEM also reported a core diameter distribution between 1.8-3 nm Fig.S51. Quantum yield measurements using fluorescein a standard dye (QY = 0.95) showed that **FCD-3** has a QY of 0.33 which is relatively high compared to other syntheses from m-phenylenediamine. **FCD-3** FTIR data shows key features at 3338 cm^{-1} (O-H/N-H), 1629 cm^{-1} (amide C=O) 1016 cm^{-1} (C-O/C-N), and 612 cm^{-1} (C-Cl). XPS data showed nitrogen was predominantely in the amine/N-heteroatom (3.99.69 eV) form, and carbon in the C-C/aromatic C-C (285.07 eV) form and the C-OH/C-O-/C-N (286.46 eV)

form. Fluorescence data shows **FCD-3** have excitation independent emission peak at 525 nm with λ_{ex} 450 nm (Fig.S5.6). Thermogravimetric analysis found that 50% of mass was lost upon heating to 650 ^{o}C, whilst the remaining 50% was able to withstand extreme heating.

The fluorescence spectrum of **FCD-3**, showed flavin like molecules which share a similar profile with a peak at 525 nm. Furthermore, pyrazine and hydroxyl motifs found shown to be present in **FCD-3** through NMR and fluorescence are found in riboflavin. These molecules may be formed during the synthesis reaction and presented on the CD surface. This is supported by the excitation indepenedent fluroescence mechanism of these carbon dots. Riboflavin-like chromophores formed from the reaction between glucosamine and *m*-phenylenediamine would then be incorporated into the core as well as presented on the surface of the nanoparticle. Furthermore, the basis of **FCD-3** cytotoxicity could be down to ROS generation coinciding with known photosensitiser properties of riboflavin[254] and fructosazine[255] in the literature. They are known photooxidising agents which destroy cellular material. Bhattacherjee *et al*.[255] show that UV-B irradiation combined with either riboflavin, fructosazine or glucoseamine caramel show a greater bacteriocidal effect on E.*coil* than each individually through an ROS mechanism.

Furthermore, results indicating nuclear localisation and DNA targeting offer promise for a novel ROS mediated PDT. Owing to their potential for PDT, **FCD-3** used in combination with cheap and accessible light emitting dioides (LEDs), with 460 nm excitation, were explored for *in vitro* cancer cell toxicity. The literature mechanism of glucoseamine self condensation to form fructosazine and 2,5-deoxyfructosazine likely occurs in this reaction. Fructosazine could then incorporated into the carbon dot core and presented on the surface as a pyrrolic-N group which can mediate a green fluorescence profile.

5.2.2 Cell studies

5.2.2.1 Cytotoxicity – selective uptake

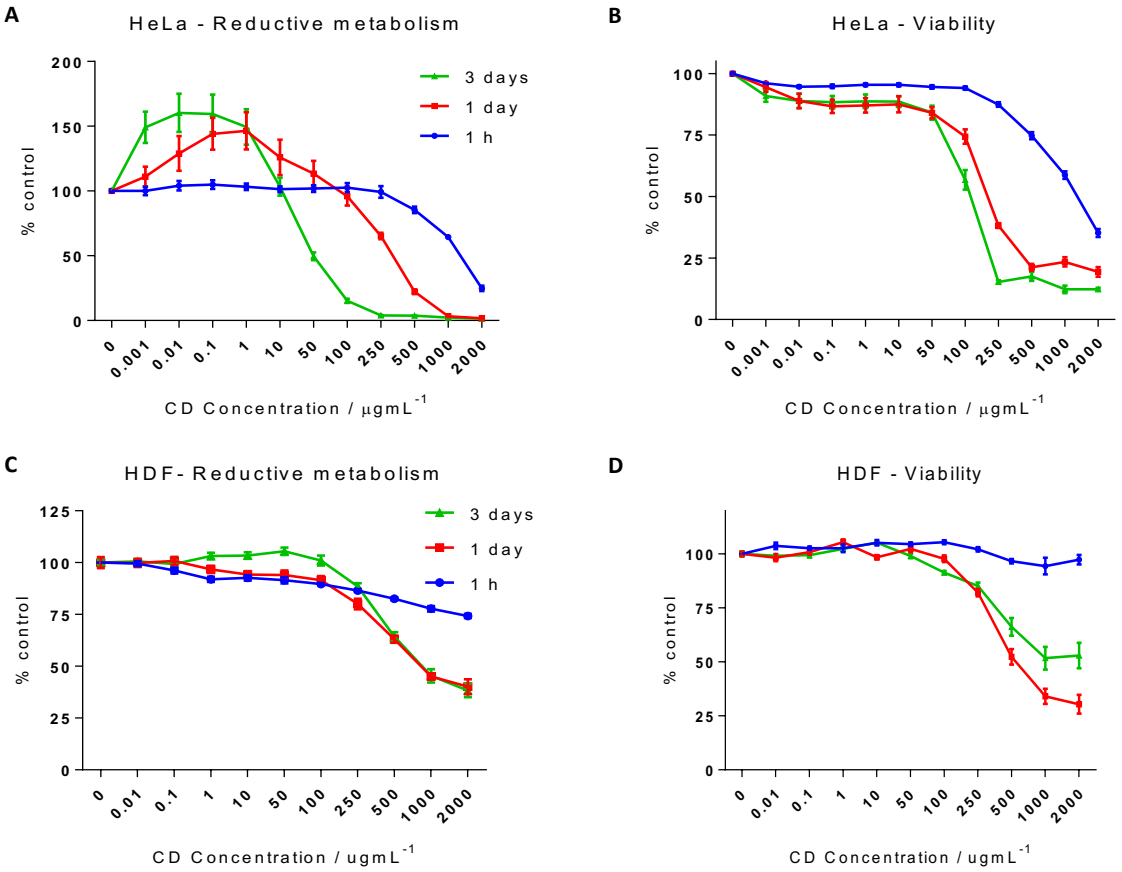

Figure 5.5 ***FCD-3*** *Toxicity and reductive metabolism data in HeLa and HDF cells treated with* ***FCD-3*** *for 2 hrs after 1hr, 1day and 3 days.*

This material named **FCD-3** was assessed for its cytotoxicity and potential for bio-application in cancer cell line HeLa and healthy cell line HDF. **FCD-3** was incubated with HeLa and HDF for 1 hour, 1 day and 3 days before toxicity experiments were performed. Figure 5.5 shows that **FCD-3** is more toxic to HeLa than HDF, likely due to the greater uptake rate and nuclear localisation. However, **FCD-3** is relatively non-toxic considering the high dosage >100 ug ml^{-1} requried at 3 days to induce cell death in both cell lines. The starting material m-phenylenediamine has associated toxicity which when incorporated into **FCD-3** is relatively non-toxic.

5.2.2.2 Selective uptake

Comparing the cellular uptake of **FCD-3** in HeLa and HDF showed that these particles are taken up more quickly by cancer cells 67% than the healthy HDF cell line 20% possibly passively. Interestingly **FCD-3** was observed in the nucleus of HeLa after 1 minute, and was localised there for up to 30 minutes before fluorescence in this area decreased. This fast nuclear targeting was not seen in HDF either through passive or active uptake. Furthermore, over a 2 hour period **FCD-3** was observed not to localise in any other organelles, observed through co-localisation experiments and confirmed with Pearson Correlation values indicating no corrolation. Values were, Mitotracker -0.0979, Late Endosome -0.0915, Early Endosome -0.0828, Golgi -0.0608, Lysosome 0.461, whilst Nucleus was 0.743. These results suggest **FCD-3** as a specific nuclear, cancer cell line targeting particle.

5.2.2.3 Localisation

Flow cytometry was used to detect FRET interaction between **FCD-3** and DNA dyes in vitro to assess **FCD-3** potential for nuclear targeting. **FCD-3** was again incubated for 2 hours in HeLa and HDF before nuclear permeating DNA dyes Enzo NuclearID-Red or DRAQ-5 were added to the cells and FRET was measured in vitro. The donor fluorescence was used as an indicator of FRET efficiency. The percentage decrease in donor signal was greater in HeLa then HDF, 82% compared 50% (Enzo) and 60% compared with 44% (DRAQ-5). This confirms results that **FCD-3** targets cancer cells and the nucelus over healthy cells and shows promise as a DNA drug delivery agent.

5.2.2.4 Killing mechanism

The ROS generated upon the treatment with **FCD-3** were first assessed to determine if this mechanism is the basis for cytotoxicity and hence PDT. If this is not the case then the hypothesis that **FCD-3** acts as a strong photothermal converter should be investigated through temperature experiments and its potential for PTT explored. Hypothesised local temperature heating effect should be investigated in the context of LED irradiation as this could be an accessible therapy treatment.

Measuring intracellular temperature increase is practically very difficult, so experimentally a number of markers such as ATP depletion, ROS generation and metabolite production can be measured alongside cytotoxicity to help give a better overview of the potential mechanism of action. Furthermore, in practice the local temperature around cells is measured as an indication of intracellular temperature increase[240]. To assess the killing mechanism of LED-irradiated **FCD-3** treated

cells, three experiments were conducted. Anaylsis of the reactive oxygen species (ROS) levels using dihydroethidium (DHE) in section 4.2.2.5, **FCD-3** metabolite production effects (5.2.2.6) and ATP depletion studies in a luciferase-luciferin based assay in 5.2.2.7.

5.2.2.5 ROS levels

ROS levels in vitro were detected through the loss in fluorescence of DHE and conducted under the same conditions as toxicity experiments in sectionn 4.2.2.1. **FCD-3** concentration of 1, 10, 50, 100 and 500 µg ml^{-1} were assessed after LED irradiation times of 30, 60 and 90 min and compared to controls (untreated cells and cells exposed to **FCD-3** but without LED irradiation), ROS levels were assessed after 1hr and compared to control. In HeLa, only at 500 µg ml^{-1} after 90 min was a reduction of 50% fluorescence measured after 1 hr, which does not corrolate with the toxicity data. Toxicity data shows that even with irradiation times of 30 & 60 min, cell viability decreased by 50% and 60% after 1 hr which was not supported by ROS levels (Figure 5.7). In HDF, similarly a lack of ROS levels at the harshest condition did not produce a significant reduction in DHE fluorescence, supporting a lack of ROS associated killing.

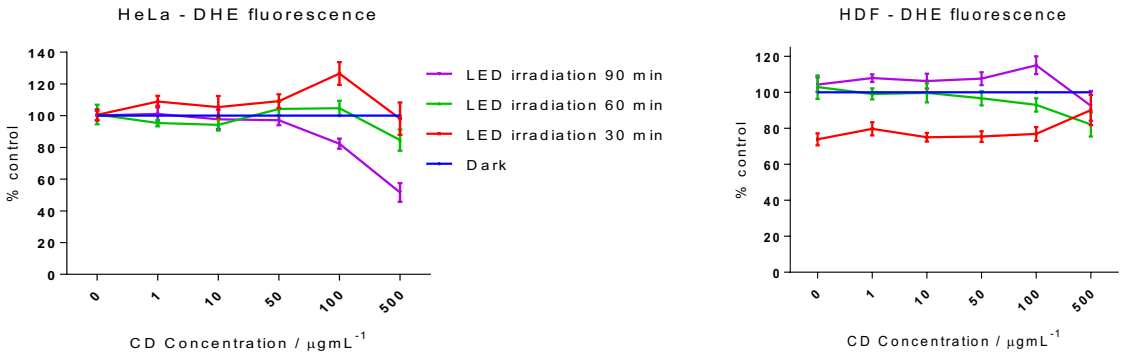

*Figure 5.6 DHE fluorescence as a measure of ROS in HeLa and HDF cells treated with **FCD-3** and LED irradiation for 30, 60 and 90 mins after 1hr.*

5.2.2.6 Metabolite production

To ascertain if metabolic products of **FCD-3** were causing toxicity upon LED-irradiation, the cell lysate post irradation was reintroduced to naïve HeLa and HDF cells and the toxicty measured. Again, under the same experimental conditions (including LED-irradiation) toxicity after 1hr on HeLa was lower, 40% than without lysate 60%. HDF showed negligable toxicty compared to control upon lysate incubation. Therefore, no additional cytotoxicty was induced by the lysate or **FCD-3** metabolites after 1 hr. NMR studies of **FCD-3** post LED-irradiation observed no structural changes supporting this.

5.2.2.7 ATP depletion assay

Indicating cancer cell growth and metabolic activity, high levels of HeLa cellular ATP can be observed through a depletion assay. Through a luciferase-luciferin assay the amount of cellular ATP was measured at 1hr, 1 day, 3 days. In this assay, luciferin is catalysed to oxyluciferin using one molecule of ATP in a visbile light (510 nm) producing reaction. At concentrations of 1, 10, 50, 100 and 500 μg ml^{-1}, **FDC-3** treated HeLa cells were irradiated for 90 mins before cell lysis and the assay was carried out. Relative to control, treatment with 1 μg ml^{-1} induced a 20% ATP level drop after 1 hr post irradiation. Furthermore, a decrease of 65 and 75 % after 1 day and 3 days respectively was observred after treatment with 1 μg ml^{-1} **FCD-3**. This trend of **FCD-3** concentration dependent ATP depletion coincides with reductive metabolism and cytotoxicity assay results under the same conditions (Figure 5.7). This result confers that **FCD-3** treatment combined with LED-irradiation results in cytotoxicity as a function of ATP depletion.

5.2.2.8 LED-irradiation cytotoxicity

Toxicity of **FCD-3** was assessed using Calcein AM and Alamar blue (AB) assays and this data was compared with toxicity data post LED-irradiation to assess **FCD-3** capability for photothermal therapy. For LED-irradiation studies, under the same conditions toxicity was assessed in the same way having introduced a 30, 60 or 90 minute LED-irradiation (λ_{ex} 420 nm) step. Directly after this step, the media was exchanged to remove non-internalised material before an incubation period and cytotoxicity assays were conducted.

For HeLa, 30 minute LED-irradiation had a toxic effect with an IC_{50} of 10 μg ml^{-1} after 1 day compared to 250 μg ml^{-1} without irradiation. Upon longer irradiation time the toxicity effect was increased and as before longer exposure up to 3 days had greater toxicity effect. Reductive metabolism followed similar trends. However, for HDF this was not the case, under even the longest LED-irradiation time (90 minutes) the toxicity did not exhibit a dose-resposnse curve within the concentration range measured (up to 500 μg ml^{-1}). Furthermore, with any of 30, 60 or 90 minute LED-irradiation, after 3 days the viability is greater than control showing cell population survival similar to non-irradiated controls. This is likely due to the lower uptake of **FCD-3** by HDF and illustrates the non-harmful effect of the LED-irradation by itself. These results show that that **FCD-3** has a cancer cell selective toxic effect which is increased by up to 25 times upon LED-irradiation.

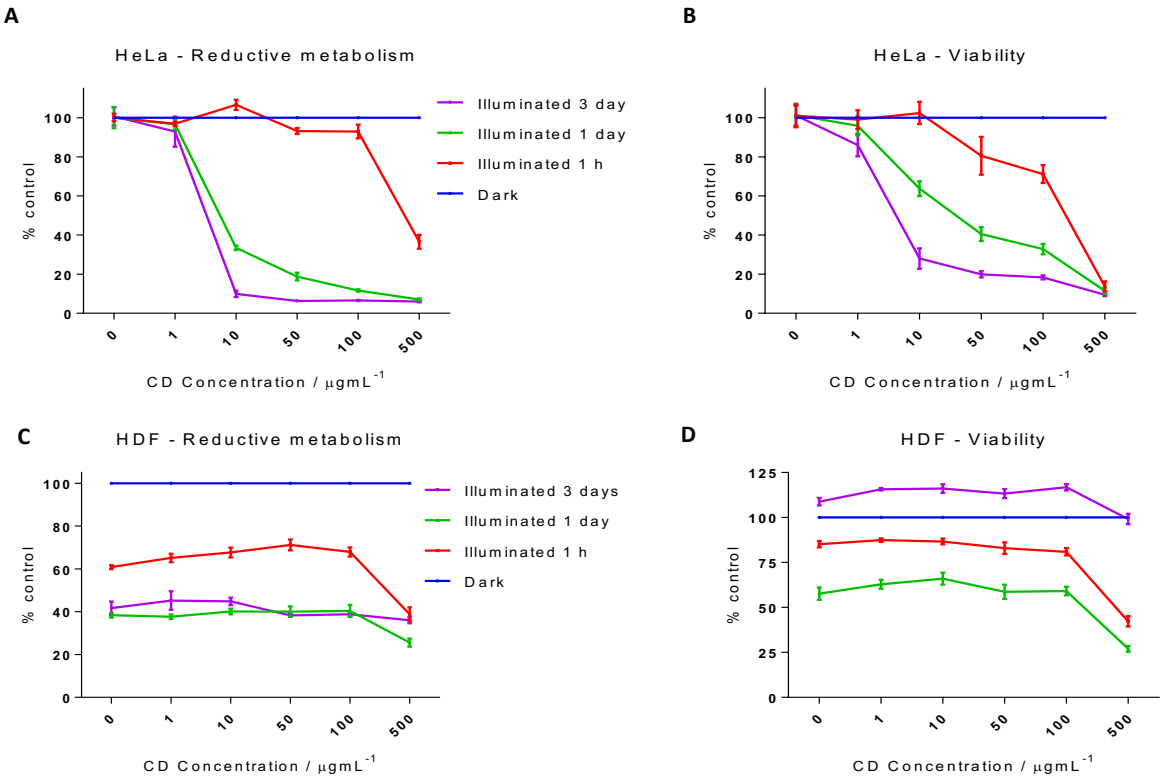

*Figure 5.7 Toxicity and reductive metabolism data for HeLa and HDF cells treated with **FCD-3** for 2 hrs and LED-irradiation for 90 mins after 1hr, 1day and 3 days. A) HeLa reductive metabolism B) HeLa viability C) HDF reductive metabolism D) HDF viability.*

5.3 Aims

Having outlined the results conducted by Stephen Andrew Hill, we aim to understand the effects observed in more detail and the underlying key features of the CD responsible for the different intracellular uptake and killing mechanism, which is not observed with the blue emissive long linker CDs (Chapter 2).

Initial experiments involved size exclusion chromatography (SEC) to investigate if there were carbon dots with distinct spectral profiles within a heterogeneous population. This would be supported by Ding *et al*. where they were able to isolate 8 carbon dots synthesised from p-phenylenediamine with distinct spectral profiles from one reaction mixture[252]. Furthermore, Jiang *et al.* saw larger nanoparticle diameter (6-10 nm) correlated with a more red-shifted fluorescence profile in carbon dots synthesised from the 3 isomers of phenylenediamine[250]. Hence, our material having a diameter distribution between 6-9 nm could feasibly be composed of CDs with differing fluorescence profiles which together produce a fluorescence peak at 525 nm.

Initial SEC interestingly fractionated our material into 2 main fractions: the small molecule 2,5-deoxyfructosazine termed **4** and a carbon dot termed **FCD-5**. Thermogravimetric analysis (TGA) data

suggested that there is organic material (around 50%) of the nanoparticle which can be destroyed by heating to 650 °C which is not incorporated in the core, supporting a core/corona model as is common with carbon dot structure with a tuneable surface. Hence, we aimed to characterise further the surface groups, determining structure and hopefully being able to correlate it to the LED induced toxicity observed.

In our work, we explored the importance of 2,5-deoxyfructosazine and its photothermal therapeutic effect when associated with a carbon dot having been synthesised in-situ as part of a facile carbon dot microwave reaction. Literature evidence suggests that passivating the surface of carbon dots leads to improved quantum yield and in some cases more red-shifted spectral properties. 2,5-deoxyfructosazine is thought to act as a passivating agent and in our system we aim to assess the fluorescence profile of our carbon dot with and without the surface associated small molecule. Furthermore, we aim to explore the implications of the surface functionality on the cytotoxicity of this material. Isolating the small molecule from the surface of the carbon dot, we were able to assess the toxicity of each component separately.

By understanding the mechanism of killing of **FCD-3** we aim to determine if our system is working through a PDT or PTT pathway or a combination of both. The fluorescence window of our material would suggest PDT methods, generating ROS as the basis for cytotoxicity. However, literature evidence also supports the idea that 2,5-deoxyfructosazine can provide energy levels within the spectral band gap of the carbon dot, facilitating energy release in the form of heat which would support a PTT pathway. Furthermore, results by Stephen Andrew Hill[256] indicate that ROS weren't generated and thus it suggests this mechanism might not be the basis for toxicity suggesting the nanoparticle confers good photothermal conversion and offers potential for PTT which would be novel at visible wavelengths.

5.4 Results and discussion.

5.4.1 FCD-3 Synthesis

Carbon dots were synthesised according to the protocol developed in the Galan group previously as described in Stephen Andrew Hill's thesis[83], as seen in scheme 5.1. Glucosamine.HCl and *m*-phenylenediamine starting materials were combined in a 1:1 H_2O:EtOH solvent mixture and heated in a domestic microwave reaction for 3 mins. A brown viscous oily material was afforded, which was green fluorescent under UV light. The glucosamine.HCl was included in this synthesis as work from our group and others[62] was shown to be a good starting material for carbon dot formation as also seen when accessing AmCD **16** synthesis in chapter 2 (section 2.2.1.1). The m-phenylenediamine component was added as it has known doping effects attributed to its nitrogen content and has been used in other literature carbon dot syntheses. Initial purification of **FCD-3** entailed dialysis purification of the crude mixture using a 10,000 MWCO cellulose membrane in H_2O overnight. **FCD-3** was freeze dried before further use. **FCD-3** was functionalised with succinic anhydride to afford acid functional groups on the surface, followed by amide coupling with 1-amino mannose in an analogous manner to that carried out with AmCD **16** as shown in chapter 2 (section 2.2.1.1 and 2.2.1.5 respectively)[1].

[1] glycan functionalisation was not carried out in this work.

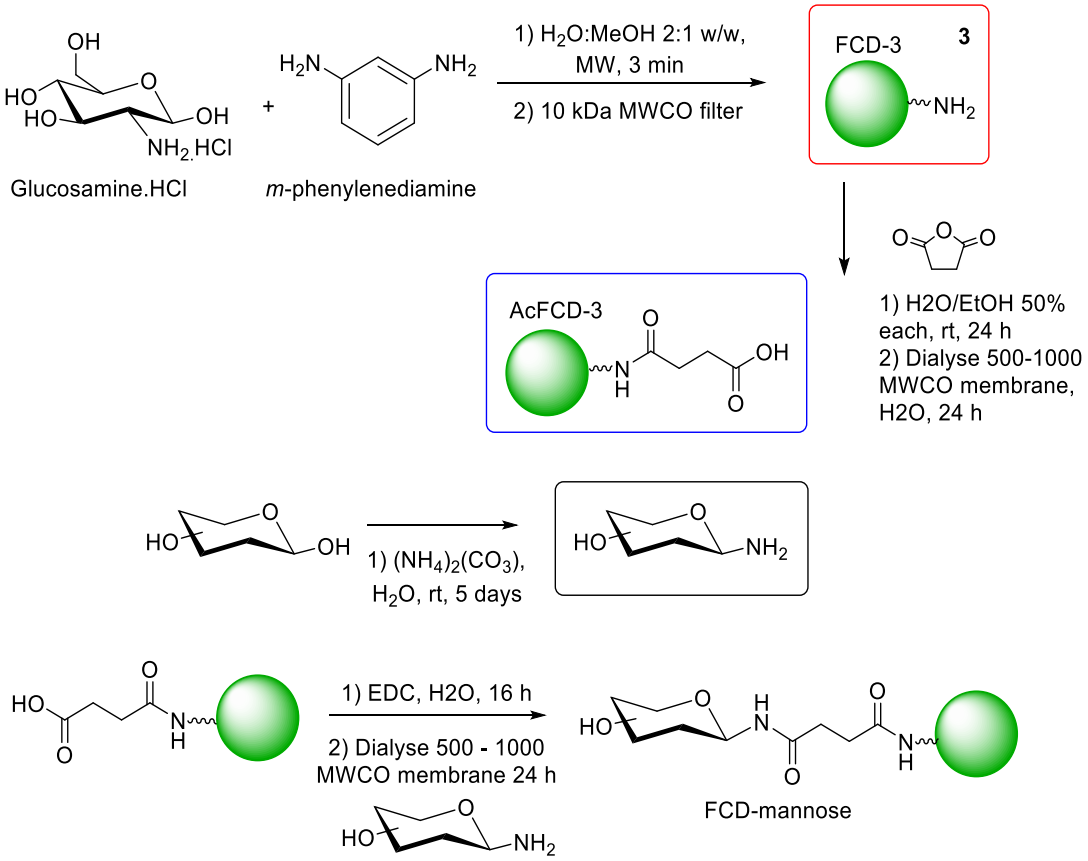

Scheme 5.1 ***FCD-3*** *synthesis*

Further purification was carried out of **FCD-3** to better understand the composition of the green CD. To that end, **FCD-3** was eluted through a sephadex G15 size exclusion column (eluting MeOH) and two main fractions were observed with numerous other smaller fractions (Scheme 5.2). The two main fractions were collected. The first was a material weakly bluish-green fluorescent by eye under UV light. The second was a green fluorescent (under UV light) material. Both fractions were further characterised by NMR and the first fraction was termed **FCD-5**.

From our initial evaluation and purication of **FCD-3** , it became apparent that the nanomaterial was comprised of an amorphous core with a small molecule or molecules coating the surface. Size exclusion choromatography (G15 Sephadex) was then used to purified the small surface molecules from bigger fragments and the core. This afforded two fractions, a green fluorescent fraction which upon further NMR characterisation was assigned to 2,5-deoxyfructosazine (**4**) and a blue fluorescent fraction which from DLS measurements gave similar size distribution 9-11 nm to the original **FCD-3**, hence we labelled it as the nanoparticle core (**FCD-5**).

5.4.2 FCD-3, 4 & FCD-5 Characterisation

4.4.2.1 Surface group determination

FCD-3, **FCD-5** and **4** were further characterised using a battery of techniques.

^{1}H NMR was used to identify **4** (Scheme 5.2) as 2,5-deoxyfructosazine which had identical NMR shifts as a commercial sample (Figure 5.9a). Hence, the main component in **FCD-3** ^{1}H NMR spectra (Scheme 5.2) is 2,5-deoxyfructosazine. Compound **4** appears to be also present on the surface of **FCD-5** in trace amounts compared to that present on the surface of **FCD-3**.

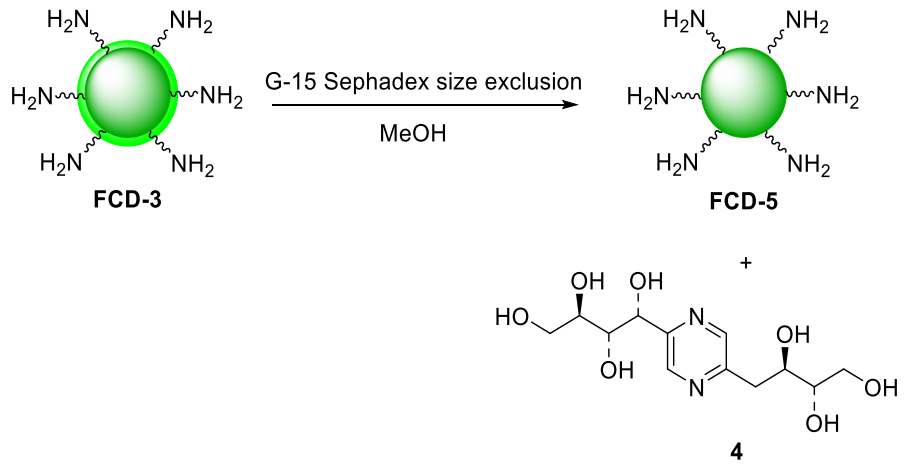

*Scheme 5.2 Purification of **FCD-5** and **4** from **FCD-3***

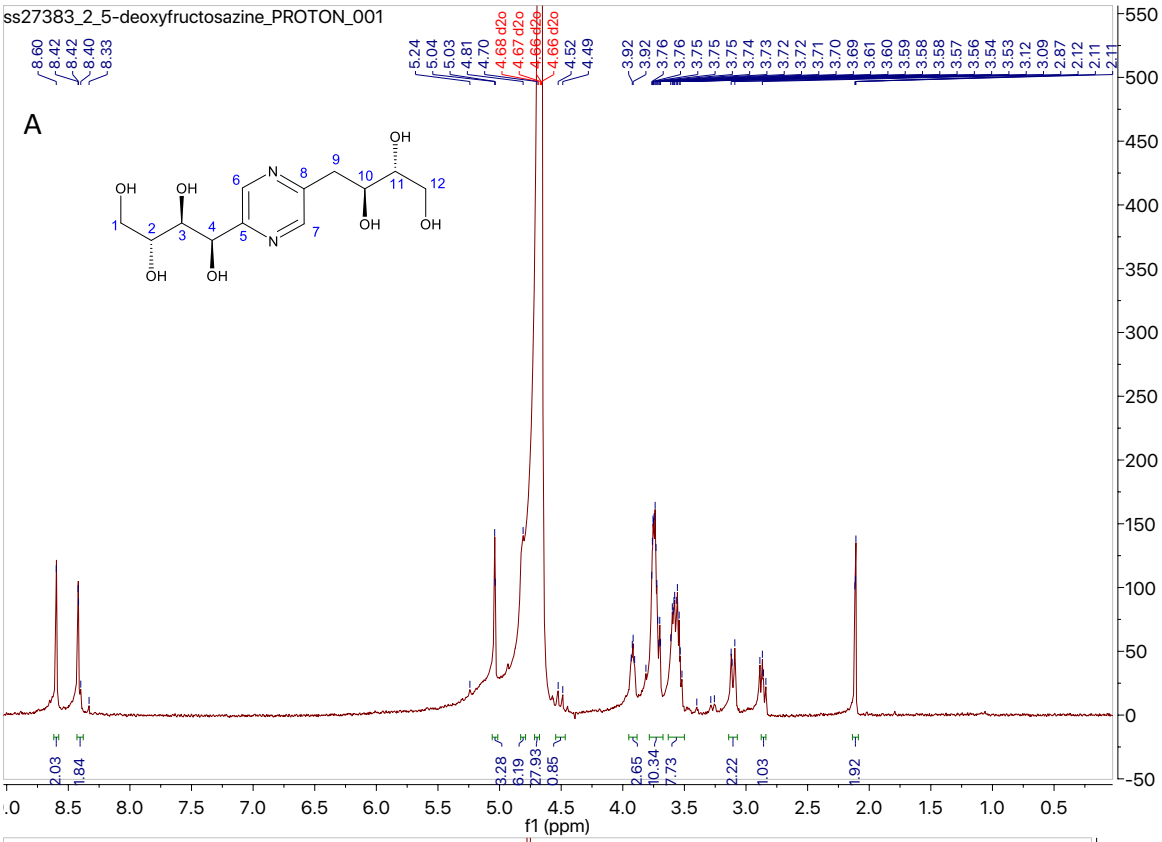
ss27383_2_5-deoxyfructosazine_PROTON_001
A
f1 (ppm)

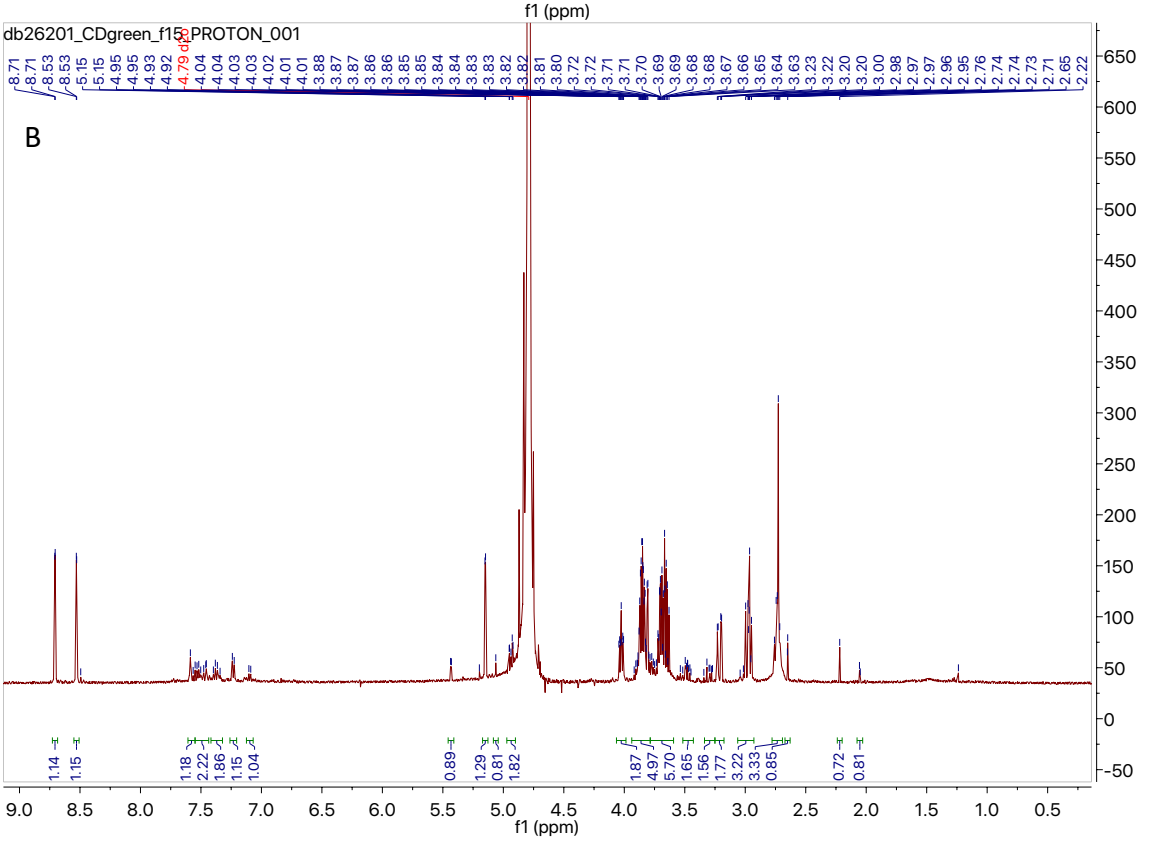
db26201_CDgreen_f15_PROTON_001
B
f1 (ppm)

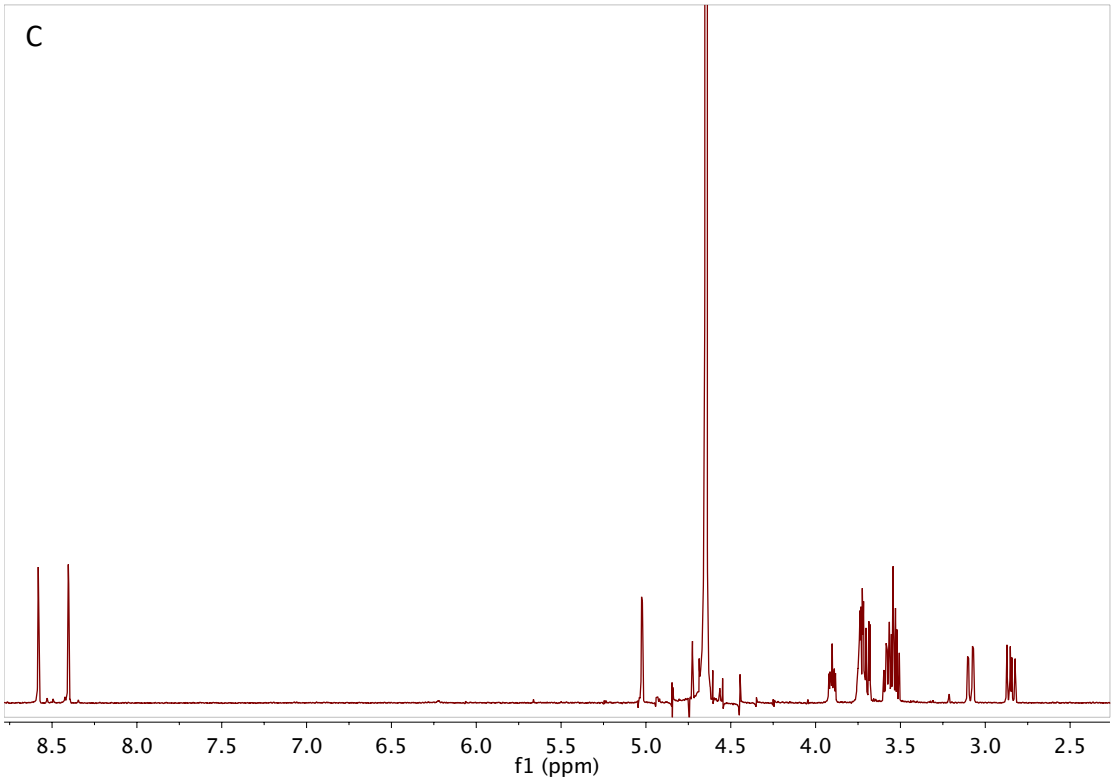

*Figure 5.8 A) ^{1}H NMR (500 MHz) of commercial 2,5-deoxyfructosazine B) ^{1}H NMR (500 MHz) of **4** C) ^{1}H NMR (500 MHz) of **FCD-3.***

5.4.2.2 Proposed Mechanism of 2,5-deoxyfructosazine formation

As previously mentioned, carbohydrates such as glucosamine have been used as a precursor for a number of carbon dot syntheses to date (section 1.4.2.2). Bhattacherjee *et al*[257]*.* showed that in a self-condensation reaction fructosazine is formed from glucosamine (Scheme 5.3). The reaction between an amine group and carbohydrates to form heterocyclic molecules which are known as advanced Maillard reaction products[255] such as fructosazine and 2,5-deoxyfructosazine. Both fructosazine and deoxyfructosazine have been found in foods including roasted peanuts and caramel[255], while the use of 2,5-deoxyfructosazine in beer production has been patented as a colourless flavour additive and is made in a controlled reaction of glucosamine[258].

The family of advanced Maillard reaction products are known to act as photosensitizing molecules in combination with UVA and UVB light to either produce free radicals or form singlet state $^{1}O_2$ which reacts locally with proteins and lipids in the cell. This is thought to be the basis for bactericidal toxicity observed in E. coli and B. subtilis upon UVB irradiation[255]. Furthermore, Bhattercherjee *et al.*[259]

showed that heat resistant E. Coli can be killed using fructosazine, which is an important consideration as strains with both virulence and heat-resistance could evolve[259].

Furthermore, studies in mammalian Caco-2 cell line from the intestine showed that fructosazine was readily taken across the epithelial barrier facilitated by natural hexose transporters GLUT1 GLUT2 and SGLT. Glucose transport via GLUT1 is known to rely on the hydroxyl groups and hydrophobic pyranose ring interacting in the protein in a non-specific way. Hence, it is proposed that fructosazine navigates the channel via the same interactions due to similar structural motifs[257].

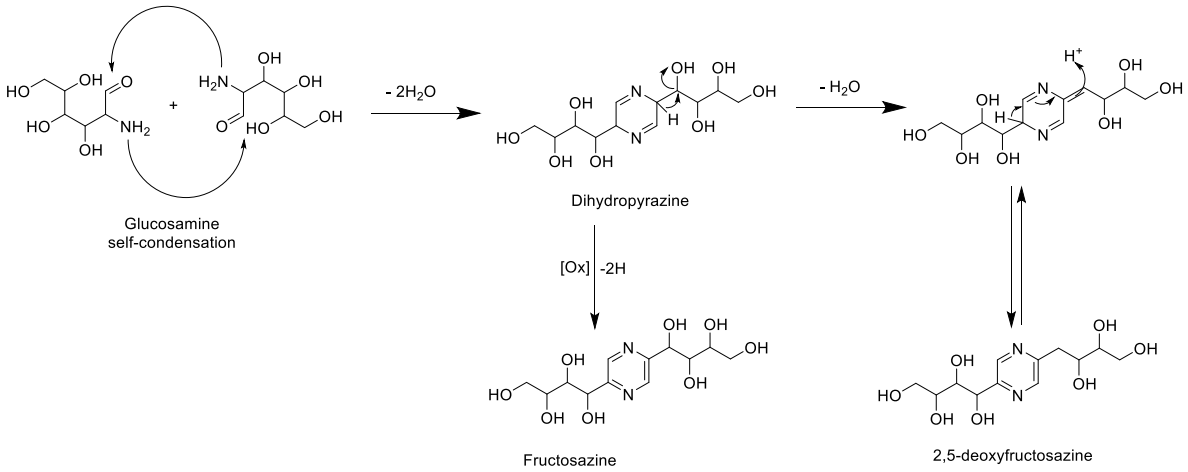

Scheme 5.3 Mechanism of fructosazine and 2,5-deoxyfructosazine formation from glucosamine.

Using ^{1}H NMR with an internal standard, the amount of 2,5-deoxyfructosazine on the surface of **FCD-3** and in the sample **4**, was calculated comparing with commercial 2,5-deoxyfructosazine. For each mg of 2,5-deoxyfructosazine in **FCD-3**, **4** had 2.14 mg. For **FCD-5**, in NMR the 2,5-deoxyfructosazine peaks were not visible. Hence the concentration was assumed to be negligable. FTIR data showed that **FCD-3** contained a peak at 3338 cm^{-1} which correspond to O-H and N-H bonds. These peaks were not present in **FCD-5**. This suggested amine functional groups on the surface could be present on the surface of **FCD-3** as seen with AmCD **16**.

5.4.2.3 DOSY of **FCD-3**, **4** and **FCD-5**

Having isolated and identified the structure of **4** from the surface of **FCD-3** further characterisation was carried out in the form of DOSY to investigate how 2,5-deoxyfructosazine was associated to the carbon dot or if it was a separate molecule. Diffusion ordered spectroscopy (DOSY) can be used to determine the diffusion coefficient of a molecule or particle in solution. The diffusion coefficient describes the molecules translational movement and hence the coefficient describes the speed of the

molecule. If a molecule or particle is bound to another particle or molecule in solution, then the diffusion coefficient will be retarded. This is therefore useful to investigate binding to nanoparticle. DOSY has been used in this way for AuNPs labelled with dye to observe whether conjugation has occurred[260]. DOSY was shown to be used to measure AuNPs 2.7 nm and 4.6 nm in size through a thiolate group[261]. Polymers up to 100 nm have been studied by DOSY, but for metallic and semiconductor particles they should be within the 1-5 nm range[262]. The diffusion coefficient of 2,5-deoxyfructosazine in the samples **FCD-3** and **4** were compared to observe if the presence of carbon dot in **FCD-3** retarded the diffusion coefficient compared to **4**.

DOSY experiment a **FCD-3** showed that 2,5-deoxyfructosazine **4** was associated with the core in solution as the core and 2,5-deoxyfructosazine shared the same diffusion coefficient of 3.83 $x10^{-6}$ cm^2 s^{-1} in **FCD-3** (Table 5.1). 2,5-deoxyfructosazine was monitored by H^1 peak at 8.53 and 8.71 ppm and CD was monitored by the peak at 3.22 ppm (Figure A.38). Diffusion coefficients which indicate no interaction between a nanoparticle and small molecule would be expected to be greater than an order of magnitude different form each other.

Commercial 2,5-deoxyfructosazine and peaks corresponding to 2,5-deoxyfructosazine in the sample **4** had diffusion coefficients of 3.56 $x10^{-6}$ cm^2 s^{-1} and 4.11 $x10^{-6}$ cm^2 s^{-1} respectively. These values are not an order of magnitude faster that seen in **FCD-3** suggesting that the smaller molecule independently diffuses at a similar speed as the NP associated form. The commercial 2,5-deoxyfructosazine diffuses slightly faster than the 2,5-deoxyfructosazine in **4** which reflects the small amount of CD remaining in this sample with which it would interact. Overall, the DOSY data was not conclusive, and further experiments are needed to confirm this interaction.

Sample	*Diffusion coefficients / x 10^{-6} cm^2 s^{-1}*	*Water diffusion coefficient/ x $10^{-6}cm^2$ s^{-1}*
2,5deoxyfructosazine	3.56	1.63
FCD-3	Fructosazine: 3.83 CD: 3.83	1.63
FCD-5	5.50	1.52
4	4.11	1.63

*Table 5.1 DOSY determined diffusion coefficients of **FCD-3,4, FCD-5** and commercially bought 2,5-deoxyfructosazine.*

5.4.2.4 TEM

Transmission electron microscopy (TEM) was carried out on a batch of **FCD-3** different to that used for the work carried out by Stephen Andrew Hill[83] and at lower resolution (1200 kV). A new batch was synthesised to confirm synthesis reproducibility and TEM allowed CD size property to be assessed between batches. Mean dimeter by TEM is 7.1 ± 4.8 nm standard deviation (SD) (a bandpass filter and thresholding were applied before diameter was determined using Fiji software) as measured from images in figure 5.9. This diameter is larger than that measured by Stephen Andrew Hill[83], perhaps in part owing to the resolution, the variation in purification, TEM sample preparation and the way the diameter was measured in Fiji. TEM therefore shows some slight difference in particle size. However, NMR data matched indicating the same material was synthesised between batches.

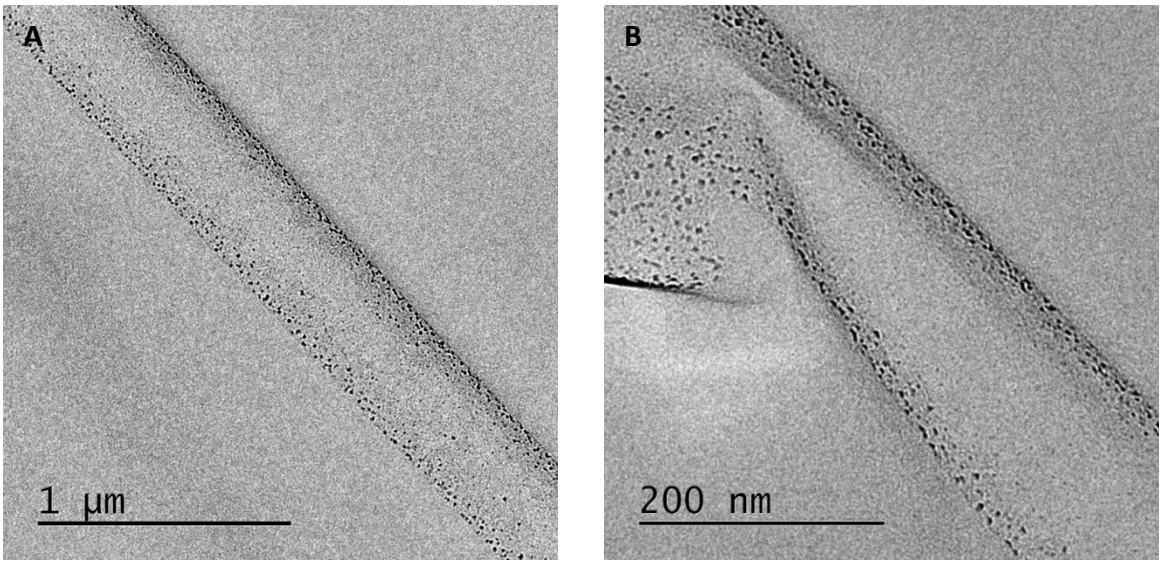

*Figure 5.9 TEM characterisation of **FCD-3**. A)&B) TEM images of **FCD-3** (1200 kV). Mean diameter 7.14 ± 4.76 nm (SD). N=704 (see supplementary figure S5.1. for histogram of size distributions).*

5.4.2.5 DLS & Zeta potential

DLS (number %) measurements show **4** and **FCD-5** as aggregated with hydrodynamic diameters of 27.2 ± 0.9 nm and 159 ± 9 nm respectively (Fig 5.10a). These values are all much larger than 8.5 ± 4.2 nm observed for **FCD-3**. This value supports TEM determined diameter of 7.14 nm ± 4.76 nm (SD) as it is the same order of magnitude but a large value due to the hydration layer observed in DLS. **FCD-5** and **4** are likely to self-aggregate in H_2O once separated from the nanoparticle **FCD-3**. Zeta potential measurements of **FCD-3**, **4** and **FCD-5** are 8.53 ± 0.79 mV, 14.2 ± 1.9 mV and -3.52 ± 1.5 mV. The surface charge of **FCD-3** reflects the measured charge of **4** and **FCD-5** in H_2O, i.e. it has a zeta potential

in between the two, meaning the charge of both **FCD-5** and **4** likely contribute to the surface charge of **FCD-3** (Fig 5.10b). The hydrodynamic diameter measured for **FCD-3** 8.523 ± 4.21 nm, in this batch is within the range 6-9 nm as measured by Stephen Andrew Hill in a different batch. The zeta potential 8.53 ± 0.79 mV and that for the Stephen Andrew Hill batch 12.05 mV are similar in that they are positive and large. However, the difference indicates difference between batches which may reflect the amount of 2,5-deoxyfructosazine on the surface which is controlled by the reaction conditions.

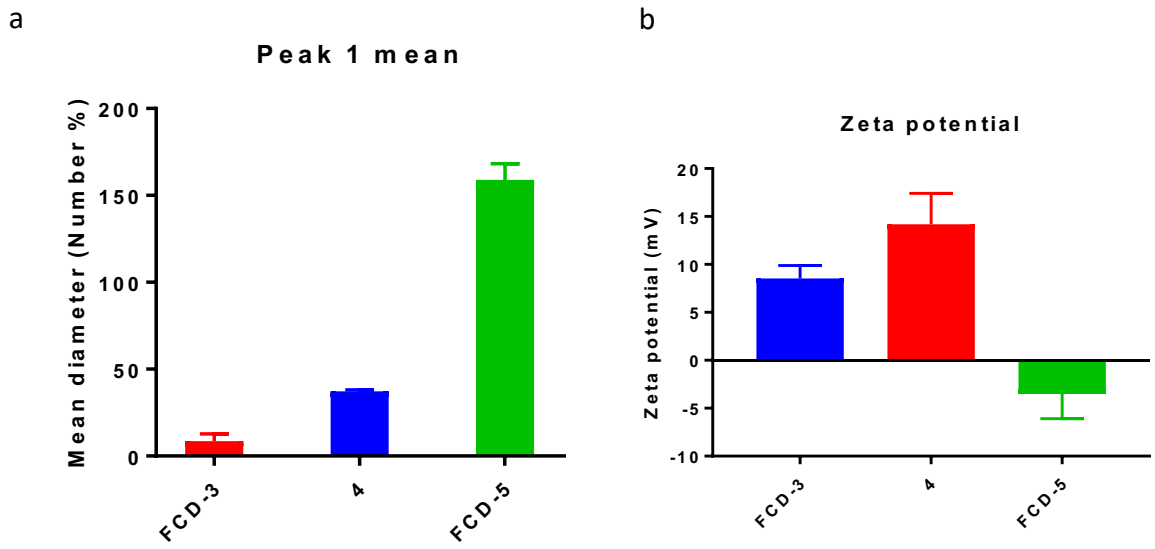

*Figure 5.10 a) DLS and b) Zeta potential of **FCD-3**,**4** and **FCD-5**.*

5.4.2.6 UV-Vis & Fluorescence spectra

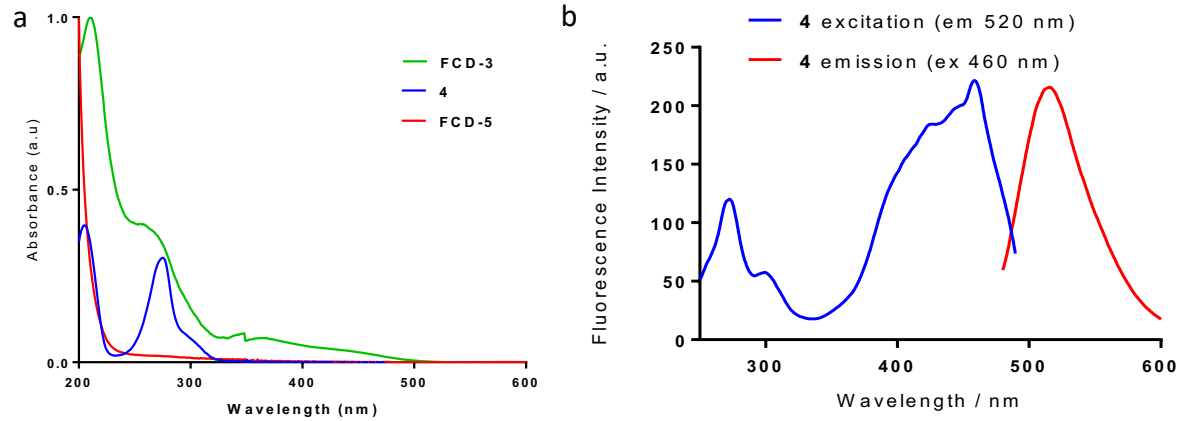

*Figure 5.11 a) UV-vis absorption spectra for **FCD-3**, **4** and **FCD-5**. b) Fluorescence excitation and emission spectra of **4**. Peak emission observed at 525 nm.*

UV-vis absorption spectra Figure 9 presents data for **FCD-3**, **4** and **FCD-5**. **FCD-3** shows a peak at 280 nm corresponding to $\pi \rightarrow \pi *$ transitions from C=C/C=N bonds and $n \rightarrow \pi *$ transitions from C=O/C=N. These features are common to many carbon dots found in the literature.[239,241] Furthermore, there is a tail toward 600 nm which corresponds to multiple optical states found in CD's. **4** shows a similar spectrum to that of 2,5-deoxyfructosazine (Figure. 5.11) owing to the 2,5-deoxyfructosazine in the sample, with a peak at 280 nm whilst CD associated peaks are not observed. **FCD-5** does not absorb much within the range 250-600 nm. All spectra show a strong absorption band < 230 nm indicating some surface aromaticity on the CD and from the fructosazine.

Fluorescence spectra of **4** seen in figure 5.11, reveals a similar excitation and emission profile to that of **FCD-3**, with an excitation peak at 250 nm and emission peak at 525 nm. This reflects that there is some CD core remaining in **4** and the fluorescence profile is made up of both 2,5-deoxyfructosazine and CD core emission.

5.4.2.7 FTIR

FTIR was carried out on **FCD-3**, **4** and **FCD-5** to investigate the surface functional groups present on the carbon dot surface and differentiate which peaks are from 2,5-deoxyfructosazine and the core (Figure 5.12). **FCD-3** had peaks at 3338 cm^{-1} (O-H stretch/N-H bend), 1629 cm^{-1} (O-H stretch/N-H stretch), 1016 (C=O stretch) cm^{-1} and 612 cm^{-1} (C-Cl stretch). **4** has peaks at 3323 cm^{-1} (O-H stretch/N-H bend), 1634 cm^{-1} (C=C stretch),1434 cm^{-1}(O-H bend), 1040 cm^{-1} (CO-O-CO stretch), 567 cm^{-1} (C-Cl stretch). **FCD-5** has peaks at 1614 cm^{-1} (C=C stretch/C=N stretch), 1326 cm^{-1}, 987 cm^{-1}, 832 cm^{-1} and 695 cm^{-1} (C-Cl stretch).

Surface quantification through fluorine NMR (section 5.4.2.1.1) shows that **FCD-3** has amine groups on the surface which are attributed to the 3338 cm^{-1} peak. **FCD-5** does not have this peak suggesting the core does not have amines on the surface. The same peak is present in **4**, however, this is likely due to O-H groups of the molecule. The peak at 1324 cm^{-1} unique to **FCD-5** could be aromatic amine (C-N) or phenol (O-H) which are both possibilities as carbon dots are known to have both sp^2 and sp^3 enriched domains on the surface.

a

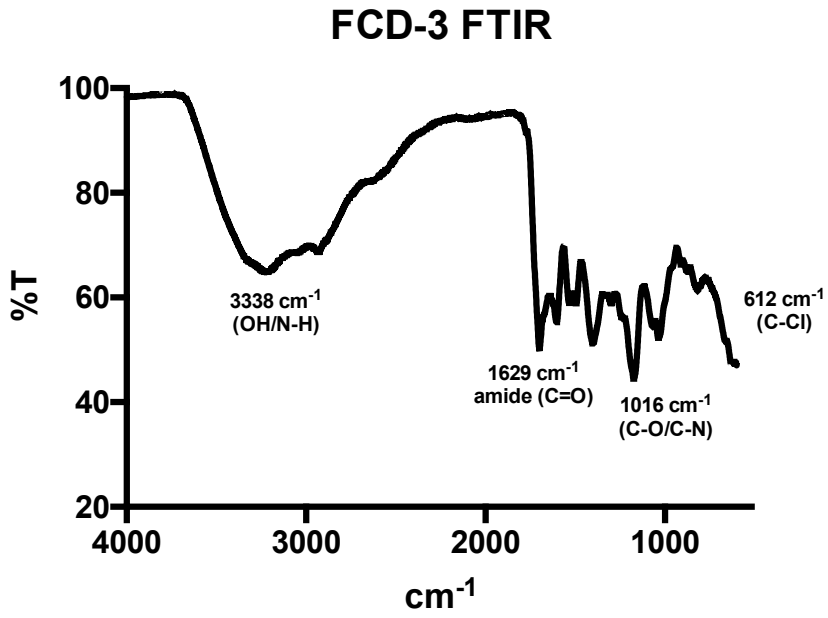
FCD-3 FTIR
100
80
60
40
20
%T
3338 cm-1
(OH/N-H)
1629 cm-1
amide (C=O)
1016 cm-1
(C-O/C-N)
612 cm-1
(C-Cl)
4000
3000
2000
1000
cm-1

b

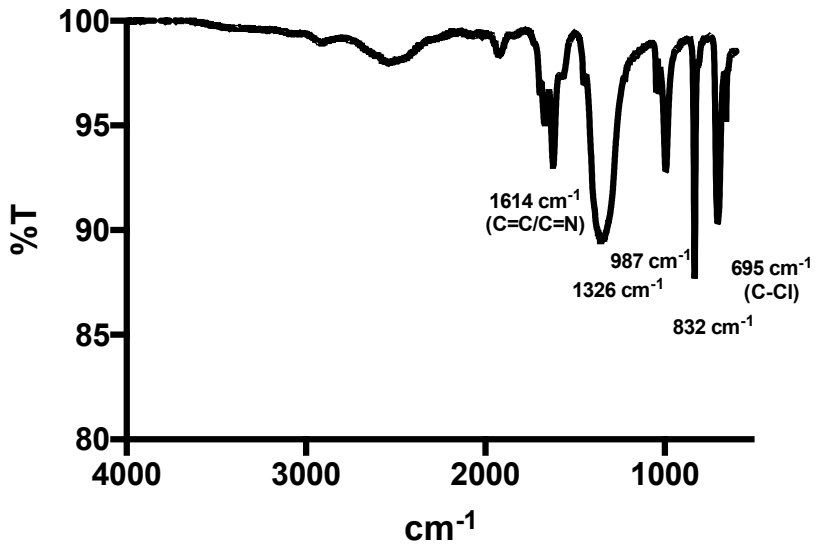
FCD-5 FTIR
100
95
90
85
80
%T
1614 cm-1
(C=C/C=N)
987 cm-1
1326 cm-1
832 cm-1
695 cm-1
(C-Cl)
4000
3000
2000
1000
cm-1

c

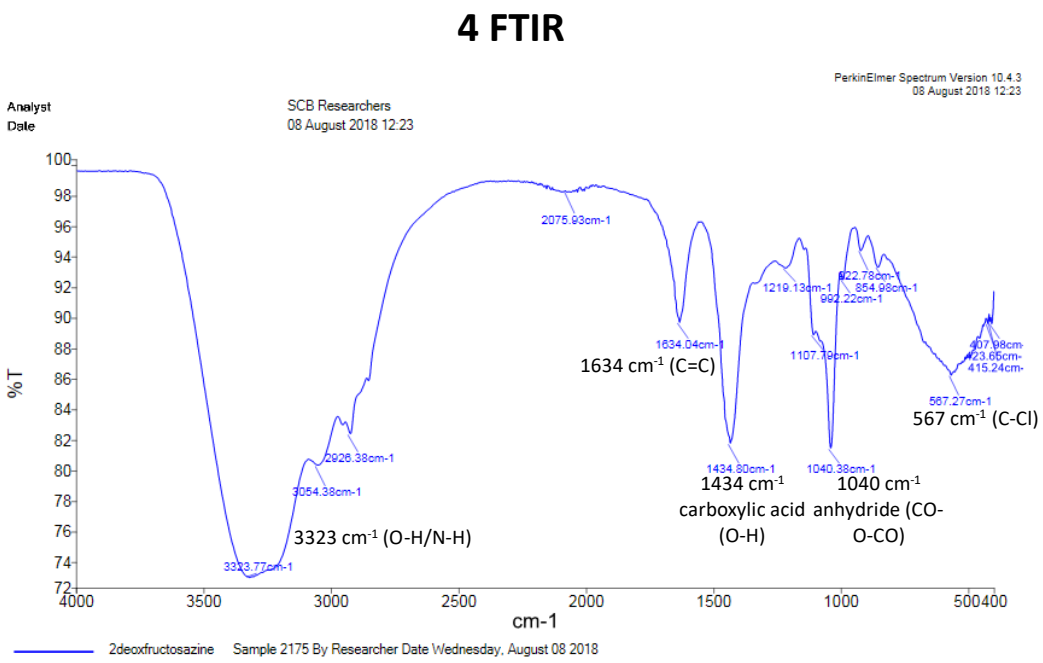

*Figure 5.12 FTIR spectra of a) **FCD-3** b) **FCD-5** and c) **4**.*

5.4.3 Cell studies

5.4.3.1 Cytotoxicity

Having identified 2 major isolated components (**4** & **FCD-5**) of **FCD-3**. Cell cytotoxicity studies were carried out where each individual component and **FCD-3** were evaluated in the absence and presence of LED ilumination and evaluated for their ability to induced cytotoxicity. These experiments would be able to help us identify which components were responsible for the bioactvity previously observed.

FCD-3, **4** and **FCD-5** were incubated with HeLa and toxicity was assessed at 1 hr, 8 hr and 24 hr as previously done in section 5.2.2.8 and results compared. For these experiments concentration of nanomaterial was corrected using the known mass of 2,5-deoxyfructosazine in each sample to be made consistent between **FCD-3** and **4**. **FCD-5** had negligible 2,5-deoxyfuctosazine present by NMR, so in each case the mass concentration used was the same as **FCD-3** (Fig.5.8).

Similar toxicity for **FCD-3** was observed in these results as those carried out by Stephen Andrew Hill (Figure 5.8), toxicity began emerging in both sets of data after 24 hr with 50 μg ml^{-1} **FCD-3** treatment and similar trends continue at higher concentration. Comparing the toxicity of **4** and **FCD-5** shows a similar concentration dependant effect to **FCD-3** at 24hrs. **FCD-5** interestingly shows comparatively lower toxicity than **FCD-3** or **4**.

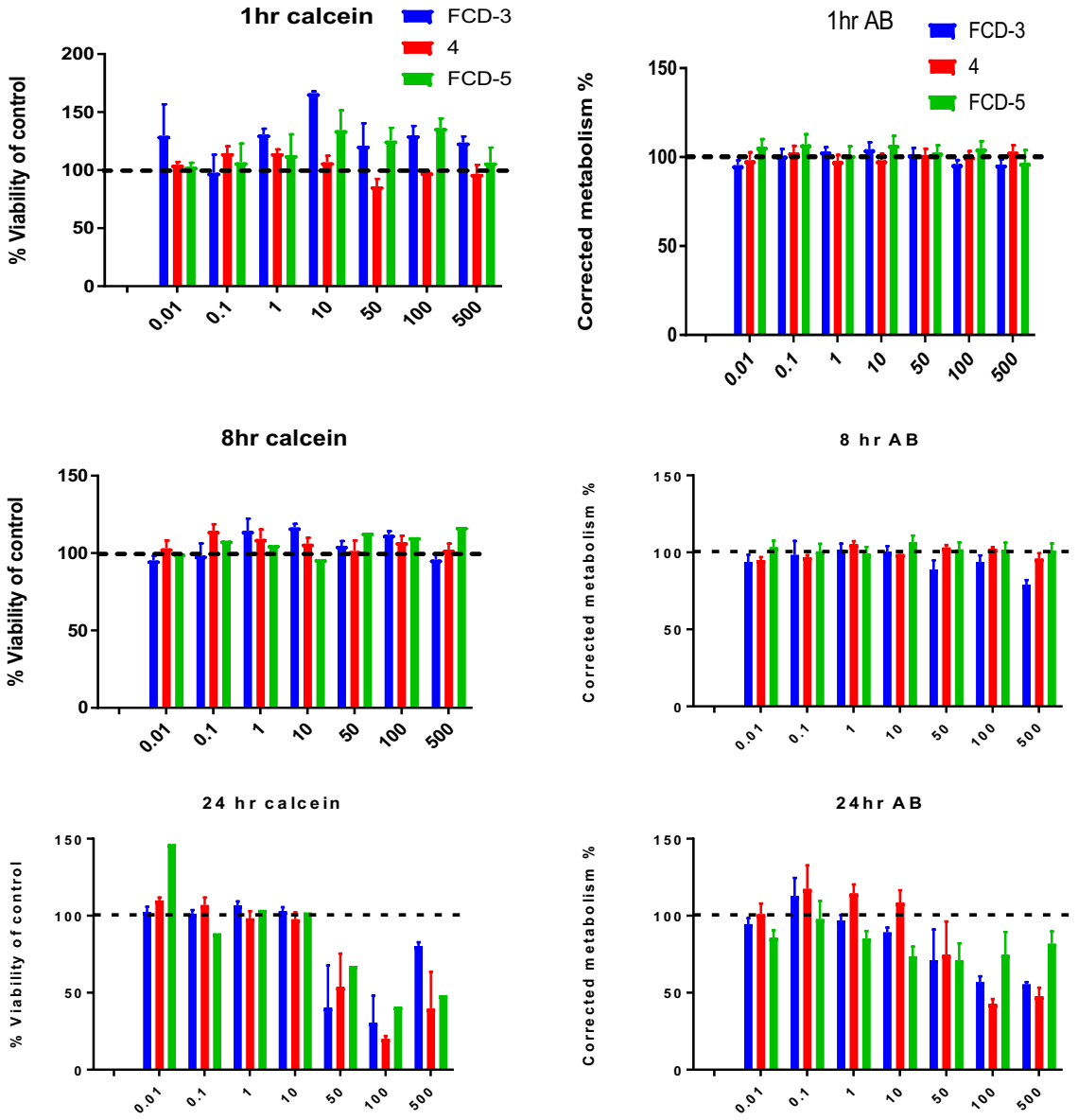

*Figure 5.13 Toxicity data of **FCD-3, 4** and **FCD-5** in HeLa cells using Calcein and AB as indicators of viability and reductive metabolism respectively. Time points 1 hr, 8 hr and 24 hr were used.*

5.4.3.2 LED-irradiation cytotoxicity

Working with CDs which absorb in the UV-visible region we were able to conduct photothermal cell experiments with cheap and easy to use LED lights (λ_{ex} 460 nm). Following the protocol previously developed, **FCD-3, 4** and **FCD-5** were assessed as toxic agents when combined with LED irradiation. Furthermore, experiments were carried out to evidence the localised heating effect we hypothesised was the mechanism by which **FCD-3** exerts toxicity. The global temperature rise of the cell media (without cells) over time upon LED irradiation was measured as a function of concentration of **FCD-3, 4** and **FCD-5**.

Toxicity and reductive metabolism assays were measured after treatment with **FCD-3, 4** and **FCD-5** after 60 minutes of LED-irradiation to determine which components cause the toxic effect observed previously with **FCD-3**. Concentrations of 50 and 100 μg ml^{-1} were chosen as good concentrations with which to see differences in toxicity between **FCD-3**, **4** and **FCD-5** (Figure 5.14). As there appeared differences in toxicity at these concentrations at 24 hr compared to control in figure 5.15. After 1 hr, 1 day and 3 days calcein and alamar blue assays were conducted. Toxicity data after 1 day and 3 day clearly show a marked decrease in cell viability compared to control for **FCD-3** only. At 50 μg ml^{-1} 20% viability is observed and 10 % at 100 μg ml^{-1}. After 3 days viability is < 10 % for both concentrations. Comparatively, **4** and **FCD-5** show no significant viability decrease at any of these concentrations or time points, and share similar viability to controls not irradated with LEDs.

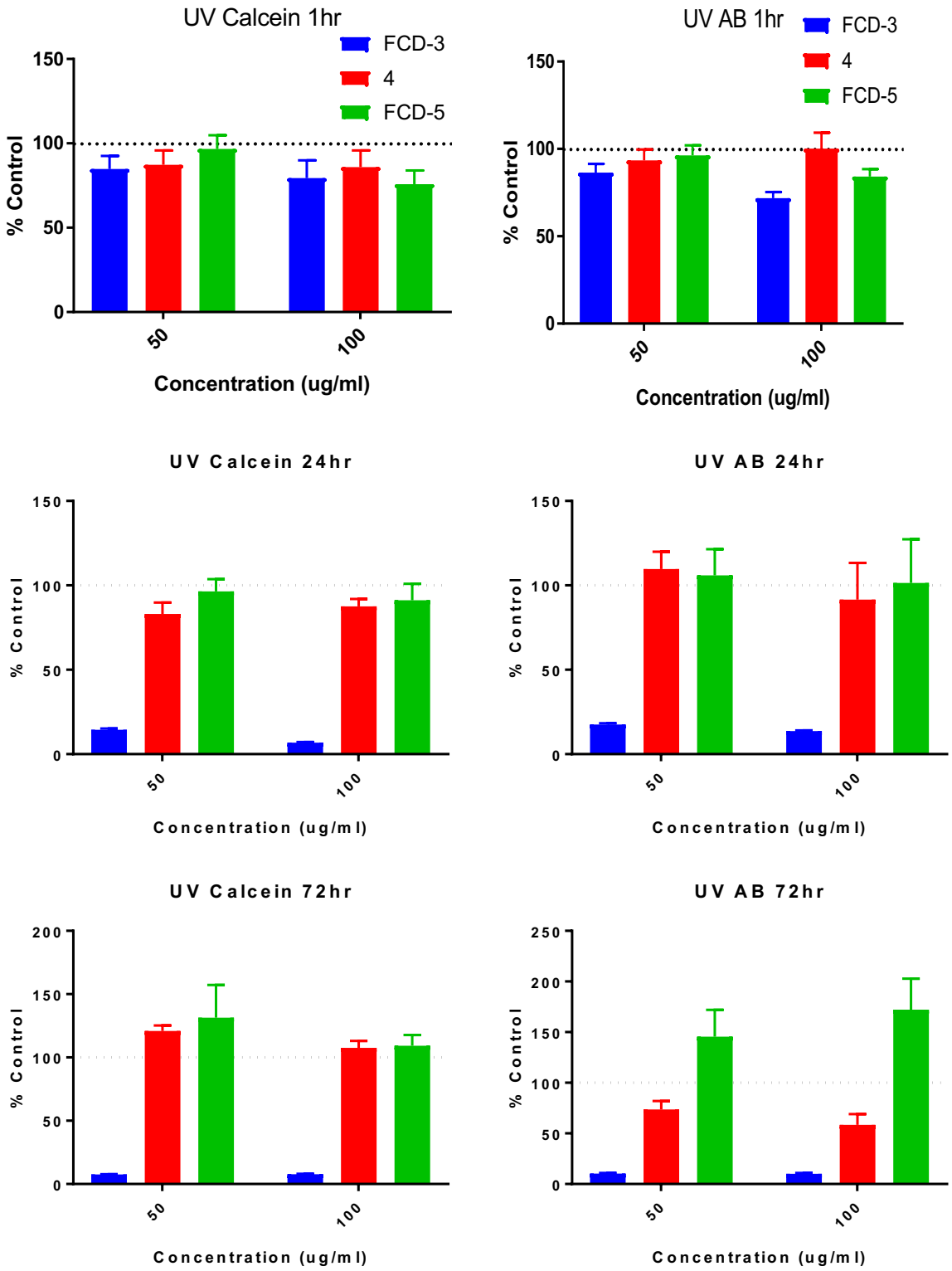

*Figure 5.14 Toxicity data of HeLa cells upon LED irradiation. Data from Calcein and AB assays assessing viability and reductive metabolism respectively are presented as % of control data. Time points 1 hr, 24 hr and 72 hr were observed. Blue bars correspond to **FCD-3**, red bars to **4** and green bars to **FCD- 5**.*

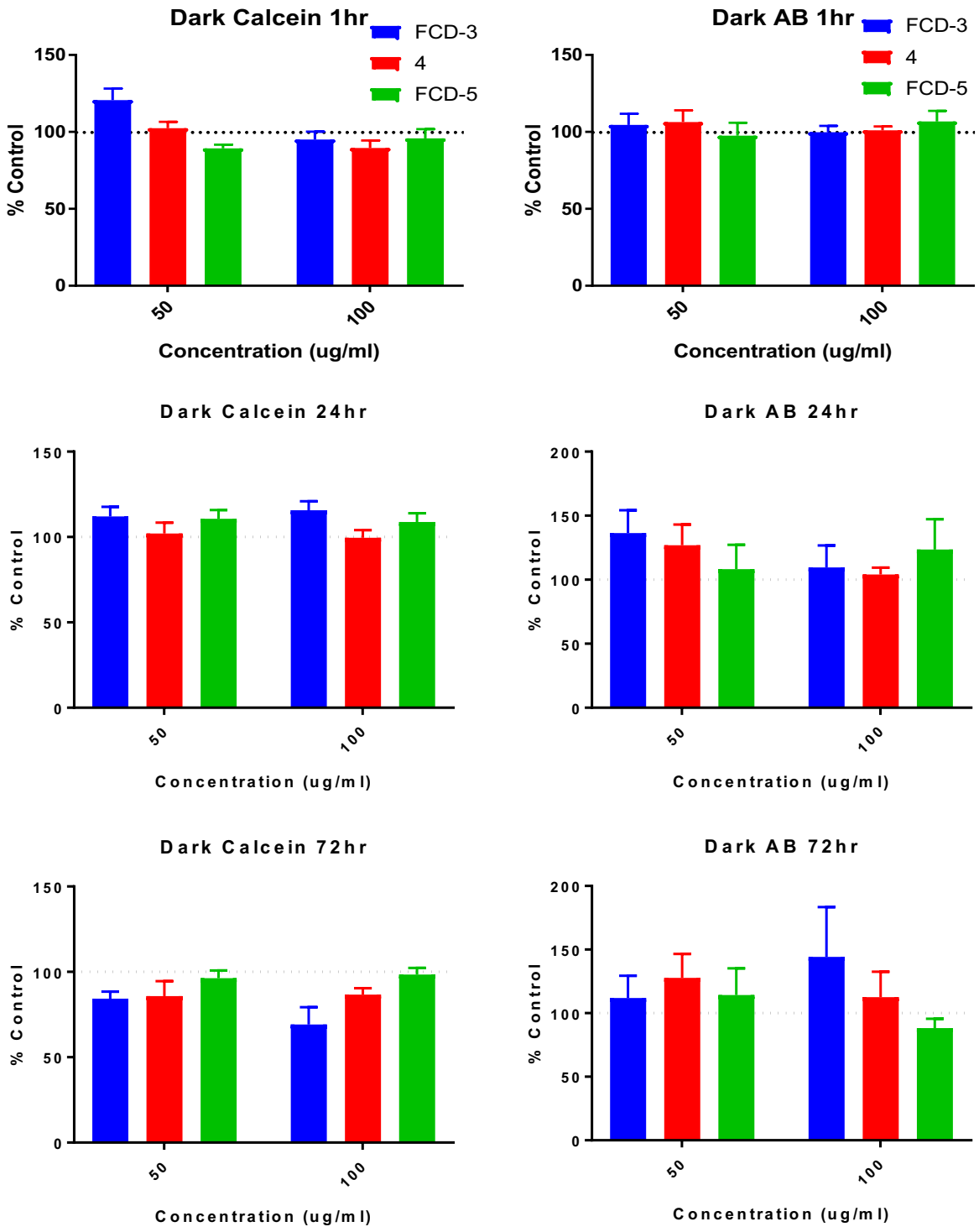

*Figure 5.15 Toxicity data of HeLa cells without LED irradiation. Data from Calcein and AB assays assessing viability and reductive metabolism respectively are presented as % of control data. Time points 1 hr, 24 hr and 72 hr were observed. Blue bars correspond to **FCD-3**, red to **4** and green to **FCD-5**.*

5.4.3.3 Control experiments

Control experiments aimed to determine whether the media (or H_2O) alone showed the same temperature change as when cells or nanomaterial were present. Control experiments were carried out under the same conditions as previous LED-irradiation experiments. **FCD-3, 4** and **FCD-5** were maintained at 50 μg ml^{-1} and irradiation time was 60 minutes. Temperature change maxima of 12-15 ^{o}C was observed for both DMEM high cell culture media and H_2O. **FCD-3** in both media and H_2O had a steeper gradient and greater temperature change then **4**, **FCD-5** or solution without nanomaterial (Figure 5.16).

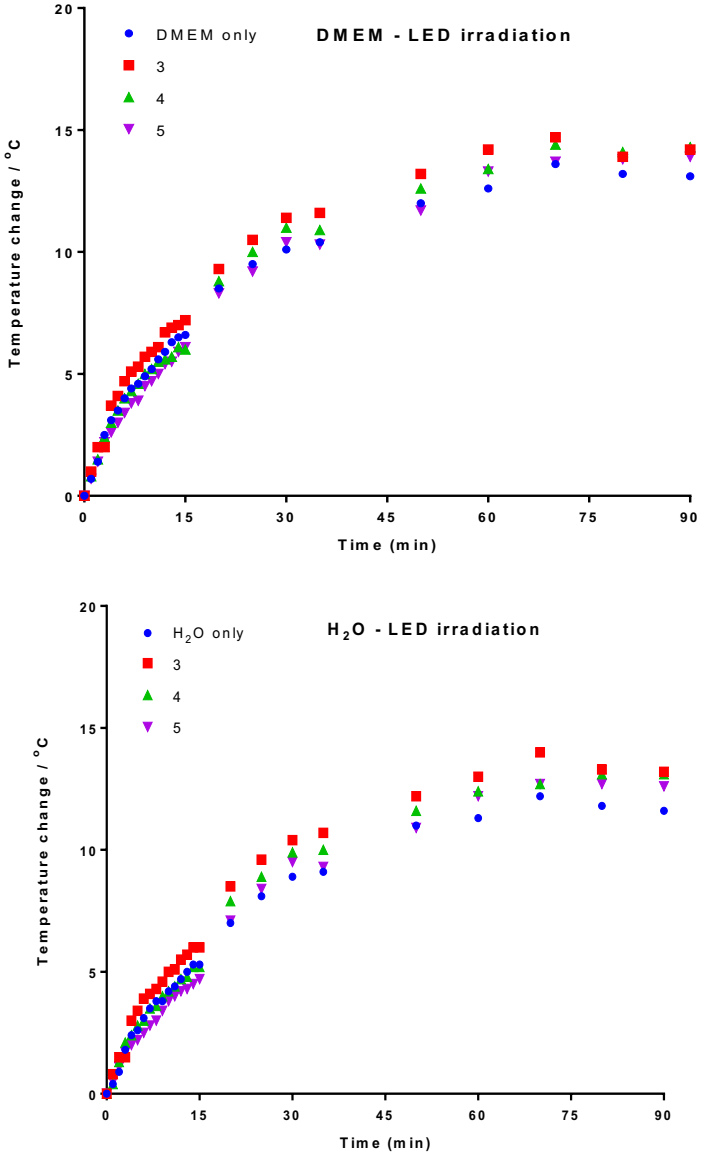

*Figure 5.16 Control experiment measuring the temperature change of H_2O and DMEM high cell culture media with nanomaterial **FCD-3, 4** and **FCD-5** in a 96-well plate without cells present. Starting temperature was room temperature of 21.4 ^{o}C in each case and temperature was recorded over 90 minutes. Blue points: Control H_2O or DMEM cell culture media only, red with **FCD-3**, green with **4** and purple with **FCD-5**.*

Treatment with **FCD-3** combined with LED irradiation was thought to create a localised heating effect at the nuclear accumulation site, inducing cytotoxicity. Control experiments were carried out with HeLa cells and **FCD-3**, **4** and **FCD-5** to observe if the temperature of the local media changed as a function of UV-irradation and nanoparticle.

HeLa cells seeded in a 96-well plate were treated with **FCD-3**, **4** or **FCD-5** at concentrations of 1, 50, 100 and 500 ug ml^{-1}, at 37 ^{o}C for 2 hours and then the temperature was measured over a 90-minute period of LED irradiation at room temperature. The temperature change was plotted as a function of time. All non-irradiated experiments show a decrease in temperature as the wells cooled to room temperature over the first 10 minutes then maintained the same temperature over the remaining eighty minutes. All LED irradiated experiments showed a similar decrease before an increase in temperature up to 7 ^{o}C greater than that at the start of the experiment and up to 12 ^{o}C greater than room temperature. **FCD-3** and **4** both show a positive concentration dependent heating effect (figure 5.17). However, this corrolation does not seem to scale with the concentrations used.

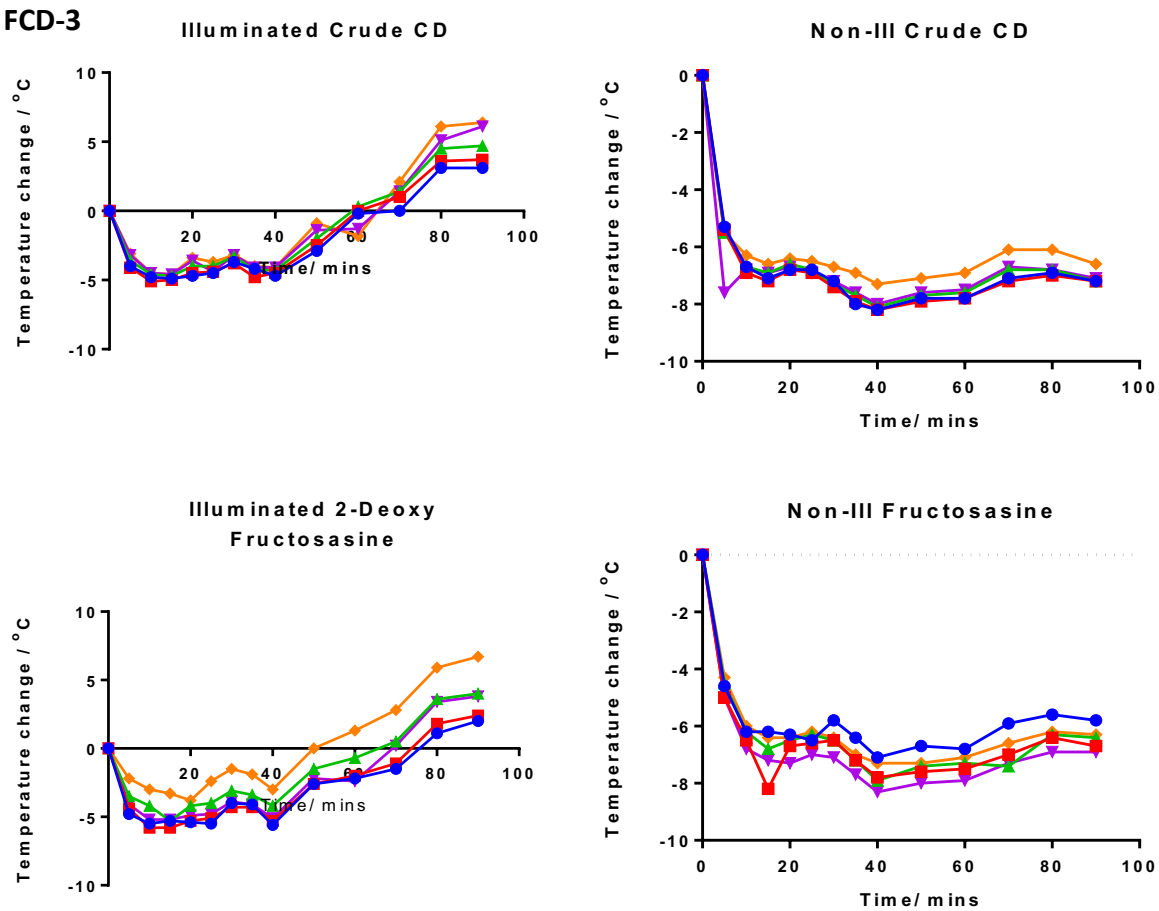

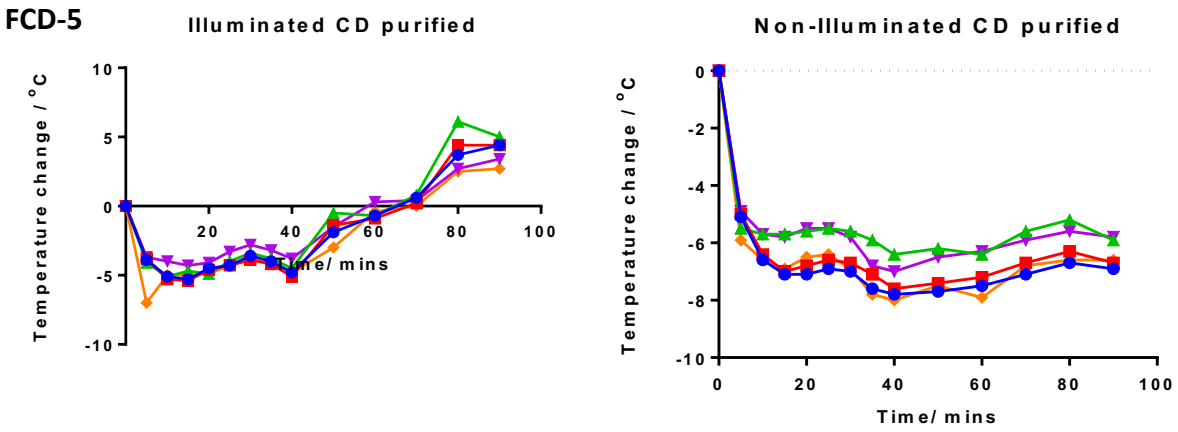

*Figure 5.17 Temperature change observed with and without LED-irradiation of DMEM media incubating HeLa cells. HeLa cells were treated with either **FCD-3,4** or **FCD-5** prior to recording and incubated at 37 °C for 2 hrs before temperature was recorded over 90 minutes of LED irradiation. Blue line: 0 ug ml^{-1}, red 1 ug ml^{-1}, green 50 ug ml^{-1}, purple 100 ug ml^{-1}, orange 500 ug ml^{-1}.*

5.4.3.4 Confocal microscopy

Confocal microscopy was used to visualise **4** in HeLa cells having been incubated with nanomaterial for 6 hrs at 10 μg ml^{-1} of **4** (figure 5.18). Grey values per treated cell were 20.7 ± 1.11 (SEM) compared to control of 7.0 ± 0.31 grey values per cell which were significantly different ($P < 0.0001$). The material **4** was fluorescent however, the 2,5-deoxyfructosazine alone is not. This suggests that the **FCD-5** CD remaining in **4** is crucial for its fluorescent property. Riboflavin molecules with known fluorescence[254] could be present in **4** could be one explanation for the fluorescence, or an interaction between the CD and 2,5-deoxyfructosazine. More work needs to be conducted to determine this.

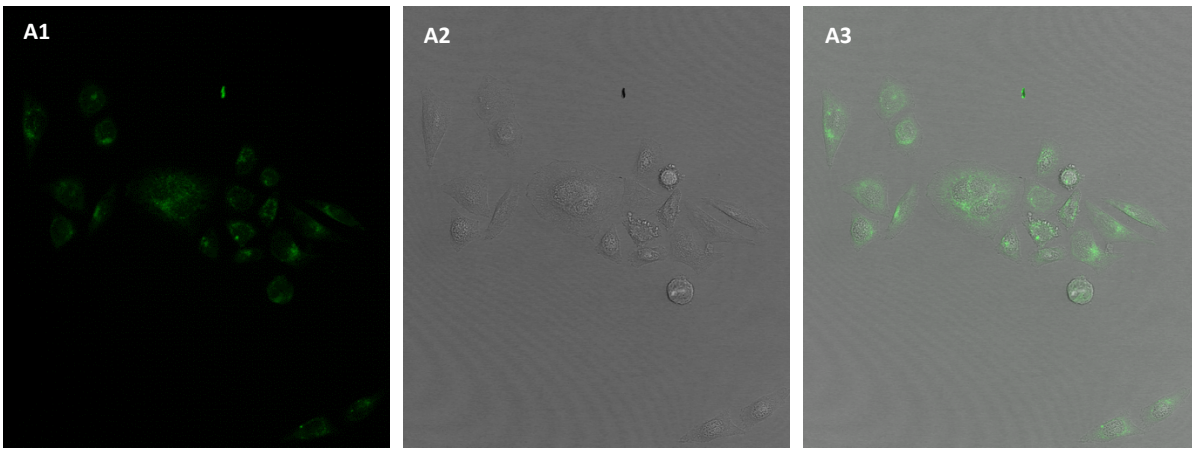

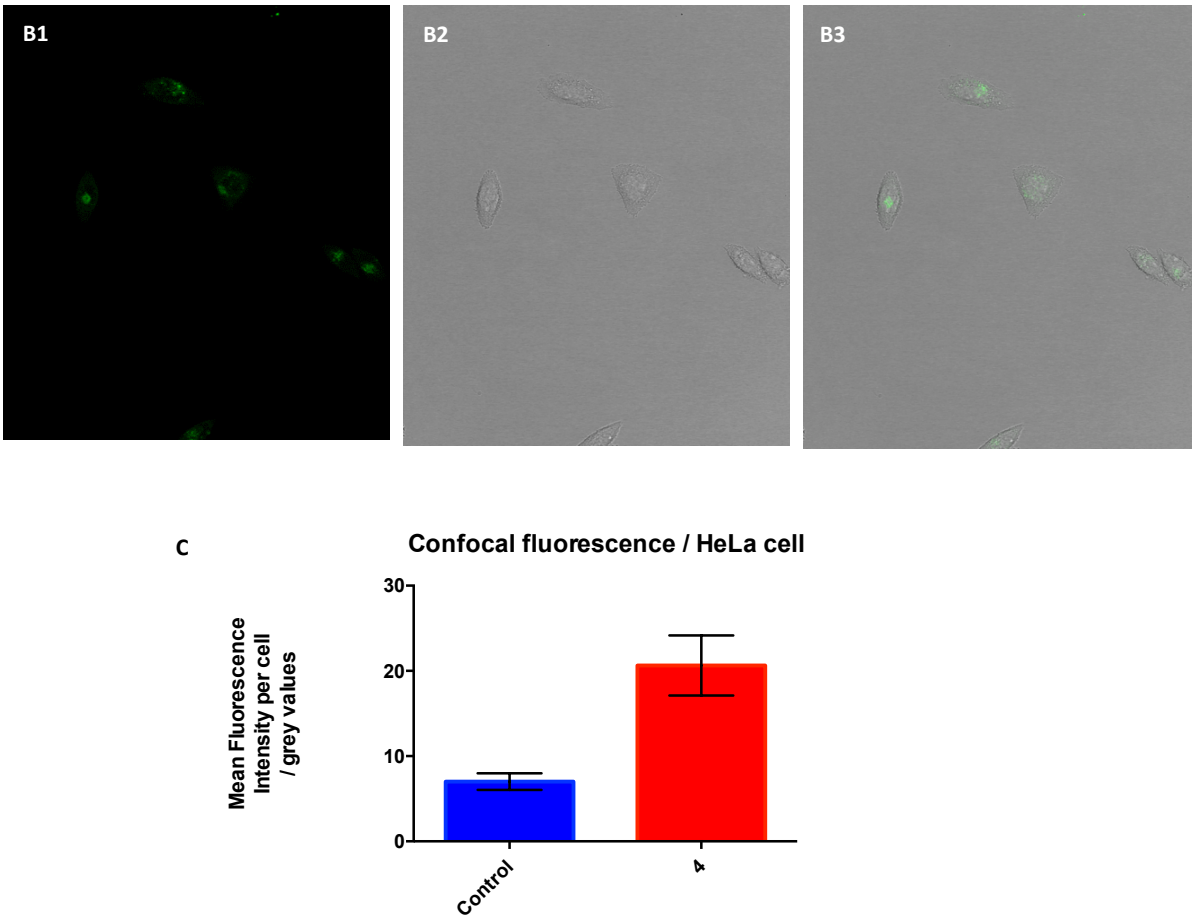

*Figure 5.18 A1) Confocal fluorescence image of **4** in HeLa cells, A2) brightfield A3) fluorescence and brightfield overlaid. B1) Confocal fluorescence image of control HeLa cells, B2) brightfield B3) fluorescence and brightfield overlaid. C) Bar chart of fluorescence in grey values per cell measured between 500-600 nm, N=100. All images are 15x15 μm.*

5.4.3.6 CLEM

Correlative light and electron microscopy (CLEM) combines the advantages of light and electron microscopy to identify novel molecular information[263]. Light microscopy (LM) provides a wide field of view of a population of cells for high-throughput analysis. Most usefully confocal microscopy can provide sub-cellular fluorescence information. Electron microscopy (EM) provides high resolution – down to an atomic level – imaging but at the cost of the field of view. In this way LM acts as a live cell imaging honing technique before cells of interest are fixed and sectioned into 70 -140 nm slices for ultrastructural imaging by EM. At this resolution nanoparticles with high electron density such as metallic gold[264] and quantum dots[44] are observed as areas of high contrast compared to background cellular density.

CLEM was carried out to visualise **FCD-3** localisation in cells. Fluorescence evidence from confocal indicates that **FCD-3** localises in both the nucleus and cytoplasm (Figure 5.19 B1). Average grey values per cell is 94 ± 62 (SEM) whilst control has 27 ± 0.33 grey values per cell which were significantly different ($P < 0.0001$). Cells used for quantification were those within the focal plane. Cells were incubated with 33.3 μg ml^{-1} **FCD-3** for 6 hrs.

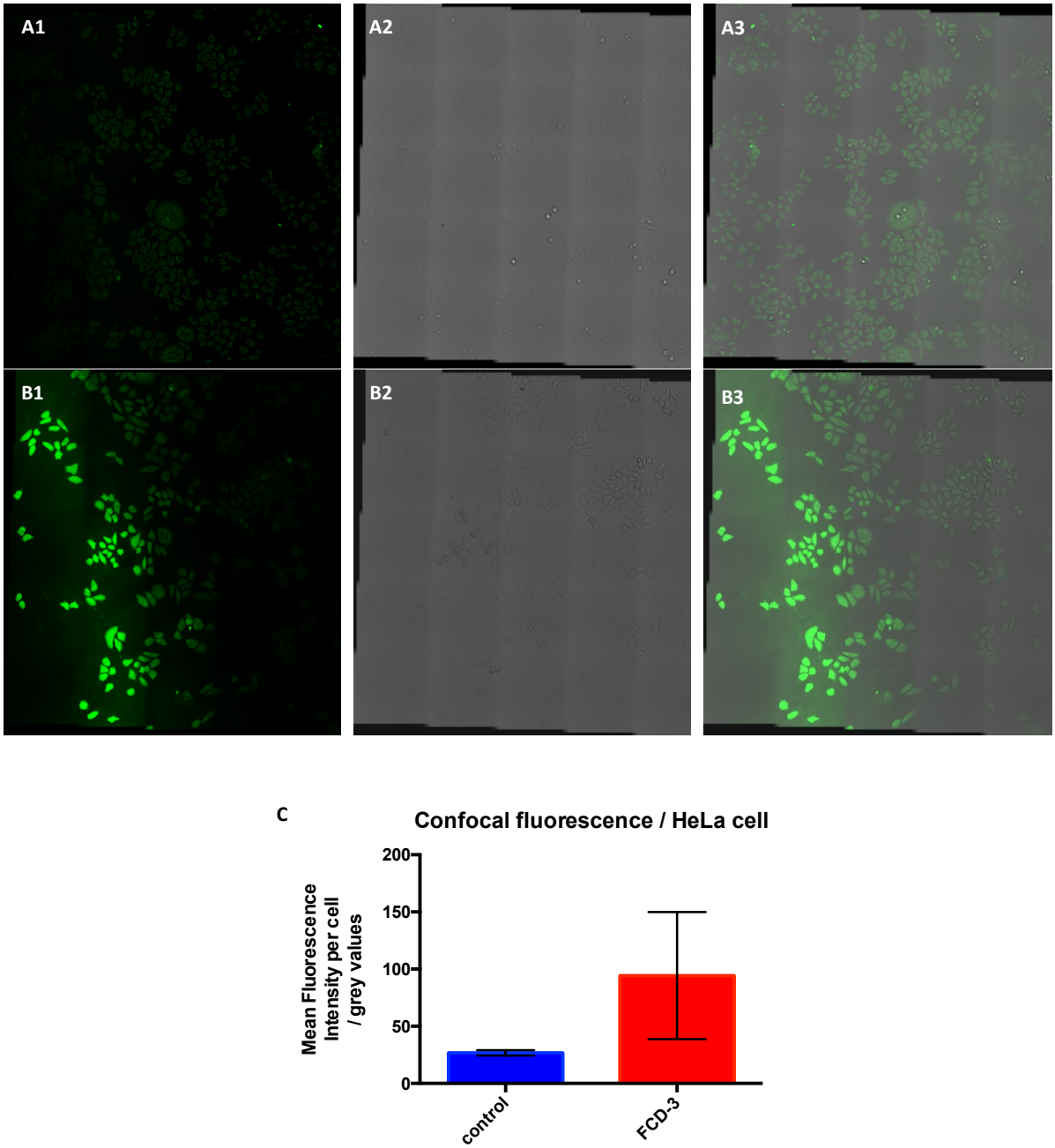

*Figure 5.19 Confocal tiled images of **FCD-3** in HeLa cells for CLEM. A1) Confocal fluorescence tiles images of control HeLa cells A2) brightfield A3) fluorescence and brightfield overlaid. B1) Confocal fluorescence image of **FCD-3** treated HeLa cells B2) brightfield B3) fluorescence and brightfield overlaid. C) Bar chart of fluorescence in grey values per cell measured between 500-600 nm, N=50. All images are 15x15 µm*

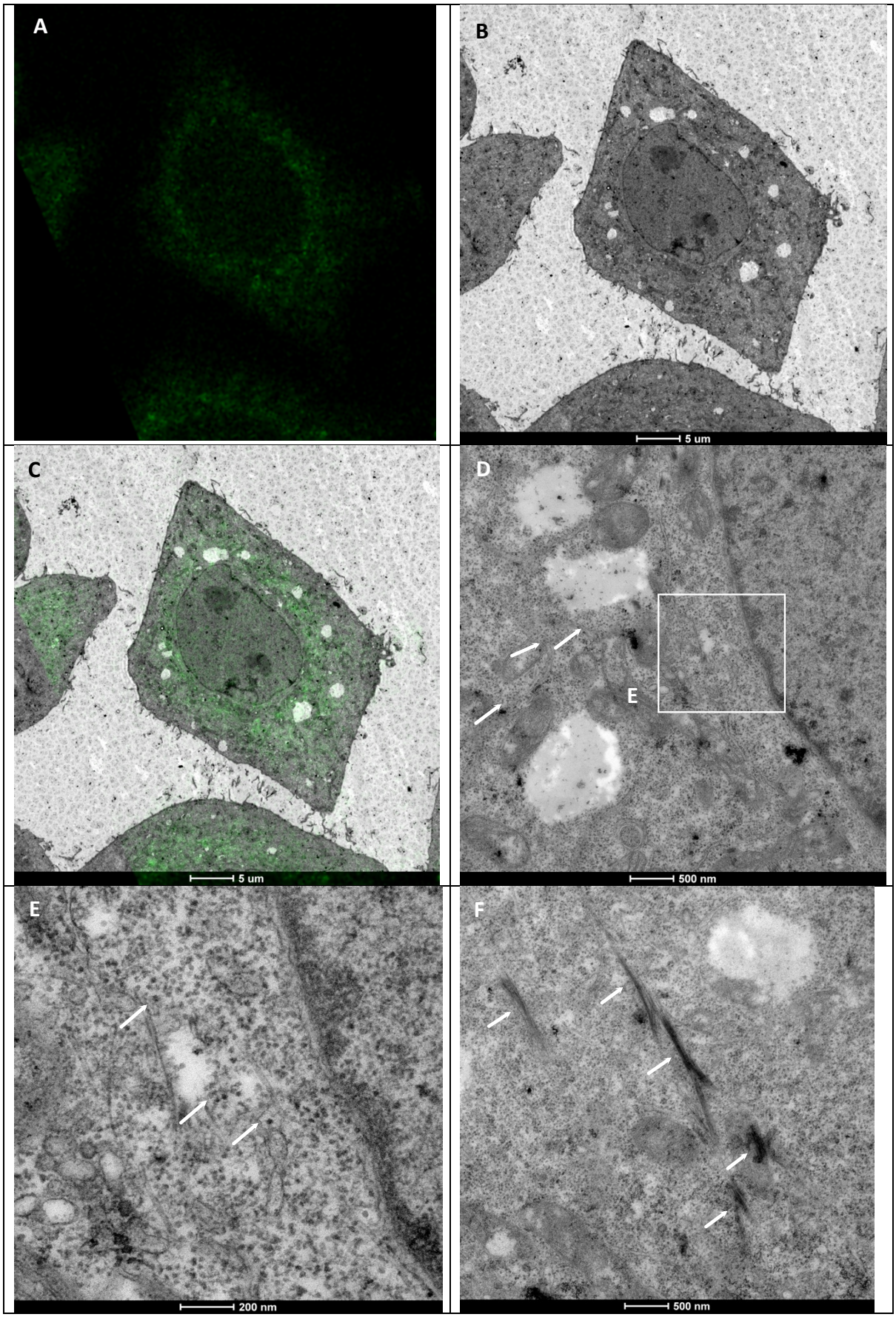

Figure 5.20 CLEM image of control HeLa cell 1 generated from confocal and EM image of the same cell overlaid. A) EM image of healthy control HeLa cell 1 B) Confocal image of healthy control HeLa cell 1. C) CLEM overlaid image of A&B. D) Magnified image of HeLa cell

Looking at these cells at higher resolution through TEM we aimed to generate further evidence for their uptake and localisation at the nucleus. Areas of high fluorescence in both **FCD-3** and control samples were imaged via EM up to 200,000x magnification. Features tens of nanometres large were observed, but all were common between control (Figure 5.20 e and S.8g&h) and **FCD-3** treated cell (Figure S.10g) suggesting them as native features such as ribosomes (~20 nm). On the nano and micron scale, features were seen which were not natural to the intracellular environment, but clearly identified as stain within certain organelles due to the very heavy contrast. Most images show this but this is well illustrated in figures S5.7 a&b, S5.8 a (control cell) and 5.20f, 5.22a and S 5.10b,c&d (treated cell). Furthermore, there were larger micron sized features which were loose pieces of stained material which were also observed covering the Formvar grid membrane in places, figure S5.8 a,g&h (control cell) and 5.22a (treated cell). Furthermore, some organelles likely golgi body or endoplasmic reticulum looked to be stained heavily, figure S 5.8f (control cell) and 5.20f, 5.22b,c&d and S5.10f (treated cell).

CLEM images of **FCD-3** treated cells were produced to identify intracellular areas from which high relative fluorescence originated. Magnified EM were then produced of these areas to observe **FCD-3** as well as imaging the nucleus at higher magnification to see if **FCD-3** could be seen, which would support FRET experiment data (section 5.2.2.3) that **FCD-3** enters the nucleus.

Figure S5.9 shows 3 cells which were all of HeLa cells incubated with **FCD-3**, 2 of which are shown at further magnification in figures 5.21 and S5.9. From all images of these cells it can be said that treatment with **FCD-3** at 33.3 μg ml^{-1} for 6hrs did not diminish the health of the cells. Cellular membrane and organelles maintain their integrity to the same degree as control HeLa cells. This supports the non-toxicity of these nanomaterials observed through cytotoxicity assays under these same conditions.

From figure 5.21, fluorescence can clearly be observed localised at high concentration at the perinuclear region, whilst also diffuse throughout the cell. EM images were taken of these areas of high fluorescence; however, no features were observed different from control cells. Figure 5.22 shows one cell with 3 regions marked in 5.22a which are magnified in 5.22b,c&d. In 5.22b,c&d organelles around the vacuole corresponding to areas of high fluorescence are stained darker in EM. Within these regions no features not found in control samples can be identified. Similar to control samples, organelles are stained heavily, and larger micron and nano sized particles are observed – which do not correlate with regions of fluorescence. Figure S5.10 shows a second HeLa cell treated with **FCD-3**.

CLEM figure S5.10 shows the same perinuclear fluorescence seen in the figure 5.21, likely due to **FCD-3** fluorescence. EM images similar to the cell in figure S5.10 a-g, only shows features also observed in control cells such as staining (Figure S5.8 a and S5.7a&b), nor does fluorescence correlate with any structures observed. Looking at the nucleus of this cell did not reveal novel features compared to control (Figure S5.8c&d).

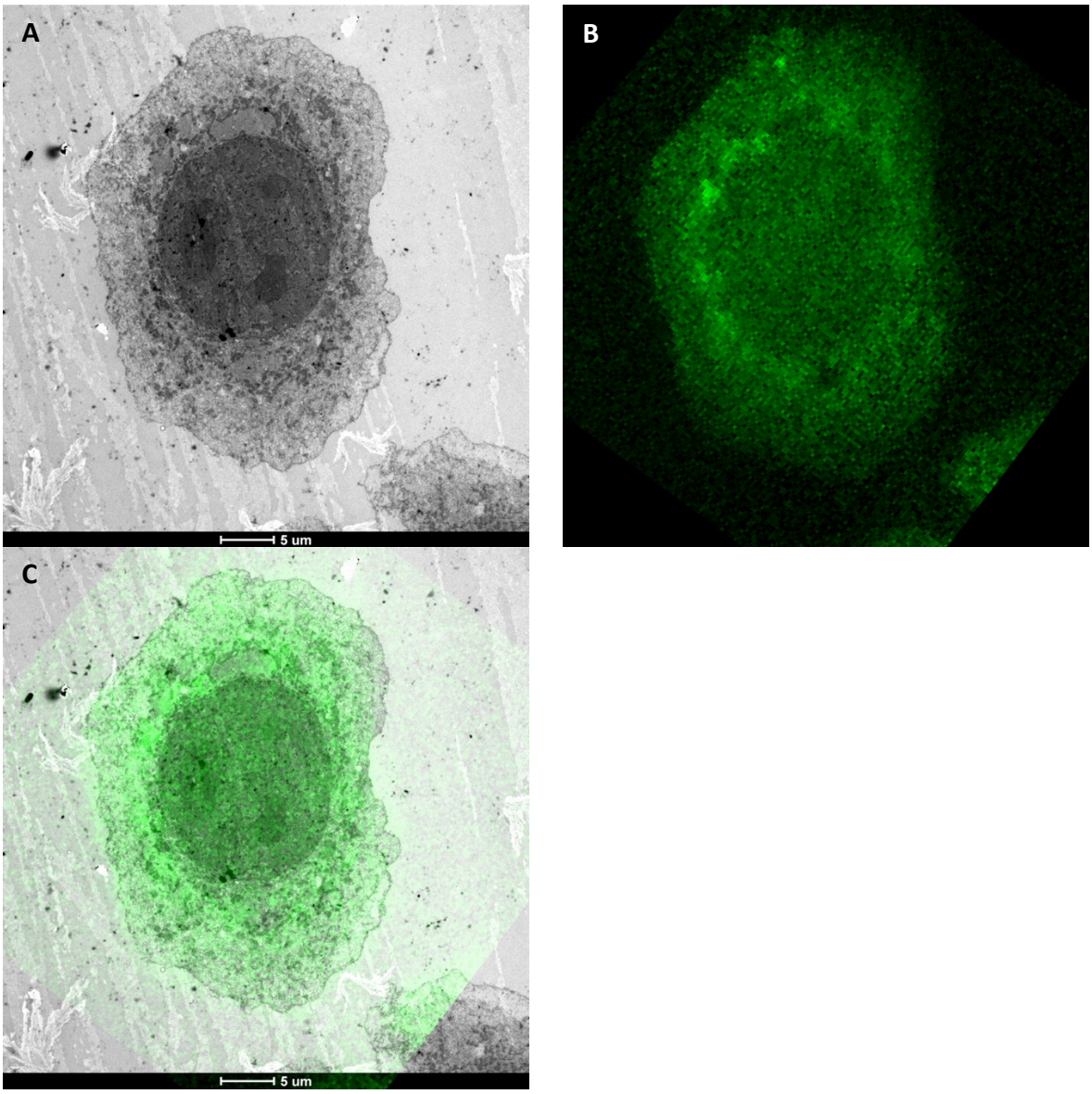

*Figure 5.21 CLEM image of HeLa cell **2** incubated with **FCD-3**. A) EM image of HeLa cell 2 incubated with **FCD-3** B) Confocal image of HeLa cell 2 incubated with **FCD-3**. C) CLEM overlap of EM and fluorescence images A&B. Areas of high fluorescence exist in the top left perinuclear region of the cell.*

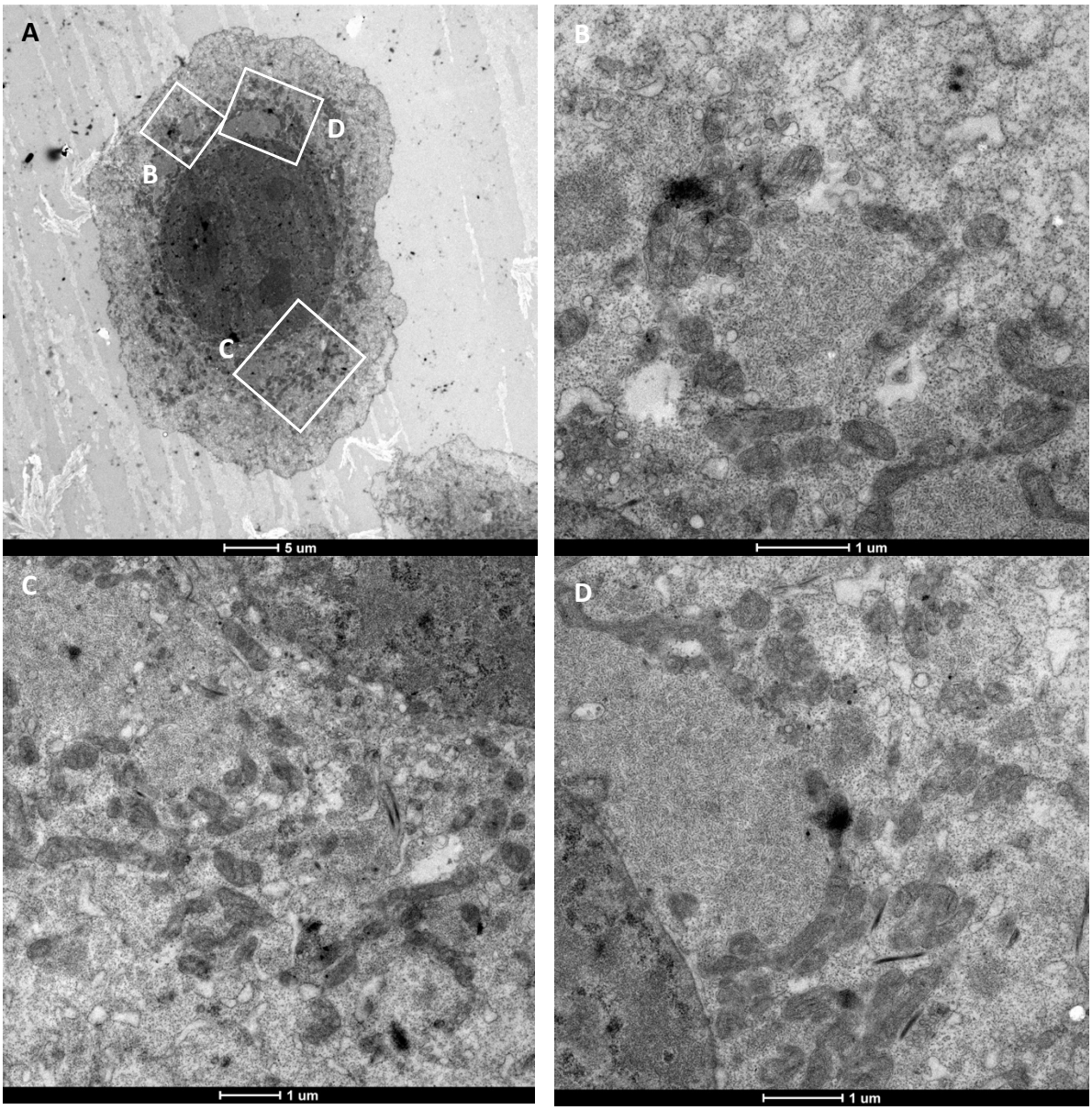

*Figure 5.22 EM images of HeLa cell 2 treated with **FCD-3**. A) Whole cell image B,C&D) areas magnified areas from A.*

Looking at confocal microscopy images of **FCD-3** treated HeLa in figure 5.22 c and S 5.10 h shows that **FCD-3** has clearly been internalised. This is evidenced by significant fluorescence observed in **FCD-3** treated cells compared to control. Fluorescence is both diffuse throughout the cytosol but also areas of high fluorescence are localised at the perinuclear region. However, no features could be identified using the high-resolution technique of EM correlating to these regions of higher fluorescence.

Working with low density carbon dots and the stained cellular background provides a challenging sample in which to observe **FCD-3** nanoparticles. This was due to uranyl acetate stain, osmium tetroxide contrast enhancing stain and resin density. Furthermore, considering the relative heavy staining of the control HeLa cells in Figures 5.23 and S 5.7&8 the carbon dots would be difficult to

detect in TEM within the cellular environment. Literature evidence assessed through Web of Science does not report carbon dot CLEM to date (as of 11th March 2020).

An abundance of fluorescence from **FCD-3** intracellularly suggests that nanoparticles in those areas are not aggregated to a degree that induced quenching. This supports the conclusion that larger features observed were stain and debris rather than aggregated nanomaterial. In order to better visualise single **FCD-3** nanoparticles an experiment using unstained cellular material with dark-field energy filtered TEM (EFTEM) could provide better contrast between the nanoparticles and cell. For example fluorescent nanodiamond of 62.7 nm diameter was observed through EFTEM which was not possible with CLEM and standard TEM.[265]

5.5 Conclusions and Future work

Owing to the low toxicity of our **FCD-3** nanoparticle to both healthy and cancerous cells without external stimulus, tight control can be exerted over cancer cell cytotoxicity through LED irradiation. Toxic effect is only present when both **4** and **FCD-5** are present in the form of **FCD-3** upon LED irradiation. The toxic effect observed in a cancerous cell line, HeLa, for this combination, is greater than the toxic effect observed for **4** or **FCD-5** alone. Through confocal microscopy we observe significant **FCD-3** uptake compared to control, suggesting that the combined CD core and 2,5-deoxyfructosazine is readily up taken by cancer cells. Furthermore, we suggest a local heating effect induced by LED irradiation when the CD core is present intracellularly which is responsible for the marked cytotoxic effect we observe after 24 hr. The LED dependent cytotoxicity is supported by general cell media temperature increase of 12 ^{o}C which agrees with previous data (section 5.4.3.4), showing a lack of correlation with ROS or metabolite production but increased ATP production. ROS production is an energy consumptive process and indicates worse photothermal conversion. The lack of ROS production and the increase in cell media temperature corroborates the idea that primary PTT effects, with high temperatures of 48-60 ^{o}C, can be achieved with **FCD-3**.

Confocal microscopy provides evidence for the uptake of **FCD-3** and **4** by the cancerous cell line HeLa. Perinuclear localisation can be seen through areas of high fluorescence intensity in confocal images. Without organelles trackers it is difficult to identify where carbon dots maybe localising. Overlaying these confocal images with EM allowed for high-resolution imaging of these areas of high fluorescence with the aim of observing **FCD-3** material. However, this did not reveal any sub-micron structures which were not observed in control samples.

Figure 5.19 depicts the uptake of **4** into HeLa cells. 2,5-deoxyfructosazine is a non-fluorescent molecule (confirmed with commercial 2,5-deoxyfructosazine), hence the green fluorescence that we observe must be due to the residual carbon dots in **4** which we know are present from NMR. Compared to **FCD-3**, **4** had 2.4 times more 2,5-deoxyfructosazine present confirmed by NMR Figure 5.8.

The CD component still present in **4** is therefore important for the fluorescence peak at 525 nm (Figure 5.11 and S5.6). The emission spectra of **FCD-3** and **4** are identical and the excitation spectra both peak at 450 nm. However, the excitation spectra differ in shape reflecting the amount of CD present in the sample (Figure 5.11). DOSY shows that CD peaks and 2,5-deoxyfructosazine share a similar diffusion coefficient suggesting they at physically associated in solution. This interaction is likely the basis for the fluorescence observed when both components are present.

The significant uptake of **FCD-3** compared to control cell line (as found by SAH) could be explained through consideration of the requirements of cancer cells. In cancer cell lines including HeLa glucose uptake is upregulated to meet metabolic demand due to fast growth and high proliferation. In HeLa this is mediated by overexpressed GLUT transporters 1 & 3[266]. Hence, the 2,5-deoxyfructosazine coated **FCD-3** which contains hydroxyl groups similar to carbohydrates could promote uptake through these channels.[257] This could be tested through active versus passive cell uptake experiments at 4 ^{o}C.

Further work which could be conducted is as follows. Improving the NIR (650 – 950 nm) absorption of our nanoparticle by including new materials into the synthesis such as NIR absorbing molecules or exploring the synthesis reaction parameters such as reagent ratios and reaction time may produce a material with the cytotoxic properties of 2,5-deoxyfructosazine and allow for absorption in the NIR region. This would facilitate *in vivo* studies to be carried out, and organ and tumour localisation studies to be investigated. Furthermore, known anti-microbial properties could be explored with **FCD-3** (2,5-deoxyfructosazine containing) and LED-irradiated before comparison to work by Bhattacharjee *et al.*[267] with fructosazine.

Further exploration of cancer cell targeting could be though functionalisation of the **FCD-5** core and recombination with **4** to form modified **FCD-3** variants with differing targeting capabilities. Following previous work in the Galan group where lactose can be used as a means to promote nanoparticle uptake in some cancerous cell lines could be investigated as a targeting agent.

5.6 Chapter 5 Experimental

5.6.1 Synthesis

1) Synthesis of FCD-3

To a solution of Glucosamine.HCl (1 g, 4.63 mmol) in deionised water (20 mL), was added *m*-phenylenediamine (0.55 g, 5.1 mmol) as a solution in MeOH (10 mL). The solution was agitated by sonication until the mixture was homogeneous and then transferred to a 250 ml Erlenmeyer flask before microwave synthesis for 3 minutes at the centre of a domestic microwave (800 W, 80 % power setting). A viscous brown solid was afforded which was then solubilised in distilled H_2O before filtering using a 10,000 MWCO Vivaspin 20 spin concentrating falcon. The bulk solution was then lyophilised to yield **FCD-3**, a brown oil-like material (1 g) before further use.

5.6.2 NMR characterisation of synthetic FCDs

FCD-3 and **4** ^{1}H NMR (500 MHz) spectra match the commercial 2,5-deoxyfructosazine spectra (all presented in figure 5.9).

FCD-3

*(*2,5-deoxyfructosazine structure):

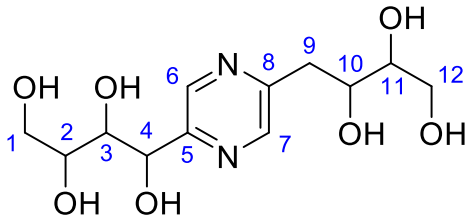

^{1}H NMR (500 MHz, Deuterium Oxide) δ 8.58 (d, *J* = 1.4 Hz, 1H, 1a), 8.40 (d, *J* = 1.4 Hz, 1H, 1b), 5.02 (d, *J* = 2.3 Hz, 1H, 4), 3.90 (ddd, *J* = 9.7, 6.2, 3.3 Hz, 1H 10,2,3,1a,12a), 3.80 – 3.65 (m, 4H, 2,3,1a,12a), 3.63 – 3.48 (m, 4H, 11,1b,12b), 3.09 (dd, *J* = 14.3, 3.3 Hz, 1H, 9a), 2.85 (dd, *J* = 14.3, 9.8 Hz, 1H, 9b).

^{13}C NMR (126 MHz, Deuterium Oxide) δ 153.95 (C5) 153.18 (C7), 144.06 (C8) 142.15 (C6), 74.39 (C11), 73.36 (C2), 71.31 (C4), 71.26 (C10), 70.99 (C3), 62.90 (C1), 62.43 (C12) , 37.49 (C9). See figures S.11 and S.12 for spectra and 2,5-deoxyfructosazine structure which the peaks here are assigned to.

4) Isolation of 4 & FCD-5 from FCD-3

FCD-3 were subjected to G15-Sephadex size exclusion column (35 x 1.7 cm) chromatography in methanol, which facilitated the separation of **FCD-3** into **4** and **FCD-5**.

5.6.2 Cell studies experimental

Confocal

$1x10^4$ HeLa cells (100 μL) were plated in a 96 well plate and left for 16 hr to adhere at 37 ^oC. The next day **4** was incubated with HeLa cells for 2 hrs at 10 $\mu g\ ml^{-1}$. Live cells were imaged using Multi-laser CLSM Leica SP8 AOBS attached to a DM I6000 inverted epifluorescence microscope at 40x magnification in buffered live imaging media (65 mW Ar laser, λ_{ex} 488 nm at 5.44% power, λ_{em} 500-600 nm).

CLEM

Confocal imaging was carried out on live HeLa cells before fixing and sectioning for electron microscopy. $2.5x10^4$ HeLa cells (250 μL) were plated in gridded confocal dishes and left overnight to adhere at 37^{o}C. The next day **FCD-3** was incubated with the cells for 6 hrs at 33.3 $\mu g\ ml^{-1}$ (300 μL). Live cells were imaged in a 50x50 μM area using Multi-laser CLSM Leica SP8 AOBS attached to a DM I6000 inverted epifluorescence microscope at 40x magnification in buffered live imaging media (65 mW Ar laser, λ_{ex} 488 nm at 5.44% power, λ_{em} 500-600 nm).

Fixing cells

Cells were fixed using sodium cacodylate solution (1 mL, 0.1 M pH 7.2 plus 2.5% glutaraldehyde) for 5 mins. Cells were then rinsed with distilled H_2O. before staining with 4% Osmium Tetroxide in H_2O (0.5 mL), for 30 mins. Cells were then stained with 0.5% uranyl acetate in H_2O (0.5 mL) for 30 mins. Samples were then dehydrated over 25 mins, with 5 mins at increasing concentration of ethanol at 70, 80 90, 96 and 100%. Epon solution (1 mL) was added to each sample and cured for 2 days using an oven. Liquid nitrogen was used to freeze and break off the confocal dish from the cured sample.

Sectioning samples

Samples were sectioned into 70 nm thick slices using a glass knife in preparation for electron microscopy. Areas chosen for each sample which were identifiable in corresponding confocal microscopy images for correlation purposes. Sections were floated on water and mounted onto Formvar/Copper TEM grids and dried overnight before imaging. TEM was carried out using a FEI Tecnai 12 120kV BioTwin Spirit TEM. Images were then correlated in Fiji image processing package. Sodium cacodylate solution was purchased from Sigma Aldrich. Uranyl acetate and osmium tetroxide were purchased from Agar scientific.

Toxicity

HeLa cells were plated at 1x10^4 cells per well (100 μL) in a 96-well plate and incubated overnight. The next day cells were incubated with either **3**, **4** or **5** in triplicate at concentrations between the range 500 μg ml^{-1} and 0.01 μg ml^{-1}. After incubation with nanomaterial for either 1 hr, 8 hrs or 24 hrs cells were washed thrice with PBS and then Calcein AM and Alamar blue toxicity assays were carried out.

LED irradiation toxicity experiments

In a 96-well plate 1x10^4 HeLa cells (100 μL) per well, were treated with **FCD-3**, **4** or **FCD-5** in triplicate for 2 hrs at 37^{o}C. For **FCD-3** and **FCD-5**, 50 and 100 μg ml^{-1} were used. For **4**, 23.8 and 47.6 μg ml^{-1} were used in place respectively. Following 2 hr exposure, plates were irradiated with LEDs for 60 mins. LED lights (λ_{ex} 460 nm) were purchased from LightingEVER ~4100057-BLUE, 12 V, 24 W. At room temperature LED lights were mounted onto a black carboard platform upon which clear 96-well plates containing cells, were stilted on Eppendorf lids with an opaque covering placed over the top. Control experiments were conducted under the same conditions in the dark without LED lights present. Post irradiation cell media was exchanged for fresh media not containing any nanomaterial and maintained at 37^{o}C. After F1 h, 24 hr and 72 hr toxicity was determined using Calcein and AB assays.

LED irradiation temperature experiments

Temperature assays upon LED irradiation followed a similar protocol as above with HeLa cells and with a non-irradiated control run in parallel. Post irradiation, cell media was not exchanged and instead the temperature of the media bathing the cells was recorded over 90 mins at a time interval of 5 mins between 0 – 40 mins and every 10 mins between 40 and 90 mins. A Thermocouple (type K from Fisher Scientific) was used to record temperature to 1 decimal place.

A second set of control temperature assays, without cells present using a similar protocol was carried out in both H_2O and DMEM cell culture media. Per well of a 96-well plate, 100 μL of media or H_2O with either **FCD-3**, **4** or **FCD-5** was placed at room temperature. Upon LED irradiation the temperature was measured over 90 mins at 1 min intervals between 0 – 15 min and every 5 min from 15 – 40 min and every 10 min between 40 – 90 min.

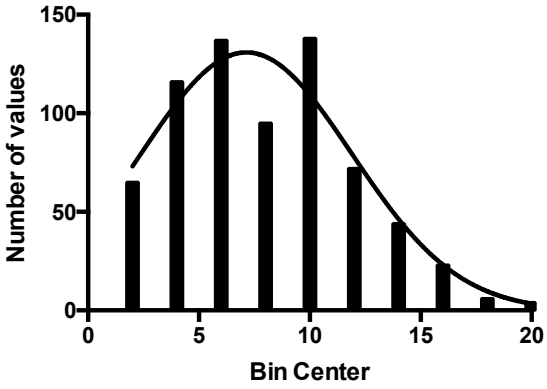

*Supplementary Figure 5.1 Histogram of TEM image of **FCD-3** carbon dots in figure 3.*

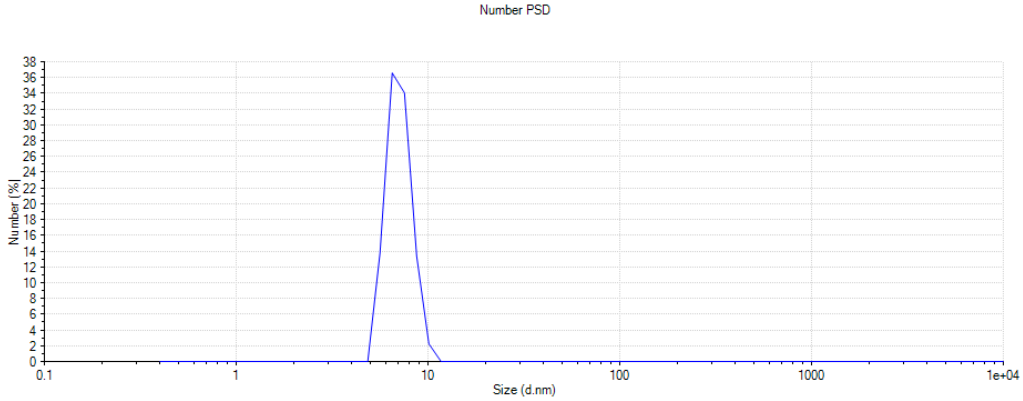

*Supplementary Figure 5.2 Dynamic light scattering average hydrodynamic diameter of **FCD-3** (% number) data. Peak between 6-9 nm.*

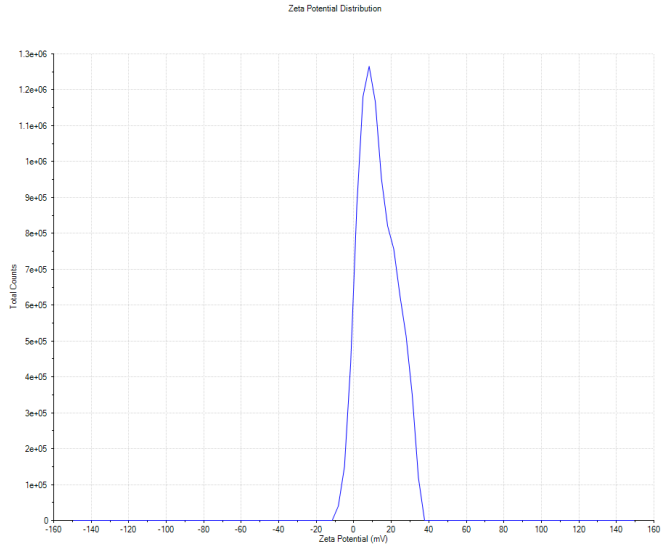

*Supplementary Figure 5.3 Zeta potential average charge of 12.05 mV of **FCD-3**.*

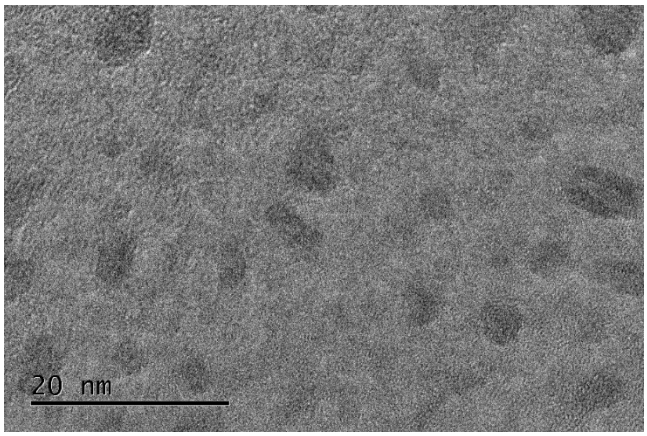

*Supplementary Figure 5.4 High resolution TEM image of **FCD-3.***

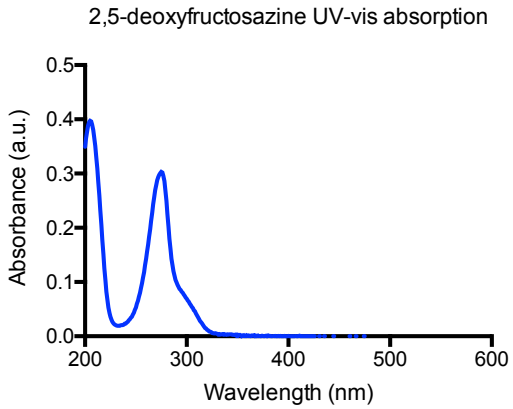

Supplementary figure 5.5 UV-vis absorption of commercial 2,5-deoxyfructosazine

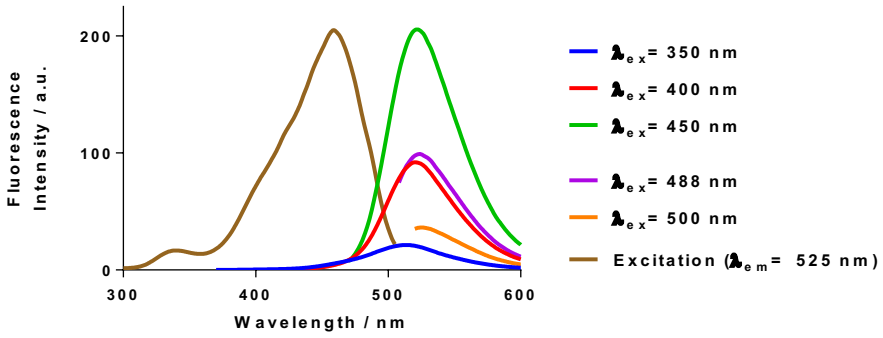

*Supplementary Figure 5.6 Fluorescence spectra of **FCD-3**. Excitation independent emission at 525 nm.*

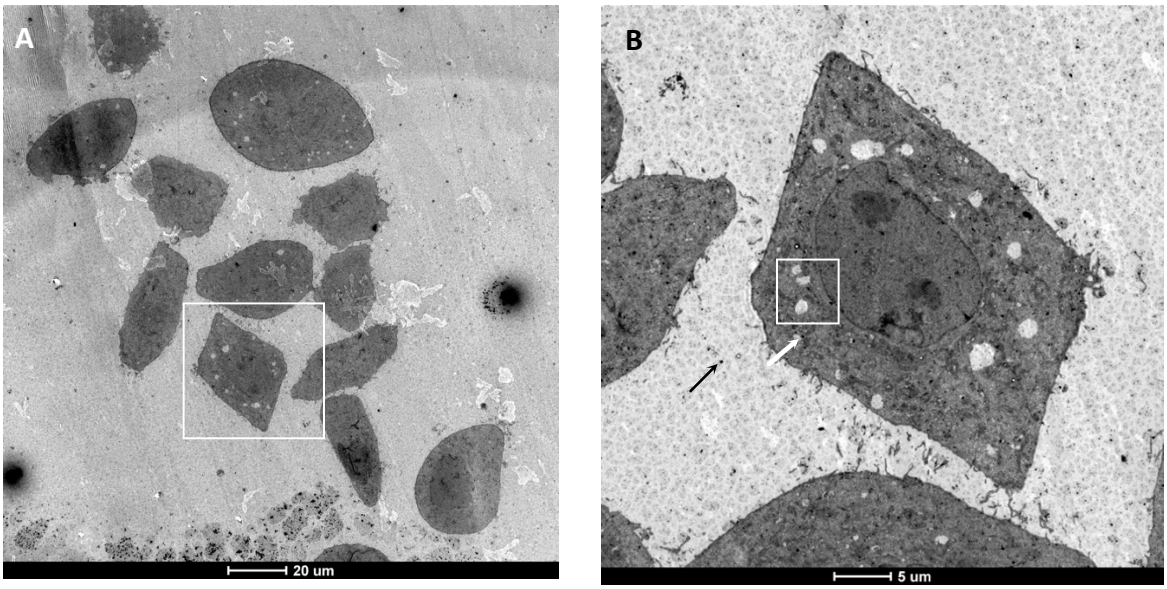

*Supplementary Figure 5.7 Healthy control HeLa cell **1** a) white box identifying the cell within amongst others on the grid. b) magnified image of cell 1, white box highlights an area of interest which is magnified in figure 14.*

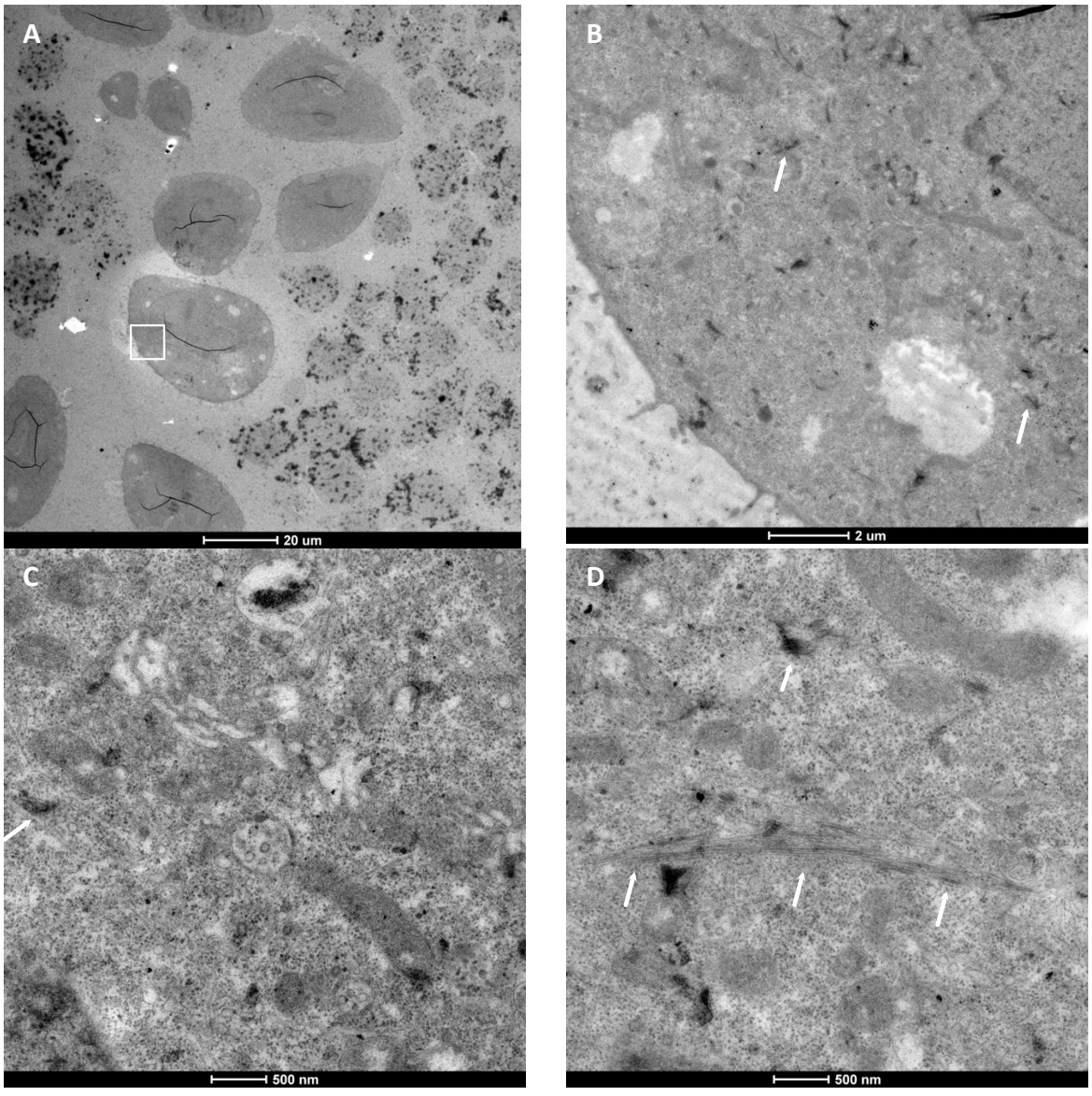

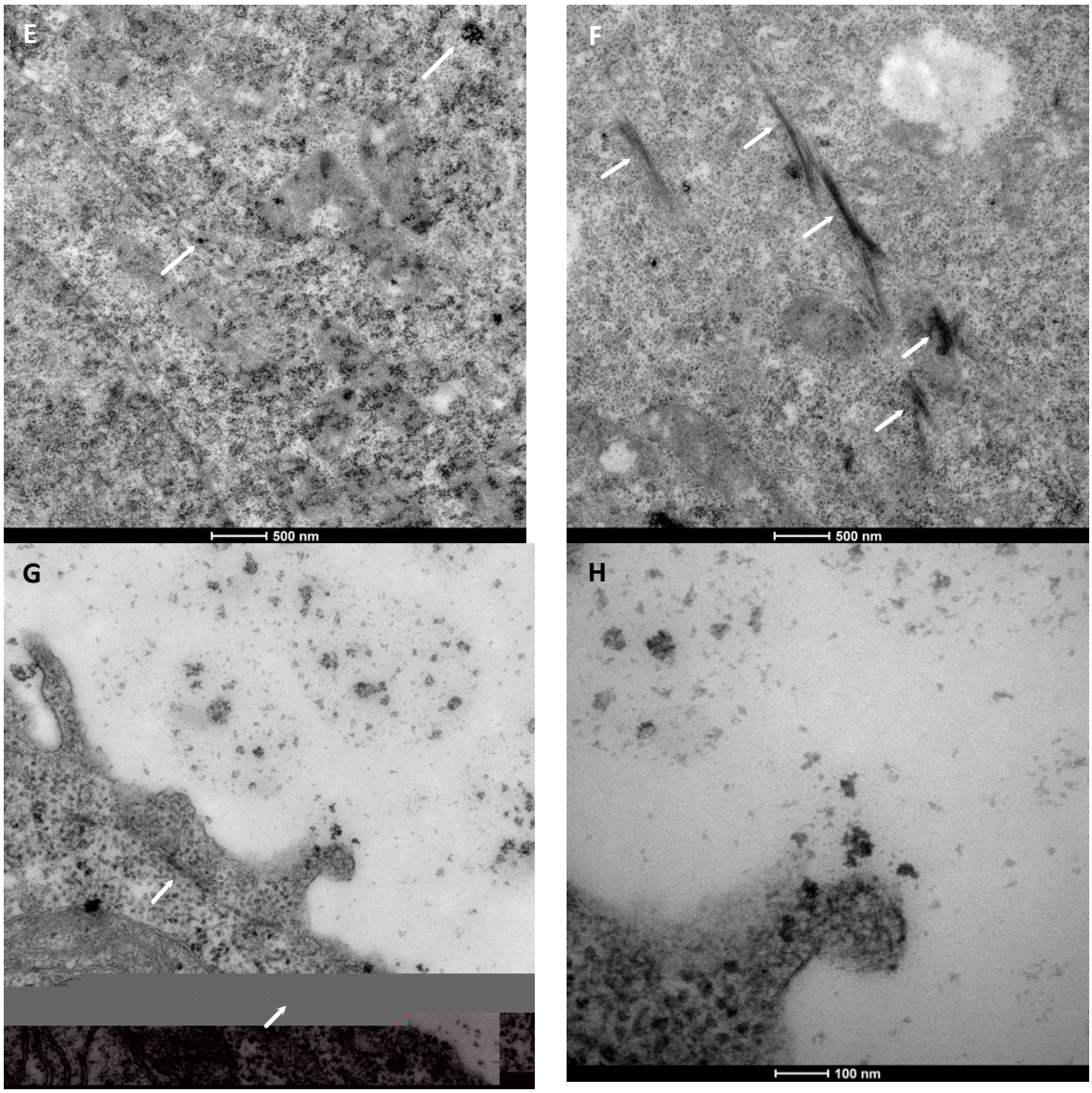

*Supplementary Figure 5.8 EM of a healthy control HeLa cell **2**. A) Shows HeLa cell in surrounding context B) Magnification of the white box in A. C,D,E,F,G,H) Area of the same HeLa cell presented in A&B. White arrows identify stained areas of potential interest.*

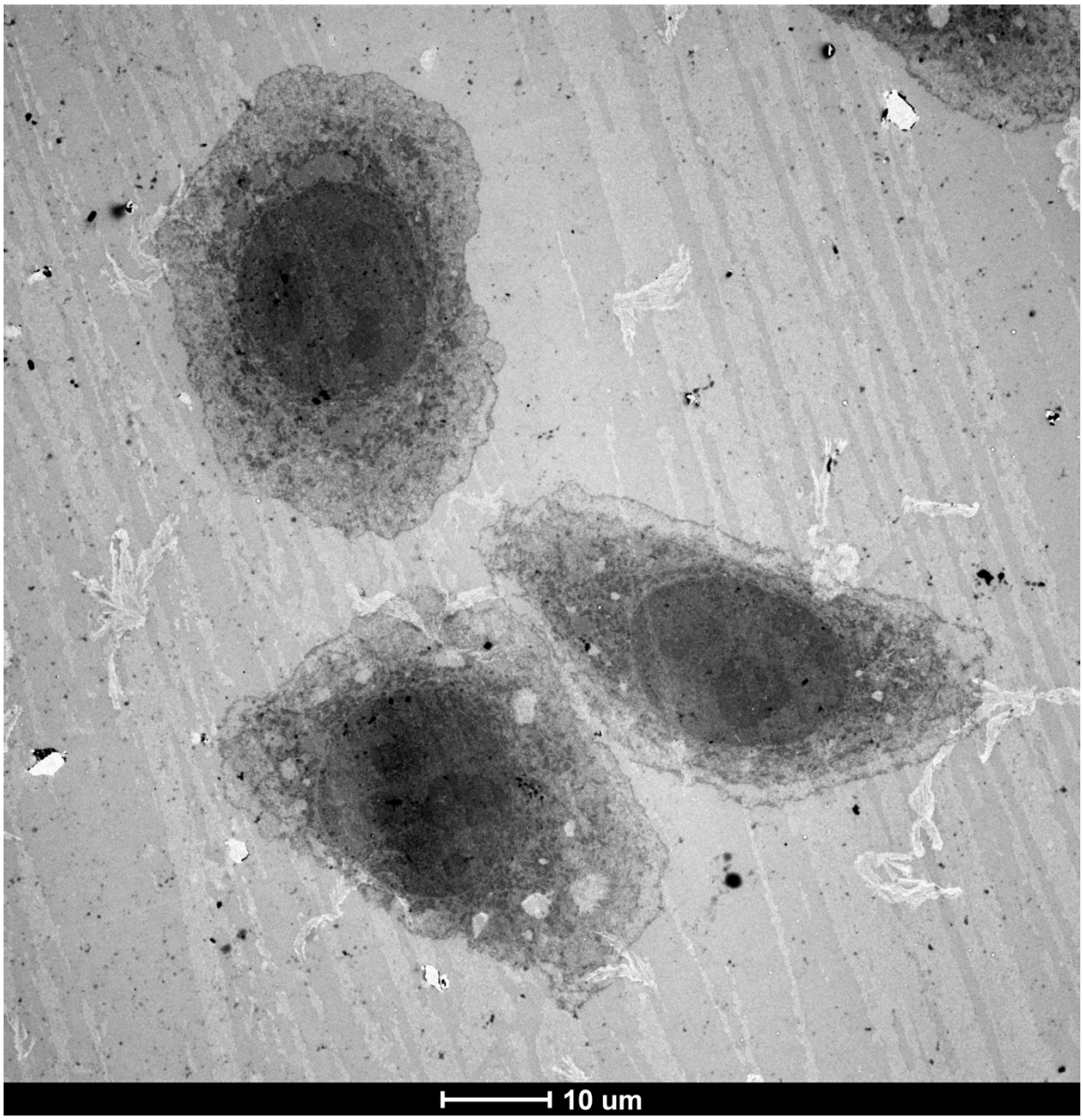

*Supplementary Figure 5.9 EM image of three **FCD-3** treated HeLa cells. Each of these cells were imaged further at higher magnification aiming to identify nanoparticle uptake.*

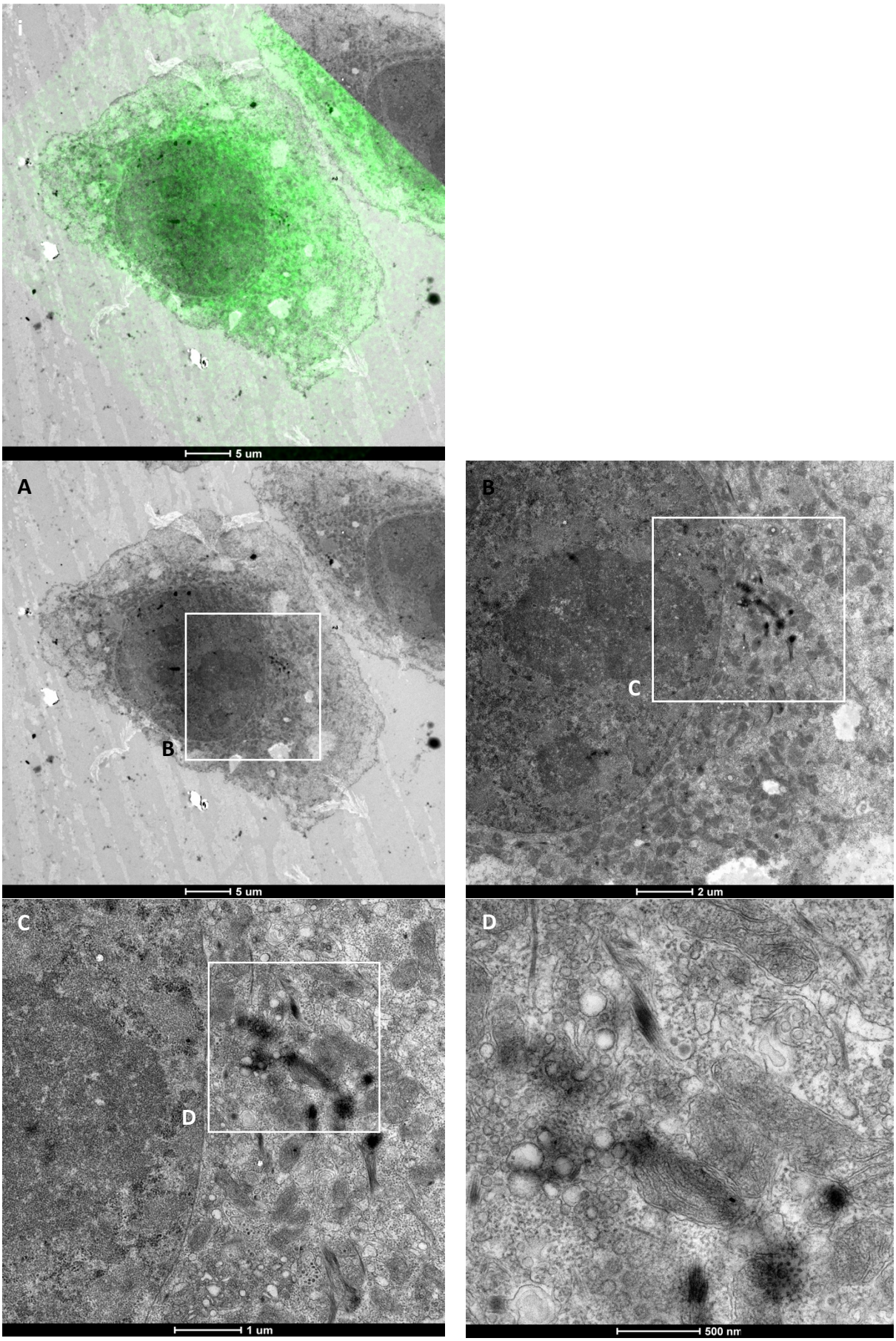
i
5 um
A
B
5 um
B
C
2 um
C
D
1 um
D
500 nm

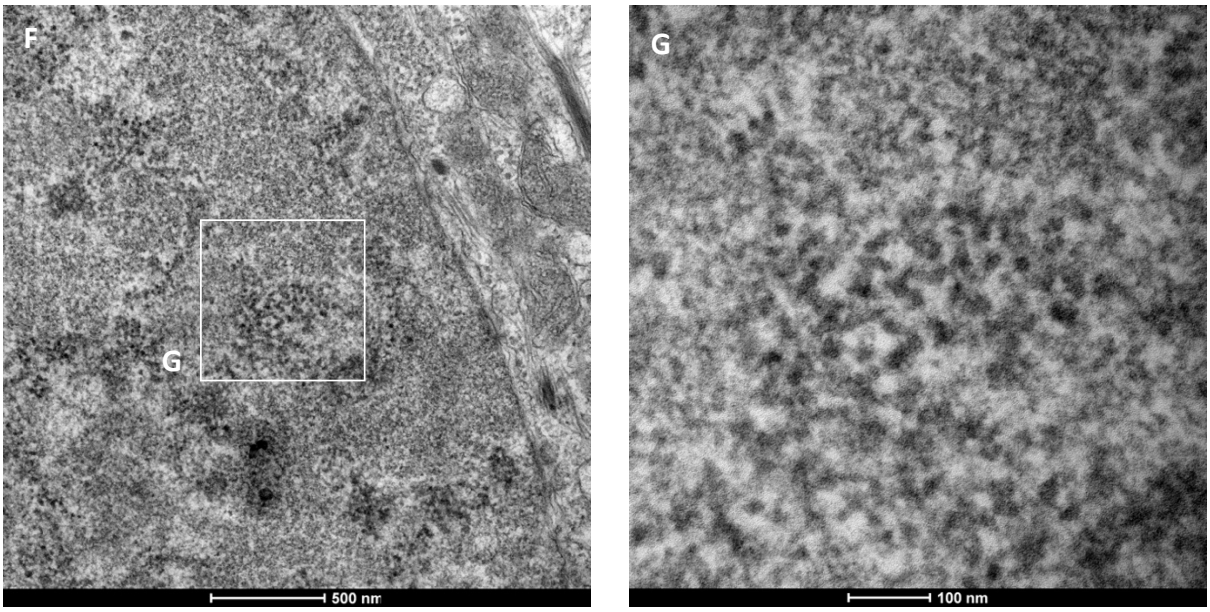

*Supplementary Figure 5.10 CLEM of a second HeLa cell **3** treated with **FCD-3**. i) shows HeLa cell EM and confocal images overlaid in a CLEM image. A) TEM image of HeLa cell **3** B) Shows a magnification of HeLa cell **3** C,D,E,F,G) Show magnified images of HeLa cell **3**. White boxes with labels indicate areas magnified in subsequent images.*

6. General Experimental

UV-Vis

UV-vis was carried out using a Carys UV-Vis 50 spectrometer (Agilent) using a 1 cm path length quartz cuvette (Thor Labs).

DLS and Zeta potential

Dynamic light scattering and Zeta potential measurements were carried out using Malvern Instrument, Zetasizer Nano-S90 ZEN1690 and Nano-Z ZEN 2600 respectively. Samples were prepared in distilled water or 0.1 M HEPES buffer with 5 mM $MnCl_2$ and 5 mM $CaCl_2$ as specified. 70 μL volume disposable micro cuvettes were used for DLS and disposable folded capillary cells DST 1070 for Zeta potential, both purchased from Malvern Panalytical.

Fluorometer

Fluorescence measurements were conducted on a PerkinElmer Fluorescence Spectrophotometer LS50B). The voltage was maintained at 700 V, whilst a 700 μL quartz cuvette was used with pathlength 1 cm for all measurements.

NMR

NMR measurements were carried out on either a Varian 500 MHz or Bruker 400 MHz machine as detailed for each spectrum in the appendix. Samples were made up to ~ 1 mg ml^{-1} in deuterated water before ^{1}H, ^{13}C or HSQC experiments were conducted.

DOSY

Diffusion ordered spectroscopy was carried out on a 500 MHz NMR machine with a relaxation delay of 2 second and samples were prepared in D_2O. Data was processed using MestReNova software, Bernstein polynomial fitting and phasing were carried out on all spectra before peak fit model was used to plot data. Diffusion coefficients from different spectra were corrected against the water peak diffusion coefficient before comparing.

Cell culture

HeLa and MDA cells (ECACC, Public Health England) were maintained in Dulbecco's Modified Eagle's medium (DMEM) with 4.5 g glucose/L. MCF-7 cells were maintained in Minimal Essential Medium (MEM). All cell lines were kept at 37^{o}C in antibiotic-antimycotic and Foetal Bovine Serum (FBS) at 10 % concentration.

Calcein AM and Alamar blue (AB) toxicity assays

These toxicity assays were carried out in tandem in all cases. Experiments were carried out in 96-well plate, post treatment cells were incubated for 1 hour in media containing 5% v/v Alamar blue, at 1 µM concentration Calcein and without FBS, total well volume 1 ml. Calcein is a measure of cell viability using Calcein AM which is reduced to Calcein (λ_{ex} 483 nm, λ_{em} 530 nm) in live cells. The alamar blue assay active ingredient is resazurin which is reduced inside live cells to fluorescent resorufin (λ_{ex} 555 nm, λ_{em} 590 nm). The amount of resazurin turnover positively correlates with cell metabolism. Dye fluorescence emission was measured using a Clariostar microplate reader. All cell culture and assay media and reagents were purchased from Invitrogen, Life Technologies (Thermo-Fisher).

AB and Calcein – IC_{50}

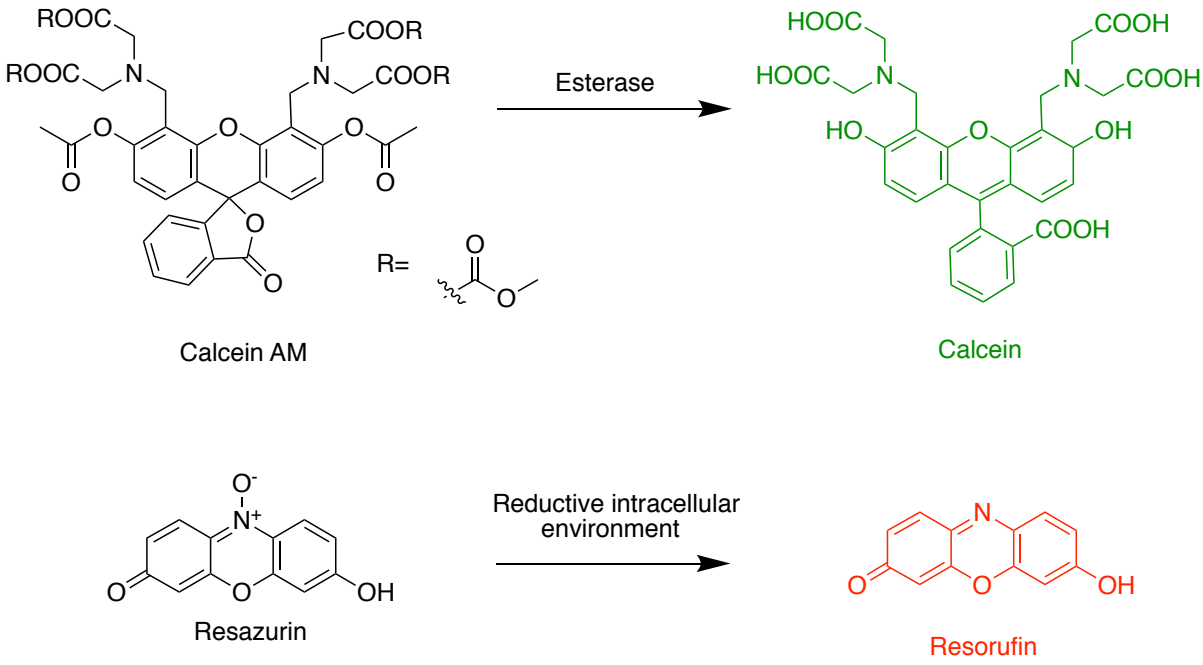

Resazurin is the non-fluorescent active ingredient in the commercially available cell metabolism test Alamar Blue. Upon incubation with cultured cells it diffuses across the cell plasma membrane where it can be reduced by cellular components to the red fluorescent Resorufin. Detecting the fluorescence of Resorufin at 590 nm allows quantification of the intracellular metabolism through a positive correlation. Increased cell metabolic activity is an indicator of cellular proliferation rather than a cell viability test.

Cancer cells proliferate more than healthy cells, meaning that they grow and divide at a faster rate. Subsequently, they require an increased level of metabolic activity facilitated by high production of

energy currencies such as NADPH, NADH, FADH. These molecules are responsible for reducing Reszurin to Resorufin during the Alamar Blue assay. Hence, living cancer cells exhibit a higher metabolic activity compared to healthy cells in the assay.

Other methods of probing this include MTT, MTT/XTT and WST assays. Commonly used is the colorimetric MTT assay which similarly involves reduction by mitochondrial reductases of the tetrazolium salt MTT to formazan. However, this requires solubilisation before its absorbance can be read.

Calcein AM is used as a means to test cell viability. Calcein AM can also cross the cell membrane and in the case of live cells, esterases present in the cytosol cleave the ester bond to produce Calcein which is green fluorescent. After this, calcein cannot cross the plasma membrane and leave the cell. Measuring fluorescence at 530 nm allows quantification of the number of live cells.

7.2 Analytical technique description

7.2.1 TEM

Transmission Electron Microscopy (TEM) involves an electron beam interacting with a sample to produce a contrast image of ultra-high resolution. This technique supersedes light microscopy in terms of resolution due to the De Broglie wavelength of electrons being much smaller than light and allowing for atomic resolution imaging.

An electron beam is produced from an emission source using high voltages commonly between 120 and 200 kV, in a vacuum. Electrons interact and pass through the sample at points of low density and are unscattered, whilst areas of higher density scatter electrons and create dark areas on the detector. The sample must be less than 100 nm thin to allow for electron transmission. In the case of carbon dot imaging; because carbon is a relatively light element, the carbon film should be made thin enough to allow for contrast with the carbon-based nanoparticles.

Scanning Transmission Electron Microscopy (STEM) is a type of TEM which has a more focused ion beam than standard methods which rasters across the sample. STEM can involve collecting only the scattered electrons from the sample using an annular dark-field detector. Combining this signal with, the dark-field image confers greater resolution. Furthermore, using STEM the elemental composition of a sample to be mapped through energy dispersive X-rays (EDX). When irradiated with electrons

elements emit characteristic x-rays which can be detected with a spectrometer. Combined with the high-resolution electron beam in STEM, a high-resolution elemental map can be made of the sample.

7.2.2 AFM

Atomic force microscopy (AFM) involves the physical probing of a sample using a scanning probe to provide atomic structural information. Resolution is much greater than with light microscopy, down to 0.1 nm. Most commonly AFM works via tapping mode to probe the surface of a sample using Van der Waal interactions between the sample and probe as the basis of signal detection. Tapping mode is an intermittent contact-based method with low level sample adhesion and friction. The AFM probe is commonly made of silicon with a high aspect ratio tip on the end with a diameter of ~ 40 nm. This large diameter means that the lateral resolution is low (~ 40 nm reflecting the tip diameter in the work presented in this thesis). However, in the height dimension, sub-nanometer resolution is detected.

The cantilever is vibrated near its resonant frequency above the sample surface using a piezoelectric modulator. As it interacts with the surface intermittently, the oscillation amplitude changes which is used to calculate the tip to surface distance, via the z-feedback loop. In order to know the height of the probe itself, a laser is reflected off the back of the cantilever, which is detected by a photodiode. This all happens as the probe is rastering back and forth across the sample to build up an image of the surface. Tapping mode also allows for phase imaging to be conducted as the tip comes into contact with the sample surface. The difference in oscillation expected (from the piezoelectric modulator input) and measured can be converted into information about the material's physical stiffness.

7.2.3 Quantum yield (Qy)

In order to assess the fluorescence potential of the singlet excited state of our carbon dots we determined the quantum yield. Quantum yield is the fluorescence emission efficiency of a molecule, defined as:

$$Quantum\ yield\ (\phi) = \frac{Photons\ emitted}{Photons\ absorbed}$$

For each carbon dot the quantum yield was determined by comparing against the widely used standard quinine sulfate. This dye is suitable for excitation in the range 310 – 360 nm and emission between 400 – 600 nm[268], similar to the spectral features of our carbon dots. This dye has a quantum yield of 54.6 % determined through independent methodology.

The absorbance of quinine sulfate is measured when < 0.1 a.u. to create a linear calibration curve and to minimise self-absorption effects and plotted against integrated fluorescence (400 – 560 nm). Using this we determined the percentage quantum yield values of our CD's in table 2.5 according to the equation[46]:

$$\phi_{CD} = \phi_{QS} \frac{I_{CD}}{I_{QS}} \frac{{\eta_{CD}}^2}{{\eta_{QS}}^2}$$

The integrated fluorescence (I_{CD}) of the CD and quinine sulfate (I_{QS}) at the same absorbance (< 0.1 a.u.) were determined experimentally over the linear portion of the absorbance v. integrated fluorescence relationship. The refractive index (η_{CD} & η_{QS}) is η = 1.33 for aqueous media and the Qy of quinine sulfate (ϕ_{QS}) 0.54. Substituting these into equation X gives:

$$\phi_{CD} = 0.546 \frac{I_{CD}}{I_{QS}} \frac{1.33^2}{1.33^2}$$

The quantum yield for each CD-saccharide can be calculated from either a single integrated fluorescence point against absorption or for more reliable values, by plotting a line of linear regression from multiple measurements of integrated fluorescence against absorption.

Then using the gradient of absorption against integrated area under the fluorescence intensity (400-560 nm) for each CD-saccharide can be standardised against the gradient of the quinine sulfate reference curve to determine the Qy[269].

$$\phi_{CD} = \phi_{QS} \frac{m_{CD}}{m_{QS}} \frac{{\eta_{CD}}^2}{{\eta_{QS}}^2}$$

The values m_{CD} & m_{QS} refer to the gradient of the calibrated absorbance against fluorescence curves.

7.2.4 DLS

Dynamic light scattering uses the detected scattered light from a nanoparticle to determine the hydrodynamic size of said particle. Particles in solution move due to Brownian motion which is measured in DLS using a laser (633 nm) and detecting the backscatter from the particle, usually at 173° to the angle of incidence. This allows for the diffusion coefficient to be measured from which the hydrodynamic size can be determined through the Stokes-Einstein equation:

$$D_h = \frac{k_B T}{3 \pi \eta D_t}$$

Where D_h = Translational diffusion coefficient (m^2 s^{-1}), k_B = Boltzmann constant ($m^2 kg$ Ks^{-2}), T = Temperature (K), h = viscosity (Pa.s.), D_t = Hydrodynamic diameter.

As particles diffuse and the detector records signals a trace is created. The frequency of fluctuations in the trace reflects the frequency of signal coming from the particles in solution. Hence smaller, faster moving particles create a trace with more fluctuations over time. This data is used to create an autocorrelation function which quantifies the time taken from a monodispersed sample signal to decay so that the signal no longer relates to the signal at time 0, which looks like a single exponential decay over time. This time taken is used to determine the translational diffusion coefficient (D_h) in the Stokes-Einstein equation, which is used to determine the hydrodynamic diameter.

When looking for monodispersion, the poly dispersity index (PDI) can indicate whether you are seeing aggregation. The PDI is a measure of the broadness of the size distribution, the larger the value the more polydispersed the sample. Between 0.05 and 0.7 size data collected is reliable. Looking at the size distribution information, number, intensity and volume can provide further information on the populations of species in a sample.

7.2.4.1 Volume, Number and Intensity distribution

Each of intensity, number and volume distribution values reported are drawn from the same correlation function and interpret the scatter signal differently. Intensity data shows the raw scattering signal observed for each peak. Larger particles which scatter more (d^6 according to Rayleigh scattering theory) will have a greater signal than the same number of particles of a smaller diameter. Hence, describing the proportion of sample making up each peak. The Z-average value reported is the mean of the intensity peaks and is best suited to describing monodispersed samples.

Number and Volume data use Mie Theory to interpret scattering data. This takes into account the scattering potential of a particle of a certain size (from the correlation function) and composition (refractive index). Number distribution represents the number of particles of that size corrected for the scattering they produce. It describes the number of each type of species in solution. The volume distribution considers the size and number of species in solution and reports the volume of space they take up based on particles being spherical. Number and volume data contain more errors than intensity data as they contain added assumptions. However, being able to look at number data can reveal smaller aggregates or monodispersed CDs which may otherwise be occluded by larger aggregates. This is useful to try and observe monodispersed carbon dots when they naturally lend to aggregate.

When investigating an aggregating population and looking at the shift from monodispersed to aggregated number data allows smaller particles to be picked up when they may be missed in intensity-based measurements. Furthermore, when looking at a titration involving 2 components such as carbon dot and lectin, comparing like for like species removes certain errors associated with number measurements.

7.2.5 Zeta potential

Zeta potential (ζ) refers to the electrochemical potential between the surface of a colloidal suspension and the dispersant it is in. The surface is usually referring to the slipping plane of the particle, where the free-flowing dispersant meets the stationary layer of dispersant associated with the particle (which is made up of an electrical double layer). The zeta potential value gained describes the net charge at the surface of a particle in a particular solution. This provides information on the colloidal stability of a particle, the higher the value the more stable it is.

Upon the introduction of an electric field (*E*), particles which have a net charge will move. Using light scattering, the velocity (V) of these particles is measured and the **electrophoretic mobility** (μ_e) which is calculated according to:

$$\mathrm{V} = \mu_e \mathrm{E}$$

And zeta potential (ζ) *is calculated according to:*

$$\mu_e = \frac{2\mathrm{e}\zeta f(k\alpha)}{3\eta}$$

Where e is the dielectric constant, η is the absolute zero-shear viscosity of the diluent and $f(k\alpha)$ is Henry's function. In the case of polar aqueous diluent $f(k\alpha) = 1.5$ and in the case of non-polar diluent $f(k\alpha) = 1$.

For ζ measurements the dispersant is required to be conductive but below 5 mS/cm, for which 0.1 M HEPES (5 mM $CaCl_2$ and 5 mM $MnCl_2$) buffer is suited with a conductivity of 4.39 ± 0.41 mS/cm. This allows for an electrical current to be applied across the cell but not too high that the electrodes overheat and blacken. As a general rule higher ζ values correspond to more monodispersed particles. However, the zeta potential value indicating aggregation is particle dependent and should be determined experimentally, through combining zeta potential and DLS data.

7.2.6 UV-Vis

Carbon dots have certain absorption characteristics seen through UV-Vis spectroscopy. Looking at this spectra can help characterise the origin of absorption, a peak between 200-250 nm can be assigned to $\pi - \pi^*$ electronic transitions in C=C and C=N aromatic domains and a peak between 250 – 350 nm can be assigned to $n - \pi^*$ electronic transitions in C=O and C=N sp^2 conjugation as well as carboxyl and amine groups in the edge states. The edge states refer to hybridised groups at the edge of graphene sp^2 or crystalline domains[270]. Often a tail into the visible region (up to 800 nm) is seen reflecting the variety of surface states that exist on CDs. Each state could be seen as imposing its own small peak which when overlaid represent the CD surface whilst the peaks at 200 – 270 nm represent the core absorption and 280 – 350 nm represent the edge states between the core and surface[271].

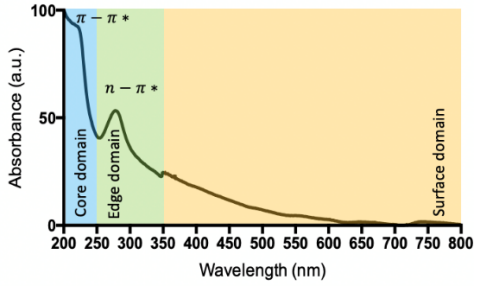

Analytical technique 1 Example UV-visible spectroscopy spectra.

7.2.7 Photoluminescence

Photoluminescence describes the light emitted following absorption of a photon by a molecule or material such as carbon dots. Multiple fluorescence centres exist in carbon dots reflecting their multiple absorption bands coming from any of the core, edge or surface states. Fluorescence resulting from core absorption, when the CD is well passivated, is excitation independent as it emits at one discrete wavelength. This is because the CD core often is similar in structure to a highly conjugated graphene molecule. Upon irradiating with higher wavelengths, the surface and edge states are excited, and they can fluorescence at a range of wavelengths red-shifted with respect to the excitation wavelength. The range of emissions reflect the range of hybridised groups and band gaps belonging to the CD.

The energy in the LUMO band will relax (vibrational relaxation) to the lowest orbital before relaxing to the HOMO band where it can fluoresce. Hence, the surface state controls the final PL properties of the CD. Overall, depending on their structure and PL origin carbon dots can exhibit excitation

dependent or independent emission. Small surface molecules on the surface of the CD can have their own PL spectra, which is excitation independent. Solvent and pH can affect the surface group PL properties and studies have been carried out to understand this effect[272].

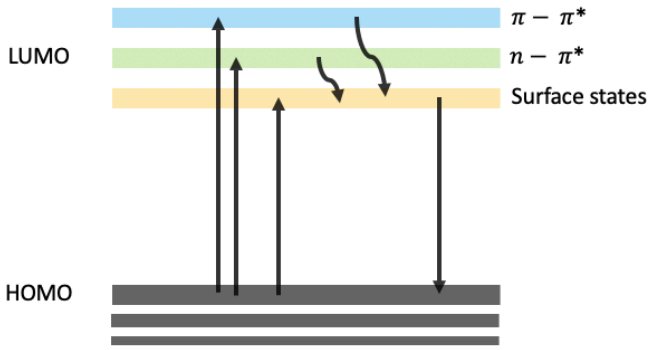

Analytical technique 2 HOMO-LUMO bands which underlie fluorescence in a molecule or particle.

2.2.8 FTIR

Fourier transformed infrared (FTIR) spectroscopy collects information on a samples IR absorption over a range of wavelengths 600-4000 cm^{-1}. Different bonds absorb light of different frequencies over this range, hence FTIR is diagnostic of bonds and therefore functional groups presence in a material. Spectra shows peaks which dip downwards when light of that particular wavelength has been absorbed, and the fingerprint region unique to a sample is below 1500 cm^{-1}. FTIR can be used in collaboration with other techniques as a means to identify a molecule. With carbon dots, it is used to identify the surface functional groups as they are accessible and able to absorb IR photons. Some CD syntheses use FTIR kinetics to observe the influence of reaction conditions on the surface functionality.

7. Appendices

7.1 NMR spectra of all synthesised molecules and CD-carbohydrates

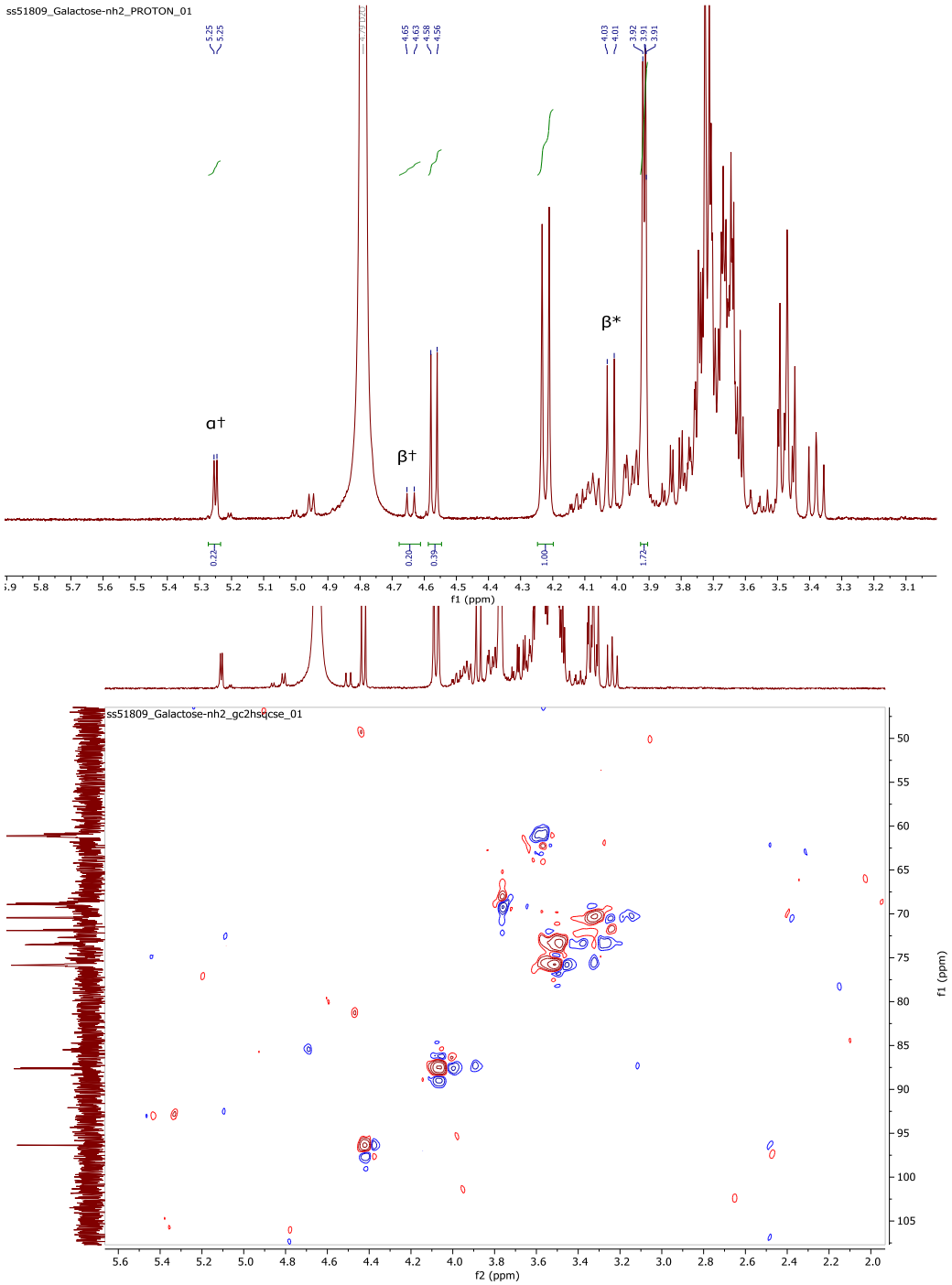

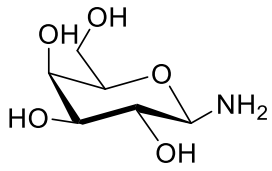

Figure A.1 ***1*** *1-Amino-1-deoxy-β-D-galactopyranoside*[95]

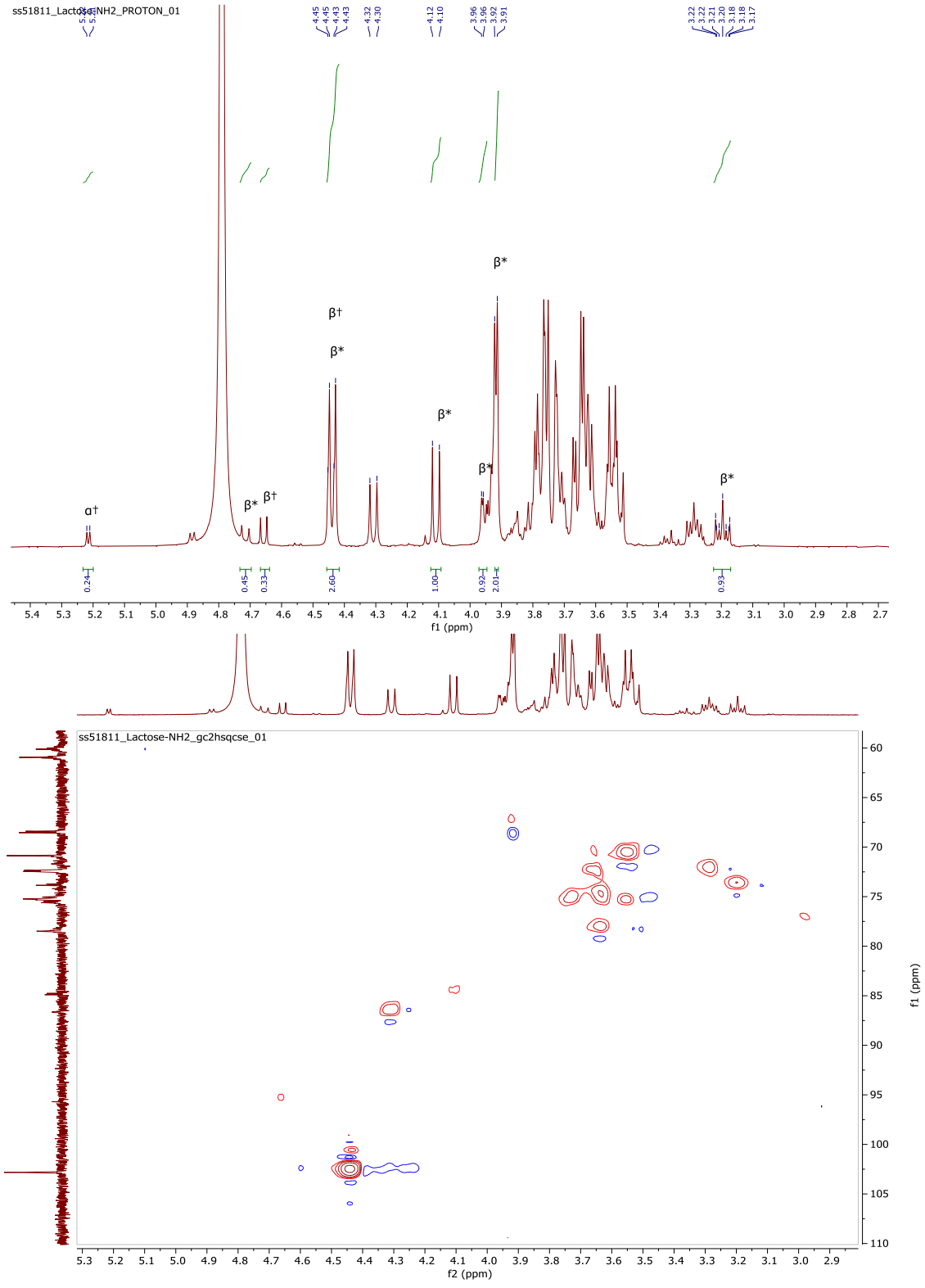

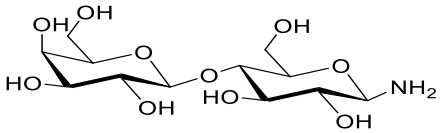

Figure A.2 **2** 1-Amino-1-deoxy-β-D-lactopyranoside[96]

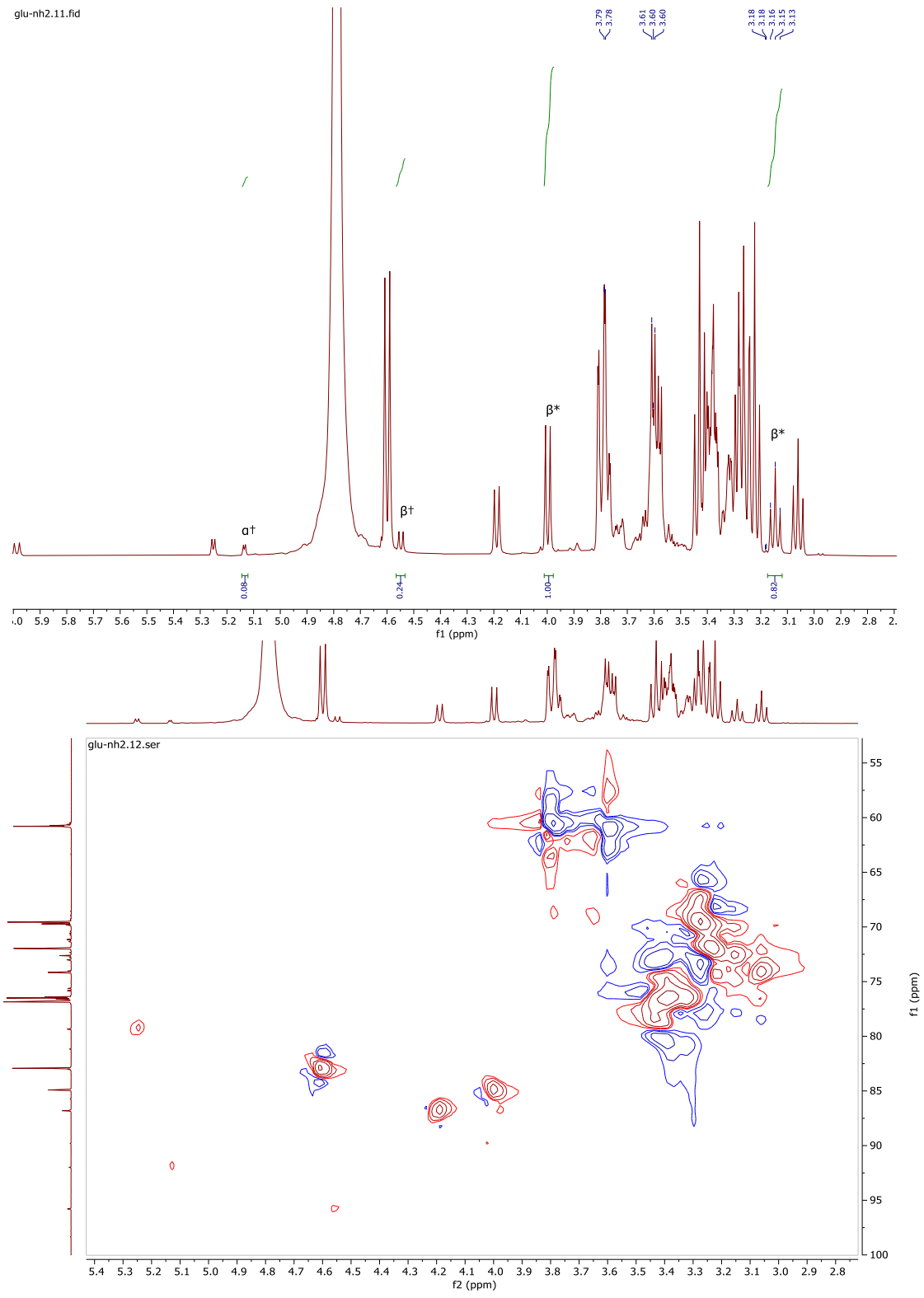

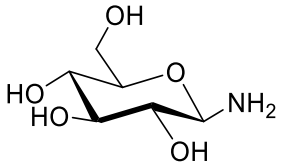

Figure A.3 **3** 1-Amino-1-deoxy-β-D-glucopyranoside[97]

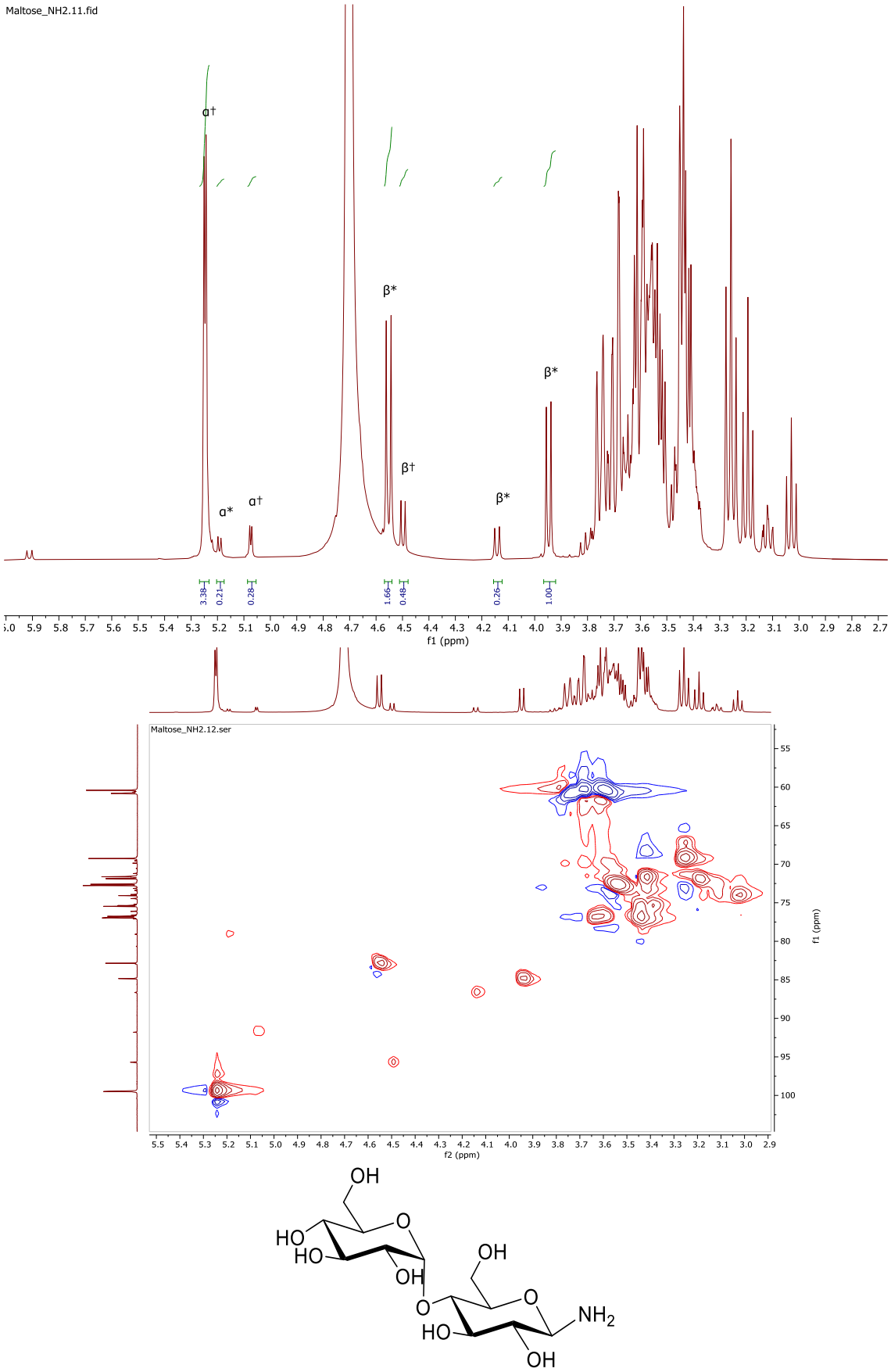

Figure A.4 **4** 1-Amino-1-deoxy-β-D-maltopyranoside[96]

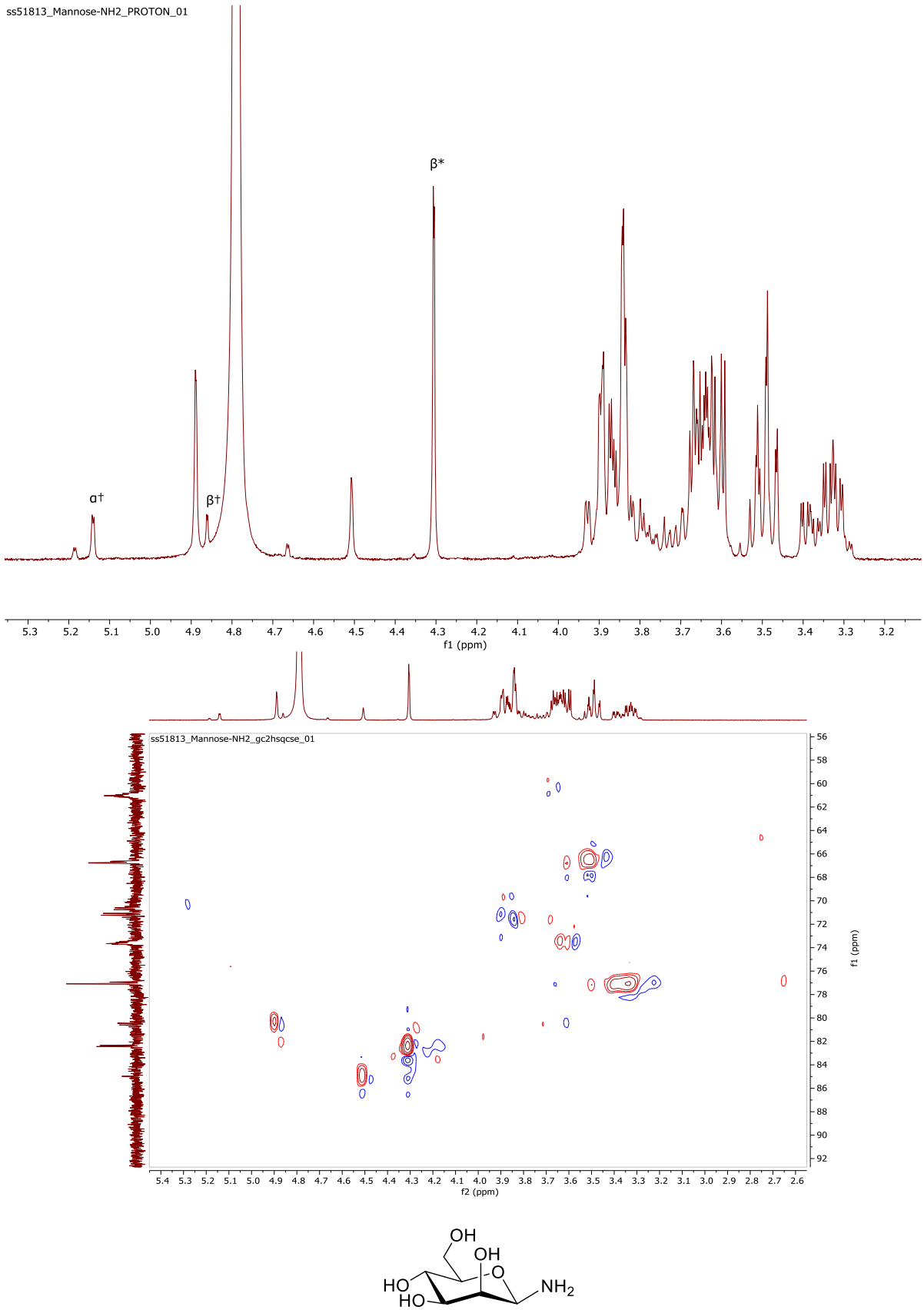

Figure A.5 **5** 1-Amino-1-deoxy β-D-mannopyranose

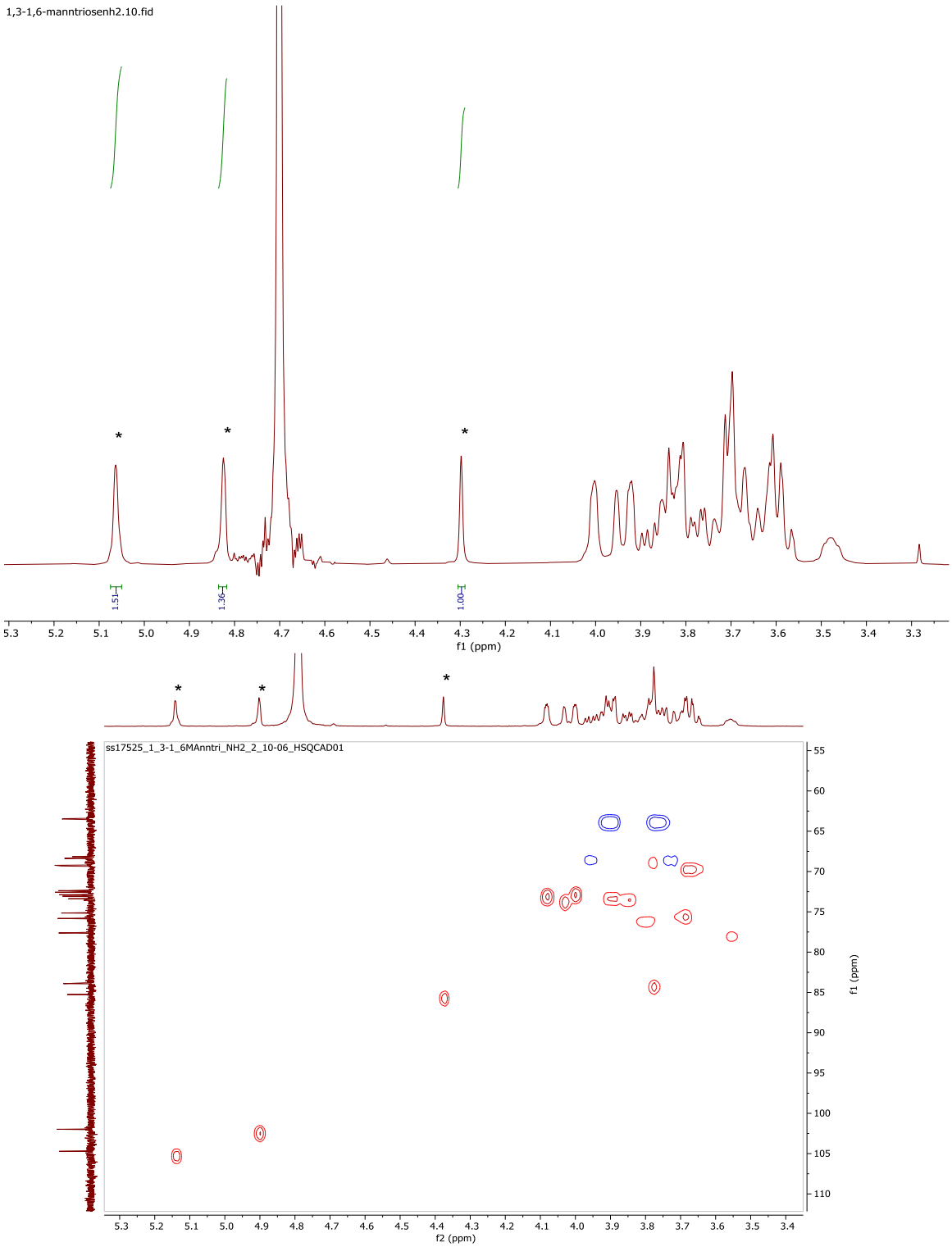
1,3-1,6-manntriosenh2.10.fid
*
*
*
1.51
1.36
1.00
5.3 5.2 5.1 5.0 4.9 4.8 4.7 4.6 4.5 4.4 4.3 4.2 4.1 4.0 3.9 3.8 3.7 3.6 3.5 3.4 3.3
f1 (ppm)
*
*
*
ss17525_1_3-1_6MAnntri_NH2_2_10-06_HSQCAD01
55 60 65 70 75 80 85 90 95 100 105 110
f1 (ppm)
5.3 5.2 5.1 5.0 4.9 4.8 4.7 4.6 4.5 4.4 4.3 4.2 4.1 4.0 3.9 3.8 3.7 3.6 3.5 3.4
f2 (ppm)

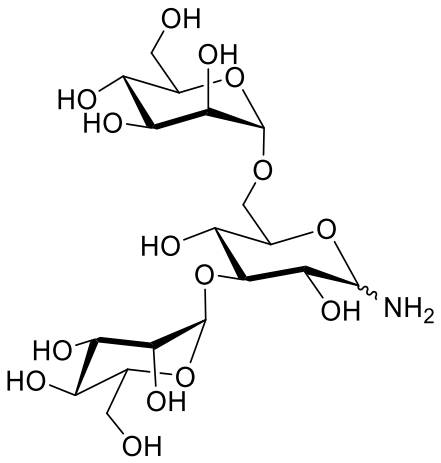

Figure A.6 **6** 3,6-Di-O-(α-D-mannopyranosyl)-1-amino-1-deoxy-D-mannopyranose

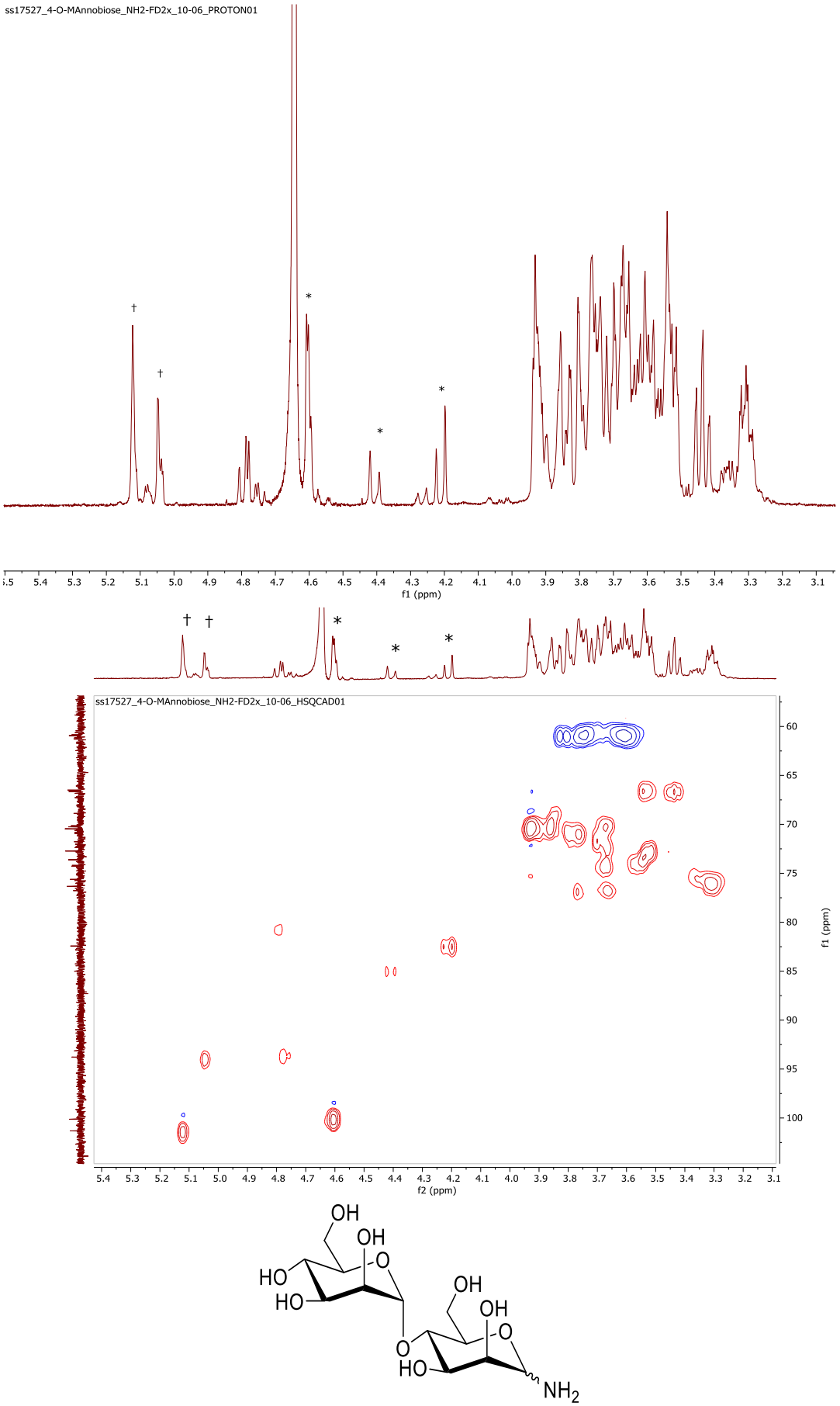

Figure A.7 **7** 4-O-(α-D-Mannopyranosyl)-1-amino-1-deoxy-D-mannopyranose

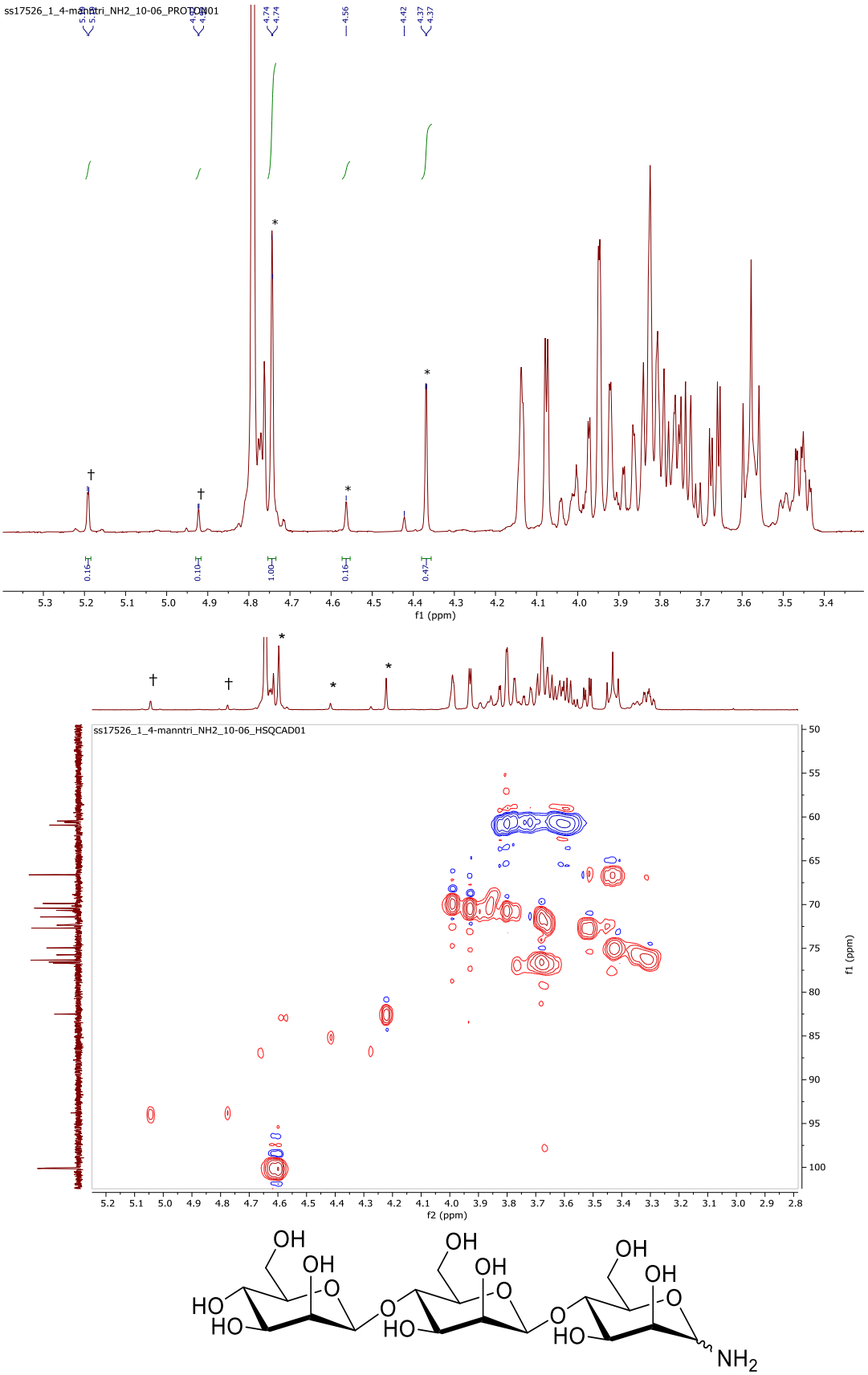

Figure A.8 **8** β-D-Mannopyranose-(1—4)-β-D-mannopyranose-(1—4)-1-amino-1-deoxy-β-D-mannopyranose.

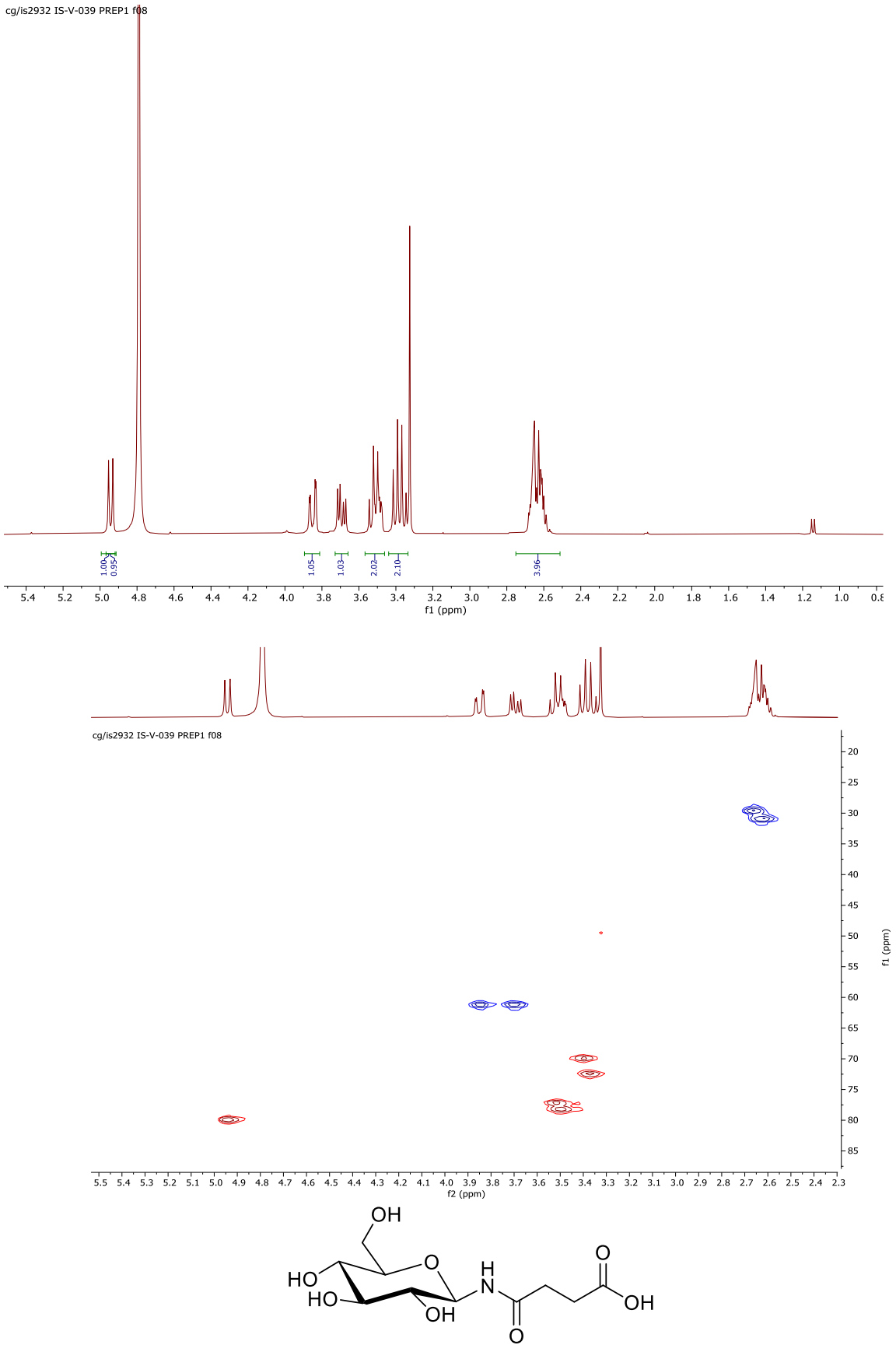

*Figure A.9 **9** 1-amino-(4-oxobutanoic acid)-β-D-glucopyranose (synthesised by another member of the Galan group)*

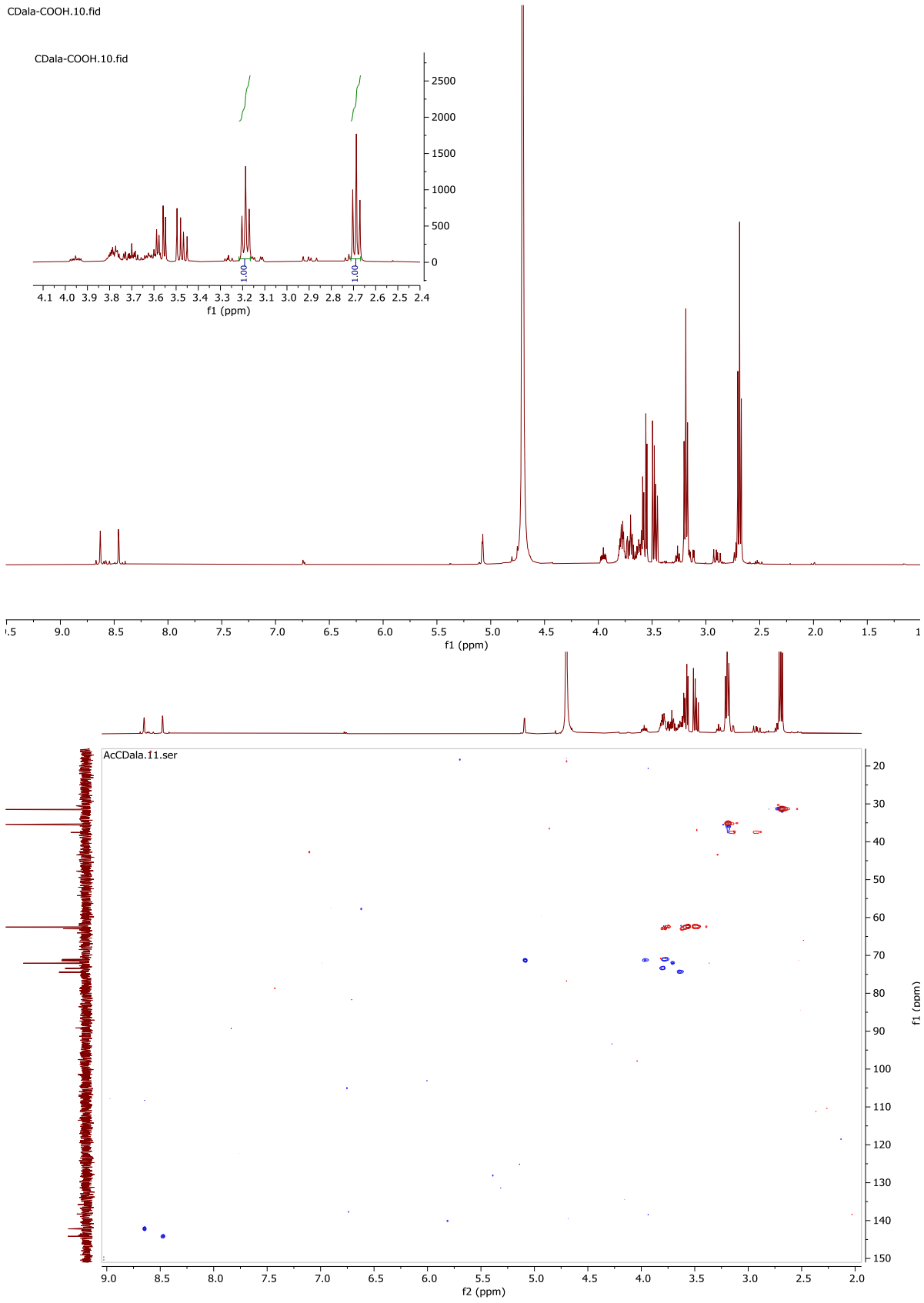
CDala-COOH.10.fid
CDala-COOH.10.fid
f1 (ppm)
f1 (ppm)
AcCDala.11.ser
f2 (ppm)
f1 (ppm)

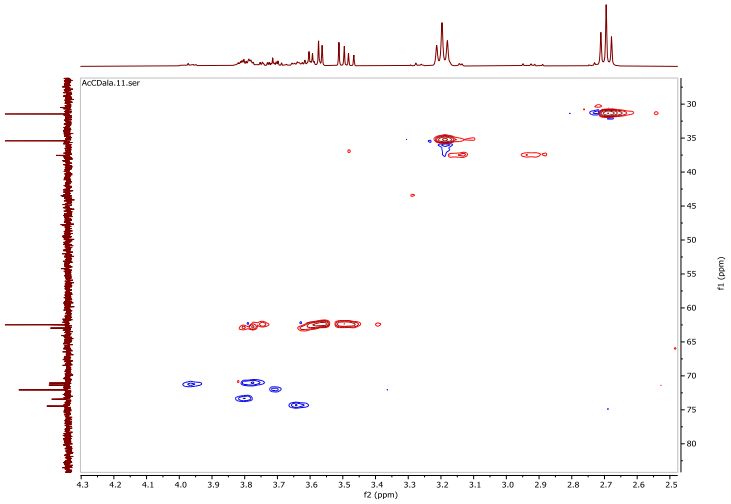

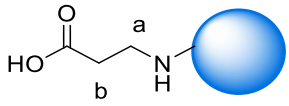

Figure A.10 **10 AcCDala**

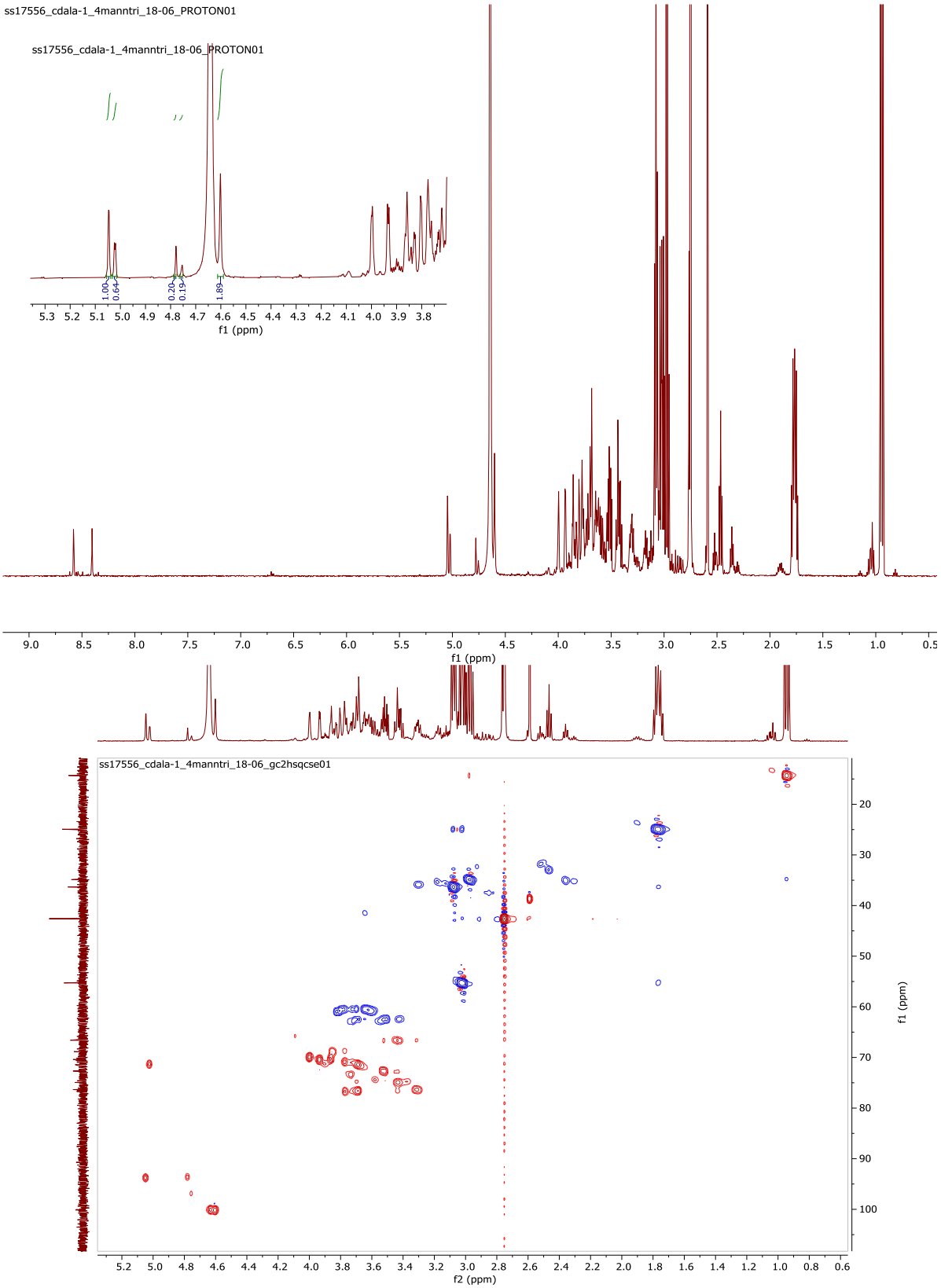
ss17556_cdala-1_4manntri_18-06_PROTON01
ss17556_cdala-1_4manntri_18-06_PROTON01
1.00
0.64
0.20
0.19
1.89
5.3 5.2 5.1 5.0 4.9 4.8 4.7 4.6 4.5 4.4 4.3 4.2 4.1 4.0 3.9 3.8
f1 (ppm)
9.0 8.5 8.0 7.5 7.0 6.5 6.0 5.5 5.0 4.5 4.0 3.5 3.0 2.5 2.0 1.5 1.0 0.5
f1 (ppm)
ss17556_cdala-1_4manntri_18-06_gc2hsqcse01
5.2 5.0 4.8 4.6 4.4 4.2 4.0 3.8 3.6 3.4 3.2 3.0 2.8 2.6 2.4 2.2 2.0 1.8 1.6 1.4 1.2 1.0 0.8 0.6
f2 (ppm)
20 30 40 50 60 70 80 90 100
f1 (ppm)

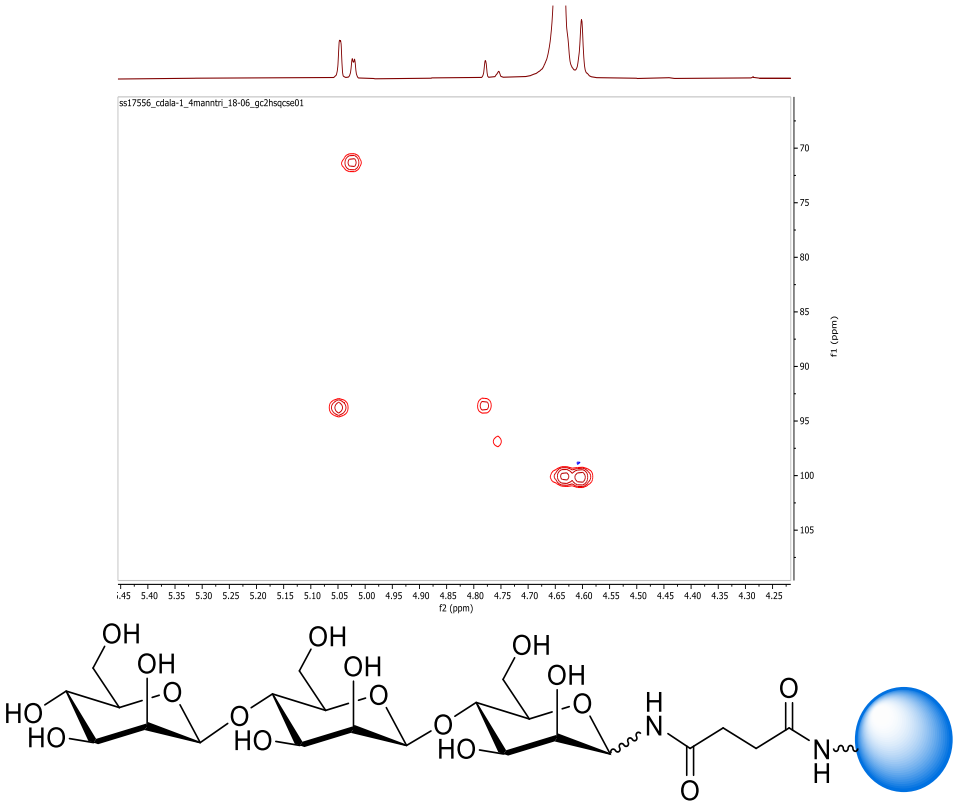

Figure A.11 **11** CDala-β-D-mannopyranose-(1—4)-β-D-mannopyranose-(1—4)-β-D-mannopyranose

CDala-1,4-mannotriose

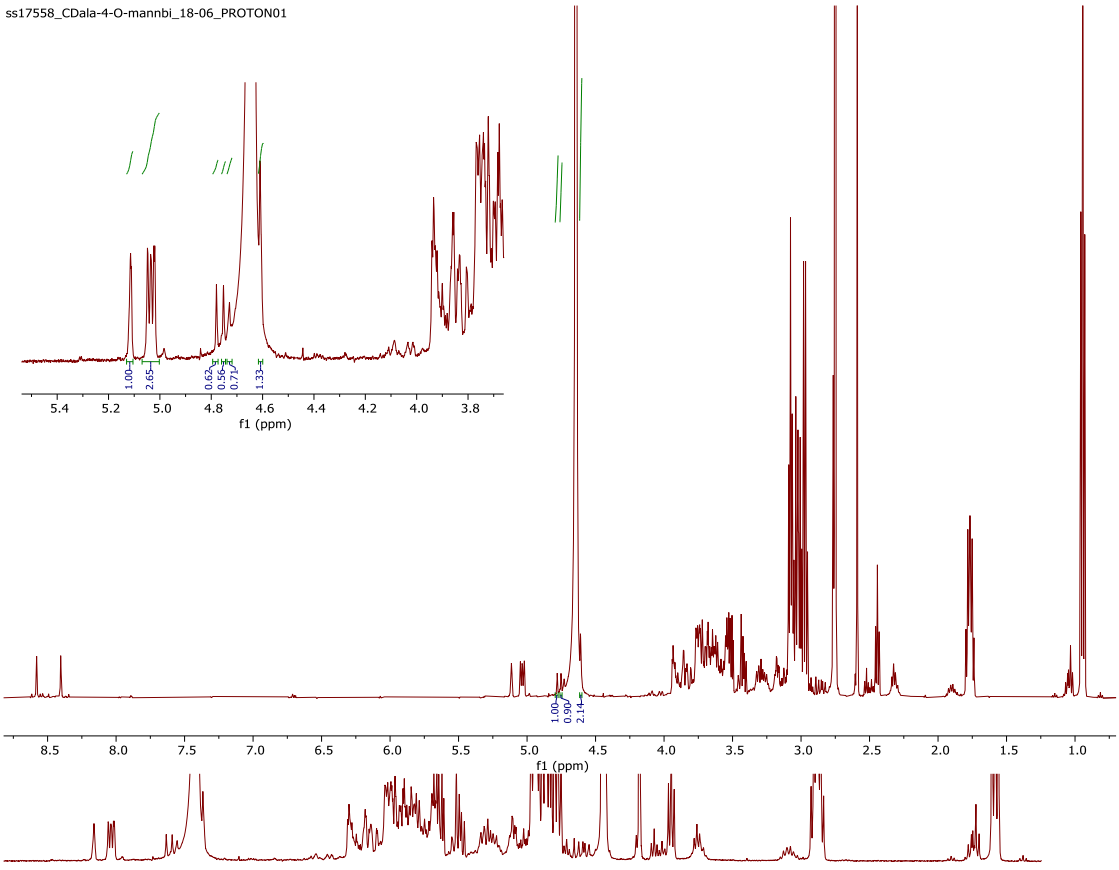
ss17558_CDala-4-O-mannbi_18-06_PROTON01
1.00
2.65
0.62
0.56
0.71
1.33
5.4 5.2 5.0 4.8 4.6 4.4 4.2 4.0 3.8
f1 (ppm)
1.00
0.90
2.14
8.5 8.0 7.5 7.0 6.5 6.0 5.5 5.0 4.5 4.0 3.5 3.0 2.5 2.0 1.5 1.0
f1 (ppm)

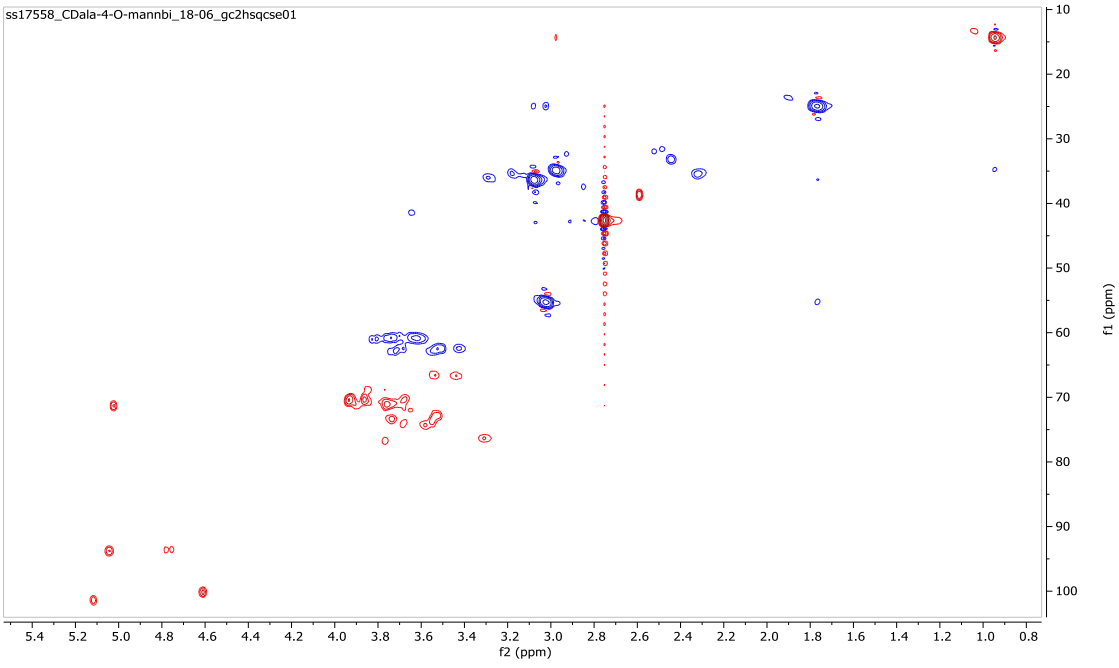
ss17558_CDala-4-O-mannbi_18-06_gc2hsqcse01
10
20
30
40
50
60
70
80
90
100
f1 (ppm)
5.4 5.2 5.0 4.8 4.6 4.4 4.2 4.0 3.8 3.6 3.4 3.2 3.0 2.8 2.6 2.4 2.2 2.0 1.8 1.6 1.4 1.2 1.0 0.8
f2 (ppm)

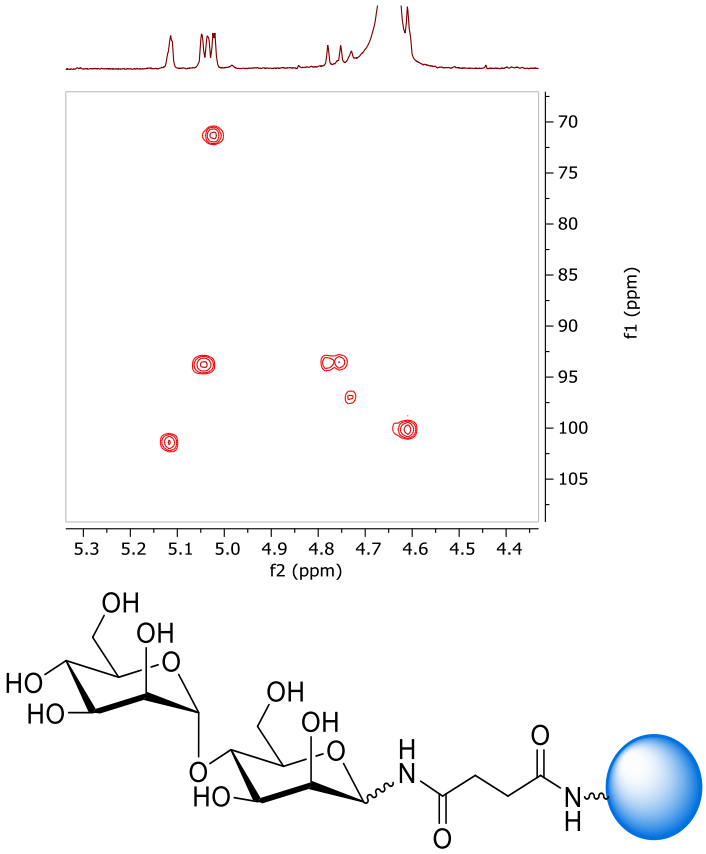

Figure A.12 **12** CDala- 4-O-(α-D-mannopyranosyl)-D-mannopyranose
CDala-4-O-mannobiose

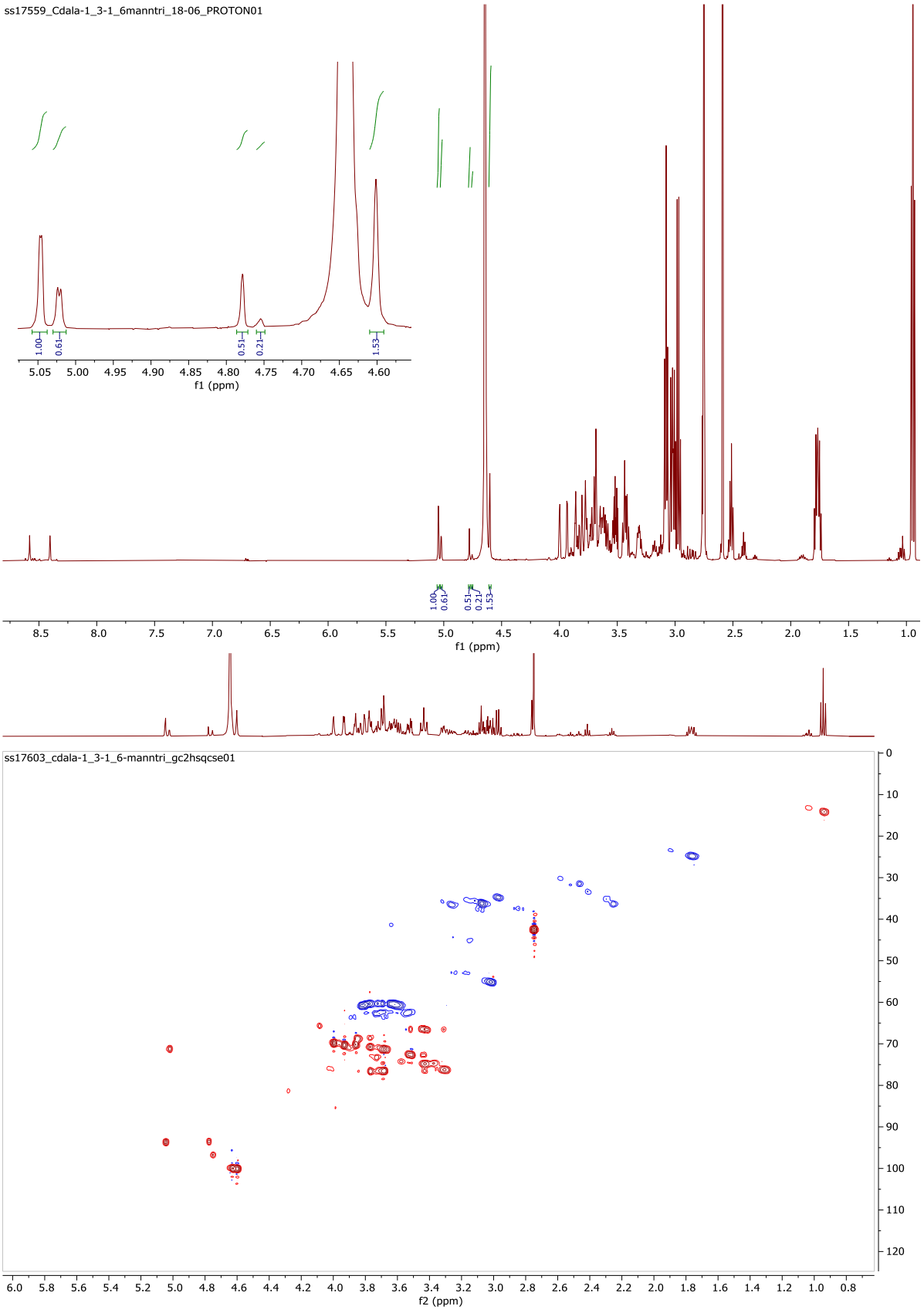
ss17559_Cdala-1_3-1_6manntri_18-06_PROTON01
1.00
0.61
0.51
0.21
1.53
5.05 5.00 4.95 4.90 4.85 4.80 4.75 4.70 4.65 4.60
f1 (ppm)
8.5 8.0 7.5 7.0 6.5 6.0 5.5 5.0 4.5 4.0 3.5 3.0 2.5 2.0 1.5 1.0
f1 (ppm)
ss17603_cdala-1_3-1_6-manntri_gc2hsqcse01
0 10 20 30 40 50 60 70 80 90 100 110 120
6.0 5.8 5.6 5.4 5.2 5.0 4.8 4.6 4.4 4.2 4.0 3.8 3.6 3.4 3.2 3.0 2.8 2.6 2.4 2.2 2.0 1.8 1.6 1.4 1.2 1.0 0.8
f2 (ppm)

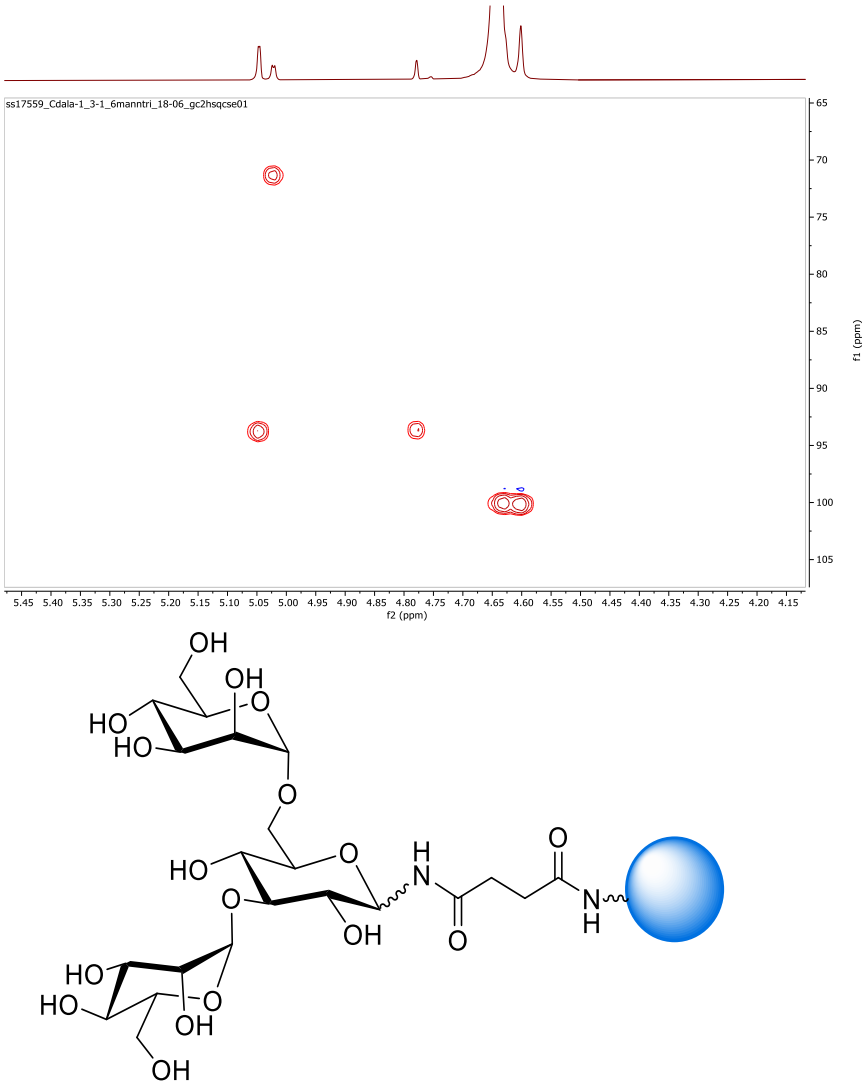

Figure A. **13** CDala-3,6-di-O-(α-D-mannopyranosyl)-D-mannopyranose
CDala-1,3-1,6-manntriose

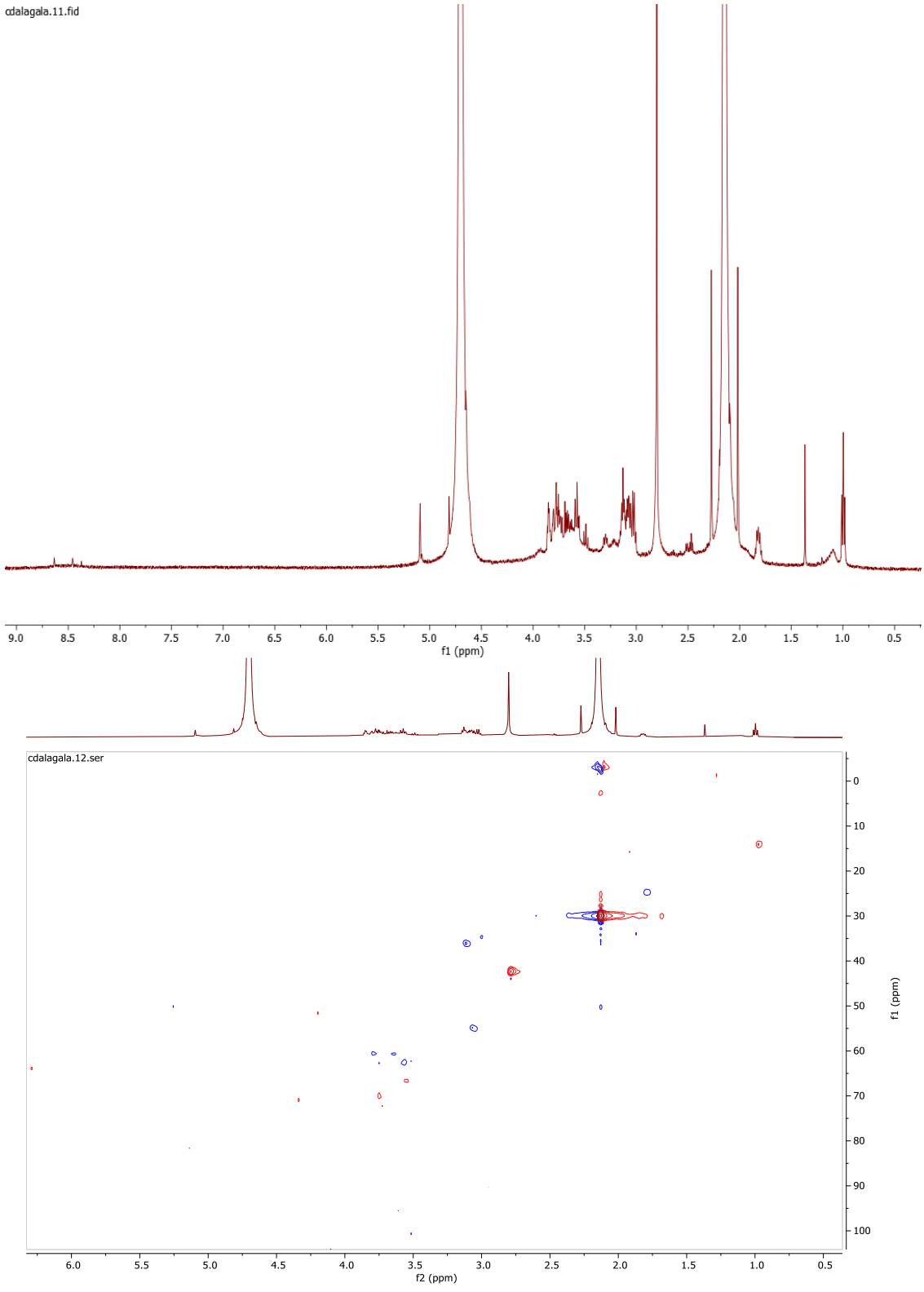

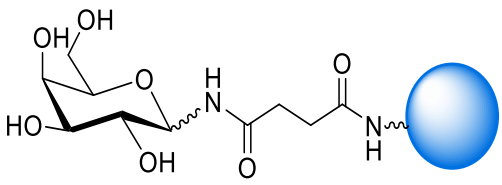

Figure A.14 **14** CDala-β-D-galactose

CDala-galactose

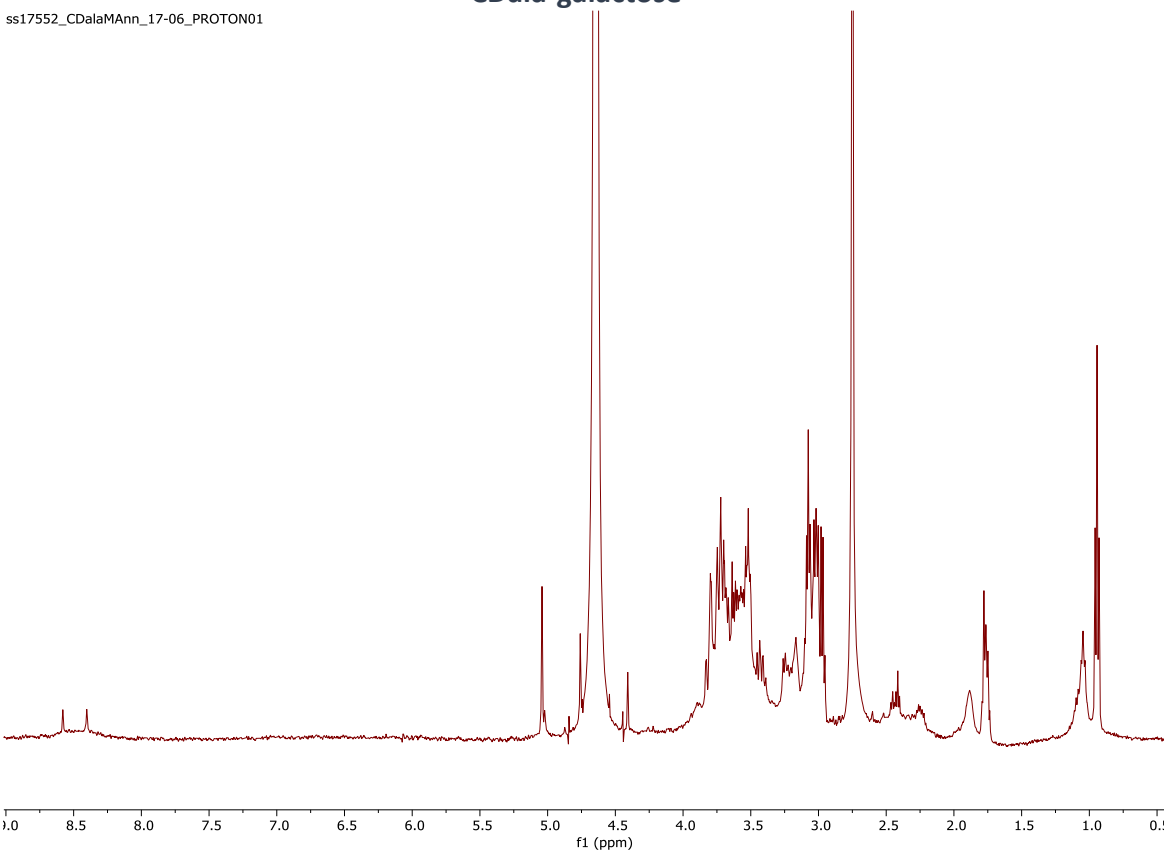

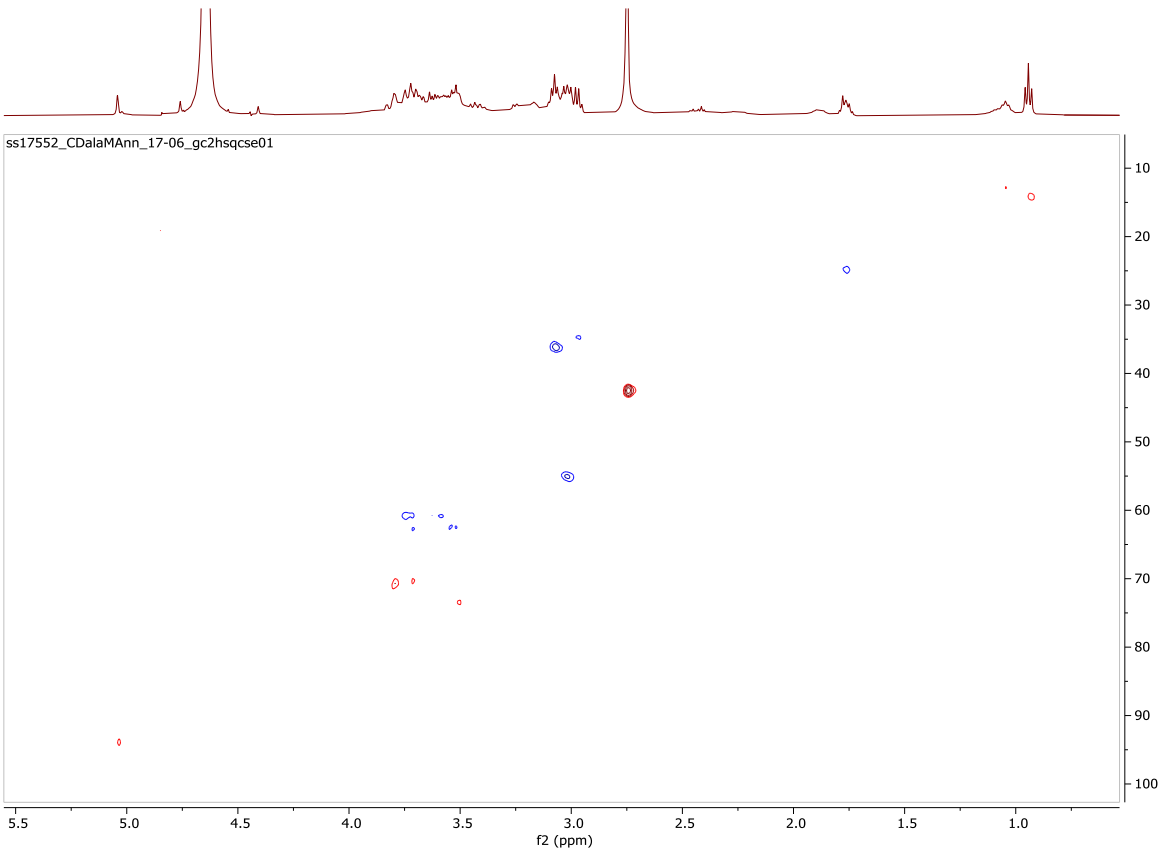

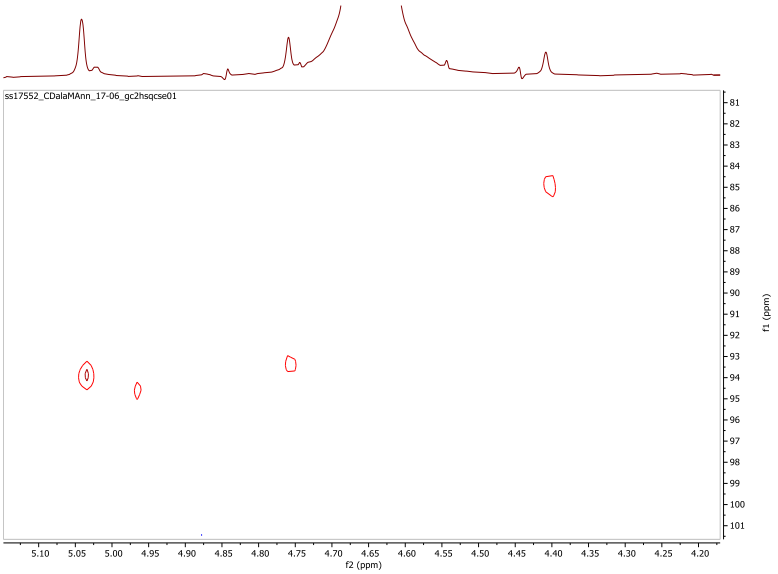

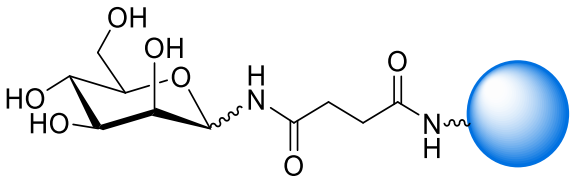

Figure A.15 **15** CDala-β-D-mannose
CDala-mannose

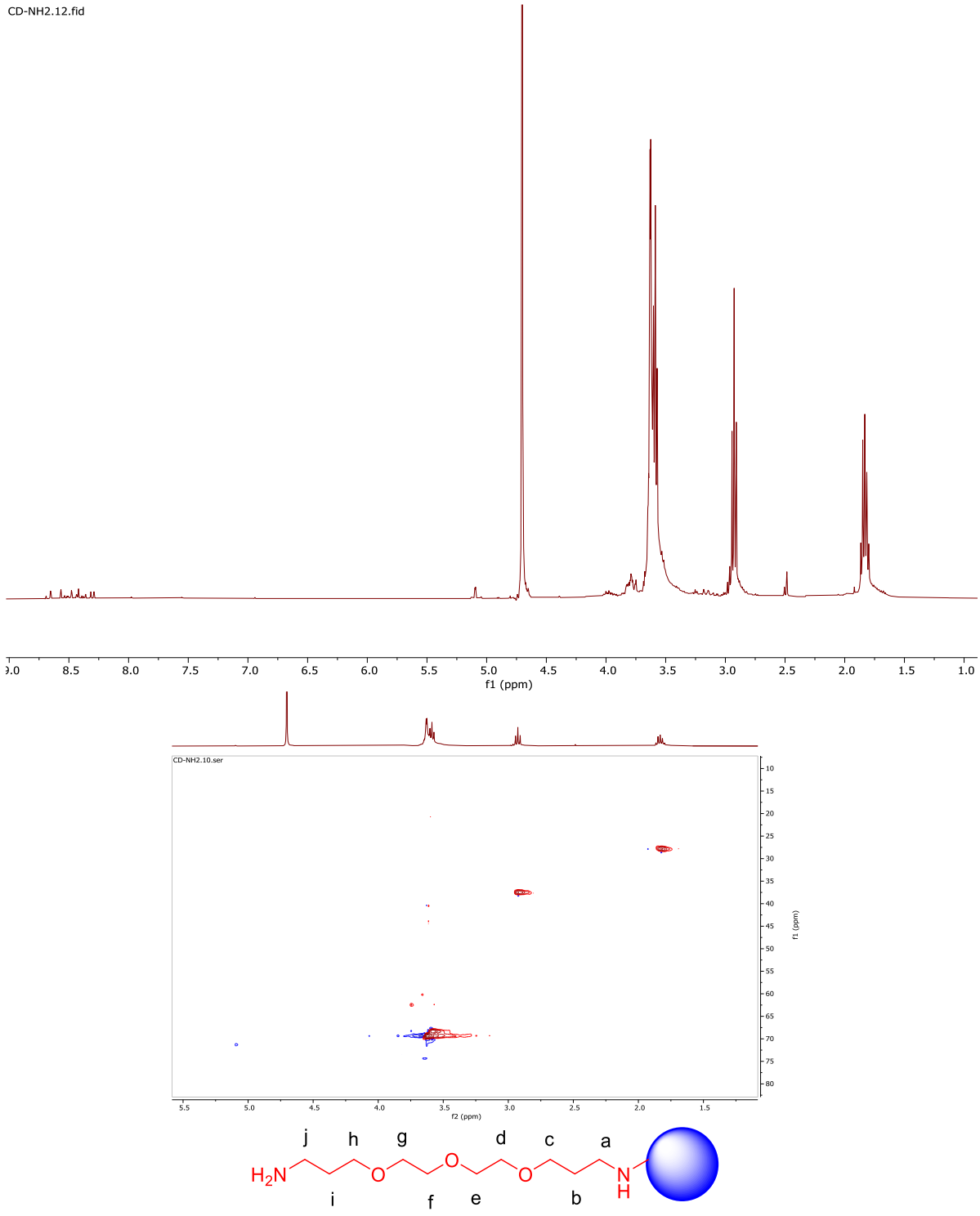

Figure A.16 **16** AmCD

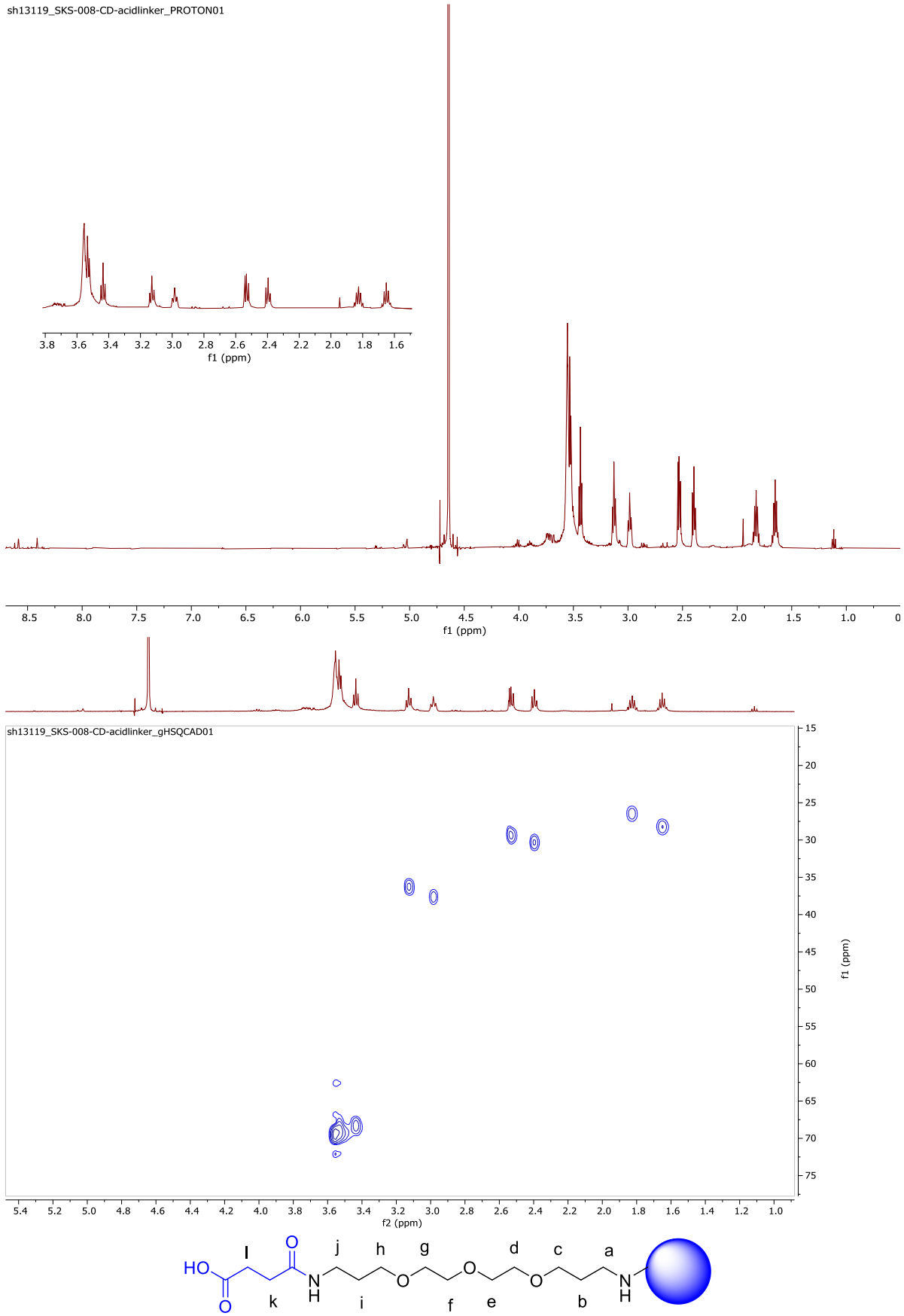

Figure A.17 **17** AcCD

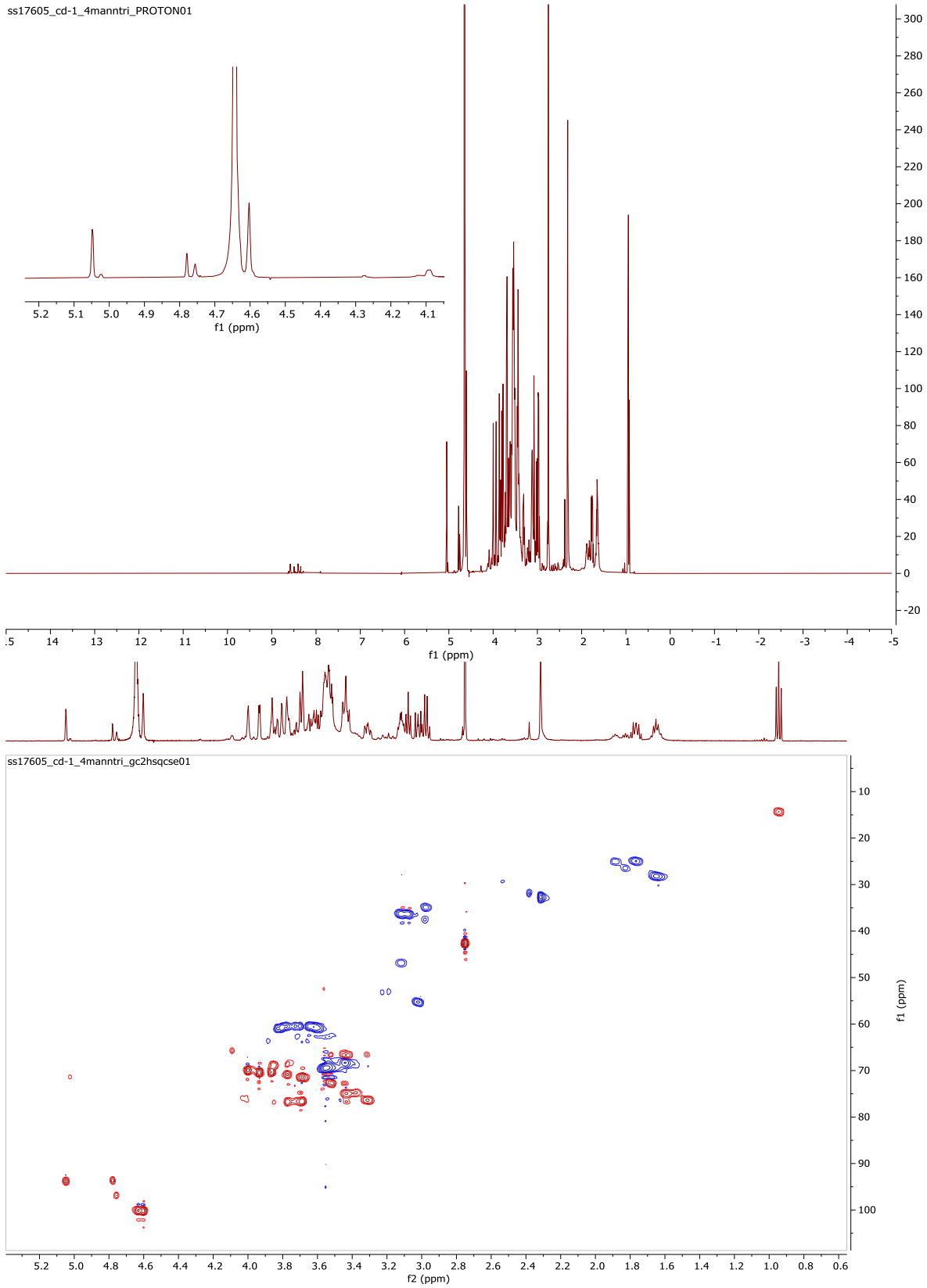
ss17605_cd-1_4manntri_PROTON01
f1 (ppm)
ss17605_cd-1_4manntri_gc2hsqcse01
f2 (ppm)
f1 (ppm)

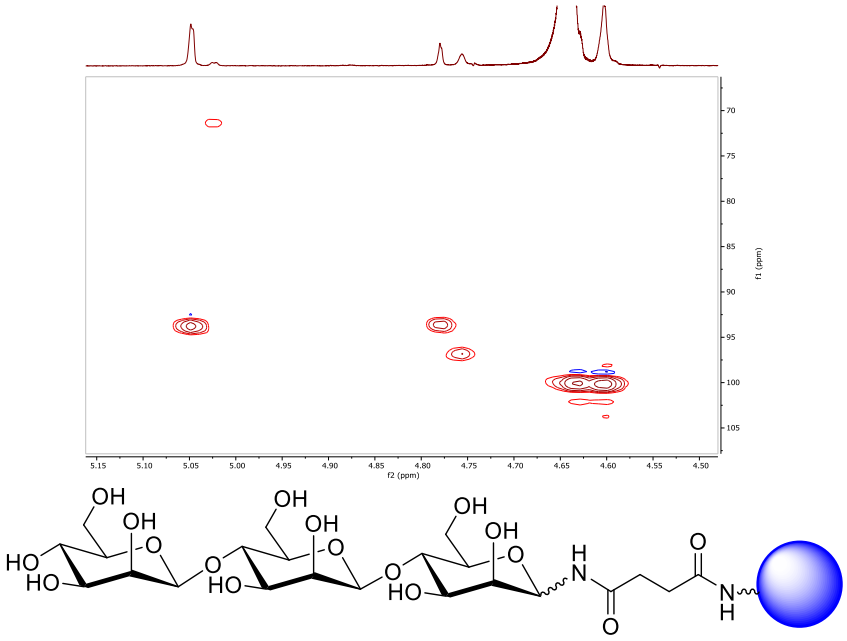

Figure A.18 **18** CD-β-D-mannopyranose-(1—4)-β-D-mannopyranose-(1—4)-β-D-mannopyranose

CD-1,4-mannotriose

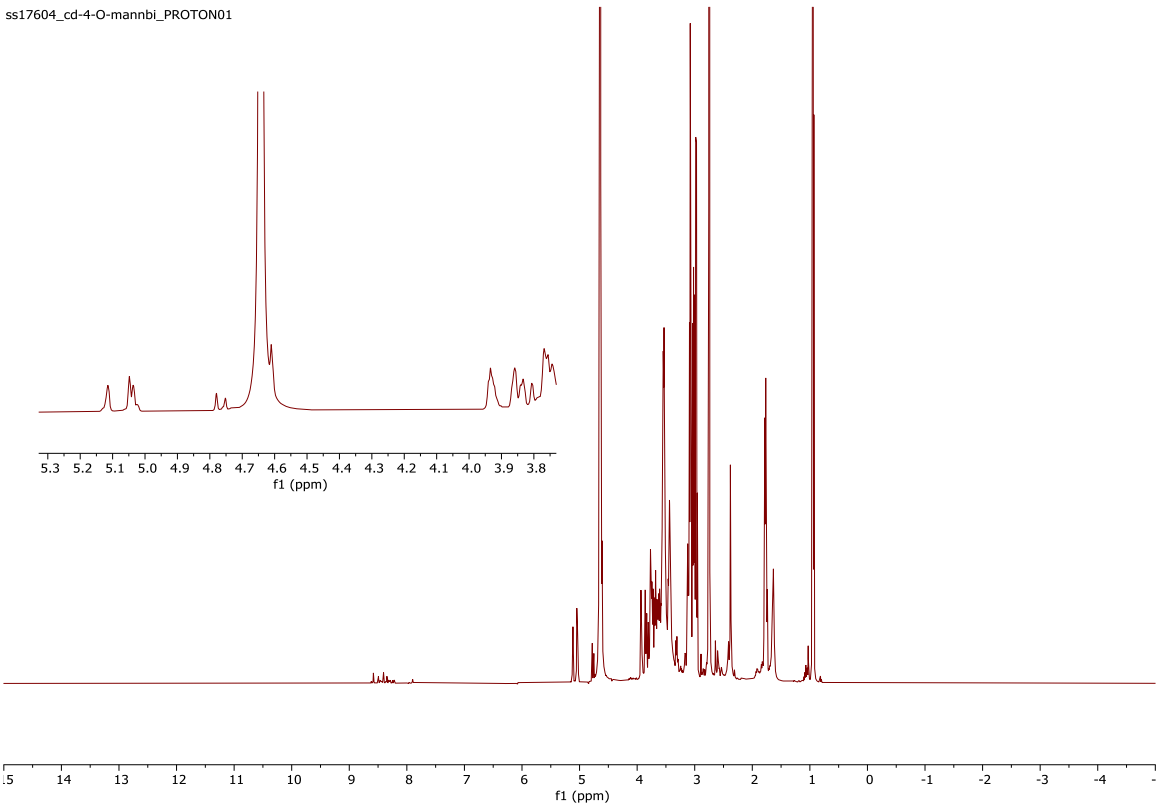

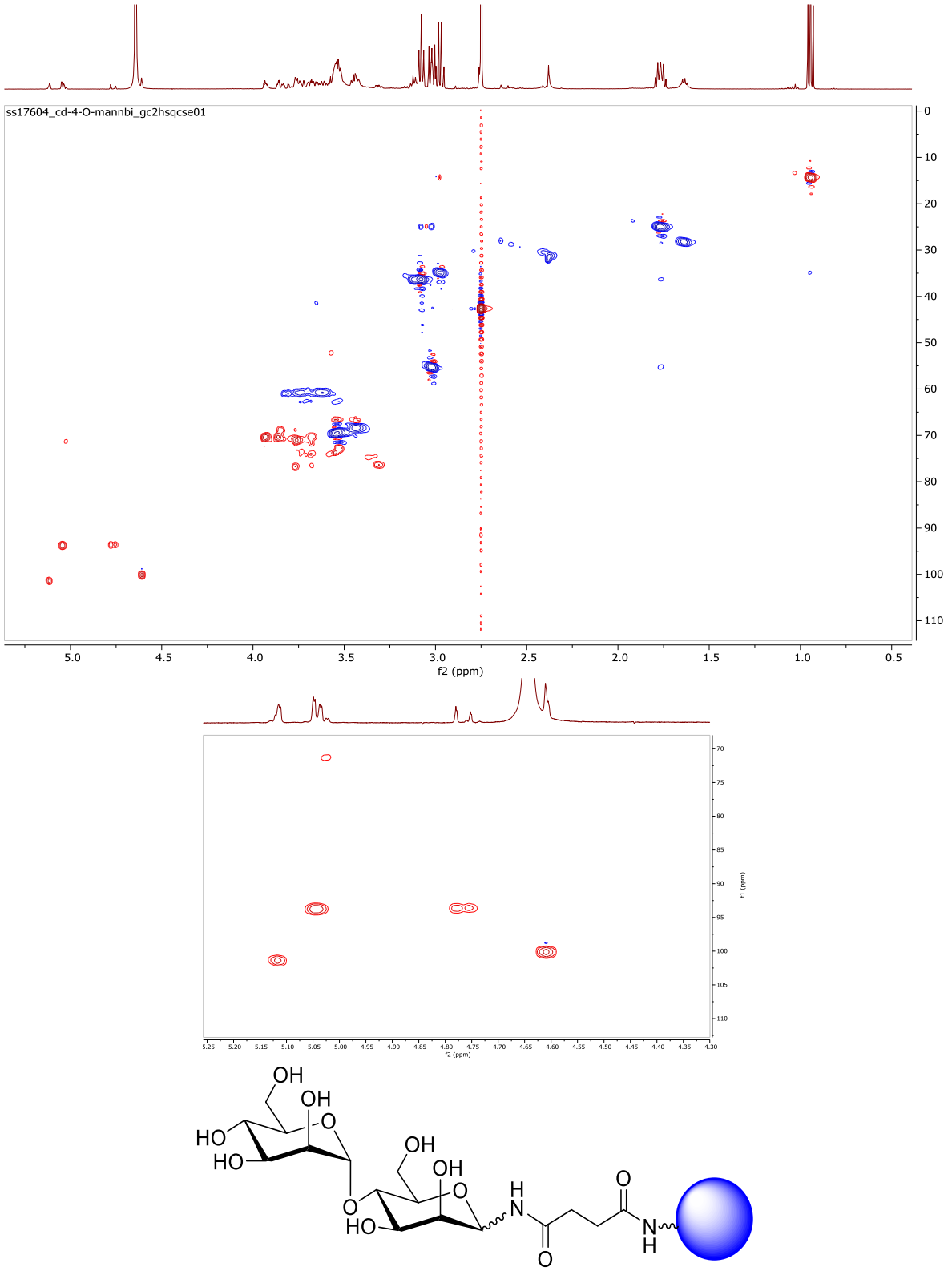

Figure A.19 **19** CD-4-O-(α-D-mannopyranosyl)-D-mannopyranose
CD-4-O-mannobiose

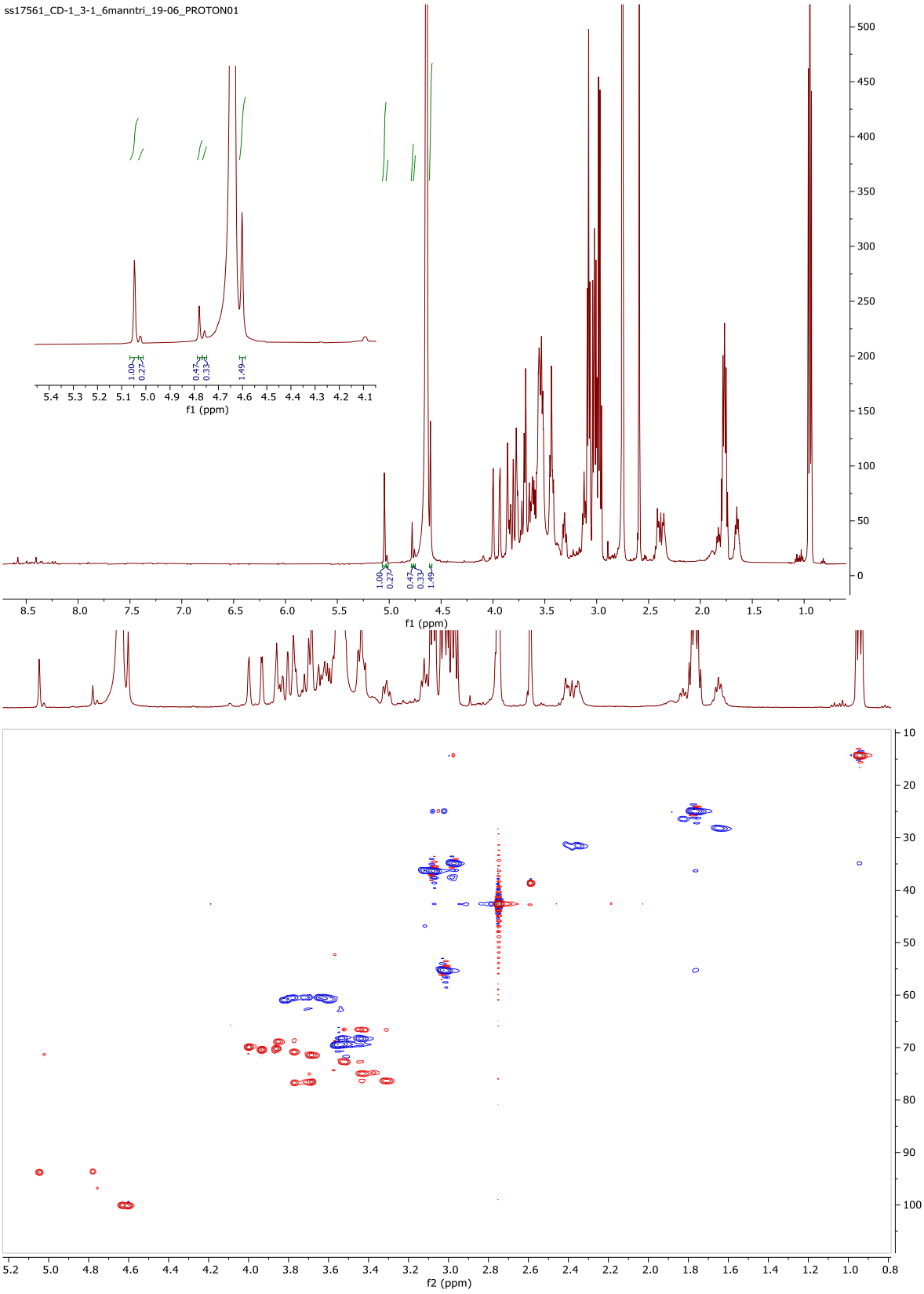
ss17561_CD-1_3-1_6manntri_19-06_PROTON01
f1 (ppm)
f1 (ppm)
f2 (ppm)

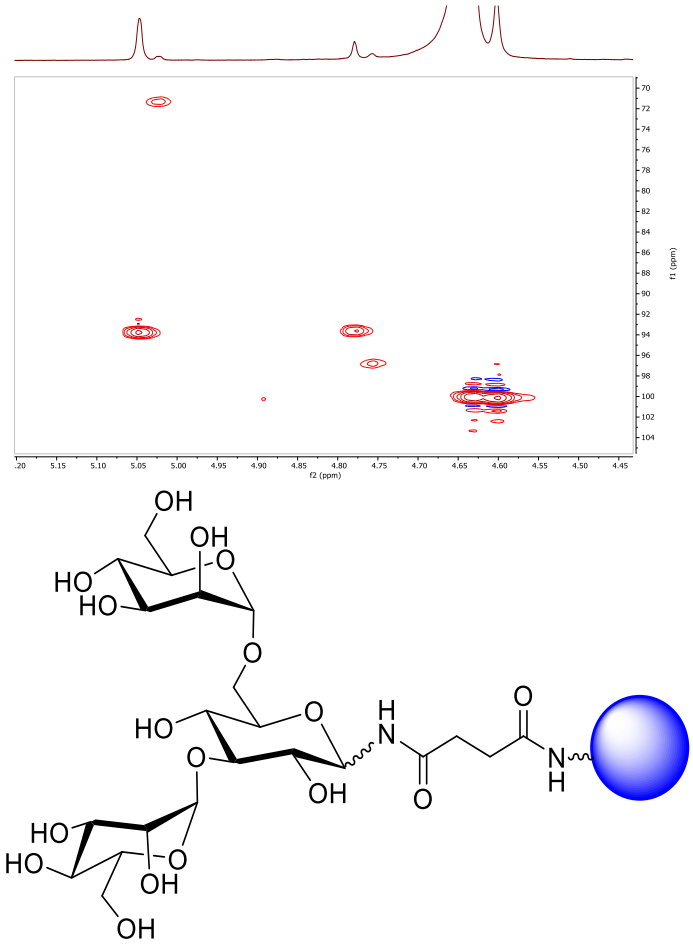

Figure A.20 **20** CD-3,6-di-O-(α-D-mannopyranosyl)-D-mannopyranose
CD-1,3-1,6-mannotriose

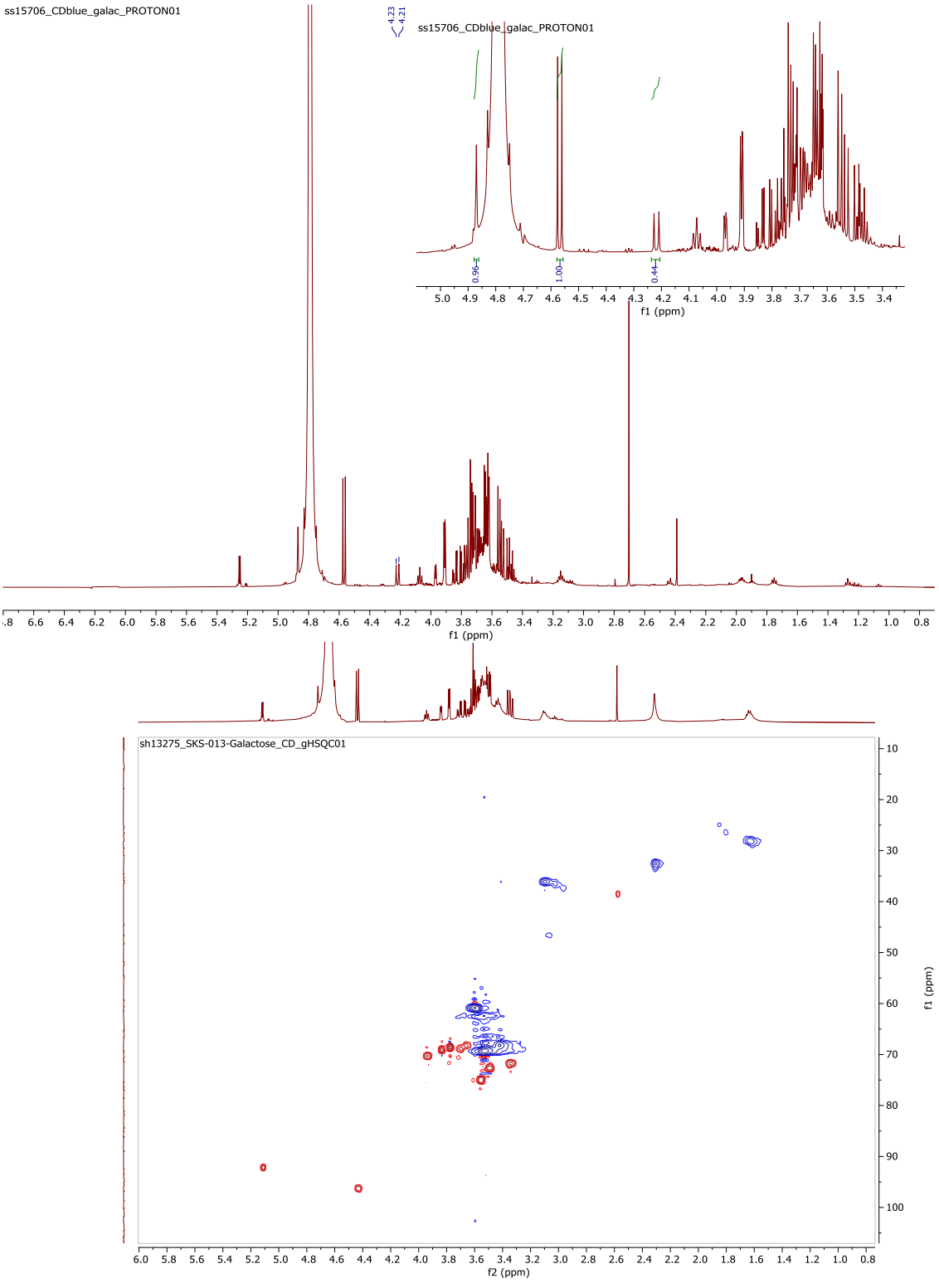

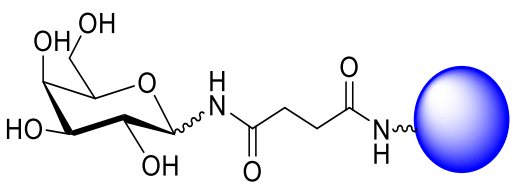

Figure A.21 **21** CD-β-D-galactose

CD-galactose

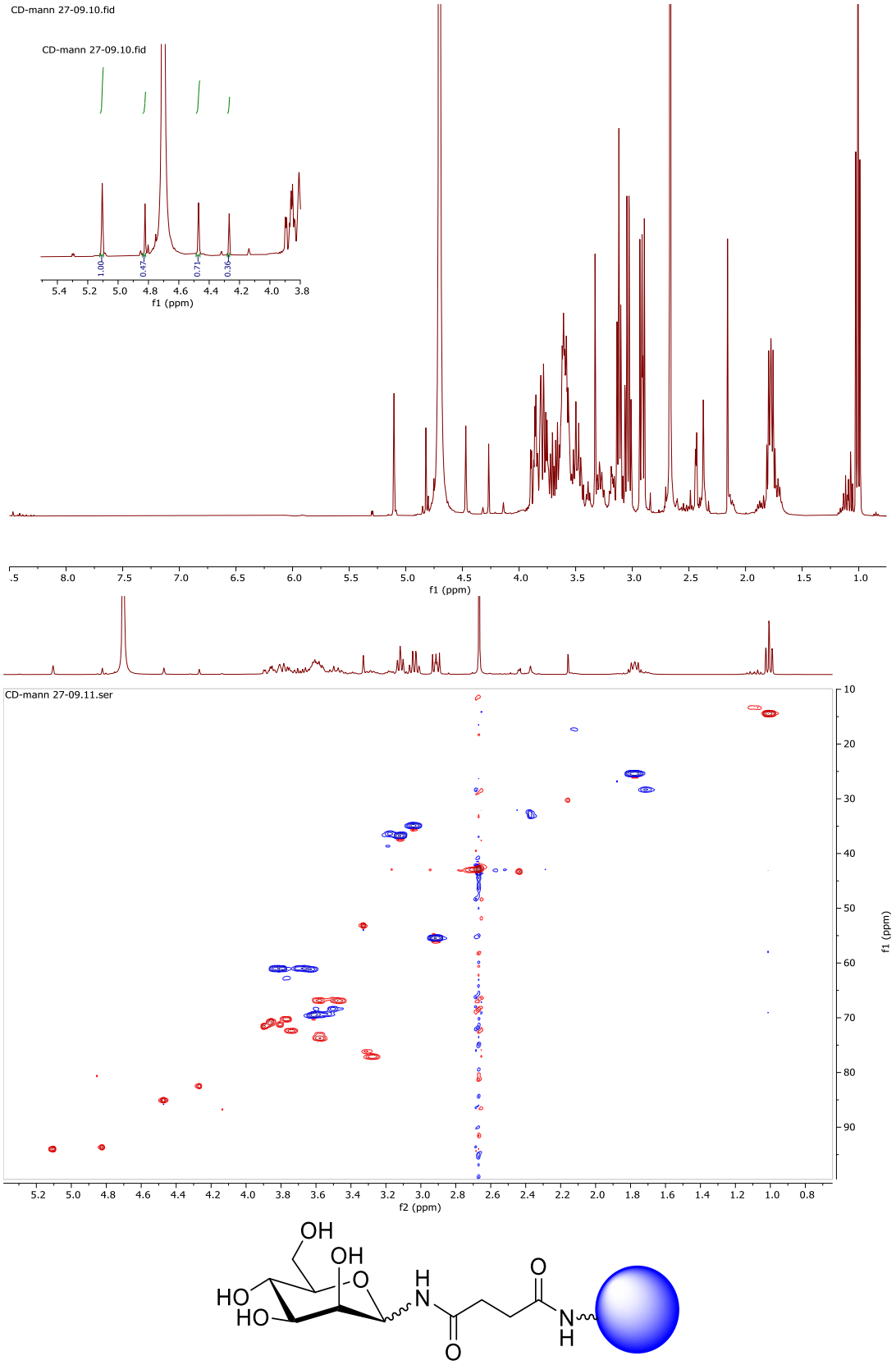

Figure A.22 **22** CD-β-D-mannose

CD-mannose

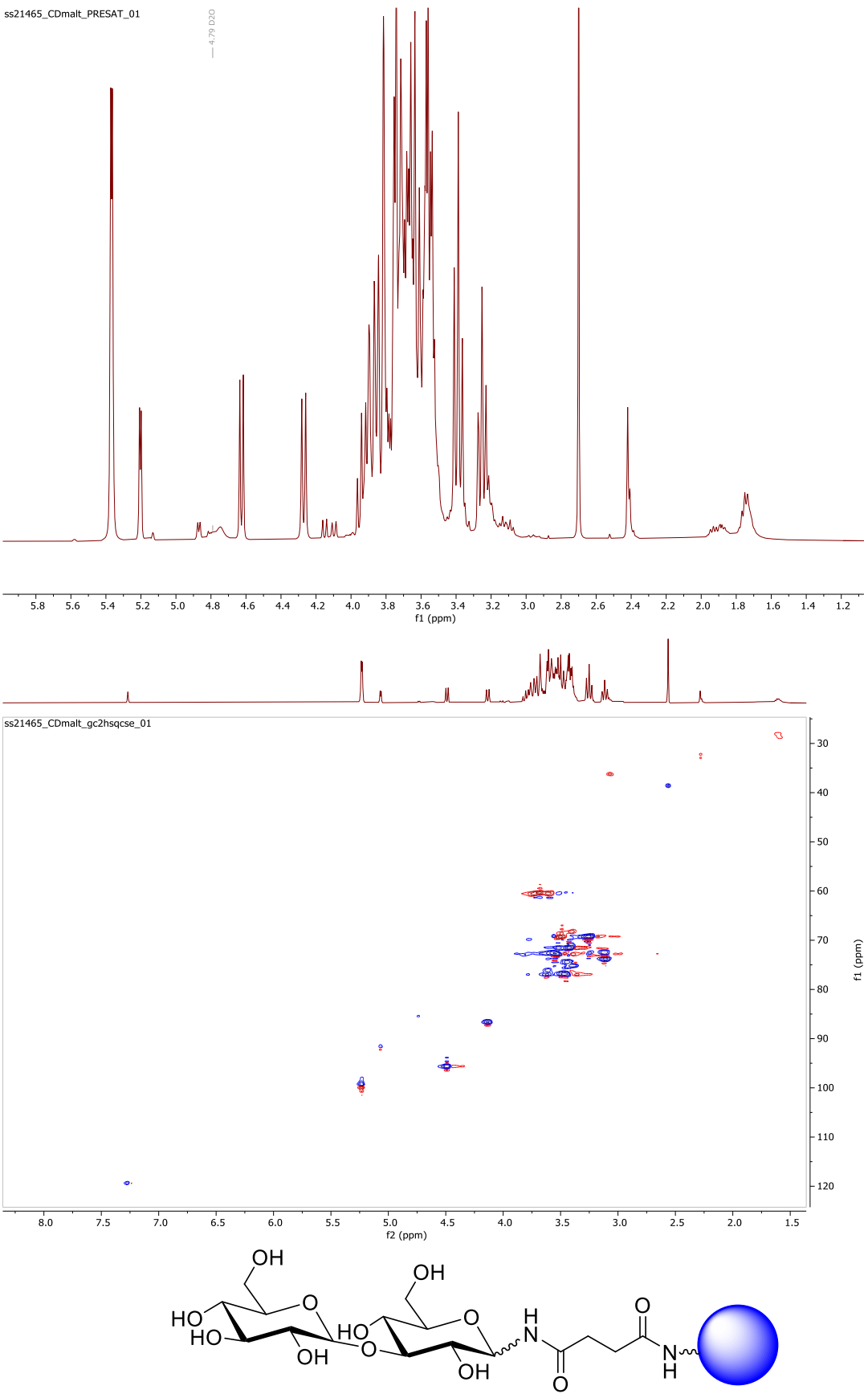

Figure A.23 **23** CD-β-D maltose

CD-maltose

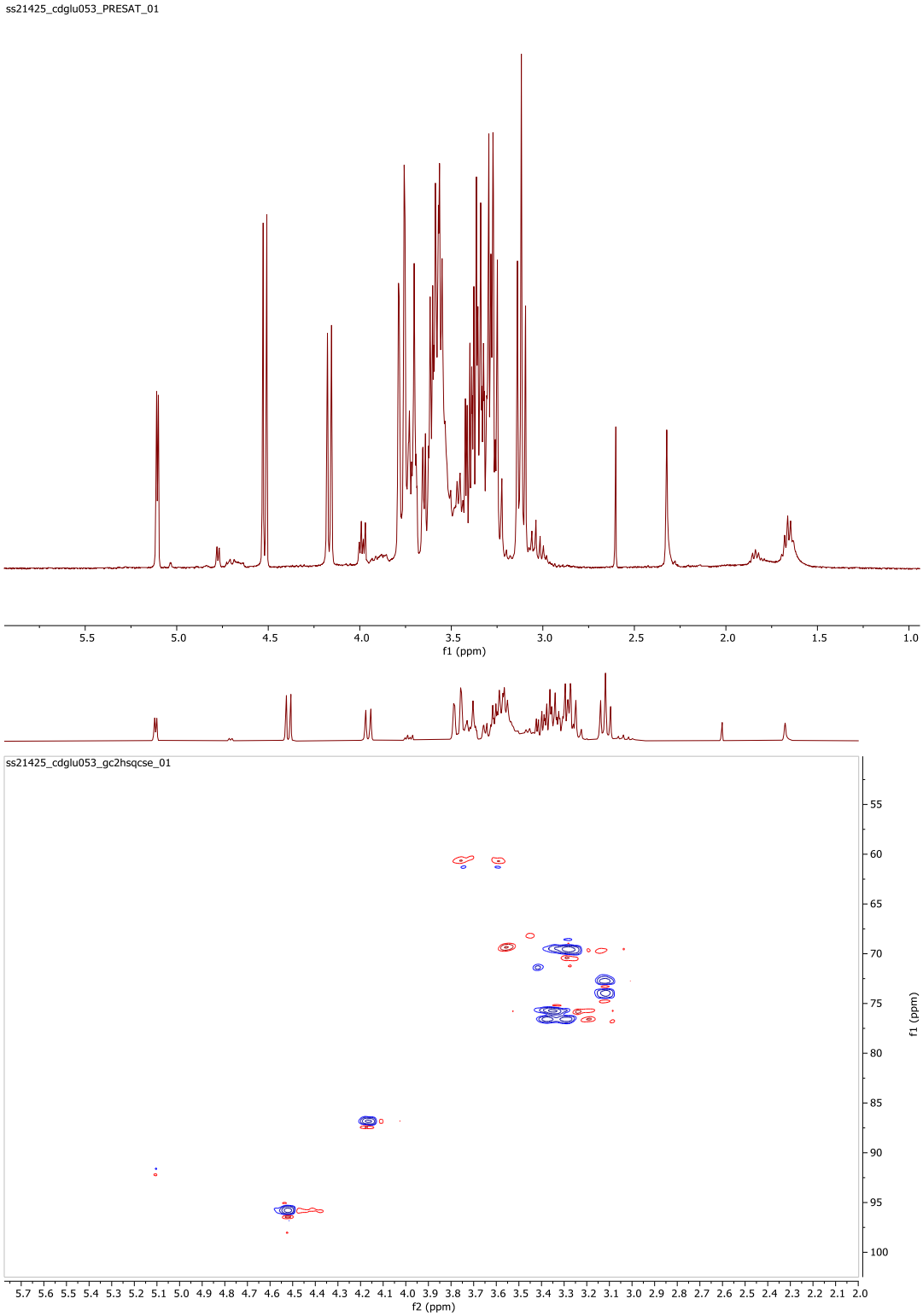

Figure A.24 **24** CD-β-D glucose

lCD-glucose

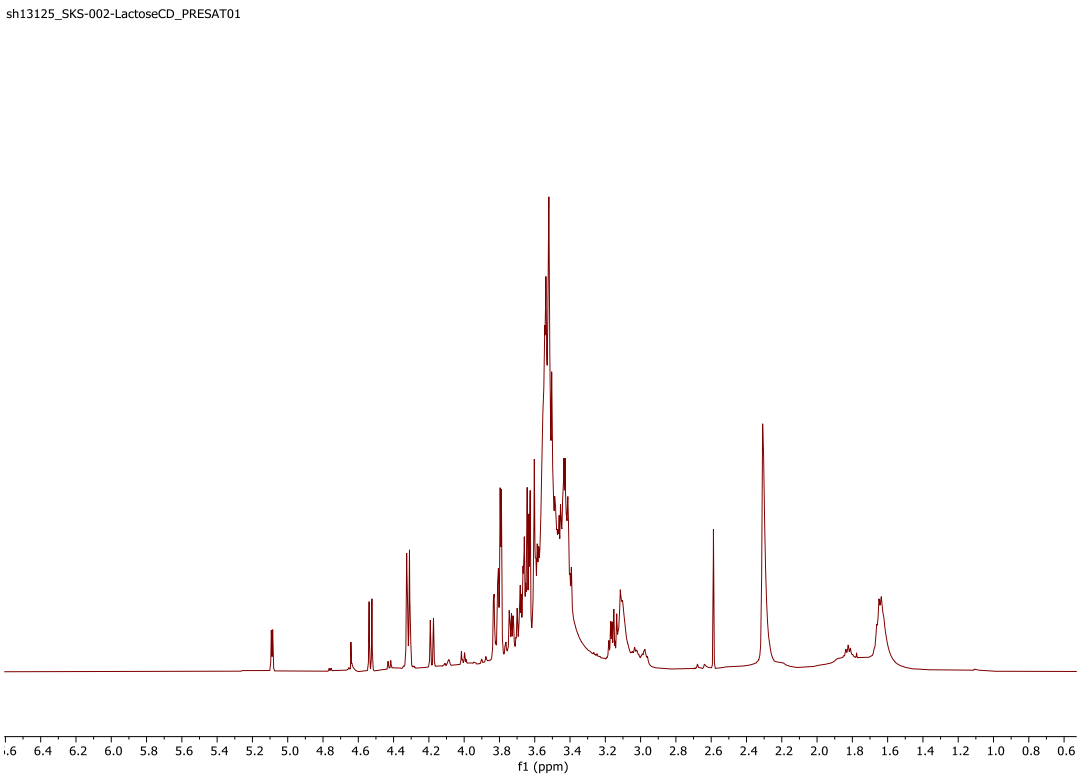
sh13125_SKS-002-LactoseCD_PRESAT01
6.4 6.2 6.0 5.8 5.6 5.4 5.2 5.0 4.8 4.6 4.4 4.2 4.0 3.8 3.6 3.4 3.2 3.0 2.8 2.6 2.4 2.2 2.0 1.8 1.6 1.4 1.2 1.0 0.8 0.6
f1 (ppm)

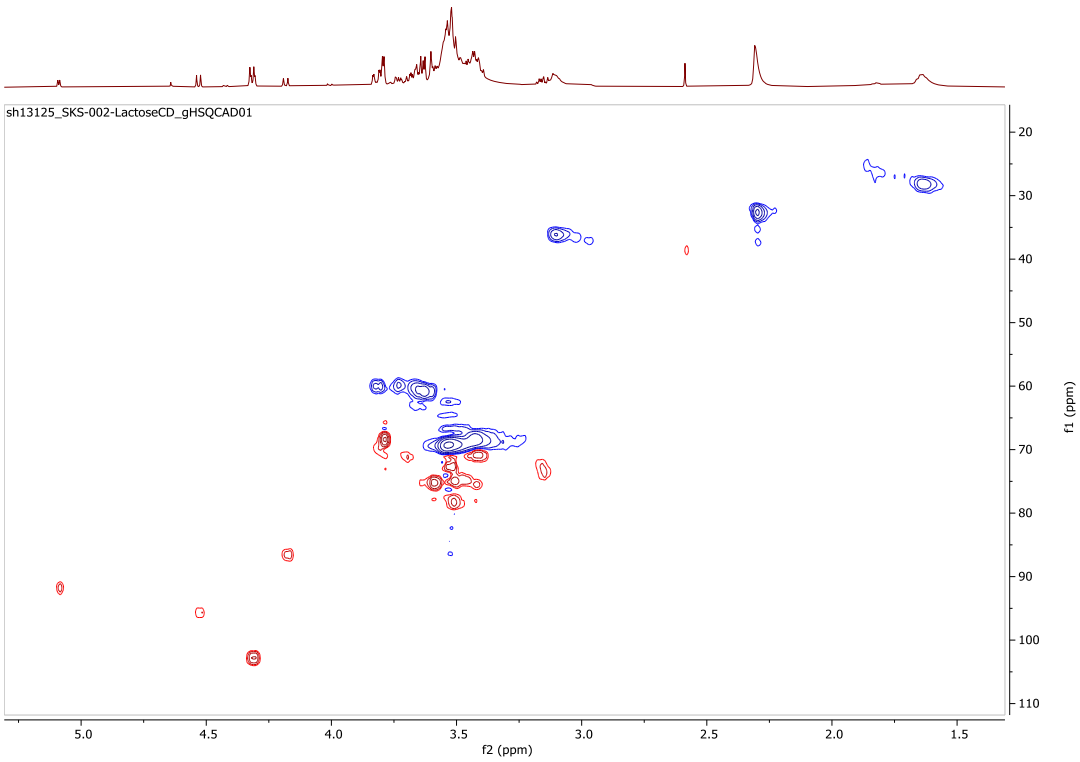

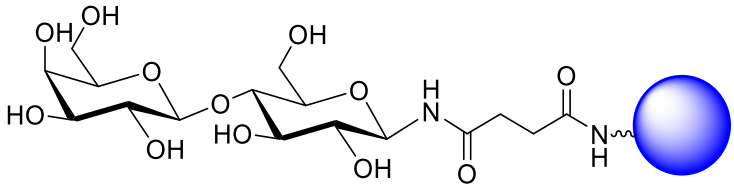

Figure A.25 ***25*** *CD-β-D lactose*
CD-lactose

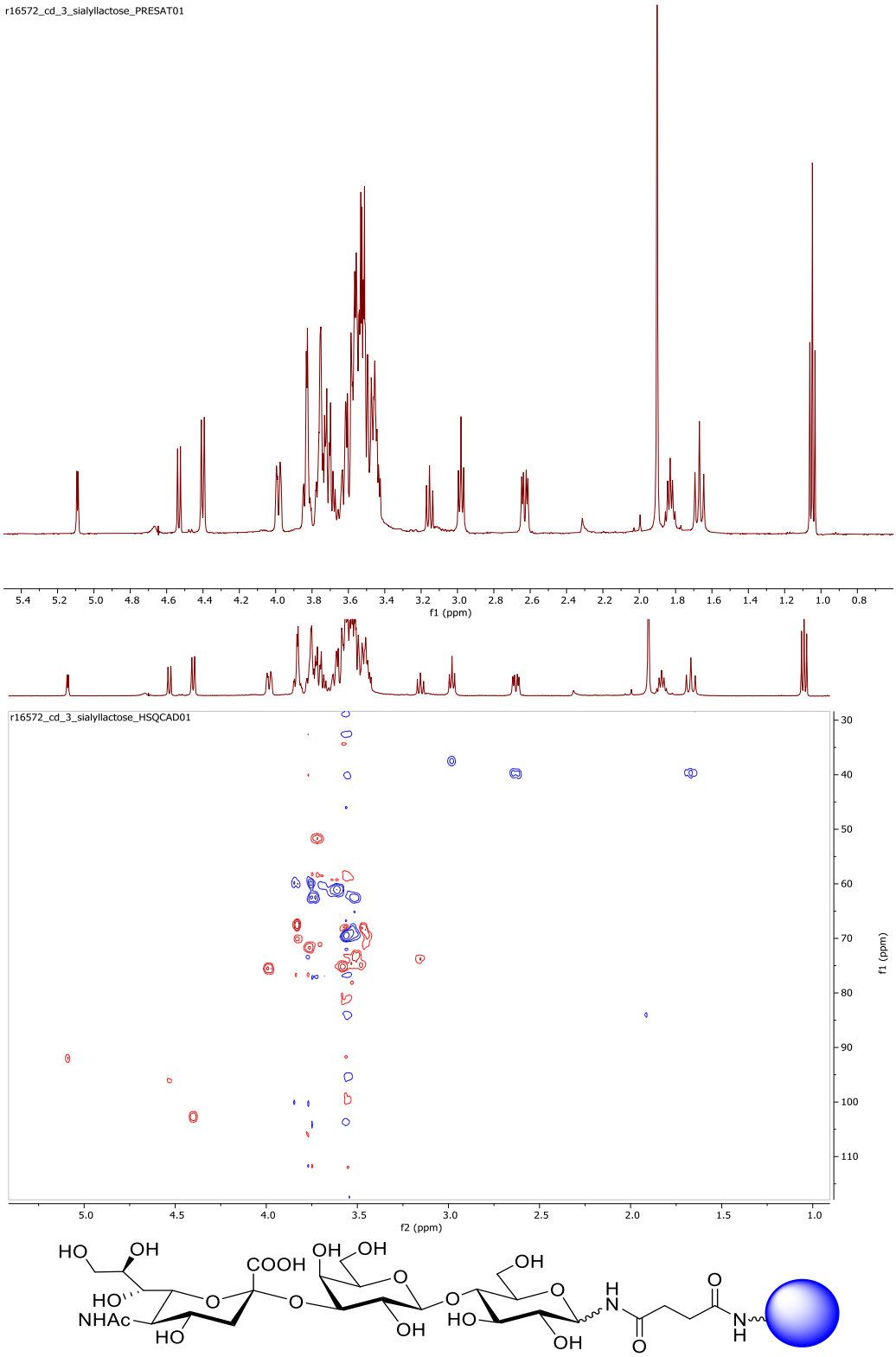

Figure A.26 **26** CD-3’-sialyl-D-lactose

CD-3’-sialyllactose

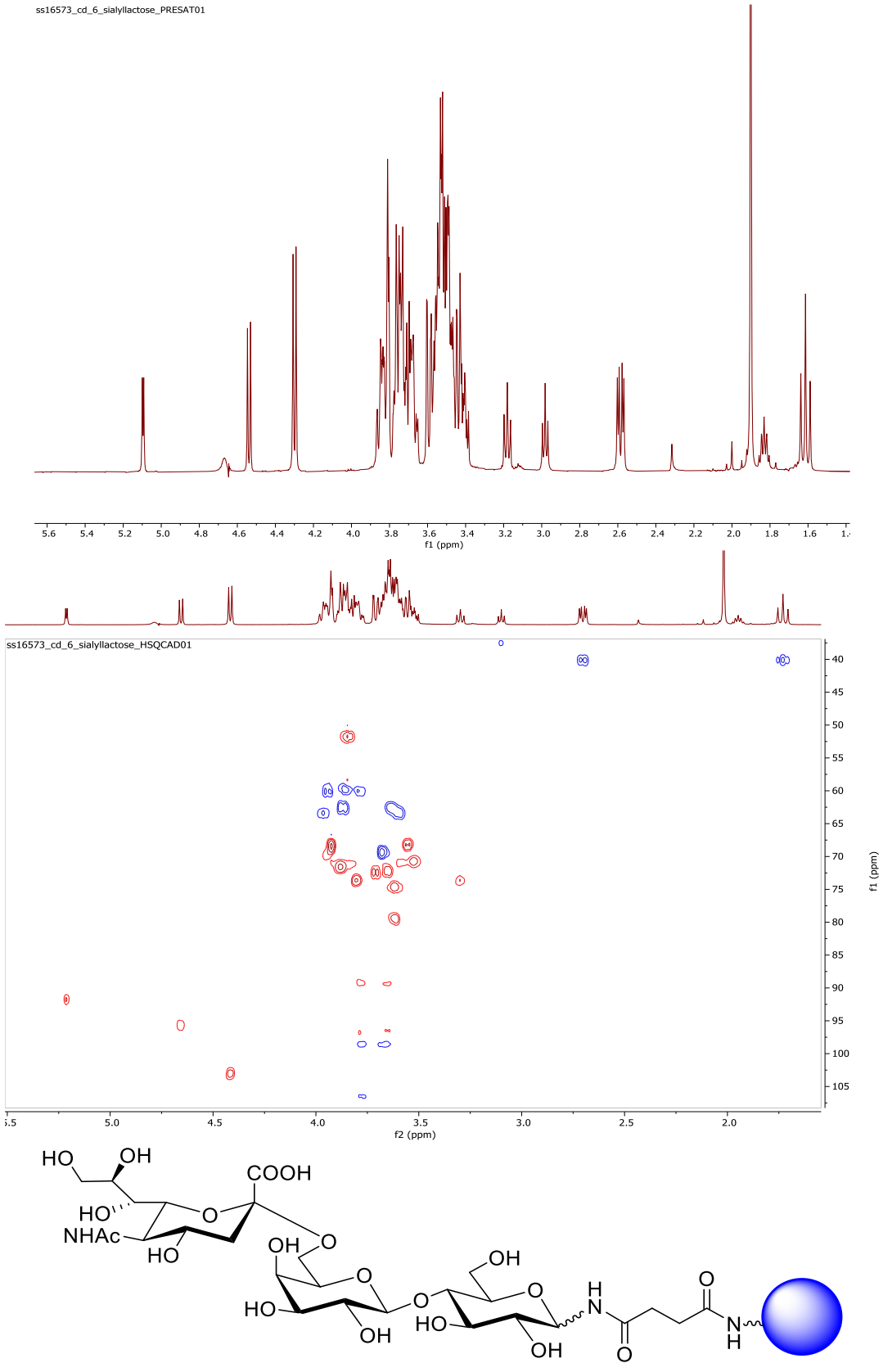

Figure A.27 **27** CD-6’-sialyl-D-lactose

CD-6’-sialyllactose

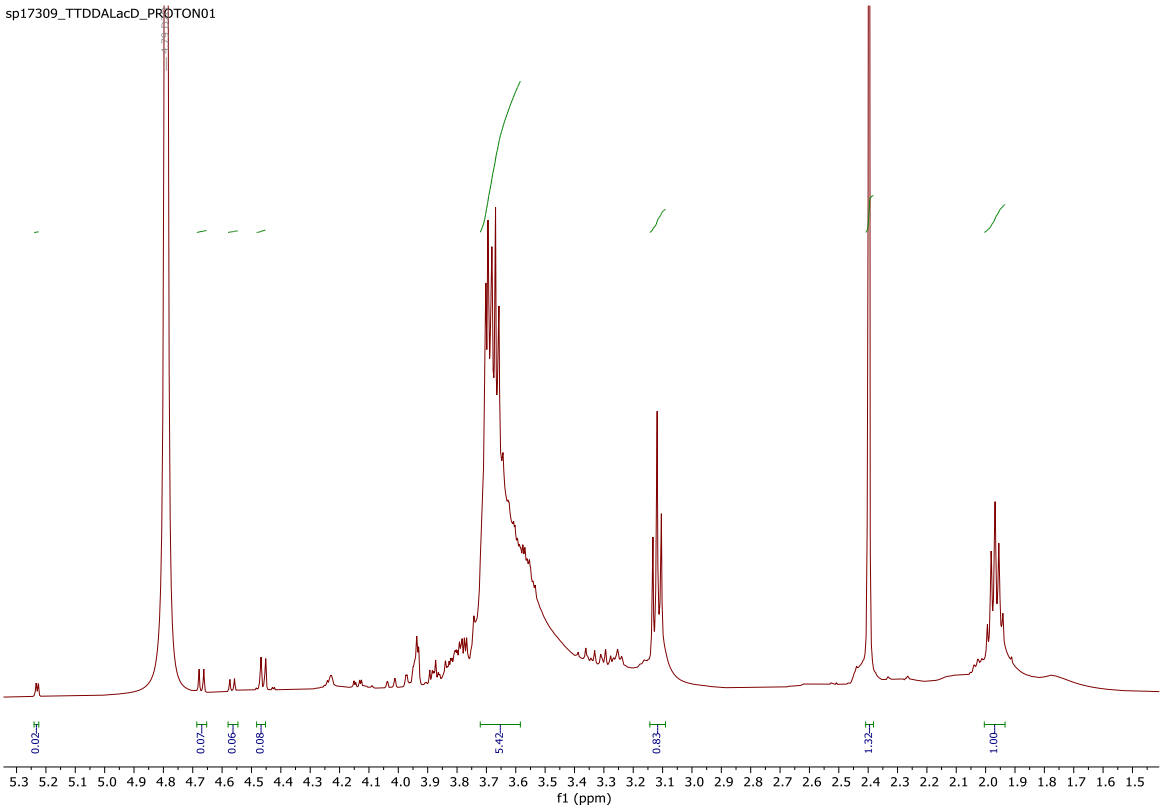

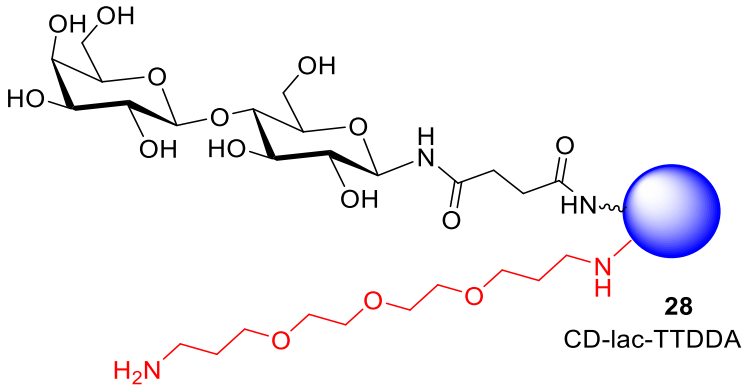

Figure A.28 **28** ^{1}H NMR (500 MHz) CD-lac-TTDDA

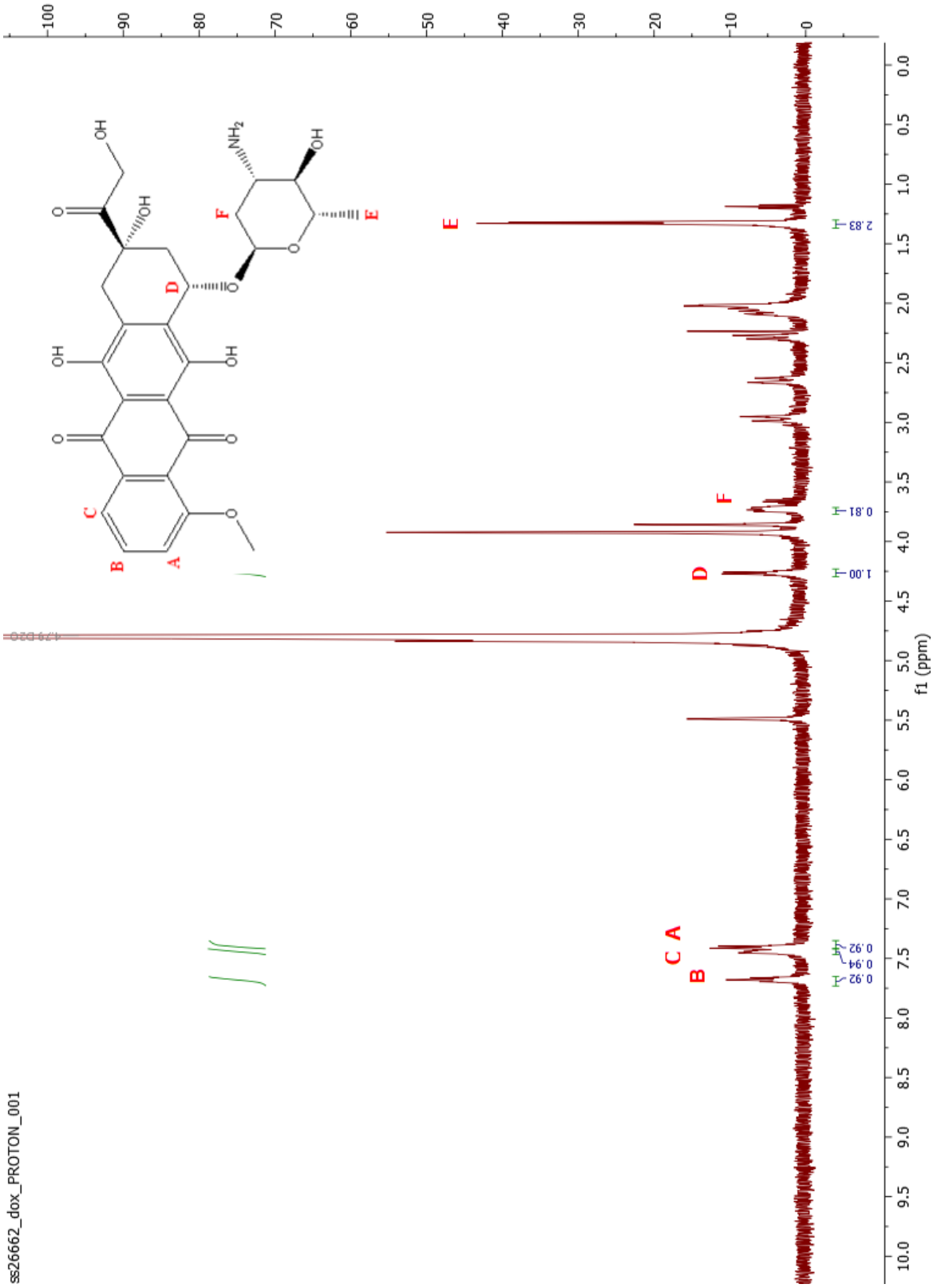

Figure A.29 ^{1}H NMR (500 MHz) Doxorubicin.HCl

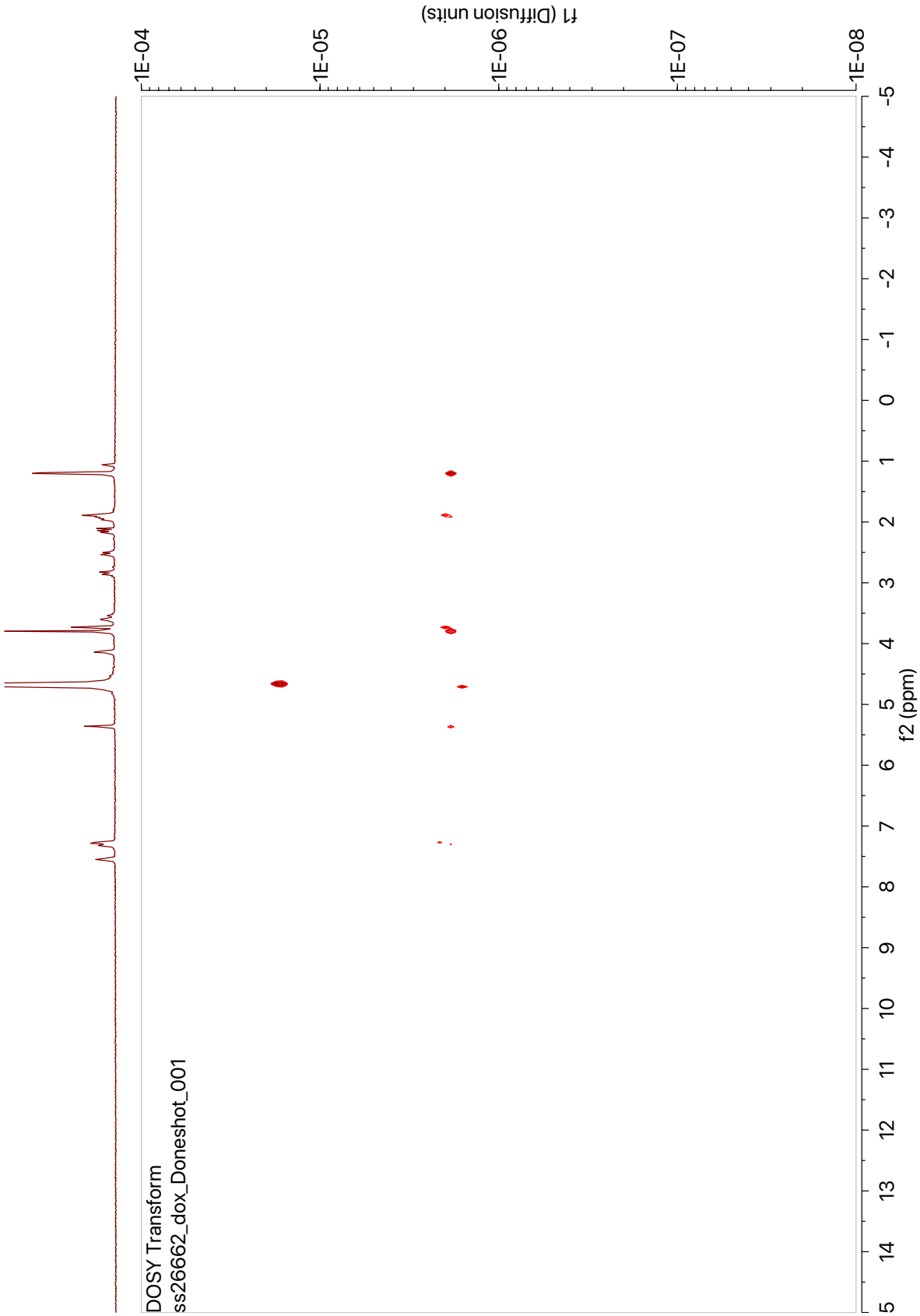

Figure A.30 *DOSY NMR (500 MHz) Doxorubicin.HCl*

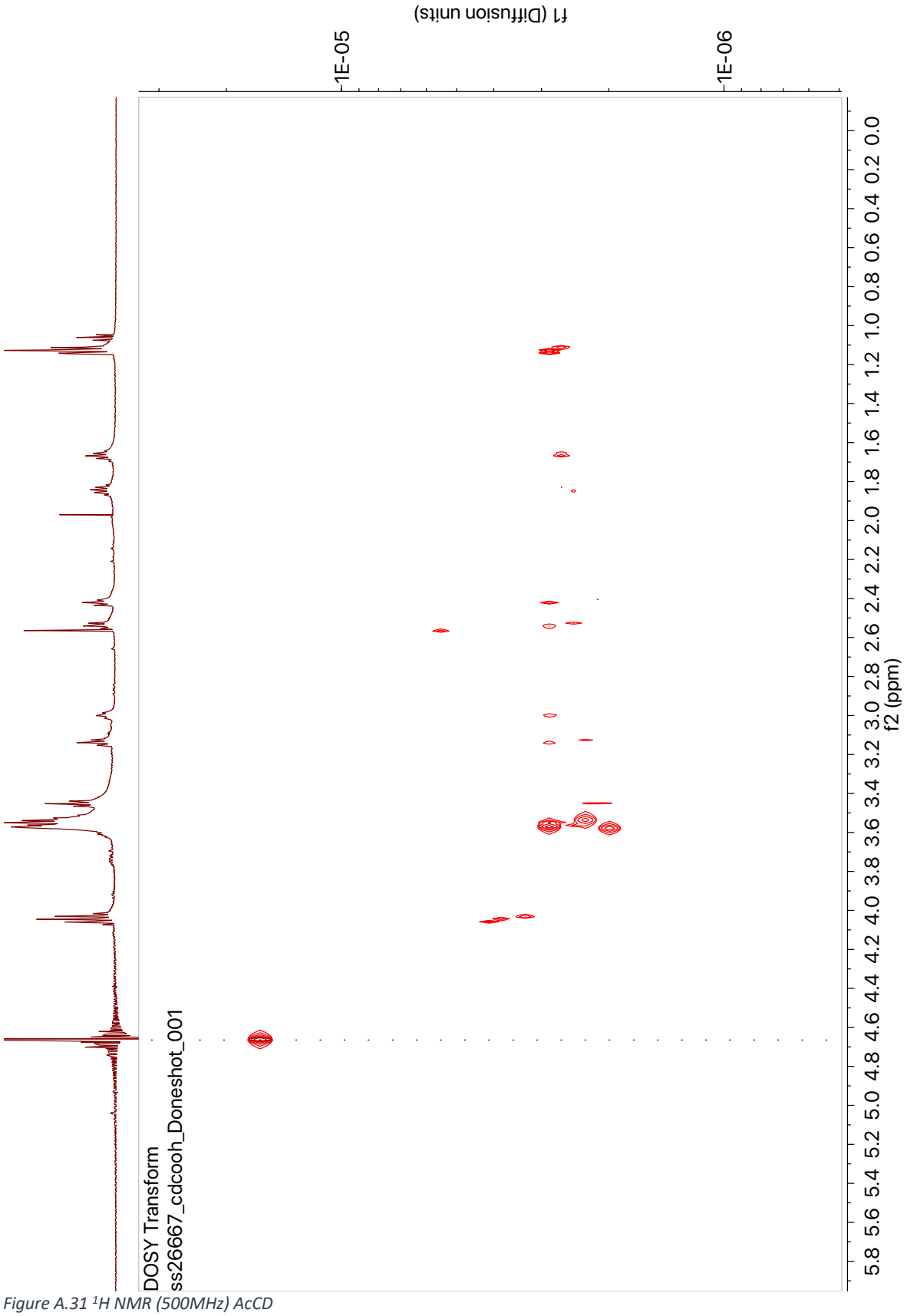

Figure A.31 ^{1}H NMR (500MHz) AcCD

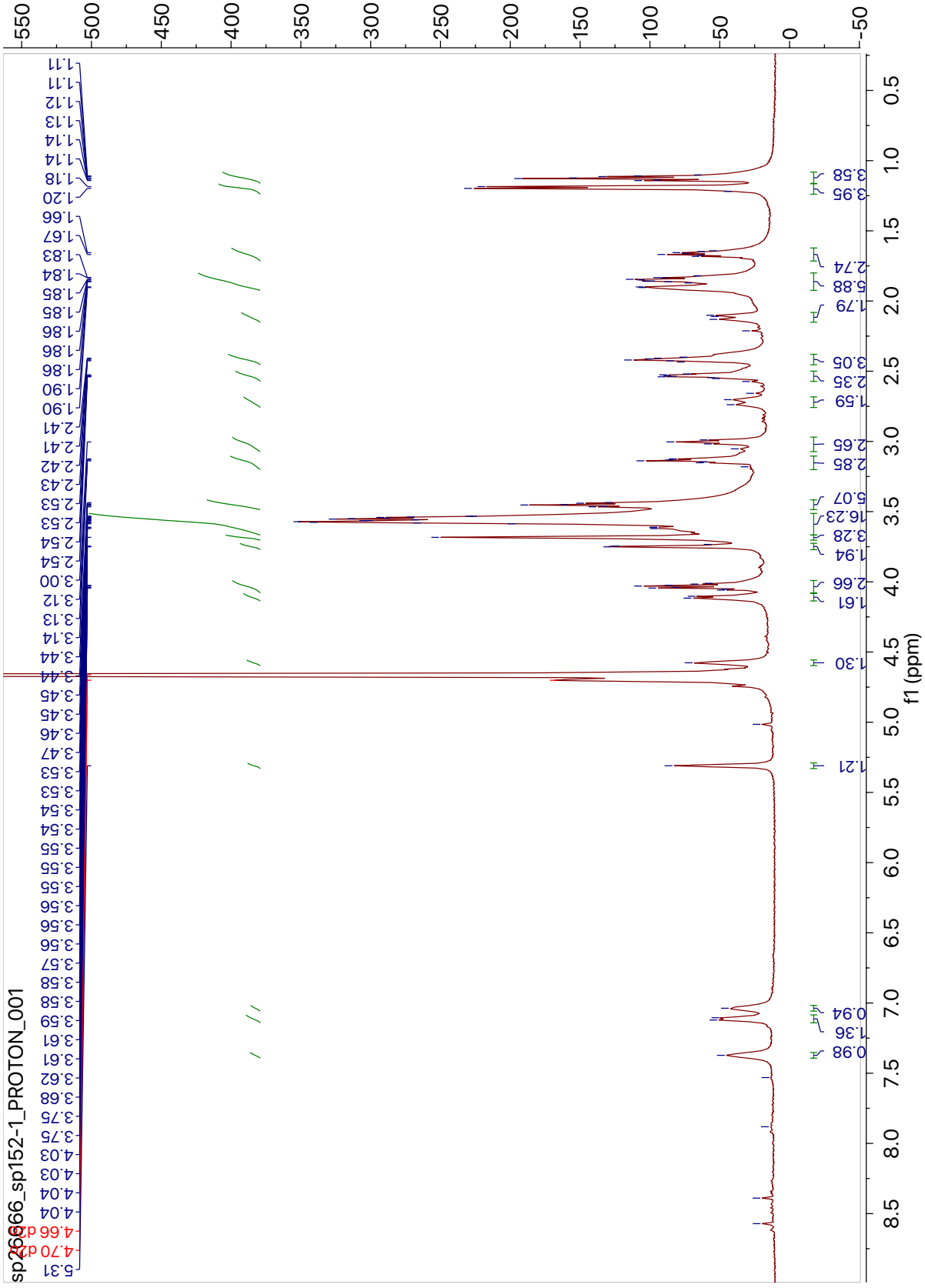

Figure A.32 ^{1}H *NMR (500 MHz)* ***C5***

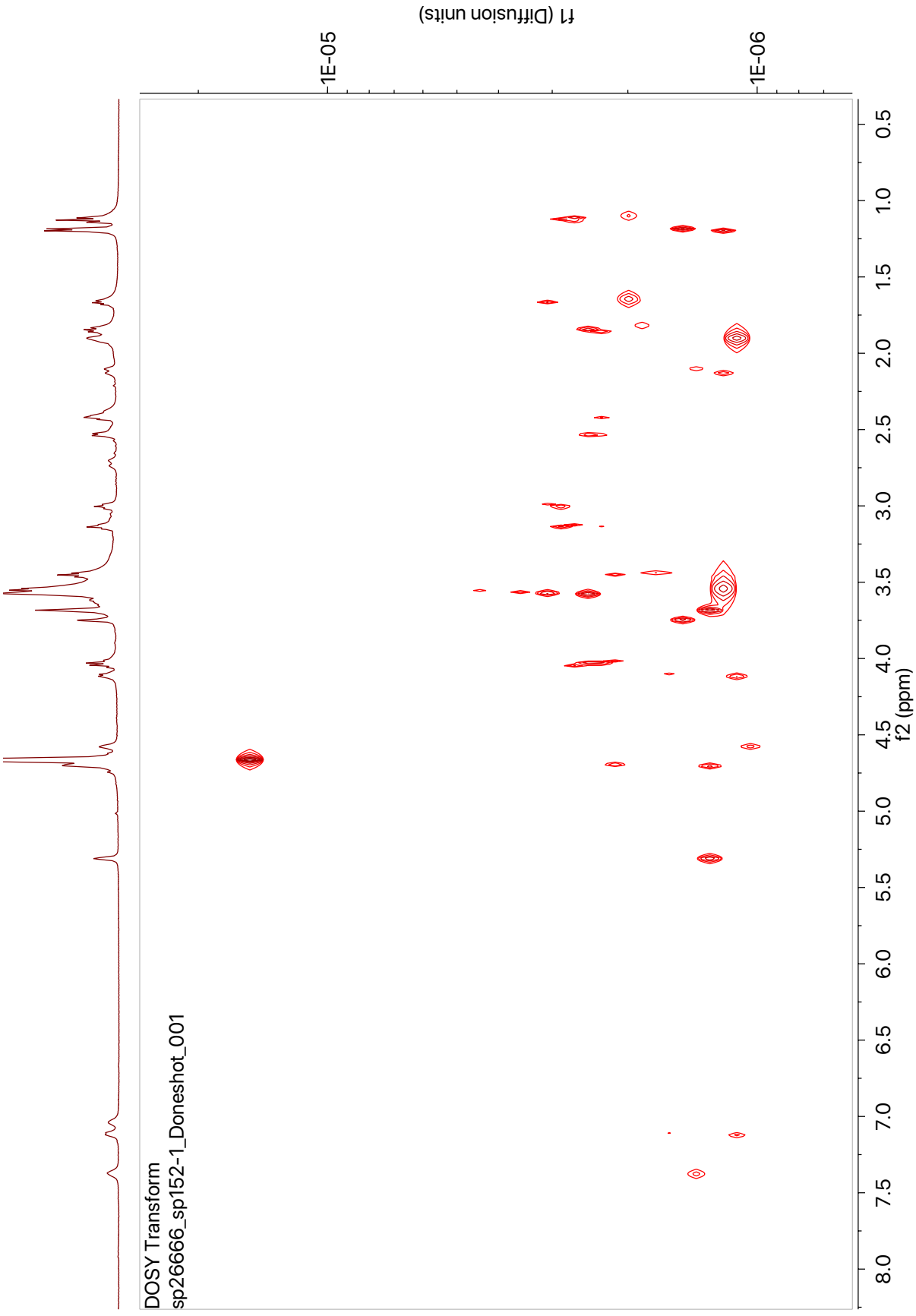

*Figure A.33 DOSY NMR **C5***

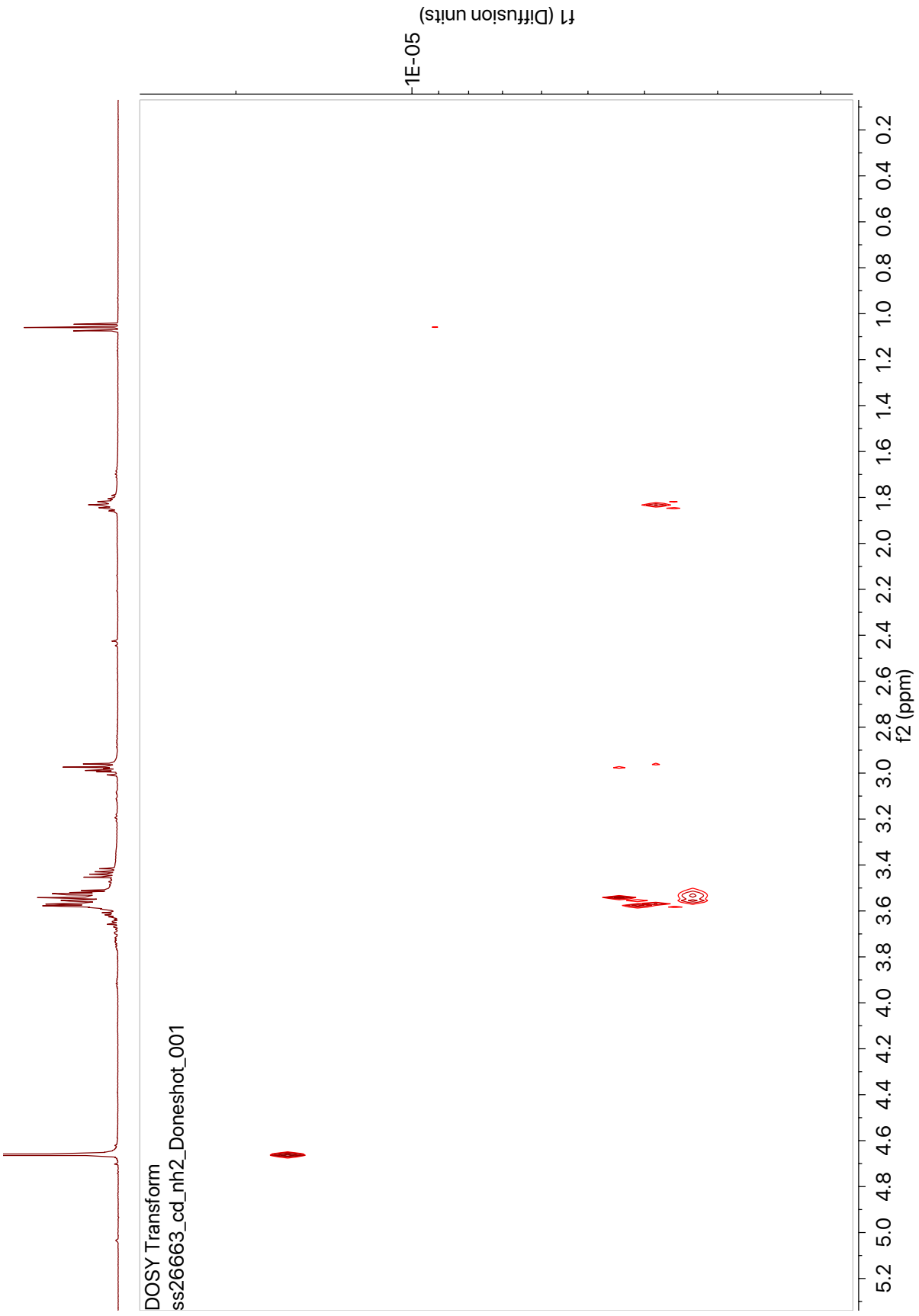

*Figure A.34 DOSY NMR AmCD **16***

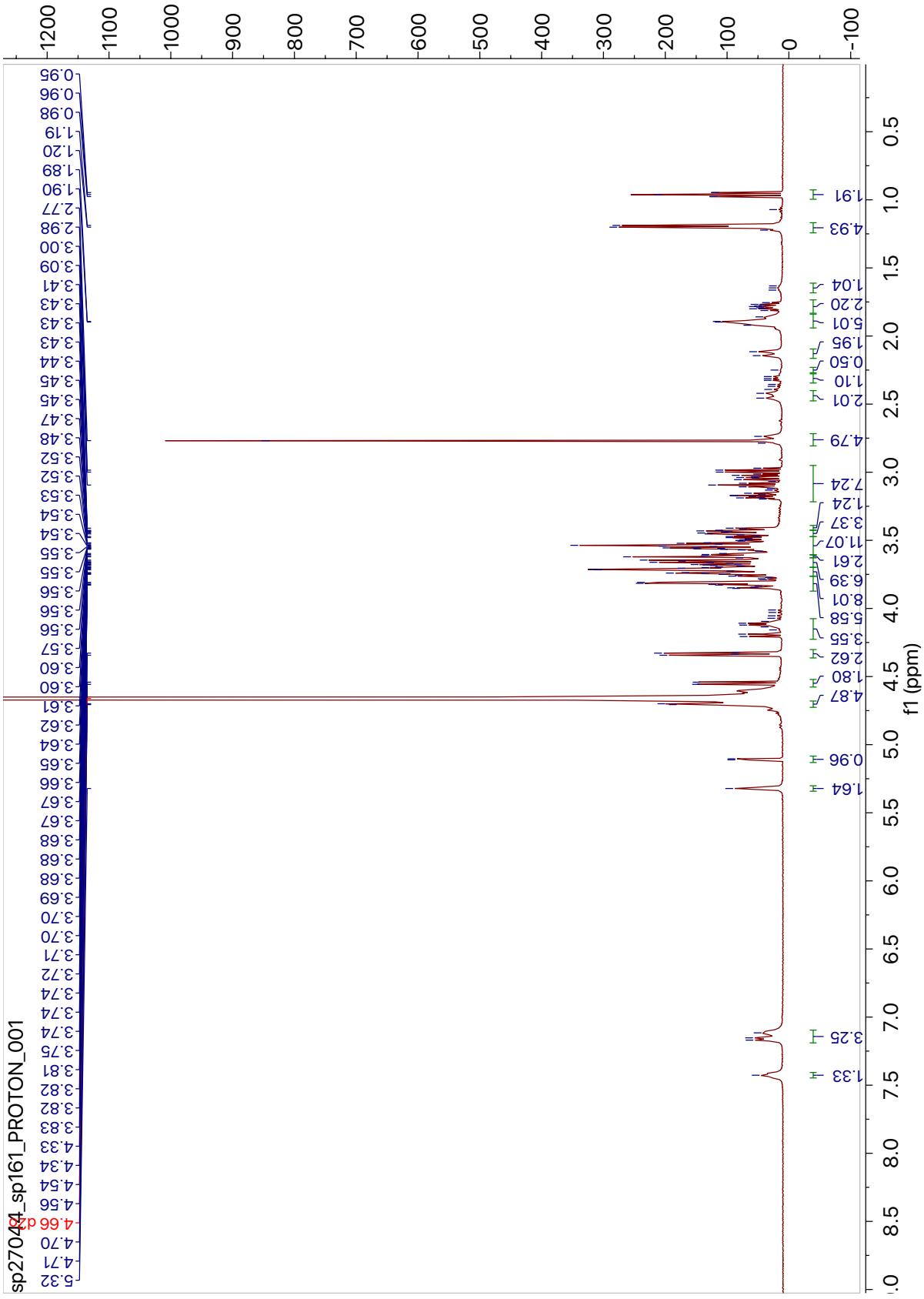

Figure A.35 ^{1}H NMR (500 MHz) ***N5***

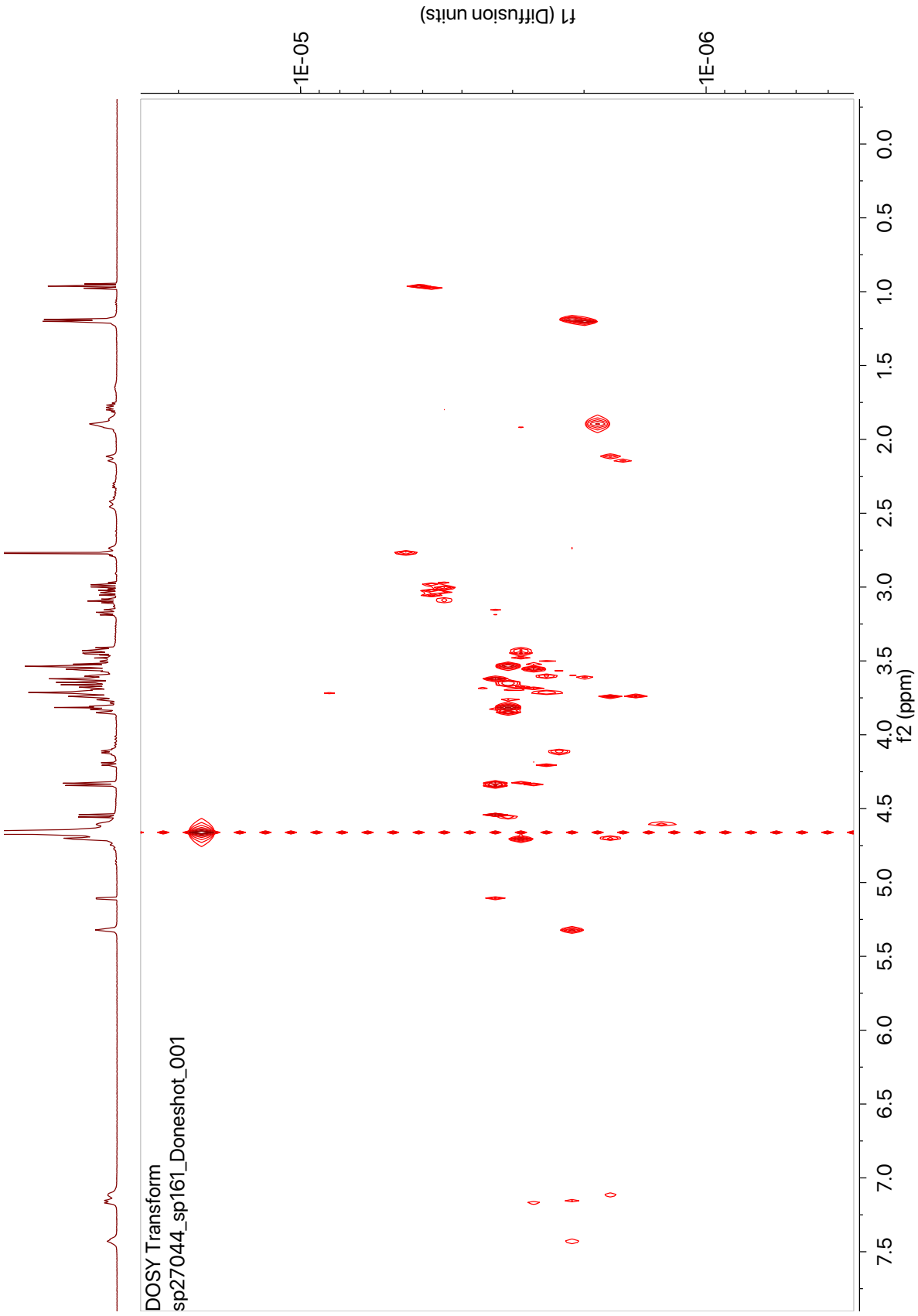

*Figure A.36 DOSY **N5***

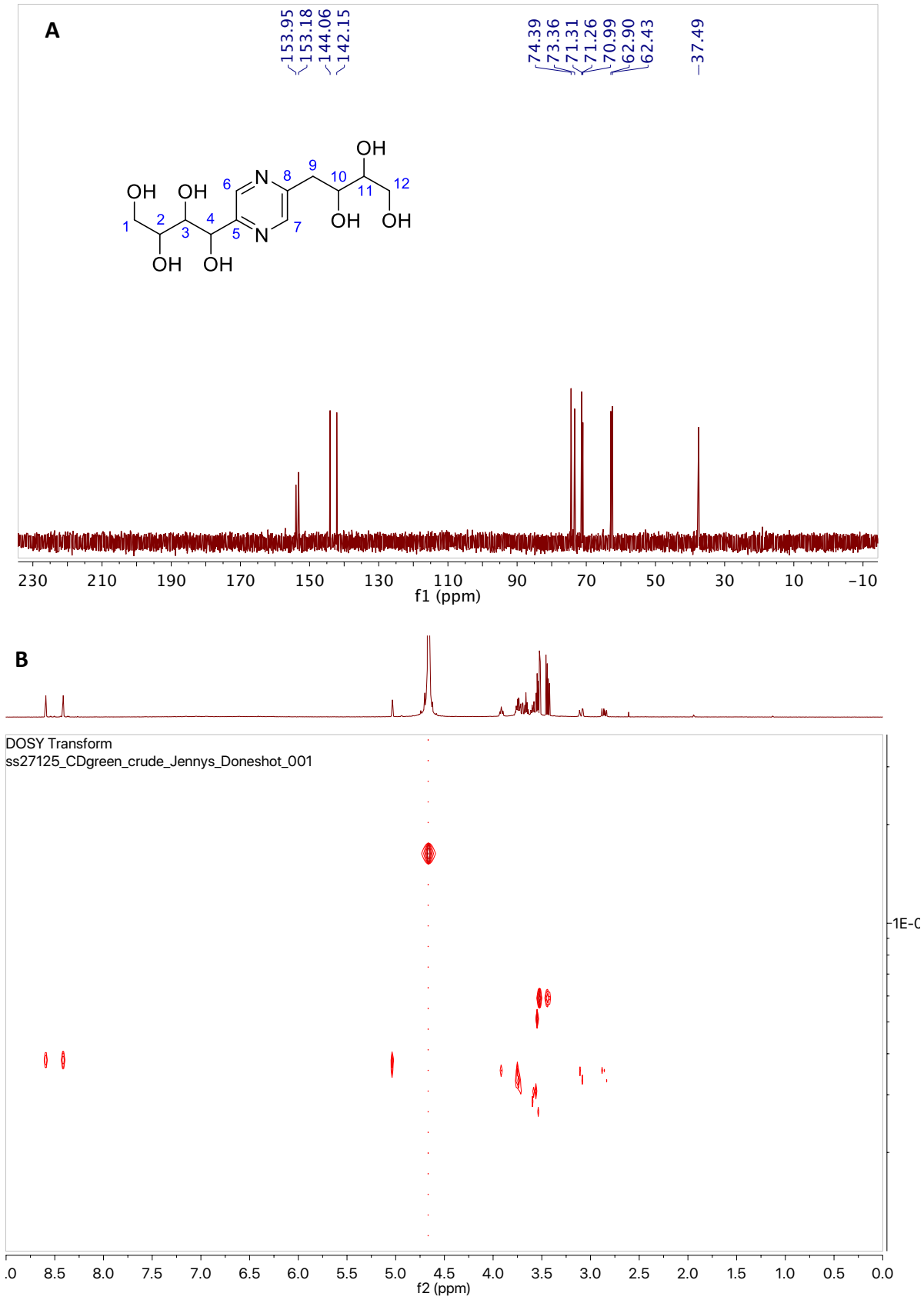

*Figure A.37 A) ^{13}C NMR (126 MHz) of **FCD-3** B) DOSY of **FCD-3.***

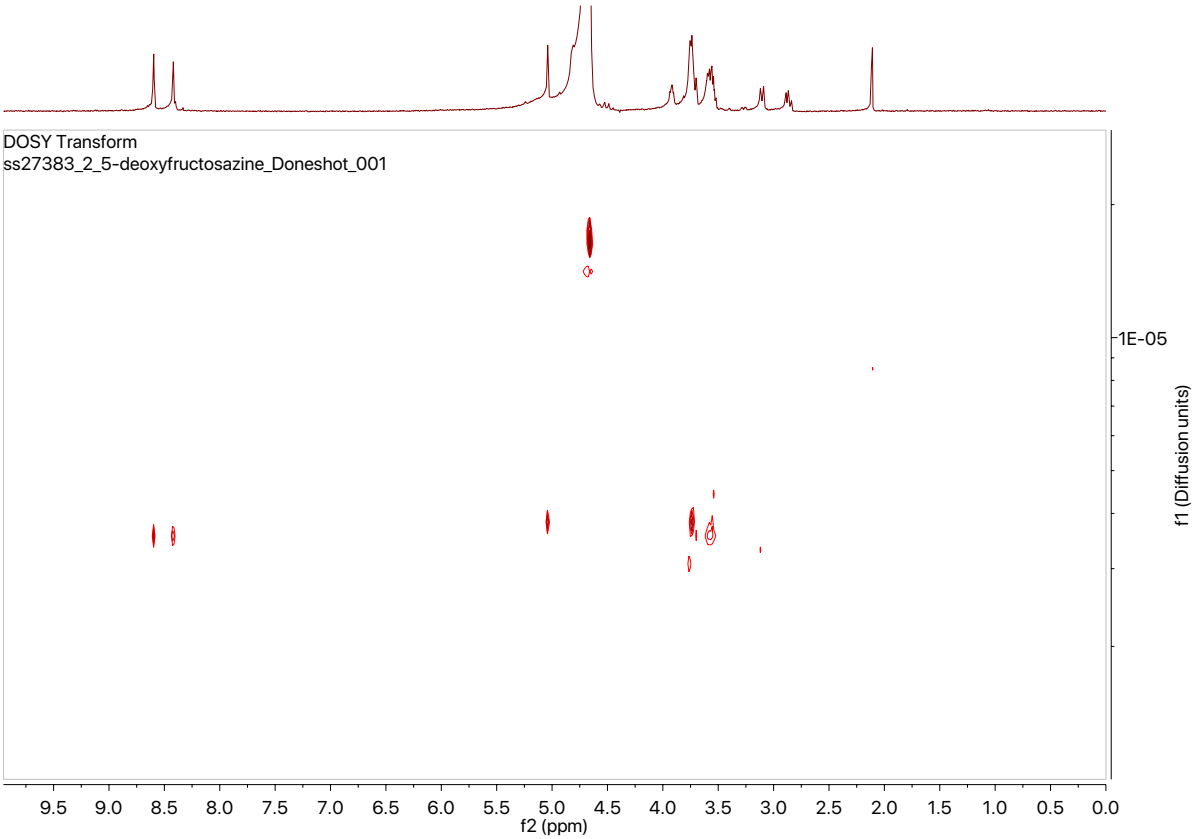

Figure A.38 DOSY of commercial 2,5-deoxyfructosazine

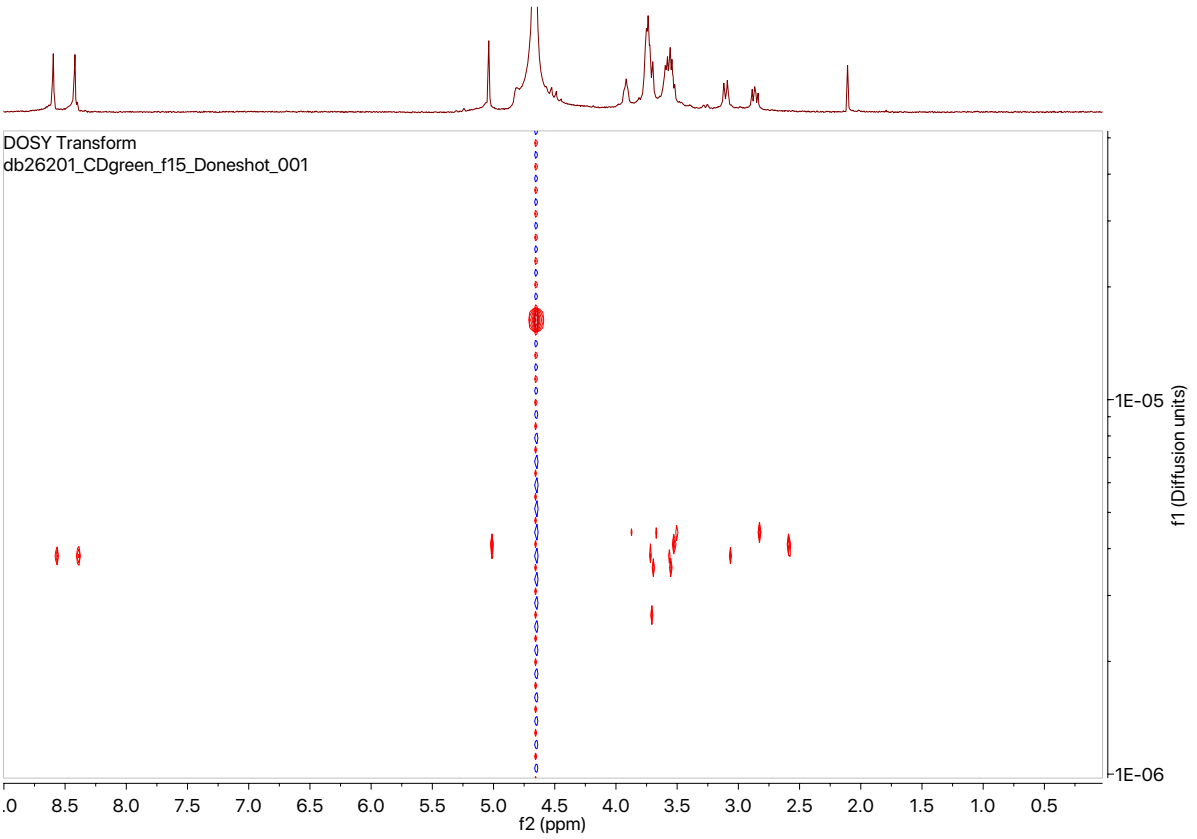

*Supplementary Figure A.39 DOSY of **4**.*

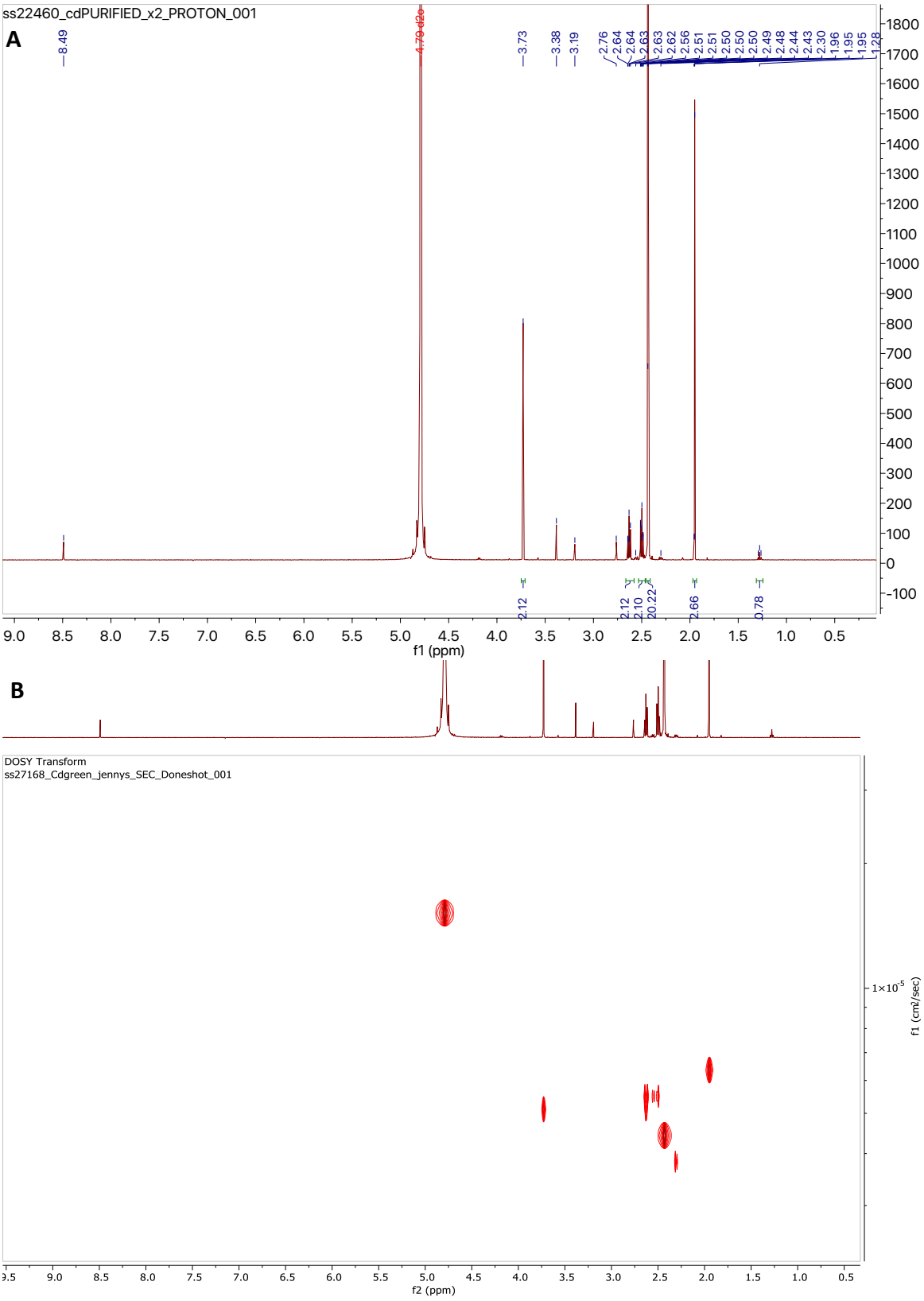

*Supplementary figure A.40 NMR A) ^{1}H NMR (500 MHz) of **FCD-5** B) DOSY of **FCD-5.***

Bibliography

1. Varki, A. *et al. Essentials of Glycobiology*. *Essentials of Glycobiology* (Cold Spring Harbor Laboratory Press, 2009).
2. Hunt, I. Chapter 25: Carbohydrates.
3. LIS, H. & SHARON, N. Protein glycosylation. Structural and functional aspects. *Eur. J. Biochem.* **218**, 1–27 (1993).
4. J., B. The Role of Glycosylation in Receptor Signaling. in *Glycosylation* (InTech, 2012). doi:10.5772/50262
5. Berg, Jeremy M., Tymoczko, John L., Lubert, S. *Biochemistry*. (Freeman, 2012).
6. Reily, C., Stewart, T. J., Renfrow, M. B. & Novak, J. Glycosylation in health and disease. *Nature Reviews Nephrology* **15**, 346–366 (2019).
7. Alberts, Bruce, Johnson, Alexander, Lewis, Julian, Raff, Keith Roberts, Walter, P. *Molecular Biology of the Cell*. (Garland Science, 2014).
8. Hart, G. W. Glycosylation. *Curr. Opin. Cell Biol.* **4**, 1017–1023 (1992).
9. Wassarman, P. *et al.* Structure and function of the mammalian egg zona pellucida. *J. Exp. Zool.* **285**, 251–258 (1999).
10. Utratna, M., Deegan, S. & Joshi, L. Exploitation of Glycobiology in Anti-Adhesion Approaches against Biothreat Agents. *J. Bioterror. Biodef.* **7**, 1–9 (2016).
11. Suzuki, Y. Sialobiology of influenza molecular mechanism of host range variation of influenza viruses. *Biological and Pharmaceutical Bulletin* **28**, 399–408 (2005).
12. 2019 Novel Coronavirus (2019-nCoV) Situation Summary | CDC. Available at: https://www.cdc.gov/coronavirus/2019-nCoV/summary.html#anchor_1580079137454. (Accessed: 18th February 2020)
13. Lundquist, J. J. & Toone, E. J. The Cluster Glycoside Effect. *Chem. Rev.* **102**, 555–578 (2002).
14. and, J. J. L. & Toone*, E. J. The Cluster Glycoside Effect. (2002). doi:10.1021/CR000418F
15. Mori, T., Toyoda, M., Ohtsuka, T. & Okahata, Y. Kinetic analyses for bindings of concanavalin A to dispersed and condensed mannose surfaces on a quartz crystal microbalance. *Anal. Biochem.* **395**, 211–216 (2009).
16. Sauer, M. M. *et al.* Binding of the Bacterial Adhesin FimH to Its Natural, Multivalent High-Mannose Type Glycan Targets. *J. Am. Chem. Soc.* **141**, 936–944 (2019).
17. Betton, G. R. Agglutination reactions of spontaneous canine tumour cells, induced by concanavalin a, demonstrated by an isotopic assay. *Int. J. Cancer* **18**, 687–696 (1976).
18. Cuatrecasas, P. & Tell, G. P. Insulin-like activity of concanavalin A and wheat germ agglutinin--direct interactions with insulin receptors. *Proc. Natl. Acad. Sci. U. S. A.* **70**, 485–489 (1973).
19. Ofek, I., Mirelman, D. & Sharon, N. Adherence of escherichia coli to human mucosal cells mediated by mannose receptors [13]. *Nature* **265**, 623–625 (1977).
20. Naismith, J. H. & Field, R. A. Structural basis of trimannoside recognition by concanavalin A. *J. Biol. Chem.* **271**, 972–6 (1996).
21. Ohyama, Y., Kasai, K., Nomoto, H. & Inoue, Y. Frontal Affinity Chromatography of Ovalbumin Glycoasparagines on a Concanavalin A-Sepharose Column. *J. Biol. Chem.* **260**, 6882–6887 (1985).
22. Concanavalin A from Canavalia ensiformis (Jack bean) Type VI, lyophilized powder | Con A | Sigma-Aldrich. Available at: https://www.sigmaaldrich.com/catalog/product/sigma/l7647?lang=en&region=GB. (Accessed: 26th February 2020)
23. Munoz, E. M., Correa, J., Fernandez-Megia, E. & Riguera, R. Probing the relevance of

lectin clustering for the reliable evaluation of multivalent carbohydrate recognition. *J. Am. Chem. Soc.* **131**, 17765–17767 (2009).
24. Edelman, G. M. & Wang, J. L. *Binding and Functional Properties of Concanavalin A and Its Derivatives III. INTERACTIONS WITH INDOLEACETIC ACID AND OTHER HYDROPHOBIC LIGANDS*. CHEMISTRY Vd* **253**, (1978).
25. Cummings, R. D. & Etzler, M. E. *Antibodies and Lectins in Glycan Analysis*. *Essentials of Glycobiology* (2009).
26. Glycosylation. Available at: https://www.uniprot.org/help/carbohyd. (Accessed: 26th February 2020)
27. Bieberich, E. Synthesis, Processing, and Function of N-glycans in N-glycoproteins. in *Advances in neurobiology* **9**, 47–70 (NIH Public Access, 2014).
28. de Leoz, M. L. A. *et al.* High-Mannose Glycans are Elevated during Breast Cancer Progression. *Mol. Cell. Proteomics* **10**, M110.002717 (2011).
29. Fukuda, M., Hiraoka, N. & Yeh, J. C. C-type lectins and Sialyl Lewis X oligosaccharides: Versatile roles in cell-cell interaction. *Journal of Cell Biology* **147**, 467–470 (1999).
30. Song, E. H. & Pohl, N. L. Carbohydrate arrays: recent developments in fabrication and detection methods with applications. *Current Opinion in Chemical Biology* **13**, 626–632 (2009).
31. Yilmaz, G. *et al.* Glyconanoparticles with controlled morphologies and their interactions with a dendritic cell lectin. *Polym. Chem.* **7**, 6293–6296 (2016).
32. Li, X. & Chen, G. Glycopolymer-based nanoparticles: Synthesis and application. *Polymer Chemistry* **6**, 1417–1430 (2015).
33. Won, S., Richards, S. J., Walker, M. & Gibson, M. I. Externally controllable glycan presentation on nanoparticle surfaces to modulate lectin recognition. *Nanoscale Horizons* **2**, 106–109 (2017).
34. Chan, P.-H. *et al.* Photoluminescent Gold Nanoclusters as Sensing Probes for Uropathogenic Escherichia coli. *PLoS One* **8**, e58064 (2013).
35. Sánchez-Navarro, M., Muñoz, A., Illescas, B. M., Rojo, J. & Martín, N. [60]Fullerene as Multivalent Scaffold: Efficient Molecular Recognition of Globular Glycofullerenes by Concanavalin A. *Chem. - A Eur. J.* **17**, 766–769 (2011).
36. Ramos-Soriano, J. *et al.* Synthesis of Highly Efficient Multivalent Disaccharide/[60]Fullerene Nanoballs for Emergent Viruses. *J. Am. Chem. Soc.* **141**, 15403–15412 (2019).
37. Palankar, R., Medvedev, N., Rong, A. & Delcea, M. Fabrication of Quantum Dot Microarrays Using Electron Beam Lithography for Applications in Analyte Sensing and Cellular Dynamics. *ACS Nano* **7**, 4617–4628 (2013).
38. Smith, A. M. & Nie, S. Chemical analysis and cellular imaging with quantum dots. *Analyst* **129**, 672–677 (2004).
39. Ikeri, H. I., Onyia, A. I. & Vwavware, O. J. The Dependence of Confinement Energy on the Size of Quantum Dots. *Int. J. Sci. Res. Res. Pap. Phys. Appl. Sci.* **7**, 27–30 (2019).
40. Data Tables | Fluorescence Quantum Yield Standards | ISS. Available at: http://www.iss.com/resources/reference/data_tables/FL_QuantumYieldStandards.html. (Accessed: 18th February 2020)
41. Sahoo, S. L., Liu, C. H., Kumari, M., Wu, W. C. & Wang, C. C. Biocompatible quantum dot-antibody conjugate for cell imaging, targeting and fluorometric immunoassay: Crosslinking, characterization and applications. *RSC Adv.* **9**, 32791–32803 (2019).
42. Guo, Y. *et al.* Dissecting Multivalent Lectin–Carbohydrate Recognition Using

Polyvalent Multifunctional Glycan-Quantum Dots. *J. Am. Chem. Soc.* **139**, 11833–11844 (2017).
43. Sun, Y. P. *et al.* Quantum-sized carbon dots for bright and colorful photoluminescence. *J. Am. Chem. Soc.* **128**, 7756–7757 (2006).
44. Benito-Alifonso, D. *et al.* Lactose as a 'trojan horse' for quantum dot cell transport. *Angew. Chemie - Int. Ed.* (2014). doi:10.1002/anie.201307232
45. Sun, Y. P. *et al.* Quantum-sized carbon dots for bright and colorful photoluminescence. *J. Am. Chem. Soc.* **128**, 7756–7757 (2006).
46. Hill, S. A. *et al.* Three-minute synthesis of sp ^{3} nanocrystalline carbon dots as non-toxic fluorescent platforms for intracellular delivery. *Nanoscale* **8**, 18630–18634 (2016).
47. Sk, M. A., Ananthanarayanan, A., Huang, L., Lim, K. H. & Chen, P. Revealing the tunable photoluminescence properties of graphene quantum dots. *J. Mater. Chem. C* **2**, 6954–6960 (2014).
48. Li, H. *et al.* Water-Soluble Fluorescent Carbon Quantum Dots and Photocatalyst Design. *Angew. Chemie Int. Ed.* **49**, 4430–4434 (2010).
49. Ye, R. *et al.* Coal as an abundant source of graphene quantum dots. *Nat. Commun.* **4**, (2013).
50. Peng, J. *et al.* Graphene quantum dots derived from carbon fibers. *Nano Lett.* **12**, 844–849 (2012).
51. Eda, G. *et al.* Blue Photoluminescence from Chemically Derived Graphene Oxide. *Adv. Mater.* **22**, 505–509 (2010).
52. Zhao, Q.-L. *et al.* Facile preparation of low cytotoxicity fluorescent carbon nanocrystals by electrooxidation of graphite. *Chem. Commun.* 5116 (2008). doi:10.1039/b812420e
53. Lu, W. *et al.* Economical, green synthesis of fluorescent carbon nanoparticles and their use as probes for sensitive and selective detection of mercury(II) ions. *Anal. Chem.* **84**, 5351–5357 (2012).
54. Zhou, J., Sheng, Z., Han, H., Zou, M. & Li, C. Facile synthesis of fluorescent carbon dots using watermelon peel as a carbon source. *Mater. Lett.* **66**, 222–224 (2012).
55. Hsu, P. C., Shih, Z. Y., Lee, C. H. & Chang, H. T. Synthesis and analytical applications of photoluminescent carbon nanodots. *Green Chem.* **14**, 917–920 (2012).
56. Zhang, Z., Sun, W. & Wu, P. Highly Photoluminescent Carbon Dots Derived from Egg White: Facile and Green Synthesis, Photoluminescence Properties, and Multiple Applications. *ACS Sustain. Chem. Eng.* **3**, 1412–1418 (2015).
57. Wang, D. *et al.* Fluorescent carbon dots from milk by microwave cooking. *RSC Adv.* **6**, 41516–41521 (2016).
58. Yao, Y. Y. *et al.* Magnetofluorescent Carbon Dots Derived from Crab Shell for Targeted Dual-Modality Bioimaging and Drug Delivery. *ACS Appl. Mater. Interfaces* **9**, 13887–13899 (2017).
59. Essner, J. B., Laber, C. H., Ravula, S., Polo-Parada, L. & Baker, G. A. Pee-dots: biocompatible fluorescent carbon dots derived from the upcycling of urine. *Green Chem.* **18**, 243–250 (2016).
60. Choi, Y., Zheng, X. T. & Tan, Y. N. Bioinspired Carbon Dots (Biodots): Emerging Fluorophores with Tailored Multifunctionalities for Biomedical, Agricultural and Environmental applications. *Mol. Syst. Des. Eng.* (2019). doi:10.1039/c9me00086k
61. Xu, H. V., Zheng, X. T., Zhao, Y. & Tan, Y. N. Uncovering the Design Principle of Amino Acid-Derived Photoluminescent Biodots with Tailor-Made Structure–Properties and Applications for Cellular Bioimaging. *ACS Appl. Mater. Interfaces* **10**, 19881–19888 (2018).

62. Hill, S. & Galan, M. C. Fluorescent carbon dots from mono- and polysaccharides: synthesis, properties and applications. *Beilstein J. Org. Chem.* **13**, 675–693 (2017).
63. Peng, H. & Travas-Sejdic, J. Simple aqueous solution route to luminescent carbogenic dots from carbohydrates. *Chem. Mater.* **21**, 5563–5565 (2009).
64. Klinger, K. M., Liebner, F., Fritz, I., Potthast, A. & Rosenau, T. Formation and Ecotoxicity of *N* -Heterocyclic Compounds on Ammoxidation of Mono- and Polysaccharides. *J. Agric. Food Chem.* **61**, 9004–9014 (2013).
65. Zhu, B. *et al.* Synthesis and evaluation of pyrazine and quinoxaline fluorophores for: In vivo detection of cerebral tau tangles in Alzheimer's models. *Chem. Commun.* **54**, 11558–11561 (2018).
66. Li, Y., Zhong, X., Rider, A. E., Furman, S. A. & Ostrikov, K. Fast, energy-efficient synthesis of luminescent carbon quantum dots. *Green Chem.* **16**, 2566–2570 (2014).
67. Wang, Z., Long, P., Feng, Y., Qin, C. & Feng, W. Surface passivation of carbon dots with ethylene glycol and their high-sensitivity to Fe3+. *RSC Adv.* **7**, 2810–2816 (2017).
68. Mintz, K. J., Zhou, Y. & Leblanc, R. M. Recent development of carbon quantum dots regarding their optical properties, photoluminescence mechanism, and core structure. *Nanoscale* **11**, 4634–4652 (2019).
69. Zhai, X. *et al.* Highly luminescent carbon nanodots by microwave-assisted pyrolysis. *Chem. Commun.* **48**, 7955 (2012).
70. Li, X., Zhang, S., Kulinich, S. A., Liu, Y. & Zeng, H. Engineering surface states of carbon dots to achieve controllable luminescence for solid-luminescent composites and sensitive Be2+ detection. *Sci. Rep.* **4**, (2014).
71. Zhai, X. *et al.* Highly luminescent carbon nanodots by microwave-assisted pyrolysis. *Chem. Commun.* **48**, 7955–7957 (2012).
72. Yang, G. *et al.* Exploring the Emissive States of Heteroatom-Doped Graphene Quantum Dots. (2018). doi:10.1021/acs.jpcc.8b01385
73. Liao, F. *et al.* Preparation of heteroatom doped poly(o-phenylenediamine) fluorescent nanospheres: Tunable fluorescent spectrum and sensing performance. *Synth. Met.* **189**, 126–134 (2014).
74. Yang, J., Chen, W., Liu, X., Zhang, Y. & Bai, Y. Hydrothermal synthesis and photoluminescent mechanistic investigation of highly fluorescent nitrogen doped carbon dots from amino acids. *Mater. Res. Bull.* **89**, 26–32 (2017).
75. Kundu, S. *et al.* Synthesis of N, F and S co-doped graphene quantum dots. *Nanoscale* **7**, 11515–11519 (2015).
76. Yang, W. *et al.* Carbon dots with red-shifted photoluminescence by fluorine doping for optical bio-imaging. *Carbon N. Y.* **128**, 78–85 (2018).
77. Mondal, S. *et al.* Efficient Photosensitizing Capabilities and Ultrafast Carrier Dynamics of Doped Carbon Dots. *J. Am. Chem. Soc.* **141**, 15413–15422 (2019).
78. Wang, T. *et al.* Carbon dots with molecular fluorescence and their application as a "turn-off" fluorescent probe for ferricyanide detection. *Sci. Rep.* **9**, (2019).
79. Krysmann, M. J., Kelarakis, A., Dallas, P. & Giannelis, E. P. Formation mechanism of carbogenic nanoparticles with dual photoluminescence emission. *J. Am. Chem. Soc.* **134**, 747–750 (2012).
80. Song, Y. *et al.* Investigation from chemical structure to photoluminescent mechanism: A type of carbon dots from the pyrolysis of citric acid and an amine. *J. Mater. Chem. C* **3**, 5976–5984 (2015).
81. Zhu, S. *et al.* The crosslink enhanced emission (CEE) in non-conjugated polymer dots: From the photoluminescence mechanism to the cellular uptake mechanism and internalization. *Chem. Commun.* **50**, 13845–13848 (2014).

82. Schneider, J. *et al.* Molecular Fluorescence in Citric Acid-Based Carbon Dots. (2016). doi:10.1021/acs.jpcc.6b12519
83. Hill, S. A. Carbohydrate-based Carbon Dots as Multivalent Glycan Platforms. (2017).
84. Hill, S. A. *et al.* Practical Three-Minute Synthesis of Acid-Coated Fluorescent Carbon Dots with Tuneable Core Structure. *Sci. Rep.* **8**, 12234 (2018).
85. Hill, S. A. *et al.* Three-minute synthesis of sp ^{3} nanocrystalline carbon dots as non-toxic fluorescent platforms for intracellular delivery. *Nanoscale* **8**, 18630–18634 (2016).
86. Likhosherstov, L. M., Novikova, O. S. & Shibaev, V. N. *New Efficient Synthesis of b-Glucosylamines of Mono-and Disaccharides with the Use of Ammonium Carbamate*. *Doklady Akademii Nauk* **383**, (2002).
87. Shangguan, N., Katukojvala, S., Greenberg, R. & Williams, L. J. *The Reaction of Thioacids with Azides: A New Mechanism and New Synthetic Applications*.
88. Avalos, M. *et al.* The structure of glycosyl amides: A combined study by NMR spectroscopy, X-ray crystallography, and computational chemistry. *Tetrahedron* **54**, 615–628 (1998).
89. Boden, S., Wagner, K., Karg, M. & Hartmann, L. Presenting Precision Glycomacromolecules on Gold Nanoparticles for Increased Lectin Binding. *Polymers (Basel).* **9**, 716 (2017).
90. Guo, Y. *et al.* Dissecting Multivalent Lectin−Carbohydrate Recognition Using Polyvalent Multifunctional Glycan-Quantum Dots. doi:10.1021/jacs.7b05104
91. Swift, T. A.. *et al.* Surface functionalisation significantly changes the physical and electronic properties of carbon nano-dots. *Nanoscale* **10**, 13908–13912 (2018).
92. Swift, T. A. Augmenting photosynthesis to enhance crop productivity using carbon dots. 206 (2018).
93. Masuko, T. *et al.* Carbohydrate analysis by a phenol–sulfuric acid method in microplate format. *Anal. Biochem.* **339**, 69–72 (2005).
94. Swift, T. A. *et al.* Surface functionalisation significantly changes the physical and electronic properties of carbon nano-dots. *Nanoscale* **10**, 13908–13912 (2018).
95. Lindner, L. & Klüfers, P. Cobalt(III) Complexes of D -Galactosylamine. *Zeitschrift für Anorg. und Allg. Chemie* **641**, 1869–1873 (2015).
96. Canales, Á. *et al. Lanthanide chelating carbohydrate conjugates are useful tools to characterize carbohydrate conformation in solution and sensitive sensors to detect carbohydrate protein interactions*. *Biochim. Biophys. Acta* **1810**, (2011).
97. Pastuch-Gawołek, G. *et al.* Small molecule glycoconjugates with anticancer activity. *Eur. J. Med. Chem.* **112**, 130–144 (2016).
98. Linek, K., Alföldi, J. & Defaye, J. Structure of glycosylamines and diglycosylamines in the arabinose, mannose, and rhamnose series. *Carbohydr. Res.* **247**, 329–335 (1993).
99. DuBois, M., Gilles, K. A., Hamilton, J. K., Rebers, P. A. & Smith, F. Colorimetric Method for Determination of Sugars and Related Substances. *Anal. Chem.* **28**, 350–356 (1956).
100. Foulger, J. H. *The use of the Molisch (a-napthol) reactions in the study of sugars in biological fluids. Downloaded from*. (2019).
101. *938 Notes improved techniques for analysis of carbohydrates in sediemnts.*
102. Lakowicz, J. R. *Principles of Fluorescence Spectroscopy*. (Springer, 2006).
103. Sekar, R. B. & Periasamy, A. Fluorescence resonance energy transfer (FRET) microscopy imaging of live cell protein localizations. *Journal of Cell Biology* **160**, 629–633 (2003).
104. Stryer, L. Fluorescence Energy Transfer as a Spectroscopic Ruler. *Annu. Rev.*

Biochem. **47**, 819–846 (1978).
105. Clegg, R. M. Fluorescence resonance energy transfer. *Curr. Opin. Biotechnol.* **6**, 103–110 (1995).
106. Berney, C. & Danuser, G. FRET or no FRET: A quantitative comparison. *Biophys. J.* **84**, 3992–4010 (2003).
107. Dos Remedios, C. G. & Moens, P. D. J. Fluorescence resonance energy transfer spectroscopy is a reliable "ruler" for measuring structural changes in proteins. Dispelling the problem of the unknown orientation factor. *J. Struct. Biol.* **115**, 175–185 (1995).
108. Preus, S. & Wilhelmsson, L. M. Advances in Quantitative FRET-Based Methods for Studying Nucleic Acids. *ChemBioChem* **13**, 1990–2001 (2012).
109. Calculate Resonance Energy Transfer (FRET) Efficiencies - The fluorescence laboratory. Available at: http://www.fluortools.com/software/ae/documentation/tools/FRET. (Accessed: 2nd March 2020)
110. Biskup, C. *et al.* Multi-dimensional fluorescence lifetime measurements. in *Multiphoton Microscopy in the Biomedical Sciences VIII* **6860**, 68601I (SPIE, 2008).
111. Chen, H., Puhl, H. L., Koushik, S. V., Vogel, S. S. & Ikeda, S. R. Measurement of FRET Efficiency and Ratio of Donor to Acceptor Concentration in Living Cells. *Biophys. J.* **91**, L39 (2006).
112. Gordon, G. W., Berry, G., Liang, X. H., Levine, B. & Herman, B. Quantitative fluorescence resonance energy transfer measurements using fluorescence microscopy. *Biophys. J.* (1998). doi:10.1016/S0006-3495(98)77976-7
113. Zeug, A., Woehler, A., Neher, E. & Ponimaskin, E. G. Quantitative intensity-based FRET approaches - A comparative snapshot. *Biophysical Journal* (2012). doi:10.1016/j.bpj.2012.09.031
114. Shrestha, D., Jenei, A., Nagy, P., Vereb, G. & Szöllősi, J. Understanding FRET as a research tool for cellular studies. *Int. J. Mol. Sci.* **16**, 6718–56 (2015).
115. How to Measure FRET - Bitesize Bio. Available at: https://bitesizebio.com/23295/how-to-measure-fret/. (Accessed: 3rd March 2020)
116. VAN MUNSTER, E. B., KREMERS, G. J., ADJOBO-HERMANS, M. J. W. & GADELLA, T. W. J. Fluorescence resonance energy transfer (FRET) measurement by gradual acceptor photobleaching. *J. Microsc.* **218**, 253–262 (2005).
117. Hellenkamp, B. *et al.* Precision and accuracy of single-molecule FRET measurements—a multi-laboratory benchmark study. *Nat. Methods* **15**, 669–676 (2018).
118. Boute, N., Jockers, R. & Issad, T. The use of resonance energy transfer in high-throughput screening: BRET versus FRET. *Trends in Pharmacological Sciences* **23**, 351–354 (2002).
119. Fluorescence Polarization (FP)—Note 1.4 | Thermo Fisher Scientific - UK. Available at: https://www.thermofisher.com/uk/en/home/references/molecular-probes-the-handbook/technical-notes-and-product-highlights/fluorescence-polarization-fp.html. (Accessed: 9th March 2020)
120. Heyduk, T. Measuring protein conformational changes by FRET/LRET. *Current Opinion in Biotechnology* **13**, 292–296 (2002).
121. Jiang, L. *et al.* Protein–Protein Affinity Determination by Quantitative FRET Quenching. *Sci. Rep.* **9**, 1–8 (2019).
122. (19) (PDF) Real-time single-molecule studies of the motions of DNA polymerase fingers illuminate DNA synthesis mechanisms. Available at: https://www.researchgate.net/publication/277412701_Real-time_single-

molecule_studies_of_the_motions_of_DNA_polymerase_fingers_illuminate_DNA_synthesis_mechanisms/figures?lo=1. (Accessed: 3rd March 2020)
123. Guo, Y., Bruce Turnbull, W. & Zhou, D. Probing Multivalent Protein–Carbohydrate Interactions by Quantum Dot-Förster Resonance Energy Transfer. in *Methods in Enzymology* **598**, 71–100 (Academic Press Inc., 2018).
124. Guo, Y. *et al.* Compact, Polyvalent Mannose Quantum Dots as Sensitive, Ratiometric FRET Probes for Multivalent Protein-Ligand Interactions. *Angew. Chemie - Int. Ed.* **55**, 4738–4742 (2016).
125. Medintz, I. L. *et al.* Self-assembled nanoscale biosensors based on quantum dot FRET donors. *Nat. Mater.* **2**, 630–638 (2003).
126. Zheng, J., Varnum, M. D. & Zagotta, W. N. Disruption of an intersubunit interaction underlies Ca 2+calmodulin modulation of cyclic nucleotide-gated channels. *J. Neurosci.* **23**, 8167–8175 (2003).
127. Ma, L., Yang, F. & Zheng, J. Application of fluorescence resonance energy transfer in protein studies. *J. Mol. Struct.* **1077**, 87–100 (2014).
128. Zhang, C. Y., Yeh, H. C., Kuroki, M. T. & Wang, T. H. Single-quantum-dot-based DNA nanosensor. *Nat. Mater.* **4**, 826–831 (2005).
129. Liu, H., Liang, G., Abdel-Halim, E. S. & Zhu, J. J. A sensitive and selective quantum dots-based FRET biosensor for the detection of cancer marker type IV collagenase. *Anal. Methods* **3**, 1797–1801 (2011).
130. Boeneman, K. *et al.* Sensing caspase 3 activity with quantum dot-fluorescent protein assemblies. *J. Am. Chem. Soc.* **131**, 3828–3829 (2009).
131. Shi, J. *et al.* A fluorescence resonance energy transfer (FRET) biosensor based on graphene quantum dots (GQDs) and gold nanoparticles (AuNPs) for the detection of mecA gene sequence of Staphylococcus aureus. *Biosens. Bioelectron.* **67**, 595–600 (2015).
132. Balaji, A., Yang, S., Wang, J. & Zhang, J. Graphene oxide-based nanostructured DNA sensor. *Biosensors* **9**, (2019).
133. Liu, L., Zhang, H., Song, D. & Wang, Z. An upconversion nanoparticle-based fluorescence resonance energy transfer system for effectively sensing caspase-3 activity. *Analyst* **143**, 761–767 (2018).
134. Zhou, D. *Quantum dot-nucleic acid/aptamer bioconjugate based fluorimetric biosensors*.
135. Shi, J., Tian, F., Lyu, J. & Yang, M. Nanoparticle based fluorescence resonance energy transfer (FRET) for biosensing applications. *Journal of Materials Chemistry B* **3**, 6989–7005 (2015).
136. Chen, N. T. *et al.* Recent advances in nanoparticle-based förster resonance energy transfer for biosensing, molecular imaging and drug release profiling. *International Journal of Molecular Sciences* **13**, 16598–16623 (2012).
137. Medintz, I. L. *et al.* Designer variable repeat length polypeptides as scaffolds for surface immobilization of quantum dots. *J. Phys. Chem. B* **110**, 10683–10690 (2006).
138. Fan, C., Plaxco, K. W. & Heeger, A. J. Biosensors based on binding-modulated donor-acceptor distances. *Trends in Biotechnology* **23**, 186–192 (2005).
139. Lasala, F., Arce, E., Otero, J. R., Rojo, J. & Delgado, R. Mannosyl Glycodendritic Structure Inhibits DC-SIGN-Mediated Ebola Virus Infection in cis and in trans. *Antimicrob. Agents Chemother.* **47**, 3970–3972 (2003).
140. Rojo, J. & Delgado, R. Glycodendritic structures: promising new antiviral drugs. *J. Antimicrob. Chemother.* **54**, 579–581 (2004).
141. Makky, A., Michel, J. P., Maillard, P. & Rosilio, V. Biomimetic liposomes and planar supported bilayers for the assessment of glycodendrimeric porphyrins interaction with

an immobilized lectin. *Biochim. Biophys. Acta - Biomembr.* **1808**, 656–666 (2011).
142. Robinson, A. *et al.* Probing lectin and sperm with carbohydrate-modified quantum dots. *ChemBioChem* **6**, 1899–1905 (2005).
143. Wang, C., Ehrhardt, C. J. & Yadavalli, V. K. Single cell profiling of surface carbohydrates on Bacillus cereus. *J. R. Soc. Interface* **12**, (2015).
144. Pal, T., Mohiyuddin, S. & Packirisamy, G. Facile and Green Synthesis of Multicolor Fluorescence Carbon Dots from Curcumin: In Vitro and in Vivo Bioimaging and Other Applications. (2018). doi:10.1021/acsomega.7b01323
145. Schlick, K. H. & Cloninger, M. J. Inhibition binding studies of glycodendrimer/lectin interactions using surface plasmon resonance. *Tetrahedron* **66**, 5305–5310 (2010).
146. Shibuya, N. *et al.* The elderberry (Sambucus nigra L.) bark lectin recognizes the Neu5Ac(alpha 2-6)Gal/GalNAc sequence. *J. Biol. Chem.* **262**, 1596–1601 (1987).
147. Goldstein, I., Winter, H. C., R. D. P. Chapter 12 - Plant lectins: tools for the study of complex carbohydrates. in *New Comprehensive Biochemistry* 403–474 (1997).
148. Teoh, S. T., Ogrodzinski, M. P., Ross, C., Hunter, K. W. & Lunt, S. Y. Sialic acid metabolism: A key player in breast cancer metastasis revealed by metabolomics. *Front. Oncol.* **8**, (2018).
149. Vajaria, B. N., Patel, K. R., Begum, R. & Patel, P. S. Sialylation: an Avenue to Target Cancer Cells. *Pathology and Oncology Research* **22**, 443–447 (2016).
150. Thordarson, P. Determining association constants from titration experiments in supramolecular chemistry. *Chem. Soc. Rev.* **40**, 1305–1323 (2011).
151. Cancer. Available at: https://www.who.int/health-topics/cancer#tab=tab_1. (Accessed: 4th February 2020)
152. Plummer, M. *et al.* Global burden of cancers attributable to infections in 2012: a synthetic analysis. *Lancet Glob. Heal.* **4**, e609–e616 (2016).
153. Immunotherapy for Cancer - National Cancer Institute. Available at: https://www.cancer.gov/about-cancer/treatment/types/immunotherapy#how-does-immunotherapy-work-against-cancer. (Accessed: 4th February 2020)
154. Blackadar, C. B. Historical review of the causes of cancer. *World Journal of Clinical Oncology* **7**, 54–86 (2016).
155. Cooper, G. . The Development and Causes of Cancer - The Cell - NCBI Bookshelf. Available at: https://www.ncbi.nlm.nih.gov/books/NBK9963/. (Accessed: 25th February 2020)
156. Cell Division, Cancer | Learn Science at Scitable. Available at: https://www.nature.com/scitable/topicpage/cell-division-and-cancer-14046590/. (Accessed: 25th February 2020)
157. Holsti, L. R. Development of clinical radiotherapy since 1896. *Acta Oncol. (Madr).* **34**, 995–1003 (1995).
158. side effects of radiotherapy - NHS - NHS. Available at: https://www.nhs.uk/conditions/radiotherapy/side-effects/. (Accessed: 4th March 2020)
159. *The Science Behind Radiation Therapy*.
160. Physiology or Medicine 1984 - Press release. Available at: https://www.nobelprize.org/prizes/medicine/1984/press-release/. (Accessed: 4th March 2020)
161. Karlitepe, A., Ozalp, O. & Avci, C. B. New approaches for cancer immunotherapy. *Tumor Biol.* **36**, 4075–4078 (2015).
162. Mohanty, R. *et al.* CAR T cell therapy: A new era for cancer treatment (Review). *Oncology Reports* **42**, 2183–2195 (2019).
163. Kimiz-Gebologlu, I., Gulce-Iz, S. & Biray-Avci, C. Monoclonal antibodies in cancer immunotherapy. *Molecular Biology Reports* **45**, 2935–2940 (2018).

164. The Story of César Milstein and Monoclonal Antibodies: The making of monoclonal antibodies. Available at: https://www.whatisbiotechnology.org/index.php/exhibitions/milstein/monoclonals. (Accessed: 5th February 2020)
165. Xu, J. *et al.* Combination therapy: A feasibility strategy for car-t cell therapy in the treatment of solid tumors (review). *Oncology Letters* **16**, 2063–2070 (2018).
166. Malhotra, V. & Perry, M. C. *Classical Chemotherapy*. *Cancer Biology & Therapy* **2**,
167. The development of tumour-specific assays for cullular response to anthracycline drugs using laser cytometry Louise J Reeve B . Sc . Department of Surgery University of Leicester Clinical Sciences Wing , Glenfield Hospital Submitted for the degree of Ph. (1999).
168. Zhang, Z. *et al.* High drug-loading system of hollow carbon dots-doxorubicin: Preparation,: In vitro release and pH-targeted research. *J. Mater. Chem. B* **7**, 2130–2137 (2019).
169. Alves, A. C. *et al.* Influence of doxorubicin on model cell membrane properties: Insights from in vitro and in silico studies. *Sci. Rep.* **7**, (2017).
170. ZhangS, H., GaoS, Y., van der Marel, G. A., van Boom, J. H. & H-J WangSlI, A. *The Journal of Biological Chemistry Simultaneous Incorporations of Two Anticancer Drugs into DNA the structures of formaldehyde-cross-linked adducts of daunorubicin-d(CG(araC)GCG) and doxorubicin-d(CA(araC)GTG) complexes at high resolution**. **268**, (1993).
171. Kumar, S., Marfatia, R., Tannenbaum, S., Yang, C. & Avelar, E. Doxorubicin-induced cardiomyopathy 17 years after chemotherapy. *Texas Hear. Inst. J.* **39**, 424–427 (2012).
172. Chatterjee, K., Zhang, J., Honbo, N. & Karliner, J. S. Doxorubicin cardiomyopathy. *Cardiology* **115**, 155–62 (2010).
173. Taymaz-Nikerel, H., Karabekmez, M. E., Eraslan, S. & Kırdar, B. Doxorubicin induces an extensive transcriptional and metabolic rewiring in yeast cells. *Sci. Rep.* **8**, (2018).
174. Chatterjee, K., Zhang, J., Honbo, N. & Karliner, J. S. Doxorubicin cardiomyopathy. *Cardiology* **115**, 155–162 (2010).
175. Lovitt, C. J., Shelper, T. B. & Avery, V. M. Doxorubicin resistance in breast cancer cells is mediated by extracellular matrix proteins. *BMC Cancer* **18**, (2018).
176. Han, J. *et al.* Chemoresistance in the Human Triple-Negative Breast Cancer Cell Line MDA-MB-231 Induced by Doxorubicin Gradient Is Associated with Epigenetic Alterations in Histone Deacetylase. *J. Oncol.* **2019**, (2019).
177. Rahman, A. M., Yusuf, S. W. & Ewer, M. S. Anthracycline-induced cardiotoxicity and the cardiac-sparing effect of liposomal formulation. *International Journal of Nanomedicine* **2**, 567–583 (2007).
178. Drug: Doxorubicin - Cancerrxgene - Genomics of Drug Sensitivity in Cancer. Available at: https://www.cancerrxgene.org/compound/Doxorubicin/133/overview/ic50? (Accessed: 8th February 2020)
179. Chang, J. B. *et al.* A novel, rapid method to compare the therapeutic windows of oral anticoagulants using the Hill coefficient. *Sci. Rep.* **6**, (2016).
180. Pardo, J., Peng, Z. & Leblanc, R. M. Cancer targeting and drug delivery using carbon-based quantum dots and nanotubes. *Molecules* (2018). doi:10.3390/molecules23020378
181. Matsumura, Y. & Maeda, H. A New Concept for Macromolecular Therapeutics in Cancer Chemotherapy: Mechanism of Tumoritropic Accumulation of Proteins and the Antitumor Agent Smancs. *Cancer Res.* **46**, 6387–6392 (1986).

182. Nakamura, Y., Mochida, A., Choyke, P. L. & Kobayashi, H. Nanodrug Delivery: Is the Enhanced Permeability and Retention Effect Sufficient for Curing Cancer? *Bioconjugate Chemistry* **27**, 2225–2238 (2016).
183. Golombek, S. K. *et al.* Tumor targeting via EPR: Strategies to enhance patient responses. *Advanced Drug Delivery Reviews* **130**, 17–38 (2018).
184. Kanwal, U. *et al.* Advances in nano-delivery systems for doxorubicin: an updated insight. *J. Drug Target.* **26**, 296–310 (2018).
185. Kong, T., Hao, L., Wei, Y., Cai, X. & Zhu, B. Doxorubicin conjugated carbon dots as a drug delivery system for human breast cancer therapy. *Cell Prolif.* **51**, e12488 (2018).
186. Shen, S., Wu, Y., Liu, Y. & Wu, D. High drug-loading nanomedicines: Progress, current status, and prospects. *International Journal of Nanomedicine* **12**, 4085–4109 (2017).
187. Ulbrich, K. *et al.* Targeted Drug Delivery with Polymers and Magnetic Nanoparticles: Covalent and Noncovalent Approaches, Release Control, and Clinical Studies. *Chemical Reviews* **116**, 5338–5431 (2016).
188. Patra, J. K. *et al.* Nano based drug delivery systems: Recent developments and future prospects 10 Technology 1007 Nanotechnology 03 Chemical Sciences 0306 Physical Chemistry (incl. Structural) 03 Chemical Sciences 0303 Macromolecular and Materials Chemistry 11 Medical and Health Sciences 1115 Pharmacology and Pharmaceutical Sciences 09 Engineering 0903 Biomedical Engineering Prof Ueli Aebi, Prof Peter Gehr. *Journal of Nanobiotechnology* **16**, (2018).
189. Bilalis, P., Tziveleka, L. A., Varlas, S. & Iatrou, H. pH-Sensitive nanogates based on poly(l-histidine) for controlled drug release from mesoporous silica nanoparticles. *Polym. Chem.* **7**, 1475–1485 (2016).
190. Sonaje, K. *et al.* Self-Assembled pH-Sensitive Nanoparticles: A Platform for Oral Delivery of Protein Drugs. *Adv. Funct. Mater.* **20**, 3695–3700 (2010).
191. Chen, W., Meng, F., Cheng, R. & Zhong, Z. pH-Sensitive degradable polymersomes for triggered release of anticancer drugs: A comparative study with micelles. *J. Control. Release* **142**, 40–46 (2010).
192. Karimi, M. *et al.* pH-Sensitive stimulus-responsive nanocarriers for targeted delivery of therapeutic agents. *Wiley Interdisciplinary Reviews: Nanomedicine and Nanobiotechnology* **8**, 696–716 (2016).
193. Ma, G. *et al.* Development of ionic strength/pH/enzyme triple-responsive zwitterionic hydrogel of the mixed L-glutamic acid and L-lysine polypeptide for site-specific drug delivery. *J. Mater. Chem. B* **5**, 935–943 (2017).
194. Mewada, A., Pandey, S., Thakur, M., Jadhav, D. & Sharon, M. Swarming carbon dots for folic acid mediated delivery of doxorubicin and biological imaging. *J. Mater. Chem. B* **2**, 698–705 (2014).
195. Qiu, L., Hong, C.-Y. & Pan, C.-Y. Doxorubicin-loaded aromatic imine-contained amphiphilic branched star polymer micelles: synthesis, self-assembly, and drug delivery. *Int. J. Nanomedicine* **10**, 3623 (2015).
196. Xing, Y., Zhang, J., Chen, F., Liu, J. & Cai, K. Mesoporous polydopamine nanoparticles with co-delivery function for overcoming multidrug resistance via synergistic chemo-photothermal therapy. *Nanoscale* **9**, 8781–8790 (2017).
197. Kim, H., Lee, D., Kim, J., Kim, T. Il & Kim, W. J. Photothermally triggered cytosolic drug delivery via endosome disruption using a functionalized reduced graphene oxide. *ACS Nano* **7**, 6735–6746 (2013).
198. Das, P., Colombo, M. & Prosperi, D. Recent advances in magnetic fluid hyperthermia for cancer therapy. *Colloids and Surfaces B: Biointerfaces* **174**, 42–55 (2019).

199. Dunn, A. E. *et al.* Spatial and temporal control of drug release through pH and alternating magnetic field induced breakage of Schiff base bonds. *Polym. Chem.* **5**, 3311–3315 (2014).
200. Yi, G., Son, J., Yoo, J., Park, C. & Koo, H. Application of click chemistry in nanoparticle modification and its targeted delivery. *Biomaterials Research* **22**, (2018).
201. Kim, E. & Koo, H. Biomedical applications of copper-free click chemistry:: In vitro, in vivo, and ex vivo. *Chem. Sci.* **10**, 7835–7851 (2019).
202. Vanegas, J. P., Scaiano, J. C. & Lanterna, A. E. Thiol-Stabilized Gold Nanoparticles: New Ways To Displace Thiol Layers Using Yttrium or Lanthanide Chlorides. *Langmuir* **33**, 12149–12154 (2017).
203. Baghbani, F., Moztarzadeh, F., Mohandesi, J. A., Yazdian, F. & Mokhtari-Dizaji, M. Novel alginate-stabilized doxorubicin-loaded nanodroplets for ultrasounic theranosis of breast cancer. *Int. J. Biol. Macromol.* **93**, 512–519 (2016).
204. Mathiyazhakan, M., Wiraja, C. & Xu, C. A Concise Review of Gold Nanoparticles-Based Photo-Responsive Liposomes for Controlled Drug Delivery. *Nano-Micro Lett.* **10**, 1–10 (2018).
205. Suk, J. S., Xu, Q., Kim, N., Hanes, J. & Ensign, L. M. PEGylation as a strategy for improving nanoparticle-based drug and gene delivery. *Advanced Drug Delivery Reviews* **99**, 28–51 (2016).
206. van den Hurk, C., Breed, W. & Dercksen, W. Nonpegylated liposomal doxorubicin. *Anticancer. Drugs* **26**, 687 (2015).
207. Rafiyath, S. M. *et al.* Comparison of safety and toxicity of liposomal doxorubicin vs. conventional anthracyclines: a meta-analysis. *Exp. Hematol. Oncol.* **1**, 10 (2012).
208. Lao, J. *et al.* Liposomal Doxorubicin in the Treatment of Breast Cancer Patients: A Review. *J. Drug Deliv.* **2013**, 1–12 (2013).
209. Yuan, Y. *et al.* Doxorubicin-loaded environmentally friendly carbon dots as a novel drug delivery system for nucleus targeted cancer therapy. *Colloids Surfaces B Biointerfaces* **159**, 349–359 (2017).
210. Yang, L. *et al.* Doxorubicin conjugated functionalizable carbon dots for nucleus targeted delivery and enhanced therapeutic efficacy. *Nanoscale* **8**, 6801–6809 (2016).
211. Liang, J. *et al.* Simple and rapid monitoring of doxorubicin using streptavidin-modified microparticle-based time-resolved fluorescence immunoassay. *RSC Adv.* **8**, 15621–15631 (2018).
212. Sun, T., Zheng, M., Xie, Z. & Jing, X. Supramolecular hybrids of carbon dots with doxorubicin: Synthesis, stability and cellular trafficking. *Mater. Chem. Front.* **1**, 354–360 (2017).
213. Yuan, Y. *et al.* Doxorubicin-loaded environmentally friendly carbon dots as a novel drug delivery system for nucleus targeted cancer therapy. *Colloids Surfaces B Biointerfaces* **159**, 349–359 (2017).
214. Kožíšek, J., Breza, M. & Ulický, C. L. *Aromatic Character of Anthraquinone Derivatives*. *Chem. Papers* **47**, (1993).
215. Liu, Z. *et al.* Supramolecular Stacking of Doxorubicin on Carbon Nanotubes for In Vivo Cancer Therapy. *Angew. Chemie Int. Ed.* **48**, 7668–7672 (2009).
216. Strauss, V. *et al.* Carbon Nanodots: Supramolecular Electron Donor-Acceptor Hybrids Featuring Perylenediimides. *Angew. Chemie - Int. Ed.* **54**, 8292–8297 (2015).
217. Li, S. *et al.* Transferrin conjugated nontoxic carbon dots for doxorubicin delivery to target pediatric brain tumor cells. *Nanoscale* **8**, 16662–16669 (2016).
218. Yu, B., Tai, H. C., Xue, W., Lee, L. J. & Lee, R. J. Receptor-targeted nanocarriers for therapeutic delivery to cancer. *Mol. Membr. Biol.* **27**, 286–298 (2010).
219. Neuwelt, E. A. *et al.* Imaging of iron oxide nanoparticles by MR and light microscopy

in patients with malignant brain tumours. *Neuropathol. Appl. Neurobiol.* **30**, 456–471 (2004).
220. Al-Nahain, A. *et al.* Target delivery and cell imaging using hyaluronic acid-functionalized graphene quantum dots. *Mol. Pharm.* **10**, 3736–3744 (2013).
221. Li, J. *et al.* Facile strategy by hyaluronic acid functional carbon dot-doxorubicin nanoparticles for CD44 targeted drug delivery and enhanced breast cancer therapy. *Int. J. Pharm.* **578**, 119122 (2020).
222. Iannazzo, D. *et al.* Graphene quantum dots for cancer targeted drug delivery. *Int. J. Pharm.* **518**, 185–192 (2017).
223. IR Spectrum Table & Chart | Sigma-Aldrich. Available at: https://www.sigmaaldrich.com/technical-documents/articles/biology/ir-spectrum-table.html. (Accessed: 5th March 2020)
224. Fu, C. *et al.* Conjugating an anticancer drug onto thiolated hyaluronic acid by acid liable hydrazone linkage for its gelation and dual stimuli-response release. *Carbohydr. Polym.* **128**, 163–170 (2015).
225. Doughty, A. C. V. *et al.* Nanomaterial applications in photothermal therapy for cancer. *Materials* **12**, (2019).
226. Jaque, D. *et al.* Nanoparticles for photothermal therapies. *Nanoscale* **6**, 9494–9530 (2014).
227. Sun, J. *et al.* Recent progress in metal-based nanoparticles mediated photodynamic therapy. *Molecules* **23**, (2018).
228. Estelrich, J. & Antònia Busquets, M. Iron oxide nanoparticles in photothermal therapy. *Molecules* **23**, (2018).
229. Mohapatra, J. *et al.* Size-dependent magnetic and inductive heating properties of Fe 3 O 4 nanoparticles: Scaling laws across the superparamagnetic size. *Phys. Chem. Chem. Phys.* **20**, 12879–12887 (2018).
230. Langer, J., Novikov, S. M. & Liz-Marzán, L. M. Surface plasmon resonance in gold nanoparticles: a review Related content When plasmonics meets membrane technology A Politano, A Cupolillo, G Di Profio et al.-Sensing using plasmonic nanostructures and nanoparticles. *J. Phys. Condens. Matter Top. Rev.* (2017). doi:10.1088/1361-648X/aa60f3
231. Vines, J. B., Yoon, J. H., Ryu, N. E., Lim, D. J. & Park, H. Gold nanoparticles for photothermal cancer therapy. *Frontiers in Chemistry* **7**, (2019).
232. De Melo-Diogo, D., Lima-Sousa, R., Alves, C. G. & Correia, I. J. Graphene family nanomaterials for application in cancer combination photothermal therapy. *Biomaterials Science* **7**, 3534–3551 (2019).
233. Robinson, J. T. *et al.* High performance in vivo near-IR (>1 μm) imaging and photothermal cancer therapy with carbon nanotubes. *Nano Res.* **3**, 779–793 (2010).
234. Yan, Y. *et al.* Stacking of doxorubicin on folic acid-targeted multiwalled carbon nanotubes for in vivo chemotherapy of tumors. *Drug Deliv.* **25**, 1607–1616 (2018).
235. Sobhani, Z., Behnam, M. A., Emami, F., Dehghanian, A. & Jamhiri, I. Photothermal therapy of melanoma tumor using multiwalled carbon nanotubes. *Int. J. Nanomedicine* **12**, 4509–4517 (2017).
236. Eom, H.-J., Jeong, J.-S. & Choi, J. Effect of aspect ratio on the uptake and toxicity of hydroxylated-multi walled carbon nanotubes in the nematode, *Caenorhabditis elegans*. *Environ. Health Toxicol.* **30**, e2015001 (2015).
237. Qiu, H., Tan, M., Ohulchanskyy, T. Y., Lovell, J. F. & Chen, G. Recent progress in upconversion photodynamic therapy. *Nanomaterials* **8**, (2018).
238. Nadort, A., Zhao, J. & Goldys, E. M. Lanthanide upconversion luminescence at the nanoscale: Fundamentals and optical properties. *Nanoscale* **8**, 13099–13130 (2016).

239. Permatasari, F. A., Fukazawa, H., Ogi, T., Iskandar, F. & Okuyama, K. Design of Pyrrolic-N-Rich Carbon Dots with Absorption in the First Near-Infrared Window for Photothermal Therapy. *ACS Appl. Nano Mater.* **1**, 2368–2375 (2018).
240. Bao, X. *et al.* In vivo theranostics with near-infrared-emitting carbon dots—highly efficient photothermal therapy based on passive targeting after intravenous administration. *Light Sci. Appl.* **7**, (2018).
241. Wu, L. *et al.* Surface passivation of carbon nanoparticles with branched macromolecules influences near infrared bioimaging. *Theranostics* **3**, 677–686 (2013).
242. Kumar, V. B., Kumar, R., Gedanken, A. & Shefi, O. Fluorescent metal-doped carbon dots for neuronal manipulations. *Ultrason. Sonochem.* **52**, 205–213 (2019).
243. Lyu, L. *et al.* Near-infrared light-mediated rare-earth nanocrystals: recent advances in improving photon conversion and alleviating the thermal effect. *NPG Asia Materials* **10**, 685–702 (2018).
244. Ash, C., Dubec, M., Donne, K. & Bashford, T. Effect of wavelength and beam width on penetration in light-tissue interaction using computational methods. *Lasers Med. Sci.* **32**, 1909–1918 (2017).
245. Chen, W. R., Carubelli, R., Liu, H. & Nordquist, R. E. *Laser Immunotherapy for Metastatic Tumors 37 PROTOCOL 37 Laser Immunotherapy A Novel Treatment Modality for Metastatic Tumors*. *Molecular Biotechnology* **25**, (2003).
246. Li, Y. *et al.* Coordination-responsive drug release inside gold nanorod@metal-organic framework core-shell nanostructures for near-infrared-induced synergistic chemo-photothermal therapy. doi:10.1007/s12274-017-1874-y
247. Hu, S. H. *et al.* Photoresponsive protein-graphene-protein hybrid capsules with dual targeted heat-triggered drug delivery approach for enhanced tumor therapy. *Adv. Funct. Mater.* **24**, 4144–4155 (2014).
248. Belkahla, H. *et al.* Carbon dots, a powerful non-toxic support for bioimaging by fluorescence nanoscopy and eradication of bacteria by photothermia. *Nanoscale Adv.* **1**, 2571–2579 (2019).
249. Jiang, K. *et al.* Red, Green, and Blue Luminescence by Carbon Dots: Full-Color Emission Tuning and Multicolor Cellular Imaging. *Angew. Chemie Int. Ed.* **54**, 5360–5363 (2015).
250. Jiang, K. *et al.* Preparation of multicolor photoluminescent carbon dots by tuning surface states. *Nanomaterials* **9**, 1–12 (2019).
251. Song, L., Cui, Y., Zhang, C., Hu, Z. & Liu, X. Microwave-assisted facile synthesis of yellow fluorescent carbon dots from o-phenylenediamine for cell imaging and sensitive detection of Fe^{3+} and H_2O_2. *RSC Adv.* **6**, 17704–17712 (2016).
252. Ding, H., Yu, S.-B., Wei, J.-S. & Xiong, H.-M. *Full-Color Light-Emitting Carbon Dots with a Surface-State-Controlled Luminescence Mechanism*.
253. Hill, S. A. *et al.* Selective photothermal killing of cancer cells using LED-activated nucleus targeting fluorescent carbon dots. *Nanoscale Adv.* **1**, 2840–2846 (2019).
254. Cardoso, D. R., Libardi, S. H. & Skibsted, L. H. Riboflavin as a photosensitizer. Effects on human health and food quality. *Food and Function* **3**, 487–502 (2012).
255. Bhattacherjee, A., Hrynets, Y. & Betti, M. Improved bactericidal capacity of UV-B radiation against E. coli strains by photosensitizing bacteria with fructosazine – An advanced Maillard reaction product. *Food Chem.* **271**, 354–361 (2019).
256. Hill, S. A. *et al.* Selective photothermal killing of cancer cells using LED-activated nucleus targeting fluorescent carbon dots. *Nanoscale Adv.* **1**, (2019).
257. Bhattacherjee, A., Hrynets, Y. & Betti, M. Transport of the Glucosamine-Derived Browning Product Fructosazine (Polyhydroxyalkylpyrazine) Across the Human Intestinal Caco-2 Cell Monolayer: Role of the Hexose Transporters. *J. Agric. Food*

Chem. **65**, 4642–4650 (2017).
258. Veen, R. V. D. A. B. B. R. B. S. H. K. O. Van. (54) BEVERAGES AND FOODSTUFFS RESISTANT TO LIGHT INDUCED FLAVOUR CHANGES, PROCESSES FOR MAKING THE SAME, AND COMPOSITIONS FOR IMPARTING SUCH RESISTANCE. (2011).
259. Bhattacherjee, A., Hrynets, Y. & Betti, M. Fructosazine, a Polyhydroxyalkylpyrazine with Antimicrobial Activity: Mechanism of Inhibition against Extremely Heat Resistant Escherichia coli. (2016). doi:10.1021/acs.jafc.6b03755
260. Miles, B. T. *et al.* Direct Evidence of Lack of Colocalisation of Fluorescently Labelled Gold Labels Used in Correlative Light Electron Microscopy. *Sci. Rep.* (2017). doi:10.1038/srep44666
261. Canzi, G., Mrse, A. A. & Kubiak, C. P. Diffusion-Ordered NMR Spectroscopy as a Reliable Alternative to TEM for Determining the Size of Gold Nanoparticles in Organic Solutions. *J. Phys. Chem. C* **115**, 7972–7978 (2011).
262. Mourdikoudis, S., Pallares, R. M. & Thanh, N. T. K. Characterization techniques for nanoparticles: comparison and complementarity upon studying nanoparticle properties. *Nanoscale* **10**, 12871 (2018).
263. What is Correlative Light and Electron Microscopy? Available at: https://www.delmic.com/correlative-light-electron-microscopy. (Accessed: 26th February 2020)
264. Fokkema, J. *et al.* Fluorescently Labelled Silica Coated Gold Nanoparticles as Fiducial Markers for Correlative Light and Electron Microscopy. *Sci. Rep.* **8**, (2018).
265. Han, S. *et al.* High-Contrast Imaging of Nanodiamonds in Cells by Energy Filtered and Correlative Light-Electron Microscopy: Toward a Quantitative Nanoparticle-Cell Analysis. *Nano Lett.* **19**, 2178–2185 (2019).
266. Rodríguez-Enríquez, S., Marín-Hernández, A., Gallardo-Pérez, J. C. & Moreno-Sánchez, R. Kinetics of transport and phosphorylation of glucose in cancer cells. *J. Cell. Physiol.* **221**, 552–9 (2009).
267. Bhattacherjee, A., Hrynets, Y. & Betti, M. Fructosazine, a Polyhydroxyalkylpyrazine with Antimicrobial Activity: Mechanism of Inhibition against Extremely Heat Resistant Escherichia coli. *J. Agric. Food Chem.* **64**, 8530–8539 (2016).
268. Eaton, D. F. *International union of pure and applied chemistry organic chemistry division commission of photochemistry reference materials for fluorescence measurement*. *Pure & Appl. Chem* **60**, (1988).
269. Lawson-Wood, K., Upstone, S. & Evans, K. *Determination of Relative Fluorescence Quantum Yields using the FL 6500 Fluorescence Spectrometer (014216_01)*.
270. Chen, Y. *et al.* Concentration-induced multi-colored emissions in carbon dots: Origination from triple fluorescent centers. *Nanoscale* **10**, 6734–6743 (2018).
271. Zhu, S. *et al.* Investigating the surface state of graphene quantum dots. *Nanoscale* **7**, 7927–7933 (2015).
272. Zhu, S. *et al.* The photoluminescence mechanism in carbon dots (graphene quantum dots, carbon nanodots, and polymer dots): current state and future perspective. *Nano Res.* **8**, 355–381 (2015).